

ESD-TR-68-23

ESD ACCESSION LIST

ESTI Call No. 62780

Copy No. 1 of 2 cys.

ESD RECORD COPY

RETURN TO
SCIENTIFIC & TECHNICAL INFORMATION DIVISION
(ESTI), BUILDING 1211

A LARGE RADIO-RADAR TELESCOPE

CAMROC DESIGN CONCEPTS

Volume I
of Two Volumes

15 January 1967

The Cambridge Radio Observatory Committee

HARVARD UNIVERSITY
MASSACHUSETTS INSTITUTE OF TECHNOLOGY
MIT LINCOLN LABORATORY
SMITHSONIAN ASTROPHYSICAL OBSERVATORY

ADU 674632

This document has been approved for public release and sale;
its distribution is unlimited.

A LARGE RADIO/RADAR TELESCOPE

CAMROC DESIGN CONCEPTS

15 January 1967

VOLUME I
of Two Volumes

CAMROC studies are supported by the
National Science Foundation (grant GP-5832)
and the participating institutions

THE CAMBRIDGE RADIO OBSERVATORY COMMITTEE

CAMROC Report 1967-1

TABLE OF CONTENTS

VOLUME I

<u>Section</u>	<u>Page</u>
CAMROC PUBLICATIONS.....	v
PREFACE	vii
SUMMARY.....	ix
1 BACKGROUND OF THE CAMROC STUDY	1-1
1.1 Introduction	1-1
1.2 The Choice of a Large Steerable Paraboloid	1-1
1.3 Philosophy Underlying the CAMROC Study Program	1-3
1.4 Performance Criteria	1-4
2 RADOME CHARACTERISTICS.....	2-1
2.1 Introduction and Background	2-1
2.2 Radome Studies	2-5
2.3 Effect of a Radome upon Antenna Economics	2-8
2.4 Effect of a Radome on System Performance	2-9
3 DESIGN REQUIREMENTS FOR EXPOSED AND PROTECTED ANTENNAS	3-1
3.1 General.....	3-1
3.2 Effect of Size	3-1
3.3 Design Considerations	3-2
3.4 Comparison of Wind and Gravity Loads on Antenna Structures	3-3
4 SEARCH FOR A SUITABLE ANTENNA CONFIGURATION	4-1
4.1 Early Configuration Studies	4-1
4.2 Conclusions of Early Configuration Studies	4-2
5 CONCEPTUAL STUDIES FOR STEERABLE PARABOLIC ANTENNAS ..	5-1
5.1 Conclusions of the Conceptual Studies	5-1
5.2 Applicability of Other Studies	5-6
6 COST ESTIMATES FOR ANTENNAS AND RADOMES.....	6-1
7 ELECTROMAGNETIC PROPERTIES OF SPACE-FRAME RADOMES ...	7-1
7.1 The Electromagnetic Properties of Large Radomes (Metal Space Frames)	7-1
7.2 Operational Experience with the Haystack Radome in Astronomical Observations	7-27
8 STRUCTURAL DESIGN FOR LARGE SPACE-FRAME RADOMES	8-1
8.1 Summary	8-1
8.2 Radome Specifications.....	8-1
8.3 Environment	8-2
8.4 Space-Frame Geometry	8-7
8.5 Structural Analysis.....	8-13
8.6 Erection Procedure	8-40
8.7 Radome Cost.....	8-40
8.8 Future Effort	8-44
8.9 References	8-46
9 OBSERVATORY INSTRUMENTATION AND FACILITIES	9-1

VOLUME I

(continued)

APPENDICES

- A Engineering Summary of a Study to Evaluate the Effects of a Radome Environment on the Performance and Cost of a Large-Diameter Radio Telescope
- B Conceptual Studies for a 400-Ft-Diameter CORT Antenna
- C Conceptual Study of a 400-Ft-Diameter Fully Compensated Cassegrain Antenna
- D CAMROC Hammerhead Antenna Concept
- E Report on a Conceptual Study of a Large Cassegrain Antenna
- F Parametric Study of a 400-Ft-Diameter Antenna Based on CSIRO Parkes Configuration
- G Engineering Summary of a Study for a 400-Ft-Diameter Radome-Housed Radio Telescope
- H Scientific Program for a Large, Steerable Paraboloid

VOLUME II

ANNEXES

RADOME (Electromagnetic)

- 1. Loss Calculation on Metal Space-Frame Radomes
- 2. Effect of Rain on Radome Performance

ENVIRONMENTAL CONSIDERATIONS

- 3. Climatic Extremes for a Large Radome Within 2 Hours of Boston, Massachusetts
- 4. Surface Wind-Speed Extremes in the United States

RADOME (Structural)

- 5. Geometric and Structural Considerations for Large Radomes
- 6. Estimate of Optimum Beam Dimensions for CAMROC 550-Ft-Diameter Space Frame When Exposed to 130-mph Wind
- 7. CAMROC Model Program
- 8. Theoretical Investigation on Buckling of Reticulated Radomes
- 9. Estimate of Critical Pressures for Model Buckling Tests
- 10. Experimental Study of Instability in Elements of Shallow Space Frames
- 11. Formulation of the Governing Equations for the Buckling of a Planar Frame

ANTENNA (Surface Considerations)

- 12. Surface Panel Geometry for Hammerhead Antenna Concept
- 13. Report to the Cambridge Radio Observatory Committee

SUPPLEMENT

Large-Diameter Rigid Radomes

CAMROC PUBLICATIONS

Engineering Design Objectives for a Large Radio Telescope, October 1965, reissued January 1966 (Two Volumes).

Objectives and Study Programs for a Regional Radio and Radar Astronomy Research Facility, February 1966.

Radomes and Large Steerable Antennas: Conference Proceedings, June 17-18, 1966.

Large Antenna Configurations, compiled by MIT Lincoln Laboratory for CAMROC Conference, June 17-18, 1966.

An Interim Report on Feasibility and Cost Studies of Radome-Enclosed Large Radio-Radar Telescopes, Prepared at the Request of the National Science Foundation, September 1966.

CAMROC Technical Memoranda No.

- 1 Performance Requirements for Study of Large Diameter Radio Telescope, prepared by MIT Lincoln Laboratory, November 29, 1965, revised March 14, 1966.
- 2 Preliminary Conceptual Studies for Large, Precision Cassegrain and CORT Antenna Configurations, prepared by MIT Lincoln Laboratory, March 8, 1966.
- 3 Space Frame Radome Geometries for Test Models, prepared by R. A. Muldoon, April 26, 1966.
- 4 General Instability Calculations on Proposed Ammann & Whitney 550-Ft-Diameter Space Frame Radome, prepared by R. A. Muldoon, April 28, 1966.
- 5 Forward Scattered Energy of Metal Space Frame, prepared by John Ruze, May 5, 1966.
- 6 Recommended Space Frame Radome Geometry and Estimate of Critical Pressures for Model Buckling Tests, prepared by R. A. Muldoon, May 10, 1966.
- 7 General Information on Existing or Proposed Antenna Systems, prepared by F. G. DeSantis, May 16, 1966.
- 8 Frame Geometry for Radome Buckling Model, prepared by R. A. Muldoon and J. F. Orabona, May 18, 1966.
- 9 Antenna Cost, Efficiency, and System Noise, prepared by John Ruze, May 23, 1966.
- 10 Loss Calculation on Metal Space Frame Radomes, prepared by John Ruze, May 24, 1966.
- 11 Dielectric Materials for use in Radome Panels, prepared by Edward B. Murphy, June 16, 1966.
- 12 Description of Large Radomes now in Use, prepared by J. F. Orabona, June 16, 1966.

CAMROC Technical
Memoranda No.

- 13 Membrane Study Requirements, prepared by Edward B. Murphy,
 June 28, 1966.
- 14 The Radome Study, prepared by John Ruze, September 1, 1966.
- 15 Estimate of Optimum Beam Dimensions for CAMROC 550-Foot
 Diameter Space Frame when Exposed to 130 mph Wind, prepared
 by R. A. Muldoon, September 20, 1966.
- 16 Antenna Cost and Surface Tolerance, prepared by John Ruze,
 October 14, 1966.
- 17 Effect of Rain on Radome Performance, prepared by John Ruze,
 November 16, 1966.
- 18 Surface Panel Geometry for Hammerhead Antenna Concept,
 prepared by John F. Hutzenlaub, January 5, 1967.
- 19 Antenna Gain Loss Due to Feed Support Blockage, prepared by
 John Ruze, February 10, 1967.

PREFACE

The Cambridge Radio Observatory Committee (CAMROC) was established in September 1965 to undertake planning studies for an advanced radio and radar astronomy research facility. The institutions and individuals responsible for the planning and conduct of CAMROC studies are listed below.

INSTITUTIONS

HARVARD UNIVERSITY
MASSACHUSETTS INSTITUTE OF TECHNOLOGY
MIT LINCOLN LABORATORY
SMITHSONIAN ASTROPHYSICAL OBSERVATORY

CAMROC

Members

Edward M. Purcell, Harvard University	}	Cochairmen
Jerome B. Wiesner, MIT		
Alan H. Barrett, MIT		
Bernard F. Burke, MIT		
John V. Harrington, MIT		
Edward Lilley, Harvard University		
Charles A. Lundquist, Smithsonian Astrophysical Observatory		
Gordon H. Pettengill, Lincoln Laboratory		
Jack P. Ruina, MIT		
Herbert G. Weiss, Lincoln Laboratory		
F. Karl Willenbrock, Harvard University		
Fred L. Whipple, Smithsonian Astrophysical Observatory		

Associates

John V. Evans, Lincoln Laboratory
Mario Grossi, Smithsonian Astrophysical Observatory
Thomas E. Hoffman, Smithsonian Astrophysical Observatory
Myle J. Holley, Jr., MIT
G. Richard Huguenin, Harvard College Observatory
Marion L. Meeks, Lincoln Laboratory
Philip Morrison, MIT
Joel Orlen, MIT
Hays Penfield, Harvard College Observatory
John Ruze, Lincoln Laboratory
Irwin I. Shapiro, Lincoln Laboratory
Carlton W. Tillinghast, Smithsonian Astrophysical Observatory

Technical-Support Groups and Individuals

Ammann & Whitney, New York, New York (antenna; radome)
Prof. J. Connor, P. H. Griggs, Department of Civil Engineering,
MIT, Cambridge, Massachusetts (radome buckling)
Electronic Space Structures Corporation, West Concord, Massachusetts
(radome electromagnetic model tests)

Technical-Support Groups and Individuals (Cont.)

Prof. D. D. Fuller, Mechanical Engineering Department, Columbia University, New York, New York (bearing-design studies)

S. D. Lewis, Prof. E. A. Witmer, Department of Aeronautics and Astronautics, MIT, Cambridge, Massachusetts (radome model test program)

Metcalf & Eddy, Boston, Massachusetts (siting)

North American Aviation, Columbus, Ohio (radome dielectric materials)

Rohr Corporation, Chula Vista, California (antenna)

Simpson Gumpertz & Heger, Inc., Cambridge, Massachusetts (antenna; radome buckling)

N. Sissenwine, I. Gringorten, Air Force Cambridge Research Laboratory (Climatology Branch), Bedford, Massachusetts (environmental studies)

Smithsonian Astrophysical Observatory, Cambridge, Massachusetts (reflector measurement studies)

Paul Weidlinger, New York, New York (antenna)

This report represents the work of many people and, whenever possible, the responsible individuals or organizations have been identified. The various technical-support groups have not reviewed this report in an integrated form, and consequently, the conclusions drawn from the study reports should be considered the views of CAMROC.

SUMMARY

The Cambridge Radio Observatory Committee has conducted technical studies for a radome-enclosed large antenna for research in radio and radar astronomy. Results of these studies show that a 400-ft fully steerable radio telescope can be conservatively designed and constructed at a reasonable cost. This report presents the results of these studies undertaken during the period from September 1965 to January 1967.

In observational radio-astronomical research, scientific progress is governed by the basic capabilities of the antenna system: spectral analysis, sensitivity (signal-to-noise ratio), polarization, and resolution. A large fully steerable precision paraboloid has unique scientific versatility because of its intrinsic broad-band spectral capability, its large aperture, and its polarization flexibility. A small auxiliary antenna and the technique of lunar occultation enable the large steerable antenna to study discrete radio sources with high resolution.

The overriding scientific versatility, the simplicity of operation, and the economical use of radiometric and radar systems led CAMROC directly to the choice of the large precision paraboloid for the diverse interests of user scientists. The areas of science open to investigation with such an instrument range from planetary studies of surface and atmospheres employing radar mapping and microwave spectroscopy, to interstellar media and gaseous nebula physics encompassing both continuum and spectral-line studies, to studies of discrete sources and the mechanisms responsible for prodigious energy generation and the basic cosmological questions. For many of the critical measurements necessary to understand the physical processes operative in the universe, construction of the CAMROC instrument would create a telescope of unprecedented versatility and power. Although a large fully steerable precision paraboloid would provide a capability of major importance, experience and engineering studies indicate that the cost would be prohibitive if the instrument must survive and operate in an exposed environment. CAMROC has completed a series of studies to investigate the technical, engineering, and economical comparisons of large telescopes with and without radome protection.

The initial phases of the CAMROC study program have concentrated on the evaluation of various antenna configurations and on the electromagnetic properties of radomes to establish both performance requirements and conceptual designs. After investigating various possibilities, CAMROC concluded that its requirement for a versatile antenna for use throughout the 300- to 6000-Mc/sec region of the spectrum can be met optimally by a large fully steerable antenna operating in conjunction with a much smaller movable parabolic reflector.

Studies of several classes of steerable reflectors showed that a conventional movable paraboloid will be less costly than movable folded-horn antennas, hybrid systems employing tilting plates and fixed paraboloids, and other configurations that could fulfill the CAMROC requirements.

The engineering and cost studies were oriented toward evaluating the feasibility and cost of fully steerable reflector-type antennas, 300 to 500 ft in diameter, that could maintain a 0.1-inch RMS surface tolerance. Subsequently, CAMROC radio and radar astronomers, when evaluating scientific programs, selected a size of 400 ft for their system-performance calculations. It is important to note that the engineering studies indicate that the design concepts that have been developed are applicable for antennas much larger than 400 ft.

Other studies disclosed that it would be extremely difficult and expensive to build an exposed 400-ft antenna that would maintain the required pointing precision of 15 arcsec and surface tolerance of 0.1 inch under even moderate winds and solar heating. Economic and engineering considerations dictated that the CAMROC antenna must use a protective radome.

As the studies progressed, it became increasingly evident that the combined cost of a 400-ft-diameter precision antenna and its radome would be dramatically lower than the cost of an equivalent antenna designed for exposed operations.

Within the protective radome environment, several attractive designs for large precision antennas have been evaluated. Independent design studies have suggested that radome-enclosed configurations should have certain common characteristics that permit large savings in cost; namely, very lightweight reflector panels can be utilized, compensation for the effects of gravity can be achieved with little complexity, the structural resonant frequency of the antenna may be comparatively low, and low-power drive and control systems may be utilized. The low weight of the reflector and the absence of overturning moments allow the bearing and support system to be small. There is a high degree of confidence in these conclusions, since they are based upon the studies of five independent designs.

The increased precision and reduced system cost that result from use of a radome completely outweigh the small increase in aperture blockage and system temperature. It is feasible to build very large space-frame radomes with completely acceptable electromagnetic properties. Experimental measurements, reinforcing theoretical studies, show that an increase in antenna diameter of about 10% will compensate for the electromagnetic effects introduced by such a radome. This modest increase in size is technically justified because it can be achieved economically.

Volume I of this progress report describes the background of the CAMROC study, the organization of the technical tasks, and the findings, to date, on antenna and radome design considerations. The first appendix is a report of an evaluation of the effects of a radome environment on the performance and cost of a large-diameter radio telescope. Six other appendices are reports on antenna-design concepts. The last appendix discusses the scientific programs made possible by the facility envisaged by CAMROC.

Volume II comprises 13 annexes, grouped broadly into categories of Environment, Radome, and Antenna, and a supplement. These are essentially "working papers" from which were derived certain findings of the CAMROC study, or which delineate in greater detail the material contained in Volume I.

**Accepted for the Air Force
Franklin C. Hudson
Chief, Lincoln Laboratory Office**

A LARGE RADIO-RADAR TELESCOPE

1. BACKGROUND OF THE CAMROC STUDY

1.1 Introduction

During the past decade, the need for radio-radar telescopes with higher sensitivity, increased resolution, and wider spectrum coverage has become increasingly evident; but progress in meeting this need has been slow, owing to the rapid escalation in cost as antennas become larger and more precise. Although specialized devices have been developed to fulfill some research requirements, it is evident that future scientific progress will be paced by innovations in instrumentation.

For many years, it has been apparent that Harvard, MIT, and the other universities in the Northeast lacked appropriate experimental facilities for radio and radar astronomy, and in the summer of 1965, joint planning studies for facilities that would satisfy this need were undertaken. The MIT Lincoln Laboratory and the Smithsonian Astrophysical Observatory have joined in these planning studies. The studies themselves have concentrated on a large (nominally 400-ft-diameter) steerable radio/radar telescope operable down to 5-cm wavelength.

1.2 The Choice of a Large Steerable Paraboloid

The next generation of instruments for radio and radar astronomy must be determined by the multiple requirements of higher resolving power, greater collecting area, and multiple-frequency coverage. These cannot be fully met by any single instrument. The choice between a single large paraboloid and an array of small paraboloids, for example, has no unique solution, as the Whitford Committee recognized in recommending that both types of instruments be built. A strong case can be made for either system, depending upon the scientific problems to be attacked; and performance criteria can be easily constructed to favor either type of instrument. The two systems are complementary. The CAMROC choice of a large paraboloid was determined by its versatility as an instrument to serve a wide variety of scientific research interests, particularly since large arrays are now being planned by other institutions.

The outstanding example of a large paraboloid in use today is the 210-ft Parkes telescope of CSIRO. Since its completion, a steady stream of important scientific results has issued from this instrument, which promises to have a long and useful scientific life. The Parkes facility exemplifies the utility of paraboloids, largely because of the great variety of measurements that can be made in a short time for only small added expenditures of capital and time. With a large properly designed paraboloid, simultaneous measurements at a number of different frequencies can be arranged without difficulty, and changes to new frequency combinations can be effected in less than an hour. In spectroscopy, in particular, large paraboloids display special effectiveness, and the recent proliferation of spectral lines available to radio astronomy lends special emphasis to the use of large paraboloids now. New lines will undoubtedly be discovered, and the capacity to change center frequency quickly and cheaply will be of great importance.

The versatility of a large paraboloid is important for the exploitation of new technical developments, the checking of new theories, and the pursuit of new discoveries; and flexibility is mandatory. The ability to undertake new measurements with a minimum of delay is a characteristic virtue of large paraboloids, and one that is not likely to wane with time. Radio astronomy is still largely a pioneering science, and new discoveries will be made that cannot be foreseen.

The versatility feature of a large paraboloid has exceptional importance to a university community, since it is easily convertible to the needs of individual scientists with different and specialized interests. The strength of the university community has traditionally been linked to this diversity.

The complementary aspects of arrays and single paraboloids are scientifically fruitful. Arrays provide highest angular resolution. However, a careful examination of the radiation patterns of arrays reveals, in all cases so far, that there is an awkward range of components in the Fourier transform that are not measured. Characteristically, these missing components correspond to the close antenna spacings and are missing for the simple reason that the elements of an array are usually spread out as far as possible to achieve maximum resolving power. The missing components can be filled in, to some extent, by taking measurements at close spacings, but only at the cost of lost observing time. When the antennas are close together, the high-resolution studies, which serve as the prime motivation for the array, cannot be made. The most economical way of obtaining the close-in Fourier components is by measuring with a single large paraboloid, which gives them directly. Therefore, the effectiveness of an array is greatly enhanced if these measurements can be made on a separate instrument. There is a further area of complementarity, for the synthesis array requires an extended period in which to complete the observation of one primary resolution area, and a "quick look" is not feasible. With a large paraboloid, reconnaissance is easy, and on-going programs are not jeopardized if interruptions occur for special purposes. Thus, the directions of research with a large array can be enhanced by a sufficiently large companion paraboloid. The CAMROC instrument can serve this need.

The use of a large paraboloid for radar astronomy has a somewhat different significance. Radio and radar astronomers have usually not shared instruments. When the largest instruments are contemplated, however, maximum usefulness dictates that all scientifically valid experiments be considered. Large paraboloids are equally useful to radar and radio astronomers and can easily be designed to be employed jointly, making possible entirely new classes of planetary observations that cannot be performed with existing instruments.

1.3 Philosophy Underlying the CAMROC Study Program

Many faculty and staff of the four CAMROC institutions have participated in the study. However, to ensure that the early conceptual studies would be as broadly based as possible and to obtain the widest variety of ideas and experience, CAMROC sponsored selected studies at industrial organizations with competence in the design of advanced structures. This enabled CAMROC to explore concurrently several different design concepts and to obtain engineering information for comparative analysis.

CAMROC's objective is the study of basic considerations that influence the design of large steerable antennas, and therefore technical justification for each fundamental design decision is required.

Although CAMROC provided limiting guide lines, the fewest possible constraints were imposed on each of the study teams. As the work progressed, the results of each study program were made available to all the other study participants. Studies were done by three broadly based structural-design organizations that do not manufacture antennas and one major antenna design and manufacturing organization. Three other industrial antenna-design and fabrication companies have participated in appropriate CAMROC technical meetings. National Radio Astronomy Observatory (NRAO) and other groups who are currently studying antenna problems joined our discussions. MIT Lincoln Laboratory structural-design engineers helped to plan and monitor about 15 CAMROC-sponsored studies; this group also undertook an independent study of one possible antenna configuration.

Wide exposure has been given to the work program as it evolved. Several progress review meetings have been held with significant participation from organizations outside CAMROC, and printed reports have had wide distribution. Useful new ideas and criticisms contributed by individuals and organizations that are not formally part of CAMROC have been welcomed. As a result of these open discussions, an important segment of the nation's radio-telescope designers and radio astronomers has become familiar with the CAMROC studies of antenna and radome performance and cost considerations.

CAMROC's engineering effort has concentrated on the antenna and radome, since these are the most costly elements in the design of a complete observatory and will require the longest development time. No constraints were placed upon the actual antenna configurations to be evaluated, provided, of course, the performance requirements could be met. Answers were sought to such questions as the type of structural configurations, the desirability of a radome, the type of control system, bearing, and data take-off equipment, etc., as influenced primarily by engineering feasibility and cost considerations.

Cost considerations occupy a position of paramount importance in the CAMROC study programs. While it has proved difficult to obtain meaningful comparative cost information on existing antennas (since they seldom are designed to the same performance and environmental specifications), previous studies have reported that the cost of exposed antennas in the 85- to 210-ft class will vary as $D^{2.3}$ to $D^{2.7}$, where D is the diameter. The proper coefficient will depend on the design constraints and environmental conditions. For antennas larger than a few hundred feet, which must function at 5-cm wavelengths, it is apparent that the cost could rise even faster than $D^{2.7}$, because: 1) the antenna beam is narrower and the pointing requirement becomes extremely stringent, 2) the reflector surface must be essentially solid, which aggravates the wind problem, and 3) the measurement, manufacturing, and thermal errors will use a larger share of the overall permissible tolerance, thereby placing more stringent limits on the structural deflection.

It is not generally recognized how severe the pointing precision requirements will be for a 400-ft microwave radio telescope. At a 5-cm wavelength, the beam is only 90-sec wide (3-db response points), and it becomes difficult to meet the pointing requirement of 1/10 beamwidth. Considering the effects of wind, approximately 10^5 ft^2 of reflector surface at microwave frequencies will be essentially solid, and the task of steering it with the required precision is indeed formidable. Within a radome, however, many design constraints are greatly relaxed, and one of the tasks of the engineering study program was to ascertain whether practical and economic antenna designs could now be achieved at an acceptable cost.

1.4 Performance Criteria

The performance criteria that have been used for studies of the proposed CAMROC 400-ft fully steerable radio telescope are outlined below. They have been modified several times during the course of the study to comply more nearly with the evolving requirements and to permit economies where relaxation did not compromise performance.

1.4.1 Antenna system requirements

	<u>Revised</u>		<u>Initial</u>	
<u>Sky Coverage</u>				
Elevation	+5° to +90°		+15° to +90°	
Azimuth	±300°		±300°	
<u>Angular Velocity</u>				
	<u>Track</u>	<u>Slew</u>	<u>Track</u>	<u>Slew</u>
Azimuth	0.2°/sec	0.6°/sec	0.25°/sec	1.00°/sec
Elevation	0.1°/sec	0.3°/sec	0.25°/sec	1.00°/sec
<u>Angular Acceleration</u>				
	<u>Track</u>	<u>Slew</u>	<u>Track</u>	<u>Slew</u>
Azimuth	0.02°/sec ²	0.05°/sec ²	0.2°/sec ²	0.2°/sec ²
Elevation	0.02°/sec ²	0.025°/sec ²	0.2°/sec ²	0.2°/sec ²

Pointing Accuracy

Absolute peak pointing accuracy shall be 15 arcsec and shall include the effects of gravity, servo tracking errors, axis gearing, alignments, readout tolerances, and temperature.

Tracking Error

The antenna shall be capable of tracking smoothly with a 3σ error not exceeding 10 arcsec (0°003).

Operational Surface Accuracy

The loss in antenna gain as a function of frequency for surface tolerances of 0.10-inch and 0.15-inch RMS is shown in Figure 1.1. When the CAMROC design criteria were initially established, the design goal was set as 0.15 inch, since it was believed that it would be very difficult and expensive to exceed this tolerance in a large antenna. With a tolerance of 0.15-inch RMS, the CAMROC reflector would still be operable at 6 Gc/sec, and, although the angular resolution would not be changed, the efficiency would be reduced to only 40% of its effective area. The specifications were revised as the engineering studies progressed and as it became evident that it would not be difficult to achieve a surface tolerance of about 0.10 inch in a radome-enclosed antenna.

The surface accuracy of the primary and secondary reflectors shall be budgeted for an RMS of the overall system as follows:

$$0.100 \text{ inch} = \sqrt{(\text{RMS}_P)^2 + (\text{RMS}_S)^2},$$

where

RMS_P = RMS of primary reflector,

RMS_S = RMS of secondary reflector.

Structural Dynamics

The lowest natural frequency of the antenna system shall be 0.2 cps (revised from 0.05 cps).

Electronic Equipment Enclosure

Provisions for 25,000 lbs of electronic gear located behind the primary reflector plus access facility to the enclosure shall be provided.

1.4.2 Environmental specifications

Ambient Temperatures

Survival -40° F to +140° F

Operational +45° F to +85° F

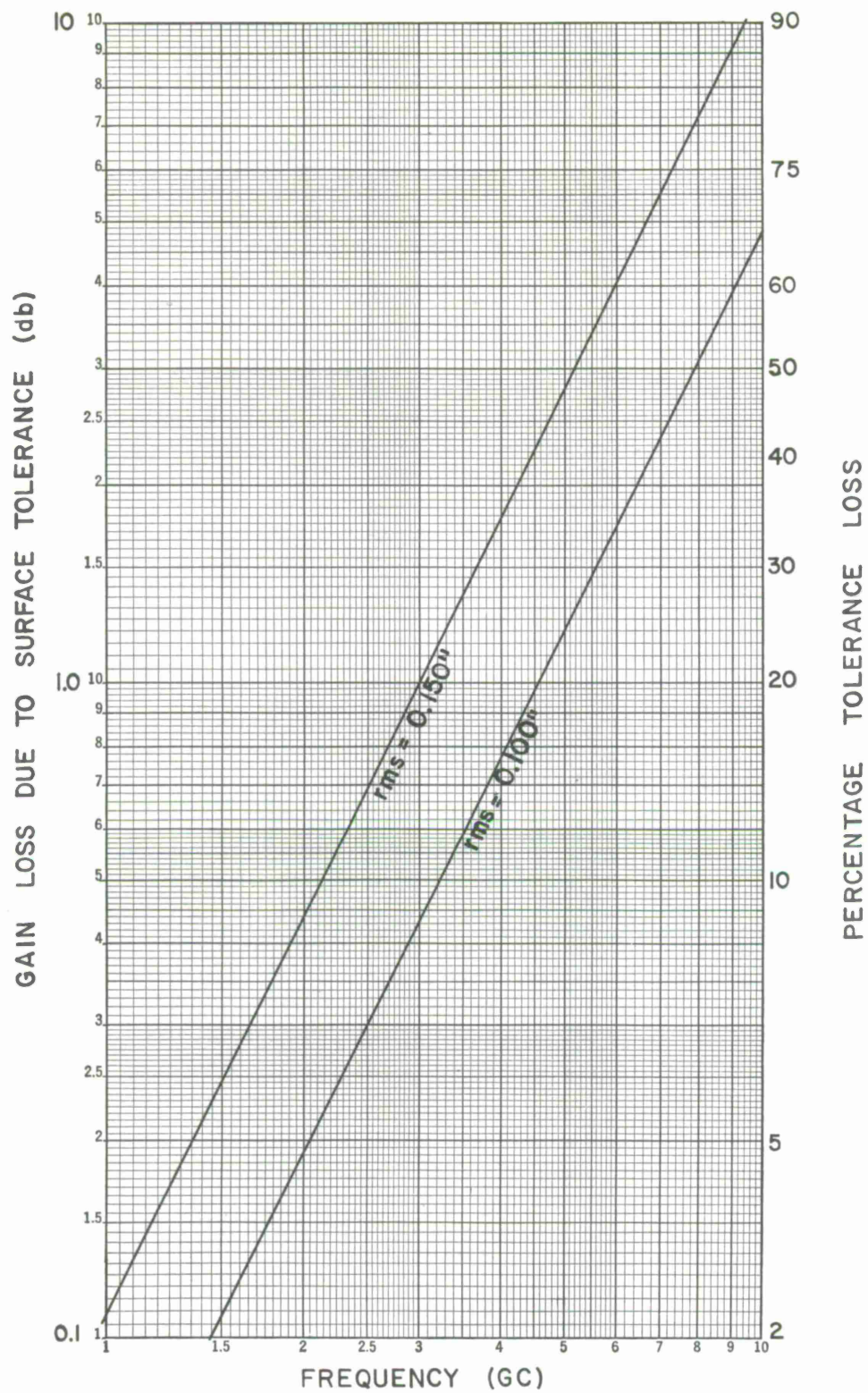


Figure 1.1. Gain loss versus surface tolerance.

Differential Temperatures

10° F from top to bottom of the radome
5° F from the center to the radome surface.

Humidity

0% to 100%.

The considerations that have been used to determine the velocity, acceleration, and servo bandwidth requirements for the CAMROC antenna are described below.

In tracking a fixed source at a range much greater than the radius of the earth with an earth-based azimuth-elevation mount, the elevation rate cannot exceed the rate of the earth's rotation. The maximum azimuth rate, however, depends upon the maximum elevation encountered, and a source passing through the zenith produces an infinite azimuth rate at that point. Azimuth rate is always maximum when the hour angle is zero, that is, when the source target is on the same meridian as the observer. This maximum rate is

$$AZ_{\max} = \Omega (\sin L + \cos L \tan EL_{\max}) ,$$

where L is the latitude of the observer, Ω is the earth's rotation rate, and EL_{\max} is the target elevation at zero hour angle. The maximum azimuth velocity required of an instrument depends, then, upon the maximum elevation at which it must be able to maintain track.

As an example, for an observer at latitude 42°5 N and a target with maximum elevation of 88°, the maximum azimuth rate required is 0.1°/sec, and the maximum elevation rate required is 0.005°/sec. Maximum accelerations are about 0.0001°/sec² in azimuth and 0.00001°/sec² in elevation.

If a Type-2 servo with essentially infinite velocity constant is considered, the necessary acceleration constant is determined from the allowable error. The half-power beamwidth of a 400-ft antenna at 6000 Mc/sec is about 0°03. Allowing 1/10 of this beamwidth for tracking error, the azimuth acceleration constant

$$K_a(az) = \frac{\text{maximum acceleration}}{\text{allowable error}} \\ = 0.01/\text{sec}^2 .$$

For elevation,

$$K_a(el) = 0.002/\text{sec}^2 .$$

Since the effect of an azimuth error on pointing angle in the slant plane decreases as the cosine of the elevation angle, the azimuth acceleration constant may be relaxed by at least a factor of 5. For both axes, then, an acceleration constant of $0.0002/\text{sec}^2$ requires for the Type-2 system a servo bandwidth of only about 0.01 cps. Using a conservative figure of about five times the servo bandwidth, the system mechanical resonant frequency need be no greater than 0.05 cps.

It is apparent that by sacrificing a very small (0.06% in the above example) amount of sky coverage, it is possible to reduce the servo bandwidth and, consequently, the mechanical resonant frequency required for tracking targets at infinite range. For scanning, for shifting targets, or for nonsynchronous earth-satellite tracking, much greater accelerations will be required. The disparity is so great that it may be well to consider a separate open-loop mode for slewing and target acquisition.

The above considerations have dictated the track-mode requirements, while the slew-mode specifications above have been chosen for operational convenience.

Provisions must be made to store acquisition velocities from the slew-mode operation so that excessive accelerations will not be required in the track mode at acquisition.

2. RADOME CHARACTERISTICS

2.1. Introduction and Background

Radomes were developed toward the end of World War II to protect microwave antenna systems on aircraft; the MIT Radiation Laboratory was responsible for much of the basic work. After the war, Cornell Aeronautical Laboratory (CAL) developed air-supported radomes as protection for ground antennas. By 1948, 55-ft-diameter air-supported radomes were commonly used in military installations.

Deterioration in the mechanical and physical properties of radome fabrics and the expense of maintenance both suggested exploration of alternative radome concepts. In 1952, Lincoln Laboratory began development of rigid radomes that could withstand severe weather for long periods, and in 1954 built several 31-ft-diameter 3/4-sphere rigid radomes made of reinforced plastic. In 1956, because of the need for still larger diameter ground radomes, metal space-frame radomes were investigated. By 1960, the 150-ft-diameter Haystack radome was erected in Tyngsboro, Massachusetts.

Since 1960, Lincoln has supported the development of computer programs for the structural analysis of highly redundant space-frame structures, for the generation of complex space-frame geometries, and for the determination of the optical blockage resulting from the frames. These programs are available to aid in improved radome design.

The types of radomes now in use can be broadly classified as air-supported and self-supporting, with the latter being further subdivided as shells and space frames.

2.1.1 Air-supported radomes

An air-supported radome is essentially an airtight coated-fabric structure supported solely by a small amount of internal air pressure. This type radome was first considered in 1946 by CAL. The prototype, erected in 1948, found general acceptance, and these radomes were used extensively throughout the United States and Canada for the protection of radar antennas against adverse weather conditions. With the later successful developments of self-supporting or rigid radomes, the air-supported models, for the most part, gradually phased out.

The Westford radome depicted in Figure 2.1 is representative of an air-supported structure. It was fabricated from orange-peel sections with vertical joints running from the base of the 12-ft-diameter crown section. The 68 main panels are stepped down to 34 toward the top and then to 17 joining the crown section. The panels are joined to each other with a bonded lap joint, with the number of joints largely determined by the available width of the material.

During construction, the radome fabric becomes a one-piece, flexible envelope; consequently, handling becomes increasingly difficult as fabrication progresses or as larger diameter structures are built. For example, the 0.07-inch thick membrane used in the 210-ft Telstar radome at Andover, Maine, weighs 60,000 lbs.

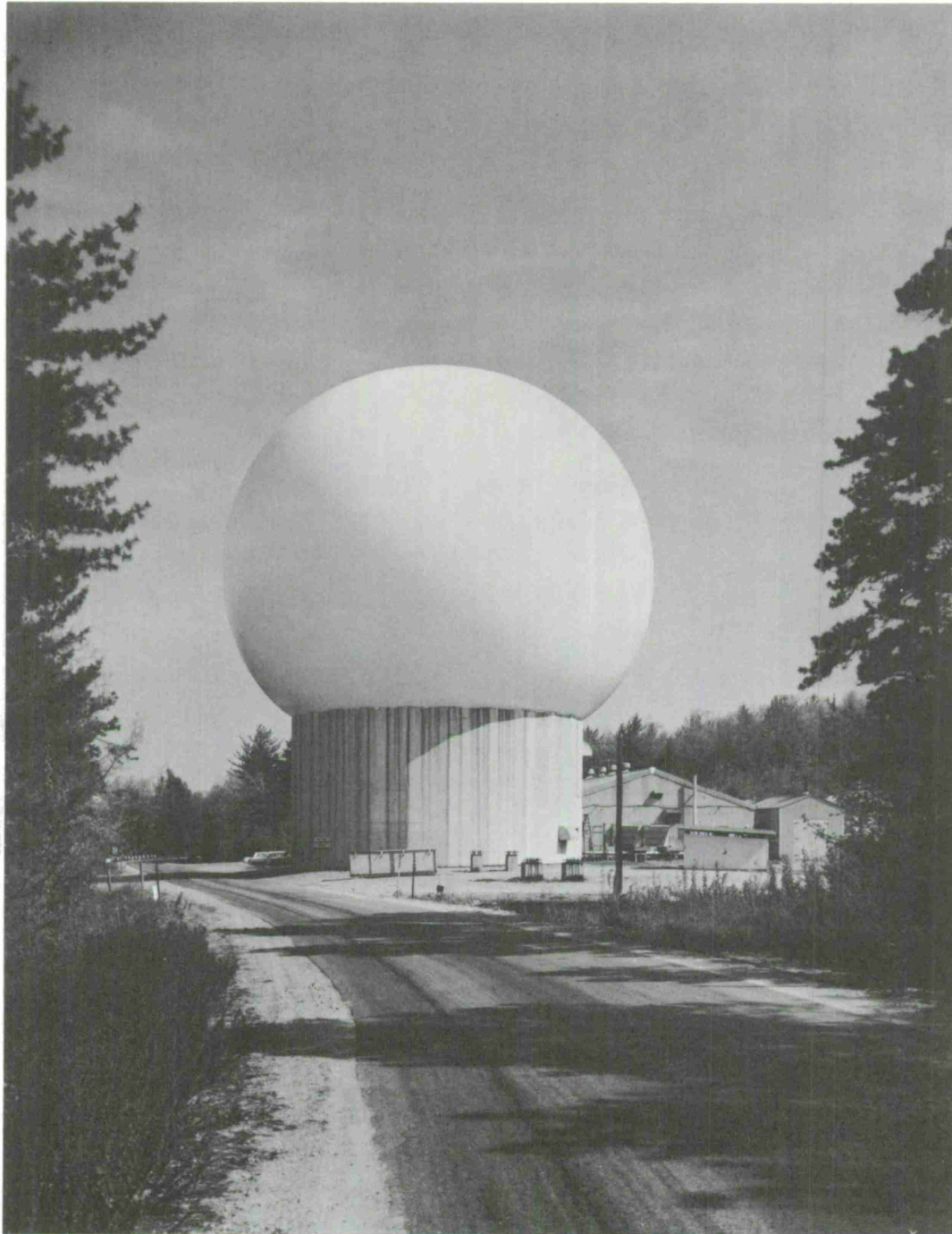


Figure 2.1. Air-supported radome at Westford installation.

Because the membrane thickness will increase with radome diameter, material approximately 0.25 inch thick would be required for a 550-ft air-supported radome. The dielectric properties associated with this thickness would be unacceptable for CAMROC. Some of the degradation in electrical performance could be eliminated by a lower density material; or a nylon fishnet could be laced to the exterior of the inflated dome so that a substantial portion of the pressure loading is carried by the nylon wire. In both cases, however, an extensive development effort would be necessary, with little certainty as to the final results.

The mechanical properties of the flexible membrane used in an air-supported structure are impaired after extended exposure to the ultraviolet radiation in sunlight, which usually means that an inflated radome must be replaced after 7 to 10 years' service. Also, with time, the material tends to absorb increasing amounts of water during rain and to retain it for longer periods. This, again, would seriously degrade the electromagnetic performance of the radome.

The inflated structure encounters its own peculiar hazards. Any debris, blowing about in high winds, can tear the membrane and cause a loss of internal pressure at a critical time. The tendency for the whole air-supported radome to lean appreciably during severe winds can be minimized by making it hemispherical, but this constraint would necessitate the use of a much larger diameter radome to contain the CAMROC antenna. All these deficiencies eliminate the inflated radome for the CAMROC application.

2.1.2 Rigid radomes

2.1.2.1 Shell structures

Rigid-shell radomes are made igloo-fashion from low-loss dielectric blocks; expanded polystyrene (polyfoam) has been used for this purpose. The outside surface is covered with a watertight skin. The largest radome of this type, shown in Figure 2.2 is approximately 30 ft.

Another type of shell radome is made from sandwich panels that have high-strength skins and a low-density core. A 55-ft radome was made this way with 1-inch-thick panels formed of glass-fabric-reinforced plastic skins with a Kraft honeycomb paper core. The panel edges were mating V-grooves and were joined together with cam-type fasteners bonded between the skins.

The required thickness of the shell-type radome increases with the diameter of the structure. This, in turn, limits the frequency range over which the enclosed antenna can operate efficiently. Because of this restriction, shell-type radomes are not acceptable for the CAMROC application.

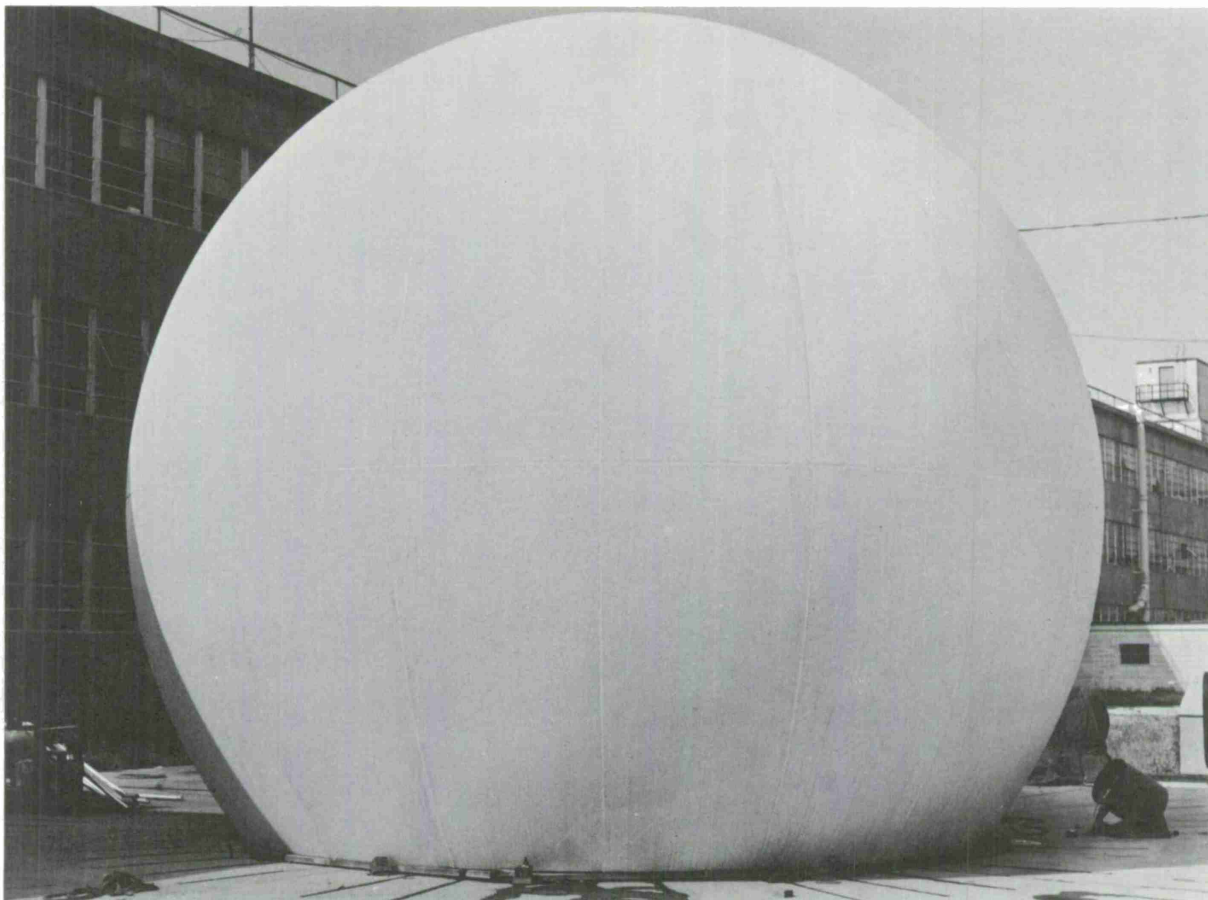


Figure 2.2. 26-1/2-ft -diameter shell-type radome.

2.1.2.2 Space-frame radomes

The space-frame radome is formed from a triangular network of load-carrying structural members that are designated as dielectric space frames or metal space frames, depending on the material used for these members. A dielectric space frame is usually assembled from fibrous-glass-reinforced plastic panels with integrally molded outstanding structural flanges and ribs.

The 55-ft CW 396A radome depicted in Figure 2.3 is a dielectric space-frame radome developed at Lincoln Laboratory to protect Air Force antennas at Arctic installations. Even though this class of radome is made of all-dielectric material, the flanges and ribs act as electric discontinuities in the radome wall, which is detrimental to the antenna-radiation pattern. For larger radomes, it was believed that metal structural members of equivalent strength would be much smaller in cross section and would thereby present less blockage area.

The evolution of the metal space-frame concept may be of interest. When the CW 396A radome was under development, it was assembled with phenolic fasteners at the behest of the electromagnetic experts who would tolerate no metal in the path of the radiated energy. However, when later these plastic fasteners were replaced with metal fasteners for a structural load test, they had no visible effect on the antenna pattern. In a subsequent crude test, aluminum tape was laid over the flanges and the ribs of the radome; a comparison of antenna test patterns with and without the tape showed very minor detrimental effects.

These encouraging results led to an electromagnetic scale-model test program that provided data on the significance of the spatial orientation of the structural members. A natural subdivision of a sphere based upon the icosahedron results in a lattice of members that tends to form a series of continuous parallel lines. When these members are collinear with the incident wave polarization, the scattering contributions tend to add in phase and alter the original distribution of energy from the antenna. This led to the random-geometry concept in which there is no alignment of adjacent members on the same great-circle arc. Scale-model tests of this type geometry proved to be quite effective electrically. The 150-ft metal space-frame radome at Haystack Hill (see Figure 2.4) and a 110-ft version built by North American Aviation are based on this geometry. The space frame requires no major development effort, and the structure can be readily designed, fabricated, and erected to meet CAMROC specifications.

2.2 Radome Studies

At the beginning of the CAMROC study, one of the basic tasks was the generation of comparative information on the performance, feasibility, and cost of large steerable antennas when they were designed for use with and without the protection of a radome. Although experience with the Haystack high-precision antenna clearly indicates that a

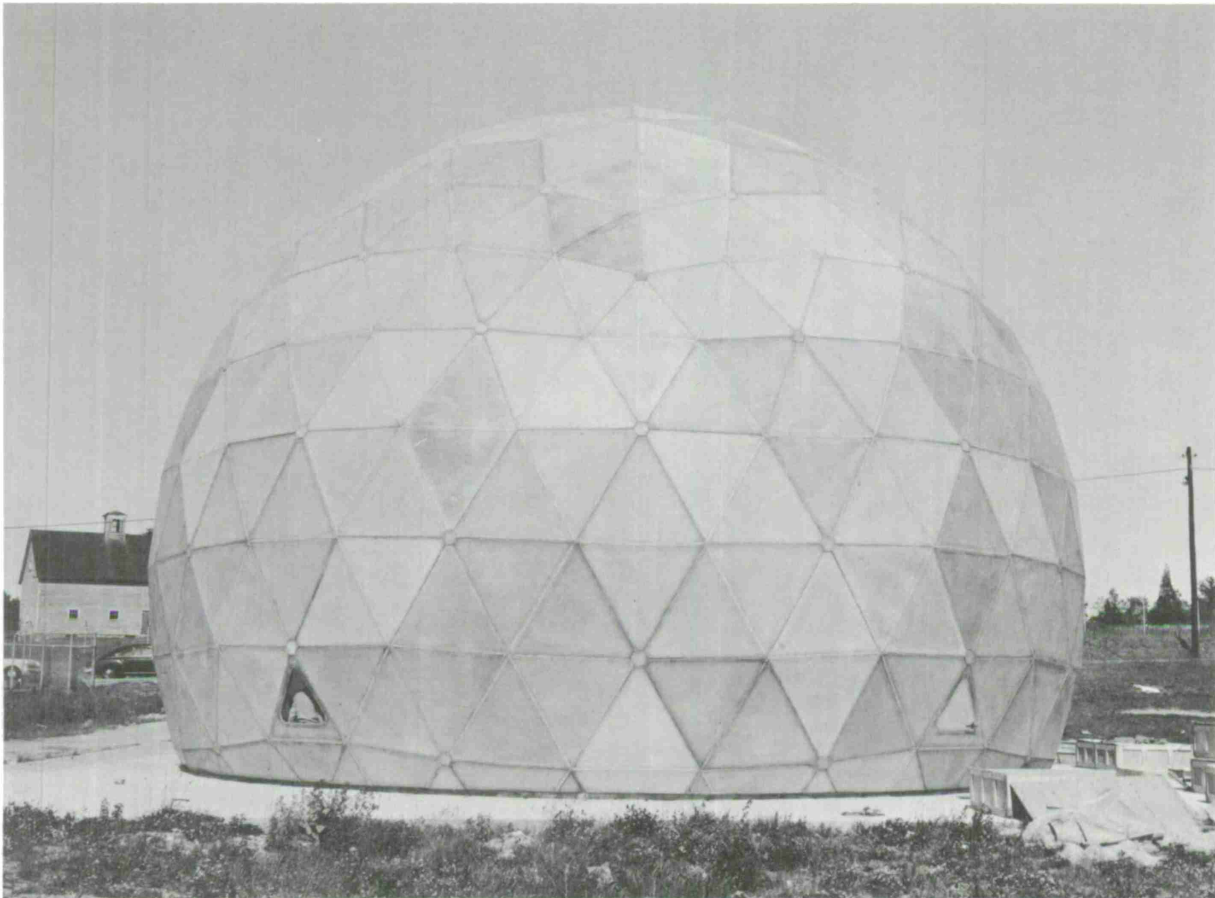


Figure 2.3. 55-ft-diameter dielectric space-frame radome.



Figure 2.4. 150-ft-diameter metal space-frame radome in use at Haystack site.

a radome permits a new approach to antenna design, with important economic consequences, particularly when the ratio of the antenna diameter to wavelength (D/λ) exceeds 1000, CAMROC obtained a completely independent evaluation of this critical question.

In February 1966, Rohr Corporation was asked to examine the radome/nonradome question. This company had recently designed and built the 210-ft Goldstone antenna for Jet Propulsion Laboratory, and thus could use the available design drawings, calculations, and field-measurement and cost data for a comparative study of a 210-ft antenna enclosed in a radome.

In addition, the work was to be extended to obtain information on the comparative costs of radome-enclosed and environmental antennas in the 100-m and 400-ft categories. (Data on an exposed 100-m antenna were available from a previous Rohr-conducted study for NRAO.) The Rohr summary report describing these studies is reproduced as Appendix A.

2.3 Effect of a Radome upon Antenna Economics

These radome studies provided unambiguous and clear conclusions about the significant changes in design philosophy and cost savings that result when an antenna is protected from the environment by a radome. Although it is evident that the importance of a radome increased rapidly with antenna size and precision, the studies revealed that both cost and performance considerations strongly dictate the use of a radome with antennas as small as 210 ft in diameter.

Although Rohr was not required to optimize the design of a 210-ft radome-enclosed antenna, the initial estimate of cost savings greater than 2.2:1 was very conservative. The results demonstrated, moreover, that it would not be feasible (at any reasonable cost) to construct an exposed, solid-surface, 400-ft-diameter antenna that could fulfill the pointing specifications (15 arcsec), even under moderate (20 mph) wind conditions.

For the radome-enclosed antenna, not only is the antenna weight reduced to about one-third, but equally important, it was determined that the drive- and control-system power requirements would be only 5% of those needed for the exposed system. Since the drive and control components on very large exposed antennas comprise a principal element in the overall cost, it was again apparent that the radome engendered highly significant economies.

This preliminary work was undertaken at a phase in the CAMROC program prior to the completion of a quantitative evaluation of the optimum design for a radome-enclosed reflector. Subsequent studies, which were able to take full advantage of greater design freedom permitted by the radome, have revealed that the comparative weights of an exposed 400-ft antenna and its radome-enclosed equivalent will differ by about 15:1. It is interesting to note that similar studies, undertaken in 1959, when the Haystack

antenna was being planned, indicated that it would be uneconomical to construct an X-band antenna even as small as 120-ft diameter, unless a radome were utilized. Consequently, the conclusions of this CAMROC study, while surprising to many, are consistent with investigations conducted by Lincoln and North American Aviation 7 years ago.

In October 1966, approximately 20 structural-design engineers from 8 different organizations attended a meeting convened to review the status of the CAMROC antenna. In order to determine if there were any residual uncertainties — from the structural designer's point of view — about the need for a radome, the following question was presented to the group:

Recognizing that the use of a radome may require the antenna diameter to be increased by approximately 10% (to obtain equivalent electrical performance) and that the cost of a radome may equal the cost of the antenna it protects, can the CAMROC objectives be fulfilled more economically with an exposed or with a radome-enclosed antenna?

The engineers at this meeting unanimously agreed that, for both structural-design and economic reasons, a 400-ft steerable antenna, suitable for operation at 6 Gc/sec, will require the use of a radome. All subsequent CAMROC antenna studies have been predicated upon the use of a radome.

2.4 Effect of a Radome on System Performance

Section 7 of this report contains theoretical and experimental information about the electromagnetic effects that a radome introduces into the performance of a low-noise antenna system. Substantial experience with the Haystack antenna and radome, as well as at other sites (largely military) that utilize radomes, has generated a body of quantitative data.

A space-frame radome introduces a small aperture blockage and also causes a small increase in overall system noise temperature. All other electromagnetic effects are minor. Studies have shown that an increase in antenna diameter of approximately 10% can fully compensate for the radome aperture blockage and the noise temperature. Since the cost of a radome-enclosed antenna is low, in contrast to that of the exposed antenna, this increase in antenna size is both reasonable and economical.

The elimination of winds, solar heating, snow, and ice from the antenna results in a significant reduction in antenna complexity and provides increased useful operating time. Since a 400-ft antenna will have an enormous surface area, which for 6-Gc/sec operation must be essentially solid, CAMROC studies have shown that it will not be economically feasible to construct a pointing and control system to fulfill the stringent pointing-angle requirements when the antenna is exposed. The use of a radome, however, greatly simplifies the pointing problem and enables the desired performance to be achieved at a reasonable cost.

3. DESIGN REQUIREMENTS FOR EXPOSED AND PROTECTED ANTENNAS

3.1 General

An exposed antenna must have definite strength, stability, and dynamic properties to withstand the effects of gravity, inertia loads, and temperature, and for survival the design must also allow for the effects of wind, icing, and snow and hail. The specified surface accuracy must be maintained in the presence of the combined effect of gravity, operational winds, and temperature. At the low angular rates needed for radio astronomy, the dynamic loads that are imposed on the structure by the drive system are very low.

For large antennas that are exposed to the elements and therefore must operate in at least moderate wind conditions, the wind loads will constitute the major source of surface and pointing error. The systematic deformations resulting from gravity and temperature effects could be corrected by the use of elementary, open-loop, slow-acting compensation techniques, but quick-response compensation techniques would have to be employed to deal with the dynamic wind forces. This more complex form of compensation requires a highly stable reference system with many sensors and control activators. A fast-response reflector compensation system has not yet been successfully utilized in a large antenna but is under study in England.*

3.2 Effect of Size

It is useful to investigate the behavior of stress, deflection, natural-frequency, and mechanical components as a given configuration is hypothetically scaled upward. In general, a linear scaling of all dimensions will not give the most efficient design, and design optimization will usually demand significant modification in the configuration as large changes in size are made; however, an analysis of the following effects of linear scaling helps to reveal problem areas in the design of very large antennas.

- 1) Gravity loads. Deflections increase as the square of the diameter; stresses increase linearly with diameter.
- 2) Wind loads. Deflections increase linearly with diameter; stresses remain constant.
- 3) Thermal environment. Deflections due to temperature differentials increase linearly with diameter; stresses remain constant.
- 4) Dynamic properties. Lowest natural frequency varies inversely as diameter.

* Burr, D. W., "An Experimental Profile Controlled Aerial," IEE Conference Publication Number 21, Design and Construction of Large Steerable Aerials, June 6-8, 1966.

- 5) Reflector tolerances. Fabrication errors of subassemblies will be essentially independent of antenna size; erection tolerances, however, will vary approximately linearly with size, owing to the limitations of the optical systems that are normally used for setting the surface.
- 6) Mechanical components. Bearing stresses due to gravity loads scale linearly, while those due to wind loads are independent of the scale size. Drive torque (and hence power) requirements behave as follows:
 - a) Inertia torque varies as the diameter to the fourth power.
 - b) Coulomb friction torque varies as the diameter cubed.
 - c) Wind torque varies as the diameter cubed.

Machining problems for precision components increase exponentially as the ratio of tolerance to size component decreases beyond certain limits. The capacities of available machine tools and transportation factors impose finite size limitations for these components.

3.3 Design Considerations

The fact that gravity-load deflections increase as the square of antenna size may appear as a severe constraint. Fortunately, this is not the case, for these reasons:

- 1) Deflection due to gravity constitutes only one component of the total error budget; it is, moreover, a predictable component. Contour errors from other sources vary either linearly with size or are invariant.
- 2) Modifications of the structural configuration (e.g., depth of trusses, method and pattern of subframing for reflector panels, etc.) can be used to stiffen the antenna structure, albeit at some increase in cost.
- 3) Gravity-load distortions can be greatly reduced by introducing, in the setting of the reflector surface, contour offsets of appropriate magnitude and direction. In addition, relatively simple deflection-control devices can be used to reduce deflection excursions further.

The earlier observation that stresses due to gravity loads increase linearly with size is valid only if the configuration is scaled linearly. If the configuration is modified to provide increased stiffness, stresses will be accordingly reduced. Since the more highly stressed portions of the antenna generally will occur near its supports, size increases in these members usually can be achieved with only minor overall effects on the inertia and deflection properties of the antenna. Where this is not the case, a higher strength material can be used or entirely new configurations may be adopted. For these reasons, it is unlikely that strength requirements will constitute a serious design problem in the diameter range proposed for CAMROC.

Assuming appropriate structural modifications as size is increased, deflections due to wind loads will increase less rapidly than size. It is apparent, however, that contour-accuracy requirements, even under a nominal operational wind velocity, will be a governing factor in the design — and hence cost — of an unenclosed dish in the precision, size, and sky-coverage range proposed for CAMROC. Aerodynamic stability may prove to be a problem for unenclosed antennas, particularly if a gravity-load deflection compensation system is employed; this can be overcome by careful aerodynamic design, by the use of structural dampers, and/or by actuating special locking or stiffening devices when wind velocities exceed the critical value.

3.4 Comparison of Wind and Gravity Loads on Antenna Structures

There appear to be some common misconceptions about the influence of wind on the behavior of an antenna system. The variable gravity loads that occur when an antenna is rotated are approximately equal to those imposed by a 45-mph wind load; consequently, since radio telescopes need to function only at winds up to 20 mph and since wind pressures vary as the velocity squared, it has been stated that antennas built for survival will also not have any difficulty in meeting performance requirements at winds of up to 20 mph. This is believed to be an erroneous conclusion, as can be seen from the discussion below.

The nominal weight of a typical reflector system may be on the order of 8 lb/ft^2 . A wind velocity of 20 mph will have a pressure load of approximately 1 lb/ft^2 . However, a 20-mph wind at a 30-ft elevation above the surface of the earth will be significantly larger at the center and at the top of the antenna (1.25 for 200 ft, and 1.5 for 400 ft of elevation). The wind-load (pressure) escalation factor is thus 1.6 and 2.25, respectively. In addition, a gust factor, which may be as high as 1.4, must be provided for, and the net effect of the height escalation and gust factor could easily produce a wind load on the antenna of 3 lb/ft^2 while the actual wind velocity on the surface was only 20 mph.

The primary reflector of the antenna will distort in a systematic manner owing to the changing gravity loads; approximately 80% of this deflection is a rigid-body rotation, 10% is a rigid-body translation, and the remaining 10% results in a distortion. The rigid-body rotation and translation components, which would produce a pointing error, can be completely calibrated out of the system. In addition, the surface distortions arising from gravity can be reduced by about a factor of 2 by bias-rigging techniques. Therefore, a more appropriate comparison of the wind and gravity effects would compare the wind-induced distortions with only that small percentage of the gravity effects that are not compensable. An examination of these factors will indicate that the winds as low as 10 to 15 mph near the ground will probably cause structural deformations and pointing errors in a solid-surfaced reflector of about the same magnitude as the residual uncompensated errors resulting from the gravity effects.

Added structural stiffness in the reflector support elements does not help in the gravity case, owing to the associated increase in weight, but it will minimize wind effects. To provide the additional structural stiffness that will be needed to make the wind effects small will involve a significant increase in material and cost.

The dynamic effect of wind on structures has received increasing attention since the collapse of the Tacoma Narrows Bridge in 1940. Design practice up to that time depended wholly on static wind loads, which were based on an arbitrary face constant that generally ignored the shape of the structure and the actual value of the wind velocity and direction at the site. Engineers have been forced to consider the possibility of wind-induced dynamic response on flexible structures, of which radar and radio telescopes are certainly among the most prominent.

The dynamic effect of wind on structures may be divided into four principal categories, depending on the shape and flexibility of self-excited oscillation:

- 1) High-frequency oscillations that are associated with long, slender structures or elements.
- 2) Cylindrical bodies, which are elements or structures whose cross-sectional shape is constant at every section along the span, showing negative slope over certain portions of the curve of attach lift force, plotted against angle of wind. These may oscillate in a bending mode. Torsional instability is also possible for this case.
- 3) Thin, flat plates placed horizontally in a horizontal wind. These may be subject to flutter if the natural frequencies in bending and torsion are not too dissimilar.
- 4) Buffeting action. This action has developed on a structure owing to the effect of some other structure relatively close up-wind. Such a condition has been reported on multiple tall stacks in line.

Many of the situations in which wind-induced oscillations are of a serious character involve circular cross sections. Consequently, considerable attention must be given to structures or members exposed to the elements in order to avoid any of the two modes of self-induced vibrations. Two methods are employed for effective action against self-induced vibrations:

- 1) Increase the natural frequency, thus raising the critical wind velocity above the anticipated wind velocity at the site.
- 2) Increase the effective damping through the installation of mechanical damping devices that act to reduce the amplitude.

In a hostile wind environment, these phenomena become increasingly critical and serve to place restraints on structural design. Local as well as system oscillations must be considered. An immediate restraint is one wherein, even with a circularly

symmetrical antenna structure, the members must be individually analyzed for local wind loads, owing to the wind escalation factor for such a large structure. Wind velocity will vary as the height, as shown in Table 3.1, where V_{30} is the velocity of wind 30 ft above local terrain. A 60-mph wind, 30 ft above the ground, would mean a 90-mph wind 600 ft above the ground.

Table 3.1. Fastest mile of wind (mph) for various height zones above ground level (inland regions)

Height zone (ft) \ V_{30}	60	67	75	80	85	90
0-50	60	67	75	80	85	90
50-150	70	80	90	95	100	105
150-400	80	90	100	110	115	125
400-700	90	100	115	120	130	135
700-1000	100	110	125	130	140	145
1000-1500	105	115	130	135	145	150

Source: American Society of Civil Engineers, "Wind Forces on Structures," Paper #3269, 1962.

For a given structural shape in a symmetrically designed antenna, wind-induced vibrations must be considered and, in all probability, will result in adding mechanical damping devices or in increasing the properties of the element. In either of these cases, additional weight must be added to the structure. These design restraints and possible additional weight in the structure will serve to increase the cost of the antenna.

In an exposed antenna, the bearing systems are likely to constitute a major problem and to assume an increasingly large percentage of total antenna cost as size is increased. To avoid excessive bearing stresses, bearing sizes must increase more rapidly than antenna size, or more appropriate bearing configurations must be adopted. In this respect, azimuth bearings present the major concern. Recent technological advances make hydrostatic bearings attractive for the larger antennas; they reduce the machining, tolerance, wear, and compliance problems of large bearings, provide smoother tracking, and allow a reduction in power requirements. A novel alternate that offers similar advantages is a flotation system. When used for exposed antennas, both hydrostatic-bearing and flotation systems may require special provisions to resist overturning moments.

While the power requirements for the drive systems of an exposed antenna increase exponentially with antenna size, this does not introduce a serious technical problem but, rather, one of economics.

When large antennas are protected from the environment, the design is usually governed by combined effects of gravity and temperature only. It might be expected that the gravity effects would override the differential temperature effects; however, with the use of deflection-compensation techniques, the gravity effects are reduced to an order of magnitude comparable to temperature effects.

When a radome is used to eliminate wind as a parameter in antenna design, new design concepts are possible because:

- 1) The major reduction in structural loads and the elimination of the problem of aerodynamic instability permit a substantially less expensive structural and mechanical design.
- 2) There is a possibility of achieving further structural efficiencies through the use of thin, stressed-skin components. This type of element cannot be employed in structures exposed to hailstones.
- 3) Maintenance, power requirements, and other operational costs are reduced.
- 4) By controlling the thermal environment, the percent of the error budget assigned to thermal distortions will be reduced, and a less stiff and cheaper design becomes feasible.

4. SEARCH FOR A SUITABLE ANTENNA CONFIGURATION

4.1 Early Configuration Studies

An early step in the planning for a new radio telescope demands the integration of the CAMROC performance requirements with contemporary design and engineering practices to determine the optimum overall concept, after which detailed studies will be required to achieve the most efficient and economical structural configuration.

Although nearly all the large steerable antennas in operation utilize a movable parabolic reflector, it appeared essential to see if the performance or economy of other configurations were of interest to CAMROC. In addition to the prime focus-fed and Cassegrain paraboloids, a possible configuration was the off-axis Cassegrain reflector, which has been studied by Bell Telephone Laboratories. Another important class, particularly where low-noise system performance is of basic importance, is the horn antenna system, such as is in use at Andover, Maine. Several derivatives of the horn antenna that permit structural simplifications also appeared to be worthy of investigation. One of these, the clam shell, offered high efficiency, low aperture blockage, and low-noise characteristics without the large structural size of the horn reflector. A still further simplification of this configuration, called CORT, has been explored at Lincoln Laboratory, because it offers many of the advantages of the horn reflector but permits scanning in elevation by rotation of a plane reflector surface.

In the six configurations to be described, the dimensions of the antenna and radome were scaled to maintain an effective aperture essentially equivalent to that obtainable from a conventional 400-ft prime focus-fed paraboloid. The relative efficiency ratings used in scaling these configurations were based upon the following factors:

- 1) The efficiency of a normal Cassegrain-fed parabolic reflector is higher than that of a focal-fed paraboloid, because the aperture illumination may be made more efficient.
- 2) The various modifications of the normal Cassegrain such as the clam shell and CORT have still higher efficiency than those of a normal Cassegrain-fed reflector, owing to the elimination of aperture blocking.
- 3) The antenna types in 1) and 2) all have losses resulting from feed spill-over and from aperture distributions that are heavily tapered in both principal planes.
- 4) The horn reflector has the highest efficiency, since it eliminates feed spill-over losses almost entirely, improves the aperture taper in one of the principal planes, and does not have aperture blockage.

It will be important to utilize a configuration for CAMROC that will permit the attainment of high efficiency over a wide frequency range. In all probability, the final system will have to permit either prime focus or Cassegrain modes of operation or perhaps use some form of Gregorian optical system that is designed to accommodate a replaceable, low-frequency feed element.

Some recent work has indicated that reflector-surface contours that are not parabolic can be utilized to provide a more efficient aperture illumination. However, since the contour modifications will be very small, the effect of these changes on the configuration can be deferred until a later phase of the program.

4.2 Conclusions of Early Configuration Studies

The early deliberations suggested that the search could be narrowed to two variations of the six configurations on the initial list: the conventional paraboloid with appropriate feed arrangement to maintain high efficiency at the longer wavelengths, and the CORT-type structure. The offset Cassegrain, while it might have merit for satellite-communication use, was deemed unacceptable for CAMROC because it has undesirable polarization effects; in addition, its intrinsically desirable reflector backup structural stiffness requires the use of two large bearings, and the configuration results in an undesirably long, cantilevered secondary feed-support system. The horn reflector did not seem structurally efficient because of its comparatively large size and large radome requirements, compared to the effective size of the useful aperture. While the clam-shell and CORT configurations have many similarities, CORT was deemed more suitable for further evaluation, since it required only one doubly curved reflector surface that did not have to rotate in elevation, whereas the clam shell required two shaped surfaces. A number of other advantages and disadvantages of each of these configurations are listed on the accompanying figures.

Because the preliminary review indicated that the CORT system might be a serious contender, it seemed wise to sponsor a more detailed examination of this class of configuration. A study contract was awarded to the firm of Ammann & Whitney in May 1966 to conduct preliminary conceptual studies of the CORT configuration and to assess its technical feasibility and cost. The final summary of this study, included as Appendix B, describes three different types of 400-ft CORT-type antennas, all enclosed within radomes. One of these schemes was based upon the original Lincoln Laboratory concept that utilized a stiff rotating cylinder; the alternate concepts used a pendulum truss and a reticulated cone. The Ammann & Whitney studies indicated that the reticulated-cone concept is feasible, and its features and cost are summarized in Section 6. It became evident during this study that, unless very economical reflector surfaces were developed, CORT would be much more expensive than conventional paraboloid antennas. Several very lightweight, low-cost reflecting surfaces were studied, one of which utilized air

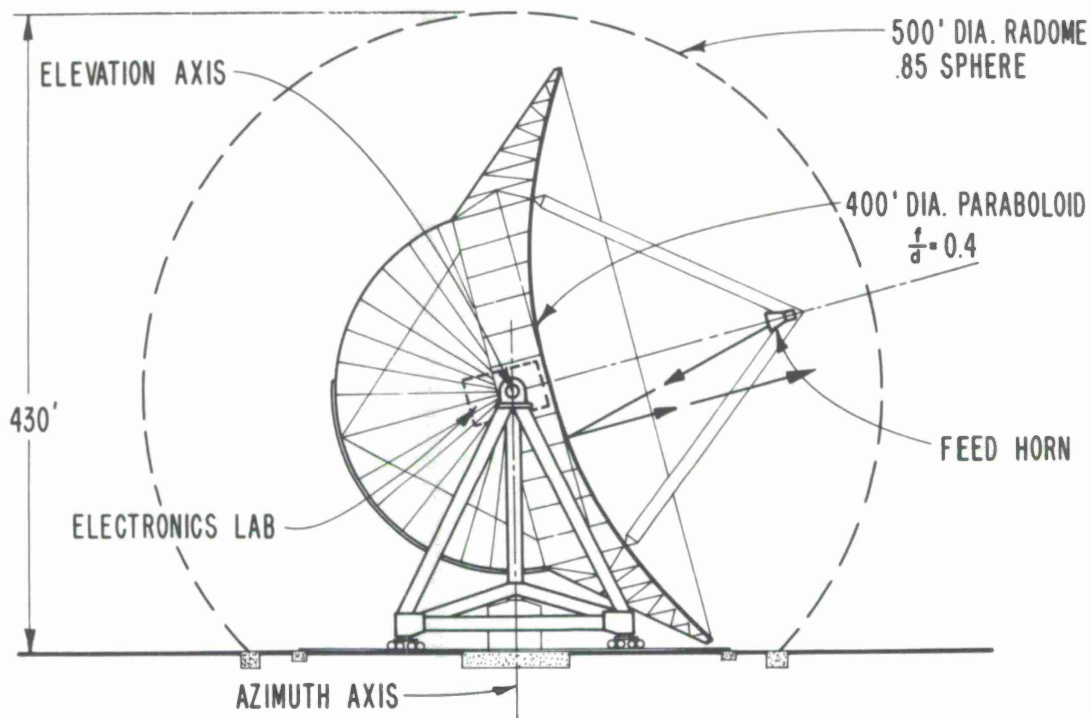
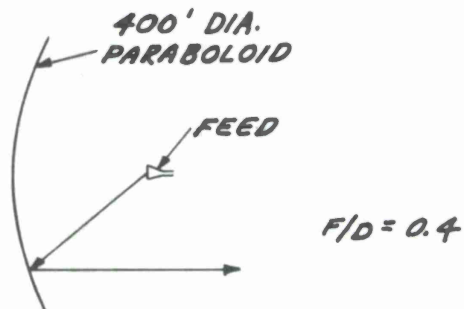


Figure 4.1. Prime focus-fed paraboloid. Estimated efficiency = 55%.



Conventional Prime Focus Fed Paraboloid

Advantages

- 1) The electromagnetic and mechanical features of this type of antenna system have been studied extensively.

Disadvantages

- 1) Long feed line or RF Box at vertex required.
- 2) High noise figure due to:
 - a) Long feed line, if used.
 - b) Primary feed spillover.
- 3) Low efficiency due to:
 - a) Space attenuation and high feed spillover.
 - b) Low directivity feed has low beam efficiency.
- 4) Feed aperture blockage.

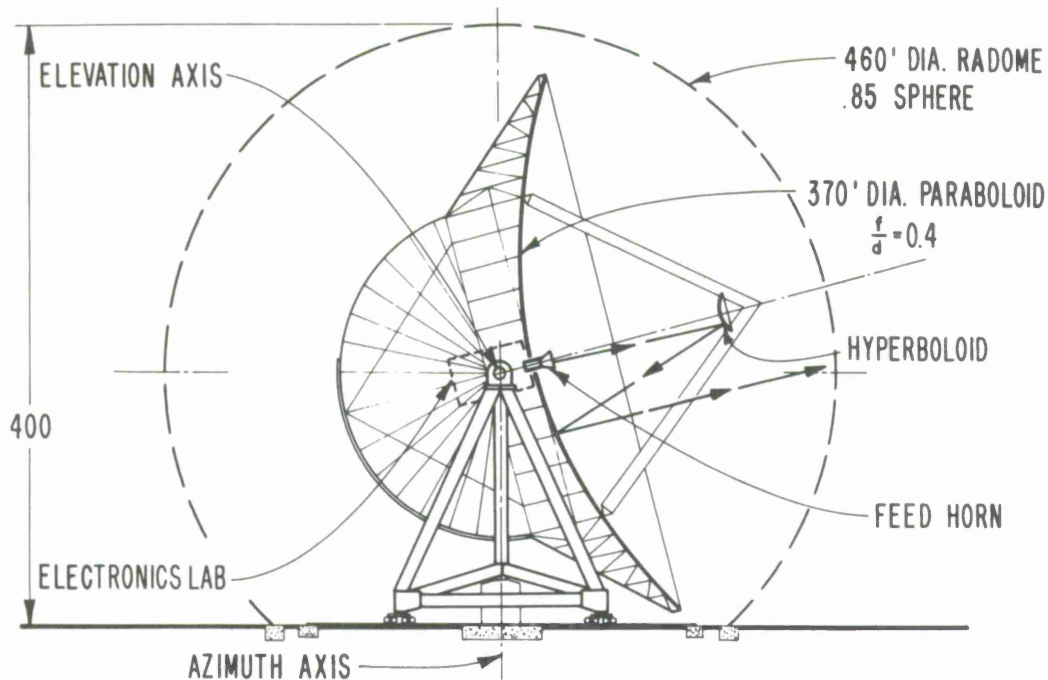
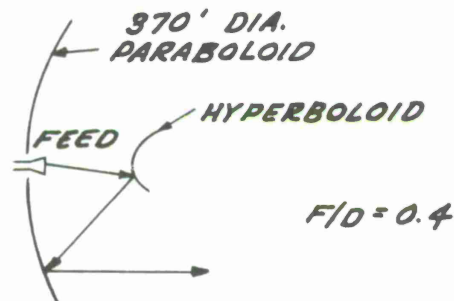


Figure 4.2. Conventional Cassegrain paraboloid. Estimated efficiency = 65% (gain equivalent to 400-ft prime focus-fed paraboloid).



Conventional Cassegrain Paraboloid

Advantages

- 1) The electromagnetic and mechanical features of this type of antenna system have been studied extensively.
- 2) Minimum length feed line.
- 3) RF Box accessibility.
- 4) Low noise figure except at low angles.
- 5) Higher efficiency due to more directive and efficient feed.
- 6) Ease of change of feed and hence of frequency and experiment.

Disadvantages

- 1) Higher noise figure at angles below 20° elevation when feed spillover hits ground.
- 2) Feed aperture blockage.

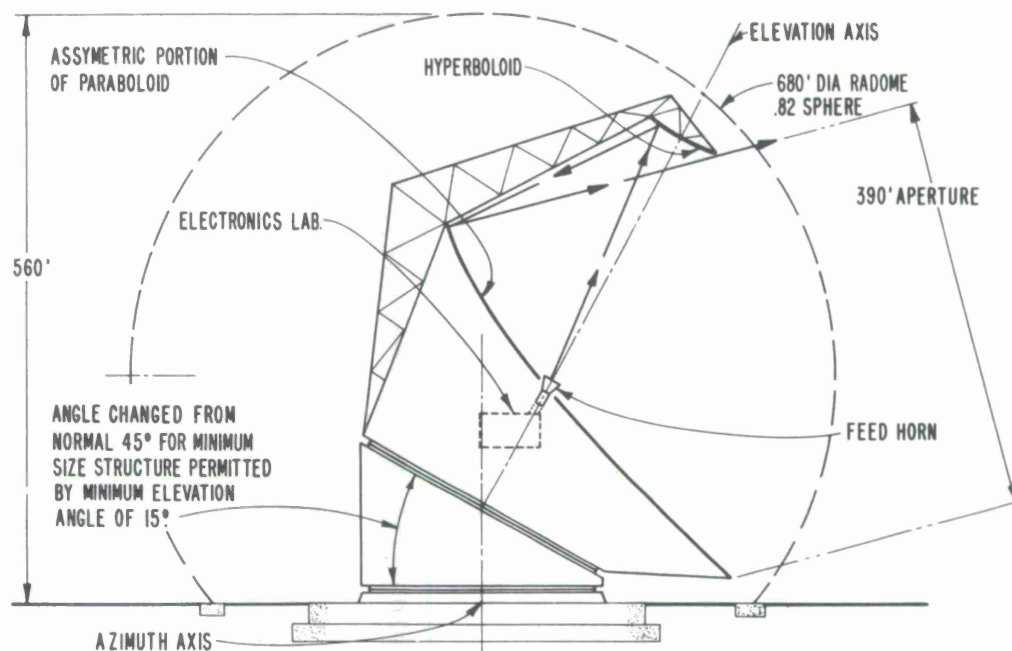
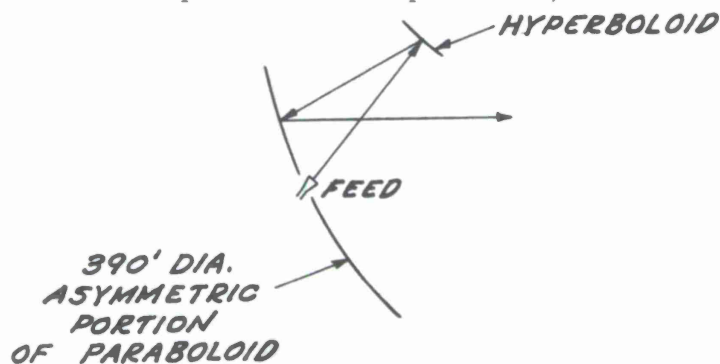


Figure 4.3. Offset Cassegrain. Estimated efficiency = 58% (gain equivalent to 400-ft prime focus-fed paraboloid).



Offset Cassegrain Paraboloid

Advantages

- 1) Low noise figure at all elevation angles.
- 2) No aperture blockage.
- 3) Minimum length feed line.

Disadvantages

- 1) Nonsymmetric reflector and panels (only left-right symmetry) – polarization effects?
- 2) Difficult rigging and measurement of precision surfaces.
- 3) Large inclined precision bearings.
- 4) Large overturning moment.
- 5) Low efficiency due to nonsymmetrical primary pattern required.
- 6) Polarization dependent upon pointing angle.
- 7) Large radome required.

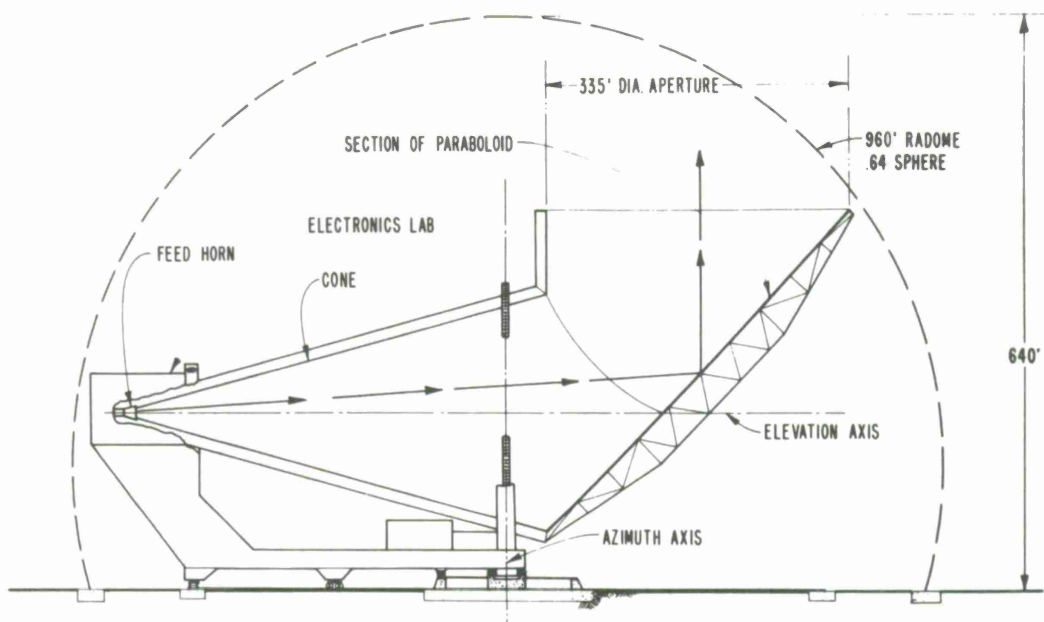
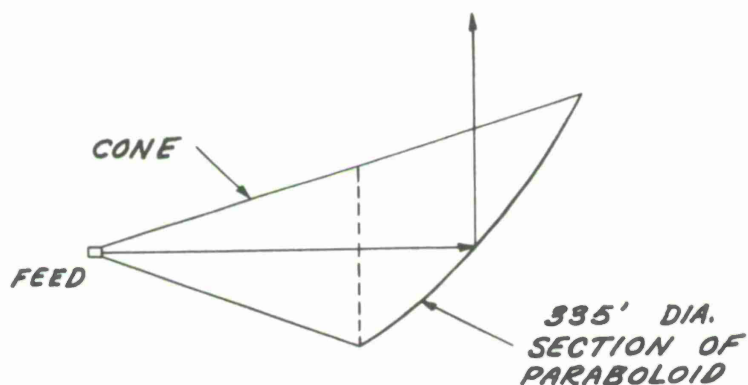


Figure 4.4. Horn reflector. Estimated efficiency = 78% (gain equivalent to 400-ft prime focus-fed paraboloid).



Horn Reflector

Advantages

- 1) Low noise due to shielded structure.
- 2) No aperture blockage.
- 3) Minimum length feed line.

Disadvantages

- 1) Large overall size.
- 2) Rotary joint required for nonrotating RF room.
- 3) No multibeam operation.
- 4) Parabolic surface not circularly symmetric.

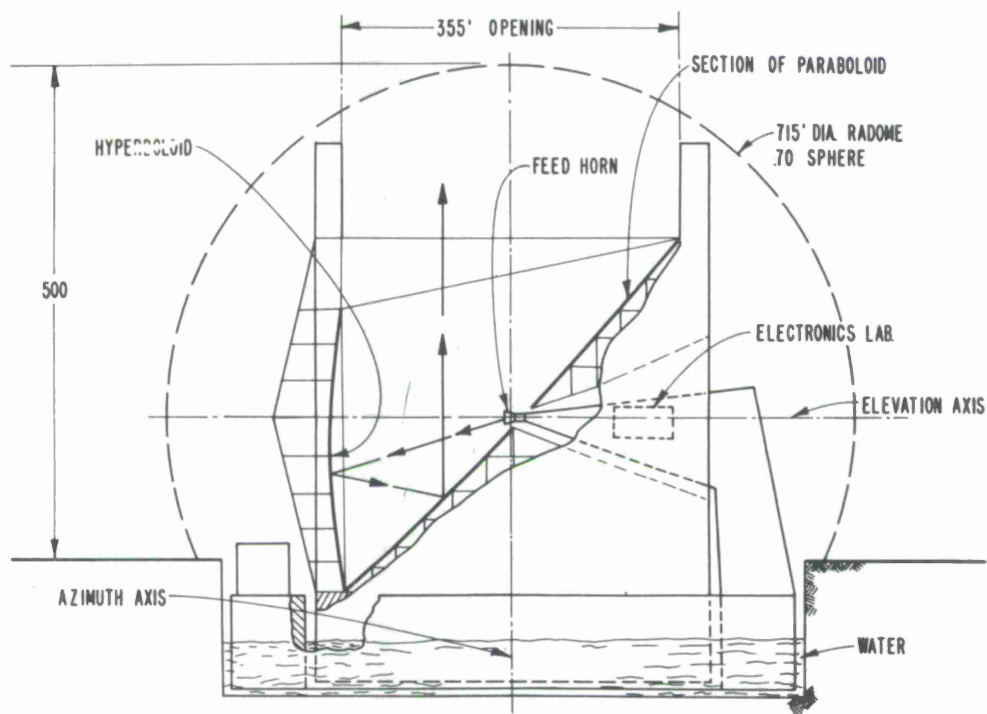
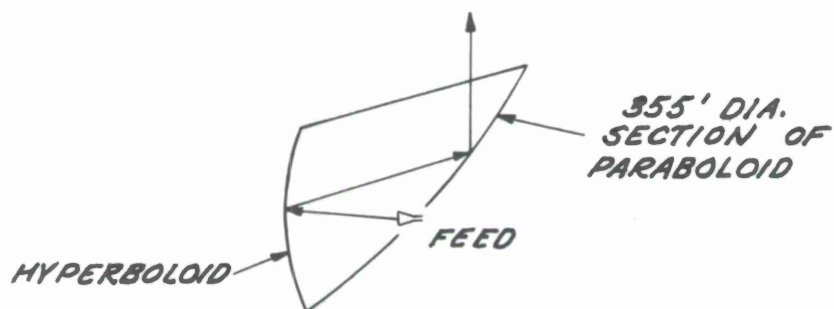


Figure 4.5. Clam shell. Estimated efficiency = 70% (gain equivalent to 400-ft prime focus-fed paraboloid).



Clam Shell

Advantages

- 1) Low noise due to shielded structure.
- 2) No aperture blockage.
- 3) Minimum feed length.
- 4) RF Box can be expanded to RF Fixed Lab.
- 5) Multiple beams possible.

Disadvantages

- 1) Two large shaped nonsymmetric reflectors required
- 2) Both reflector surfaces not fixed with respect to gravity.

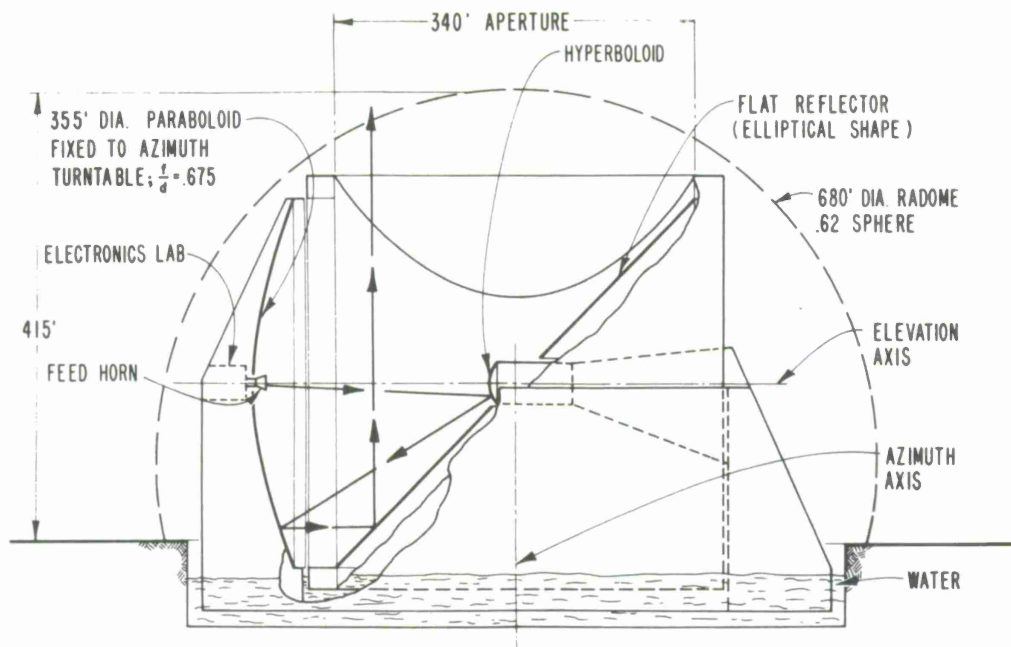
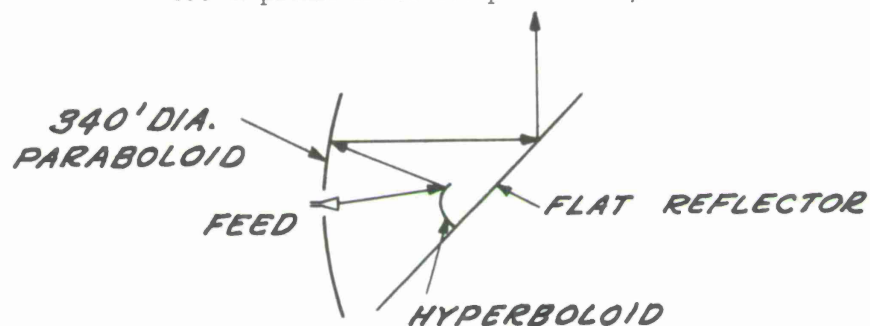


Figure 4.6. CORN. Estimated efficiency = 75% (gain equivalent to 400-ft prime focus-fed paraboloid).



CORN

Advantages

- 1) Low noise due to shielded structure.
- 2) No aperture blockage.
- 3) Minimum length feed line.
- 4) RF Box can be expanded to Laboratory rooms (fixed to gravity).
- 5) Convenient multifrequency and multi-beam operation.
- 6) Parabola remains fixed with respect to gravity.
- 7) Position of mirror not critical.
- 8) Only surface subject to changing gravity forces is a plane — easily rigged and controlled.

Disadvantages

- 1) Two large reflecting surfaces.

pressure to compensate for the variable gravity-deflection components. Nevertheless, conclusions of this study indicated that the cost of the CORT configuration would be appreciable in excess of that of the standard paraboloid antenna. This excess cost is attributable to the need for two reflectors and their backup structures, instead of one as in the simple paraboloid figuration, and for the requirement for a movable shield and a very large and deep radome. Despite its higher cost, the CORT configuration has many attractive features.

5. CONCEPTUAL STUDIES FOR STEERABLE PARABOLIC ANTENNAS

By the summer of 1966, engineering studies had provided data that permitted two basic decisions on the conceptual approach to be followed by CAMROC:

- 1) From the standpoint of both engineering and economics, the antenna must be protected from the environment.
- 2) The movable parabolic reflector appeared to be significantly more economical than other reflector systems.

Within these constraints, CAMROC decided to select the most appropriate antenna configuration by comparing quantitatively a spectrum of interesting concepts. To do this, five 4-month conceptual design studies of steerable parabolic reflectors were initiated in mid-1966, four under subcontract with industrial organizations and one utilizing the CAMROC-allocated resources at Lincoln Laboratory:

Conceptual Study of a 400-Ft-Diameter Fully Compensated Cassegrain Antenna,
by Ammann & Whitney

CAMROC Hammerhead Antenna Concept, by MIT Lincoln Laboratory

Report on a Conceptual Study of a Large Cassegrain Antenna by Paul
Weidlinger

Parametric Study of 400-Ft-Diameter Antenna Based on CSIRO Parkes
Configuration, by Simpson Gumpertz & Heger Inc.

Engineering Summary of a Study for a 400-Ft-Diameter Radome-Housed
Radio Telescope, by Rohr Corporation

The final summary reports of these five studies became available in December 1966, and are reproduced as Appendices C through G.

5.1 Conclusions of the Conceptual Studies

An examination of the five reflector studies indicates that a number of basic characteristics appear to be common to each concept. The main features of each configuration study are shown in Table 5.1, and simplified sketches of the concepts are shown in Figures 5.1 through 5.5. The determination that certain common characteristics should govern the design of a large high-precision low-cost antenna is a significant achievement, inasmuch as the studies were performed by five organizations working with a moderate degree of independence. These common features, not listed in any specific sequence, are:

- 1) Lightweight reflector panels. These studies have indicated that the weight of the panel is clearly reflected throughout all other parts of the structure, and for minimum cost, it is necessary to employ the lightest weight panel that will fulfill the tolerance and strength requirements. Panel weight is the only load that does not contribute to the structural stiffness, and it must be minimized.

Table 5.1. Tabulation of configuration studies

Study	Reflector			Antenna pedestal	Rotating support system and drives	Interface reflector to elevation axis	Weight (tons)	
	Configuration	Gravity compensation technique	Type of panels				Elevation	Azimuth
Ammann & Whitney	Reticulated shell backup structure with compensation	Computerized position controlled jacks at corners of panels. Open loop control.	Isosceles triangular shape. Average 26 ft on 2 sides. Oriented on 2 sides. Form squares or rectangles. Jacks at either 4 or 8 panel corners.	Not considered in study.	Not considered in study.	Small-diameter bearings supporting shell and two axisymmetric spine trusses.	400 ft - 770	400 ft - 965
	Aluminum panels - steel backup							
Rohr	Radial rib truss structure. Optimization of I/x for members by special shapes. All aluminum structure.	Undetermined at this time.	Rings of panels that are trapezoidal in shape. One stand-off stud at each panel corner.	Space frame yoke-tower mounted-trunnions 130 ft apart. 65-ft radius elevation gear, which is also used as counterweight.	Two 24-inch diameter antifriction bearings for elevation axis. 40-ft-diameter hydrostatic thrust bearing with antifriction bearing for radial loads.	130-ft-diameter main circular truss in backup structure. Interconnecting trusses.	400 ft - 290	400 ft - 575
Simpson Gumpertz & Heger	Radial trusses with circumferential stabilizing members and spiral purlins to simulate a shell. All aluminum structure.	None used.	Rings of panels averaging 13 ft radially and 4 ft circumferentially. Each adjuster will support one point on two panels.	Not considered in study.	Not considered in study.	50-ft-diameter hub with elevation interconnect at 43-ft diameter. Steel weldment construction of truss.	300 ft - 198 400 ft - 448 500 ft - 893	Not considered in study.
Paul Weidinger	Vertical trusses and horizontal purlins with compensation.	Precalculated forces that are proportional to elevation angle and gravity vector. Open loop.	Rectangular panel singly curved, assembled in rectangular coordinate orientation. Panels are 4 ft x 13 ft.	Space-frame yoke bearing from concrete cellular turret diagonally up to the end of elevation axis. Intermediate towers, from yoke to elevation axis, which support series of elevation bearings and drive units.	8 antifriction bearings approximating 2 to 3 ft in diameter. Azimuth turret of concrete. Cellular design is supported on tower mounted hydrostatic thrust bearing - 50-ft diameter.	Integrated vertical truss and horizontal purlins at the eight vertical truss sections.	300 ft - 413 400 ft - 580 500 ft - 810	300 ft - 633 400 ft - 1015 500 ft - 1680
	Aluminum panels - steel trusses.							
Lincoln Laboratory	Vertical trusses and horizontal purlins with compensation. Steel trusses - aluminum panels.	Precalculated deformations that vary with elevation angle.	Rectangular panel singly curved, assembled in rectangular coordinate orientation. Panels are 4 ft x 13 ft.	A 360-ft long doubly cantilevered horizontal truss, which is integral with a turret. The truss assembly rotates on a bearing 40 ft in diameter atop a 150-ft high tower.	Series of 8-52-ft diameter hydrostatic support systems for elevation rotation designed to rotate about horizontal truss. 40-ft-diameter hydrostatic thrust bearing for azimuth rotation.	Integrated vertical truss surface at the eight vertical truss stations.	300 ft - 442 400 ft - 946 500 ft - 1603	300 ft - 680 400 ft - 1430 500 ft - 2469

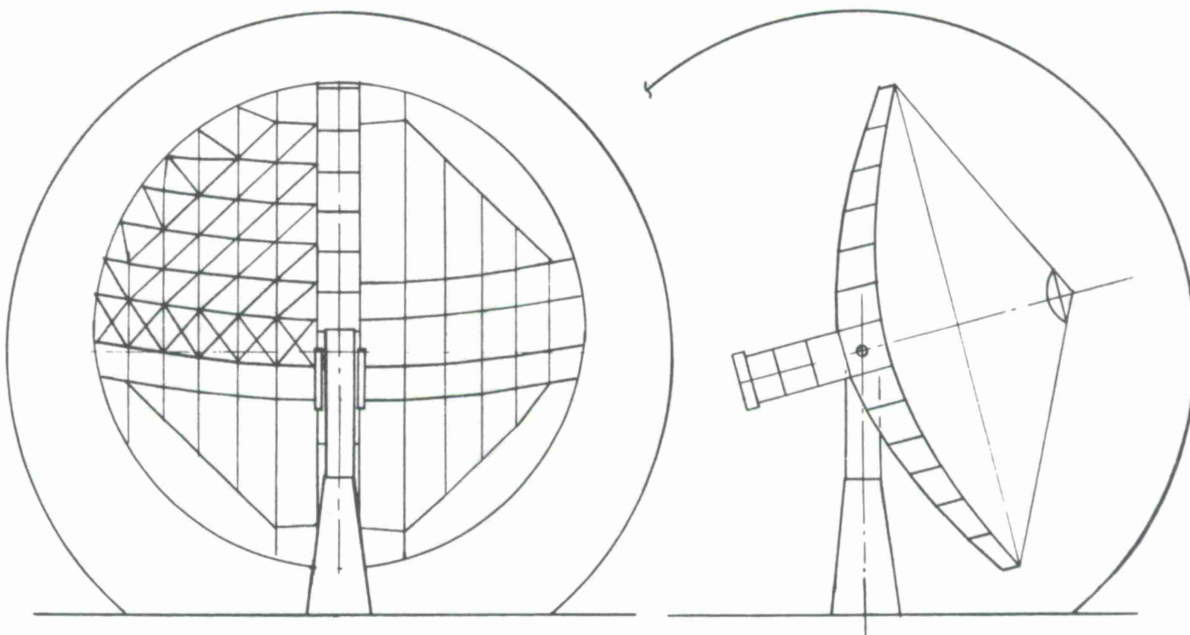


Figure 5. 1. 400-ft-diameter Ammann & Whitney configuration.

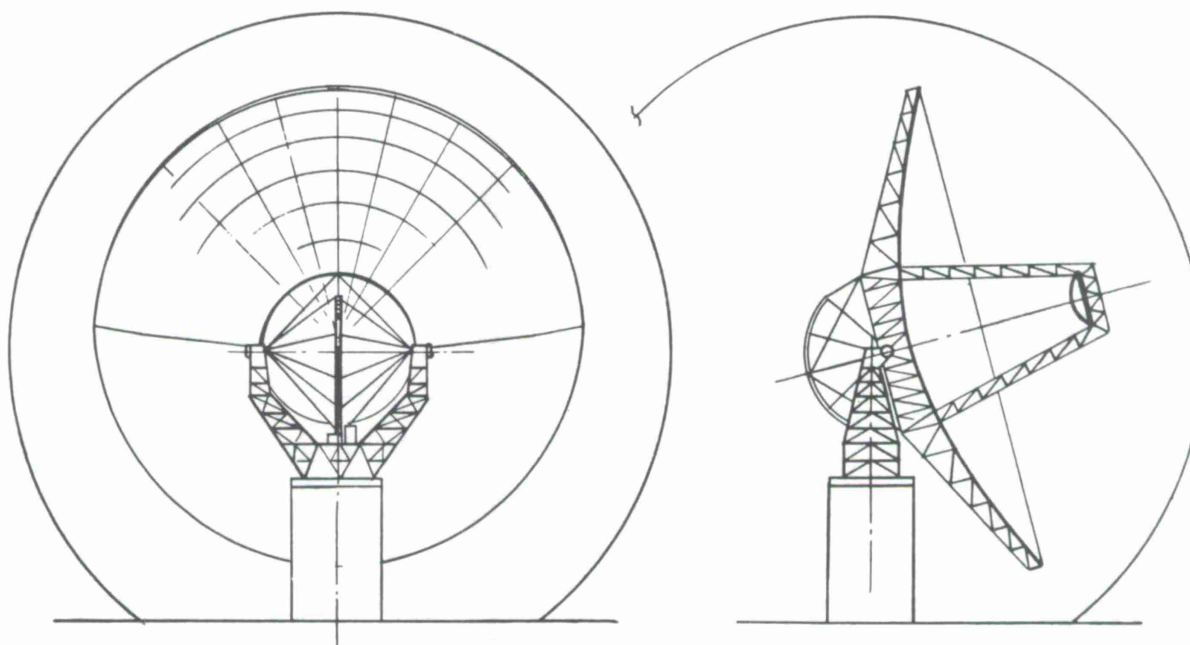


Figure 5. 2. 400-ft-diameter Rohr configuration.

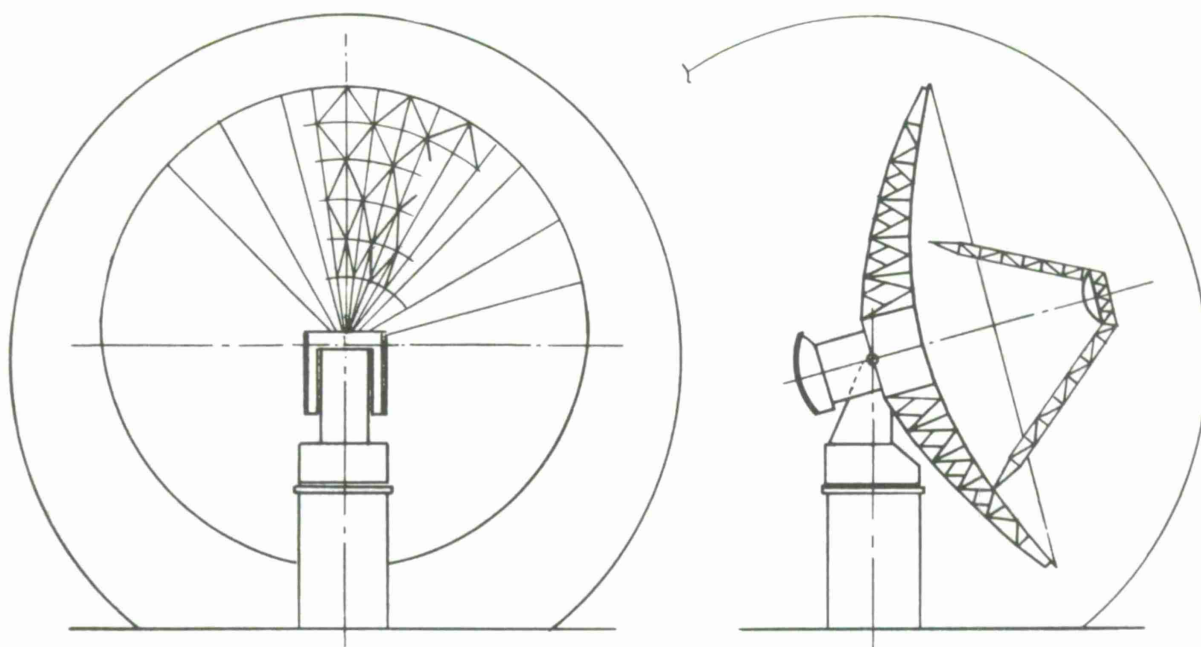


Figure 5. 3. 400-ft-diameter Simpson Gumpertz & Heger configuration.

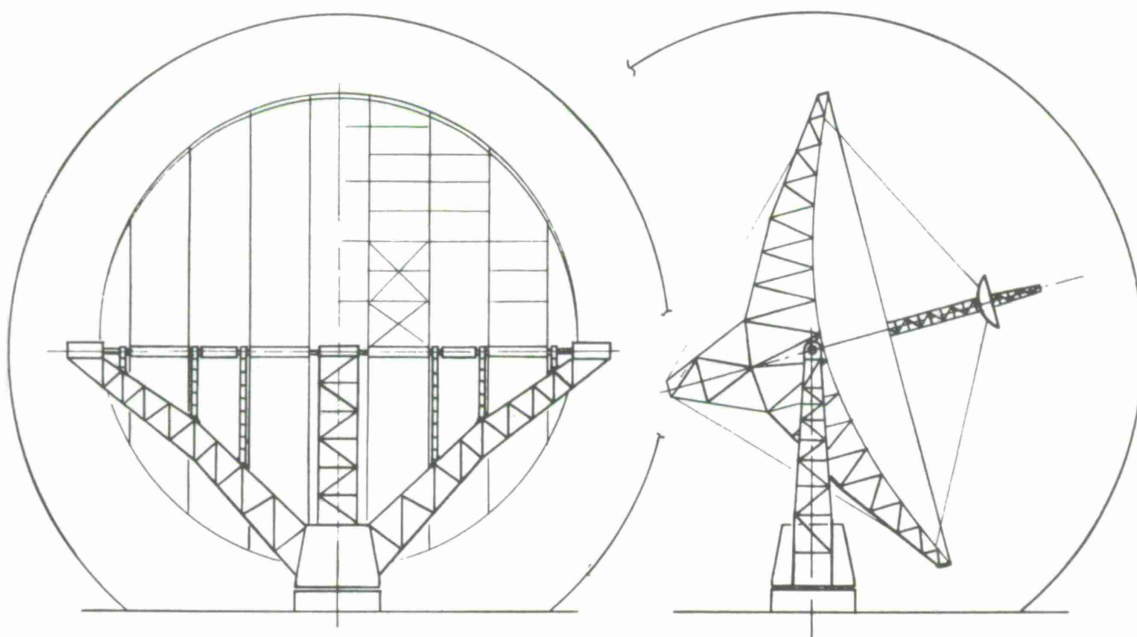


Figure 5. 4. 400-ft-diameter Weidlinger configuration.

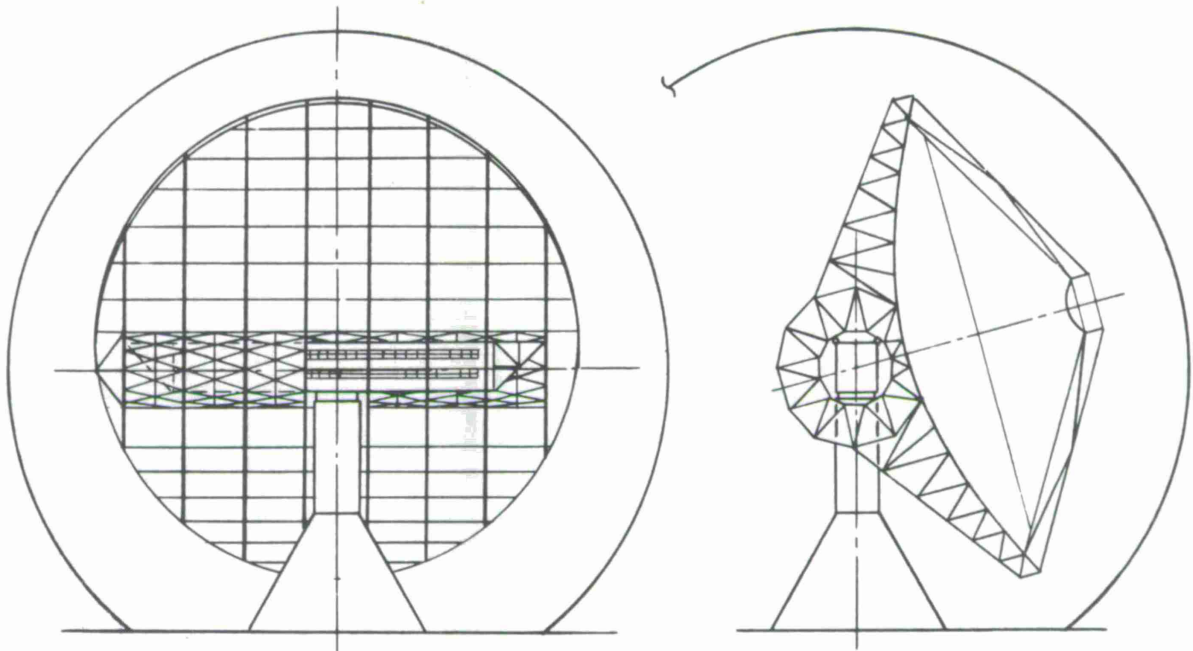


Figure 5.5. 400-ft-diameter "Hammerhead" MIT Lincoln Laboratory configuration.

- 2) Suitability of small-diameter bearing and pedestal. The absence of large overturning moments, the ability to employ a balanced system, and the comparatively light weight of the moving structure permit the use of a comparatively small (30 to 40 ft in diameter) azimuth bearing. This allows the use of small, low-cost foundations and compact pedestals, and helps reduce the stiction and pointing-precision problem.
- 3) Magnitude of uncompensated deflections. When the backup structure of a 400-ft reflector was designed for stress consideration, the deformation of it could easily exceed 1.0-inch RMS (before compensation). The studies have indicated that it is reasonable to design this type of a lightweight backup structure, based only upon strength considerations, and then to compensate for its deflection by the use of open-loop variable displacement or force-control systems in order to meet the specified 0.1-inch RMS surface tolerance.
- 4) Low-horsepower requirements. The absence of variable wind forces and a need for operation at comparatively low rotation and acceleration rates have permitted the use of azimuth and elevation drive components having comparatively low torque and horsepower. A principal design constraint appears to be that of tracking smoothness; but with an appropriate bearing system, probably hydrostatic, the performance requirements can be adequately met with less than 5 hp.

The cost estimates related to the studies are summarized in Section 6.

5.2 Applicability of Other Studies

During the course of the conceptual studies, other parallel work was found to be potentially relevant to CAMROC objectives, although not directly funded by CAMROC. Two of these related activities are summarized below.

5.2.1 National Radio Astronomy Observatory homology study

Dr. Sebastian Von Hoerner of NRAO has been investigating the mathematical concepts underlying the optimum design of a structure that employs "equally soft" support points, so that the structure will deform from one paraboloid to another as it is rotated in elevation. NRAO has developed a computer program that goes through this process directly for structures of limited size. Although specific engineering designs have not emerged from Von Hoerner's studies, his concepts have been provocative and have alerted the structural designers to this different viewpoint. One of the CAMROC studies, the analysis and optimization of the configuration by Simpson Gumpertz & Heger, extends this type of approach to larger, more complex antenna structures that remain essentially parabolic in contour during rotation. Further work along the lines suggested by Von Hoerner could conceivably result in still more efficient structures. The "Homology Concept" is particularly applicable to radome-enclosed antennas, where gravity is the dominant contour-determining effect.

5.2.2 North American Aviation (NRAO-sponsored) floating-sphere study

One design for a large steerable antenna that periodically is suggested for consideration is based on the use of a large rotatable spherical radome that is employed to support an integral paraboloidal reflector system. In this concept, the pointing of the antenna is accomplished by actually rotating the fully spherical radome, which is supported on either a water or an air-flotation system or on a number of discrete hydrostatic pads. This concept, named "The Eyeball," is currently being investigated by North American Aviation, Inc., under a subcontract with NRAO. Several versions were studied at MIT Lincoln Laboratory in 1959-1960.

While the initial impressions of this particular type of antenna system were favorable, more detailed studies revealed a number of basic engineering problem areas that severely influenced the overall feasibility and, more importantly, the cost of this class of system. While the use of an air-pressure bearing instead of a water bearing permitted a better distribution of the sphere weight over the surface of the shell, it did result in the need for substantial amounts of air-blower power and did not drastically simplify the drive and control problem.

Areas of concern with the "Eyeball" configuration are: 1) the transmission of the horizontal wind forces to the foundation, 2) the overturning torque of the sphere resulting from skin friction of the wind, 3) the isolation of the reflector surface from the deformations of the spherical radome, and 4) the introduction of drive forces and electrical power to the sphere.

There appear no unique attributes of this type of configuration that greatly simplify the use of reflector-compensation techniques or that give it any special advantages over a conventional Cassegrain antenna and separate radome combination. Based on what is known about this type of configuration, it was evident that the movable radome and its pointing mechanism would be substantially more costly than a stationary radome, and that the savings that would be gained by the integrated paraboloidal surface would be lost in maintaining this surface within the required accuracy.

6. COST ESTIMATES FOR ANTENNAS AND RADOMES

It is important to consider the performance characteristics of the CAMROC antenna so that its cost may be put in proper perspective. With a diameter of 400 ft, it will have approximately 2-1/2 times the area and 10 times the precision of the largest fully steerable antenna now in operation (Jodrell Bank). It will also have approximately 3-1/2 times the area and 2-1/2 times the surface precision of the recently completed 210-ft-diameter Goldstone antenna of Jet Propulsion Laboratory. Previous studies have shown that the cost of an exposed fully steerable antenna will increase proportional to the antenna diameter raised to the 2.5 power (the exponent on the diameter may vary from $D^{2.3}$ to $D^{2.7}$ depending upon the required precision and environmental constraints) times the reciprocal of the allowable surface tolerance. Following conventional designs, the proposed CAMROC antenna would be costly.

The most relevant cost experience to use for comparative purposes is that of the recently completed 210-ft Goldstone antenna, since we are concerned with U. S. costs and not with those in Germany, Britain, or Australia. If the \$13 million cost of this antenna were scaled to allow for its change in diameter to 400 ft in accordance with a conservative $D^{2.3}$ scaling relationship, the cost would exceed \$40 million (see Appendix A) even if the tolerance remained at 0.25 inch. This cost would increase substantially if it were possible to build a 400-ft structure with a precision of 0.1 inch instead of 0.25 inch and, at the same time, to improve the pointing precision by the required factor of 5. There is considerable engineering evidence that technical limitations would preclude the achievement of the CAMROC design goals even in moderate wind conditions with a 400-ft exposed antenna. While this conclusion may seem somewhat surprising, it should be recognized that the CAMROC performance requirements are very stringent because of the desire to operate at wavelengths as short as 5 cm. This short wavelength calls for a reflecting surface that is essentially solid (holes must be no larger than 0.25 inch), and the wind, snow, and ice loads that this structure, with its large surface area, would have to sustain would be essentially equivalent to those of a solid-surface structure.

During the past 6 months, the first firm information regarding the cost of 300- to 500-ft fully steerable precision antennas and radomes has become available. With these data, it is now apparent that, when a radome is used, the reduction in the cost of a 400-ft 0.1-inch RMS tolerance antenna is so substantial when contrasted to an exposed antenna that, even with the cost of the radome included, there still remains a very significant saving. Perhaps of equivalent significance is the engineering evidence, which indicates that antennas fulfilling the CAMROC goals can be constructed at low engineering risk and without the utilization of exotic materials, massive tonnages, or unusual fabrication techniques.

Each of the five groups working on antenna-concept studies was asked to prepare cost estimates for its specific reflector configuration, based upon a diameter of 400 ft and a surface tolerance of 0.10-inch RMS, and to evaluate the variation of antenna cost with moderate changes in diameter and surface tolerance. Because the study teams employed different costing procedures and item breakdown for their estimates, the cost information from each configuration report has been normalized and collated into this section.

One unexpected outcome of the five configuration studies has been the general similarity in the overall basic characteristics that each group considered appropriate for a radome-enclosed antenna. For example, each team recommended a minimum-weight design, a small azimuth bearing, low-horsepower drives, and lightweight surface panels; each design successfully achieved contour compensation at a small cost. Consequently, the cost estimates for each of the configurations do not differ greatly and can be reasonably well represented by the itemized cost breakdown shown in Table 6.1. Since the cost analysis of the Hammerhead effort was more complete than those available from the other four configuration studies, it has been used as the basis for the costs in Table 6.1. It is interesting to note that the variation in the antenna costs based upon the comparative weights for the different configuration is surprisingly small (less than 20%), as can be seen in Table 6.2.

The radome costs shown in Table 6.1 are derived from those given in Section 8 of this report, with the main difference being the addition of cost estimates for the air-circulation and heating systems. The radome used in this study is a 0.75 sphere 550 ft in diameter, which is compatible with a 400-ft antenna. As shown in Table 6.1, the engineering and engineering supervision costs do not vary significantly with diameter. This was done since it was felt that the engineering task actually varies only slightly with size since the same calculations and analyses must be performed. For this reason, the cost of 400 ft was developed and then reduced or increased slightly for 300 and 500 ft.

The variation of the antenna and radome costs versus size, based upon the data in Table 6.1, is plotted in Figure 6.1. The summation of these two curves gives us a total structural-mechanical system cost, as shown in Figure 6.2.

By way of comparison, the Rohr study (see Appendix A) to evaluate the influence of the radome on antenna cost, showed that a radome-enclosed antenna would cost substantially less than an exposed antenna. The shaded region in Figure 6.2 spans the range of estimates of the cost of an exposed 400-ft antenna with a 0.1-inch RMS tolerance. It is based on the previously discussed cost-versus-diameter relationship of $D^{2.3}$, modified to allow for the increased precision.

Table 6.1. Estimate of cost versus size

<u>Item</u>	<u>Primary reflector diameter (ft)</u>		
	<u>300</u>	<u>400</u>	<u>500</u>
1. Primary reflector	\$ 941,000	\$ 1,934,000	\$ 3,087,000
2. Secondary dish	56,000	100,000	195,000
3. Reflector support structures	56,000	127,000	243,000
4. Laboratory space behind reflector (300 ft ²)	94,000	94,000	94,000
5. Tower, foundation	170,000	372,000	693,000
6. Azimuth bearing	165,000	262,000	385,000
7. Azimuth drive	64,000	74,000	85,000
8. Elevation bearing	427,000	703,000	1,051,000
9. Elevation drive	96,000	106,000	116,000
10. Miscellaneous items	<u>1,050,000</u>	<u>1,233,000</u>	<u>1,433,000</u>
Construction Total	3,119,000	5,005,000	7,382,000
Engineering	1,000,000*	1,250,000*	1,600,000*
Engineering supervision	700,000*	850,000*	1,100,000*
Contingency 25%	<u>1,200,000</u>	<u>1,775,000</u>	<u>2,520,000</u>
Grand Total	6,019,000	8,880,000	12,602,000
<u>Radome diameter (ft)</u>			
	<u>412</u>	<u>550</u>	<u>688</u>
1. Radome structure	\$ 2,536,000	\$ 4,734,000	\$ 8,036,000
2. Air circulation and heating	<u>566,000</u>	<u>1,000,000</u>	<u>1,566,000</u>
Construction Total	3,102,000	5,734,000	9,602,000
Engineering	650,000*	700,000*	800,000*
Engineering supervision	200,000*	300,000*	400,000*
Contingency 25%	<u>1,000,000</u>	<u>1,685,000</u>	<u>2,700,000</u>
Total Radome Cost	4,952,000	8,419,000	13,502,000
Total Antenna and Radome	\$10,971,000	\$17,299,000**	\$26,104,000

* The cost of the engineering and engineering supervision for radome-enclosed antennas in the 300- to 500-ft size range does not depend strongly on the diameter.

** At this phase in the CAMROC study program, the cost projection of 19.5 million for the antenna-radome system is valid for planning purposes. ("An Interim Report on Feasibility and Cost Studies of Radome Enclosed Large Radio-Radar Telescopes," CAMROC Report, September 1966).

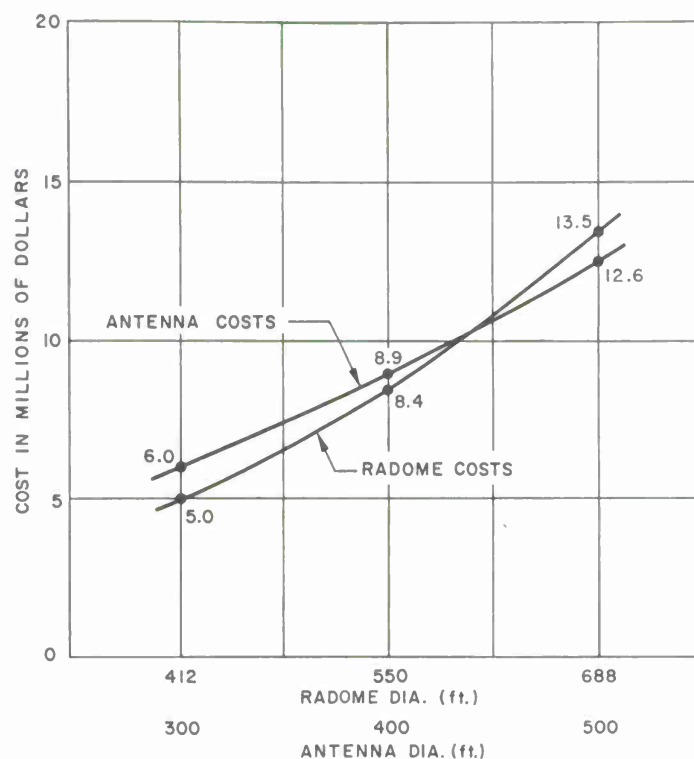


Figure 6.1. Estimated cost for a protected antenna and its radome versus diameter.
Notes:

- 1) Excludes real estate and RF equipment.
- 2) Radome costs are based on a 0.75 sphere with coincident axes of antenna and radome.

Table 6.2. Variation of antenna cost estimates

Costs from all studies (in millions of dollars)				
	Lincoln concept	Minimum	Maximum	Average cost
Antenna costs	8.9	8.4	10.4	9.2
Radome costs	8.4	8.4	8.4	8.4
Total	17.3	16.8	18.8	17.6

From the data in Figure 6.2, it can be seen that the cost of a radome-enclosed antenna will be very much lower than that of a comparable exposed antenna. At a diameter of 400 ft, the structural-mechanical systems costs are estimated to be \$17.3 million for the CAMROC installation, whereas those for an exposed antenna would exceed \$80 million. Even at this high cost, the pointing accuracy of the exposed antenna would not meet the CAMROC requirements in modest winds.

Another task during these studies was the derivation of cost versus surface tolerance for various antenna diameters. For the case of environmental antennas, it has been found that, at a given diameter, cost is an inverse function of tolerance. In the case of the CAMROC study, the various concepts must be discussed separately, since this relationship varies with the compensation techniques used. The Simpson Gumpertz & Heger study states that with its concept, which uses no compensation, cost is an inverse function of tolerance. This is as expected, since in this respect the configuration is similar to that of an exposed antenna. At the other extreme is the Ammann & Whitney study, which completely relies on compensation. Here, costs do not vary with tolerance so long as the required tolerance remains within the tolerance limits of the jacking system (RMS = 0.064 inch). To achieve a better surface accuracy than this would require a more precise system of jacks and controls, and thus there would be a step in the cost curve when this tolerance was exceeded.

The other studies use partial compensation and lie somewhere between these two conditions. No attempt has been made to evaluate fully the equation of this curve other than to conclude that it rises quite slowly, since tolerance in these cases can be improved by a redistribution of material, improvement in control tolerance, and a reduction in panel tolerance.

The curves for cost versus surface accuracy are shown in Figure 6.3 for a diameter of 400 ft. The fully compensated concept is constant (\$8,400,000) until the required tolerance reaches 0.064-inch RMS, at which point there is a step in the cost curve. The partial-compensation concepts (\$8,900,000 at 0.10-inch RMS) are shown only as a slightly sloping line and have not been truly derived from cost estimates. The no-compensation concept is shown as an inverse function of the tolerance, and the cost of this concept was estimated to be \$12,000,000 (at an RMS of 0.10 inch).

All the five studies, which were conducted independently, clearly establish the major savings in cost of the antenna-radome system over an exposed antenna of equivalent size.

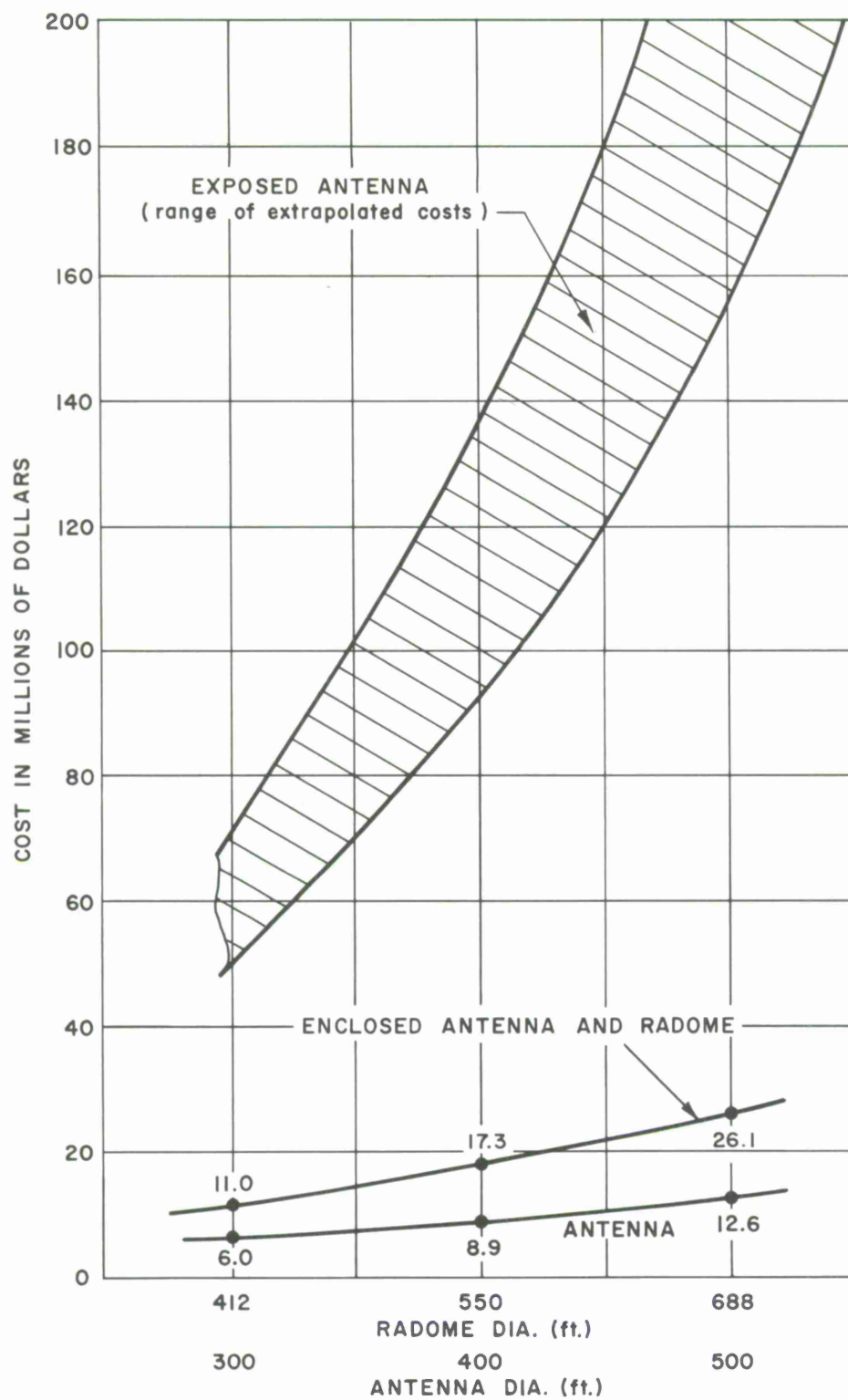


Figure 6.2. Costs for exposed and radome-enclosed antennas (0.10-inch RMS).

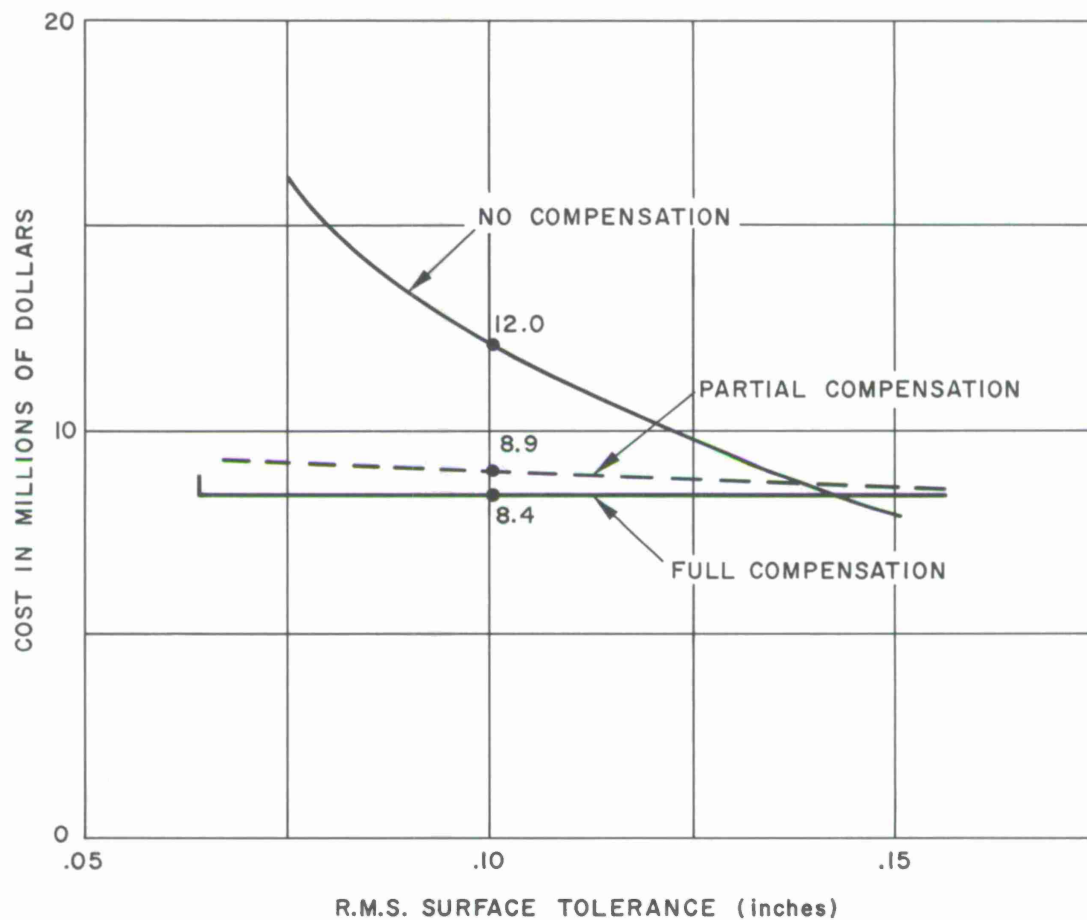


Figure 6.3. Antenna cost versus tolerance at 400 ft in diameter. Notes:

- 1) Based on 1966 costs, excluding real estate and its development costs, RF equipment, and radome.
- 2) The no-compensation curve is based on conservative cost estimates.

7. ELECTROMAGNETIC PROPERTIES OF SPACE-FRAME RADOMES

7.1 The Electromagnetic Properties of Large Radomes (Metal Space Frames)

The electromagnetic effects of a metal space-frame radome stem from factors that affect the radiative or receptive properties of the enclosed antenna. The major effects, such as loss of gain and a small increase in noise temperature, can be quantitatively calculated. The other effects are so small that they cannot be estimated and, owing to inherent instrumental effects in the antenna itself, can be measured only with considerable difficulty, if at all.

The electromagnetic effects of radomes must be balanced against the beneficial effects described in previous sections. Further, the importance of these effects must be evaluated in relation to the type of measurements to be performed and the inherent limitations of an unprotected antenna. As an example, the loss of gain must be considered in light of the fact that the radome permits us to build a larger and more precise antenna at a lower cost. In the same manner, the small increase in noise temperature must be evaluated in terms of the increase in operating time of the radome-enclosed antenna, and the more precise surface (higher gain) and pointing that can be achieved for many experiments.

In the following sections, we discuss the various electromagnetic radome effects, pointing out the extent of our knowledge and indicating areas where additional work is proceeding. In giving calculated and experimental data on the 150-ft Haystack radome, the structure that has been most thoroughly investigated, it should be realized that this radome was designed many years ago for stringent military use in the Arctic. A modern space frame, optimized by computer structural computation and designed for normal wind specifications, would have lower antenna-aperture blockage, which would result in a proportionately lower loss, less scattered energy, and lower noise temperature. It can also be expected that minor effects that are barely measurable in the Haystack system would become negligible.

7.1.1 Loss of antenna gain

The loss of enclosed antenna gain occurs in two ways: 1) blockage of the antenna aperture by the metal space-frame members, and 2) energy reflection and absorption from the radome dielectric membrane.

7.1.1.1 Space-frame blockage

The metal space-frame members shadow or block a portion of the antenna radiating aperture. This fraction therefore detracts from the antenna axial field. Figure 7.1 shows the aperture blockage of a precise model of the Haystack radome obtained by photographic means. It is evident that the radiating aperture is obscured by a network of members. In evaluating this photograph we should also consider that all antennas inherently suffer from aperture blockage by their feeds and feed supports. Figure 7.2 shows this feed shadowing for the Haystack antenna.

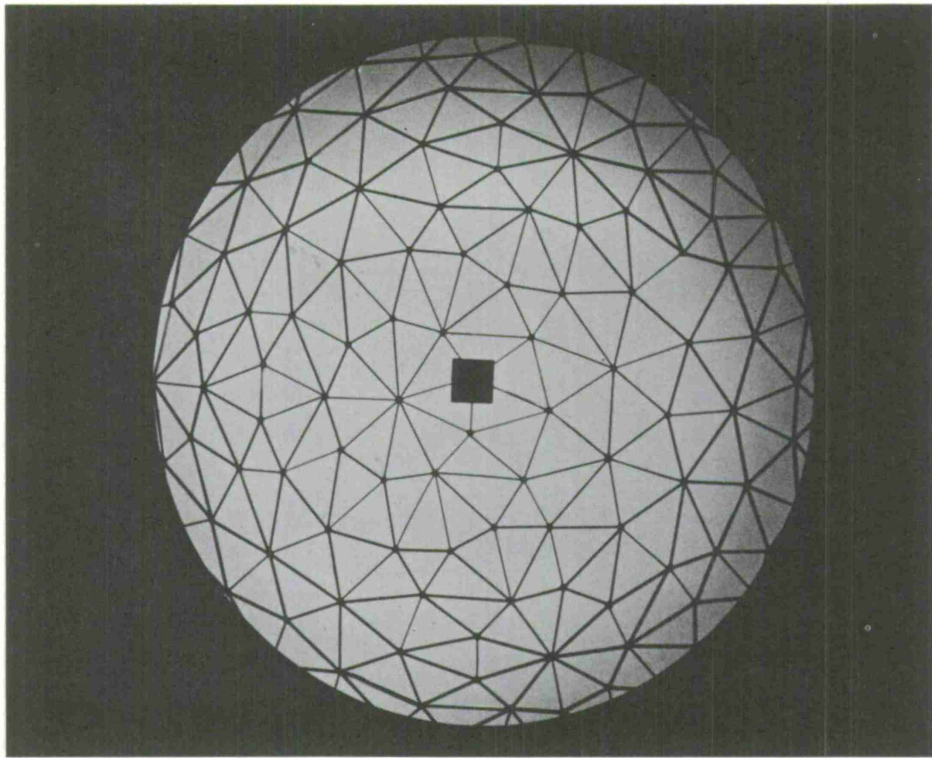


Figure 7.1. Shadowgraph of a metal space-frame radome.

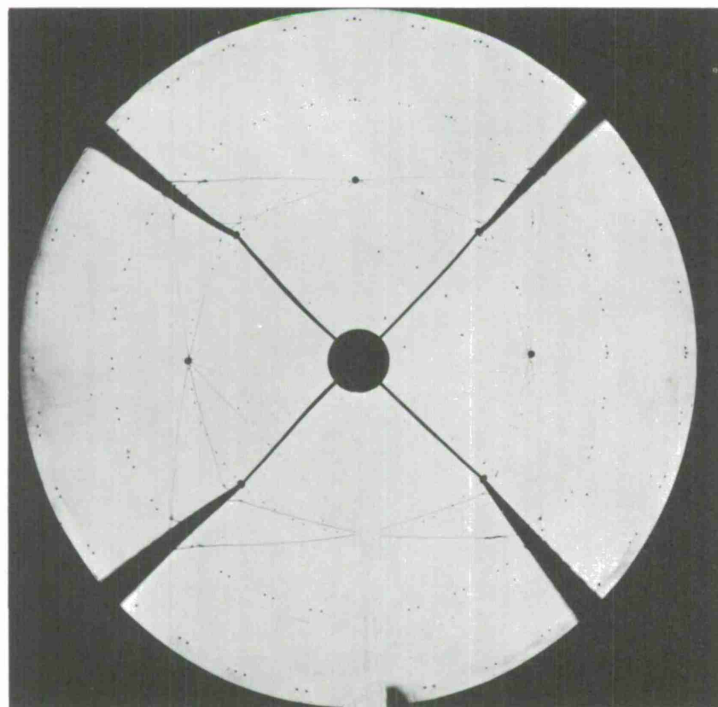


Figure 7.2. Shadowgraph of antenna feed-support system.

In the CAMROC system, the subreflector will be about 40 to 60 ft in diameter and the feed supports about 200 ft long. In an outdoor antenna, this feed system must be designed for survival conditions. A radome enclosure will reduce the bulk of the feed-support blockage and in part compensate for the inherent radome space-frame blockage.

In the short wavelength or optical limit, if the radome is assumed a flat sheet, the fractional loss of gain is simply twice the fraction of the area blocked, or

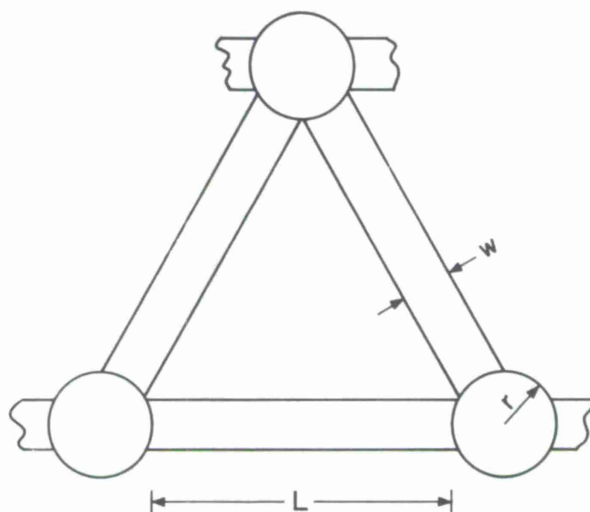
$$\frac{\Delta G}{G} = 2\eta \quad (1)$$

This flat plain blockage naturally depends on the size (width) of the members and on the openness of the structure, that is, the average member length.

A reasonably accurate formula (exact for equilateral triangles and 2% in error for member lengths varying $\pm 10\%$) (see Figure 7.3) is

$$\eta = \frac{2\sqrt{3} w}{L} \quad (2)$$

where w is the width of the members, and L is their average length.



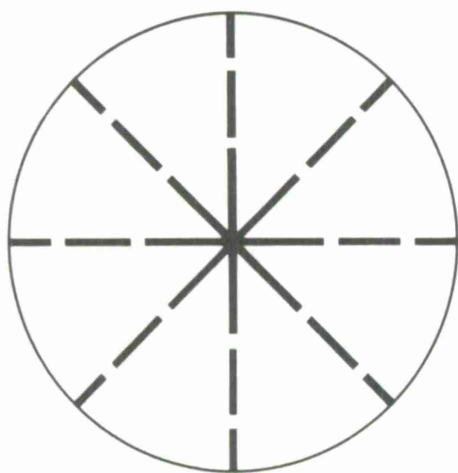
$$\text{BLOCKAGE} = \frac{2\sqrt{3} w L}{(L + 2r)^2} + \frac{2\pi}{\sqrt{3}} \left(\frac{r}{L + 2r} \right)^2 = \eta_m + \eta_h$$

Figure 7.3. Geometry for blockage calculation.

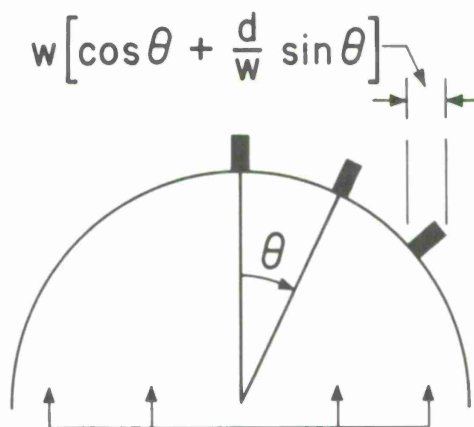
It is obvious that, for low blockage, we wish to make the members thin and the cell size large.

For the practical spherical radome, the above formulas must be modified by a curvature factor. This factor arises in a number of ways (see Figure 7.4):

- 1) Members lying along great circles through the beam axis are foreshortened by the cosine of the angle of incidence when projected on the antenna aperture. Their blockage effect is therefore reduced.
- 2) Members orthogonal to these great circles appear more concentrated at the edge of the aperture by the cosecant of the incident angle (venetian-blind effect). These members therefore increase the aperture blockage.
- 3) Members orthogonal to the great circles are further viewed from the side at the aperture edge.
- 4) Finally, these effects, which are radially dependent, must be weighed by the aperture illumination function.



GREAT CIRCLE MEMBERS



PLANE WAVE

ORTHOGONAL MEMBERS

Figure 7.4. Limiting disposition of members.

The curvature factor can be obtained from prepared curves (given in Annex 1) for a given radome-to-antenna-diameter ratio and for a specified member depth-to-width aspect ratio. These curves assume that the number of members in the aperture is large and that they are uniformly distributed over the aperture. Alternately, the spherical optical blockage can be exactly computed by an electronic computer projection program.

Equations (7-1) and (7-2), modified by the curvature factor, then give our estimate of the high-frequency effective-aperture blockage and of the loss of axial gain. Typical values for a 150-ft metal space frame are:

<u>Effective Optical Blockage</u>		
	η_e	Gain loss
Haystack	11%	1.0 db
Modern space frame	4%	0.4 db

At longer wavelengths, the effective blockage increases as the scattering cross section of members parallel to the electric vector is greater than the optical cross section. Since this increase is greater than the decrease in the orthogonal-polarization case, the average scattered energy of a large number of randomly oriented members rises as the frequency drops.

For circular members, this relative scattering cross section can be precisely calculated. In Figure 7.5 we show this result for the two polarizations and their average. It should be noted that the average scattering cross section is equal to the optical cross section as long as the wavelength is less than 10 times the cylinder diameter. The scattering cross section of rectangular and special-shaped members can be calculated by numerical integration, and the result is shown for the former in Figure 7.6. In general, the relative cross section increases with member depth; however, deep members can be made thinner or longer, owing to their greater structural strength.

At times, suggestions have been made that specially shaped members, elliptical or ogival, would considerably reduce the radome-scattered power. The use of such members does not appear very promising; calculations for elliptical cylinders show only a nominal reduction over rectangular members of the same depth-to-diameter ratio (in fact, a disadvantage when structural strength is considered). Furthermore, the attachment of the radome membrane to such shaped members becomes a problem.

On the basis of the above analysis and similar work,^{1,2} the metal space-frame loss can be estimated at the frequencies of interest.

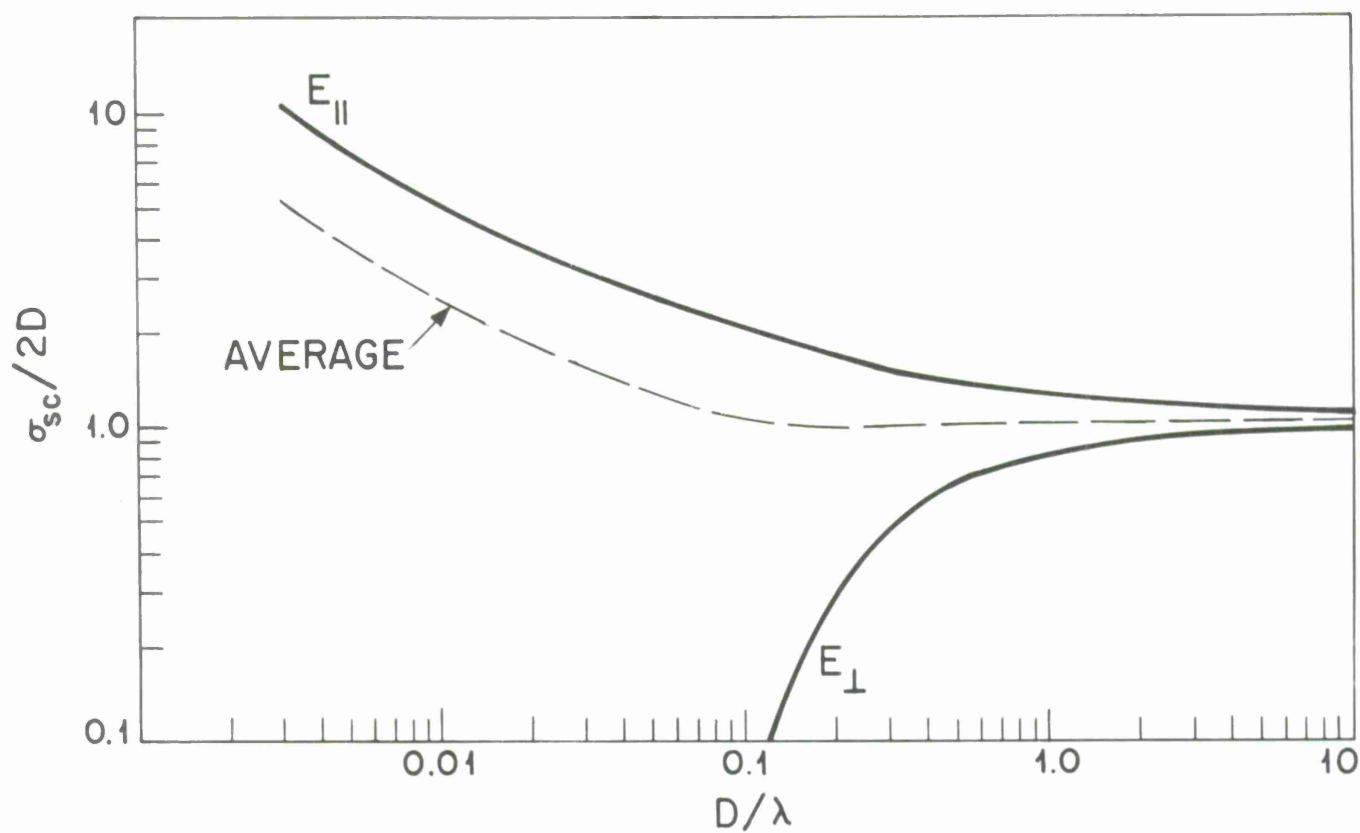


Figure 7.5. Total scattering cross section, round metal cylinders.

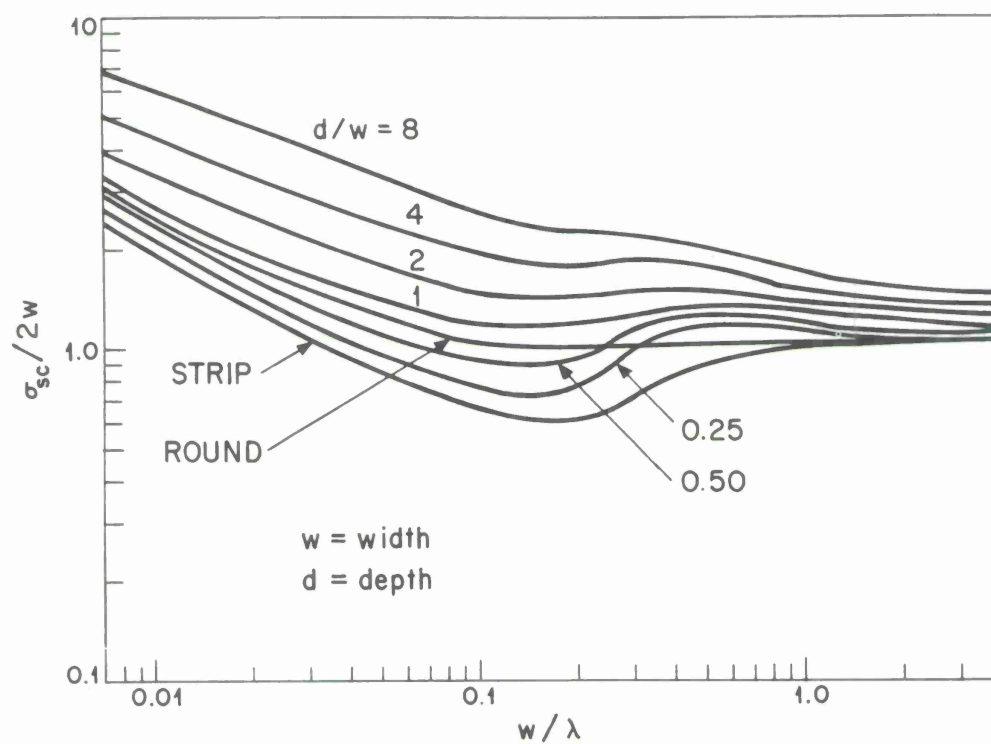


Figure 7.6. Total average scattering cross section, rectangular cylinders.

The radome loss can also be electrically measured. Such measurements are not practical on the full-scale installation, because the radome can generally not be removed. Even for smaller radomes that can be removed, the precision of measurement is not sufficient, owing to the time interval between measurements. Radome-loss measurements are therefore made on a model basis at a scaled higher frequency. To obtain precise loss information, an accurately scaled model of half the radome is periodically rotated in front of the radiating antenna. Figure 7.7 shows an experimental setup.

These model loss measurements have their limitations, namely:

- 1) Accuracy is probably no better than 0.05 to 0.10 db. This is due to the stability of the equipment and to heat waves over the transmission path.
- 2) The required scaled frequency sets a limit on the range over which measurements can be made, owing to the availability of stable signal sources of sufficient output -- that is, to measure the Haystack loss at 2 cm with a 10-ft scaled radome requires a signal source of 1.33 mm (225 Gc/sec).

Figure 7.8 shows a typical experimental run on the 10-ft Haystack model. The region where the antenna is unobstructed and then completely covered is evident. Since the measurement is made rapidly, the accuracy depends largely on the short-term equipment stability and on our calibration-standard attenuators.

Figure 7.9 shows the results of a number of measurements on the Haystack radome and on a modern 160-ft space frame. Comparison is made with the theoretical predictions, which appear pessimistic by about 10%. However, it would appear that the theoretical space-frame loss values are very good estimates and may be used to evaluate structural designs.

The question naturally arises, "What metal space-frame loss are we to expect on a CAMROC system with a 550-ft radome and a 400-ft antenna?" The answer naturally depends on the structural design, on the required safety factors, on the permissible stress levels, and on the provisions made for radome buckling under severe conditions. Designs proposed by structural engineers under the CAMROC program have been analyzed for metal space-frame loss (see Figure 7.10). These indicate that, if rectangular steel members are used (4-5 inches wide and 15 inches deep) with an average length of 30 ft, the field loss (voltage) would be about 8%, or a little less than 0.8 db (nominal wind specifications, 130 mph). This loss may be reduced by a greater certainty in the buckling criteria or by lower wind specification, and it may be increased by a desire for a higher safety factor. Until a final design is available, no more definite figure can be given.

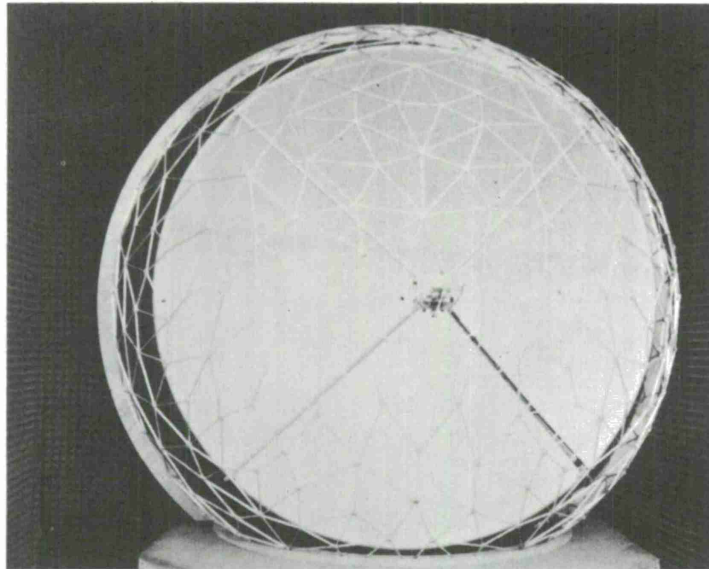


Figure 7.7a. Test antenna and model radome as used for pattern and loss measurements through the radome.

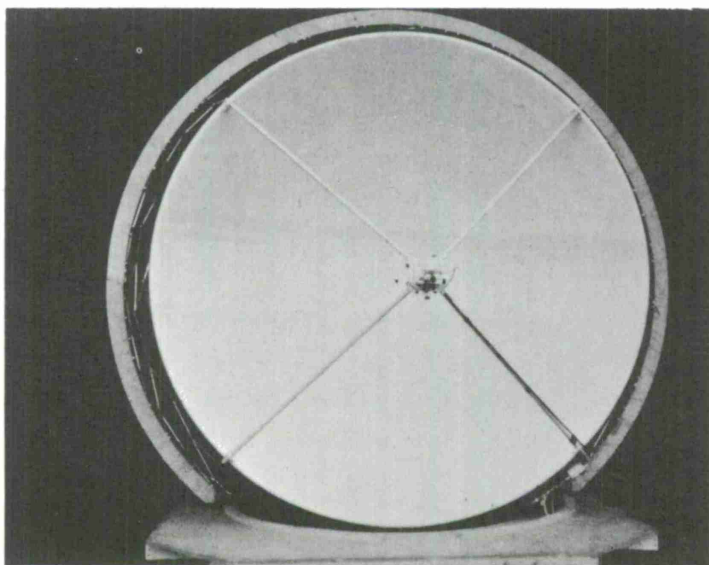


Figure 7.7b. Test antenna with radome in off position.

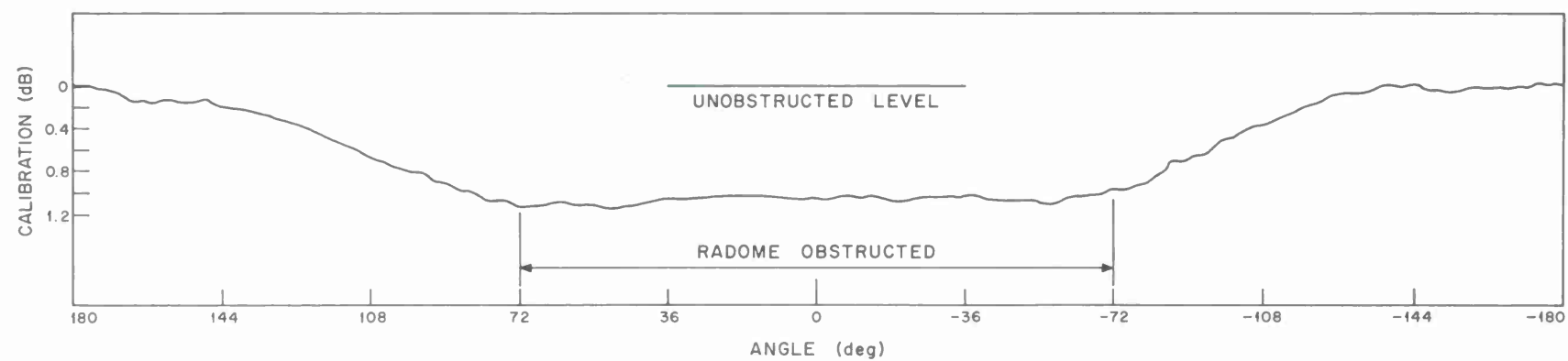


Figure 7.8. Haystack vertical polarization loss.

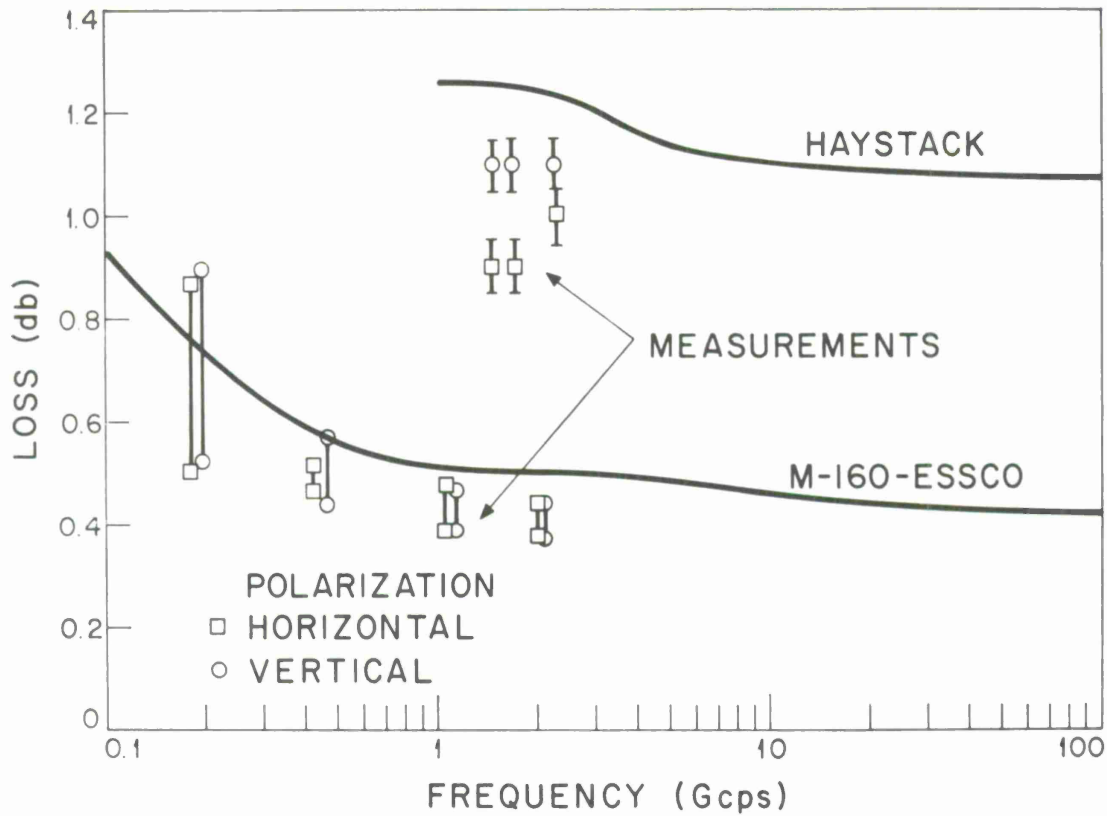


Figure 7.9. Metal space-frame loss, theoretical (heavy lines) and experimental.

7.1.1.2 Membrane losses

The membrane (metal space-frame covering) loss has two components, namely, an ohmic and a reflection loss.

a) Ohmic loss. For a thin dielectric loss panel, the fractional energy absorbed is

$$\frac{2\pi}{\lambda} \tan \delta$$

For impregnated Fiberglass panels, 0.050 inch thick, we have ($\epsilon = 4.0$, $\tan \delta = 0.01$) at 6000 Mc/sec:

$$\frac{2\pi}{\lambda} (0.05\sqrt{4} (0.01)) = 0.003 ;$$

that is, for the usual radome material, the panel ohmic loss expected for the CAMROC system is less than 0.015 db.

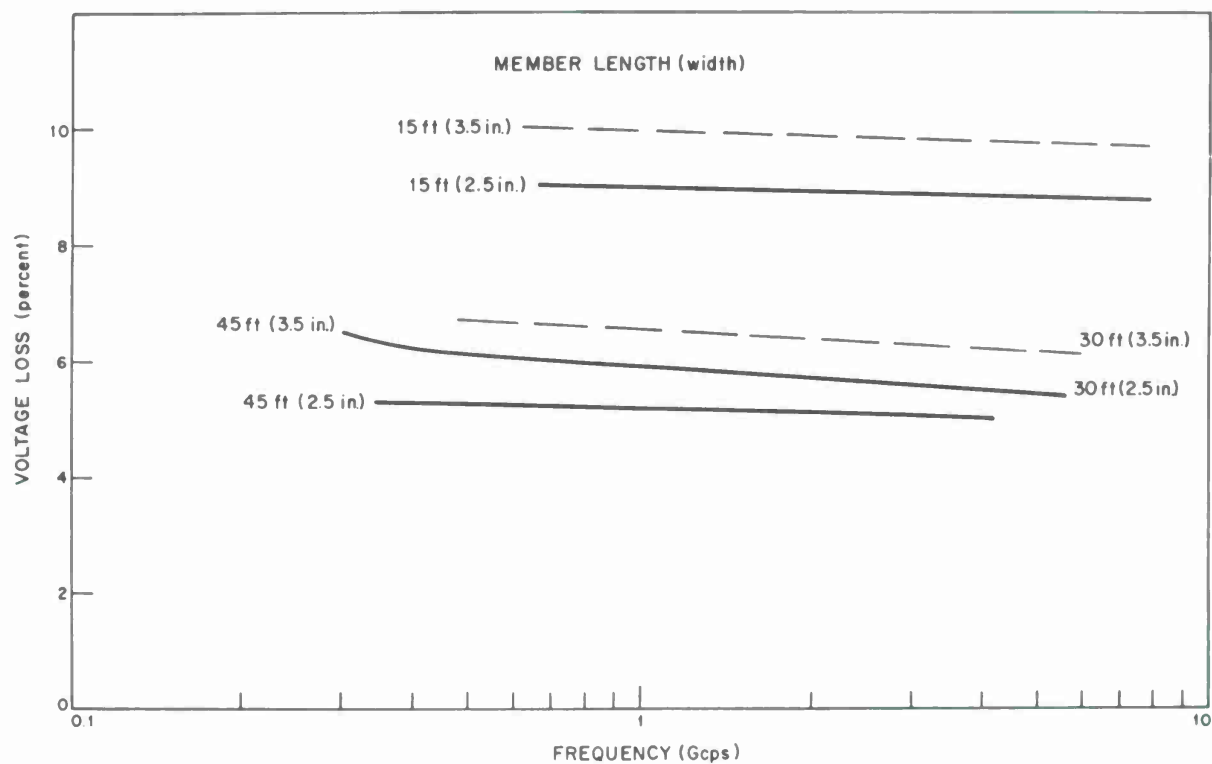


Figure 7.10a. Member voltage loss. Radome, 550 ft; antenna 400 ft; antenna, taper 12 db.

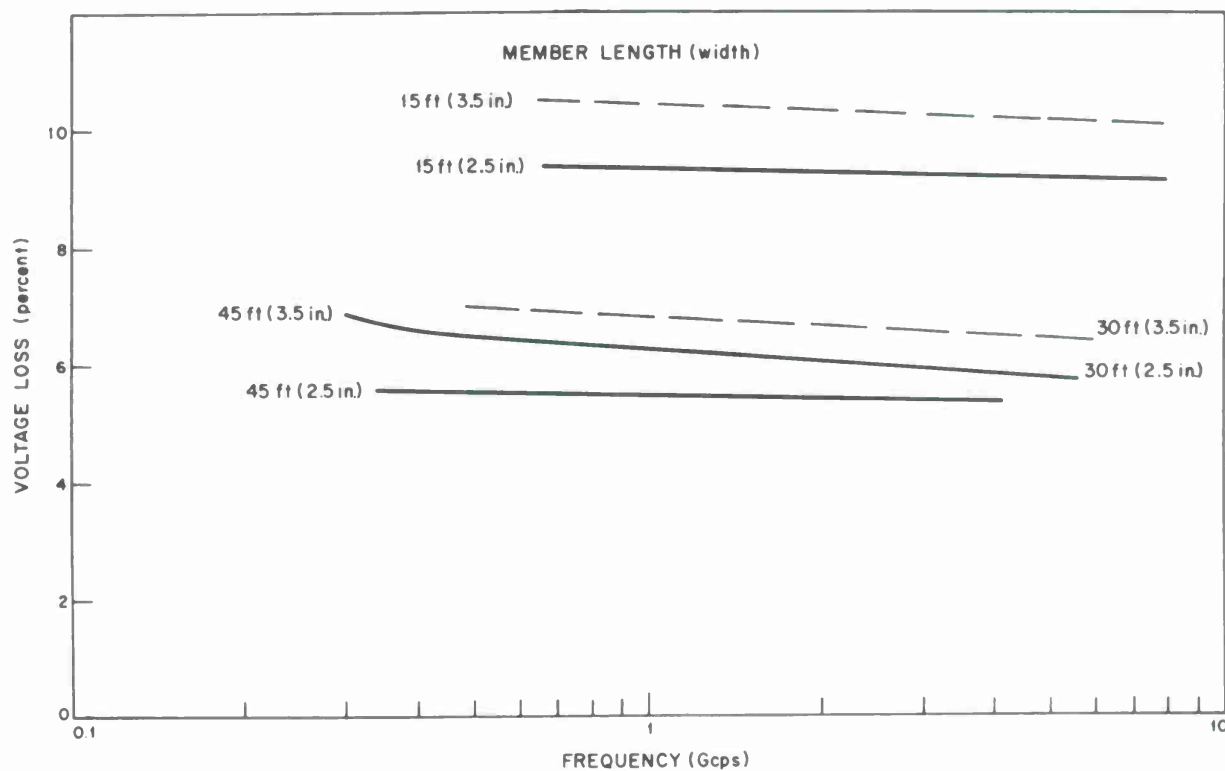


Figure 7.10b. Member voltage loss. Radome, 550 ft; antenna, 400 ft; antenna, taper 0 db.

b) Reflection loss. The power reflected from a thin dielectric panel is given by

$$|p|^2 = \frac{(\pi\delta)^2}{\lambda} (\epsilon - 1)^2 .$$

For the suggested CAMROC panels, we have (at 6000 Mc/sec)

$$|p|^2 = \frac{(\pi \times 0.050)^2}{2} (4 - 1)^2 = 0.055 \text{ (0.25 db)} ;$$

that is, the reflected power is about an order of magnitude greater than the absorbed power. However, it decreases as the square of the frequency and therefore will be negligible over the lower half of the operating band. The loss calculated is at normal incidence. For a spherical membrane the loss increases in one plane and decreases in the other. It has been shown that the average loss is very close to that calculated at normal incidence.

c) Membrane astigmatism. Owing to the sphericity of the radome, the transmission through the radome membrane depends slightly on the relation of the polarization vector to the local plane of incidence. The emergent phase front then has a slight aberration. Because the phase error has different signs in the two principal planes, the effect is similar to astigmatism in optics.

Calculations on the suggested CAMROC panels would indicate a gain reduction factor of about 0.9975 (about 0.01 db); this is at 6000 Mc/sec and would become correspondingly smaller at lower frequencies.

d) Membrane-thickness variation. Inherent variation in the thickness of the membrane panels, due to the manufacturing process, will produce phase errors in the emergent wave front. This effect is identical to surface-tolerance errors on the enclosed antenna and may be similarly calculated.

Assuming nominal 50-mil Fiberglas panels with a 5-mil standard deviation in thickness, we would then have for the loss-of-gain factor

$$\frac{G}{G_0} = 1 - \left(\frac{2\pi\Delta t}{\lambda}\right)^2 = 1 - \left(\frac{2\pi \times 0.005}{2}\right)^2 = 0.9997 ,$$

an entirely negligible quantity.

7.1.1.3 Gain loss due to boresight error

Radome boresight shifts have been extensively investigated for military tracking radars. By use of split-beam techniques on a model basis and by observation of the tracking jitter obtained, indications are that the radome boresight shifts are about 1/200 of a beamwidth.

This angular shift is an order of magnitude smaller than that due to the angular-tracking precision of the enclosed antenna and amounts to about a 0.00025-db gain loss.

7.1.1.4 Total gain loss

Tabulating the above losses, we have

Space-frame blockage	0.8	db
Membrane losses		
Ohmic	0.02	db
Reflection	0.25	db
Astigmatism	0.01	db
Thickness variation	0.002	db
Boresight shift	<u>0.0003</u>	<u>db</u>
Total	1.1	db at 6000 Mc/sec

The principal losses are the space frame, which is essentially independent of frequency, and the membrane reflection, which depends on the square of the frequency. Figure 7.11 shows the frequency independence of these losses for the higher loss Haystack system.

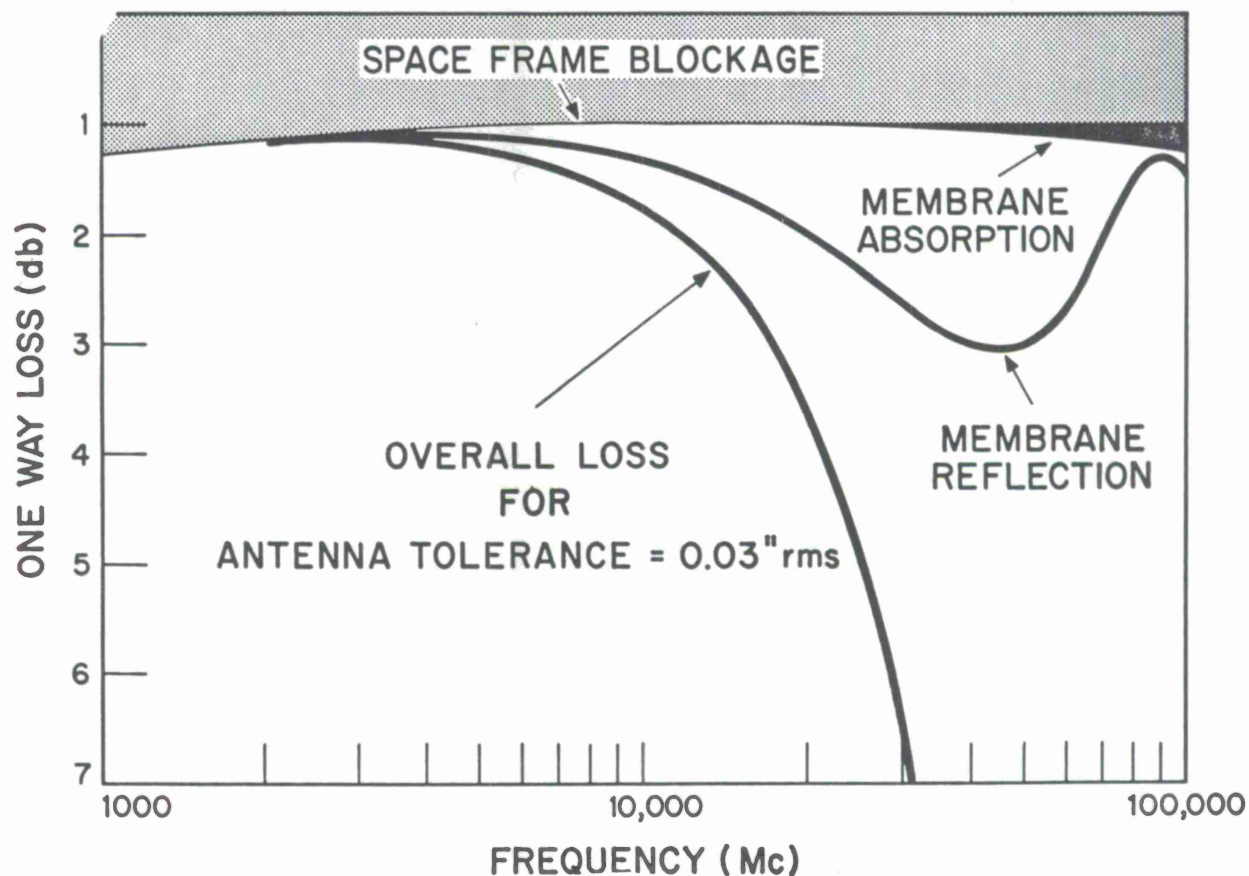


Figure 7.11. Haystack radome and reflector losses.

7.1.2 Antenna pattern degradation

Since the metal space frame scatters and the radome membrane reflects a portion of the incident energy, the directive pattern of the enclosed antenna is modified. As this energy is removed from the desired beam, the result is a loss of axial gain, as discussed in the previous section.

The spatial energy distribution of an ideal antenna is really quite good, with nearly 100% of the radiated energy being concentrated in an angular cone enclosing the main beam and the first few side lobes. By an ideal antenna we mean one where

- 1) All the input energy appears in an in-phase aperture and preferably with some illumination taper. This implies that the parabolic surface has no profile errors.
- 2) There is no aperture blockage.

Antennas that approach this ideal, like a large horn, horn reflector, and other no-blockage systems, should have extremely small far-out side-lobe levels as low as 20 db below isotropic. Such systems are therefore very low-noise devices and not liable to man-made interference.

Normal parabolic antennas have a number of defects whereby all the input energy is neither utilized by the radiating aperture nor scattered by aperture obstructions. These defects may be listed as

- 1) Ohmic losses in the feed structure. This energy is not radiated, but it does contribute to the system noise temperature.
- 2) Spill-over energy either over the reflector rim in a focal-fed system or over a Cassegrain subreflector. Typically, this energy may be 10% of the total (high-efficiency feeds) to 30% for lower-efficiency systems.
- 3) Feed or subreflector blockage and that caused by their supports. Typical values of scattered energy are 10% to 20%. Haystack has a calculated value of 11%.
- 4) Perturbation of the emergent wavefront by the reflector-surface profile errors, and scattering of energy out of the main-beam direction. For the CAMROC system at the extreme frequency of 6000 Mc/sec (5 cm) and with an RMS tolerance of 0.10 inch, about 33% of the aperture energy will be scattered. At 3000 Mc/sec, this percentage is 10%.

Energy scatter due to reflector tolerance and to Cassegrain subreflector spill-over is directed close to the axial direction, that is, in a half-cone angle of up to 20° , whereas focal-fed spill-over and aperture-blockage effects are scattered over wide angles and even to the rear of the reflector.

This lost energy markedly increases the theoretical side-lobe levels of an ideal aperture, especially in the region beyond the first few side lobes. This discussion can be made clearer if we consider that fundamentally, if we scatter 10% of the input energy isotropically, the radiation level must be 10 db below isotropic, regardless of the nature of the antenna.

The importance of the additional scatter due to a radome therefore strongly depends on the quality of the enclosed antenna; that is, an ideal antenna such as a horn reflector would have more degraded characteristics than a typical Cassegrain paraboloid.

To obtain the effect of a radome on the antenna pattern, we have taken scale-model patterns on the Haystack geometry with and without the radome. The measured data are shown in Figures 7.12 and 7.13.

We note the

- 1) Decrease in axial gain of 1 db,
- 2) Unchanged half-power beamwidth and unchanged first few side lobes,
- 3) Increased side-lobe levels farther out from the main beam.

Recorded data of the above type do not readily present the desired information. In Figure 7.14 we have plotted only the side-lobe peaks for the two cases and have drawn a smooth curve through each set. We can then see the radome contribution in various portions of the radiation pattern.

Assuming that the radome contribution forms an incoherent power addition, we can abstract the radome-scatter pattern from the two curves. This is shown in Figure 7.15.

It is seen that the radome-scatter pattern has a large axial beam due to the coherent forward-scattered energy and a side-lobe tail due to wide-angle forward scatter and backscatter redirected by the radome-enclosed reflector.

On theoretical grounds, we would expect that approximately half the total radome scatter is directed forward and half into the rear. Most of the forward energy is concentrated in the axial beam and in a narrow forward cone⁴ of about 10 to 20 beamwidths.

Measured curves of this sort can aid in predicting both the increased susceptibility of a radome-enclosed antenna to spurious interference and its increased noise temperature. On this basis, we would expect about a 6-db increase in spurious interference for the Haystack system, and less for CAMROC, owing to its smaller space-frame scatter.

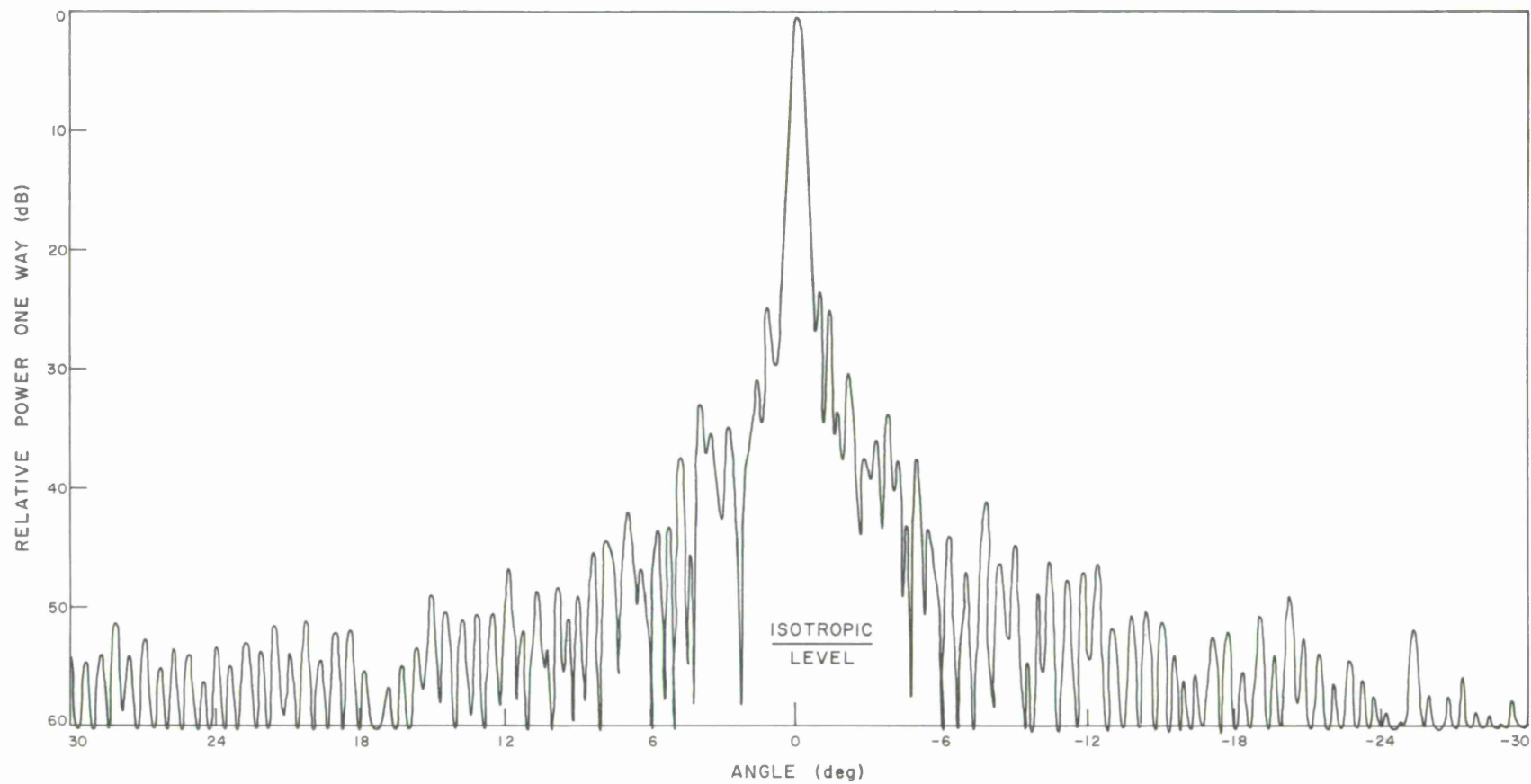


Figure 7.12 Haystack antenna pattern without radome; horizontal polarization; frequency, 20.3 Gc; model scale, 1:15.

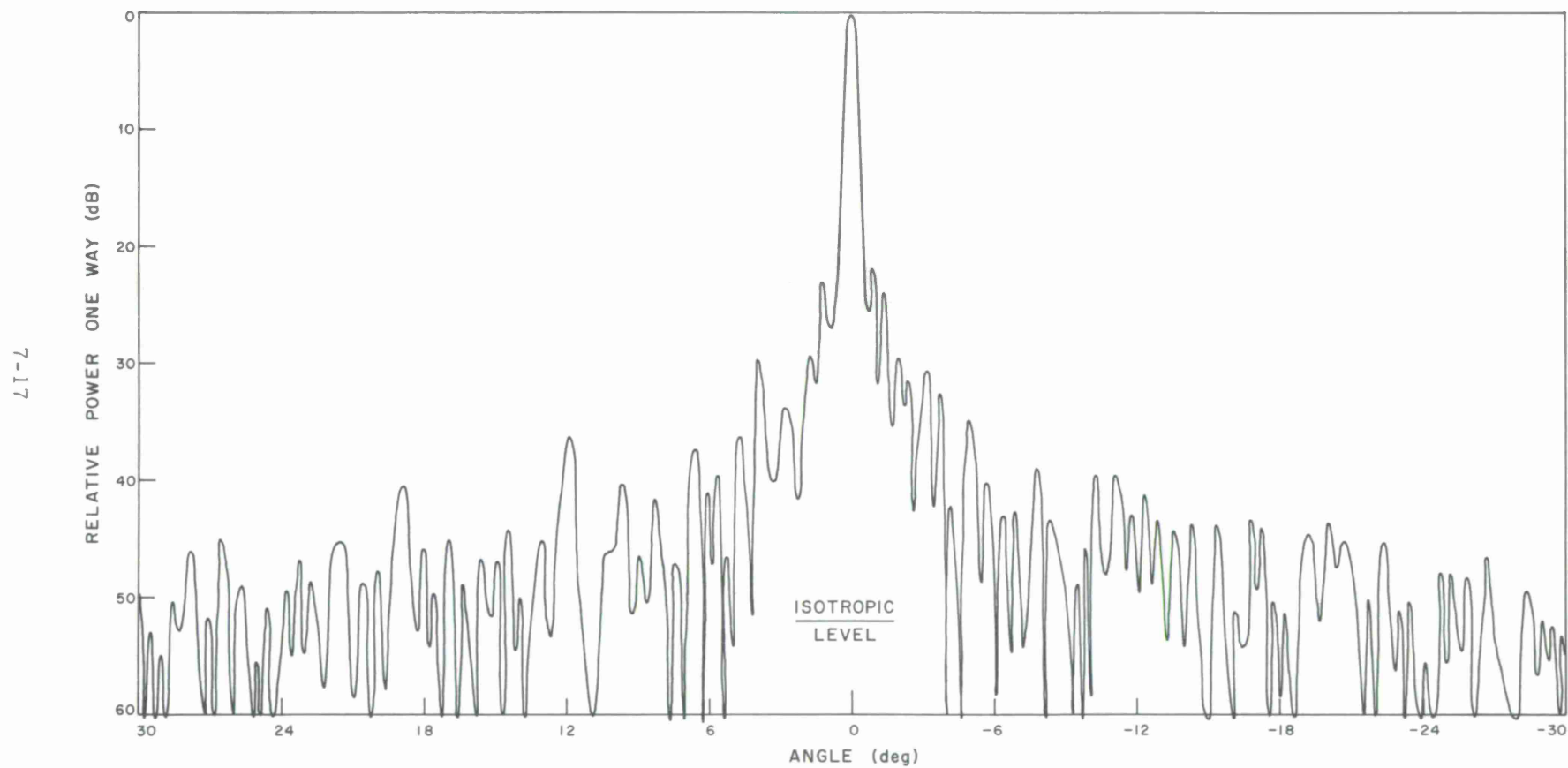


Figure 7.13 Haystack antenna pattern with radome; horizontal polarization; frequency, 20.3 Gc.

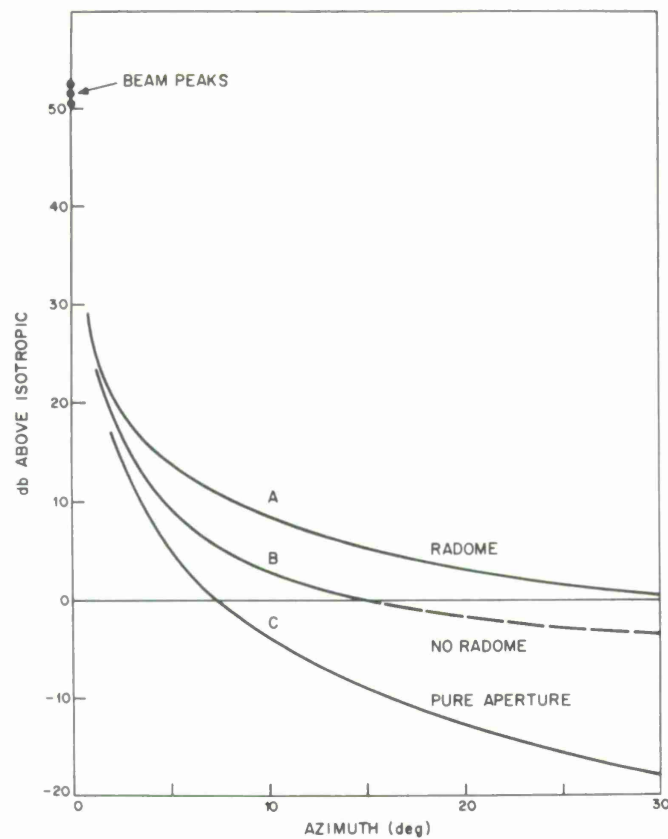


Figure 7.14 Haystack pattern; frequency, 1360 Mc/sec; HPBW, $\sim 0.4^\circ$; antenna gain, 51.5 db; radome loss, 1 db; focal point feed.

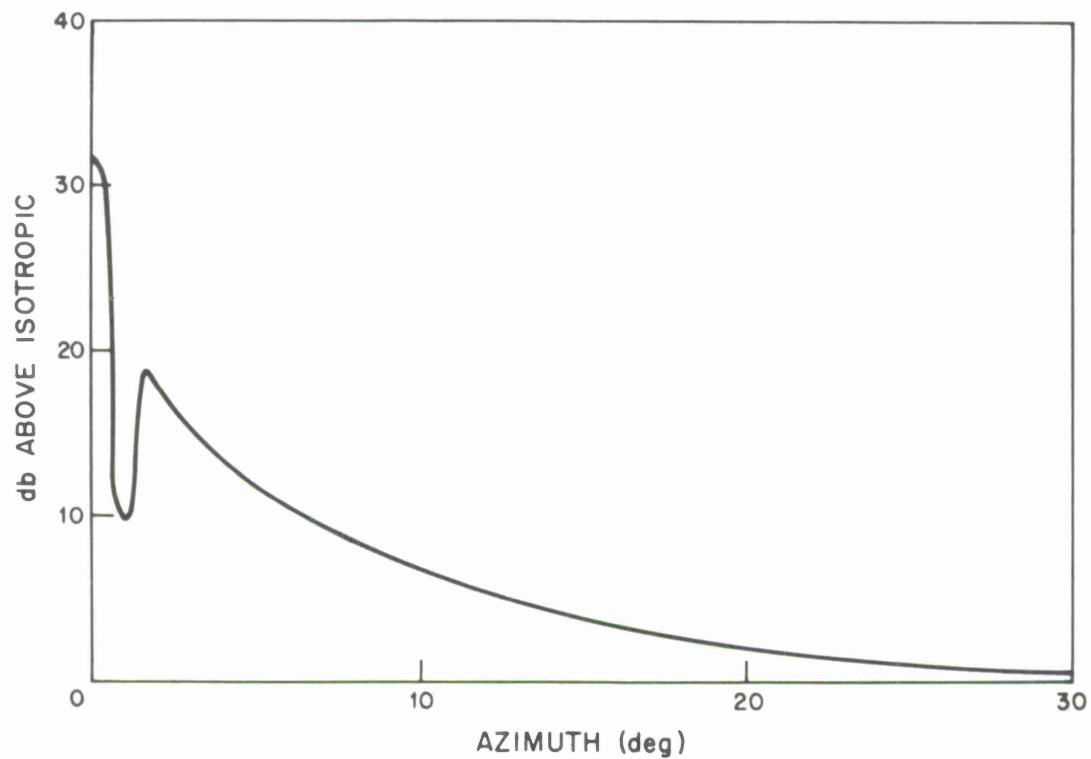


Figure 7.15 Haystack radome disturbance; frequency, 1360 Mc/sec; radome loss, 1 db; antenna HPBW, 0.4° ; antenna gain, 51.5 db.

This increase is probably measurable in an actual installation, and the sun could be used as a spurious source. However, man-made interference has a wide dynamic range, and we question whether the comparatively small reduction in interference rejection of a radome-enclosed antenna is frequently operationally significant for a typical paraboloid.

It is planned in the course of the CAMROC development effort to test extensively the proposed radome design on a scale-model basis by means of on-off pattern measurement. Such work, although basically simple, requires both a measurement over a wide dynamic range and a test site free from spurious reflections. The experimental data of Figures 7.12 and 7.13 could not be extended beyond $\pm 30^\circ$ from beam axis, owing to site limitations.

7.1.3 Increase of antenna noise temperature

It has, at times, been erroneously assumed that if the radome loss is 1 db (20%), the increase in noise temperature should be $0.20 \times 290^\circ \text{K}$. The radome loss is not an ohmic loss, but is almost entirely due to energy scattered out of the antenna aperture. To determine the noise contribution, we must know or estimate the spatial distribution of this scattered energy and determine that fraction that impinges on the warm earth or is absorbed by the membrane.

7.1.3.1 Membrane ohmic loss

First let us consider the membrane ohmic loss. This was calculated above as

$$\frac{2\pi t}{\lambda} \sqrt{\epsilon} \tan \delta = 0.003 ,$$

or

$$0.003 \times 290^\circ \text{K} = 0.85^\circ \text{K} ;$$

that is, the currently planned CAMROC panels will have a contribution of less than 1° at the extreme frequency of operation. At lower frequencies, the noise temperature decreases directly as the frequency. Furthermore, the use of other (thinner) membrane material would reduce this noise contribution.

7.1.3.2 Radome-scattered energy

The radome (space frame and membrane) scatters energy both in the forward and rearward hemispheres. The forward-scattered energy is confined largely to a narrow cone 10 to 20 antenna beamwidths in diameter. For narrow-beam systems, this forward-scattered energy does not contribute significantly to the system noise temperature at any usable elevation angle. Furthermore, for a Cassegrain geometry, this scatter would be masked by subreflector spill-over, hitting the warm earth at low elevation angles.

However, the back-scattered energy, which is close to half the total, is widely scattered. For the CAMROC system at 3000 Mc/sec (0.65-db radome loss), the total loss is 14%; the back-scattered energy is 7%. If all this energy hit the warm earth, the temperature contribution would be 20° K. Fortunately, most of this back-scattered energy is redirected by the antenna reflector into the cold sky.

The radome noise contribution for the Haystack system was calculated, at various zenith angles, by estimating the fraction of energy that hit the ground. The results of these seemingly rough calculations are shown in Figure 7.16. These were calculated at 7.5 and 15.0 Gc/sec, where the radome loss was 1.2 db (24%) and 1.7 db (32%), respectively.

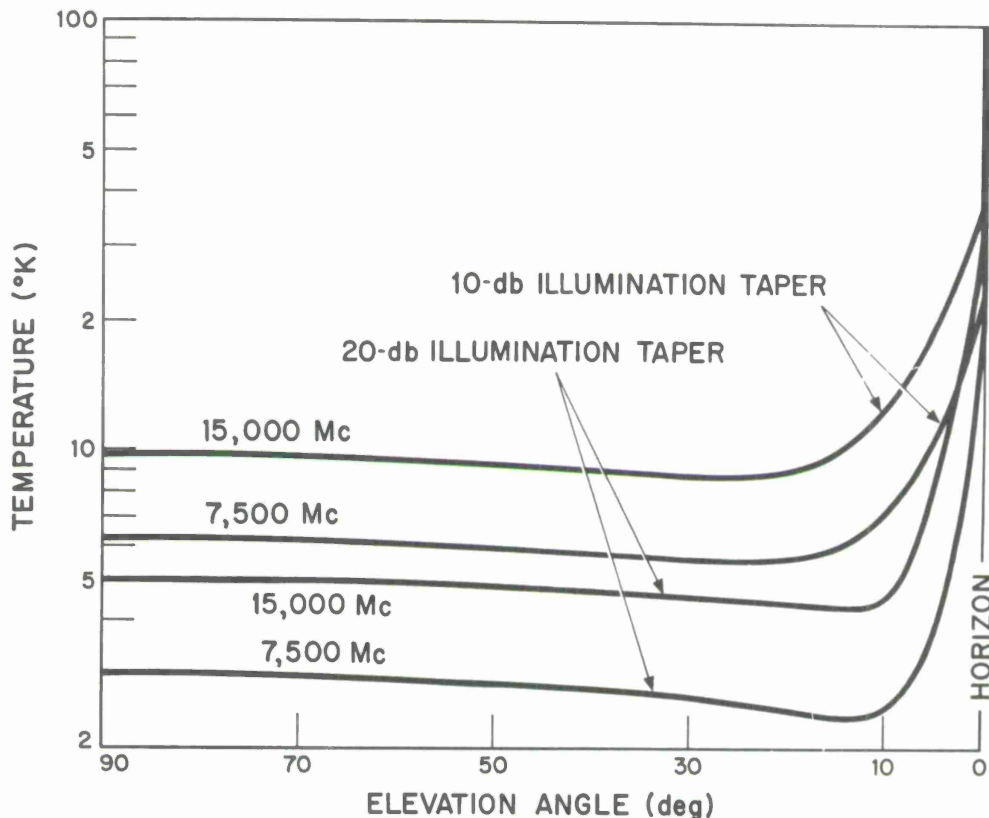


Figure 7.16 Calculated Haystack radome noise contribution.

Actual Haystack noise measurements indicated that after the sky temperature, wave-guide feed, and estimated outside antenna temperature were removed, the remaining radome contribution checked our rough estimates within the measurement errors. Figure 7.17 shows some of the measured data.

On the basis of these data, we come to the conclusion that the radome noise contribution of the proposed CAMROC system will be less than 8° K at all frequencies.

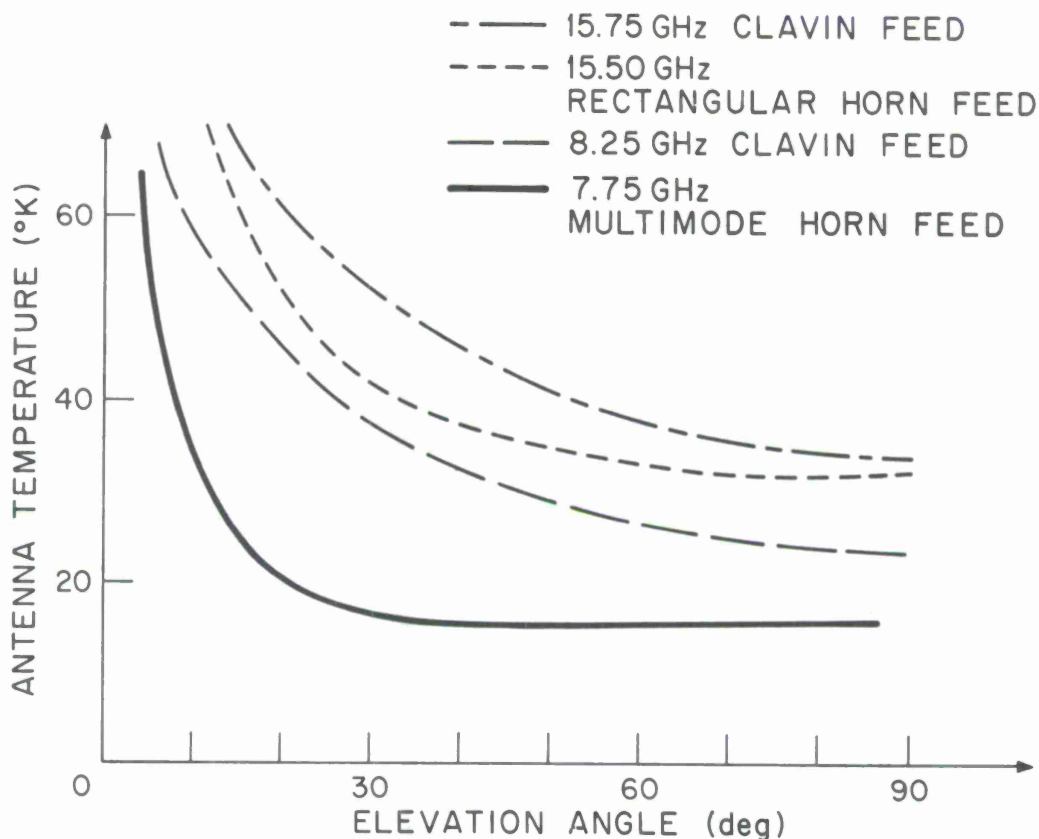


Figure 7.17 Measured Haystack noise temperature.

The noise budget may be written:

Haystack (measured at 7750 Mc/sec)	18° K
Spaceframe calculated (Figure 7.16)	6° K
Membrane adsorption (0.032 inch thick)	1° K
Typical low-noise paraboloid	11° K
	18° K

The higher noise temperature (23° K) measured with the lower efficiency Calvin feeds indicates not that the radome contribution is higher but that the same antenna outside would have a higher noise temperature. In general, the actual noise temperature measured on an outdoor or enclosed antenna depends on the feed losses, antenna efficiency, spill-over energy, and the antenna illumination, so that actual measurements with various feeds will vary.

7.1.4 Gain variation and polarization effects

A typical metal space frame has about 1000 individual members. Depending on the relative size of the enclosed antenna, the number projected on the antenna-aperture plane may vary from 100 to 300. Haystack, which is a particularly dense (high-blockage) structure, has about 300 structural members in the radiated beam.

As we scan the antenna and look through different portions of the radome, we would expect to observe slight variations or granularity in the received signals due to a few more or less members in the antenna beam. However, we would expect this granularity to be at most a few parts in a hundred.

Since the loss of the Haystack metal space frame is 1 db, we would, on theoretical grounds, expect a gain variability of about 0.01 db (0.2% in received source temperature).

The disturbance is small and difficult to measure and separate out from other instrumental effects. Further, there are very few data on the gain stability of outdoor or unobstructed antennas when we consider such small variations. The gain change with zenith angle due to feed defocus or droop and/or surface-tolerance change is well known, and for some systems is an order of magnitude or more higher. Thermal changes and wind gusts also produce significant changes, but ones on which little systematic data are available.

To investigate the radome effect, if any, the optical blockage was computed for various portions of the radome with the following results. (For the Haystack radome with uniform illumination, the variation would decrease with aperture taper and with lower-blockage radome.)

<u>Look angle</u>	<u>Blockage %</u>	<u>Ratio</u>
1	12.224	1.023
2	11.945	1.000
3	12.076	1.011
4	12.250	1.026
5	12.058	1.010
6	12.086	1.012
7	12.104	1.013

The data from the above table are plotted in Figure 7.18. We note that for the Haystack radome it is possible to find positions where the loss differs by 0.02 db.

We have attempted to determine experimentally the gain variability by means of scale-model measurements. Unfortunately, the effect we are looking for is so small that, at present, it is not certain whether a gain variation of 0.05 db exists or whether it is due to some instrumental effect as yet uncovered.

The same situation exists in regard to the gain loss as a function of the polarization. In this case, no definite effects have been found in the Haystack operational system. However, scale-model measurements indicate a variation of signal strength of about ± 0.075 db or an RMS of 0.02 db. To eliminate instrumental effects of the changing polarization (rotating joints, ground reflection, etc.), the polarization is held constant and the scale-model radome is rotated about the antenna-beam axis. The result is a noise-like signal shown in Figure 7.19. Owing to the peculiar nature of this response, we suspect this is an unknown instrumental effect.

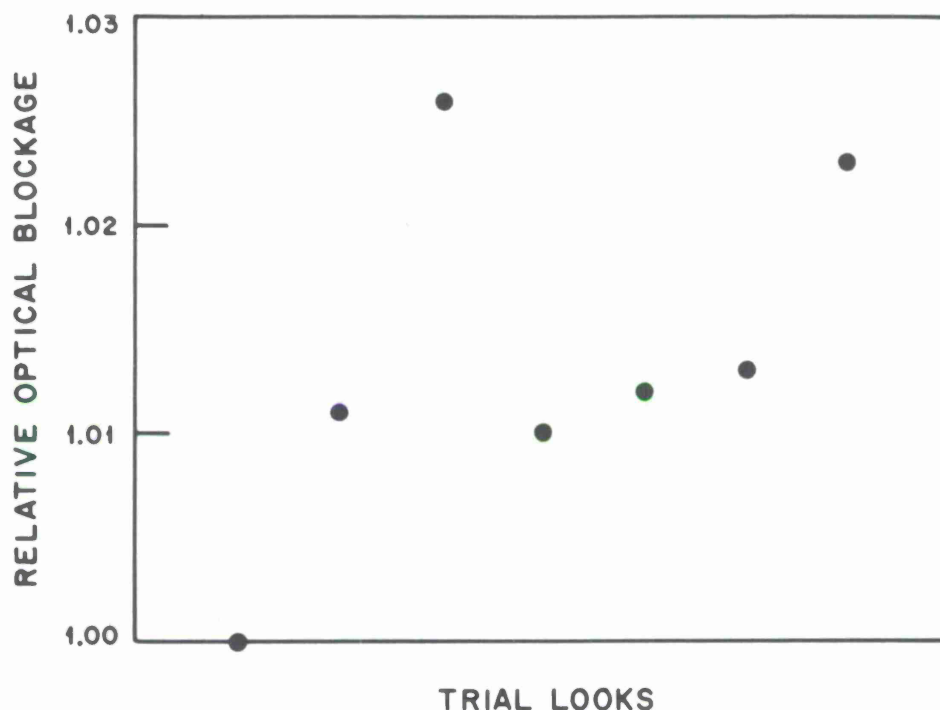


Figure 7.18 Calculated optical blockage of Haystack radome at various look angles; uniform illumination.

Theoretically, the transmission through a metal grid of equiangular polygons or through a completely random geometry should not be polarization dependent. Since the Haystack geometry may not be completely random, the two orthogonal components of each member were summed on an electronic computer. The ratio of these two sums is shown in Figure 7.20. This figure indicates that, in the long wavelength limit, if we were to rotate the polarization, the maximum change in the blockage loss would be 2%. For a 1-db space-frame loss, this would imply a 0.5% modulation of the received flux. For the lower-loss CAMROC design, this modulation would be 0.3%. This figure is conservative since there also will be more members in the antenna-beam aperture. This radome polarization effect will disappear at short wavelengths.

It should be emphasized that the effect illustrated is for the low-frequency limit and should disappear when the member cross section approaches a fraction of a wavelength. In the high-frequency limit (members over a wavelength), the effect would not be measurable.

In this connection it should be pointed out that very few data exist on the gain-polarization variations inherent in the enclosed antenna. To our knowledge, no one has attempted measurements of gain variations less than a few tenths of a db. Completely symmetric antennas should theoretically have no gain-polarization effects. Unsymmetric antennas, such as the horn reflector, have a theoretical gain-polarization dependence, typically 1.029 (0.126 db).

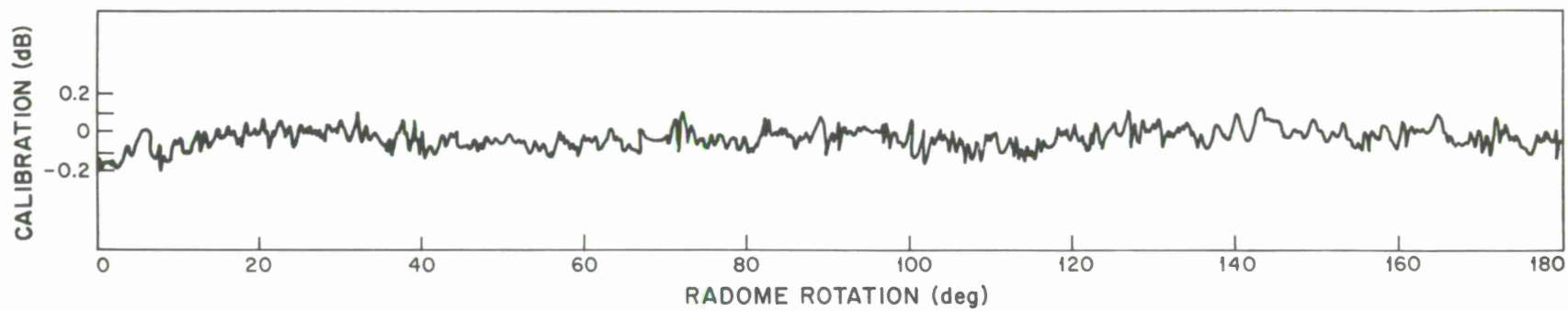


Figure 7.19 Haystack radome, polarization granularity (measured on scale model).

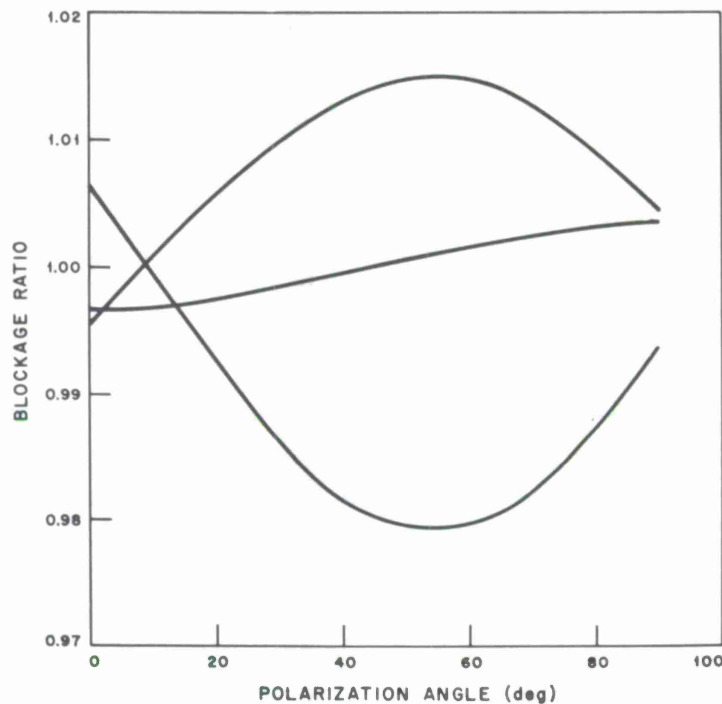


Figure 7.20 Ratio of blockage for two orthogonal polarizations for three different look angles, Haystack geometry.

7.1.5 Effect of rain

We would expect that, owing to the high dielectric constant of water and its high loss tangent at microwave frequencies, the effect of moisture and water on the radome would be deleterious, affecting both the transmission and the noise temperature. Great care must therefore be taken so that the radome membrane material does not absorb water. This condition is met by epoxy-impregnated Fiberglas sheets and various mylar-tedlar combinations.

The effect of actual rain depends on how much water there is on the radome and how it is distributed. The amount of water depends, naturally, on the rain rate and on the size of the radome. A radome collects water in proportion to the square of its diameter, whereas the run-off is proportional only to its circumference.

The nature of the run-off is also of prime importance. If the run-off occurs in uniform films, the energy scattered depends on the square of the film thickness in wavelengths, whereas if the run-off is in streams or rivulets, scattered energy is proportional to the cube of the stream diameter in wavelengths. Both the film thickness and the stream diameter depend inversely on the average run-off velocity. Therefore, treating the membrane surface or using special material to enhance rapid run-off will cause thin films or streams with consequent smaller electromagnetic effects.

The electromagnetic effects could be calculated if the nature of the flow were known. Unfortunately, this seems to be an extremely complex problem with no general agreement, at the present time, as to the film thickness or the stream diameter as a function of rain rate and radome size.

Experimental data are also sparse. To obtain such data on a large radome, it is necessary to monitor system performance over a considerable period of time. This has been done on the Andover installation, operating at 4 Gc/sec, which has a 210-ft inflatable radome. The results have been reported⁵ and are also summarized in Annex 2 of this report.

Briefly, the Andover results indicate that for low-to-moderate rain rates (0.1 to 2.5 mm/hr or 0.04 to 0.1 inch/hr), the measured transmission loss is 1 to 2 db and the increase in noise temperature is 25 to 70° K. The question has been raised as to whether these results are applicable to a metal space-frame radome with Fiberglas membranes.

In addition to these system-performance results, measurements have been made on a 55-ft radome, simulating the effects of rain by means of garden sprinklers.⁶ These results indicated transmission losses about an order of magnitude lower than the Andover results for the same rain rates. In addition, by treating the surface to obtain rapid run-off, transmission losses as low as a few tenths of a db were obtained for very heavy rain rates of 1 inch/hr.

Unfortunately, few data are available for the Haystack installation. As mentioned, to obtain meaningful information, provision must be made to monitor system performance at the comparatively rare times of significant rainfall. It is known that the Haystack system temperature at 15 Gc/sec increases by 50 to 100° K during periods of heavy rain. However, the radome-rain effect has not interfered with the Haystack observational program. Precise radio-astronomy observations could not have been made in any case at centimeter wavelengths.

In evaluating the radome-rain effects relative to the CAMROC program, it should be realized that heavy rain occurs only 0.1% of the time and moderate rain only 1%, while over 90% of the time it does not rain at all. In contrast, at a height of 200 ft (average height of 400-ft antenna), a 30-mph wind is exceeded 10% of the time, and only 10% of the time is the wind less than 10 mph.

As part of the CAMROC study program, an attempt will be made to obtain a better understanding of the run-off problem on a large radome, and use will be made of membrane material that enhances rapid run-off. In addition, means will be investigated to channel the rain water into high-velocity flow.

Although the CAMROC radome will collect three to four times as much water per run-off area, its electromagnetic degradation due to rain will probably not be so severe as that of Haystack, since the wavelength is three or four times longer.

7.2 Operational Experience with the Haystack Radome in Astronomical Observations

The use of the Haystack 120-ft paraboloid for observations in radio astronomy has generated direct information on the electromagnetic effects of radomes, thus providing a full-scale test of the parameters developed through theory and model experiments. The measurements made so far have been in the following categories:

- 1) Contribution to system noise temperature.
- 2) Polarization effects,
- 3) Reduction of aperture efficiency,
- 4) Constancy of gain and system noise temperature.

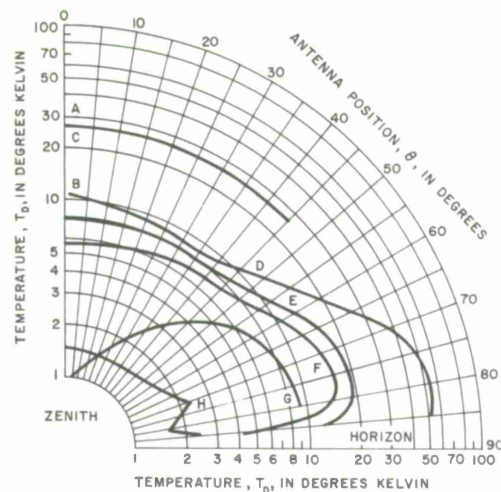
The most complete checks have been made at 8 Gc/sec and 15.5 Gc/sec, plus measurements of system noise at 1.6 Gc/sec. The results quoted in the subsequent sections are taken from Meeks⁷, system noise temperature and diminution of aperture efficiency; Allen⁸, polarization effects; and Allen, Burke, and Crowther⁹, constancy of gain and systems noise temperature.

7.2.1 System noise temperature

The ideal method of determining the radome contribution to the system-noise temperature is to measure the antenna temperature as a function of zenith angle with and without a radome. Unfortunately, this is not practical, as it would involve either removal of the radome or use of an identical antenna outside.

However, we can obtain an estimate of the radome contribution by comparing the Haystack radome-enclosed antenna with a similar large antenna outside. Figure 7.21 shows the measured data on some typical geometries. It should be noted that the antenna temperature varies considerably with the type of antenna, whether it is focal-point fed or Cassegrain, and whether it has feed supports. Curve D is that for a well designed Cassegrain geometry and indicates a zenith temperature of about 11° K. As we approach the horizon, there is a considerable increase in the noise temperature, due to the sub-reflector spill-over energy, now hitting the warm earth. The elevation angle where this becomes dominant depends on the magnification of the Cassegrain geometry.

Figure 7.22 shows the measured data on the Haystack antenna, using high-efficiency horn feeds. We note a zenith noise temperature of 18 and 22° K at 7.75 and 15.75 Gc/sec, respectively.



- A. HORN-FED PARABOLOID, FIBERGLASS STRUTS
 - B. HORN-FED PARABOLOID, NO STRUTS
 - C. STANDARD CASSEGRAIN, FIBERGLASS STRUTS
 - D. STANDARD CASSEGRAIN, METAL STRUTS
 - E. NEAR-FIELD CASSEGRAIN, SUBREFLECTOR $f=13"$
 - F. AS E, NO STRUTS, MYLAR SUPPORT
 - G. CONICAL HORN REFLECTOR, 27" APERTURE
 - H. HORN REFLECTOR, 5' APERTURE
- (CRAWFORD HILL SITE, REFERENCE 7)

Figure 7.21 The 6-Gc noise performance of a 16-ft paraboloid ($l/D = 0.375$); from D. C. Hogg and R. A. Semplak, "An Experimental Study of Near Field Cassegrainian Antennas," BSTJ pp. 2677-2704, November 1964.

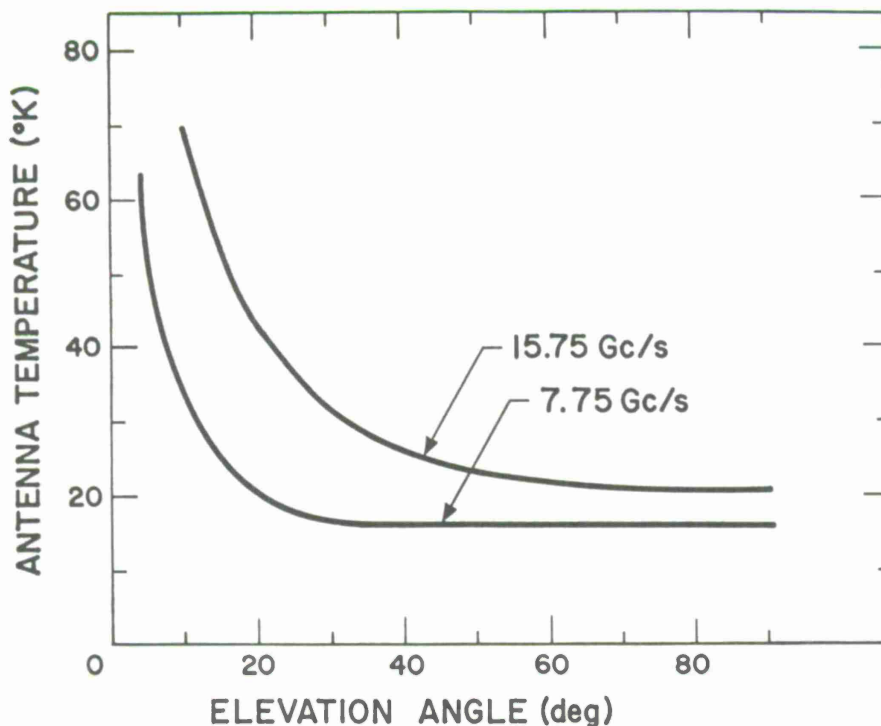


Figure 7.22 Antenna temperatures; Haystack antenna (horn feeds).

It is of interest to compare these measurements with the theoretical predictions in the previous section. We have

	<u>7.75 Gc/sec</u>	<u>15.5 Gc/sec</u>
Radome scatter (Figure 7.16)	6°	10°
Membrane absorption	1°	2°
Typical Cassegrain	<u>11°</u>	<u>11°</u>
	18°	23°
Measured Haystack (zenith)	18°	21°

The agreement between the Haystack-measured results and those of a typical Cassegrain with the added radome contribution indicates that the radome effect is about as expected. The general shape of the two sets of curves as a function of elevation angle is also encouraging. However, this comparison cannot be carried too far, because the two systems have different magnifications.

The actual measured temperature at Haystack naturally depends on the efficiency of the feeds used. Figure 7.23 shows the results with Clavin feeds. These compact, broad-band feeds have about 20% greater spill-over and consequently higher noise temperatures. It is believed that, if data on a comparison antenna with Clavin feeds were available, outdoors subtraction of our measured results would yield the same radome contribution.

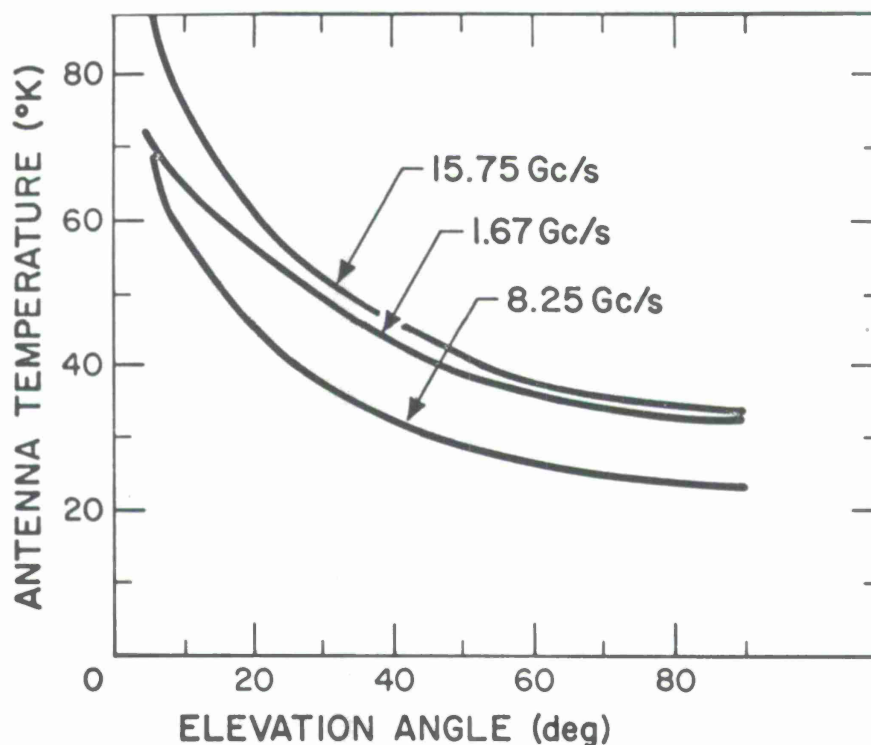


Figure 7.23 Antenna temperatures; Haystack antenna (Clavin feeds).

In addition to the above measurements, using the 120-ft antenna, measurements were also made using sky horns. A pair of scaled horns was constructed, with beam widths of about 25° at 1.6 and 8 Gc/sec. These were used to measure background antenna temperatures inside and outside the Haystack radome. The measurements were made with great care, using liquid nitrogen and room-temperature loads as calibration references. The VSWR was measured across the radiometer band at both frequencies, and outside and inside the radome. No changes were found in these VSWR measurements. After correction for VSWR and atmospheric emission, the background antenna temperatures with the horns were 3°K and 5°K at 1.6 and 8 Gc/sec, respectively. We expect a cosmic background temperature of 3 to 4° at these frequencies, and evidently the far-side-lobe contributions to the horn temperatures were negligible.

The measured differences between the antenna temperature inside the radome and outside are given in Figures 7.24, 7.25, and 7.26. In Figure 7.24, the ground emission is effectively shielded from the horn by the Haystack reflector and the noise-temperature radome contribution turns out to be 14°K at both frequencies. In Figures 7.25 and 7.26, the radome temperature contributions may be observed to increase because this shielding is absent.

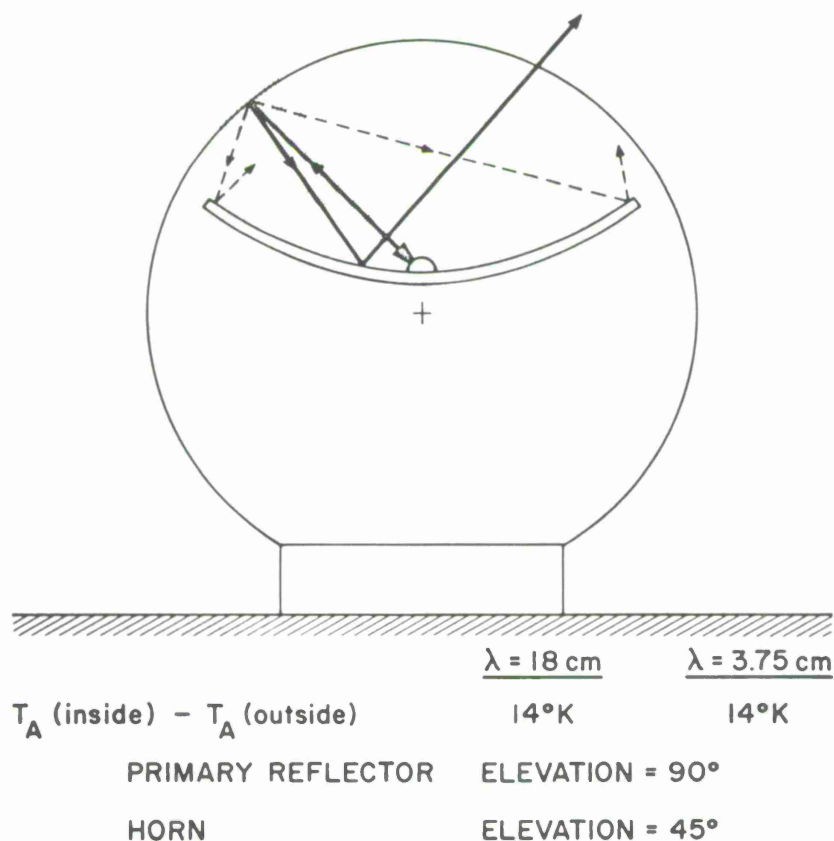


Figure 7.24 Radome noise-temperature measurement.

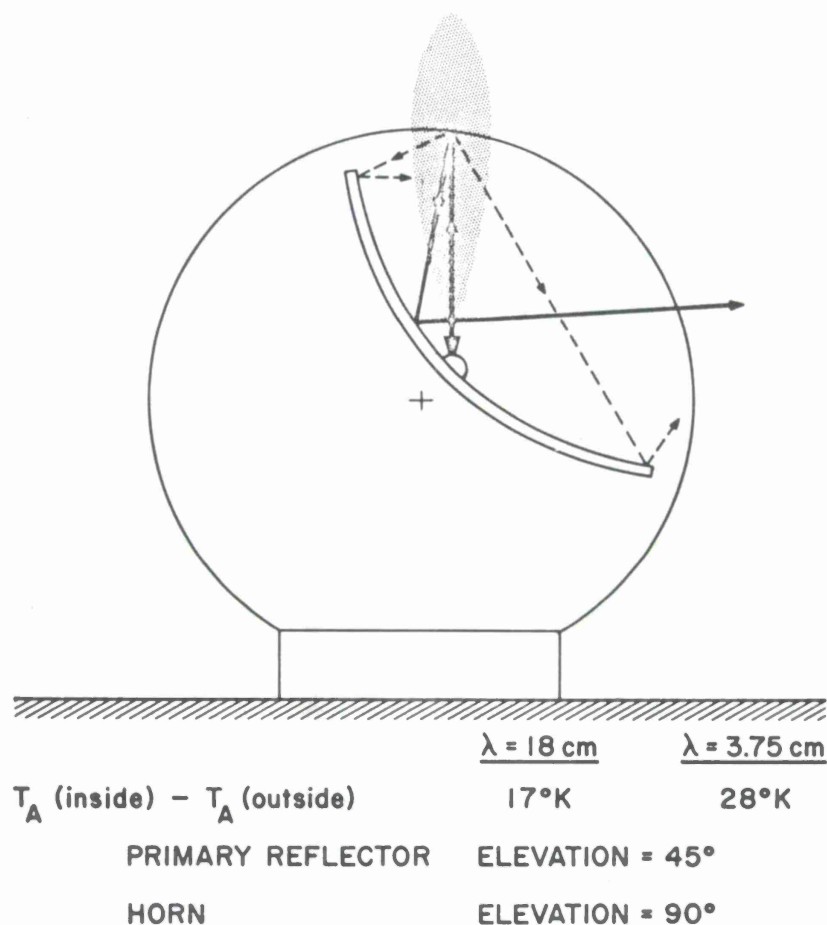


Figure 7.25 Radome noise-temperature measurement.

It will be noted that the radome temperature contribution with the sky horns is greater than that obtained with the 120-ft antenna. Some of this is due to the precision in this difficult measurement. There is also some question as to whether the sky-horn determination is representative of the 120-ft antenna since the radome scattering members are illuminated differently in the two cases.

7.2.2 Polarization effects

An intensive study of the Haystack radome has been completed by Allen,⁸ who made polarization measurements, at 8 Gc/sec, 15.25 Gc/sec, and 15.75 Gc/sec, of a number of radio sources. The Crab Nebula (M1) was mapped as a function of polarization as well as of brightness, and the instrumental effects were checked at a variety of zenith angles and azimuths. The Orion Nebula was chosen as a reference source whose polarization should be small or zero. The total instrumental polarization was measured, and it appears to be almost entirely due to the rotating joint in the polarimeter and not to the radome. The observed instrumental polarizations are given in Table 7.1. The sharp change between 15.25 and 15.75 Gc/sec is a certain indication that a sharply tuned element in the system, such as the rotating joint, is responsible.

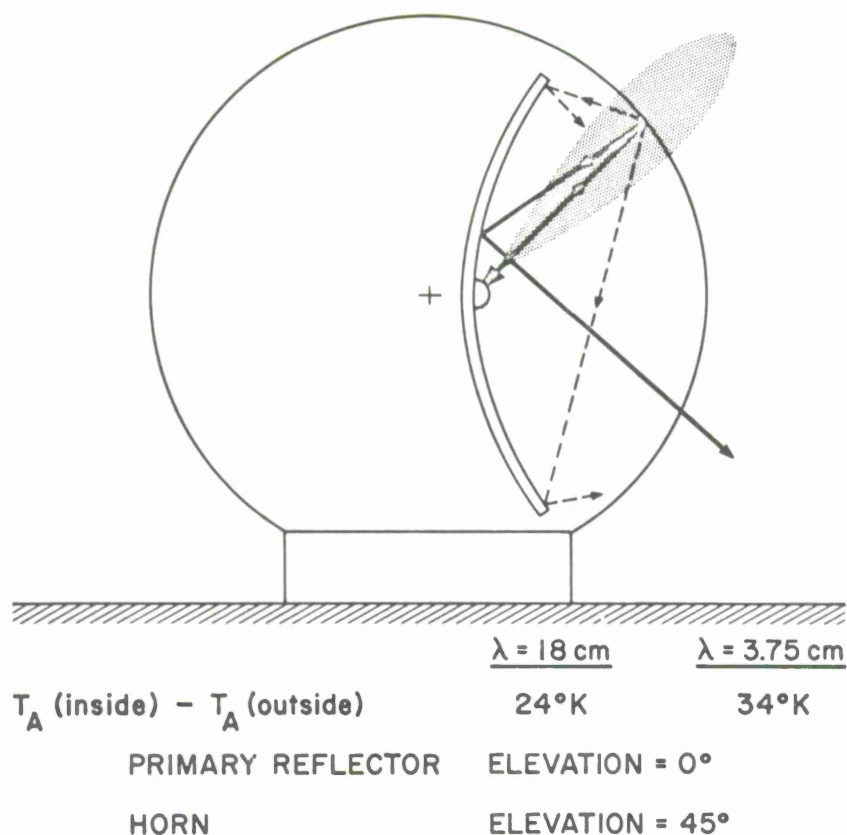


Figure 7.26 Radome noise-temperature measurement.

Individual measurements were made with short integration times to see if local "granular" polarization was present. The variance of single measurements of approximately 0.6%, with the corresponding variance in angle, was completely attributable to random receiver noise, and no radome effect could be discerned.

Table 7.1 Polarization measurements with Haystack

Frequency (Gc/sec)	8.25	15.25	15.75
Instrumental polarization (%)	1.05 ± 0.1	2.1 ± 0.22	0.98 ± 0.17
(parallactic angle)	$56^\circ \pm 6^\circ$		
Total polarization, M1 (%)	8.0 ± 0.1	(M1 was resolved at these frequencies)	
(parallactic angle)	$147^\circ \pm 4^\circ$		
Variance in polarization, single measurement	---	0.69	0.53
Variance in angle, single measurement	---	17°	29°

The observed polarization for the Crab Nebula, M1, agrees with the determination by other authors to within the quoted errors. From the measurements it is concluded that instrumental polarization effects were determined to within 0.1% for the entire system and that radome polarization effects are less than 0.1%.

7.2.3 Diminution of aperture efficiency

The loss in aperture efficiency due to the Haystack radome has been computed, using the theory outlined in Annex 1. The aperture blockage of the space frame and the reflectivity of the membrane at frequencies of 8 Gc/sec and 15.5 Gc/sec were taken into account in the calculation. The overall aperture efficiency of the Haystack antenna has been measured at both these frequencies by observing bright radio sources whose fluxes are known. If the estimates of the radome loss are assumed, it then becomes possible to compute the RMS deviations in the surface tolerance of the antenna. The tolerance computed in this way turns out to be 50 mil. Table 7.2 shows the measured efficiencies and the losses assigned to surface-tolerance deviations and radome loss. The breakdown in terms of radome loss and surface tolerance is, of course, not unique. The radome loss might be higher in principle and the RMS surface error smaller. However, an optical survey of 240 points on the Haystack reflector gives an RMS error of 52 mil, confirming the calculations.

7.2.4 Constancy of system

Stability of gain and system noise are important requirements for a radio-astronomy system, and, for certain types of measurements, lunar-occultation measurements especially, the effects of a radome over small changes in pointing angle are particularly important. The constancy of antenna gain has been checked by tracking strong radio sources through the radome, by setting the gain modulator so that the antenna-noise contribution from the radio source is canceled out, and by noting the differential changes in antenna temperature. The changes could be due to two causes: change in antenna gain or change in noise contribution from the system, especially the radome. In order to separate the two effects, the antenna is offset to look at the cold sky, the gain modulator is set to null, and the antenna tracks the cold sky through the same region of the radome that was covered when the radio source was tracked.

Measurements have been made by Allen, Burke, Crowther⁹ using the 8-Gc/sec maser radiometer of the planetary radar system. So far, all results have been negative, with all fluctuations observed being attributable to clouds or to random noise fluctuations. The system is sufficiently low noise to enable 0.1° K effects to show clearly with 10-sec integration time. The radio source Cassiopeia A gives an antenna temperature of approximately 50° K, and it was thus possible to look for gain changes of 0.2% (0.01 db). The measurements so far indicate that gain changes of this order of magnitude must be rare, since none has been observed.

Table 7.2. Haystack efficiencies

	db	%
Clavin feed at 7750 Mc/sec		
50% aperture efficiency	66.4	50
Reflector tolerance (0.050 RMS)	-0.8	
Radome loss	-1.2	
	<hr/>	
Net gain	64.4	31.5
Measured	64.5	32.3
Clavin feed at 15,500 Mc/sec		
50% aperture efficiency	72.4	50
Reflector tolerance	-3.0	
Radome loss	-1.7	
	<hr/>	
Net gain	67.7	16.9
Measured	67.3	15.4
Multimode feed at 7750 Mc/sec		
64% aperture efficiency	67.5	64
Reflector tolerance	-0.8	
Radome loss	-1.2	
	<hr/>	
Net gain	65.5	40.4
Measured	66.0	44.2
Rectangular horn at 15,500 Mc/sec		
64% aperture efficiency	73.5	64
Reflector tolerance	-3.0	
Radome loss	-1.7	
	<hr/>	
Net gain	68.8	22
Measured	69.0	23

The related question, of small-scale changes in antenna temperature, has been investigated closely, since there had been preliminary indications that such effects might exist. Meeks⁷ and Allen⁸ reported small discrete changes in antenna temperature of approximately 0.2° K at 8 Gc/sec, which appeared at given azimuth and elevation. The angular scale was of the order of one beamwidth. Such effects could be caused either by a small-scale "granularity" in the radome contribution to antenna temperature or by weak interfering transmitters in far-out side lobes of the antenna pattern. The effect seemed rather large to be attributed to the radome directly, since no theoretical interpretation appeared reasonable; but the importance of such an effect would be so great that a careful investigation was warranted.

The tests with the maser radiometer on Cassiopeia A were negative, but a check was made by observing the cold sky through the same part of the radome in which Allen⁸ had seen the most clearly marked effects while observing the radio source 3C84 (Perseus A). The effect seen earlier exhibited an amplitude of 0.3° K, a signal easily detectable with the maser. No effect was seen, and an upper limit of 0.1° K for this part of the radome was measured. It was concluded, therefore, that the noise "granularity" must be caused by weak interfering transmitters in distant side lobes.

It should be noted that the receivers had very different pass bands. The 8-Gc/sec radiometer employed earlier utilized a tunnel diode amplifier with a 1-Gc/sec bandwidth and was therefore vulnerable to interference, while the maser used in the later tests was relatively narrow-band, with a 10-Mc/sec bandwidth having a center frequency that had been chosen to be as free of interference as possible.

Large-scale and long-term effects by the radome on the gain have not been investigated as fully, because the dominant gain changes caused by thermal effects have masked any effects attributable to the radome. Most measurements are made with respect to reference sources, and such relative measurements show internal consistencies of the order of 1%.

7.2.5 Pointing perturbations

In the pointing calibration of Haystack at 8 and 15.5 Gc/sec, no deviations in the axis of the beam have been found that could be assigned to radome effects. The pointing calibration made on bright radio sources gives an RMS pointing error of $0^{\circ}003$. Sources have been tracked for periods of 30 min with the antenna pointed off the center of the source at the half-power point. In this time interval, the pattern of the space frame in front of the antenna changes appreciably, but no deviations were found that could not be attributed to small errors in the pointing servo system.

7.2.6 Phase perturbations

The interferometric use of large paraboloids, in conjunction with smaller elements at large distances, has proved to be such a powerful tool that it is important to establish that phase fluctuations induced by the radome will not compromise use of a large paraboloid in such an enclosure. The Haystack antenna has been used successfully as one element of a phase-stable interferometer by Rogers et al. Phase errors were carefully investigated, and no variation in phase shift could be found that was not attributable to random noise fluctuations. The wavelength used was 18 cm, and from the data an upper limit of 0.6 cm can be placed on the variations in electrical path length induced by the radome. This is a conservative upper limit, and in actuality the variability in phase shift may be one or two orders of magnitude smaller.

7.2.7. Electromagnetic characteristics of a 550-ft radome

The Haystack radome contributes approximately 7° at 7.75 Gc/sec and 12° at 15.75 Gc/sec to the system noise when the antenna is directed toward the zenith. The loss in gain due to aperture blockage is 1.1 db at X-band, and agrees with theory. Radome polarization effects at X-band and the K_u -band amount to less than 0.1%. "Granularity" of gain is less than 0.2%, over a scale of one beam width, and antenna temperature variations over the same scale are less than 0.1° K.

Following are estimated performance characteristics of 550-ft metal space-frame radome for 400-ft antenna

- 1) Loss of gain

Metal space frame	Depends on structural-design stress levels, wind specification, and knowledge of buckling criteria. Present state of the art: 0.8 db. Loss essentially independent of frequency.
Membrane	Depends on membrane thickness and dielectric constant. Loss varies as square of frequency. Present design: 0.25 db at 6000 Mc/sec, less than 0.06 db below 3000 Mc/sec
	Total loss estimate: 1.1 db at 6000 Mc/sec 0.8 db below 3000 Mc/sec
Boresight shift	One to two hundredths of a beamwidth [*]
Pattern degradation	No change in main beam and first few side lobes. Far-out side-lobe level increased 3 to 6 db.
- 2) Increased noise temperature

Metal space frame	Depends on space-frame loss and antenna illumination taper. Independent of frequency. Probable value about 8° measured on Haystack.
Membrane	Depends on membrane loss and directly on frequency. Calculated at 6000 Mc/sec < 1° K. Total noise increase < 9°K at 6 Gc/sec
- 3) Gain variability

Due to nonuniformity or lack of complete randomness of metal space frame. Calculated for Haystack ±0.01 db.*
- 4) Polarization gain variability

Due to nonuniformity or lack of complete randomness of metal space frame.*

*Measurements with Haystack indicate that the effect is smaller than other instrumental errors.

8. REFERNECES

1. Kennedy, P. D., "An Analysis of the Electrical Characteristics of Structurally Supported Radomes," Ohio State University Report No. 722-8, November 1958.
2. Kay, A. F., "Electrical Design of Metal Space Frame Radomes," IEEE Trans. on Ant. and Prop., vol. AP-13, no. 2, pp. 188-202, March 1965.
3. Friis, R. W., and May, A. S., "A New Broad-Band Microwave Antenna System," Electrical Engineering, pp. 97-100, March 1958.
4. Ruze, J., "Forward Scattered Energy of Metal Space Frame," CAMROC Technical Memorandum No. 5, May 5, 1966.
5. Giger, A. J., "4 Gc Transmission Degradation due to Rain at the Andover, Maine Satellite Station," BSTJ, p. 1528, September 1965.
6. Cohen, A., and Smolski, A., "Effect of Rain on Satellite Communications Earth Terminal Rigid Radomes," Microwave Journal, p. 111, September 1966.
7. Meeks, M. L., "System Noise Temperature and Diminution of Aperture Efficiency," 1966.
8. Allen, R. J., "Polarization Effects," 1966.
9. Allen, R. J., Burke, B. F., and Crowther, P., "Constancy of Gain and System Noise Temperature," 1966.

8. STRUCTURAL DESIGN FOR LARGE SPACE-FRAME RADOMES

8.1 Summary

The general specifications of the radome and the overall environment to which it will be exposed are reviewed. A discussion is presented of a method for geometrically dividing a spherical surface into a network of beams, and the computer programs for carrying out this operation are described.

Emphasis has been placed on the development of computer-design techniques for the structural analysis of a space-frame radome. One of the computer programs combines a generalized stiffness analysis of space-truss structures with a beam-column analysis. By utilizing iteration techniques, an optimum size of the beam can be generated as a function of the geometrical configuration and applied loading. This program is currently in the final stages of development.

Another area of great emphasis has been the evaluation of the general instability of large structures. One of the primary motivations for this emphasis is that only approximate techniques are currently available and there is relatively little experience with structures as large as the nominal 550-ft-diameter radome. The general equations have been formulated and programmed for solution on an IBM/360 computer, and the program is in final stages of testing. A description is presented of the experimental program that has been initiated in support of the theoretical investigations. These studies and computer programs will be instrumental in ensuring an efficient and reliable radome.

Studies have been carried out to evaluate the membrane, which is an important element in the radome system. The thickness requirements, electrical performance, methods of manufacture, and methods for attaching to the beams are being studied. Membrane analysis and design studies are continuing.

Studies to establish an overall design for the radome have provided preliminary data on the general feasibility of the structure, on its cost, and on the electromagnetic performance characteristics. The activities under way should provide the basis for establishing a final design concept during 1967.

8.2 Radome Specifications

In contrast to the enclosed antenna the radome must protect, many of the major features of a radome can be established fairly readily. For example, electromagnetic, structural, and cost considerations indicate that a truncated spherical structure appears to be a desirable configuration for the radome. The electromagnetic performance requires that the protective dielectric skin be very thin. Since the radome will have a very large diameter, the requirement that the skin be thin eliminates single-wall shell, sandwich, and inflatable radome construction in favor of a metal space-frame structure covered with a thin dielectric skin. A triangular framing configuration has been selected as an efficient scheme for resisting the shell loads produced by the wind.

The major parameters that influence the size of the radome include:

- 1) Antenna diameter and focal length.
- 2) Distance between the center of antenna rotation and the vertex of parabola.
- 3) Minimum angle of depression of the antenna.
- 4) Feed-support length.
- 5) Allowable offset between the center of the sphere and the center of rotation of the antenna.
- 6) Minimum clearance between the antenna and the radome.

Figure 8.1 is a typical antenna-radome configuration study of the CAMROC facility. This figure illustrates the variation of radome size with minimum elevation angle and with various amounts of offset between the center of the sphere and the center of rotation of the antenna. The minimum clearance between the antenna and the radome was set at 40 ft for this sketch, but clearances as small as 15 ft may be practical. The ratio of height to diameter was held constant at 0.765. This figure shows the variation of radome size with minimum depression angle. As in most engineering solutions, the final selection will be the result of the most satisfactory trade-off among the variables of cost, electromagnetic performance, and structural requirements.

8.3 Environment

A radome exists for the sole purpose of sheltering the enclosed antenna from the natural environment (see Annexes 3 and 4).^{1,2} It must protect the antenna from the adverse effects of wind, snow, sun, rain, ice, and hail. It also provides a closed, artificial environment in which temperature extremes and gradients can be modified to more tolerable levels.

8.3.1 Wind

Of the environmental elements, the wind imposes the most severe loading on the radome. The structural design of the radome must then guarantee the mechanical integrity of the radome against the peak design wind loads. The specification of the design wind must include the magnitude of the wind velocity, the gust intensity and duration, and the escalation of wind velocity with height. The probability of occurrence of these conditions must be established for an acceptable risk, in terms of the anticipated life of the radome and for a given site location.

It has been proposed that the design lifetime of the radome should be at least 25 years* and that the radome should survive environmental conditions that exhibit a 1% risk of occurring in this time span. Figure 8.2 depicts a wind-velocity map of the United States. The velocity values are those that can occur in a 25-year period with a 1% risk at a height of 50 ft above ground level. It is noted that in the inland New England area of interest, there is a 1% probability of reaching wind velocities of 86 mph in a 25-year time period. The inland New England wind environment is more moderate than many

*The radome design lifetime likely may be chosen to be 30 or more years.

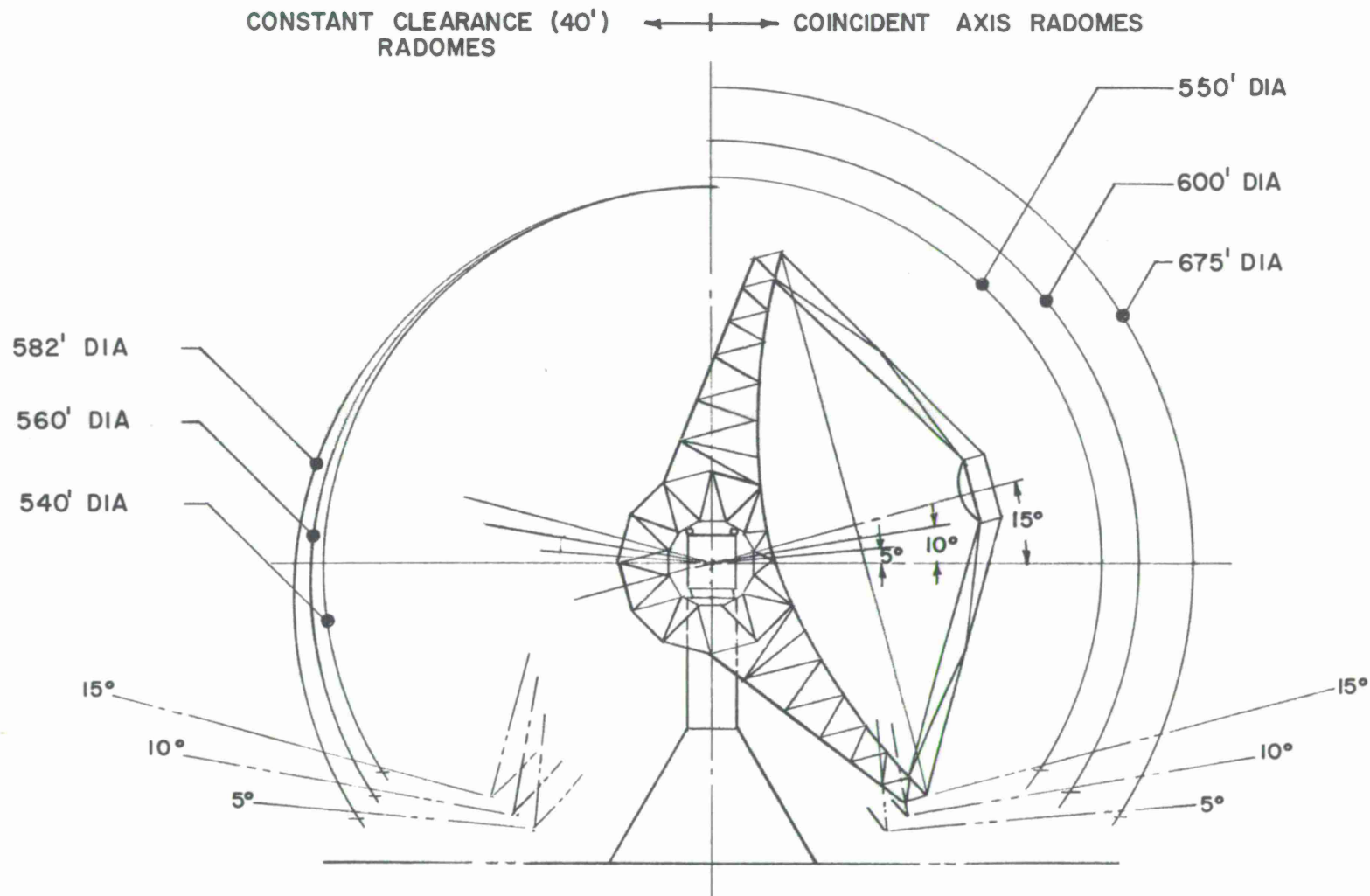


Figure 8.1. Typical antenna-radome configuration study, CAMROC facility; variation of radome size with minimum elevation angle for a 400-ft-diameter reflector. (See p. 8-2 for further discussion of antenna-radome clearance.)

other regions in the United States. All velocity measurements from which the map is developed represent observations averaged over a 5-min period.

Data from five inland weather stations over a 25-year period provide the basis for estimating the increase in wind velocity as a function of height above ground. The results are presented in Figure 8.3 for the condition of 1% risk in 25 years. The wind gust factor as a function of gust duration for different steady 5-min average wind speeds is plotted in Figure 8.4 for the 1% risk during 25 years' criterion. By means of Figures 8.2 through 8.4, the variations over the radome of wind velocity, gust velocity, and duration are readily obtained. It is recognized that the local wind velocity at the site is dependent on the surrounding terrain and on the number, size, and orientation of the buildings in the complex. However, when this information becomes available for a specific site, velocity adjustments can be estimated either through selected wind-tunnel tests or from available data.

8.3.2 Snow

Typical of snow data for the New England area are those from the Boston Weather Bureau, which indicate that, within a radius of approximately 60 miles of Boston, there exists a 1% probability that, within a 25-year span, 30.0 inches of snow will fall within a 24-hr period.

Experience at smaller radome installations indicates that the accumulation of snow on a radome is confined to a polar cap having a central angle of approximately 30°. It has also been reported that the total accumulation in the cap region is substantially less than the snow fall measured on an adjacent, flat, horizontal surface, although no measured data are available.

If it is assumed that a maximum of 30.0 inches of wet (7.8 lb/ft^3) snow falls within a 24-hr period and is completely retained within the cap region, then the maximum radial pressure will still be less than that developed by the design wind speed. A combination of high winds and substantial snow accumulation on the dome is unlikely. Thus, snow loading is not considered to be a major structural consideration. However, because the forces imposed by the snow load are unlike those due to the wind, the resulting stresses must be investigated.

8.3.3 Rain, ice, hail, and temperature

The rain, ice, hail, and maximum and minimum temperatures that could be experienced in the western part of Massachusetts for the case of a 2% risk over the 25-year span are summarized in Table 8.1. These parameters do not exert any major influence on the structural design of the radome. However, they will have some effect on the design of secondary elements, i. e., heating equipment, membrane attachment, and sealant.

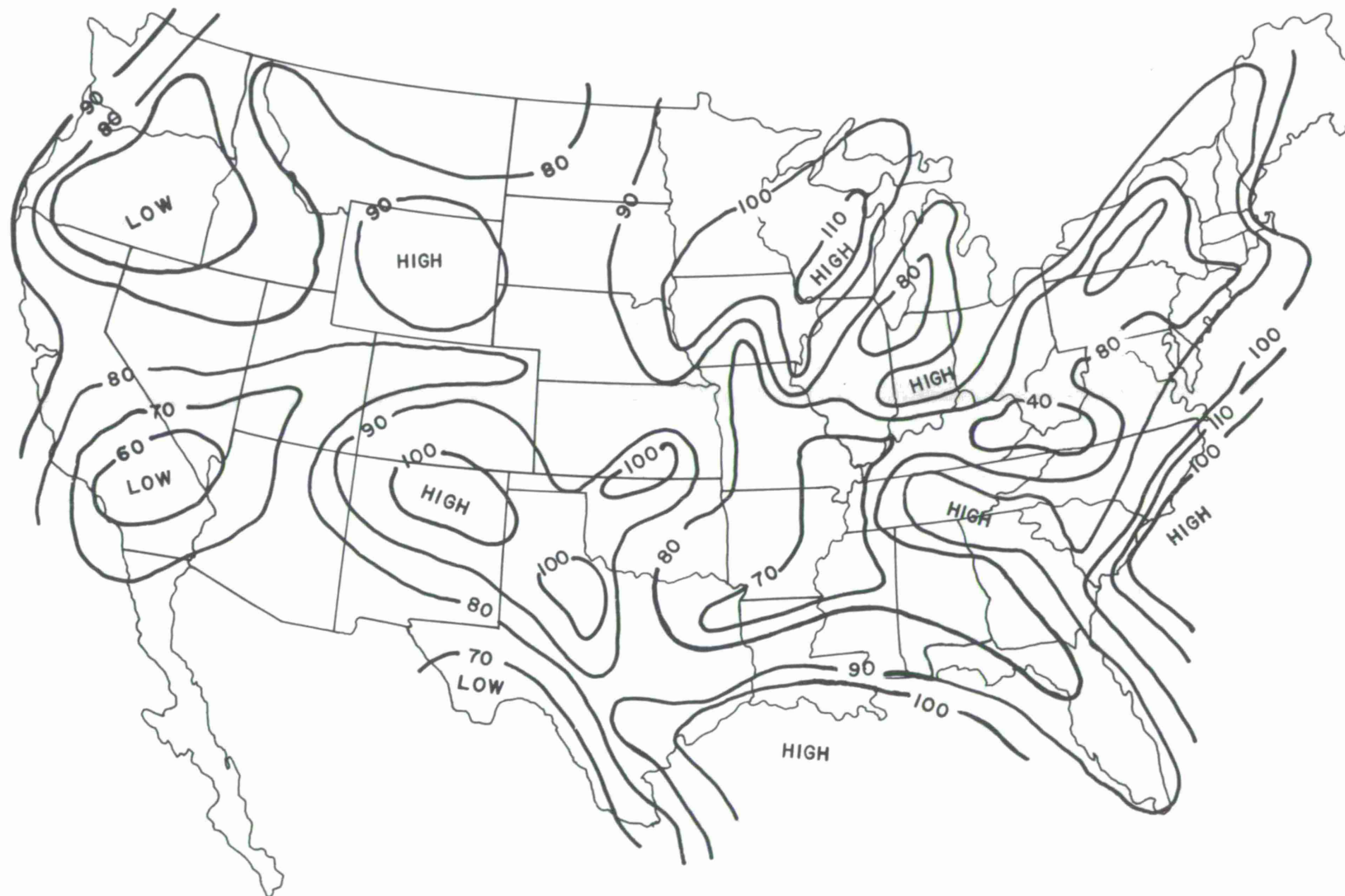


Figure 8.2. Wind-velocity map of the United States; isopleths of 1% of 25-year maximum 5-min wind in mph.

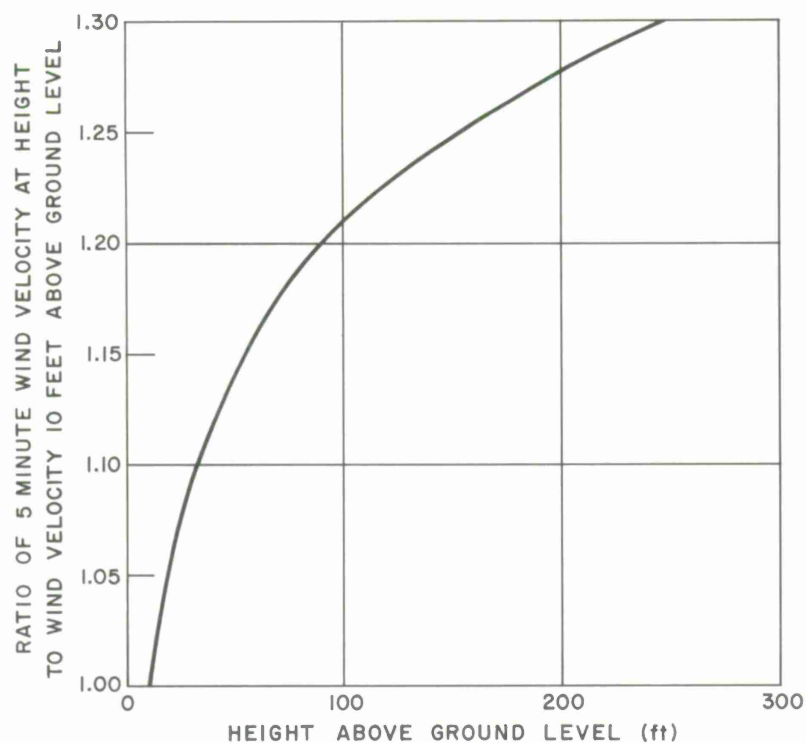


Figure 8.3. Wind-velocity data from five inland weather stations, 25-year period. Ratio of velocity at heights up to 300 ft versus that at 10-ft ground level.

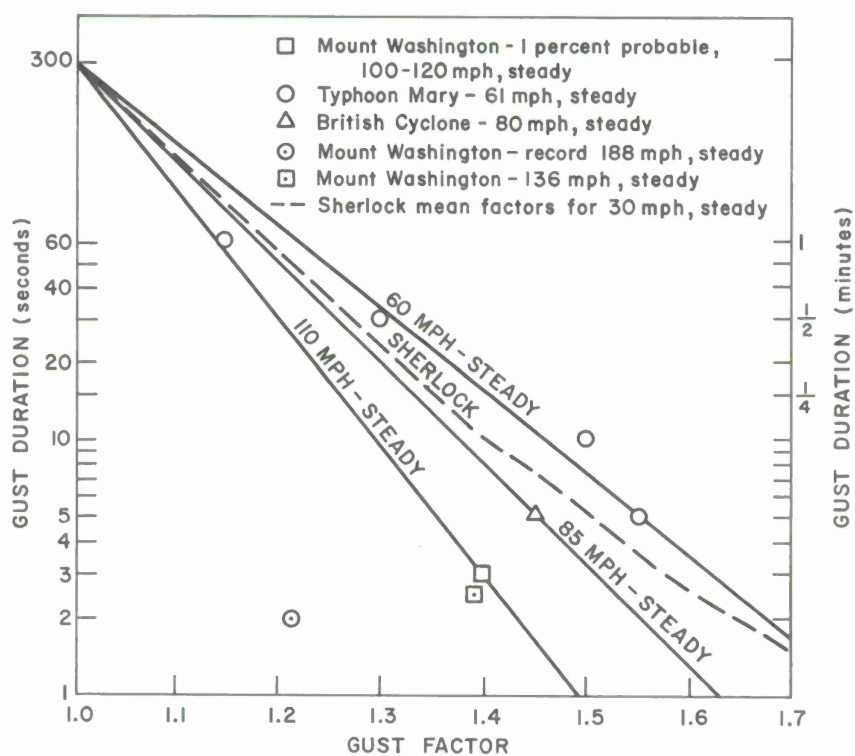


Figure 8.4. Estimated 1% probable gust factor for 5-min steady wind.

Table 8.1. Summary of secondary environmental conditions in Massachusetts area for structural design of radome

		Duration			
		5 min	1 hr	6 hr	24 hr
Rainfall (inches/hr)*		12.00	3.09	1.13	0.40
Minimum temperature, January **		-23° F			
Maximum temperature, July **		+107° F			
Rime ice (estimated maximum)		3.5 inches at sea level 5.0 inches at 1000 ft			
		25-year risk (%)			
Hail	Diameter (inches)				
	{ 1.00	71			
	{ 1.25	44			
	{ 1.50	30			
* 1% risk of occurring in 25-year span.					
** 2% risk of occurring in 25-year span.					

8.4 Space-Frame Geometry

Because the CAMROC antenna will be used mostly for sky observation and at elevations where low-angle ground scatter will not interfere with antenna performance, the choice between uniform and random space-frame geometries for the 550-ft CAMROC radome will depend on the relative optical blockage and on the economics of fabrication and erection for these frame types (see Annex 5).³ The uniform geometry has been investigated first, because of the comparative ease in generating a relatively simple uniform division of the whole structure into convenient sections.

The radome geometry was developed by considering an icosahedron, which consists of 20 equilateral triangles and 12 vertex points arranged as shown in Figure 8.5. Each vertex point falls on the surface of the sphere, which can be made to circumscribe the icosahedron. By locating the centroid of one of the triangles, elevating this point to the circumsphere, and drawing chords from this point to the apices and midpoints of the sides of the triangles, the triangle is subdivided into six congruent triangles, as shown in Figure 8.6. The congruent triangle AEG is now further divided. This process consists in the development of a triangular-type grid composed of 15 to 20 points that fall on the surface of the sphere and the associated chordal connections (corresponding to the beam elements) between these vertex points. Once this basic unit has been established, all the vertex points and beam members in the radome space frame can be developed through a series of reflections and/or rotations of the basic unit.

A computer program is in operation that performs these reflections and rotations on the basic input unit. A subroutine is also in operation that develops all the necessary input information from a convenient specification of the vertex points in terms of polar

coordinates and an identification of the beam members by vertex points. By means of these programs, three uniform geometries have been defined. These geometries represent candidates for use in the CAMROC radome application.

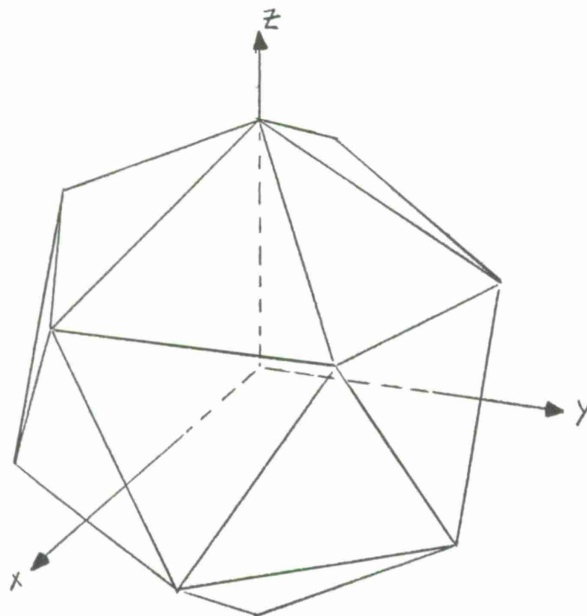


Figure 8.5. Icosahedron used in development of radome geometry.

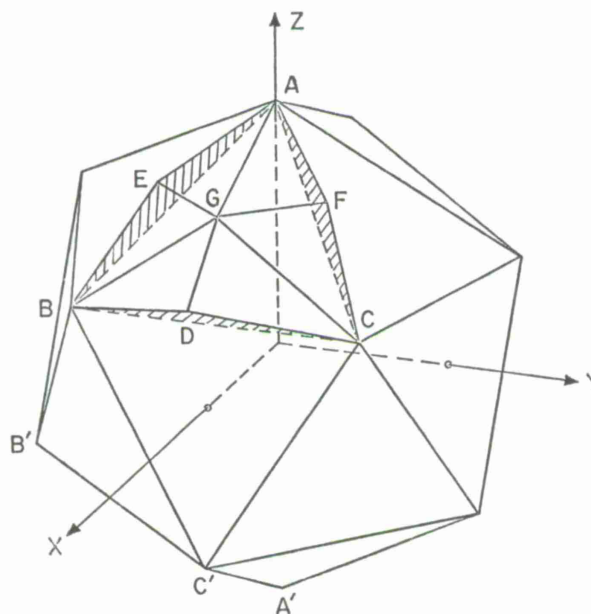


Figure 8.6. Breakdown of icosahedron used in development of uniform space-frame radome geometry.

In order to obtain some estimate of the effect of beam length on the structural performance of space-frame radomes, geometries with nominal beam lengths of 30, 40, and 50 ft were developed. The number and length of beams distributed about the surface of the 550-ft CAMROC space-frame radome, as determined by the computer program, are shown in the geometries in Figure 8.7. The number of beams, number of hubs, and the total length of beams are plotted as a function of beam length in Figure 8.8. The data points correspond to the computer output for the three geometries that have been developed, and the curves represent an approximate formula.

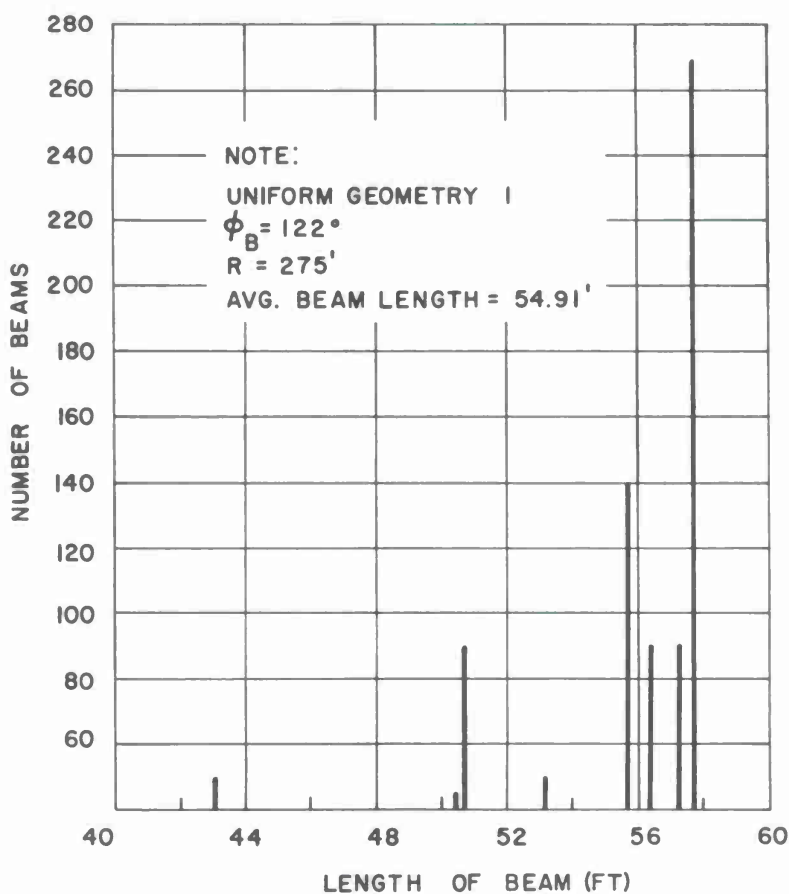


Figure 8.7a. Distribution of number and length of beams in 550-ft-diameter space-frame radome (ϕ_B is defined in Figure 8.8.)

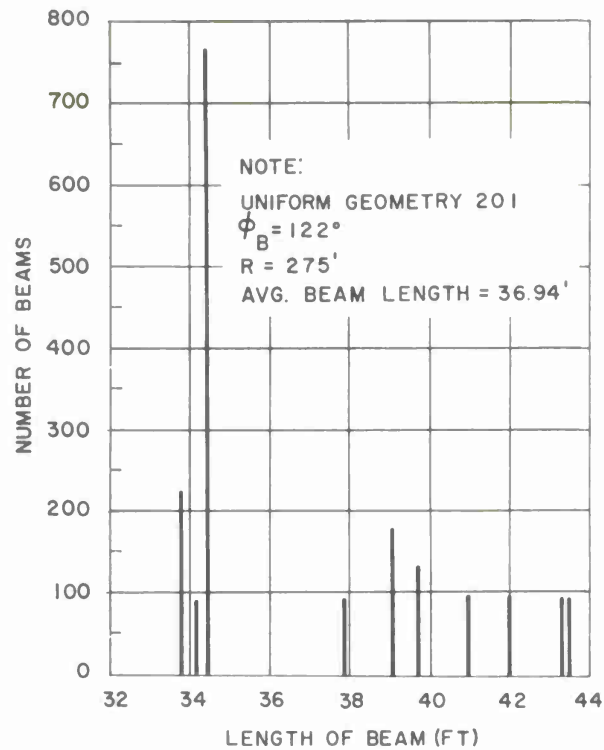


Figure 8.7b. Distribution of number and length of beams in 550-ft-diameter space-frame radome (ϕ_B is defined in Figure 8.8).

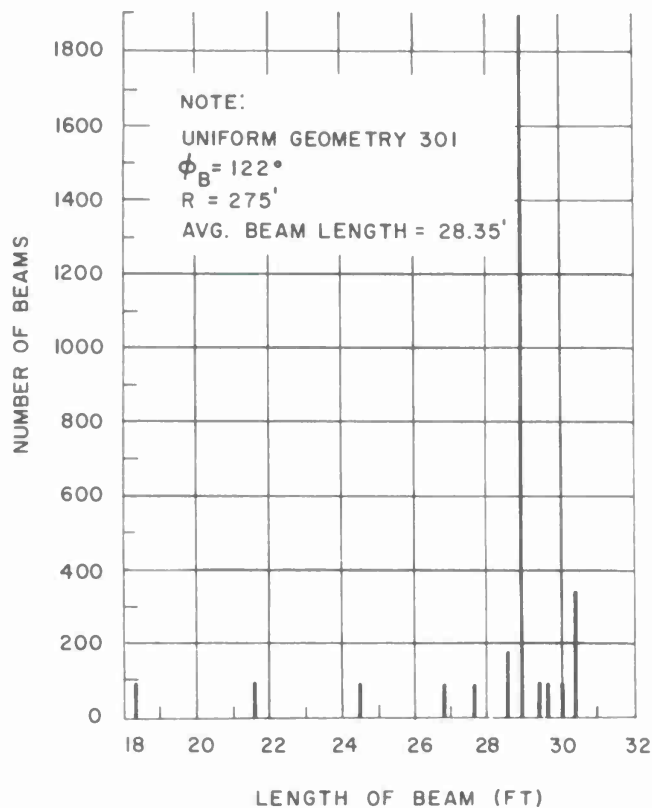


Figure 8.7c. Distribution of number and length of beams in 550-ft-diameter space-frame radome (ϕ_B is defined in Figure 8.8).

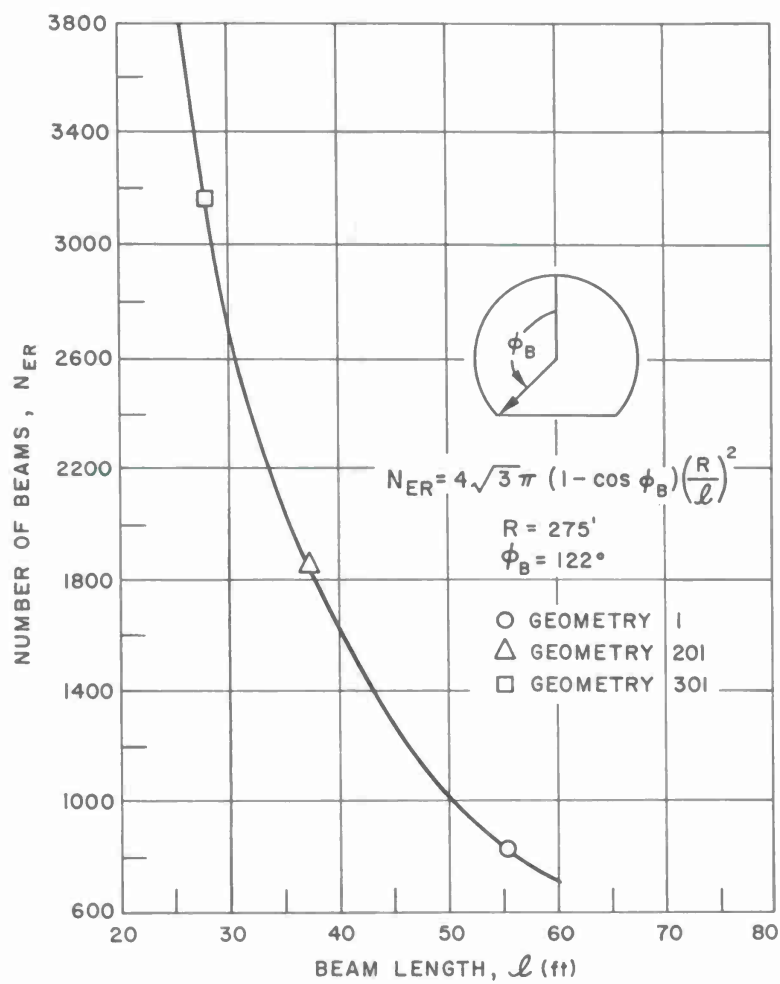


Figure 8.8a. Number of beams in 550-ft-diameter space-frame versus beam length.

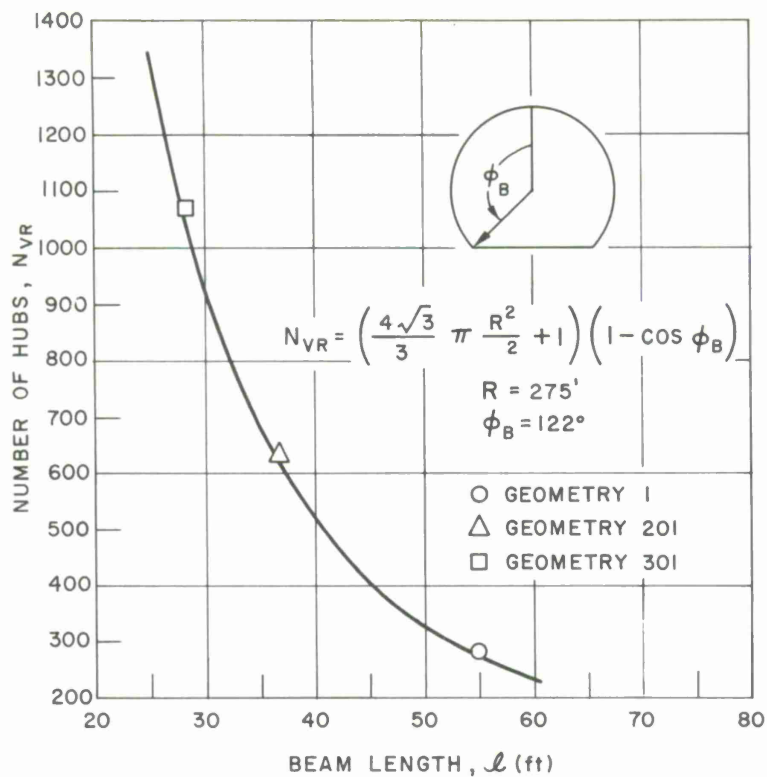


Figure 8.8b. Number of hubs in 550-ft-diameter space-frame versus beam length.

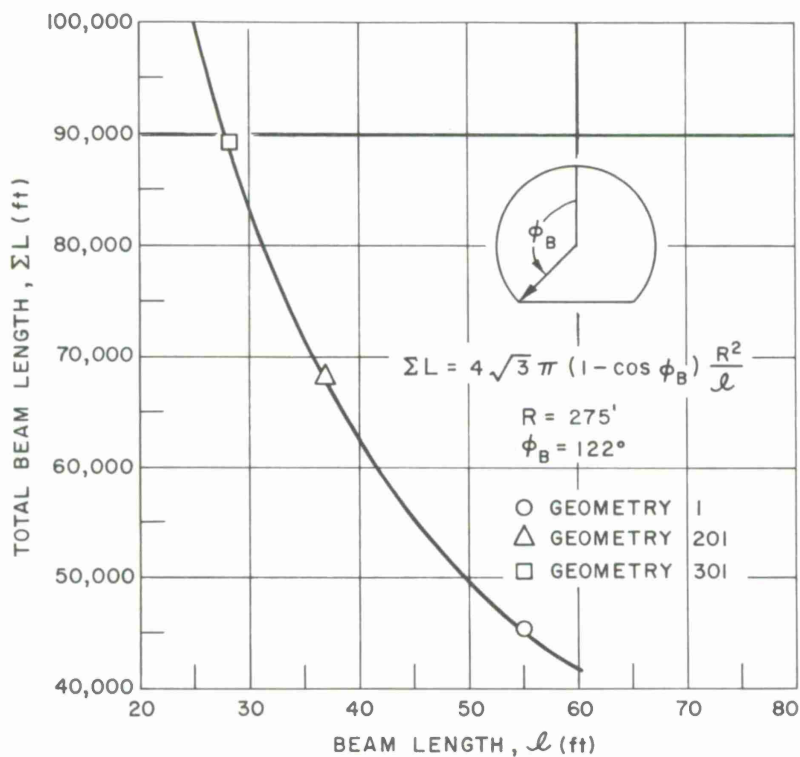


Figure 8.8c. Total length of beams in 550-ft-diameter space-frame versus beam length.

8.5 Structural Analysis

8.5.1 Introduction

In order to design a radome that is structurally reliable and has the best possible electromagnetic performance, an extensive analysis is required. The program of analysis that will be used in the design of the CAMROC radome is described in this section. In Section 8.5.2, the types of load to which the radome will be exposed are briefly reviewed, and the modes of failure that must be prevented are indicated. Next, in Sections 8.5.3 and 8.5.4, the analysis of the general instability of the structure and the detailed stress analysis of the individual beam members are discussed. The extensive use of a digital computer is necessary for both these analyses because of the large number of beams to be analyzed. The needed programs being developed are described.

The analysis and design of the membranes are of vital importance to the electromagnetic performance of the radome. What has been done and is being done is described in Section 8.5.5.

Finally, in Section 8.5.6, some of the preliminary methods of space-frame analysis are outlined and preliminary estimates of the member sizes are made.

8.5.2 Loading and modes of failure

8.5.2.1 Loading

There are two primary loading conditions to which the radome will be exposed:

- a. Dead-weight loading. The radome will be subjected to its own dead weight.
- b. Wind loading. After the radome has been completed, it will be subjected to the wind requirements discussed in Section 8.3. The design wind loading must be combined with the dead-weight loading to obtain the total loading applied to the radome under this condition.

8.5.2.2 Modes of failure

Before the modes of failure that can be experienced by the frame are considered, it will be helpful to review briefly the functional behavior of the structure.

It is to be noted at the outset that the frame provides the primary load-carrying capability for the radome. The differential pressure on the radome caused by the wind is resisted by the membrane panels, as shown in Figure 8.9. In supporting the pressure loading, large tensile stress resultants T are developed in the membrane, as shown in Figure 8.10a.

The unbalanced forces in the y direction where the membranes are attached to the beam produce a lateral loading $2T \sin \alpha$, which must be supported by the beam. The distribution of lateral loading is approximately triangular, as shown in Figure 8.10b. The transverse loads on the individual beams are, in turn, redistributed by "shell-type"

action of the entire frame structure into primary axial loads in the beams (load P in Figure 8.10b). The primary axial stresses in the frame are finally reacted at the base of the structure by the foundation. Thus, each member has a combined axial and transverse loading, requiring a general beam-column analysis for every beam in the structure. The dead-weight loading of the structure is distributed throughout the frame in a similar fashion.

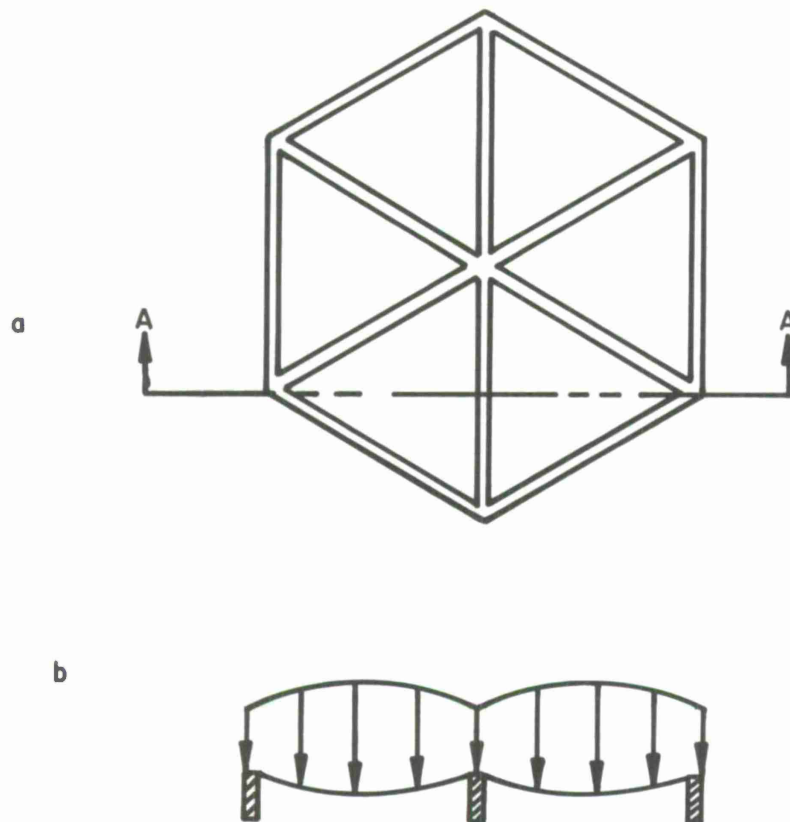


Figure 8.9. Typical radome panel grouping: a - Typical plane grouping. b - Section A.A of panel grouping.

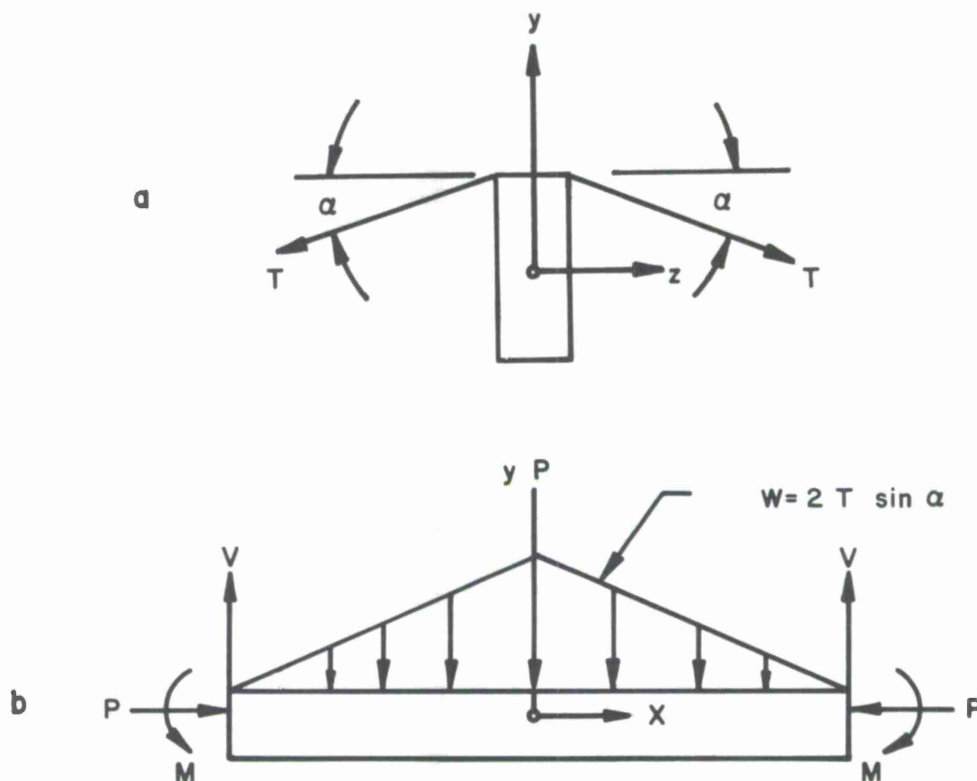


Figure 8.10. Forces on typical radome beams: a -Cross section of beam indicating membrane forces. b- Typical beam isolated from structure.

There are two primary modes of failure that must be examined:

a. Failure of individual members. The failure of individual members will occur when the allowable tensile or compressive stress for the material is exceeded. The failure of a member as a beam column can occur in either of two possible modes. The first mode is failure of the beam column in the plane of the membrane (this is the z direction in Figure 8.10a). This is generally the "weak" axis of the member because the member will usually be deeper than it is wide. A torsional mode of failure is possible but, with planned beam cross-sectional dimensions, is not likely. In the case of failure about the "weak" axis, the only transverse loadings that need be considered in conjunction with the axial load are the appropriate dead weight of the member and the wind-pressure loading that occurs before any panels are installed. The second mode of member failure occurs about the "strong" axis (in the y direction in Figure 8.10). In this case, there will be large transverse loadings on the beam from the adjacent membranes. The stresses due to beam-column action about the strong axis must not exceed the allowable stress for the material.

b. General instability of the radome frame. This mode of failure involves the entire radome framework and is possible even when the individual members have been designed so as to prevent failure as beam columns.

In addition to these modes of failure for the complete structure, failure must be prevented in the partially erected radome. Since erection stresses depend so greatly on the details of the erection and the methods of bracing during erection, they cannot be considered at the present time. During later phases of the program, however, when the details of the design have become firm, the erection bracing and procedure must be checked against the possibility of failure during erection.

8.5.3 General instability^{4, 5, 6}

8.5.3.1 Introduction

Although the maximum stresses in the radome may be well within the capacity of the frame material, that is, below the yield strength, the structure can still fail as a result of general instability, i. e., a buckling collapse of several adjacent panel groups. At present there are no reliable solutions that relate the elements of the applied load and the parameters of the space frame in order to predict the buckling capacity of the structure. Approximate solutions that replace the framework by an equivalent spherical shell with extensional and flexural stiffness similar to the space frame are sometimes attempted. However, this approach is questionable, primarily because the characteristic length of buckle in the equivalent shell is of the same order of magnitude as the member lengths in the radome frame.

For any distributed, arbitrary load acting on the surface of the radome, a plot of the load intensity versus the frame deflection will yield the load at which the space frame becomes unstable. A nonlinear load-deflection analysis of this kind is considered to be the most practical and reliable method for studying general instability. The nonlinearity of this method derives from the effect of the changing geometry on the equations of equilibrium, from the influence of the varying axial force in a member on the flexural rigidity of the member, and also from any nonlinearity of the stress-strain properties of the frame material. It is estimated that stress-strain nonlinearity will not be significant for the frame materials of interest. Then, if general buckling does not occur within the linear stress-strain region of the material, the load at the initiation of nonlinear stress-strain behavior can be accepted as the upper buckling limit.

Even when the nonlinearities are limited to the effects of geometry change and the influence of the varying axial force on the flexural rigidity of the member, the analysis is still computationally complex. The complexity derives from the fact that the computation must proceed using small load increments and also from the very large number of member elements in the structure. Fortunately, the existence of large-capacity computers and the evolution of programs for the analysis of complex structures permit nonlinear analyses of this kind.

The most acceptable procedure for the development of a buckling criterion for space-frame radome structures consists in blending the analytical and the experimental. Thus, if a reliable, computer-implemented, theoretical solution is developed, then the separate variables — geometry, member properties, wind-load distribution, imperfections — can be readily introduced in successive computer runs. Hence, a computer-implemented analysis is judged to be an essential prerequisite for the design of an efficient radome structure. However, in order to verify the theoretical method, the analysis must be complemented by an experimental investigation. For this purpose, the physical models are not required to represent in any great detail either the entire radome or the anticipated load distribution.

8.5.3.2 Theoretical analysis

8.5.3.2.1 Formulation of the governing equations*

a. Assumptions. The material is considered to be linear elastic and the strain to be negligible with respect to unity. It is also supposed that the rotation ω of the tangent to the centroidal axis is sufficiently small that $\omega^2 \ll 1$. This restriction requires ω to be less than about 15° and is not too severe.

b. Derivation of the equations. The differential equations and boundary conditions consistent with the geometrical approximation ($\omega^2 \ll 1$) are derived by applying the principle of virtual displacements. The planar case is considered first, and the results are then extended to the three-dimensional case. The relations between the end actions and end displacements are expressed in matrix form,

$$\underline{F} = \underline{K} \underline{U} + \underline{F}_0 \quad , \quad (8-1)$$

where \underline{F} is the end-action matrix, \underline{U} contains the end displacements, and \underline{F}_0 contains nonlinear terms due to the rotation of the chord. The elements of \underline{K} are also nonlinear functions of the axial force.

c. Solution procedure. The solution procedure involves combining an incremental loading technique with a corrective procedure. It is assumed that the system is linear within a load increment and that the tangent stiffness matrix \underline{K}_T evaluated at the position prior to the load increment is used. The incremental equations have the form

$$\Delta \underline{F} = \underline{K}_T \Delta \underline{U} = (\underline{K} + \underline{K}_G) \Delta \underline{U} \quad , \quad (8-2)$$

* The formulation, herein summarized, was carried out by Simpson Gumpertz & Heger Inc., with independent verification by Prof. Jerome Connor, Civil Engineering Department, MIT; see Annexes 8 and 11.

where \underline{K} is the same as in (8-1) and \underline{K}_G is due to the nonlinear geometric terms in \underline{F}_0 . Actually, \underline{K}_G is defined by

$$\Delta \underline{F}_0 = \underline{K}_G \Delta \underline{U} \quad . \quad (8-3)$$

After a certain number of load increments have been applied, the displacements are corrected by iterating on the exact equations; e. g., equation (8-1). The relations for the $(n + 1)$ th cycle are

$$\underline{F}^{(n+1)} = \underline{K}^{(n)} \underline{U}^{(n+1)} + \underline{F}_0^{(n)} \quad , \quad (8-4)$$

where $\underline{K}^{(n)}$, $\underline{F}_0^{(n)}$ are evaluated at $\underline{U}^{(n)}$. The displacements predicted by the incremental approach are used as a starting value for (8-4). Once convergence is obtained, the incremental approach is continued, using \underline{K}_T evaluated at the corrected displacements.

8.5.3.2.2 Adaptation and development of computer programs for stability analysis*

a. Linear elastic solution. The linear solution for a statically indeterminate elastic structure considers the geometry, topology, boundary conditions, elastic properties, and applied loads to obtain a gross solution giving joint or nodal displacements, boundary forces, and joint forces acting on each structural component or member.

A displacement method of analysis has proved tractable and economical to solve on a digital computer. The solution process can easily be segmented into a linear series of steps, leading to the solution of the global problem. These steps are:

- 1) Compute member stiffness matrices from properties.
- 2) Modify to account for member force releases.
- 3) Assemble global stiffness matrix from member matrices and topology.
- 4) Compute effects of member loads.
- 5) Assemble load vectors.
- 6) Modify stiffness matrix and load vectors to account for boundary force releases.
- 7) Solve for joint displacements.
- 8) Compute member end and joint forces.

A number of computer programs utilizing such analysis techniques are now available. Considerations for their use include generality, efficiency, capacity, and reliability. The program discussed here, in addition to satisfying these criteria, is also readily modified. The program is called the stiffness analysis of the STRUctural Design Language, or STRUDL. STRUDL itself is an applications subsystem of the Integrated Civil Engineering System, ICES, now under development in the Department of Civil Engineering at MIT.

*Implementation of stability analysis on the computer, as herein described, is currently being carried out by Simpson Gumpertz & Heger Inc., in cooperation with Prof. R. D. Logcher, Civil Engineering Department, MIT.

STRUDL and its stiffness analysis are now operational in the Civil Engineering System Laboratory, CESL, at MIT on an IBM System/360 Model 40. Work is continuing on improving its efficiency and reliability and on its documentation. The present version runs on the System/360 under the CESL Monitor. STRUDL will shortly be converted to operate under the control of Operating System/360.

b. Evaluation of nonlinear analysis formulation. A computer program has been written for the nonlinear solution of a very simple two-degree-of-freedom problem. This problem corresponds to a model structure tested during the summer of 1966, the results of which are available and used for comparison.

Initial solutions show a good correspondence between experimental and analytic tests. Differences are sufficiently small to be attributable to the differences and variations in material properties. The solution technique is solved directly for each point on the load-deflection curve.

In order to evaluate the effects of various nonlinear terms in the formulation, analytic tests were also made neglecting first the effect of curvature on the axial stiffness and second this effect and the effect of chord rotation. The critical buckling loads for these cases were increased by 10% and 30%, respectively. Thus, it does not appear possible to neglect either effect.

Only preliminary work has been done in evaluating the incremental loading-displacement correction technique. No feeling has yet been gained on increment sizes or on the number of increments between corrections. It does appear from this simple model that the number of cycles of iteration needed in a correction will be modest.

c. General nonlinear analysis for instability. Because of the segmentation of the linear analysis of STRUDL and of its modularity, it is quite feasible to modify and expand this system to perform nonlinear analysis. When directed toward the radome analysis, the task of creating such a program can be separated into 1) development within STRUDL, 2) implementation and tune-up as a special program, and 3) production running. Work has started at CESL on the first area. The latter tasks will be carried out by Simpson Gumpertz & Heger Inc.

The nonlinear analysis will proceed as the linear analysis and will contain a cycling control mechanism. The process flow is shown in Figure 8.11. Changes in the STRUDL stiffness-analysis-process components for the nonlinear analysis include:

- 1) Creation of a control-iteration routine.
- 2) Modification of the member-stiffness calculation for the effects of axial load and end displacements.
- 3) Modification of the load vector calculation to operate on load increments and partial total loadings.

- 4) Modification of the solution algorithm to trap a recovery procedure to indicate joint instability.

Stability criteria must also be studied.

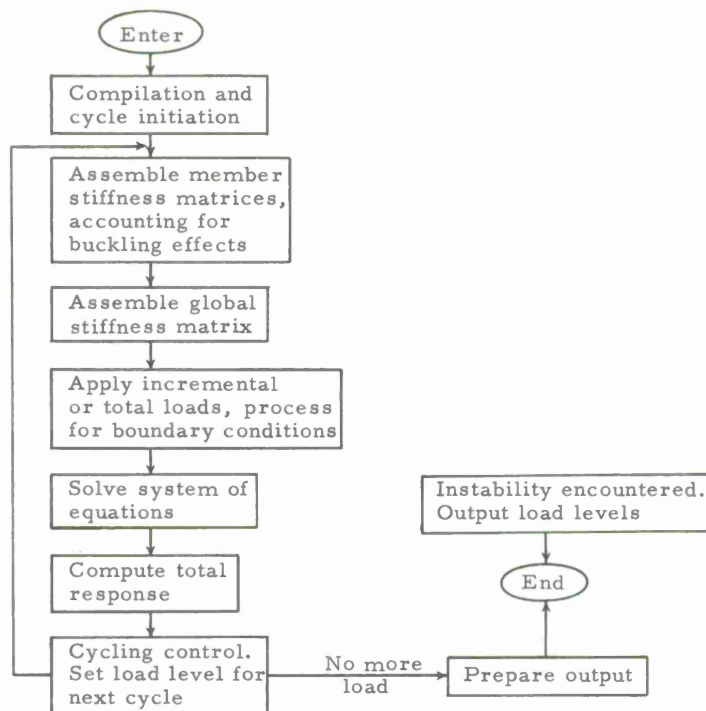


Figure 8.11. Nonlinear analysis processes.

Work is currently proceeding on these modifications and on new STRUDL language commands. Commands will allow the specification of total loading conditions that can be segmented, or of incremental loading conditions for which load levels may be specified for all increments. A limited amount of output may be specified with the NONLINEAR ANALYSIS command to provide output after each cycle, which will be useful for monitoring the analysis.

The following limitations will initially govern:

- 1) Only prismatic members are treated.
- 2) Distributed member loads are not treated (i. e., loads are concentrated at joints).
- 3) Nonlinear material properties are not considered.
- 4) Shear deformations are neglected.
- 5) Postbuckling behavior will not be tracked.

Each of these limitations can be eliminated with further development and is probably desirable for use with the final CAMROC radome design. Items 1), 2), and 4) are not difficult to include in the analysis.

Performance of the computer program is of interest because of the size of the structure to be treated. An initial estimate of the analysis speed on a Model 65 System/360 indicates a solution speed of 1-1/2 to 2-1/2 sec per joint per cycle for a structure of the 150- to 200-joint size. If a need for about 20 cycles for a solution is considered, the time for the solution of a 180-joint structure would be 90 to 150 min of machine time. Analysis of the full radome, about 1000 joints, may involve on the order of 15 hr, depending upon how peripheral equipment is used.

d. Schedule. It is expected that the program will be operational by May 1, 1967.

8.5.3.3 Space-frame model buckling tests⁴

To establish the validity of the critical buckling load predictions that will be obtained from the computer analysis, an experimental investigation of the critical buckling loads for a model space-frame structure has been undertaken. All the essential elements of the radome structure are included in the model design except the skin. Consideration will be given to including this parameter after the initial frame-buckling tests have been completed.

a. Metal frame model design. Because of space limitations in the test area at MIT, the model diameter was fixed at 14 ft. A random-geometry formulation that had been developed and used for a previous radome application and that showed some promise as a candidate for the CAMROC system was selected for the model space frame. To avoid interference with the development of the buckle, a spherical surface with an included half-angle of 52° was designed.

For ease in fabrication and assembly, a rectangular cross section was adopted for the beam members, while the hub design was fashioned from two flat disks, one positioned along the top and one along the bottom of the beams at the intersection of the beam members. To develop maximum rigidity at the joints, the individual disks are 1.5 inches in diameter, 0.220 inch thick, fashioned from 4158 steel, heat treated to Rockwell "C" 33, and secured to each other by means of two #4 bolts passing through each member at the joint. In order to develop a buckling failure at a minimum load, the beam members were fabricated from 7075-T6 aluminum. A preliminary buckling analysis⁷ established the member cross-sectional dimensions at 0.250 inch wide and 0.313 inch deep. The hubs and beam members are depicted in Figures 8.12a and 8.12b.

The model will be assembled by supporting all the hubs from a mandrel whose diameter is 8.0 inches less than that of the space frame. The beams will then be drilled, reamed, and bolted in place. Finally, when the model radome has been completed, all hubs will be released from the mandrel except the anchor hubs at the base. The mandrel is shown in Figure 8.12c.

b. Metal frame model test. A whiffle-tree loading apparatus that will permit the application of load increments up to 100 lb per joint is being designed. Some 64 joints equally distributed about the zenith will be loaded. The mandrel will be equipped with joint stops that will limit the deflections and thereby prevent excessive deformation of the frame. This precaution will permit the experiments to be repeated after the replacement of any damaged members. Strains and deflection measurements will be recorded at selected locations during each test.

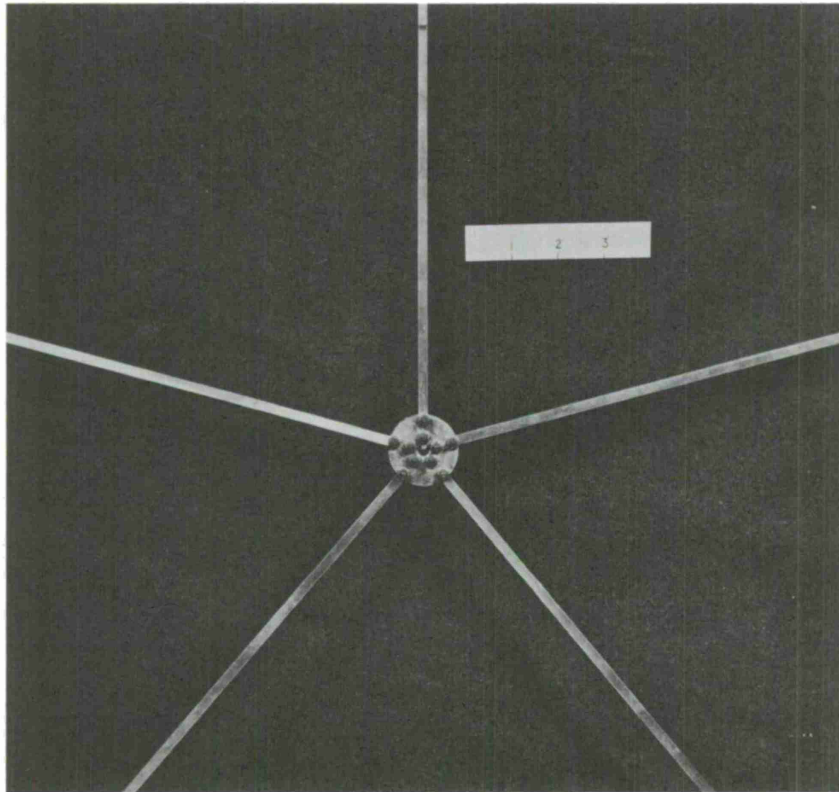


Figure 8.12a. Beam-hub design for 14-ft-diameter test model.

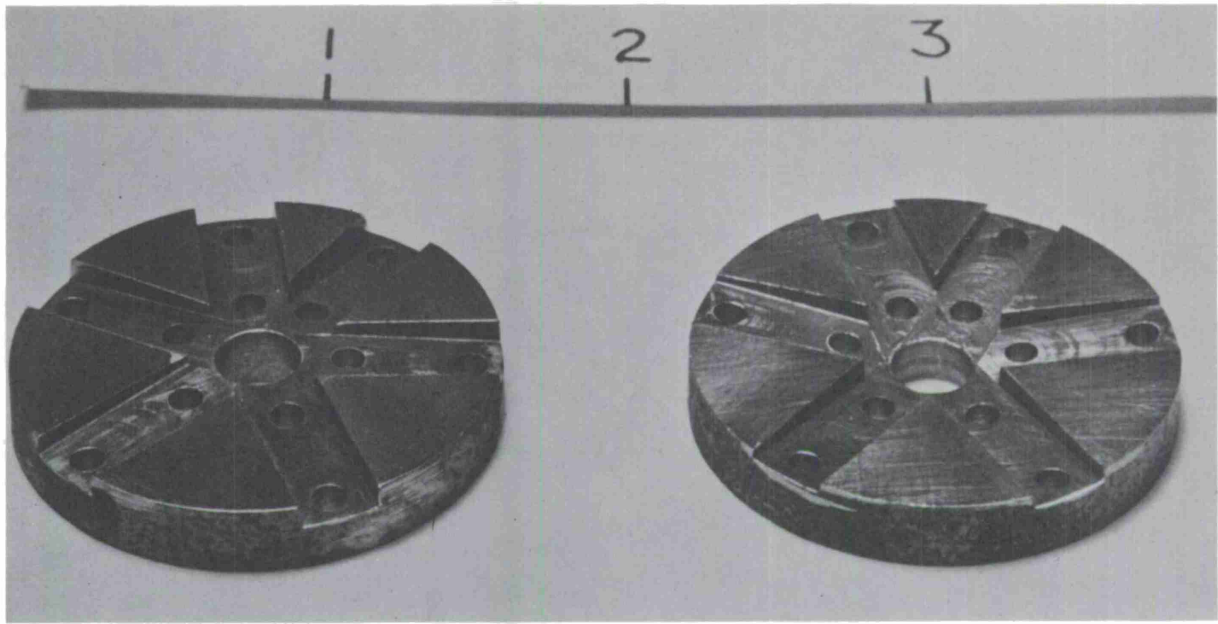


Figure 8.12b. Typical hubs for test model.

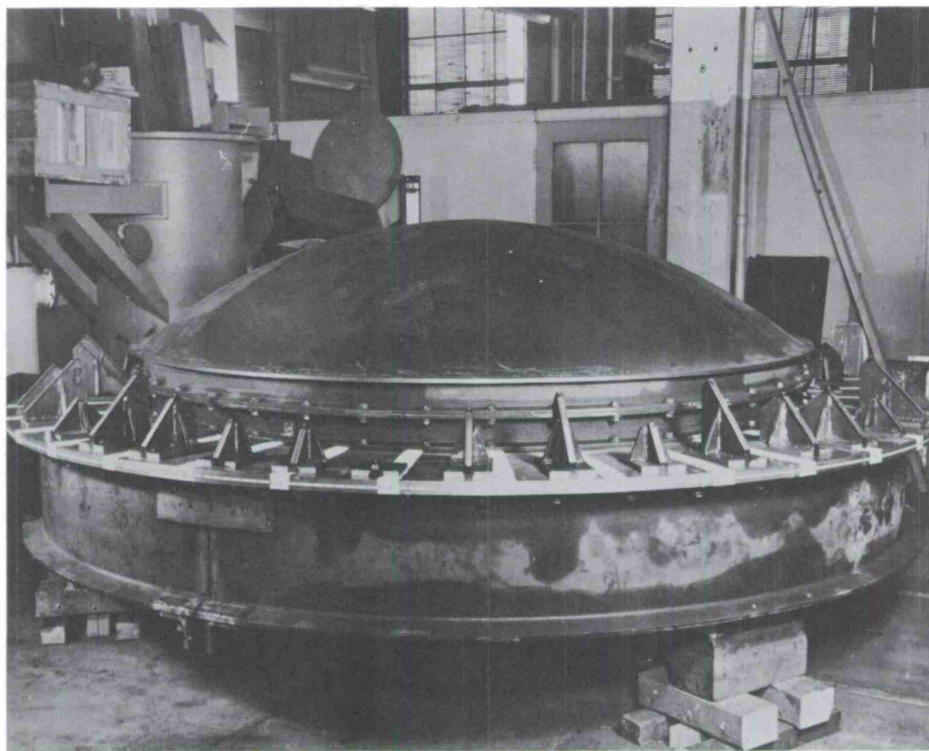


Figure 8.12c. Mandrel for radome model tests.

c. Plastic frame model tests.⁸ The models consist of a unit hexagonal frame of the type that is continuously repeated over a spherical surface to form the conventional space-frame radome structure (see Figure 8.13).

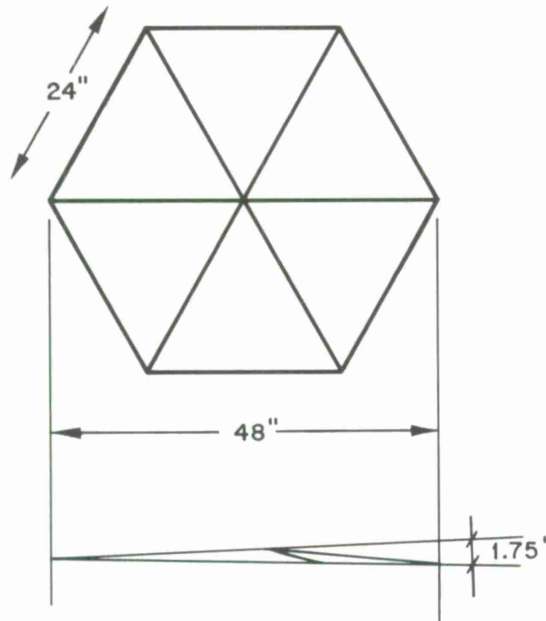


Figure 8.13. Plastic model dimensions.

These component tests are designed to provide preliminary checks for evolving computer-implemented analysis, and to provide backup for the primary model studies should the latter encounter serious unanticipated delays.

The Structural Models Laboratory of the MIT Civil Engineering Department recently completed a series of tests on the unit hexagonal framework. All the models were of plastic and had the geometry shown in Figure 8.13. Two rectangular member shapes, 0.7 by 0.7 inch square and 0.35 inch wide by 0.7 inch deep, were used. Preliminary studies included both methyl methacrylate (Plexiglas) and polyvinyl chloride (Boltaron 6200) models; however, success in obtaining 100% rigid joints with the methyl methacrylate models (with PS-18 cement) led to the selection of acrylic members.

For statistical purposes 12 models, 6 of the 0.7 \times 0.7-inch cross section and 6 of the 0.35 \times 0.7-inch cross section, were fabricated and tested. The material modulus of elasticity was approximately 500 ksi. For imposed vertical displacements at the apex joint, measurements were taken of the applied load versus the apex joint vertical

displacement. Typical load versus deflection curves are shown in Figure 8.14. The 0.35×0.7 -inch cross-section models failed by weak-axis Euler buckling of the individual inclined struts. The 0.7×0.7 -inch models buckled in a symmetrical snap-through mode. The postbuckling behavior (e. g., the unloading branch of the load versus deflection curve for the 0.7×0.7 -inch models) was readily obtained because the loading system was one that imposed the displacement and not the load. After unloading, the models could be retested as desired.

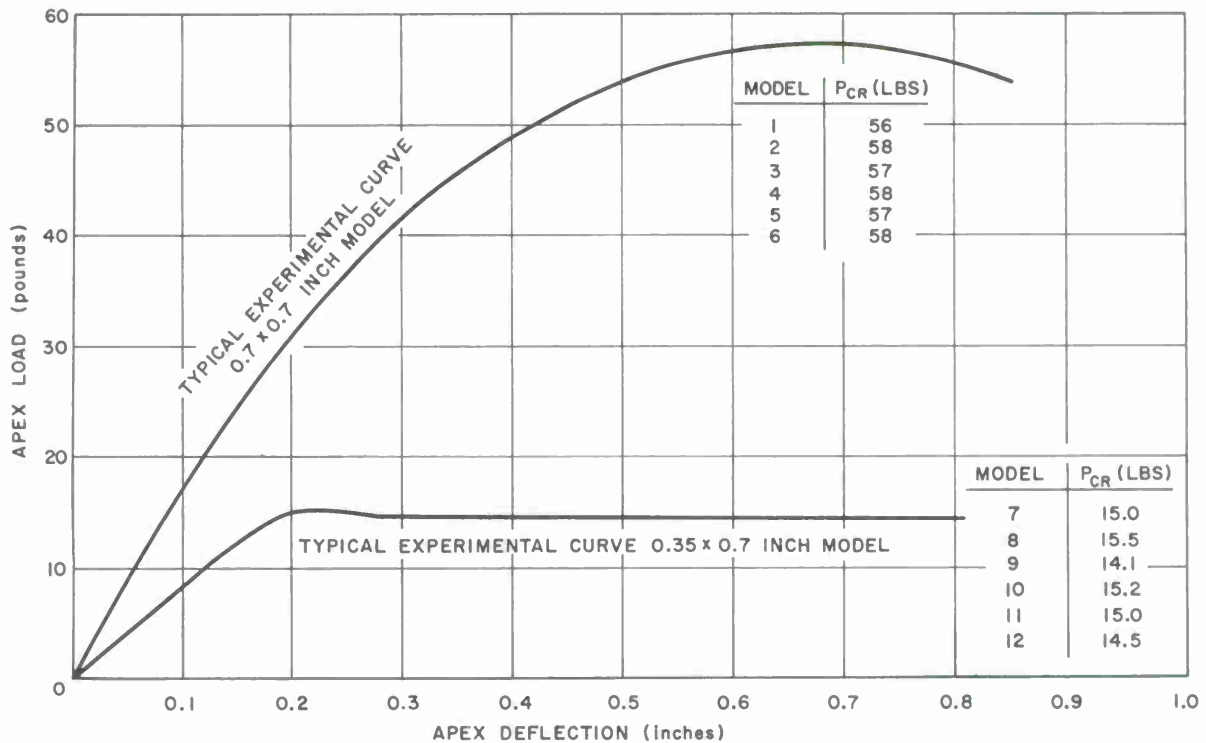


Figure 8.14. Acrylic model results.

Future testing will include:

- 1) An experimental study comparing the behavior of steel frame models with the acrylic models.
- 2) An experimental study comparing the behavior of smaller scale acrylic models to those already tested. After the smaller scale has been justified, a 20° or 30° segment of the radome will be remodeled in acrylic to study the buckling behavior of a larger portion of the total radome.

8.5.4 Development of computer program for radome stress analysis

The stress analysis of the CAMROC radome involves modifying and extending several existing computer programs, developing new ones where required, and linking the separate elements into a complete design process.

The finished program, to be called STAR (STructural Analysis of Radomes), will require that a batch of vertex points and beam members corresponding to $1/6$ of an icosahedral triangle ($1/120$ of the spherical radome area) be read into the program. The first section of the program will then develop all the vertex points and beam members for the complete radome structure, and by utilizing a Fourier fit to the measured wind-tunnel pressure-distribution data, the program will determine the forces acting at each vertex point and the intensity of the triangular load distribution acting along the length of each beam. This information will be assembled in proper sequence by the computer and punched out on cards or written on tape for immediate entrance to available structural programs. This portion of STAR is now operational. Three geometries (described in Section 8.4) have been developed and are ready for the structural-analysis phase.

Part of the information developed in the first portion of the program will be used as input to the STAIR program.⁹ By means of STAIR and preliminary estimates of the cross-sectional dimensions of the beams, the axial load acting on each member in the frame will be calculated. The remaining information on the transverse loads will be coupled with the STAIR results, and the maximum stresses in each beam member in the space frame will be determined by means of a beam-column analysis program. This latter portion will be repeated until the minimum acceptable beam dimensions for every member in the frame are developed. This procedure will be used with different geometries and the optical blockage of each final structure computed. The space frame that yields the minimum optical blockage is regarded as the most efficient.

It is expected that the radome computer analysis will eliminate the need for large safety factors, thus reducing the beam dimensions and minimizing the cost and optical blockage of the structure. Also, it is anticipated that a large number of frame geometries can be investigated in the search for the most efficient space frame for the CAMROC application.

8.5.5 Membrane design considerations

The determination of a suitable material for use in a 550-ft-diameter metal space-frame CAMROC radome is currently under investigation at North American Aviation, Inc., Columbus, Ohio. The mechanical, electrical, and fabrication problems constitute the main effort of this investigation.

Preliminary reports on the first two categories are presented below:

8.5.5.1 Mechanical

For the membrane study, it has been assumed that the structure must be designed to withstand a 130-mph wind and that the beam lengths in the space frame will fall between 30 and 45 ft with a minimum beam width of about 3 to 4 inches. These sizes have been chosen to study the membrane design and attachment problem and do not imply the selection of a beam design. Then the stresses and deflections developed in various membrane materials when covering 30-ft and 45-ft equilateral triangles and when exposed to the maximum local pressure ($c_p = 1.6$) engendered on a spherical radome by the 130-mph wind (0.48 psi) are under evaluation. The edge loads required to maintain tautness and a suitable method for engaging the membrane to the limited beam width are also under investigation. Also, estimates of the effects of fatigue, creep, weathering characteristics, water absorption, and degradation of mechanical properties with time on membrane performance are being made.

8.5.5.2 Electrical

It is required that the membrane produce a lowest possible loss in the electromagnetic transmission at frequencies as high as 6000 Mc/sec. For a typical dielectric constant of 4.0, the low loss requirement will be met with a membrane thickness of about 0.04 to 0.05 inch. If the dielectric constant is increased, the thickness must be decreased.

8.5.5.3 Fabrication

Owing to the size of the triangular cells that must be covered, it is apparent that the membrane will be fashioned in rectangular strips because of the Fiberglas reinforcement that will then be joined and processed to give the appropriate triangular area. The method of seaming, the number of seams, and the effect of the seams on the performance of the antenna are under investigation.

8.5.5.4 Preliminary results

A review of vinyl-reinforced Fiberglas and Mylar-Dacron-Tedlar composite materials indicated that these materials have acceptable electromagnetic and mechanical properties that resulted in small stresses in relation to the yield stress. However, the deflections under the design loads and the elongation and creep under the initial tautness load were considered excessive.

Attention was concentrated on various polyester resin systems reinforced with Fiberglas woven fabric. The calculated stresses, deflections, and edge slopes are summarized in Tables 8.2 and 8.3 along with the appropriate physical and mechanical properties for some 10 variations of glass plies and weaves. Table 8.2 lists the results for the 45-ft equilateral triangle, while Table 8.3 contains the results for the 30-ft equilateral triangle.

To maintain panel tautness under an average wind of 10 mph, and thus to minimize the possibility of a fatigue failure, the edge load that must be applied to maintain a minimum deflection and fixed slope under the dead weight plus 10-mph wind load is calculated and presented in Tables 8.4 and 8.5 for the 30- and 45-ft triangles, respectively.

No substantial results are available yet on panel fabrication, attachment methods, or costs.

Table 8.2. 45-ft equilateral triangle exposed to uniform pressure, $q = 0.48$ psi

Panel thickness (inch)	Modulus of elasticity $\times 10^6$ (psi)	Allowable membrane stress (psi)	Computed maximum stress (psi)	Computed deflection at center (inches)
0.03-0.05	1.57-1.63	16,000-17,800	7,500-10,820	14-16

Table 8.3. 30-ft equilateral triangle exposed to uniform pressure, $q = 0.48$ psi

Panel thickness (inch)	Modulus of elasticity $\times 10^6$ (psi)	Allowable membrane stress (psi)	Computed maximum stress (psi)	Computed deflection at center (inches)
0.03-0.05	1.57-1.63	16,000-17,800	5,800-8,200	8-9

Table 8.4. 45-ft equilateral triangle exposed to uniform pressure corresponding to 10-mph wind load plus dead load

Panel thickness (inch)	Computed deflection at center (inches)	Edge load lb/in	Initial edge load required to maintain $0^\circ 30'$ slope (lb/in)
0.042	3.5	14.2	23.9
0.050	3.4	18.2	39.7

Table 8.5. 30-ft equilateral triangle exposed to uniform pressure corresponding to 10-mph wind load plus dead load

Panel thickness (inch)	Computed deflection at center (inches)	Edge load lb/in	Initial edge load required to maintain $0^\circ 30'$ slope (lb/in)
0.042	2.04	11.5	15.3
0.050	2.05	13.9	18.0

Note: All materials were fabricated from various combinations of the following Fiberglass cloths: #120, 128, 164, and 181. The same Hetron polyester resin was used throughout. The numbers are for the 45° direction to the weave in the Fiberglass cloth.

8.5.5.5 Electrical analysis of membrane effects

A number of possible combinations of laminations and joints to give the desired thickness and size for very large dielectric panels have been studied. These differ as to type of laminate overlap and the number and thickness of laminations used. The various combinations studied have been previously defined as to mechanical properties. Their effect on electromagnetic performance will be discussed here.

The various lay-ups defined previously consist of three to five plies, with overlapping seams within each ply. The overlapping seams cause an increase in overall laminate thickness equal to that of a single ply at each seam and equal to twice the thickness of one ply at seam intersections. Transmission of energy through the panel is affected by each thickness and the relative area occupied by each, according to the following relationship:

$$T = a T_A + b T_B + c T_C ,$$

where a is the percent of area occupied by thickness A , and T_A is the voltage transmission coefficient for thickness A , etc. For the six laminate combinations considered, transmission loss, thus computed, ranges from 0.28 to 0.39 db. The small thickness increase resulting from overlap is of little consequence, transmission loss being governed almost entirely by the overall laminate thickness, irrespective of the seams.

The alternate means of obtaining large panels by lapping and bonding of completed, smaller sized panels was also considered as above. For the same nominal overall thickness of the panel, the transmission loss was calculated to be only slightly greater than that for panels fabricated by lapping one ply at a time during lay-up. The difference is on the order of a few hundredths of a db. Calculations were based on the use of laminate with a relative dielectric constant of 3.99 and a loss tangent of 0.046. Variation of loss with frequency for the worst case considered (0.046-inch membrane, 1.0-inch lap joint) is presented in Table 8.6.

Table 8.6. Variation of loss with frequency for 0.046-inch membrane, 1.0-inch lap joint

f(Gc/sec)	Voltage transmission coefficients		Relative area		Overall loss (db)
	Membrane	Joint	Membrane	Joint	
3	0.994	0.976	0.948	0.052	0.067
4	0.989	0.957	0.948	0.052	0.118
5	0.983	0.931	0.948	0.052	0.179
6	0.976	0.899	0.948	0.052	0.260

For further discussion of electromagnetic properties of metal space-frame radomes, see Section 7.1.

8. 5. 6 Preliminary analysis^{10, 11, 12, 13}

8. 5. 6. 1 General

The primary objective of the preliminary calculations contained in this section is to evaluate the general feasibility of the radome. To judge the feasibility of the radome, reasonable estimates are needed of the member sizes so that the electromagnetic performance, weight, and cost of the structure can be evaluated. In addition, a preliminary analysis provides an understanding of the primary parameters of the problem. It is understood that these preliminary calculations are not a substitution for the rigorous, detailed analysis of the stresses and the general stability described in the previous sections.

In order to make the preliminary calculations tractable, it is necessary to make assumptions. These should be clearly seen at the outset. The primary axial loads in the members and the evaluation of the general stability of the structure will be accomplished by means of the equivalent-shell technique. By transforming the space frame into an equivalent shell, advantage can be taken of the many solutions that exist for spherical shells under a variety of loading. This technique has been found to give reasonably good results in the analysis of framed domes. The axial loads so calculated will be used in conjunction with the lateral loads produced by the action of the wind on the membrane to examine the beam-column action of the members. The axial load will be assumed to act at the centroid of the section. In these calculations, the membrane will not be relied upon to provide primary lateral support of the beams. That is, the beams in the structure must have inherent structural stability. The loadings considered in the preliminary calculations will include both wind loads and dead-weight loads.

8. 5. 6. 2 Computation of axial loads — equivalent-shell technique

Hrennekoff¹⁴ has shown that a network of equilateral triangles of side length L can be transformed into an equivalent membrane plate having a thickness

$$t = \frac{2A_s}{L\sqrt{3}} \quad , \quad (8-5)$$

where A_s is the cross-sectional area of the beams. The elastic modulus of the plate has been assumed to be the same as that for the beams, namely E_s . If ϵ_s is the strain in the beam, the axial load P in the beam can be expressed as

$$P = E_s \epsilon_s A_s \quad . \quad (8-6)$$

This can be written in terms of the equivalent thickness as

$$P = E_s \epsilon_s \frac{\sqrt{3}}{2} L t \quad . \quad (8-7)$$

Now the strain, ϵ_s , along the beam can be expressed in terms of shell strains as

$$\epsilon_s = \epsilon_\theta \cos^2 \alpha + \epsilon_\phi \sin^2 \alpha + \frac{\gamma}{2} \sin 2\alpha, \quad (8-8)$$

and

$$\epsilon_\theta = \frac{N_\theta - \nu N_\phi}{E_s t}, \quad (8-9)$$

$$\epsilon_\phi = \frac{N_\phi - \nu N_\theta}{E_s t}, \quad (8-10)$$

$$\frac{\gamma}{2} = \frac{(1 + \nu) N_{\phi\theta}}{E_s t}, \quad (8-11)$$

where α is the angle between the beam and the θ axis, γ is Poisson's ratio, and N_ϕ , N_θ , and $N_{\phi\theta}$ are the meridional, hoop, and shear-stress resultants, respectively. The axial load can be expressed as

$$P = \frac{\sqrt{3}}{2} L \left(N_s - \frac{N_t}{3} \right), \quad (8-12)$$

where

$$N_s = N_\theta \cos^2 \alpha + N_\phi \sin^2 \alpha + N_{\phi\theta} \sin 2\alpha, \quad (8-13)$$

$$N_t = N_\theta \sin^2 \alpha + N_\phi \cos^2 \alpha - N_{\phi\theta} \sin 2\alpha. \quad (8-14)$$

Thus, when the shell stresses are known, the beam stresses can be computed as a function of the length and the angle between the beam and the θ axis.

8.5.6.3 Lateral loading – the beam-column problem

The lateral loads on the beams are produced by the wind loading transferred to the beams by the membranes and the dead weight of the beam itself. The lateral wind loading is assumed to have a triangular distribution, and the dead-weight loading of the beam is assumed to be uniformly distributed. A third case can be considered as a wind loading on the beam itself before the membranes have been installed. This third case can also be assumed as uniform. These various loadings are shown on beams isolated from the frame shown in Figure 8.15. In the figure, L_e is the distance between the inflection points (zero moment) on the beam and is a measure of end fixity. If the wind pressure at any point is taken as $C_p q$, where C_p is a pressure coefficient and q is the dynamic pressure,

$$W'_{WL} = \frac{\sqrt{3}}{3} C_p q L. \quad (8-15)$$

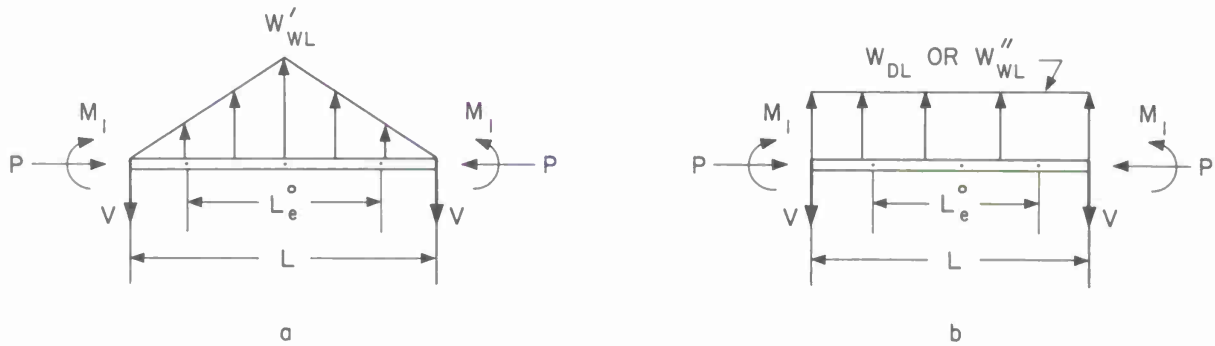


Figure 8.15. Lateral loading on typical beams: a, Triangular lateral load distribution. b, Uniform lateral load distribution.

The dead-weight running load W_{DL} is a function of the total weight of the beam and the angle of the beam axes relative to the gravity vector. The wind running load W''_{WL} is a function of the cross-sectional geometry of the beam, a drag coefficient that can be conservatively taken as 2.0, and the angle between the beam axes and the wind vector as well as its "shading" by other members.

The maximum stress at the center of the beam column from the wind loading can be expressed to a good approximation as

$$\sigma = \frac{P'}{A_s} + k' \frac{M'_0}{Z_z}, \quad (8-16)$$

where

$$k' = \frac{1}{\beta_1^2 P' L^2} \left(1 - \frac{\pi^2 E_s I_z}{\beta_1^2 P' L^2} \right), \quad (8-17)$$

$$\beta_1 = \frac{L_e}{L},$$

P' is the axial load in the beam associated with the specific loading condition being investigated,

Z_z is section modulus about z axis,

I_z is moment of inertia about the z axis, and

$$M'_0 = \frac{W'_{WL}}{24} \beta_1^2 (3 - \beta_1). \quad (8-18)$$

The orientation of the beam axes with respect to the radome geometry is shown in Figure 8.16.

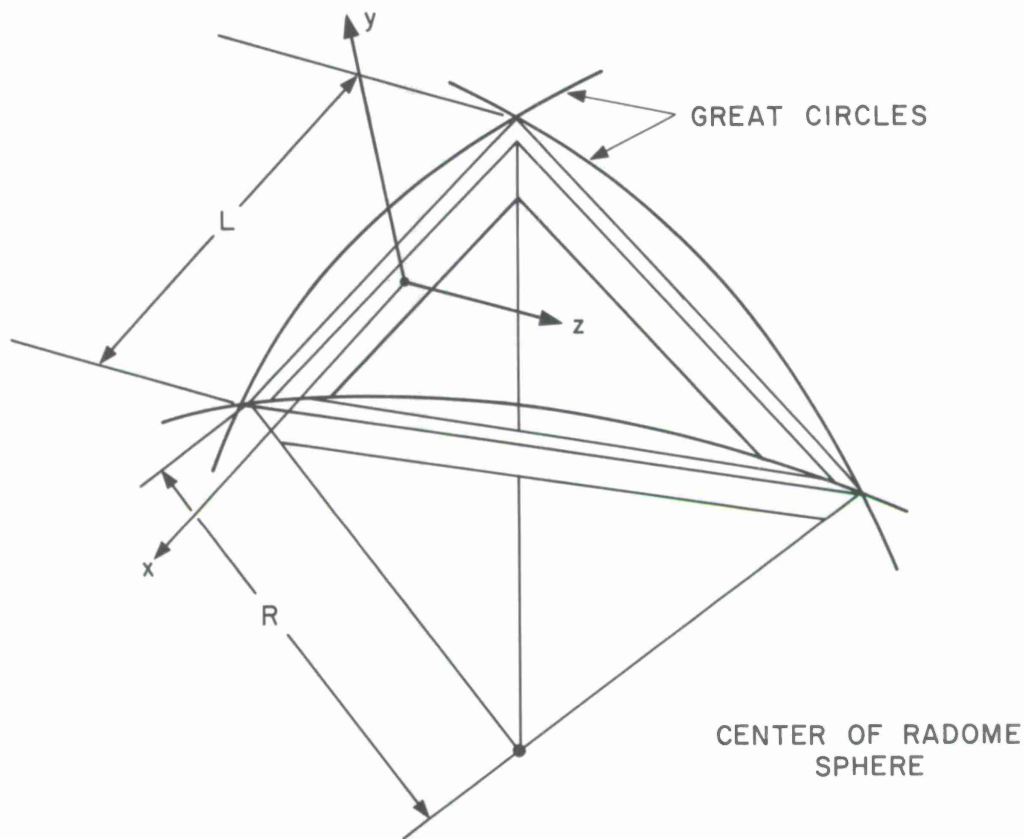


Figure 8. 16. Typical beam layout on radome.

For a satisfactory design, the magnitude of the stress computed from equation (8-16) must be less than the allowable stress specified for the material. In addition, when the membranes are assumed to be ineffective for lateral support,

$$P < \frac{\pi^2 E I_y}{(\beta_1 L)^2} \quad (8-19)$$

For the dead-weight loading condition, the maximum stress at the center of the beam can be expressed as

$$\sigma'' = \frac{P''}{A_s} + k'' \frac{M_0''}{Z_y} \quad (8-20)$$

where

$$k'' = \frac{1}{\beta_2^2 P'' L^2} \left(1 - \frac{\pi^2 E_s I_y}{\beta_2^2 P'' L^2} \right) \quad (8-21)$$

P'' is the axial load associated with the specific loading condition being investigated,

Z_y is the beam section modulus about the y axis,

I_y is the beam moment of inertia about the y axis,

$$M_0'' = \frac{W''}{8} L^2 \beta_2^2, \quad \text{and} \quad (8-22)$$

W'' is an appropriate combination of W_{DL} and W_{WL}'' .

The value of the end-restraint parameter is a function of the stiffness, which is supplied by the various members that intersect at a joint. If the stiffness of all the members that intersect at a joint, except the beam under consideration, is taken as K , then the plot in Figure 8.17 (see reference 15) can be used to estimate the value of β . Neglecting the torsional stiffness of the beams and any reduction or increase in stiffness from axial loads, the end restraint K for bending about the z axis for a framework of equilateral triangles will be $9 E_s I_z / L$. For bending about the y axis, the end restraint K will be about $15 E I_y / L$. Thus, according to Figure 8.17, it can be seen that an effective length ratio of 0.8 will be conservative for practical construction.

8.5.6.4 General instability — equivalent-shell technique

The buckling of a spherical shell under a uniform pressure loading can be expressed as

$$P_{cr} = K E \left(\frac{t}{R} \right)^2, \quad (8-23)$$

where

P_{cr} = buckling pressure,

E = elastic modulus,

R = shell radius, and

t = shell thickness.

The data for buckling pressure generally have a fair amount of scatter because of initial imperfections. For radome design, a value of 0.3 has commonly been used for K . Tests conducted by Witmer¹⁶ on model radomes and spherical shells indicate that this value gives good results.

In order to use equation (8-23) for space-frame shells, an effective value of the modulus and shell thickness must be obtained. These effective values are determined by equating the extensional and bending stiffness of a beam to an equivalent shell element. This gives

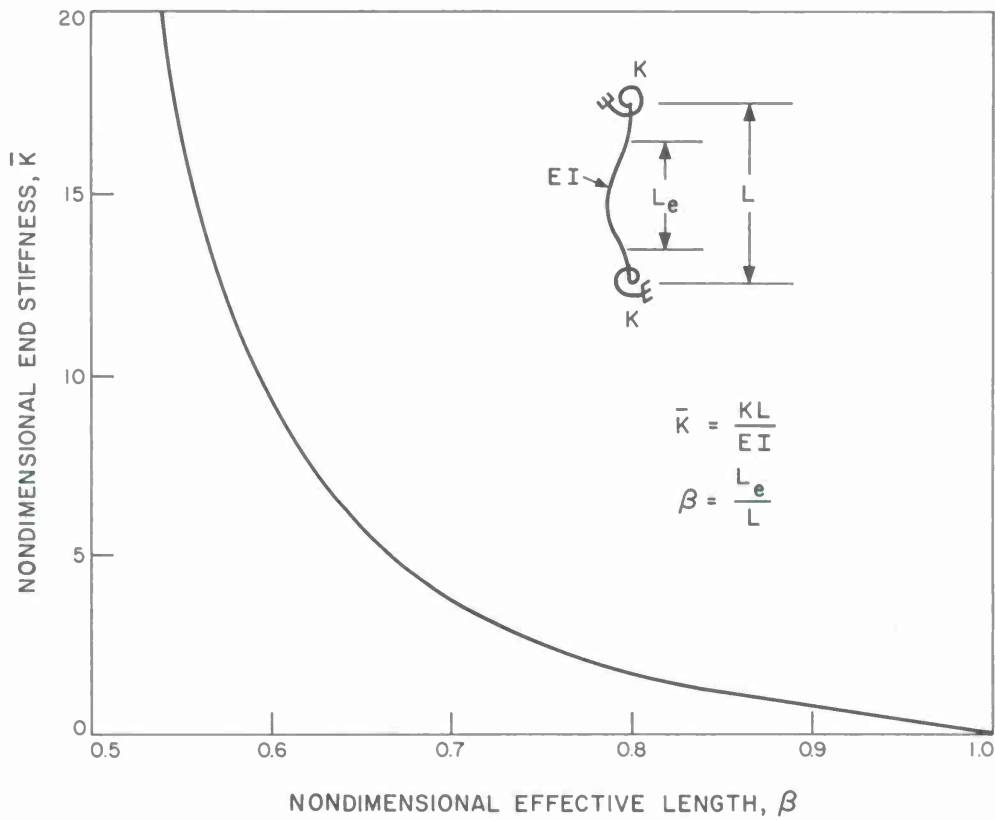


Figure 8.17. Effective length as a function of elastic end restraint.

$$E_s A_s = E_e t_e L_e, \quad (8-24)$$

$$E_s I_z = \frac{E_e t_e^3 L_e}{12}, \quad (8-25)$$

where L_e is the length of the equivalent shell element represented by the beam. As noted above, for a network of equilateral triangles of side length L , the equivalent plate of the same modulus is

$$t = \frac{2 A_s}{\sqrt{3} L}. \quad (8-26)$$

For a material E_e , the equivalent length L_e will be $\sqrt{3}/2 L$. Using this in equations (8-24) and (8-25) gives

$$t_e = \sqrt{\frac{12 I_z}{A_s}}, \quad (8-27)$$

$$E_e = \frac{E_s A_s}{\frac{\sqrt{3}}{2} L \sqrt{\frac{12 I_z}{A_s}}} \quad (8-28)$$

Substituting equations (8-27) and (8-28) into equation (8-23) with a value of $K = 0.3$ yields

$$P_{cr} = 1.2 E_s \frac{\sqrt{A_s I_z}}{LR^2} \quad (8-29)$$

8.5.6.5 Estimate of member sizes

The member sizes in the radome are established as follows:

1) The moment of inertia of the beam in its weak direction, I_y , must be sufficient to support the axial load from the combination of design wind and dead weight, the axial load from dead weight (plus forces due to wind on the radome within or without membranes), and the axial load induced by the pressure loading that will produce general instability. The membrane will not be considered as providing any buckling restraint for any of these conditions.

2) The moment of inertia of the beam in its strong direction, I_z , must be sufficient to support the axial load from the combination of design wind and dead weight and to prevent general instability at the design wind speed. The beam also must be sufficient to resist lateral loading on the beam produced by the wind loads on the membranes.

An overall picture of the beam axial forces in the radome is given in Figure 8.18. The axial forces due to the wind loading were estimated on the basis of a preliminary STAIR computer run and represent the most severe loads at a given value of the meridional coordinate ϕ . The dead-weight stresses are based on a nominal weight of 2400 tons for the radome. It can be seen that the wind loads far outshadow the dead-weight loads for the structure. A plot of the maximum bending moment at the center of the beam is given in Figure 8.19.

The loads in Figures 8.18 and 8.19 were used to estimate the cross-sectional dimensions of the radome beams. In this estimate, the membrane was assumed ineffective in providing lateral support for the beams. To provide a reasonably efficient

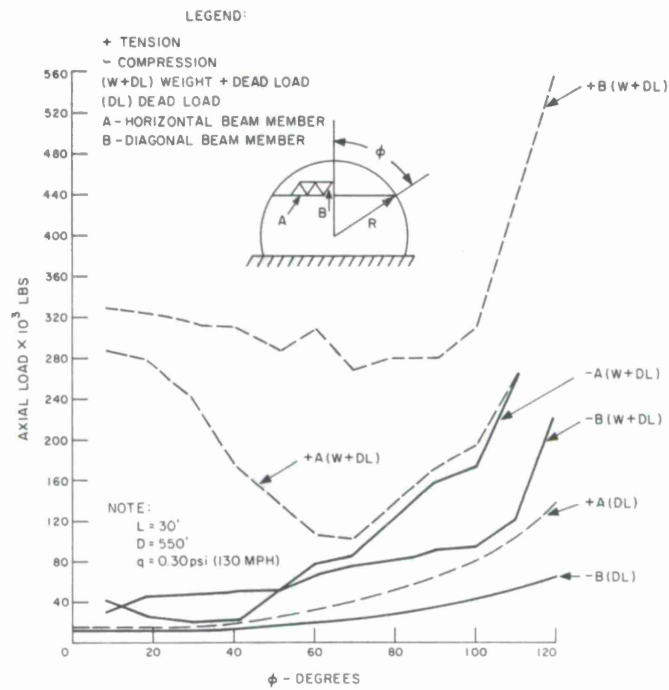


Figure 8. 18. Estimated maximum axial loads in beams due to wind and weight.

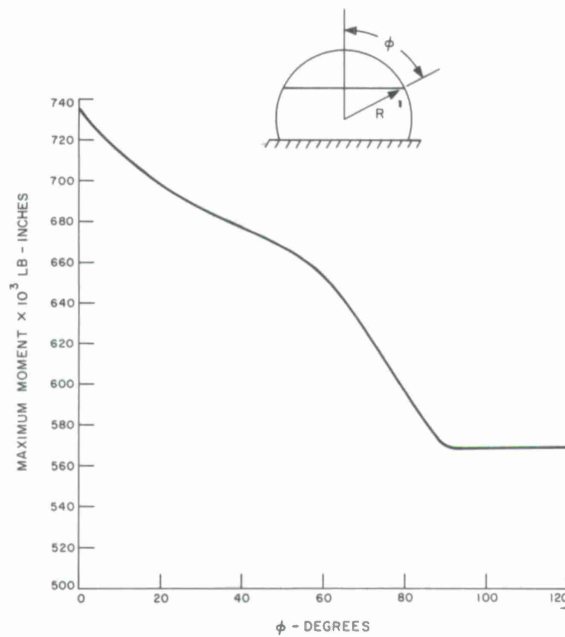


Figure 8. 19. Estimated maximum bending moment developed in beam member by wind loading.

structure, the dimensions of the beam were allowed to vary to account for the variable stress distribution in the radome. A 30-ft beam length and a 15-inch beam depth were chosen, and two beam types were selected. Beam type A is a horizontal or hoop beam and beam type B is a diagonal beam that makes a 60° angle with the hoops. It is believed that these two beam types provide a reasonable representation of the radome geometry. The results of the calculations are shown in Figure 8.20. It is noted that structural sizes were estimated for four regions of the dome. Regions I and II comprise the greater portion of the structure, while regions III and IV, which are considerably smaller, represent the highly stressed base area. The minimum size was governed by the requirement for general stability of the structure. The great proportion of the beams are 4 inches wide. Wider beams are required in the base region especially for the highly stressed hoop beam.

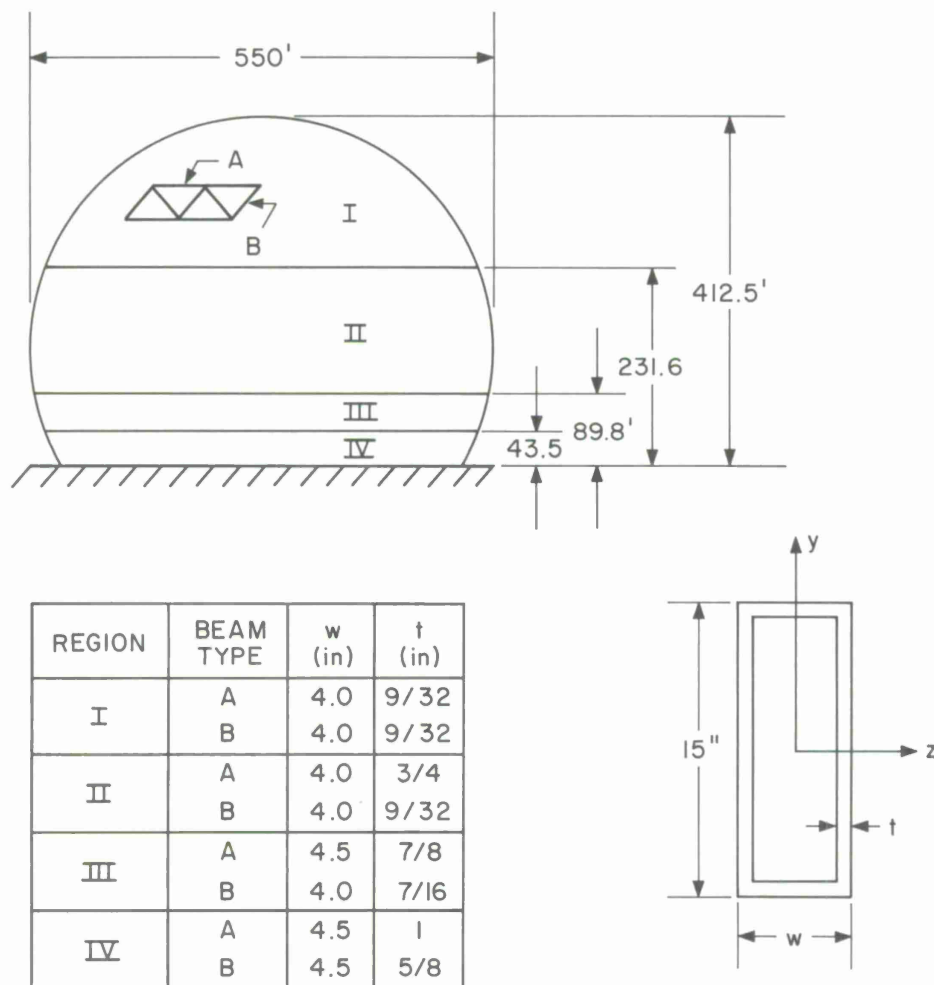


Figure 8.20. Estimated beam cross-sectional dimensions.

For the preliminary calculations made in this section, the beam cross sections in the four regions of the sphere have been sized for the maximum load in that region. No factor of safety over this maximum load has been considered. Most of the beams in the four regions of the sphere, however, will automatically have a factor of safety because they are more lightly loaded than the maximum. For the final design, each beam will be evaluated by a systematic criterion for a safety margin. One possibility for this criterion is that every beam must have a load-carrying capability equal to or greater than 1.5 times the highest load that would be experienced by the beam over a period of 30 years; this matter is currently under consideration.

It has been found that the optical blockage of a space frame can be estimated as^{13,17}

$$\eta = \frac{0.8785}{4\pi} \frac{\Sigma L}{R^2} \left[\frac{\sin \theta}{1 + \cos \theta} h + b \right], \quad (8-30)$$

where

η is the fraction of the antenna plane shadowed by the beams,

ΣL is the total length of the beams in the complete spherical radome frame,

h is the beam depth,

b is the beam width,

$\theta = \sin^{-1} R_A / R,$

R_A is the antenna plane radius, and

R is the radome radius.

The blockage of a frame composed of 30-ft-long beams having a rectangular cross section of 15 inches by 4 inches will be about 8.5% (0.76 db) in the 3000- to 6000-Mc/sec region, and 8.9% (0.80 db) in the 300- to 600-Mc/sec region.

It is to be emphasized that the beam dimensions in Figure 8.20 represent an estimated design. This design cannot be considered optimum. The final design will, of course, be based upon the rigorous analysis described in Sections 8.5.3 and 8.5.4.

If the membrane were counted upon to provide lateral support for the beams, the blockage and the weight of the structure would be decreased. Alternative methods of lateral bracing such as Fiberglas ropes are also a possibility. Various types of lateral support are currently under investigation.

8.6 Erection Procedure^{16,17}

Several methods have been advanced for the erection of the 550-ft-diameter CAMROC space-frame radome. The most efficient and least costly methods utilize the antenna pedestal as a scaffolding to support men and equipment during erection. (Thus, both radome and antenna are erected simultaneously.) Although the method is independent of the enclosed-antenna design, the case of the Hammerhead antenna is outlined below in some detail.

Erection of the radome will start by mounting a standard tower crane on tracks on top of the Hammerhead. This crane might be the same one used to construct the tower and to erect the structural steel trusses. As shown in Figure 8.21, a stationary boom will be used to hold a float or staging for the riggers. The azimuth drive of the Hammerhead will be used to slew the rig into position over the work. Past experience has shown that the radome may lack stability until it is built well beyond the equator. Temporary guys will be desirable. This method of erection allows the rig to swing clear of the guys.

As the radome nears completion, the tower crane will be extended and moved toward the center of the Hammerhead, as shown in Figure 8.22. A tower boom will be used to hold staging for workers. The radome frame will be erected first; then the surface panels will be applied by a similar method.

Following completion of the dome, the secondary reflector and support structure will be suspended from the dome, as shown in Figure 8.23, during erection of the antenna structure. Upon completion of the antenna, these will be lowered into place and attached. This method is similar to that used for the Haystack antenna.

8.7 Radome Cost

Based on a preliminary structural analysis, a cost for the radome was estimated. Table 8.7 presents the schedule for this estimate. As can be seen, the cost of the radome can be divided into three main items: 1) the foundation, 2) the steel framework, and 3) the dielectric membrane panels. The design and engineering costs are not included in this section but are incorporated in Section 6 of this report.

The foundation cost is based on the lift and overturning loads produced on a 550-ft-diameter 75% sphere exposed to a 130-mph wind. Basically, the foundation consists of a trench 10 ft deep and about 14 ft wide into which are put a reinforced concrete pier and footing and then appropriately backfilled. On top of the concrete pier is a bolted steel based ring that will provide the accurate mounting surface needed for the radome. This type of construction is standard and has been used successfully on many existing radome structures. It will be noted that the cost of the foundation does not include any surfacing of the area enclosed by the radome base circle. This area may eventually have buildings

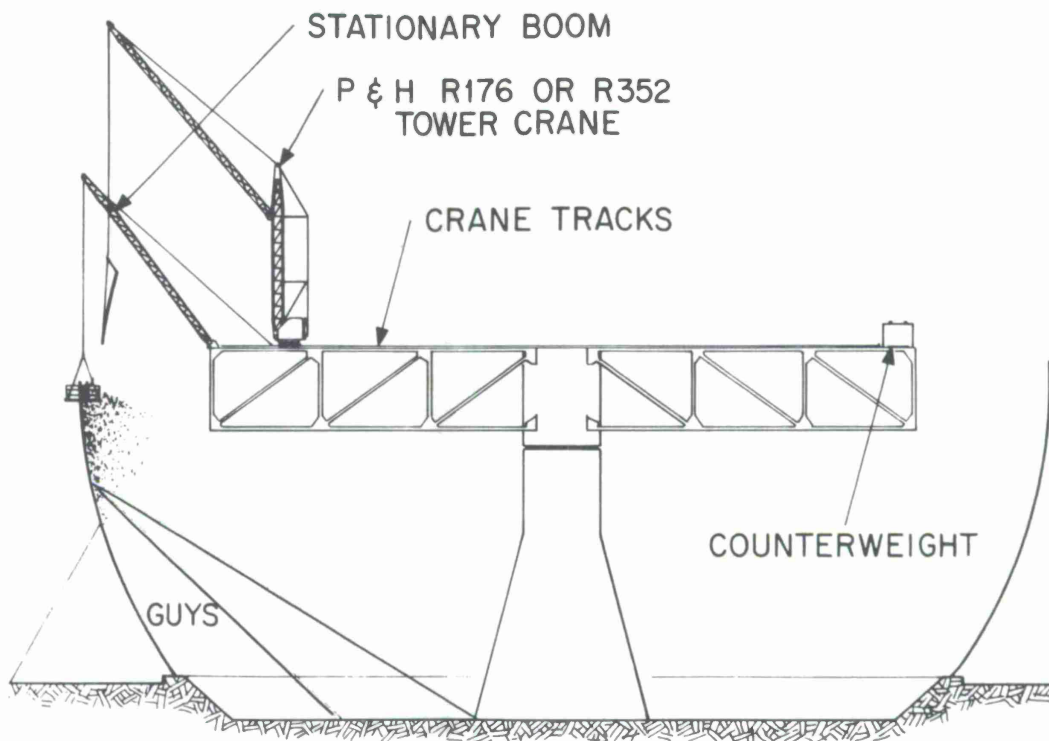


Figure 8.21. Radome erection — start.

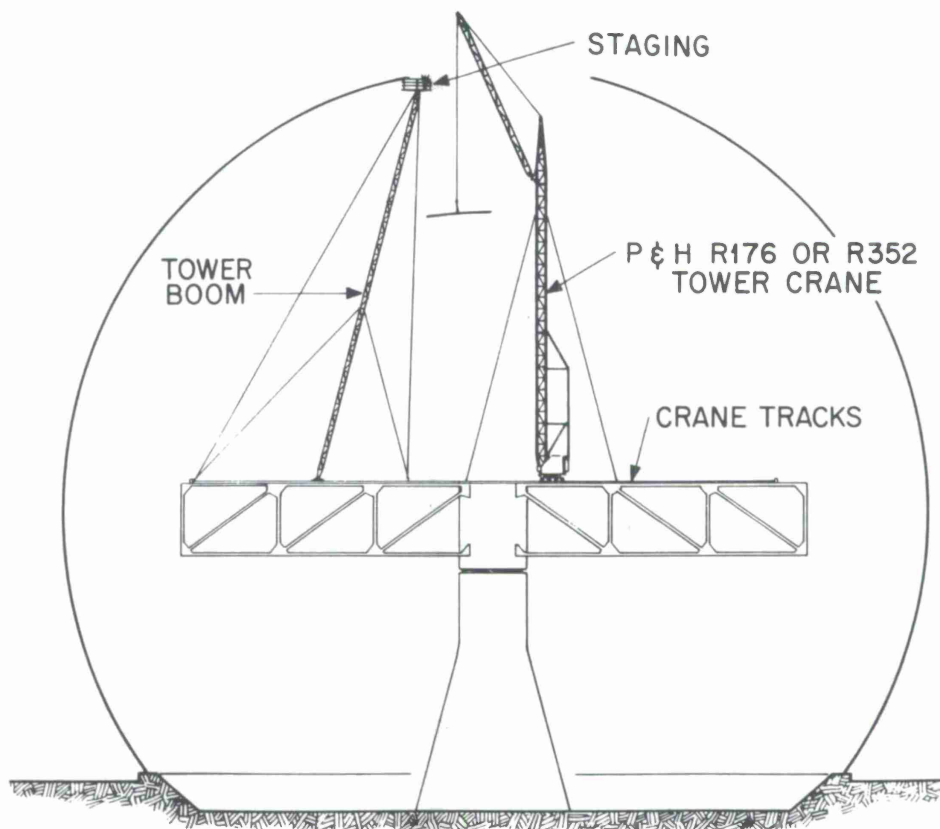


Figure 8.22. Radome erection — finish.

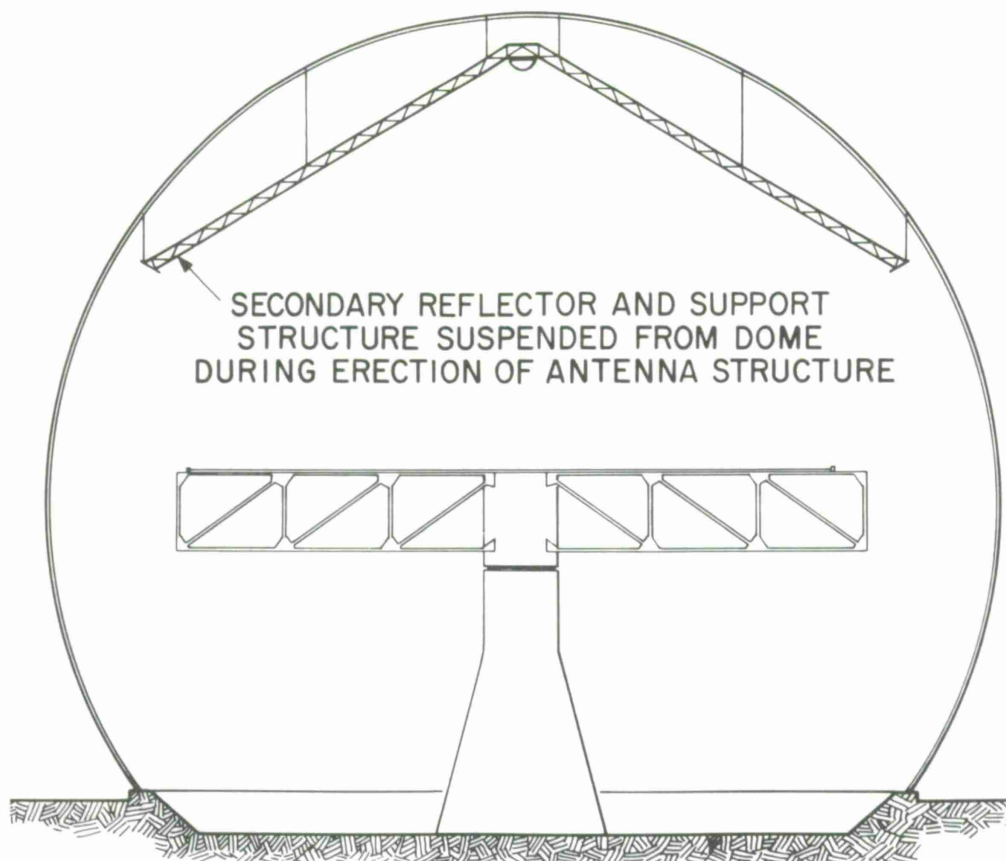


Figure 8.23. Secondary reflector in radome.

Table 8.7. Estimated radome cost schedule for 550-ft 75% sphere

Excavation	7500 yd ³ \$3.00/yd ³	= \$	22,500	
Concrete	4150 yd ³ \$50.00/yd ³	=	207,500	
Base ring	175 tons \$600.00/ton	=	105,000	
Installation	175 tons \$200.00/ton	=	<u>35,000</u>	
				370,000
Fabrication of steel framework	2400 tons \$600.00/ton	=	1,440,000	
Erection of steel framework	2400 tons \$400.00/ton	=	<u>960,000</u>	
				2,400,000
Fabrication of panels	713,000 ft ² \$1.50/ft ²	=	1,069,500	
Installation of panels	2630 panels \$150/panel	=	394,500	
Miscellaneous				500,000
Total				4,734,000
10% contingency				473,000
Total				5,207,000

or walks, or possibly the entire surface will be finished with blacktop. Also, no costs have been included for access.

The largest single item of cost is the fabrication and erection of the steel framework. Again, this cost was based on the weight of the steel framework needed for a 550-ft-diameter 75% sphere exposed to 130-mph wind. The beam construction consists generally of a top and bottom chord tied together with web lacing. This construction will make possible a minimum weight of radome with the least difficulty in fabrication since local reinforcing can be added to the beams without complicating the construction. It is believed that the weight that was used for the estimate is sufficiently conservative to allow for ample reinforcing of the basic structure. The erection cost is based upon the use of the antenna pedestal, as indicated in a previous section. This should allow for a fairly reasonable cost for the erection of the radome frame.

The final major item of cost is the fabrication and installation of the Fiberglas dielectric panels. Based on past experience, the unit cost of \$1.50 psf of surface area is felt to be reasonable for the type of material proposed. On the other hand, the installation cost of the panels is a direct function of detail design of the panel attachment and the schedule of installation relative to the framework erection. At this stage of estimation, however, the cost given is believed to be reasonable.

The miscellaneous category includes such items as bolts, fittings, and waterproofing materials. The 10% contingency is meant to account for minor deviations in the costs as listed. It is important to note that the following items have not been included in the cost:

- 1) Radome heating and ventilating.
- 2) Site preparation.
- 3) Engineering costs.
- 4) Access tunnels.
- 5) Lighting.

As of the present time, the total radome cost, excluding the above-listed items, is estimated at \$5,207,000. A more comprehensive cost estimate is given in Section 6.

It is of interest to examine the variation of the radome cost with radome diameter. The radome diameters for protecting antennas of 300 and 500 ft will be 412 and 688 ft, respectively. For the smaller diameter the cost is estimated to be \$2,790,000, and for the larger diameter the cost is estimated to be \$8,840,000. The bases for these estimates are the same as for the 550-ft-diameter radome described above. A plot of the radome cost as a function of diameter is given in Figure 8.24.

In the scaling of the costs, the radome foundation and the panels varied approximately as the square of the diameter while the steel frame cost varied approximately as the cube. Although it is a conservative assumption, the cost of other items was held to be constant over this range of radome sizes.

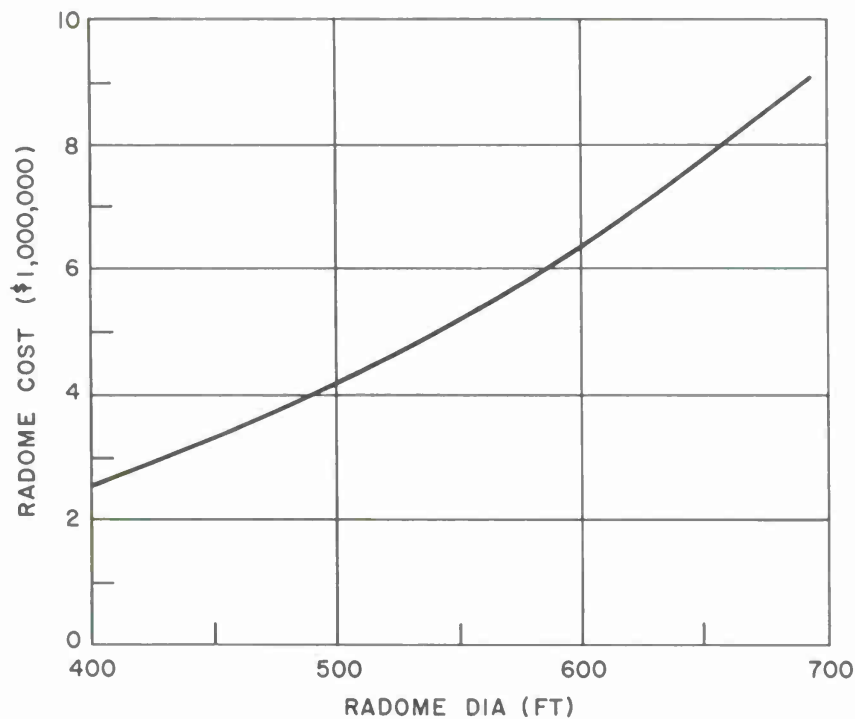


Figure 8.24. Radome cost versus diameter.

8.8 Future Effort

Studies now in progress to which a considerable amount of effort has already been devoted will be pursued to completion. These include the development of the STAR computer program (see p. 8-26) to permit a linear stress analysis of space-frame radomes, the analysis and experimental confirmation of a buckling criterion that relates the applied wind loading to the parameters of the space frame, and the selection of an optimum membrane material for the CAMROC application.

8.8.1 Design wind

Once the site of the CAMROC facility is fixed, then an exact specification of the design wind, including the maximum anticipated steady-state value, which exhibits a 1% risk over a 25-year span, the escalation of wind with height, and the associated gust intensities and durations, will be made. This information will be based on a study of the best available data obtained from the weather station closest to the site. These results will be adopted for the radome analyses.

When the configuration of the CAMROC complex, consisting of the radome, the tower mount, and associated adjacent buildings, has been designed and the relation of the complex to the topographical features of the site established, then wind-tunnel tests to deter-

mine the influence of these factors on the pressure distribution about the radome will be undertaken.

8.8.2 Heat and ventilation

The design, cost, and feasibility of heat and ventilation equipment shall be considered. This equipment is necessary to minimize temperature extremes and to alleviate undesirable thermal gradients that can deform and distort the surface of the antenna and thereby seriously degrade its operational efficiency. It will allow the immediate removal of snow and ice, which will permit a continuous operation of the facility during inclement weather.

8.8.3 Internal pressurization

The effect of introducing an internal pressure within the radome to modify the pressure distribution and to reduce the compressive loads that are developed during an infrequent but severe wind storm will be evaluated. If this method is feasible, the radome can be built using smaller size beam members based on lower design winds and can thus effect an improvement in optical blockage for the radome.

8.8.4 Membrane tests

When one membrane material has been chosen for use in the radome, then a triangular panel whose dimensions and panel-attachment details are identical to the largest triangular panel to be used in the radome will be constructed and rendered airtight. The membrane will then be tested by introducing air pressure equal to the maximum developed on the radome by the design wind speed and the behavior of the membrane recorded. Also, using the same fixture, the fatigue properties of the membrane will be determined at reduced air pressures by flexing the membrane at cyclic rates consistent with the range of predicted wind gusts at the site.

8.8.5 Radome section tests

A full-scale radome section consisting of at least six triangles will be instrumented, made airtight, and exposed to increasing positive overpressures through air evacuation until the maximum design wind load is reached. The stresses and deflections will be monitored at the selected locations during the tests. The uniform loading will permit a precise analysis of the stresses and deflections. Comparison of these calculated results with the measured output will help determine the effects of joint rigidity and the beam restraint due to the membranes on radome performance.

The test will also yield a severe and realistic appraisal of the performance of the full-scale beam, hub, and joint components.

8.9 References

1. Sissenwine, N. , and Gringorten, I. , "Climactic Extremes for a Large Radome within 2 hours of Boston, Massachusetts," see Annex 3.
2. Sissenwine, N. , and Gringorten, I. , "Surface Wind-Speed Extremes in the United States," see Annex 4.
3. Muldoon, R. A. , "Geometrical and Structural Considerations for Large Radomes," see Annex 5.
4. Lewis, S. D. , and Witmer, E. A. , "CAMROC Model Program," see Annex 7.
5. Simpson Gumpertz & Heger, "Theoretical Investigation on the Buckling of Reticulated Radomes," vol. I, see Annex 8.
6. Simpson Gumpertz & Heger, "Theoretical Investigation on the Buckling of Reticulated Radomes," vol. II, July 8, 1966.
7. Muldoon, R. A. , "Estimate of Critical Pressures for Model Buckling Tests," see Annex 9.
8. Griggs, P. H. , "Experimental Study of Instability in Elements of Shallow Space Frame," see Annex 10.
9. "STAIR Instruction Manual," MIT Lincoln Lab. , Manual No. 48, March 1962.
10. Hansen, R. C. , "Microwave Scanning Antennas," Academic Press, New York, 1964.
11. Foerester, A. F. , "Stress Distribution and Stability Criteria of Spherical Ground Radomes Subjected to Wind Loads," Proceedings of the OSV-WADC Radome Symposium, vol. I, June 1958.
12. Muldoon, R. A. , "Dynamic Buckling of Space Frame Radome Models," MIT Lincoln Report No. 71 G-3, February 15, 1962.
13. Muldoon, R. A. , "Estimate of Optimum Beam Dimensions for CAMROC 550-ft-Diameter Space Frame When Exposed to 130-mph Wind," see Annex 6.
14. Hrennekoff, A. , "Solution of Problems in Elasticity by the Framework Method," J. Appl. Mech. , January 1942.
15. Shanley, F. R. , "Strength of Materials," McGraw-Hill Book Company, New York, 1957.
16. Witmer, E. A. , "Static Tests of Spherical Shells and Space-Frame Radome Structures," Part 1-TTR Program, Aeroelastic and Structures Research Laboratory, MIT, Data Report 98-1, June 1961.
17. Muldoon, R. A. , "Optical Blockage of Haystack Space Frame Radome Geometry," MIT Lincoln Lab. Memo. , December 1964.
18. Ammann & Whitney, "Large-Diameter Rigid Radome," see vol. II, Supplement.
19. Stetson, P. , "CAMROC Hammerhead Antenna Concept," Radomes and Large Steerable Antennas, Conference Proceedings, June 17-18, 1966.

9. OBSERVATORY INSTRUMENTATION AND FACILITIES

The antenna and the radome constitute the two major elements of capital expense, and they require the longest time for planning, design, and construction. Consequently, the early CAMROC efforts have focused on these system elements. Nevertheless, preliminary studies on some other components are under way.

The CAMROC scientific plans require, in addition to the main antenna, a smaller antenna, on a movable baseline, that will operate cooperatively as an interferometer. Although it is not specified in detail, we also envision a movable secondary element that could be transported from station to station at distances on the order of hundreds of miles. The objectives for such joint use of interferometric instrumentation and the large primary CAMROC antenna are discussed in Appendix H.

The size and the cost of the projected antenna make it worthwhile to use sophisticated radiometric receiving equipment in order to exploit fully its performance capabilities. It is evident that very low-noise receiver amplifiers should be employed, and when appropriate, they should be cryogenically cooled. The radiometric systems should cover the complete useful frequency range of the antenna, with special emphasis on specific spectral lines. To the maximum degree possible, multiple-frequency radiometers will be planned, so as to permit simultaneous observations, thereby enhancing the operational utility of the facility. Because the state of the art is continuously changing, we do not plan to prepare detailed designs for the receiving equipment until approximately 18 months prior to the date when the antenna is scheduled to become operational. Nevertheless, the studies being undertaken will provide realistic cost and performance estimates.

A very high-power radar transmitter will be planned for use at the observatory. To minimize RF losses, the transmitter and the associated receiver components will most likely be physically located in close proximity to the reflector, probably in the pedestal tower. Since the radar should be capable of operating at several different wavelengths, the transmitters will be designed to be rapidly interchangeable, but will utilize common power supplies, cooling units, timing systems, etc.

A flexible computer control system will be incorporated for both pointing control and data processing. The computer will also monitor and record the operation of all the equipment systems at the facility. Time-shared control provisions will enable the antenna to be commanded remotely from a distant terminal via telephone lines. In addition, means will be included to enable the telescope-pointing information and output data to be displayed and monitored remotely. This capability should enable use of the telescope as a classroom instruction tool.

Studies have started to prepare both preliminary plans for the many scientific components required at the site and estimates for appropriate instrumentation shops, test laboratories, and other supporting facilities. These planning activities will progress to the point where realistic cost and schedule estimates can be prepared by July 1967; but the detailed planning and design for these ancillary elements will not commence until approximately 1 year after the antenna system has been authorized.

APPENDIX A

ENGINEERING SUMMARY
OF
A STUDY TO EVALUATE THE EFFECTS OF A RADOME ENVIRONMENT
ON THE PERFORMANCE AND COST
OF A
LARGE-DIAMETER RADIO TELESCOPE

Prepared for
THE CAMBRIDGE RADIO OBSERVATORY COMMITTEE

October 21, 1966

ROHR CORPORATION
ANTENNA DIVISION
CHULA VISTA, CALIFORNIA

ABSTRACT

A cost and performance analysis has been conducted on the effect of a radome on the design of a large-diameter radio telescope.

The results have shown that for an environmentally designed 210-ft-diameter telescope the cost is estimated at \$5 million more than its radome-housed counterpart. For a 400-ft-diameter telescope, this cost difference is estimated at a significant \$27 million.

From a performance standpoint, a 400-ft-diameter telescope exposed to environmental conditions cannot economically be designed to meet the CAMROC pointing accuracy requirement of 15 arcsec (peak 3σ). The controlled radome environment, however, does permit achievement of this tolerance and greatly simplifies the mechanical and servo-drive subsystems and permits keeping the structural dynamics within tolerable limits.

From the results of this study, a radome-housed telescope is recommended for the CAMROC program.

TABLE OF CONTENTS

<u>Section</u>		<u>Page</u>
1	INTRODUCTION	A-1
2	SUMMARY AND CONCLUSIONS	A-2
3	DESCRIPTION OF THE TELESCOPES UNDER STUDY	A-9
4	RESULTS OF THE 210-FT-DIAMETER ENVIRONMENTAL ANALYSIS	A-11
5	RESULTS OF THE RADOME-HOUSED 210-FT-DIAMETER ANALYSIS	A-11
6	COMPARISON OF RESULTS	A-29
7	PERFORMANCE AND COST COMPARISON OF THE 210-FT- AND 100-M-DIAMETER RADIO TELESCOPES	A-31

1. INTRODUCTION

This report summarizes the engineering analyses conducted to evaluate the performance and cost differences between an environmentally designed (no radome) and a radome-housed large-diameter radio telescope. The study was designed to assist CAMROC in determining the advantages, disadvantages, and economics involved in the design of radio telescopes that are subjected to full environmental conditions as compared with the radome-housed telescopes. (The radome itself is not part of this study.) This study was funded in part by the National Science Foundation under grant GP 5832.

The need for this study stems from the absence of realistic cost data on large-diameter radio telescopes. This first study was based on an existing environmentally designed antenna that would serve as the basis for cost reference. The Jet Propulsion Laboratory's 210-ft-diameter environmental antenna, a recently completed program, was utilized since design and final cost and field-measured performance data were available. Additional data were also made available through the results of a 100-m fully steerable radio telescope study developed by Rohr for the National Radio Astronomy Observatory.

The first objective was to develop a radio-telescope specification that would be applicable to either the radome-housed or the environmentally designed radio telescope. The surface tolerance specified was 0.150-inch RMS and was kept constant for each design. The pointing accuracy specified was 15 arcsec (3σ). For the JPL environmentally designed antenna, this tolerance was measured at 90 arcsec, owing mainly to the magnitude of the wind-load deflections on the antenna. Consequently, it was not possible to keep the pointing-accuracy tolerance constant for each design without major redesign to the existing JPL antenna. The wind loadings specified were 25-mph precision and 120-mph survival, and the drive requirements, for precision operation, were $0.25^\circ/\text{sec}$ velocity and $0.2^\circ/\text{sec}^2$ acceleration and $0.25^\circ/\text{sec}$ and $0.02^\circ/\text{sec}^2$ drive to stow. The above wind and drive requirements differed somewhat from the existing environmentally designed antenna; however, it was determined that these differences were minor and would not materially affect the results.

The next objective of the study was to reevaluate the environmentally designed 210-ft-diameter antenna to comply with the above radio telescope specification except in the area of pointing accuracy and to reevaluate its costs. In general, portions of the design were simplified; this included the removal of the master equatorial, dome, its separate tower, and windshield, as well as the offices, laboratories, and operating and machine rooms. As modified, the 210-ft antenna represented a realistic cost and performance approach to a large-diameter, environmental, fully steerable radio telescope.

Using the antenna parameters developed for the radome: no-radome study comparison, the telescope was redesigned to take advantage specifically of the radome

environment. Complete costs of this system were then determined. Despite the minor restriction of using the original 210-ft geometry for the radome-housed antenna, the conclusions clearly demonstrated the advantages that can be gained by enclosing a large-diameter antenna in a radome.

Gravity-load deflection-compensation techniques were not considered for this study because the additional time and effort required to investigate fully all possible approaches and their effects on the design and cost of the telescope were not within the scope of this program. Since the main purpose of this study was to establish firmly the cost trend between the radome-housed and the environmentally designed radio telescopes, the use of compensation devices would not drastically alter this result.

As stated, the study was undertaken with a single main purpose in mind. That is, it would establish the relative cost between an environmental and a radome-housed large-diameter radio telescope. The study was planned in such a way that each design would have as closely as possible the same ultimate performance. The results of the study would then allow direct and simple comparison of the costs of the instruments for both the environmental and nonenvironmental designs, and should also uncover the advantages and disadvantages and reasons why the radome should or should not be recommended for the CAMROC telescope.

The study has satisfied the above purpose.

2. SUMMARY AND CONCLUSIONS

The most significant parameters that influence the design and cost of a large-diameter radio telescope are the operational and survival wind velocities. These two parameters have a significant effect on surface accuracy, pointing accuracy, drive power, survivability, system stiffness, and overall weight. As a result, the environmentally designed antenna is more costly, since the lightest weight structure generally is the most economical.

The weight-to-cost relationships for the material, fabrication, and erection of structures have been firmly established by the steel and aluminum industries. These relationships are applicable for large antenna structures except in those areas where extreme accuracy must be achieved and in the mechanical, servo, and foundation components, since these components can be significantly affected by other variable requirements (i.e., environmental, soil conditions, etc.), and therefore do not follow the weight-to-cost relationship.

For either the radome-housed or the environmentally designed antenna, a study of the effect on total cost of engineering, material, manufacturing, and erection, for a wide range of antenna diameters has shown that:

- 1) Engineering costs are a constant percentage of the total cost.
- 2) Manufacturing and erection cost percentages reduce as the antenna diameter increases.
- 3) Material costs increase significantly as the antenna diameter increases (except for the radome-housed antenna because of the significant reduction in cost of all mechanical components).

It follows that the cost of the radome-housed telescope, since it weighs considerably less and requires very little drive power, is significantly lower than that of the environmentally designed instrument.

The following chart (Figure 1) summarizes the cost and weight relationships for the antenna diameter range of interest (see also Figures 2, 3, 4, and 5). Note that for a 210-ft-diameter antenna, there is approximately a \$5 million saving for the radome-housed telescope and an estimated \$27 million saving for the 400-ft-diameter radio telescope, which should be more than adequate to overcome the radome costs. Also, notice that the cost ratio of the environmental versus nonenvironmental telescopes increases as the antenna diameter increases. It is felt that an optimized 400-ft-diameter telescope designed specifically for the radome environment will improve this ratio even further.

Figure 1. Cost and weight summaries.

Diameter		210 ft		100 m (328 ft)	
		Environmental*	Nonenvironmental†	Environmental**	Nonenvironmental
Weight	Million of lbs	4.8	1.6	11.6	3.9 [‡]
	Ratio	3	1	7.3	2.4
Cost (Less engineering and profit)	Millions of dollars	9.4	4.3	30.0	13.2
	Ratio: environmental nonenvironmental	2.20	1	2.28	1
	Approximate dollars/lbs	2.0	2.7	2.6	3.4
* Based on JPL contract - W. O. 420 † Based on MIT study - W. O. 748 ** Based on NRAO study - W. O. 215 ‡ Based on an equivalent stiffness extrapolation					

2.1 400-Ft Design Criteria

This study, although limited in scope, represents a first look at the economics of a radome on the design of a large-diameter radio telescope. The cost trend has been firmly established; however, full advantage of the radome environment was not utilized.

Millions
of Pounds

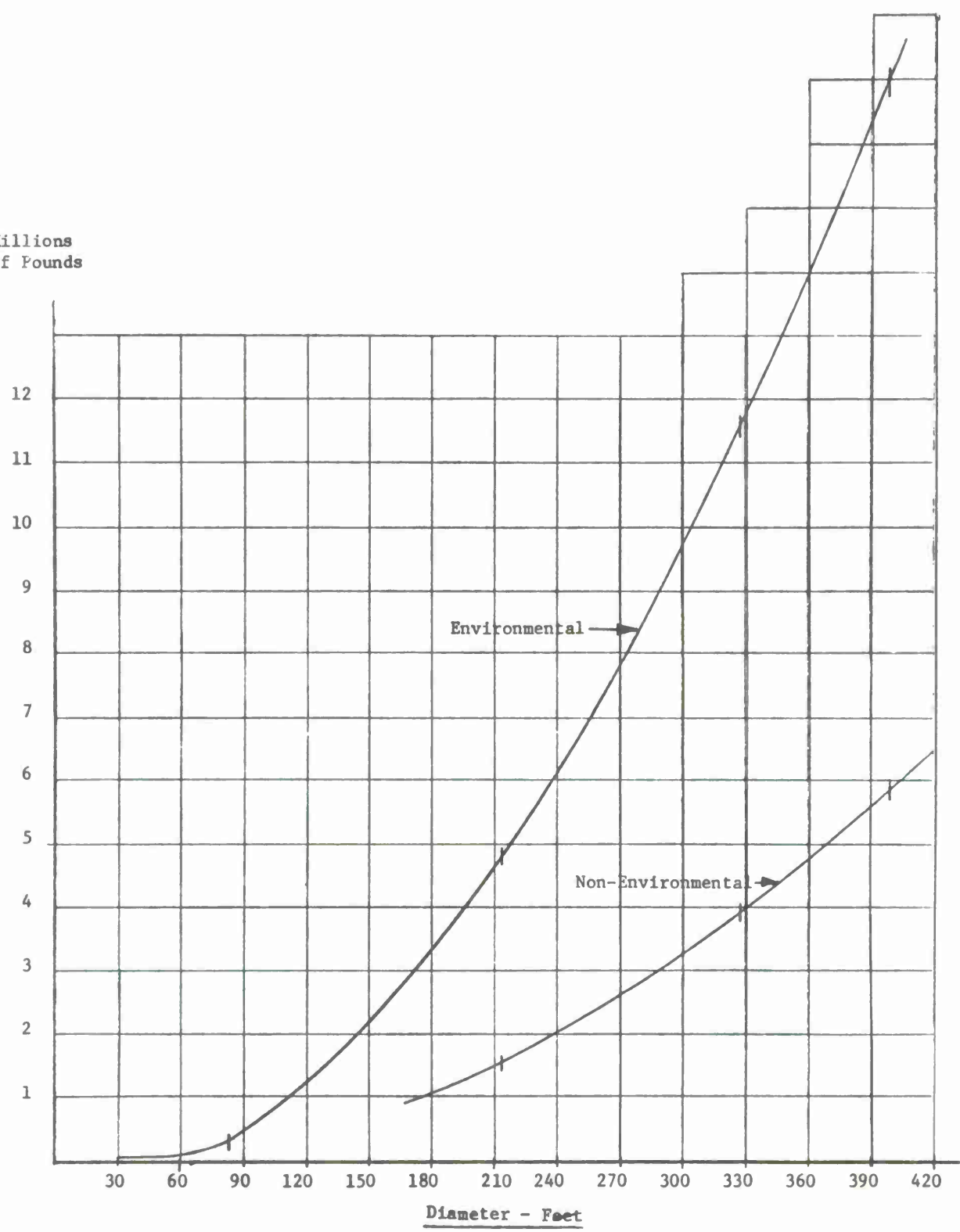


Figure 2. Large-diameter antenna study; weight versus diameter curves.

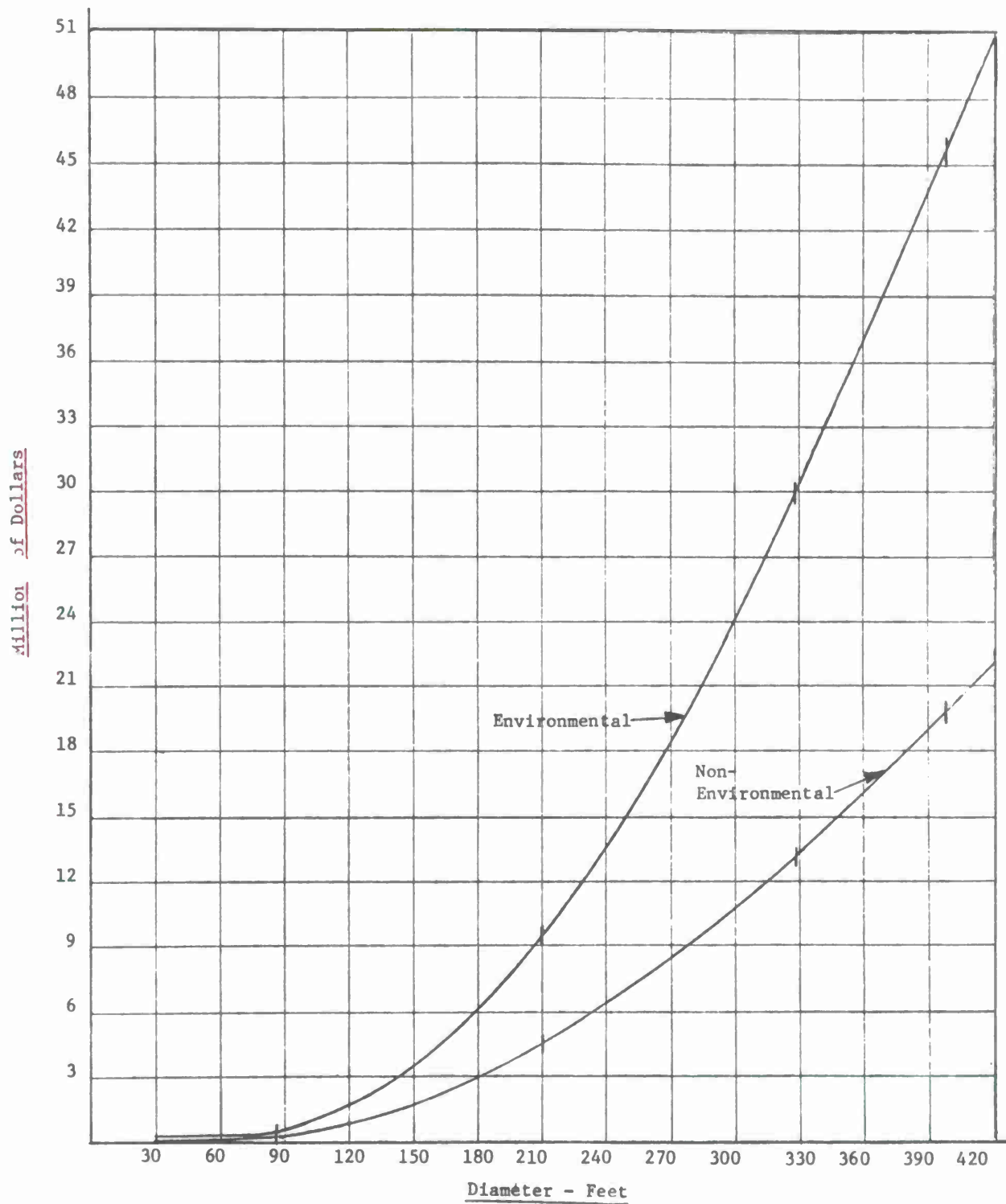


Figure 3. Total costs, in millions of dollars. (Excludes engineering, profit, and shipping costs.)

Millions
of Dollars

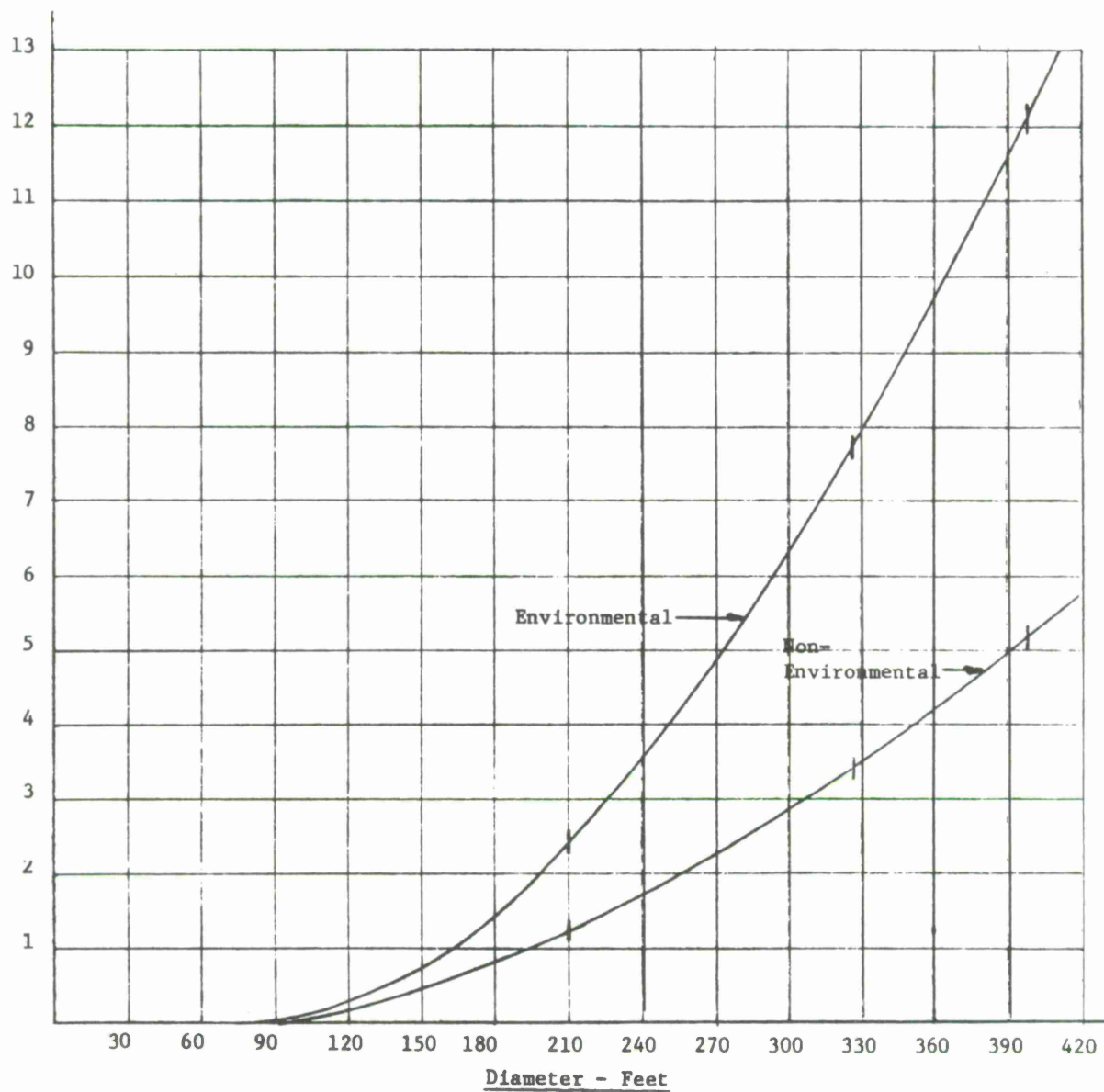


Figure 4. Erection costs.

Millions
of Dollars

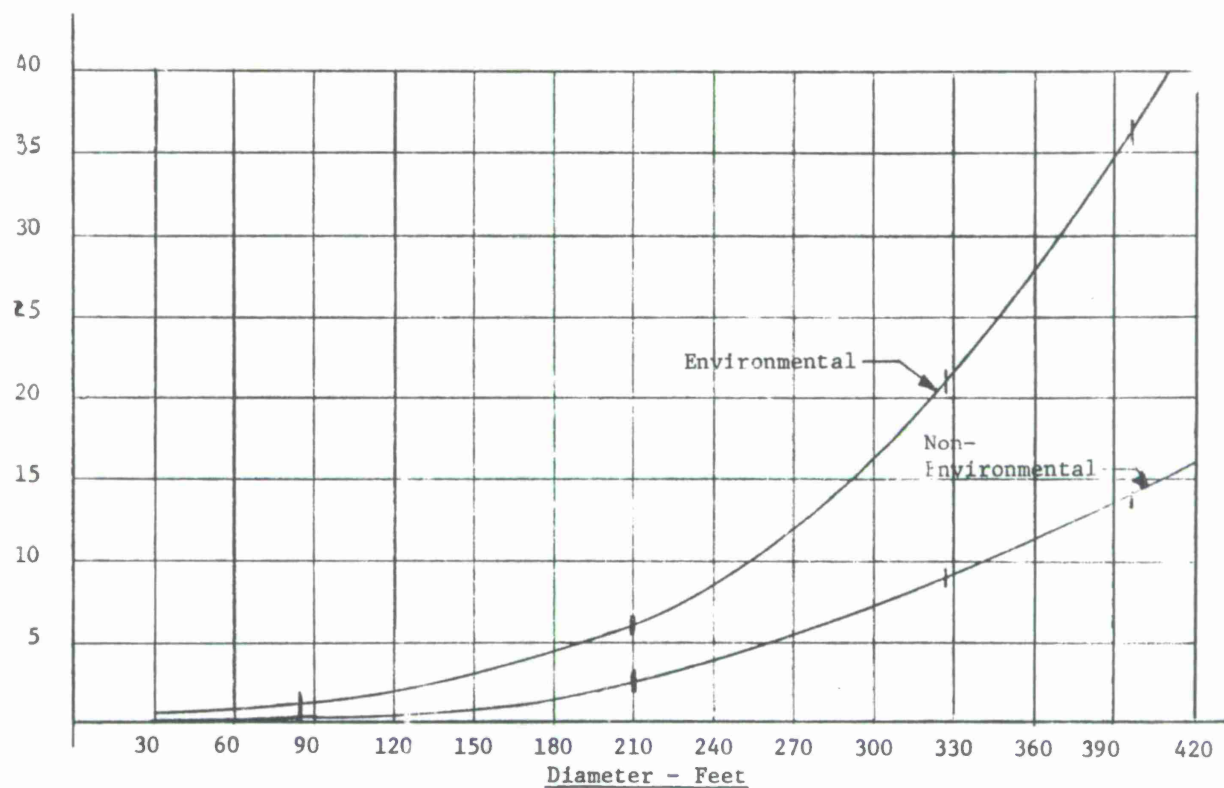


Figure 5. Manufacturing costs.

Since the only vector that we are trying to overcome is gravity, the least weight design would represent the best, technically and economically. Stress levels will be very low owing to the absence of wind; therefore, very lightweight member sections can be utilized. However, the structural limitation of $L/r = 200$ (where r is the least radius of gyration and L the length of the member) presents a lower limit on member sizes, hence weight and cost.

In order to optimize the design of a 400-ft-diameter radome-housed telescope, it is suggested that the following be fully evaluated in the attempt to make full use of the radome environment.

- 1) A very lightweight surface-panel design should be developed, since the surface-panel weight represents a very large portion of the externally applied load. The panels should be extremely rigid, to keep their own deflection small. Special heavy walkway panels will have to be provided.
- 2) The use of aluminum for the reflector backup structure bears investigation. Theoretically, either steel or aluminum will produce the same gravity-load deflection pattern (except for externally applied loads from the surface panels). However, the aluminum structure would reduce the elevation counterweight and inertia, which would result in a lighter weight pedestal. While material and fabrication costs are higher for the aluminum structure, the shipping and erection costs would be smaller.
- 3) In order to keep the weight of all secondary members, hoop trusses, etc., minimized, a very lightweight high r member section should be developed.
- 4) All rib trusses should be kept shallow to minimize member length and L/r , elevation counterweight, and inertia.
- 5) Deflection-compensation techniques should be fully investigated to determine their effect on controlling deflections, minimizing weight, and reducing cost.
- 6) An optimized reflector-support girder and elevation-wheel structure configuration must be developed and should have at least the following characteristics:
 - a) A reflector surface that has circular deflection contours.
 - b) A reflector surface that has a transverse parabolic deflection pattern (homology).
 - c) Minimum counterweight.
 - d) Location of axis of rotation very close to the center of gravity.
 - e) Lightweight.
 - f) Extreme rigidity.
 - g) Economy.

Figure 6 represents a relative comparison of the differences between a radome-housed and an environmentally designed telescope.

Figure 6. Comparison between the environmental and radome-housed telescope.

	Nonenvironmental radome (MIT)	Environmental no-radome (JPL)
Weight	Low	High
Gravity	Same	Same
Wind	None	High
Ice and snow	None	High
Thermals	Reduced	Δt 10°; $\pm 60^\circ$
Performance	Deflection design	Strength design
Required natural frequency	Low	High
Overturning moment on azimuth bearing	None	High
Overall environment	Mild	Severe
Drive power	Low	High
Rigidity	Low	High
Repeatability	Very important	Not significant (since other errors are much larger)
Axis friction	Very important	Not significant from a servo-design standpoint; other errors are so much greater. However, owing to mass and inertia, a "frictionless" bearing is still required.
Readout system	On-axis 2-1/2-arcsec encoders.	a) Geared on-axis cam compensated b) Optical link - master equatorial - < 18 arcsec
Axis alignments	Critical	Not critical (a small portion of the total tolerance)
Servo systems	Electrical - low power - antibacklash	Hydraulic - high power - antibacklash
Reliability	Not critical	Critical due to severity of environment.

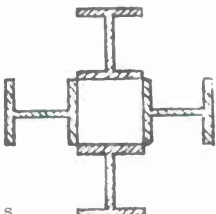
3. DESCRIPTION OF THE TELESCOPE UNDER STUDY

The JPL 210-ft-diameter antenna was used as the basis for this first study because actual cost and field performance data were available. Since the existing engineering, including the computer analysis, could be readily utilized, an economical study could be completed in a short schedule.

We realize that there are many types of mounts that could be utilized. Most of these have been studied by Rohr, and their advantages and disadvantages explored.

Utilizing the geometry of the 210-ft-diameter antenna would in certain ways restrict the study. Its use actually places a restraint favoring the environmentally designed telescope; however, it was decided that the results, advantages, disadvantages, and cost trend for the radome-housed telescope design could still be firmly established. Where it was possible to modify the geometry of the radome-housed telescope, this was accomplished, and Figure 7 summarizes these differences.

Figure 7. Geometric differences and concept changes between the JPL and MIT 210 ft.

	Nonenvironmental radome (MIT)	Environmental no-radome (JPL)
Elevation wheel	Single	Double
Elevation bearing	Single	Double
Hydrostatic bearing	Reduced pad size (approx. 30-inch by 40-inch) - 3 required - lower power	40-inch x 60-inch pads - 3 required
Alidade	Single member sections - weight is 1/5 of JPL - greatly simplified structure	Built-up member sections 
Pedestal		
Wall thickness	30 inches	42 inches
Height	27 ft	46 ft
Drives	2 per axis 1/10 of stiffness	4 per axis
Servo	Electric 1/20 of hp	Hydraulic

To acquaint the reader with the telescope designs that were studied, the following is a brief, general description. All concepts utilized Cassegrain optics with a focal-length-to-diameter ratio of 0.42. The surface is comprised of individually adjustable aluminum panels (outer panels are perforated to reduce wind loadings and torques). The reflector backup structure is structural steel and consists of radial rib trusses that support the adjustable panels and a rectangular girder-support system. (A diamond-shaped girder is utilized for the 328-ft-diameter concept.)

The reflector-supporting structure or alidade, which rotates about the azimuth axis, is a large-framed pentahedron with three base points supported by a large-diameter azimuth hydrostatic thrust bearing, while the two top points support the elevation bearings. Azimuth and elevation gear drives are mounted on the alidade structure.

The azimuth-rotating structure is carried on an azimuth hydrostatic thrust bearing whose runner is mounted on top of the concrete pedestal. A pintle bearing defines the azimuth axis and carries all horizontal loads to the top of the pedestal at its center.

Elevation motion is carried on four self-aligning spherical roller bearings (the 210-ft radome concept utilizes two self-aligning spherical roller bearings).

The elevation wheel is supported by the elevation bearings and supports the reflector's main support girder (for the 210-ft no-radome concept, the elevation-wheel structure is a dual-wheel concept).

Azimuth and elevation motions of the antenna are operated by antibacklash servo-controlled hydraulic drives (for the 210-ft radome concept, antibacklash electric drives are utilized).

The following conceptual drawings depict the environmental and nonenvironmental radio telescopes:

Title	Drawing no.
210 environmental (no-radome)	SK-1355
210 nonenvironmental (radome)	SK-2040
328 environmental (no-radome)	SK-1589

4. RESULTS OF THE 210-FT-DIAMETER ENVIRONMENTAL ANALYSIS

As stated, the 210-ft-diameter environmentally designed antenna was reevaluated in consonance with the CAMROC specification.

This permitted the removal of certain components, such as the master equatorial (optical link) readout loop, which permitted the removal of its supporting tower, the protective windscreen, and the dome. Furthermore, the A & E facilities, consisting of the large offices, laboratories, shops, and operating and machinery rooms, were also deleted from the cost.

Figures 8, 9, and 10 present original results excerpted from the 210-ft-diameter program. These characteristics are unchanged because they were not materially affected by the basic CAMROC radio-telescope specification.

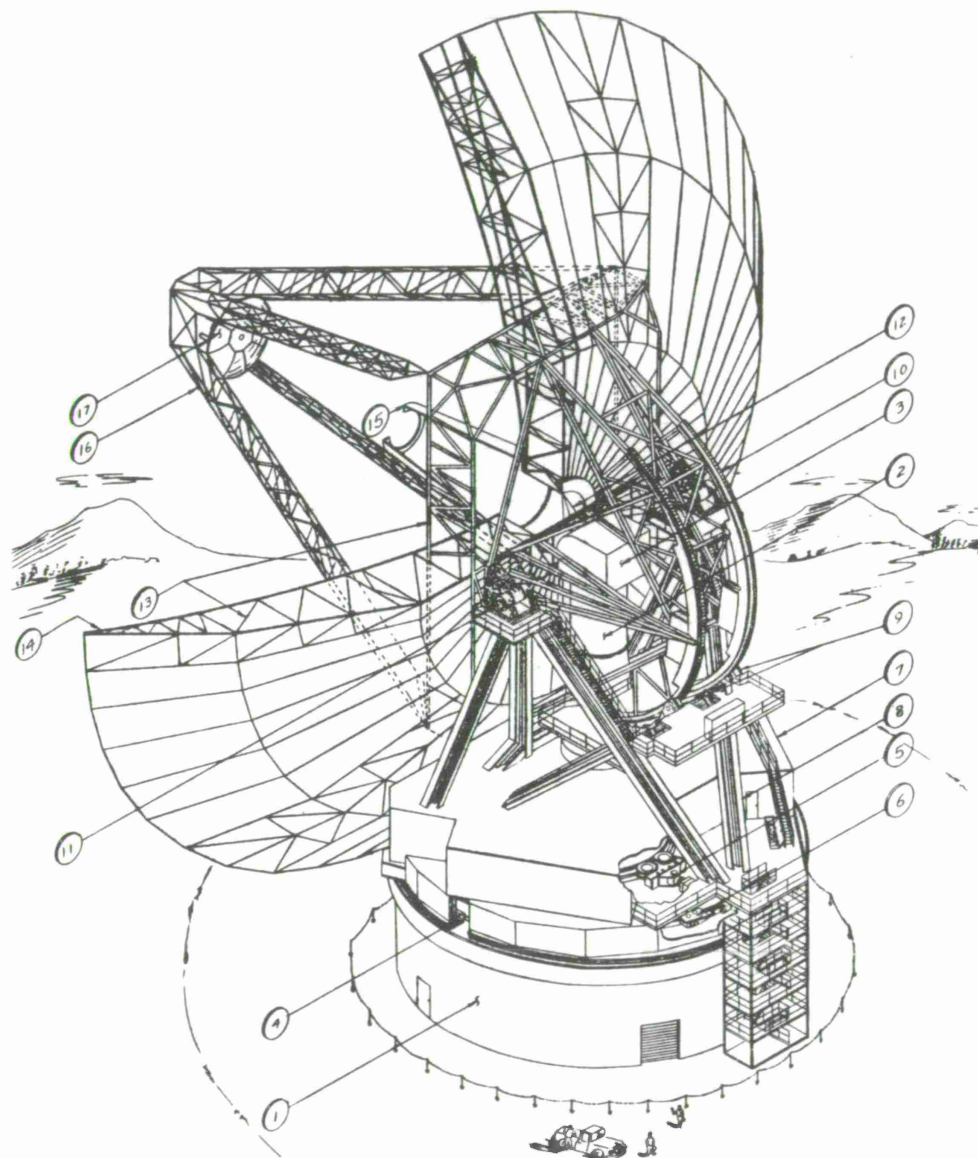
5. RESULTS OF THE RADOME-HOUSED 210-FT-DIAMETER ANALYSIS

As stated, the 210-ft-diameter environmental radio telescope was completely reanalyzed. The geometry of the reflector and alidade remained essentially fixed; however, owing to the radio-telescope sky coverage requirement of 15° above the horizon, the reflector was located 10 ft closer to the axis of rotation (refer to SK-2040); second, the dual elevation-wheel structure was replaced with a single elevation wheel; and third, the double elevation-bearing assemblies were reduced to single-bearing assemblies, tied together with a simple rotating shaft (no offset is required at the intersection of the azimuth and elevation axes to clear the master equatorial).

TOTAL AAS WEIGHT
CFS AND JPL COMPONENTS

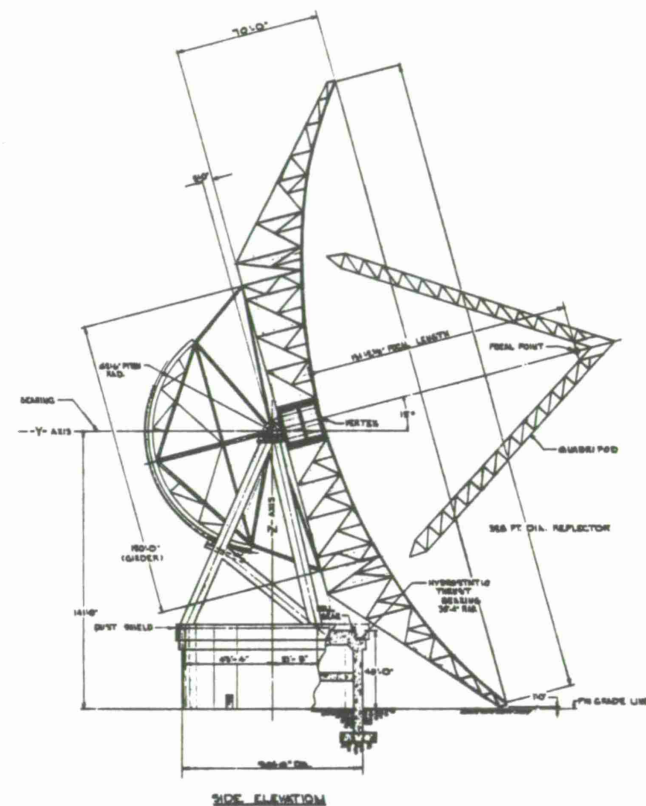
ITEMS		UNIT OF POUNDS
1	PEDESTAL	19049000
2	INSTRUMENT TOWER	1243000
3	EQUATORIAL ROOM	2000
4	AZIMUTH THRUST BEARING	210000
5	AZIMUTH RADIAL SHEAR BEARING	103000
6	AZIMUTH DRIVE ASSEMBLY	84000
7	EQUIPMENT AND CONTROL HOUSE	351000
8	ALIDADE	1242000
9	ELEVATION DRIVE ASSEMBLY	130000
10	BACK UP STRUCTURE (ELEVATION WHEEL AND COUNTERWEIGHT)	400000
11	ELEVATION BEARING ASSEMBLY	142000
12	INTERMEDIATE REFERENCE STRUCTURE (INCLUDING OPTICAL EQUIPMENT)	7000
13	PRIMARY REFLECTOR STRUCTURE	546000
14	PRIMARY REFLECTOR SURFACE	63000
15	FEEDCONE	48000
16	QUADRIPOD	24000
17	SUBREFLECTOR AND ADJUSTMENT MECH	17000
	LIGHTING AND UTILITIES	6000
	LADDERS AND PLATFORMS (REFLECTOR STRUCTURE)	7000
	CABLES AND CABLE WINDUP (ALIDADE STRUCTURE)	40000
	ELEVATION TRUSS, SPACE FRAME AND ELEVATION AXIS STRUCTURE	73000
	HYDRAULIC POWER SUPPLY	43000
	AZIMUTH BEARING PADS	35000
	CONTROL CONSOLE	4000
	TOTAL	15583000

* 7000 LBS FOR INTERMEDIATE REFERENCE STRUCTURE
IS FOR FUTURE ADDITION



210 environmental (no-radome). Drawing no. SK-1355.





328 environmental (no-radome). Drawing no. SK-1589.

Figure 8. Results - 210-ft environmental analysis.

Component		Major component weight breakdown (lbs)		
Reflector		678,000		
Elevation wheel		930,000		
Elevation counterweight		600,000		
Alidade		1,500,000		

Surface accuracy	Pointing accuracy		Structural dynamics (locked rotor frequency)	Drive power
0.170 inch achieved	0.025° * achieved	Analog pointing mode cam compensated	1.6 cps achieved	200 hp per axis
0.250 inch specified	0.033° * specified			
	0.013° * achieved	Master equatorial mode	1.5 cps specified	
	0.015° * specified			

* Note: These two pointing modes do not meet the CAMROC radio-telescope specification requirement of 0.004°.

Figure 9. Surface-accuracy error tables.

Error source 1σ - RMS - (inches)	Manufacturer's tolerance on panels	Alignment tolerance on panels	Gravity 45° to horizon	Wind 30 mph $\alpha = 0, \psi = 0$	Thermals $\Delta t = 10^\circ$
Panels	0.060	0.060	0.031	0.056	0.003
Structure	-	-	0.074	0.043	0.020
$\Sigma 1\sigma$	0.060	0.060	0.105	0.099	0.023
$1\sigma^2 \times 10^{-6}$	3600	3600	11,000	9801	529
$\Sigma 1\sigma^2 \times 10^{-6}$	28,530				
$RSS = \sqrt{\Sigma 1\sigma^2}$	$\sqrt{0.028530} = 0.170 \text{ arcsec} < 0.250 \text{ arcsec (JPL specification requirement)}$				

The radome-housed antenna must resist gravity loads and reduced thermal loadings. Since reducing the weight or gravity loading of the structure results in less stress and less deflection, theoretically a practically "weightless" structure could result. However, practical considerations place a lower restriction on the minimum sizes and materials that can be utilized. For example, structural local buckling or L/r considerations plus the ability to fabricate and erect accurately very light special structural configurations emerge as constraints. A complete static and dynamic three-dimensional analysis for the radome-housed antenna has been conducted based on the above ground rules.

Figure 10. Pointing-accuracy error tables - no radome - the 210-ft-diameter environmental design.

Elevation axis: $\theta_{xx} - \text{arcsec} - 3 \sigma$						
Wind velocity - 30 mph	Deadload 45° to horizon	Windload $\alpha = 0$ $\psi = 120^\circ$	Thermals $10^\circ \Delta t$	Align- ment (RSS)	Gusty wind	Tracking
Reflector assembly*	16	-	Worst case about azi- muth axis	23	-	-
Antenna-mount assembly†	-	6		24	-	-
Servo system	-	-	-	-	Worst case all in	13
Readout system	-	-	-	10	Azimuth axis	-
$\Sigma 3 \sigma$	16	6	-	35	-	13
$3 \sigma^2$	256	36	-	1190	-	169
$\Sigma 3 \sigma^2$	1190					
$RSS = \sqrt{\Sigma 3 \sigma^2}$	$\sqrt{1190} = 41 \text{ arcsec} = 0.011^\circ 3 \sigma$					
Azimuth axis: $\theta_{yy} - \text{arcsec} - 3 \sigma$						
Reflector assembly	-	35	-	-	{ -	-
Antenna-mount assembly	-	29	27	-		-
Servo system	-	-	-	-	28	13
Readout system	-	-	-	10	-	-
$\Sigma 3 \sigma$	-	64	34	10	28	13
$3 \sigma^2$	-	4100	1150	100	780	169
$\Sigma 3 \sigma^2$	6299					
$RSS = \sqrt{\Sigma 3 \sigma^2}$	$\sqrt{6299} = 80 \text{ arcsec} = 0.022^\circ$					
Summary - azimuth and elevation						
$3 \sigma - \text{peak} - \text{arcsec}$		Azimuth		Elevation		
3σ		80		41		
$3 \sigma^2$		6299		1651		
$RSS = \sqrt{\Sigma 3 \sigma^2}$		$\sqrt{7950} = 90 \text{ arcsec} = 0.025^\circ < 0.033^\circ \text{ (210-ft spec.)}$				

Note: The maximum error contributor is wind and amounts to approximately 71 arcsec. In terms of variance (σ^2), this represents 62% of the total error budget.

* Datum plane alignment: 22 arcsec; Subreflector alignment: 12 arcsec

† Azimuth-axis alignment: 18 arcsec; Elevation-axis alignment: 18 arcsec

After calibration, these errors can be assumed to have 10% repeatability or 0.10 (35) = 3.5 arcsec; also, 90% of the gravity errors can be compensated. With these compensations, the resulting space pointing vector is:

$$\begin{aligned} \sqrt{(3 + 36 + 13 + 169) + (4100 + 1150 + 100 + 780 + 169)} &= \sqrt{6520} \\ &= 81 \text{ arcsec with the maximum error contributor being wind} \\ &\text{(approximately 75% in terms of } \sigma^2 \text{).} \end{aligned}$$

Figure 11 summarizes the results of the radome-housed telescope study.

Figure 11. Results - 210-ft radome-housed analysis.

Component	Major component weight breakdown (lbs)	Surface accuracy	Pointing accuracy	Structural dynamics (locked rotor frequency)	Drive power
Reflector	453,000	0.145 inch calculated	0.004° (15 arcsec)	1.0 cps calculated	10 hp
Elevation wheel	450,000			0.5 cps recommended	per
Elevation counterweight	240,000	0.150 inch specified	(repeatability)	0.3 cps required	axis
Alidade	350,000				

5.1 Reflector and Pedestal

In philosophy, the radome-housed reflector can be allowed to deflect many inches at the tip as long as the reflector maintains a parabolic shape within the gravity-load RMS stipulated and is extremely repeatable within the pointing-accuracy requirements.

Analysis of the reflector proceeded along the lines of reducing all radial ribs and hoop-truss members to minimum size predicated on the structural buckling (L/r) required by AISC Code, where the L/r is limited to a maximum of 200, since these restrictions do place a lower limit on the structural design. The reflector's main rectangular support-girder and elevation-wheel structures were scaled down (member area only) to maintain approximately equivalent stiffnesses with respect to the original design. The goal here was to achieve a 0.115-inch RMS (45° to horizon-gravity loading only) for the radome-housed antenna. The comparable RMS for the no-radome antenna was 0.074-inch RMS. Theoretically, reducing the weight of the structure while keeping the geometry constant would produce identical deflections for gravity loadings only, except for the external loads from the surface panels.

It was possible to reduce the weight of the reflector 50% while maintaining the same geometry. Unfortunately, the above-mentioned AISC Code L/r restrictions prevented further weight reduction. The RMS was calculated as approximately 0.090 inch for gravity only (45° to horizon).

For the radome antenna, Figure 12, a surface-accuracy chart, assumed that the thermal differentials will be one-half of the no-radome design ($\pm 5^\circ$) and that there will be no wind-load deflection.

Based on the above, the RSS tolerance of 0.170 inch was kept constant. The gravity-load RMS for the reflector, 45° to horizon, therefore varied as follows:

No-radome: 0.074 inch 1σ ; 0.222 inch 3σ
 Radome - $1/2$ thermals: 0.115 inch 1σ ; 0.345 inch 3σ .

Consequently, the reflector and elevation-wheel assembly was analyzed for a gravity-load RMS goal from 45° to the horizon of 0.115 inch, as well as being capable of surviving the worst stress condition. (See Figure 13 for final results.)

Figure 12. Surface-accuracy error tables (initial budget) — 210-ft radome housed.

Error source 1 σ – RMS – inches	Manufacturer's tolerance on panels	Alignment tolerance on panels	Gravity 45° to horizon	Wind 30 mph $\alpha = 0, \psi = 0$	Thermals $\Delta t = 10^\circ$
Panels	0.060	0.060	0.031	-	0.002
Structure	-	-	0.115	-	0.010
$\Sigma 1 \sigma$	0.060	0.060	0.146	-	0.012
$1 \sigma^2 \times 10^{-6}$	3600	3600	21,330	-	144
$\Sigma 1 \sigma^2$		28,674			
$RSS = \sqrt{\Sigma 1 \sigma^2}$	$\sqrt{0.028674} = 0.170 < 0.250 \text{ inch}^*$				
* Note: The MIT specification requirement was revised to 0.150 inch.					

Figure 13. RMS table — final results of the CAMROC study.

Error source 1 σ — RMS — inches	Manufacturer's tolerance on panels	Alignment tolerance on panels	Gravity 45° to horizon	Thermals $\Delta t = 5^\circ$
Panels	0.060	0.060	0.031	0.002
Structure	-	-	0.090	0.010
$\Sigma 1 \sigma$	0.060	0.060	0.121	0.012
$1 \sigma^2 \times 10^{-6}$	3600	3600	14,600	144
$\Sigma 1 \sigma^2$	21,944			
RSS = $\sqrt{\Sigma 1 \sigma^2}$	$\sqrt{0.021944} = 0.145 \text{ inch}$			
CAMROC specification	0.150 inch			

After the scaling down of all structural members in the reflector and the elevation wheel, a three-dimensional static analysis was conducted. The computer programs employed were STAIR, STIFFEIG, and Path Length. The STAIR pin-jointed structural-analysis program was handled by the IBM 7094, Mod. II computer. The analysis was for one quadrant of the reflector elevation-wheel assembly, using the applicable boundary conditions for structural symmetry and antisymmetry. A total of 724 joints and 2510 bars were used to analyze this quadrant (1 hour computer time per analysis) for which deflections, reactions, and internal stresses due to gravity were computed. From the static displacements of all structural joints (227) located at the reflector surface, the surface accuracy (RMS) and reflector pointing error were computed, using the Path-Length program.

Since there is no wind acting on the antenna, the balance of the component parameters were selected to comply with the system natural frequency (locked rotor) of stiffness requirements. For example, the alidade was redesigned and all member sizes were significantly modified. Since the alidade is a rigid, rather than a pinned, structure, the STIFFEIG program was utilized; it takes into account end restraints for computing deflection, rotations, and spring constants.

The servo-accuracy requirement of 5 arcsec limited the acceleration lag error to less than 2 arcsec. This required a locked-rotor frequency of approximately 0.3 cps, which represented a significant stiffness reduction (a factor of 28) from the JPL 210-ft-diameter antenna, which has a locked-rotor frequency of 1.6 for the azimuth axis.

To find the lowest natural frequency of the reflector and elevation-wheel assemblies, the structure, as used in the STAIR analysis, was simplified and modeled to fit within the size limitations of a three-dimensional structural dynamic analysis program called STIFFEIG. All the reflector-structure static displacements from the STAIR analysis were matched to the static displacements of the modeled structure. When the ratio of these deflections approaches unity, then the stiffnesses of the two structures are matched. Once this compatibility is achieved, the structural dynamic analysis portion of the STIFFEIG program is run to determine the lowest six natural frequencies and mode shape deflections of the reflector and elevation-wheel assembly. With these data reduced, reflector-elevation-wheel lumped parameter models can be developed for incorporation into the overall system lumped parameter models. The analysis was conducted for the zenith-position (SS Boundary Condition) and the horizon-position (AS Boundary Condition) dynamic models.

For the dynamic analysis of the entire system, a 15° lumped model was analyzed using two Rohr-developed programs:

- 1) DYNEL for the elevation-lumped model.
- 2) DYNAZ for the azimuth-lumped model.

A group of differential equations describing the mass and stiffness characteristics of the lumped parameter model of the 210-ft antenna system are used to compute elements for the mass Matrix A and stiffness Matrix C. With these two matrices known, the natural frequencies of the model are solved using the eigenvalue subroutine CARAC5.

As a result, it followed that the stiffnesses of all components could be significantly reduced, thereby drastically cutting costs. For example, the stiffness of the alidade was reduced by a factor of 5, permitting the use of single rather than expensive built-up sections. All mechanical component stiffnesses (drives and bearings) were reduced by a factor of 10. This permitted utilizing very inexpensive gear reducers, standard bearings and housings, a reduction of the hydrostatic bearing pad sizes, etc. All spring and mass characteristics were revised and the two 15° of freedom lumped parameter

dynamic models were rerun. The result was 0.96 cps for the elevation axis and 0.93 cps for the azimuth axis. This was still too high, considering the 0.3 cps required. It was concluded that further reduction of stiffnesses would not significantly alter the above results, and it would require drastic revisions to the overall geometry to make further large-scale cost reductions.

It is recommended that a minimum locked-rotor frequency be specified as 0.5 cps to guard against discrepancies between the calculated versus the actual measured values.

In the next phase of the study, the pointing accuracy was reanalyzed. The specification requires a peak error of 15 arcsec repeatability. This is a minuscule tolerance for a structure of this magnitude, and consequently represents a major problem area. The reflector assembly from a gravity-loading standpoint must be an extremely repeatable structure, since it will be mandatory to calibrate out the gravity-load pointing error. Alignment of axes and datum planes must be held to less than 10 arcsec to accommodate calibration. Thermal differentials of only 5° on the structure can present a significant pointing error. For this structure, a 17-arcsec error has been calculated. It may, therefore, be necessary to control thermally the entire structure with a $\pm 2^\circ$ tolerance. Control of this type would be impossible outside a radome. A precision on-axis readout encoding system (19 bit) having a total axis error of less than 5 arcsec is required. Axes errors from the servo system must also be kept to less than 5 arcsec. Axes frictions become very critical and must be kept as low as possible. The result of the pointing-error analysis indicates a peak error of approximately 21 arcsec is possible if the gravity and alignment errors are calibratable and thermals are held to less than $\pm 5^\circ$ (see Figure 14).

5.2 Gear-Drive Considerations

Although there are many possible drive systems for the antenna, this study has been restricted to gear drives. A number of possible geared drives have been evaluated, and the following approaches have been found to be potentially applicable:

- 1) Floating single pinion.
- 2) Dual pinion with electrical antibacklash.
- 3) Dual pinion with mechanical antibacklash.

In the floating single-pinion drive, the backlash is reduced to a tolerable value by utilizing tight gearbox tolerances and by crowding the main pinion into the bullgear to eliminate final mesh backlash. This approach has been computed to give a backlash of about 4 arcsec with best available tolerances. This will cause a servo error due to backlash of about 2 or 3 arcsec above the antibacklash drive. The thermal environment of a radome is obviously required.

Figure 14. Pointing-accuracy table.

Elevation axis		Gravity (nonrepeatability)	Thermals 5° - Δt	Alignment*	Tracking
Error source (arcsec)					
Component					
Reflector assembly		8	0	17	-
Antenna-mount assembly		-	0		-
Servo system		-	-	-	5
Readout system		-	-	5	-
Σ 3 σ		8	0	< 18	5
(3 σ) ²		64	0	315	25
Σ (3 σ ²)		404			
RSS = √Σ (3 σ) ²		√404 = 20 arcsec = 3 σ			

Error source (arcsec)		Thermals 5° - Δt	Alignment	Tracking	
Component					
Reflector assembly		3	-	-	
Antenna-mount assembly		14	-	-	
Servo system		-	-	5	
Readout system		-	5	-	
Σ 3 σ		17	5	5	
(3 σ)		290	25	25	
Σ (3 σ) ²		340			
RSS = √Σ (3 σ) ²		√340 = 18 arcsec			

Resultant: Azimuth + elevation = $\sqrt{404 + 340} = \sqrt{744} = 27 \text{ arcsec}$

Note: Datum and axis alignments have been held to 10 arcsec maximum. Since axis alignment errors can be calibrated, it is assumed that 10% of the alignment errors will remain as residuals. This reduces the resultant space pointing vector to approximately 21 arcsec, with the maximum error being the 17 arcsec due to 5° thermal differentials.

* RSS applies since alignment errors are random.

A dual pinion drive with electrical antibacklash is the type normally used for precision antenna applications. The Comsat 85-ft antenna system uses this type of drive. The two gearboxes are mechanically independent except for their common connection to the bull gear. Antibacklash bias torque is generated by the servo-drive motors. There are two possible antibacklash drive schemes applicable to this type of drive, the unidirectional and the bias drives:

- 1) In the unidirectional drive, each drive motor and gearbox provides torque in one direction only — the other gearbox and motor provides a slight restraining torque to eliminate backlash. One motor and gearbox must be

capable of providing the full peak load, and only one gearbox provides the drive stiffness. This approach allows the use of a simpler power servo, since each motor provides only unidirectional torque (see Figure 15).

- 2) In the bias drive, both motors are biased to provide a countertorque at zero load to eliminate gearbox backlash. Varying load torques are supplied equally from the two motors and gearboxes. See Figure 15 for a plot of individual motor torques versus load demands. In this type of drive, the two motors and gearboxes share the peak load (not quite equally) and both gearboxes act in parallel for drive stiffness. The servo system must provide bidirectional torque control for both motors.

A dual-pinion mechanical-antibacklash drive provides a bias torque on the pinions from a mechanical connection between the two gearboxes. This approach allows the use of a straightforward single-motor servo system. It is sensitive to thermal effects and gearing tolerances, which usually preclude its use in nonradome antennas. For the radome-housed antenna, the environment and lower power gearing requirements may allow its use. Further investigation is required to establish definitely its feasibility.

If the antenna system were to be constructed in the near future, the bias-drive dual-pinion approach currently appears advantageous owing to its proved capabilities. Further investigation of alternate approaches is warranted.

The characteristics of the drives for a radome-housed antenna are low stiffness, low friction, and low backlash. High-quality gear reducers such as those used on present 85-ft antennas are costly, possess a stiffness too high for the radome requirement, and have a backlash of between 0.005 inch to 0.010 inch and a breakaway friction of less than 7-inch lbs. These latter two characteristics are achievable since the gears were ground. It appears that a friction type of drive designed specifically for radome application (i.e., low backlash, low friction) may be considerably less expensive, while supplying the most favorable characteristics.

5.3 Control and Drive System - General

The overall control-system arrangement, illustrated in Figure 16, employs a control computer for all digital data handling. The specified modes of control operation (Slave, Manual, and Slew) are mechanized so that each is independent of the other except for the power drive. Slew inputs are applied directly to the drive-rate servo. Manual hand wheel inputs develop error signals from a multispeed synchro system. These errors are amplified and shaped by analog servo amplifiers before being applied to the rate servo. The Slave (digital) command inputs are generated within the computer, compared to the encoded antenna position, and compensated before D/A conversion and application to the analog control system. The digital computer functions illustrated in Figure 16 are typical of those desired for radio astronomy; the detailed arrangement of this equipment, however, is not the subject of this study.

Note: Solid line represents bias drive. Dashed line represents unidirectional drive.

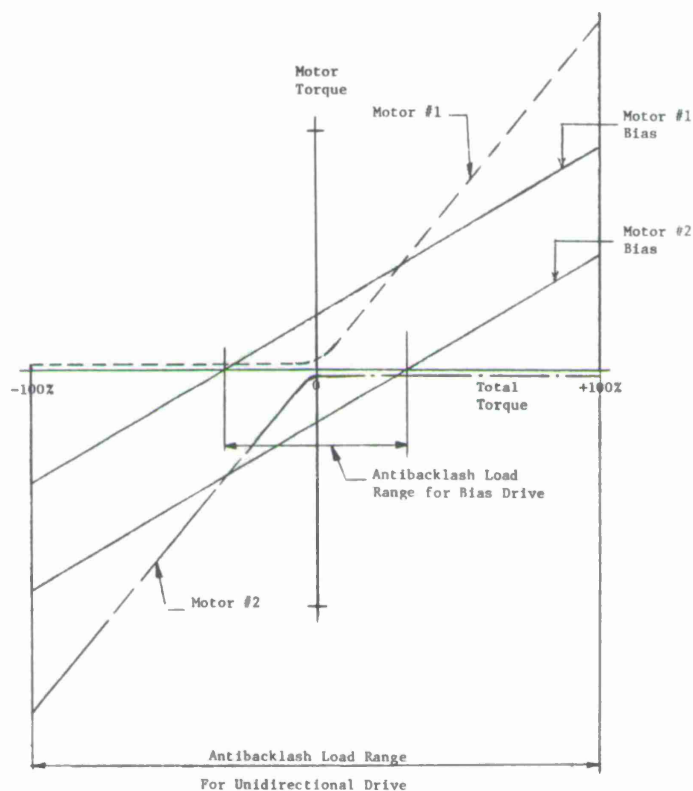
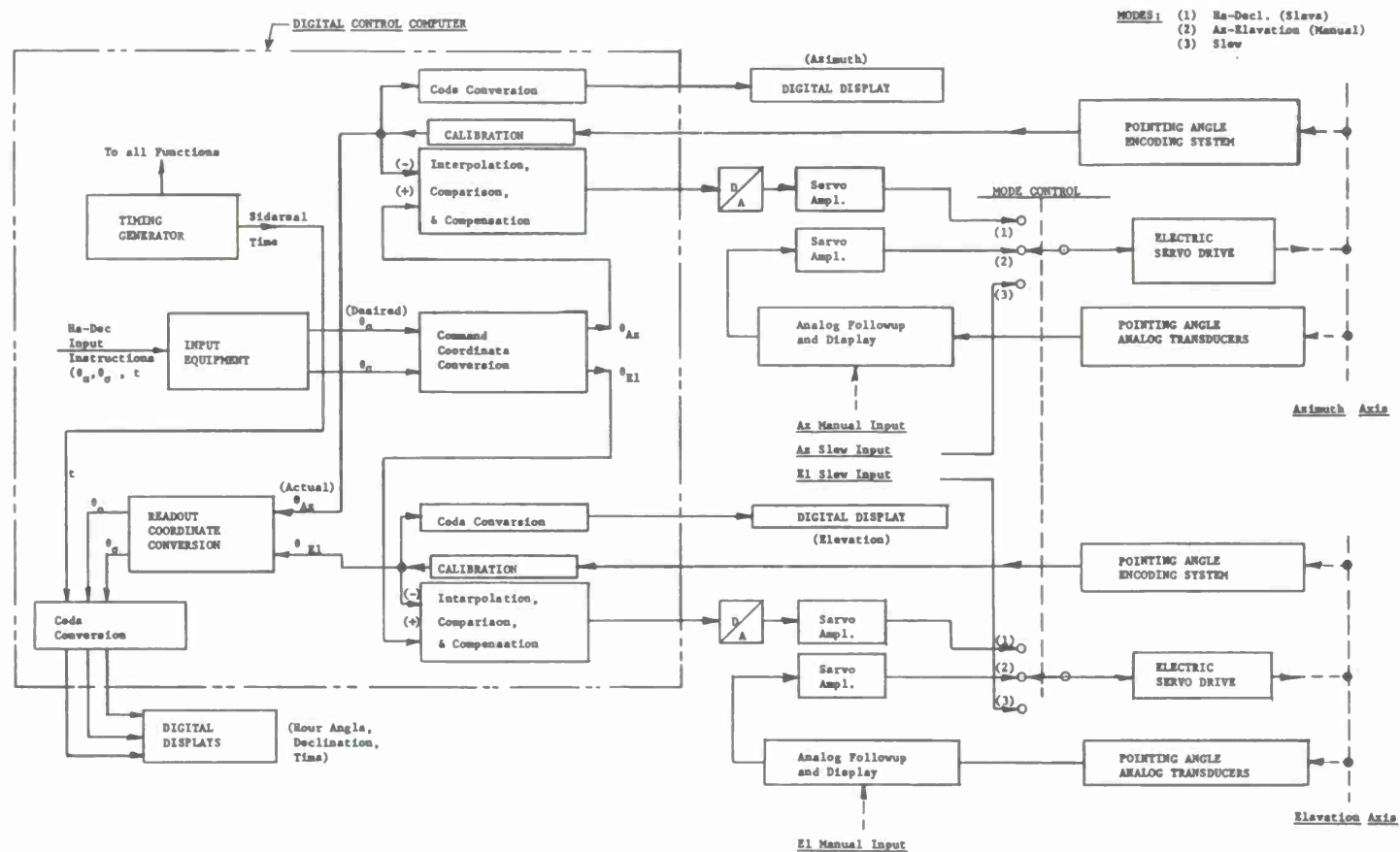


Figure 15. Comparison of bias and unidirectional drive torques.

The servo drive for each axis is a 10-hp rated antibacklash electric-motor system, as shown in Figure 17. Two identical motors, each driven by a solid-state power amplifier, are used on each axis. Antibacklash is provided through an electrical bias into the amplifiers. A common-rate loop using the rate feedback from both motors provides a very stiff drive system. This system is a low-power version of the system successfully employed on the Comsat 85-ft antenna. The M-G sets used in the Comsat system can be replaced with solid-state amplifiers owing to the lower power requirement.

The servo-control electronic equipment can be totally solid state. Modular construction as used on the Comsat system will provide convenient maintenance. All control equipment except the control console itself can be housed in one or two standard 19-inch racks.

The recommended precision data system is a direct on-axis 19-bit encoder similar to the Wayne-George BD-19. This system will require special axis couplings to realize its inherent accuracy. Output is a continuous parallel 19-bit natural binary.





5.4 Servo-System Considerations (Effect of Structure on Servo Accuracy)

The basic servo drive and control equipment for the system can be of conventional proved design. However, the accuracy (see Figure 18) of the control system is strongly affected by the following basic antenna parameters:

- 1) Lowest structural resonant frequency.
- 2) Drive system (gearing) stiffness.
- 3) Antenna axis friction.

The lowest structural resonant frequency limits the servo bandwidth, which in turn limits the acceleration constant K_A of the servo. With the Type II servo systems used for antenna control, the target-following error is predominantly acceleration lag. Hence, the servo lag error is inversely proportional to K_A . Since K_A varies as the square of servo bandwidth, the lag error is greatly increased as the servo bandwidth is reduced. With a near-optimum servo-loop design and a minimum structural resonance of 0.3 cps, the peak lag error for celestial targets is a tolerable 1.4 arcsec. If the structural resonance is lowered to 0.1 cps, the lag error increases to 13 arcsec, too high a value for a 15-sec total system accuracy. This lag error can be somewhat reduced by feed-forward techniques on long-term celestial target tracks; however, this approach is not applicable for short-term error reduction owing to the low bandwidth of the servo system (0.025 cps for 0.1-cps structural resonance). It is recommended that the antenna structural-mechanical design be based on a minimum resonant frequency of 0.3 cps.

The drive-system stiffness and the antenna-axis friction determine the servo error due to friction effects at the typical low tracking velocity required for celestial tracking. With the predicted friction torque variations of 50,000 lb-ft and a composite drive system (rate servo and gearing) stiffness of 5×10^9 lb-ft/rad, the computed peak friction error is 2.4 arcsec. A significant increase in friction or decrease in drive stiffness will cause this error to increase to intolerable levels. Attaining this predicted friction error requires a drive-gearing stiffness of 10^{10} lb-ft/rad. This is a much higher value than would be required to meet the natural-frequency criteria. The only alternative to designing for gearing stiffnesses on this order of magnitude is to reduce axis friction drastically. It appears that attainment of lower axis friction requires the use of small-diameter, low-friction axes bearings and great attention to friction sources, such as seals, cable mechanisms, etc.

Conclusions and Recommendations - Servo-System Errors

There are two key sources of error that strongly affect structural-mechanical design. These are the breakout friction and the servo lag errors. All the other servo errors are essentially independent of the structure and are not likely to increase above the predicted values.

Breakout-friction error can only be held to the value listed if drive stiffness is very high compared to the breakout friction. As can be seen in the calculations, a factor of 10 reduction in gearing stiffness (to 10^9 lb-ft/rad) would increase this error by

more than a factor of 5 (to 11 arcsec). Therefore, the drive stiffness must be kept high unless friction is correspondingly reduced.

Figure 18. Summary of servo-system errors.

Error source	Peak error (arcsec)
Breakout friction	2.0
Servo noise	2.4
Servo drift	<0.5
Resolution (digitizing)	1.7
Servo lag	1.4
Backlash	0 (antibacklash drive)
RSS error (3σ) (per axis)	3.9 arcsec per axis

The servo lag error computed herein requires a minimum structural natural frequency of 0.3 cps. Reducing the structural frequency to 0.1 cps from 0.3 cps will increase the lag error nearly a factor of 10 (error of 13 sec). Use of feed forward of commanded acceleration can be used to reduce the error. This considerably complicates the controls and is useful only on long-time tracks where acceleration can be accurately predicted.

It is recommended that structural and mechanical design be based on a 10^{10} lb-ft/rad drive stiffness if axis friction is 50,000 lb-ft and on a 0.3 cps minimum structural natural frequency.

5.5 Readout-System Considerations

Four basic types of readout systems were considered:

- 1) Instrument tower and mount system.
- 2) Geared readout system.
- 3) On-axis encoding system.
- 4) Optically linked readout system.

The wind-deflection error eliminating features of systems (1) and (4) are not required for radome operation; therefore, these systems are not recommended owing to their higher cost and complexity. Either a geared readout system with cam compensation or a direct on-axis encoding system can provide adequate readout-system accuracy. Owing to its present availability and greater simplicity, the direct on-axis encoding system is recommended. (The computed error per axis for this system is 4 arcsec.)

Special attention must be given to the couplings connecting the encoders to the antenna axis. In the present error analysis, the basic encoder and the couplings are predicted to have about equal errors. Large-diameter couplings and encoder location to minimize antenna bearing-mount effects on the encoder and coupling are required.

Regardless of the type of readout system selected, some calibration of the encoded position to correct for repeatable errors is required. As discussed elsewhere, the elevation axis position may deviate as much as 18 arcsec owing to structural deflections. This calibration correction is accomplished in the control computer.

5.5.1 Readout-system accuracy

There are two major sources of error:

- 1) The basic encoder, which is specified as the Wayne George BD-19, accurate to 2.5 arcsec peak.
- 2) The error of the couplings and local deflections — special couplings will be required to attain high accuracy. Use of such couplings in a radome environment should give a coupling error of 3 arcsec maximum. The expected system error peak is: $RSS = (3\sigma) \text{ error } [(3 \text{ arcsec})^2 + (2.5 \text{ arcsec})^2]^{1/2} = 4.0 \text{ arcsec}$ for either axis.

5.6 Suggested Control-Computer Configuration

For efficient radio-astronomy operation, computer-controlled sidereal-coordinate antenna operation is recommended. The block diagram arrangement of an overall control system employing this type of control is shown in Figure 2. Here, a control computer provides all digital data handling.

In digital (Slave Mode) operation, input instructions in tape, card, or manual form are inserted through the input equipment. These inputs, in sidereal coordinate form, may range from a single right-ascension-declination command for several hours' operation to a time-coded series of hour-angle-declination instructions at time intervals down to about 1 per sec. The input equipment, operating in conjunction with the station timing source, converts these instructions to hour-angle-declination inputs at a repetition rate of 1 per sec maximum. The resulting instructions are then coordinate converted to the required azimuth and elevation positions by the Command Coordinate Converter. The azimuth-elevation command data are interpolated to provide real-time command inputs at a repetition rate of about 5 per sec, compared to the corrected antenna-position feedback from the encoders, and compensated to provide proper servo loop characteristics. This gives a continuous digital rate command that is converted to analog form in the D/A converter and fed to the antenna power servos.

The encoded antenna position is modified by applying the required antenna calibration and refraction corrections. The corrected antenna position is converted to decimal form for actual boresight azimuth-elevation display and applied to a readout coordinate converter to generate sidereal coordinate displays. This approach allows convenient correction for repeatable antenna structural deflections in one step for both control and display.

The control computer may be time shared with other system functions, such as data logging, coordinate computation, etc. A fairly high-capacity computer is required, since coordinate conversion requires computation of several sine and cosine functions and several multiplications and divisions at an accuracy level of about 2^{19} . By minimizing the number and speed of coordinate conversions using the approach described above, it is expected that the required computer capability can be attained in a small general-purpose computer. JPL is currently using a SDS 910 machine to accomplish most of the functions required; expansion of the existing facilities of the Deep Space Network to incorporate full computer control is expected in the next few years.

6. COMPARISON OF RESULTS

The results and conclusions from the JPL 210-ft-diameter environmentally designed antenna would be greatly magnified for the 400-ft-diameter antenna. In fact, the analyses have shown that the effect of wind on the design of the 400-ft-diameter antenna is uneconomical and technically not feasible in the areas of pointing accuracy, natural frequency, and drive requirements. Furthermore, thermal differentials must be controlled in order to minimize pointing error, and this can be achieved only with a radome.

For the 210-ft-diameter environmental antenna, it took 200 hp per axis to drive the antenna in 50-mph winds at a velocity of $0.1^\circ/\text{sec}$. Since axis torques and forces vary as the diameter is cubed and squared, respectively, the horsepower required to drive a 400-ft-diameter antenna at the same velocity approaches very large limits — a factor of 8 over the 210-ft antenna.

The structural stiffness required for the 210-ft antenna to maintain 28-arcsec pointing error under a 30-mph wind with a 33% gust factor was 1.5 cps lowest structural frequency. The resulting stiffness requirements for all components predicated on supporting the 5 million lbs of mass and corresponding inertia significantly affected the cost of the instrument. In fact, the gear-reducer stiffness requirement was so high that for all practical considerations the upper limit had been reached for the type of reducers utilized for this program.

Considering the fact that the 210-ft-diameter antenna was designed for a pointing accuracy of 0.033° with dead load compensated and 0.015° (54 arcsec) with dead load compensated utilizing the master equatorial (optical) readout, the 15 arcsec (0.004°) required by the CAMROC specification for the 400-ft antenna, which is a very small tolerance for a structure of this size, would appear to be a requirement that could not be achieved without the use of a radome.

The overall design approach for an environmentally designed antenna must make allowance in the surface-accuracy and pointing-accuracy error budgets for the operating wind requirement. For the JPL 210-ft-diameter antenna, the surface accuracy for the 30-mph wind conditions, including the wind deflection of the structure and panels, was

0.099-inch RMS. In terms of variance (σ^2), this represented approximately 33% of the total surface-accuracy error budget. The pointing accuracy due to the 30-mph wind condition with a 0.33 gust factor was 71 arcsec. In terms of variance (σ^2), this represented 62% of the total pointing-accuracy error budget, exceeding the total CAMROC pointing requirement of 15 arcsec by approximately a factor of 5. The structural, mechanical, and servo stiffnesses that would be required to satisfy this error requirement for the CAMROC 400-ft antenna would require a tremendous increase in weight (stiffness), which defines cost.

Consequently, significant engineering and economic advantages can be gained if a large-diameter antenna is housed in a radome. Some of these are:

- 1) There is a considerable reduction in weight (3:1), hence cost (2.2:1); therefore, a much larger diameter antenna can be procured. In fact, the final cost analysis indicated a \$5 million saving for the 210-ft-diameter radome-housed telescope.
- 2) Mechanical drive components and axis bearing requirements are reduced (20:1 in horsepower alone), which significantly influences the structural-mechanical configurations available for use in a radome-housed concept, since very small azimuth bearings can be utilized.

Other factors brought out by the study are:

1) L/r consideration

For a radome-designed antenna, one of the major structural limitations is the $L/r = 200$ requirement. Since this requirement places a lower limit on the antenna weight, hence cost, the least weight to radius of gyration member sections must be developed and utilized throughout the design.

2) Axis frictions

For accurate servo-drive performance, axis frictions, which are a small part of the accuracy and torque requirements for environmentally designed drives, become very important for the radome-housed telescope design, thus leading to the conclusion that a small-diameter low-friction (hydrostatic) azimuth bearing should be utilized.

3) Pointing accuracy

Achieving a pointing-accuracy requirement of 15 arcsec without a radome for a structure of this magnitude is not technically feasible. In fact, this requirement represents a significant problem area even for the radome-housed antenna. First of all, the structure must be extremely repeatable with negligible hysteresis or nonlinearity. The system will have to be calibrated completely so that all repeatable errors, such as gravity deflection, axis alignment, etc., will be minimized so that they become

negligible. Thermal errors on a structure of this magnitude are significant, and a thermally controlled radome may be required to have an antenna meet the 15-arcsec accuracy.

Servo and readout subsystems must be very accurate, better than 1/3 of the no-radome environment, since on-axis errors of less than 5 arcsec for these subsystems are the maximum permissible tolerance. These tolerances can, however, be achieved with present-day equipment.

Pointing errors created by wind loadings, including gust, would require a structural stiffness so great as to be uneconomical. To accept wind errors, which are transient phenomena, would be intolerable in order to achieve a 15-arcsec pointing-accuracy requirement. Therefore, a radome appears highly desirable.

4) Gear drives

The gear-drive systems must be of the antibacklash type, since gear-reducer backlash errors will approach 0.004° , which is not tolerable from the antenna-pointing standpoint. High-quality reducers with ground gears were tested for backlash and friction on an 85-ft antenna. The test results were 0.005 and 0.010 inch for backlash and breakaway frictions of less than 7-inch lbs. In order to keep backlash to a minimum and to minimize axis friction, ground gears are recommended.

5) Summary

From the mechanical, structural, servo, and economic viewpoints, a large-diameter radio telescope must be housed in a radome in order to meet the technical requirements of the CAMROC program within a reasonable cost.

7. PERFORMANCE AND COST COMPARISON OF THE 210-FT- AND 100-M-DIAMETER RADIO TELESCOPES

The following tables compare the JPL 210-ft-diameter advanced antenna system, the 328-ft-diameter NRAO study, and the 210-ft-diameter MIT study. To arrive at comparable cost evaluations, the RMS tolerances were equalized; the corresponding weight and cost ratios are shown in Figure 22 (also refer to Figures 2 and 3).

The 100-m- and 210-ft-diameter environmental-designed radio telescopes are predicated on similar concepts having the same performance. A cost and performance comparison was made on the 100-m with the 210-ft-diameter antenna. This study indicates that the cost of the larger diameter antenna varies closely to the diameter raised to the 2.7 power. This increase in cost for the larger diameter telescope is due to:

- 1) The environmental conditions, which are must more severe for the larger diameter antennas.
- 2) The accuracy requirements, specifically pointing accuracy.

- 3) The additional complexity of the mechanical components (drives and bearings) due to the wind loadings on the larger diameter antenna.
- 4) The antenna-stiffness parameter requirements, which increase inversely as the diameter is squared.
- 5) The additional complexity in the manufacture and erection of the larger structural sections.

It is also pointed out that the dollar-per-lb cost is higher for the radome antenna as compared with its no-radome counterpart, which is as expected.

Figure 19. Comparison of results of the 210-ft-diameter environmental and nonenvironmental radio telescopes.

	Environmental	Radome housed	Remarks
Total rotating weight on the azimuth axis	4,200,000 lbs	1,600,000 lbs	An almost 3:1 reduction
The surface accuracy for both was kept constant at:	0.170-inch RMS 0.250 inch specified	0.170-inch RMS 0.145 inch calculated 0.150 inch specified	Which contains the error effects from all sources
Pointing accuracy	36 arcsec for tracking loop mode 54 arcsec optical link mode 90 arcsec analog mode	15 arcsec repeatability (22 arcsec calculated)	*
Locked-rotor frequency of either axis	1.6 cps and 1.8 cps where a 1.5 cps is required	Calculated is \approx 1.0 cps where a 0.5 cps is recommended and a 0.3 cps required	
The resonant frequency of the reflector— symmetrical mode: antisymmetrical mode:	4 cps 2.55 cps	5 cps 3.4 cps	
Dead load RMS of reflector as a change from 45°/horizon	0.074-inch RMS	0.090-inch RMS	Here we were striving for an RMS of 0.115 inch; therefore, more weight can be removed; however, the concept must be changed
Calculated overall RMS - 1σ	0.170 inch (0.250 inch specified)	0.145 inch (0.150 inch specified)	
Weight of the entire elev. rotating structure	2,293,000 lbs	1,213,000 lbs	An almost 2:1 reduction
Rotating inertia	100,000,000 slug ft	\approx 50,000,000 slug ft	
Axis horsepower	200, which is required to drive to stow - 50-mph wind	10 hp - for acceleration	This is a tremendous difference
Drives	4 per axis	2 per axis	
Servo system	Hydraulic antibacklash	Electric antibacklash	Very accurate servo system required
Azimuth bearing	Hydrostatic	Hydrostatic	Axis frictions must be kept very low—smoothness of motion must be very high
Foundation	10,000,000—2500 yds	6,000,000—1500 yds	
Cost ratio	2:2	1	

*Which implies that the antenna structure can be allowed to deflect many inches as long as it maintains a parabolic shape within the surface tolerances desired. Since the actual pointing errors of concern are the nonrepeatability, hysteresis, and nonlinearities in the structure, this requirement dictates that the reflector, gears, drives, bearings, readouts, and servo system must be extremely repeatable and accurate, having very low friction and very small nonlinearities.

Figure 20. Comparison of characteristics of the 210-ft-diameter environmental and nonenvironmental radio telescopes

	Nonenvironmental radome (MIT)	Environmental no-radome (JPL)
Gravity deflection		
RMS - zenith	0.116 inch	0.096 inch
RMS - horizon	0.122 inch	0.101 inch
RMS - 45° horizon	0.090 inch (0.115-inch goal)	0.074 inch
RMS goals - gravity only	0.115 inch	0.074 inch
Overall RMS	0.145 inch (5° Δt)	0.170 inch (30-mph wind, 10° Δt)
Spec. Requirement	0.150 inch	0.250 inch
Pointing accuracy		
3σ - overall	27 arcsec	0.025° (90 arcsec)
3σ - after compensation	≈ 21 arcsec	0.023° - 30-mph wind, analog
Spec. - 3σ	15 arcsec repeatability (on-axis encoder)	0.033° - 30-mph wind, mode
Spec. - 3σ overall		0.015° - optical mode (master equatorial)
Dead load only - reflector	21 arcsec calibratable 8 arcsec noncalibratable	18 arcsec calibratable 8 arcsec noncalibratable
Structural dynamics		
Reflector frequency - symmetrical mode	5 cps	4 cps
antisymmetrical mode	3.4 cps	2.55 cps
Locked-rotor frequency azimuth and elevation axes	0.93 and 0.98 cps calculated, respectively	1.6 and 1.8 cps
Required minimum	0.3 each axis	1.0 each axis
Spec.	0.5 each axis	1.5 each axis
System stiffness	0.2×10^{10} ft-lb/rad	1.0×10^{10} ft-lb/rad
Gear-drive stiffness	6×10^6 ft-lb/rad for each gear reducer	2.2×10^7 ft-lb/rad for each gear reducer
Axis-drive stiffness	2.6×10^{10} ft-lb/rad	26×10^{10} ft-lb/rad
Minimum recommended axis-drive stiffness	1.0×10^{10} for 50,000 ft-lb of friction	-
Number of drives	2 drives per axis	4 drives per axis
Rate servo stiffness	1×10^{10} ft-lb/rad	5×10^{10} ft-lb/rad
Wind velocity		
Precision	-0-	(50% solid and 50% porous) 25 mph
25% degraded	-0-	35 mph
Survival	-0-	120 mph

Figure 20. (Cont.)

	Nonenvironmental radome (MIT)	Environmental no-radome (JPL)
Velocity		
Precision operation	0.25°/sec	0.25°/sec
Slew	1°/sec	1°/sec
Drive to stow	0.25°/sec	0.25°/sec — wind 50 mph
Snow	-0-	40 psf
Ice	-0-	1/2 inch solid
Acceleration		
Precision operation	0.2°/sec ²	0.2°/sec ²
Slew	0.2°/sec ²	0.2°/sec ²
Drive to stow	0.02°/sec ²	0.02°/sec ²
Speed range	0.001°/sec to 0.25°/sec	0.001°/sec to 0.25°/sec — winds from 0 to 35 mph
Thermal differential	0 to 5° F	0 to 10° F
Readout system	< 4 sec 2-1/2-arcsec encoders	< 18 sec — master equatorial
Axis alignments	< 10 sec each	< 20 sec each
Servo system		
Accuracy	< 5 sec	< 13 sec
Drive power		
Antibacklash	10 hp/axis required	200 hp/axis required (50- mph drive to stow, 0.1° sec velocity)
Axis ratio	15000:1	28800:1
Weight (lbs)		
Ref. struct. (inner)	258,000	385,000
Ref. struct. (outer)	195,000	293,000
Backup (elevation wheel)	450,000	930,000
Feed support (cone)	40,000	47,000
Quadripod	30,000	38,000
Counterweight	240,000	600,000
Total rotating mass	1,213,000	2,293,000

Figure 20. (Cont.)

	Nonenvironmental radome (MIT)	Environmental no-radome (JPL)
Inertias — lb-ft sec ² × 10 ⁶		
Inertia about elevation axis	56	106
Inertia about cross-elevation axis	51	96
Inertia about boresight (I_6^z)	51	97
I_z (horizon look)	61	115

Figure 21. Comparison tables of the 210-ft and 100-m telescopes.

	JPL 210-ft environmental	NRAO 328-ft environmental (concept 2)	MIT 210-ft radome-housed
Reflector	Rectangular girder — 56 ft × 97 ft — vertex 13 ft deep — radial ribs $f/d = 0.423$ deflection shape — circular contours — zenith	Rectangular girder — 88 ft × 200 ft — 18 ft deep at vertex — radial ribs $f/d = 0.423$ deflection shape — circular contours — zenith	Rectangular girder — 56 ft × 97 ft — vertex 13 ft deep — radial ribs $f/d = 0.423$ deflection shape — circular contours — zenith
Weight and center of gravity of reflector from elevation axis	Weight — 604,000 lbs Arm — 30.4 ft	Weight — 2,200,000 lbs Arm — 21.5 ft	Weight — 405,000 lbs Arm — 20.4 ft
Reflector surface	Solid surface for 50% of diameter — perforated surface for outer 50% of the diameter — independently adjustable panels		
Weight on elevation bearings	2,300,000 lbs	3,570,000 lbs	1,200,000 lbs
Ratio of reflector- support girder to reflector diameter	Length Width 0.46 0.27	Length Width 0.61 0.24	Length Width 0.46 0.27
Feed support	Quadripod 90 ft high; base support — 56 ft × 97 ft	Height — 122 ft base diameter — 173 ft	90-ft-high bipod — base 97-ft spread
Elevation wheel	Diameter — 83 ft 2 wheels	Diameter — 125 ft 2 wheels	Diameter — 83 ft 1 wheel
Elevation counter- weight	548,000 lbs	340,000 lbs	231,000 lbs
Alidade	Height — 77 ft base diameter — 76 ft 8 inches weight — 1,500 kips 56 ft between eleva- tion bearings	Height — 100 ft base diameter — 90 ft weight — 2,300 kips 88 ft between eleva- tion bearings	Height — 77 ft base diameter — 76 ft 8 inches weight — 350 kips 56 ft between eleva- tion bearings
Elevation bearing	Quantity — 4 spherical roller bearings 24 inches \emptyset per axis — two each side	Quantity — 4 spherical roller bearings 30 inches \emptyset per axis — two each side	Quantity — 2 spherical roller bearings — 20 inches \emptyset per axis — one each side
Azimuth bearings	<u>Thrust bearing</u> 3 hydrostatic bearing pads on a 76 ft 8 inch \emptyset runner — pad size 40 inches × 60 inches <u>Radial bearing</u> 3 radial roller bearings 15-ft radius	<u>Thrust bearing</u> 3 hydrostatic bearing pads on an 87-inch \emptyset runner <u>Radial bearing</u> 30-ft \emptyset — 3 equally spaced trucks on a 30-ft \emptyset collar	<u>Thrust bearing</u> 3 hydrostatic bearing pads on a 76-ft 8-inch \emptyset runner — pad size 30 inches × 40 inches <u>Radial bearing</u> 3 radial roller bear- ings — 15-ft radius
Drives	Countertorque drive system — 4 reducers per axis — 200 hp- tangential link-backup roller mounting arrangement. Two 9- inch wide bull gears for elevation and one 9-inch for azimuth.	Countertorque drive system — 4 reducers per axis. Tangential link-backup roller mounting arrange- ment. Two 12-inch wide bull gears for elevation and one 9- inch wide bull gear for azimuth.	Countertorque drive system — 2 reducers per axis. Tangential link-backup roller mounting arrange- ment. A 4-inch wide bull gear required for each axis.

Figure 21. (Cont.)

	JPL 210-ft environmental	NRAO 328-ft environmental (concept 2)	MIT 210-ft radome-housed
Drives (cont.)	<u>Bull-gear diameter</u> elevation - 83 ft azimuth - 70 ft	<u>Bull-gear diameter</u> elevation - 125 ft azimuth - 81 ft	<u>Bull-gear diameter</u> elevation - 83 ft azimuth - 70 ft
Pedestal	Height - 46 ft walls - 42 inches thick weight - 10,000 K	Height - 40 ft 87-ft \emptyset wall - 3.5 ft thick - top deck reinforced concrete steel girder config- uration weight - 13,800,000 K	Height - 27 ft wall - 30 inches thick weight - 6,000 K
Servo system	Hydraulic system is required to provide accu- racy requirements. Countertorqued principle must be utilized to eliminate backlash in re- ducer/bull-gear assembly. Servo system errors must be held to 13 arcsec on each axis.		Electric antibacklash system - servo sys- tem errors must be held to 5 arcsec on each axis.
Readouts	Master equatorial on- axis optical link < 18 arcsec accuracy. Geared readout for analog mode.	Precision geared for on-axis readouts < 10-arcsec accu- racy.	On-axis precision 19 bit encoders < 5- arcsec digital readout systems error.

		JPL 210-ft environ- mental	NRAO 328-ft environ- mental (concept 2)	MIT 210-ft radome- housed	Remarks
Pointing accu- racy - arcsec uncalibratable		54	75	15	
Surface accu- racy - 1σ - RMS best-fit parabola	Specification require- ments include dead- load, windload, ther- mals, panel-manufac- turing, and field-setting tolerances	0.250 inch	0.250 inch	0.150* inch	*Includes deadload, reduced thermals, panel manufacturing and setting tolerances
	As calculated	0.170 inch	0.234 inch	0.145 inch	
Locked-rotor frequency	Required for either axis	1.5 cps	0.5 cps	0.5 cps	
	As computed or az. measured el.	1.6 cps 1.8 cps	0.74 cps 1.01 cps	0.93 cps 0.98 cps	
Servo bandwidth	Azimuth and elevation	0.2 cps	0.1 cps	0.08 cps	
Acceleration	Azimuth and elevation	0.2°/sec ²	0.2°/sec ²	0.2°/sec ²	
Velocity	Azimuth and elevation	0.50°/sec* 0.20°/sec*	0.50°/sec* 0.25°/sec*	0.25°/sec 0.20°/sec	*Up to 30 mph *Up to 45 mph
Drive hp required per axis		200	200	10	
Drive to stow	Elevation axis	50 mph	45 mph		60 mph using least windage stow path
Stowed	Elevation axis	120 mph	100 mph		Independent stow locks elevation
Weights of structural components	Feed support	pounds 41,000	pounds 65,000	pounds 22,000	Struct. A36
	reflector surface	60,000	155,000	60,000	6061-T al. panels
	refl. struct. & el. whls.	1,651,000	3,010,000	887,000	struct. A36
	counterweight	548,000	340,000	231,000	lead
	total at elev. axis	2,300,000	3,570,000	1,200,000	struct. A36
	alidade	1,500,000	2,300,000	400,000	struct. A36
	Weight of structural	3,800,000	5,870,000	1,600,000	Struct. A36
	weight of mechanical	400,000	370,000	40,000	bearings & reducers
	weight on top of pedestal	4,200,000	6,240,000	1,640,000	struct. & mech.
	weight of concrete	10,000,000	13,800,000	6,000,000	including rebar
	Total weight on soil:	14,200,000	20,000,000	7,640,000	

Figure 22. Weight and cost summary: environmental and nonenvironmental 210-ft-diameter and 100-m.

Ratio	(Diameter) ¹ (Diameter) ² (Diameter) ³	210 ft Ø		328 ft Ø		Remarks
		Environmental	Radome	Environmental	Radome	
		1	1	1.56	1.56	
		1	1	2.44	2.44	
		1	1	3.80	3.80	
Weights on (lbs)	Elevation bearings	*	†	**		
	Azimuth bearings	2,300,000	1,200,000	3,600,000		
	Soil	4,200,000	1,600,000	6,240,000		
Calculated RMS (1σ)		14,200,000	7,600,000	20,000,000		
		*	†	**		
		0.170 inch	0.150 inch	0.250 inch		
Eq. weight for eq. deflection		0.150 RMS		0.150 RMS	0.150 RMS	RMS set equal in order to have a common base for cost comparison
	Elevation bearings	2,600,000	Same as	6,400,000	3,000,000	
	Azimuth bearings	4,800,000	above	11,600,000	3,900,000 ‡	
	Soil	15,800,000	(basis)	29,500,000	13,300,000	
Cost (millions of dollars) (less engineering costs, which are common)		9.4	4.3	30.0	13.2	These include the on-site installation
Approximate \$/lb		2.0	2.7	2.6	3.4	
		Less all A & E offices, labs, shops, equipment room, master equatorial, etc.	same	same	same	

* Based on JPL contract - W. O. 420.

† Based on MIT study - W. O. 748.

** Based on NRAO study - W. O. 215.

‡ Based on an equivalent stiffness extrapolation.

APPENDIX B

CONCEPTUAL STUDIES FOR A 400-FT-DIAMETER CORT ANTENNA

Prepared for
THE CAMBRIDGE RADIO OBSERVATORY COMMITTEE

November 1966

AMMANN & WHITNEY
NEW YORK, NEW YORK

TABLE OF CONTENTS

<u>Section</u>		<u>Page</u>
1	INTRODUCTION	B-1
2	SUMMARY AND CONCLUSION	B-1
3	DESIGN CRITERIA	B-2
4	CORT CONFIGURATIONS	B-3
5	COMPONENT DESIGN OF RETICULATED CONE CORT SYSTEM.....	B-9
6	COST ITEMS	B-21
7	COST ESTIMATES	B-22

1. INTRODUCTION

The CORT-type antenna system as conceived by the MIT Lincoln Laboratory has the highest electrical efficiency of any of the concepts that have been proposed, owing both to the elimination of feed aperture blocking and to its efficient shielding system. However, two large reflecting surfaces are required by the system as compared to one in the Cassegrain system. In order to compare the relative merits of CORT with more conventional antennas, preliminary design studies and cost estimates are required.

This report covers a 400-ft-diameter CORT-type antenna and two alternative CORT schemes, all enclosed within radomes. Rough cost estimates for all three concepts were made, and a detailed cost estimate for the most economical scheme is presented. Although the design of the radomes is not part of this study program, its cost, derived from a previous report, is included in the estimate in order to obtain an overall construction cost of the complete antenna system. The design studies and cost estimates for an alternate Cassegrain antenna concept will be the subject of a separate report.

This work is performed under the guidance of the MIT Lincoln Laboratory with funds provided under a National Science Foundation grant.

2. SUMMARY AND CONCLUSION

The original CORT antenna system conceived by the MIT Lincoln Laboratory (Figure 1) and two alternate CORT schemes, the pendulum truss concept (Figure 3) and the reticulated cone concept (Figure 5), were studied.

It was found that the overall cost of the original scheme is excessive because a very stiff rotating cylinder and a large-diameter radome are required. The pendulum truss scheme is not economically feasible since it requires a very large radome, a complicated system of drives, and a complex shield. A reticulated cone concept is feasible, and its features and cost are summarized in this report.

During the study, it became evident that unless very economical reflector surfaces were developed, CORT would be much more expensive than the conventional Cassegrain antennas. The primary reflector surface developed is a curved, perforated steel plate. Since the surface does not move relative to gravity, it can be cambered to offset the dead-load deflection. For the mirror surface, panels made of thin gauge metal sheet glued to prestressed wire take maximum advantage of the plane's simplicity and are recommended. The deflection of the mirror during altitude rotation will be compensated by air pressure, which varies with the normal component of the weight of the plane.

The overall cost of the CORT system is given in Table 3. It is felt that the cost of the CORT configuration will appreciably exceed that of the Cassegrain configuration. The excess cost is attributable to the need for two reflectors and their backup instead of one as in the Cassegrain configuration, to the shield, and to the need for a very large and deep radome.

3. DESIGN CRITERIA

The performance criteria of the antenna system and the environmental specifications as furnished by the MIT Lincoln Laboratory are as follows:

- 1) Sky coverage
Elevation: +15° to +90°
Azimuth: ±300°
- 2) Angular velocity (both elevation and azimuth)
Tracking: 0.25° /sec
Slew: 1.00° /sec
- 3) Angular acceleration
0.04° /sec² (both elevation and azimuth)
- 4) Speed range
The antennas shall be capable of operating smoothly at all velocities from 0.001° /sec to 0.25° /sec.
- 5) Pointing accuracy
Operational peak pointing accuracy: 15 sec. This shall include the effects of gravity, temperature, axis gearing, read-out tolerances, alignments, and servo tracking errors.
- 6) Operational surface accuracy
0.15-inch RMS (normal) - overall system tolerance to be budgeted in accordance with the following expression:
$$0.15 = \sqrt{(RMS_p)^2 + 1/2 (RMS_m)^2 + (RMS_s)^2}$$

RMS_p = RMS of fixed paraboloid . . (normal)
RMS_m = RMS of mirror (normal)
RMS_s = RMS of secondary reflector (normal)
The limiting cases of this expression are:
RMS_m = 0.21 inch if RMS_p = 0.00 inch and RMS_s = 0.00 inch or
RMS_p = 0.15 inch if RMS_m = 0.00 inch and RMS_s = 0.00 inch
- 7) Structural dynamics
The lowest natural frequency of the antenna systems shall be not less than 0.1 cps.
- 8) Electronic-equipment enclosure
Provision for 25,000 lbs of electronic gear, plus access facility located behind the primary reflector.

- 9) Ambient temperature
Survival: -40°F to $+140^{\circ}\text{F}$
Operational: $+45^{\circ}\text{F}$ to $+85^{\circ}\text{F}$
- 10) Differential temperature
 10°F to bottom, 5°F side to side
- 11) Humidity
 0% to 100%

4. CORT CONFIGURATIONS

4.1 General

In all CORT configurations, a 400-ft-diameter paraboloid reflector similar to those used for conventional antennas is used. However, the reflector does not rotate in elevation. Elevation sky coverage is provided instead by a 400-ft \times 566-ft elliptical reflecting plane placed in front of the paraboloid. This reflecting plane functions as a rotating mirror in which the paraboloid can "see" the sky.

The mirror rotates about an axis that is a prolongation of the axis of the paraboloid to provide altitude coverage. The optics are such that the mirror lies in a 45° plane when pointing at the zenith and rotates into a vertical plane when pointing at the horizon.

Both paraboloid and mirror are mounted on a turntable that rotates about a vertical axis, causing the azimuth motion.

Because the center of the mirror can be placed at the focus of the paraboloid, the instrument may be operated as a prime focus instrument by placing the feed at this point. If, instead, a hyperboloidal secondary reflector is placed at the center of the mirror, and the feed is placed on the dish, the antenna will operate as a Cassegrain instrument. This latter arrangement has the advantage of requiring no movable fittings between the electronic feed capsule and its support. It is expected that a CORT antenna will be capable of operating in either mode, depending upon the requirements of the experiment being performed.

4.2 The Original CORT Concept

Figure 1 shows how the configuration was applied in the original concept developed by MIT Lincoln Laboratory. The mirror is mounted in a cylinder that is supported on two sets of rollers. Because the axis of the cylinder is a prolongation of the paraboloidal axis, the rollers drive the barrel and therefore the mirror through its altitude motion.

The cylinder, which extends beyond the mirror, is open at the end to permit the paraboloid to see the mirror. It is also pierced to provide an opening by which the mirror sees the sky. This tight enclosure arrangement is responsible in a large part for the high efficiency of the concept.

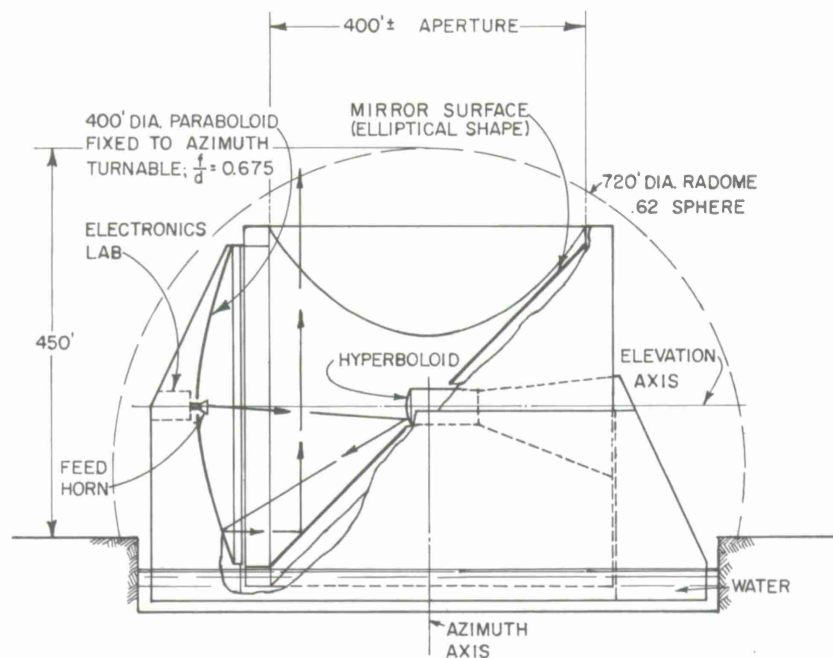


Figure 1. CORT.

Preliminary computations indicated that gravity load causes large deflection of the rotating cylinder unless the cylinder is made very stiff or reinforced with many diaphragms. This cylinder deflection in turn affects the very deflection of the mirror. Because a stiffened cylinder proved to be quite heavy, two alternative CORT schemes were developed. For identification purposes, we have called the first alternate the pendulum truss concept and the second the reticulated cone concept.

4.3 The Pendulum Truss Concept

As can be seen in Figures 2 and 3, the mirror is supported on trusses that bear on a longitudinal cantilever girder, which in turn rotates independently of the azimuth motion about a vertical axis. By driving the cantilever about a horizontal axis (Drive D1) and a vertical axis that is independent of azimuth motion (Drive D3), the mirror can be made to follow its correct path.

The advantage of using a two-axis drive to simulate a one-axis motion in this way lies in the behavior of the elements of the mirror plane. Any horizontal line drawn on the mirror surface remains horizontal as the structure rotates. If this horizontal is imagined as a long hinge below which is suspended a structural framework, it can be seen that

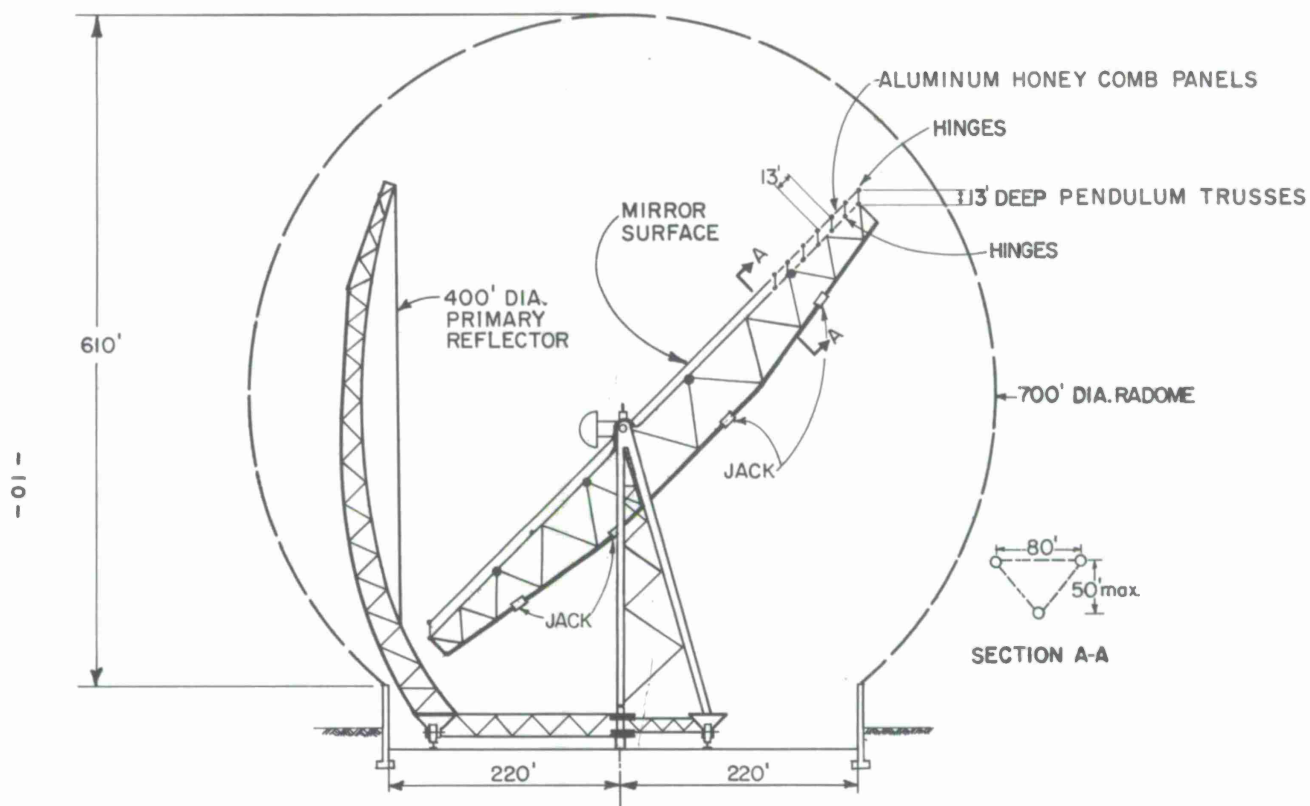


Figure 2. Pendulum truss scheme.

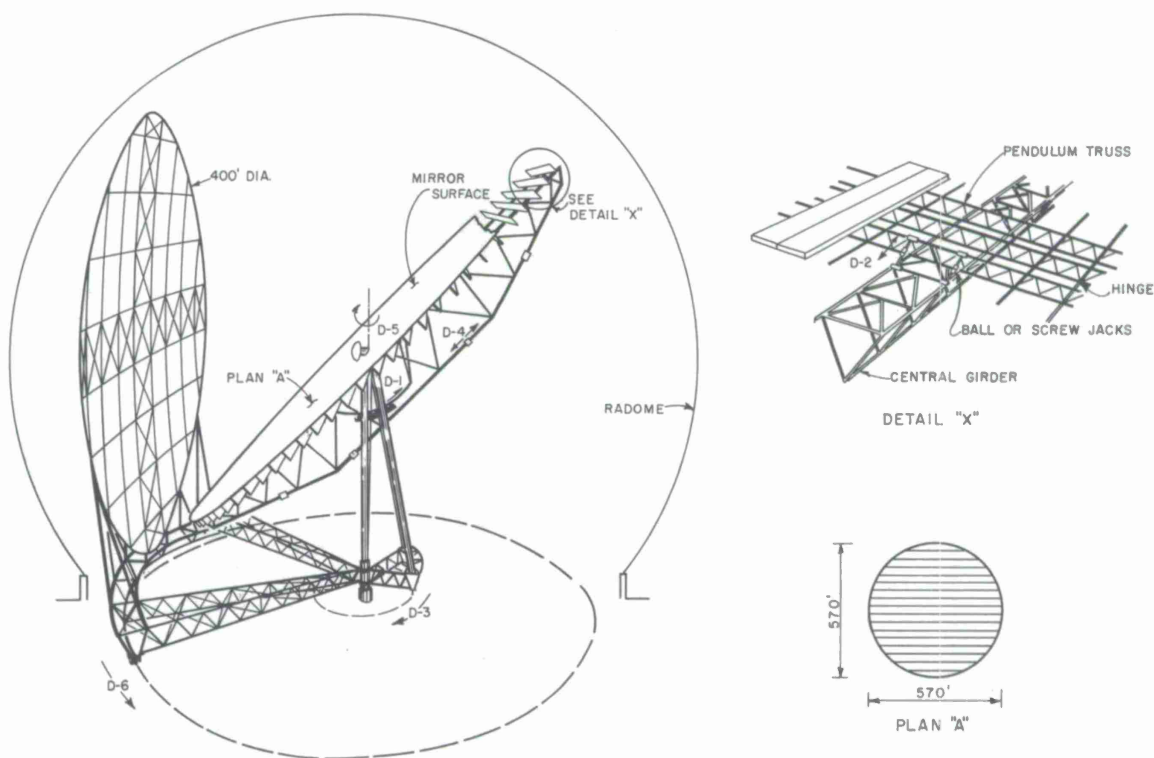


Figure 3. Pendulum truss scheme.

the structural framework never changes its attitude relative to the gravity reactor. Gravity-caused deflections never change and can be cambered out, making the frame infinitely stiff even though built of finite (and actually very light) material.

Because of uncertainties due to friction, it was decided to rely on a Drive D2 rather than on gravity to ensure that the suspended trusses remained vertical. In this case, further economies were to be realized by supporting the truss from beneath rather than from above, making the trusses into elongated inverted pendulums.

The paraboloid, like the pendulum trusses, does not move relative to gravity, nor does the turntable. These items are also effectively infinitely stiff. The only structural elements that deflect owing to motion of the antenna are the cantilever girder that carries the pendulum trusses and the mirror surface that spans between the trusses.

The mirror surface spans a relatively short distance and, as will be discussed later, can easily be made adequately stiff. The large cantilever girder, however, cannot be economically stiffened. Instead, it will be compensated by placing jacks (Drive D4) within the structural system. Because the girder deflections are predictable, the jack strokes can be programmed in advance as a function of the elevation of the antenna; no feedback is needed.

When the mirror undergoes rotation about a vertical axis independently of azimuth rotation, the prime focus or the secondary reflector mounted in the mirror must remain unrotated. Drive D5 is shown schematically as a device that rotates equal and opposite to the motion of D3 to accomplish this.

While the geometric concept seems attractive, preliminary development of the design showed it to be quite expensive. The primary reasons are:

- 1) The required radome is 700 ft in diameter and 610 ft high. The cost of the radome alone would be more than \$13,700,000.
- 2) The structural steel required for the antenna is more than 9,600,000 lbs.
- 3) The enclosure or shield will be very complicated and costly.
- 4) An exceptionally large mirror is required.
- 5) The six drives (D1 to D6 noted above) and hinge connections at the pendulum trusses add considerable cost.

The concept study was therefore dropped.

4.4 The Reticulated Cone Construction

In this scheme, shown in Figures 4 and 5, the mirror rotates about the horizontal axis, as in the original CORT concept. However, the cylinder has been replaced by a reticulated cone not only to reduce the amount of structure but also to stiffen the structure

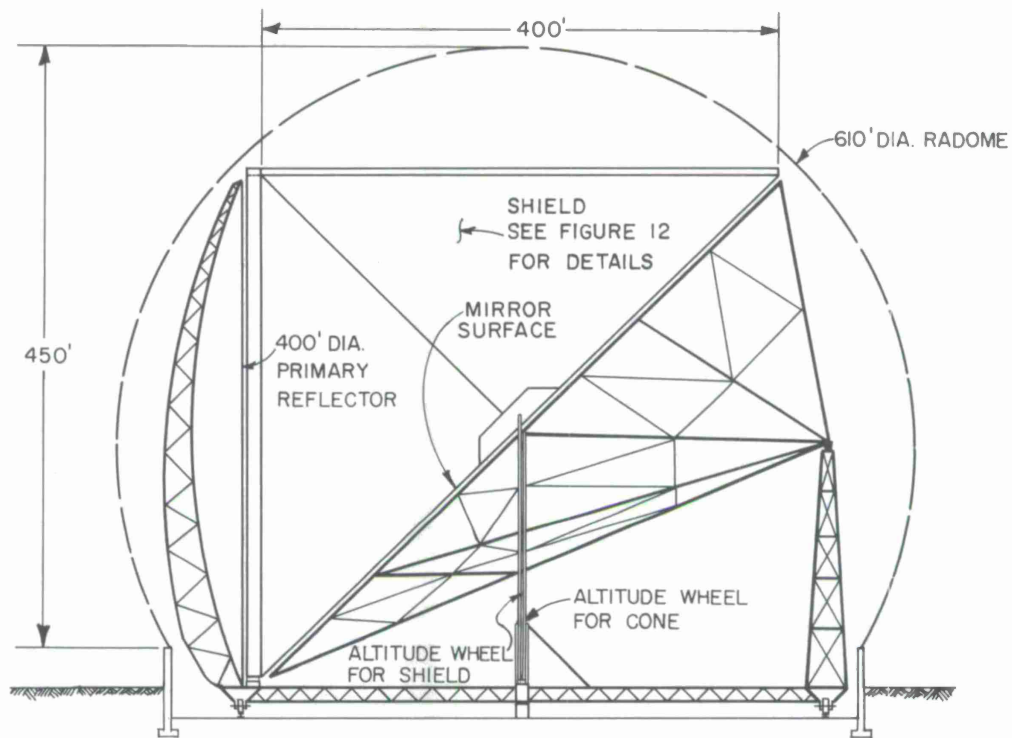


Figure 4. Reticulated cone scheme.

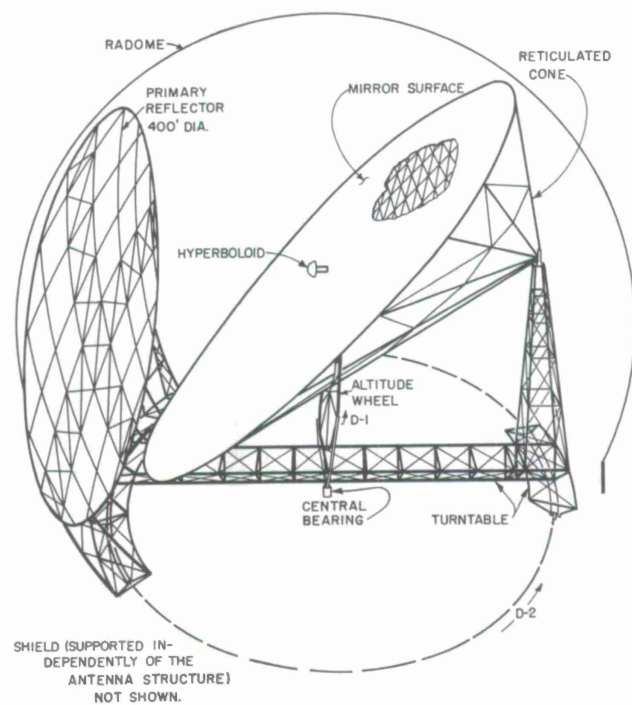


Figure 5. Reticulated cone scheme.

for minimum deflection. The shield is supported independently of the antenna structure so that its distortion will not affect the antenna. The antenna, therefore, will be a deflection design, and the shield, a strength design. Both the antenna and the shield can be driven by the same drives.

The mirror surface is supported by a space truss strong enough to span over the 400 ft by 566 ft ellipse, but not stiff enough to satisfy the deflection criteria. As in the case of the pendulum truss concept, we judge it to be more economical to compensate the deflection than to resist it.

The compensation method is based upon the unequal stiffness of the mirror structure in the in-plane direction and the out-of-plane direction. In the plane of the mirror, the backup structure is very stiff and the deflections in this direction are not significant. No compensation for in-plane motion is required. Deflections normal to the mirror plane are caused by the bending of the structure system and are relatively large. Since their deflections degrade antenna performance, they are compensated.

The stiffness of the mirror structure in the in-plane direction is uncoupled from the out-of-plane of direction. That is, the framing system was designed so that loads applied in the mirror plane do not cause deflection normal to the plane. This is accomplished by permitting no connections from the plane to the cone except at the perimeter and by providing in-plane framing with as little eccentricity as possible. As a result, the deflections are proportional to that component of the mirror weight that is normal to the mirror plane, and can be compensated by a uniform air pressure on the mirror plane that varies with the elevation angle of the antenna. The air pressure will not exceed a few inches of water.

The deflection of the mirror support (the elliptical perimeter of the reticulated cone) in a direction normal to the surface is the only other element that contributes a deflection during altitude rotation. Compensation for this deflection is not quite so simple, but computer studies show the elliptical perimeter to be quite stiff. The peak plane distortion after bias rigging is only about 1/4 inch, indicating an RMS error of about 0.10 inch due to gravity if no compensation is used. Optimizing of the framing will halve this value, and simple member compensation by jacking will reduce it to an insignificant value.

As in the case of the other CORT concepts, the paraboloid and turntable structure do not deflect owing to gravity.

5. COMPONENT DESIGN OF RETICULATED CONE CORT SYSTEM

5.1 Primary Reflector and Support

The angle between the primary reflector and gravity does not change as the antenna rotates. No matter how flexible its structure is, dead load will have no effect on its shape. The framing should therefore be developed to produce minimum deformation due to thermal gradients rather than due to loads. Our investigation indicates that as little three-dimensional behavior as possible should be invoked. Therefore, simple vertical cantilever trusses spaced 50 ft apart are used to carry the load to the turntable.

The reflector surface is a curved-perforated steel plate weighing about 1.25 psf, cambered to offset dead-load deflection. The plates are supported by purlins, spaced 13 ft on center, that span between the vertical trusses. The 8.5-lb/linear ft purlins are cambered for dead-load deflection. If necessary, the support system can be enclosed in insulation to maintain its shape, and the reflector surface may be covered with low-dielectric, high-insulation polyurethane. See Figure 6 for support details.

The total weight of the primary reflector support system is 520,000 lbs consisting of 310,000 lbs for the vertical trusses and 210,000 lbs for the purlins.

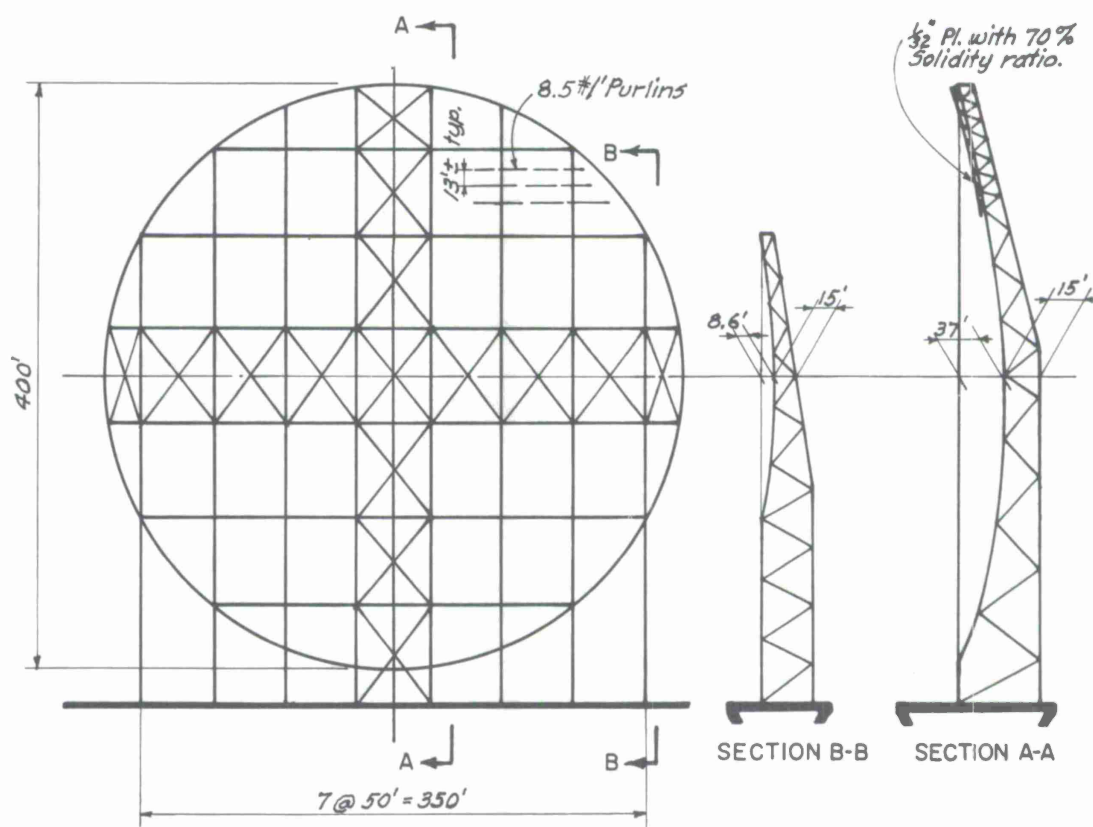


Figure 6. Primary reflector.

It should be noted that this is not a least-weight design, but rather a cost design. Many of the surface elements used in the mirror design proved to be considerably lighter, but they were not used since the stiffness requirements made them expensive. The primary reflector skin is unusual for an antenna in that it can be designed with no regard to deflections due to loads.

5.2 Reticulated Cone

The reticulated cone is supported at its center on an altitude wheel and at the end on a steel tower. The altitude rotation is controlled by Drive D1, as shown in Figure 5. Most of the total weight of the reticulated cone is transmitted to the ground, directly through the altitude wheel and indirectly through the central bearing. The end reaction of the cone is only a small fraction of the total weight.

In order to find the deflections and stresses in the reticulated cone, an idealized system shown in Figures 7, 8, and 9 was analyzed by computer. The sectional areas of the members used were reduced several times until practical minimum sections were obtained. As the members were reduced, the deflections remained nearly constant. This was because the reduction in member stiffness was offset by a reduction in weight. The sizes of the members were generally governed by column and local buckling, bending of members, and fabrication and erection considerations.

The lengths, sections, weights, and maximum stresses in the major members are listed in Table 1.

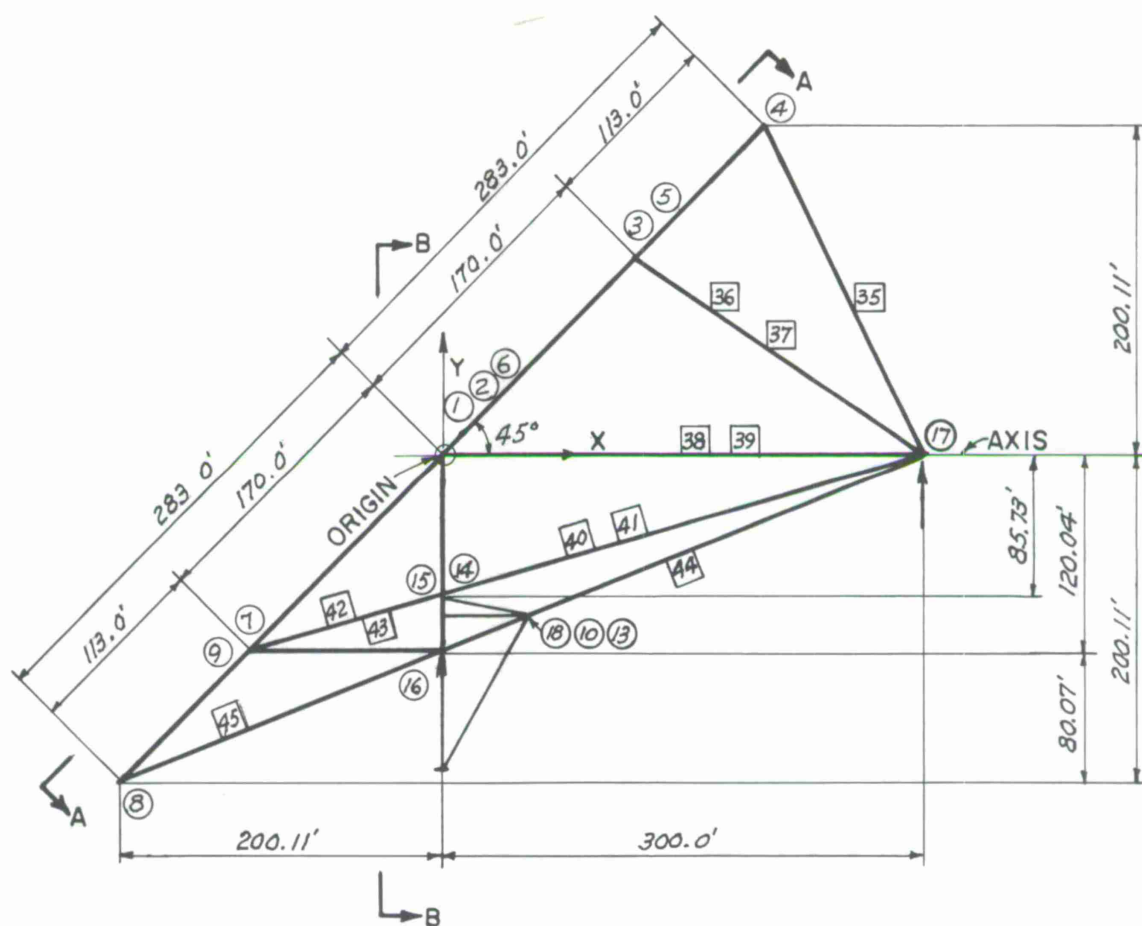
Since the normal deflection of the mirror surface can be compensated for its own deflection by air pressure, the most critical deflections of the reticulated cone are those of the edge of the mirror where the surface is supported. These deflections are shown in Figure 10. The maximum deflection normal to the plane after rigging is 0.25 inch, indicating an RMS error of about 0.10 inch due to gravity if no compensation is used, which is within the permissible limits.

The weight of the main members and the bracing, including details of the reticulated cone, is about 2,750,000 lbs.

5.3 Mirror Reflector Surface

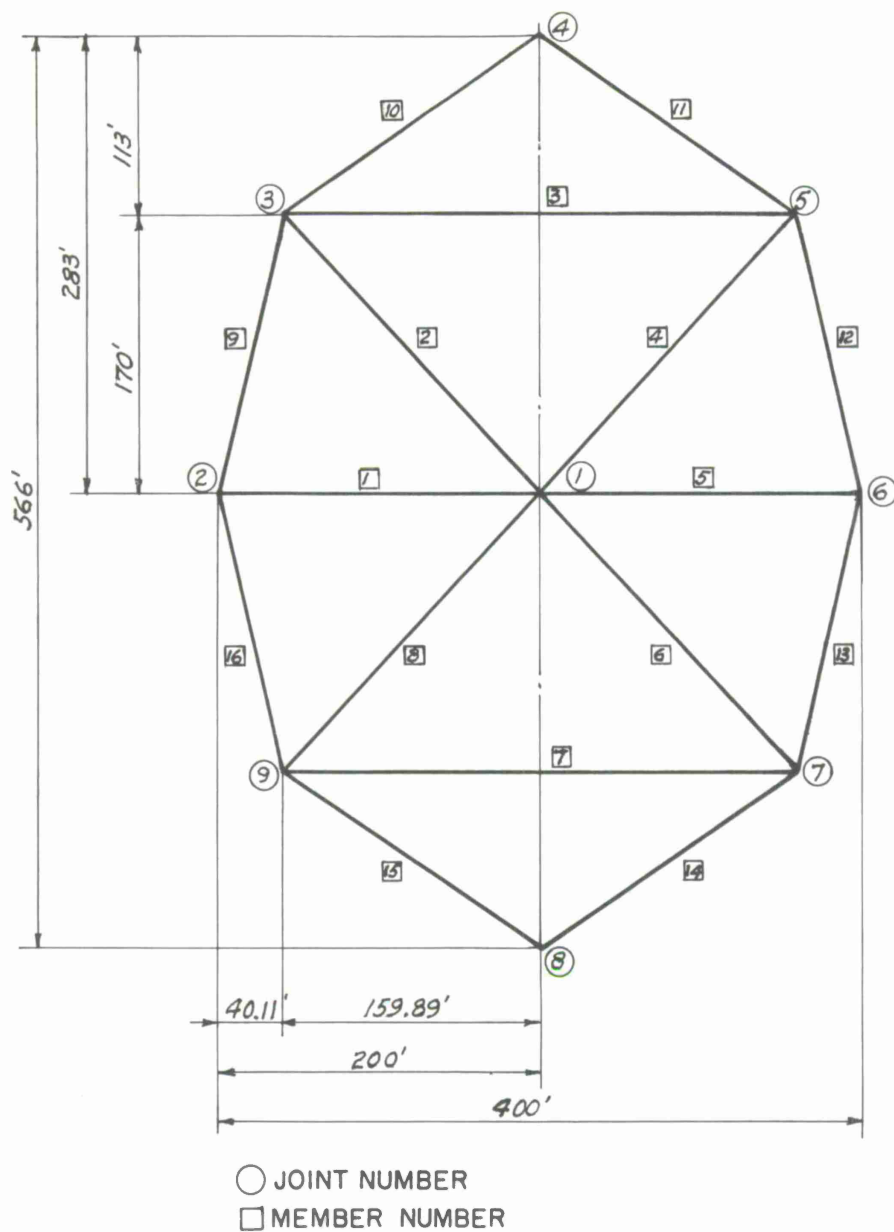
As noted previously, the mirror surface is supported by a space truss that, in turn, is connected by hinges to the reticulated cone. The following surface materials have been studied:

- 1) Steel and aluminum mesh, prestressed and unprestressed.
- 2) Expanded metal screen.
- 3) Wires (prestressed) of steel, aluminum, and Fiberglas.
- 4) Fiberglas-reinforced plastic sheet with metallic paint.



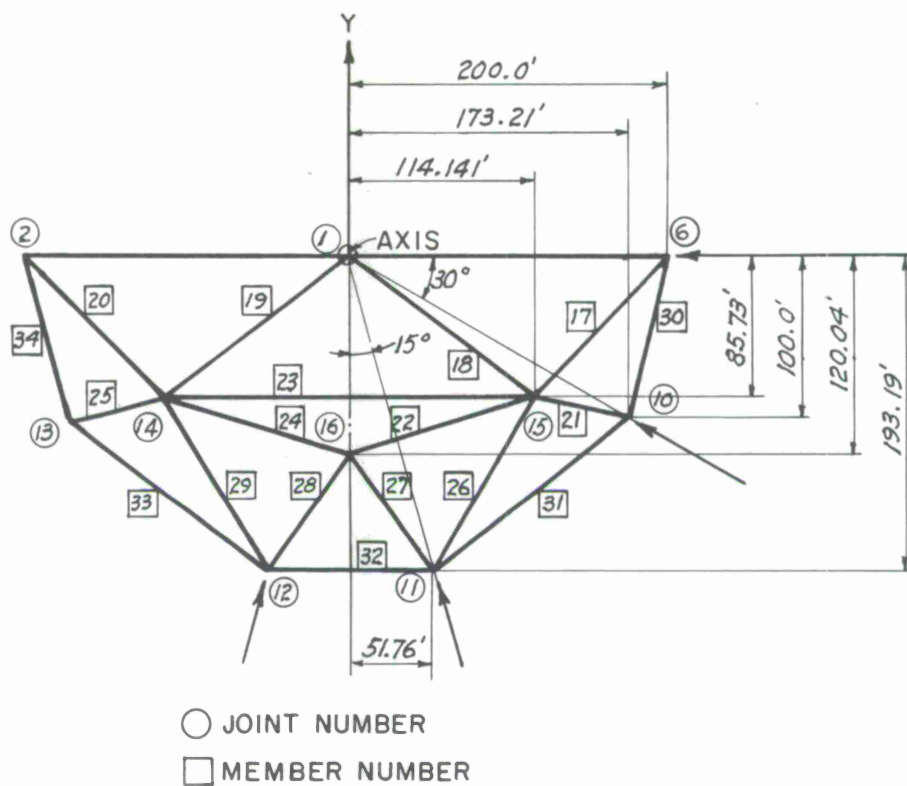
○ JOINT NUMBER
 □ MEMBER NUMBER

Figure 7. Cone configuration.



SECTION A-A

Figure 8. Cone configuration.



SECTION B-B

Figure 9. Cone configuration.

Table 1. Reticulated cone members (bracing not included).

Member no.	Length (ft)	Diameter (inches)	Thickness (inch)	Weight (lbs/ft)	Axial stress (ksi)	Bending stress (ksi)
1 to 8		(Included in flat plane framing)				
9	174	20	0.4	82	2.3	4.9
10	196	22	0.5	112	0.4	
11	196	22	0.5	112	0.6	
12	175	20	0.4	82	2.6	
13	175	20	0.4	82	3.8	
14	196	22	0.5	112	2.2	
15	196	22	0.5	112	2.2	
16	174	20	0.4	82	3.9	
17	121	14	0.3	48	4.0	
18	142	16	0.3	55	5.6	
19	142	16	0.3	55	4.6	4.5
20	121	14	0.3	48	4.0	
21	61	7	0.3	24	21.0	2.0
22	119	14	0.3	48	4.7	
23	228	26	0.5	140	6.9	6.9
24	119	14	0.3	48	2.1	
25	61	7	0.3	24	2.9	
26	124	14	0.3	48	7.8	
27	89	11	0.3	38	1.5	
28	89	11	0.3	38	2.0	
29	124	14	0.3	48	7.9	
30	103	12	0.3	41	9.1	
31	153	18	0.4	75	3.7	
32	103	12	0.3	41	9.3	
33	153	18	0.4	75	3.5	
34	103	12	0.3	41	1.4	
35	223	26	0.5	140	1.0	
36	268	30	0.6	195	1.7	8.1
37	268	30	0.6	195	1.7	
38	360	41	0.8	360	6.0	11.0
39	360	41	0.8	360	6.0	
40	332	38	0.8	328	3.7	
41	332	38	0.8	328	3.7	
42	133	16	0.3	55	1.0	
43	133	16	0.3	55	0.6	
44	263	30	0.6	195	0.7	
45	215	25	0.5	137	1.7	
46	200	23	0.5	137	5.9	
47	200	23	0.5	137	5.9	
48	181	21	0.5	113	0	
49	181	21	0.5	113	0	
50	122	14	0.3	48	0	
51	122	14	0.3	48	0	
52	127	15	0.3	51	7.9	
53	127	15	0.3	51	7.9	
54	60	7	0.3	24	11.5	

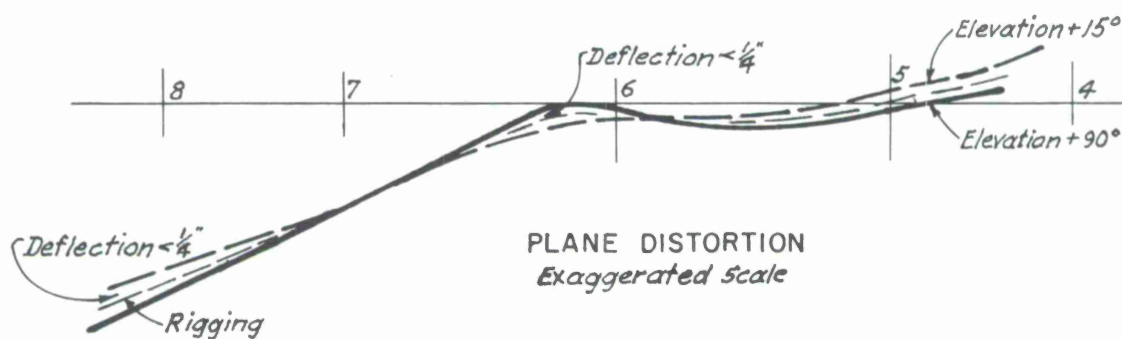
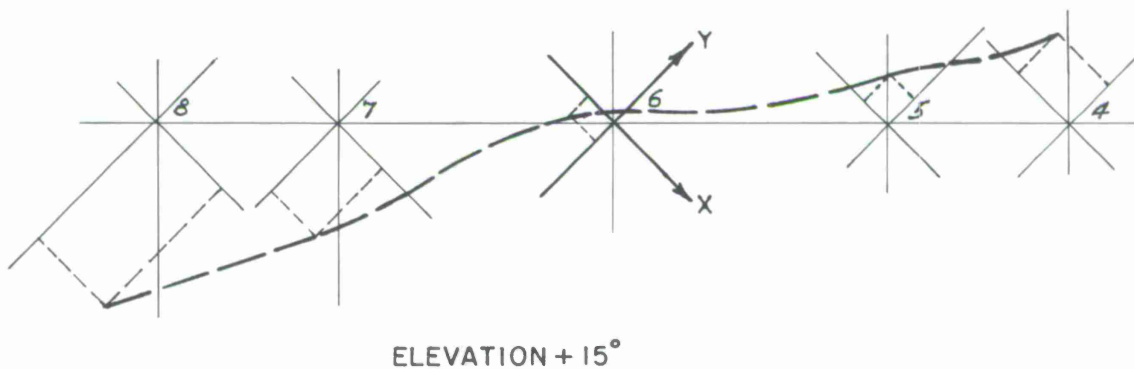
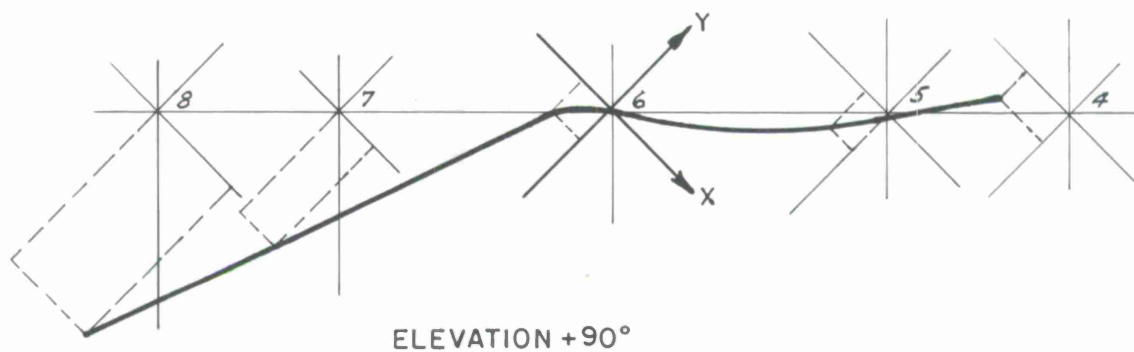


Figure 10. Cone deflection.

- 5) Solid steel and aluminum sheet, with and without stiffeners.
- 6) Perforated steel and aluminum sheet, with and without stiffeners.
- 7) Corrugated steel sheet.
- 8) Gypsum with metallic paint.
- 9) Polyurethane panels with metallic paint.
- 10) Honeycomb sandwich panels of aluminum, paper, plastic, polystyrene, and balsawood.
- 11) Rigid panels on prestressed wires.
- 12) Metal textile.

Because the mirror is a plane, very light skins can be used by prestretching them over a frame. Since the tension ensures a precise plane, the premium paid for an accurate surface is low.

It was found that the most efficient surface is thin-gauge sheet metal glued to prestressed wires in 20 ft by 20 ft panels. The panel frames, made of alloy steel, can be used as the main material of the space truss (see Figure 11 for details of the panel construction). Each individual panel can be removed from the space truss for tuning or adjustment. Since the wires are under high tension at all times, the four edge members of the panel are always under compression. In order to prevent their buckling, special fixtures are required for support in the weak direction during fabrication and during the removal of the panels from the space truss. Once the panels are attached to the space truss, they will become an integral part of the truss system and can be used as the main material of the truss.

5.4 Space-Truss Mirror Backup

The design of the space truss is governed by the loading when there is a failure in the air-pressure control system. It was felt that ultimate-strength design theory should be used for such loading. Since the edge members are primarily under bending and the space-truss members under axial loads, these two types of stresses can be considered as nonadditive under the ultimate-strength concept. However, an alloy steel with a higher yield point was used in the edge members to ensure the elastic behavior of the reflector surface and the space-truss system under normal loading conditions.

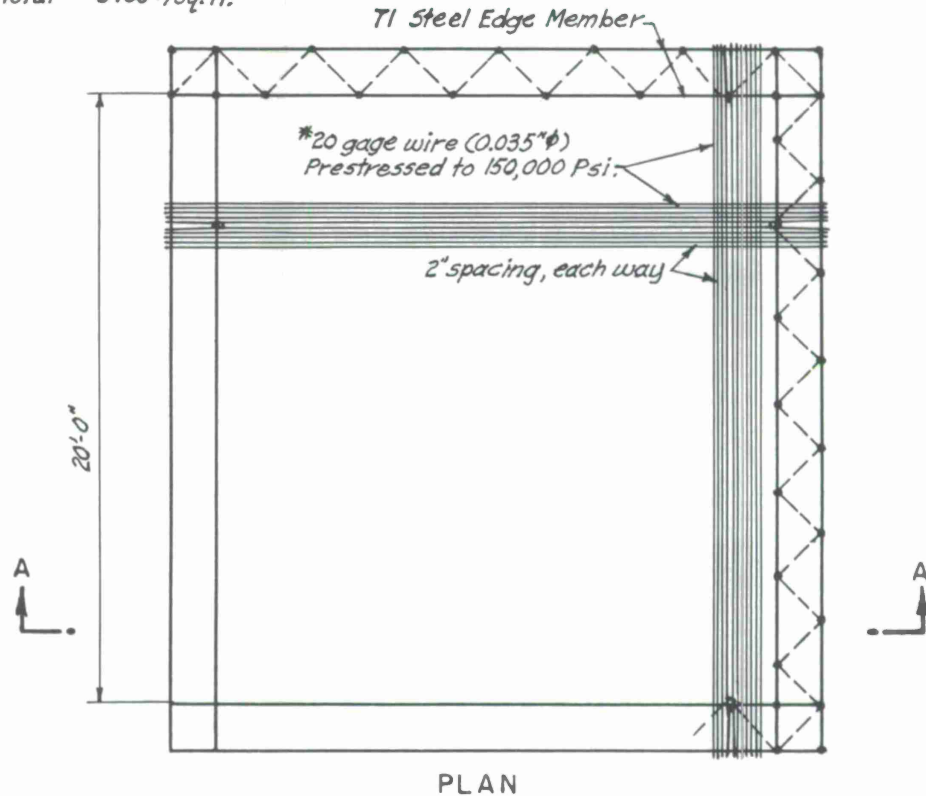
The weight of the mirror surface exclusive of the edge members is 0.30 psf. The total weight, including details of the space truss, is 1,300,000 lbs.

5.5 Air Pressure Control System

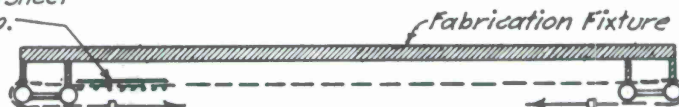
The air pressure will vary from 0 at 0° elevation to 1-1/2 inches of water at 90° elevation. Conservatively, we have assumed that the antenna, which slews through this

MIRROR SURFACE

Steel Metal — 0.18*/sq. ft.
 Wires — 0.05
 Glue, etc. — 0.07
 Total = 0.30*/sq. ft.



#38 (0.0060") gage steel sheet
 with 70% solidity ratio.



ALTERNATE A

Grooves, tackings, fasteners
 or resistance welding.



ALTERNATE B

Fabrication Fixture required.
 Jack frame to pretension wires.

SECTION A-A

Figure 11. Mirror surface panels.

range in 1-1/2 min, must have a precise surface during this time to be ready to track. The pressure therefore can be varied at rates up to 1 inch/min.

Preliminary studies show that the air pressure can be controlled to the required accuracy by equipment commercially available. The equipment includes three 50,000 cfm fans, outlet devices in multiple, connecting ducting, controls, air-tight membranes, and spray coating.

5.6 Shield

The shield is separated from the antenna structure. It will be a space-truss structure either covered with Fiberglas-reinforced plastic or coated with metallic paint or covered with sheet metal. The shield is supported at two locations: one is near the primary reflector, the other support is a half-ring parallel to the altitude wheel so that both the antenna and the shield can be driven by the same drive, as shown in Figures 4 and 12.

Since the deflection of the shield is not critical, the structural design is based on strength rather than on deflection. However, 15-ft-deep trusses are used to reduce the deflection to a reasonable limit. The maximum deflection of shield after cambering is about 9 inches, which is considered permissible.

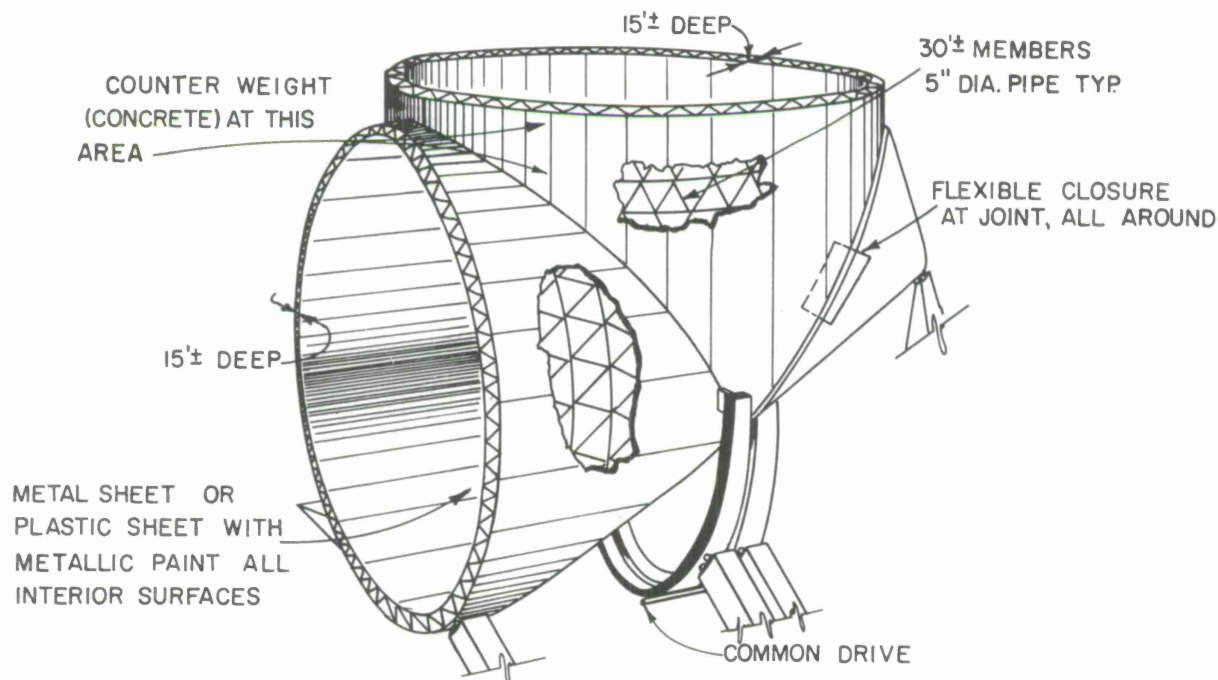


Figure 12. Shield detail.

The total weight of the shield is 860,000 lbs, which includes 130,000 lbs for the vertical ring, 120,000 lbs for the wheel, and 610,000 lbs for the partial cylinder. About 160,000 ft² of Fiberglas-reinforced plastic sheet is required as the covering for the space truss.

5.7 Turntable and Reticulated Cone Supports

The turntable consists of two truck girders. One supports the vertical cantilever trusses of the primary reflector, and the other supports a tower that carries the end of the reticulated cone. A longitudinal girder connects the two truck girders.

The two truck girders are 10-ft-deep triangular box girders with azimuth wheels attached. The longitudinal girders are latticed triangular boxes. The major portion of the weight of the reticulated cone is transmitted to the central bearing through a V-frame that is connected to the longitudinal girder.

The weight of the turntable is as follows:

Truck girder at primary reflector	93,000 lbs
V-frame	107,000
Tower at end of cone	24,000
Truck girder at end of cone	11,000
Longitudinal beam	180,000
Total	415,000 lbs

5.8 Hyperboloid (Secondary Reflector)

The hyperboloid surface is made of aluminum honeycomb sandwich panels. It is supported by a horizontal girder cantilevered from the tower at the end of the cone, as shown in Figure 13. It is completely separated from the mirror surface so that the mirror rotation about a horizontal axis will not affect it. Since the cantilever arm does not move relative to gravity, its deflection can be cambered during fabrication.

The weight of the hyperboloid and supporting system is about 65,000 lbs.

5.9 Drives

Azimuth rotation is controlled by the drive schematically designated as D2 in Figure 5. Because the framing has been arranged to bring most of the antenna weight over the central pintle bearing, the contribution of friction to the power requirements of D2 is quite small. We estimate that 100 hp total will be required.

Power will be delivered to the wheels on the turntable trucks. The wheels are standard crane wheels, and the track standard crane rail machined and set to the required accuracy. We do not believe that hydrostatic bearings are needed, since only a small portion of the weight is supported at the outer perimeter.

Altitude rotation is controlled by drives schematically designated as D1 in Figure 5. If the antenna structure were counterweighted to eliminate torque on these drives, the dead-load deflections would be excessive. The counterweight is therefore placed on the

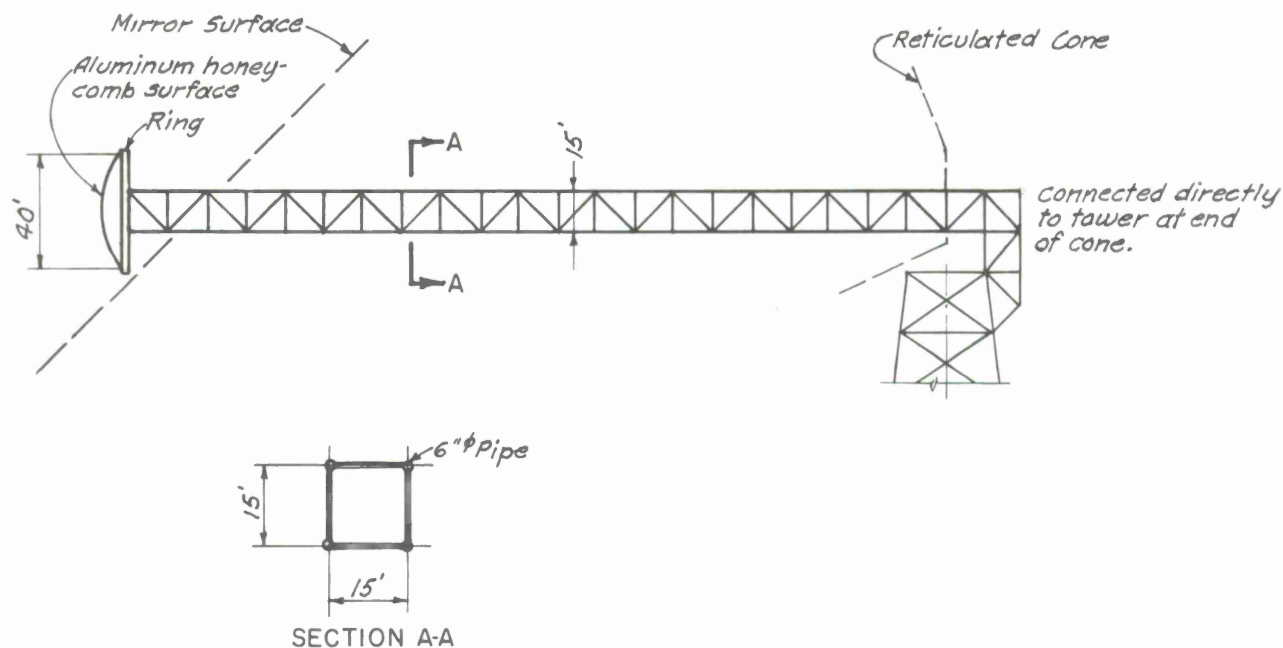


Figure 13. Secondary reflector support.

shield, permitting low deflections and low drive torques, and the altitude power required was held to 100 hp maximum.

5.10 Bearings

The load on the central bearing is about 4,600,000 lbs. To reduce friction and stick slip during azimuth rotation, hydrostatic bearings were assumed.

For altitude rotation of the reticulated cone, rollers are used at the altitude wheel. However, these rollers only carry the cone weight; they do not drive it. The drive forces will be applied by a squeeze mechanism to a continuous curved plate. This permits simple equalizing of cone and shield motion and relieves the high friction requirements that would otherwise be required at the junction of rollers and tires.

Because the structure was proportioned to transmit a very light load at the truncated end of the cone, a light standard bearing of the radial thrust type can be used. Further design development may show the need for a larger bearing to permit access to the electronic equipment at the center of the mirror. However, this will present no feasibility or appreciable cost problem.

5.11 Radome

A spherical radome 610 ft in diameter and 450 ft high is assumed for cost purposes. The construction of the radome is not covered in this report, but cost curves developed in a MIT Lincoln Laboratory report entitled "Large Diameter Rigid Radomes" dated April 1965 were used.

6. COST ITEMS

For the cost estimate, it was assumed that the construction contracts are to be awarded in 1966. Applicable escalation of costs should be used when actual construction timing is determined. This is a valid procedure provided all cost estimates are based on the same assumption. It was also agreed that the following items should be included in the Ammann & Whitney cost estimate:

- 1) Radome.
- 2) Structural steel.
- 3) Reflector surfaces.
- 4) Counterweights.
- 5) Structural compensation systems.
- 6) Altitude and azimuth:
 - a) bearing,
 - b) gear boxes,
 - c) rollers,
 - d) motors,
 - e) rails, tracks, or canals.
- 7) Major bearings (pintle or altitude).
- 8) Ladders and access or elevators, passageways.
- 9) Drive power wiring.
- 10) Cable wrap system.
- 11) Hoists for equipment enclosure.
- 12) Hoists for repair and maintenance.
- 13) Brakes and bumpers.
- 14) Laboratory within radome.
- 15) Offices, storage rooms, etc., within radome.
- 16) Drive control system.
- 17) Space for electronic-equipment enclosure.
- 18) Surface checkout and tuning.
- 19) Engineering.
- 20) Contingencies.

The following items were not estimated. They should be estimated by the CAMROC Committee or others and added to the enclosed estimate to obtain the overall antenna cost.

- 21) Coordinate conversion computer and data-reduction system.
- 22) Radome temperature-control system.
- 23) Laboratory and equipment.
- 24) Electronic-equipment enclosures.
- 25) All RF equipment.
- 26) Station power (substation and standby).
- 27) Conduit for all wiring.
- 28) Site work:
 - a) access road,
 - b) parking,
 - c) utilities,
 - d) paving, grading, drainage, and landscaping.

- 29) Insurance.
- 30) Local taxes.
- 31) Real estate.
- 32) Power, except drives.
- 33) Administration by CAMROC.
- 34) Off-site inspection and testing.
- 35) Borings and soil testing.

7. COST ESTIMATES

7.1 Structural Steel Weights and Unit Price

The total weight of structural steel required for the reticulated cone CORT system is 5,910,000 lbs. The weights of various components are given in Table 2.

Table 2. Structural steel weights in pounds.

Mirror framing and reticulated cone	4,050,000 lbs
Primray reflector support	520,000
Turntable including truck girders and tower	415,000
Shield	860,000
Secondary reflector support	65,000
Total	5,910,000 lbs

The basic unit price used for structural steel is based on an actual bid in 1959 for a similar structure with the following modifications considered:

- 1) Escalation of cost versus time.
- 2) Difficulty of fabrication and/or erection.
- 3) Type of steel used.
- 4) Location of structure.
- 5) Size of the job.

From the above considerations, a unit price of \$1.15 was obtained for the fabrication and erection of the antenna structural steel.

7.2 Costs

The cost estimates for Items 1 to 20 inclusive of the CORT reticulated cone concept are given in Table 3.

Table 3. Cost estimates.

The Ammann & Whitney cost estimate for Items 1 to 20 of the CORT reticulated cone concept are as follows:

Antenna structural steel 5,910,000 lbs at	\$ 1.15	\$6,800,000
Counterweight (concrete) 210 yd ³ at	\$100.00	21,000
Mirror reflector surfaces 177,000 ft ² at	\$ 4.00	710,000
Primary reflector surfaces 137,000 ft ² at	\$ 5.00	685,000
Secondary reflector surfaces 2,000 ft ² at	\$ 20.00	40,000
Azimuth rails 262,000 lbs	\$ 1.00	262,000
Azimuth wheels 14,000 lbs	\$ 3.15	44,000
Azimuth motor		40,000
Azimuth gearbox, etc.		50,000
Altitude tires 13,000 lbs	\$ 1.40	18,000

Table 3 (Cont.)

Altitude rollers, bearings	\$ 60,000	
Altitude bull wheel	10,000	
Altitude motor	40,000	
Altitude gearbox, squeeze drive, etc	250,000	
Drive control system	200,000	
Center bearing	200,000	
Bearing at end of cone	40,000	
Ladders, access, elevators, passageways	100,000	
Drive, power wiring, cable wrap system	350,000	
Hoist for equipment enclosure	50,000	
Hoist for repair and maintenance	10,000	
Brake and bumper	50,000	
Mirror hinges	150,000	
F. R. P. sheets (shield and air-pressure control)	560,000	
Air-pressure control system (fans, outlet devices, ducting, control, coating)	300,000	
Foundation at rail and bearing	230,000	
Space for electronic equipment on antenna (11,200 ft ³)	30,000	
Surface checkout and tuning	200,000	
Antenna Costs		\$11,500,000
Radome	\$8,000,000	
Radome floor	285,000	
Laboratory within radome	135,000	
Offices, storage rooms, within radome (5,000 ft ²)	90,000	
Radome Cost		8,510,000
Radome and antenna engineering, supervision of construction and contingencies (25%)		5,003,000
Total		<u>\$25,013,000</u>

APPENDIX C

CONCEPTUAL STUDY OF A 400-FT-DIAMETER
FULLY COMPENSATED CASSEGRAIN ANTENNA

Prepared for
THE CAMBRIDGE RADIO OBSERVATORY COMMITTEE

December 1966

AMMANN & WHITNEY
NEW YORK, NEW YORK

TABLE OF CONTENTS

<u>Section</u>		<u>Page</u>
1	INTRODUCTION.	C-1
2	THE CONCEPT	C-1
3	COMPONENT DESIGN	C-4
4	SURFACE-COMPENSATION SYSTEM	C-20
5	ERRORS	C-23
6	DESIGN CRITERIA	C-25
7	COST ESTIMATES	C-26

1. INTRODUCTION

In order to determine the relative cost and engineering feasibility of a 400-ft-diameter CORT antenna and a 400-ft-diameter Cassegrain antenna, each enclosed within a radome, conceptual studies were made for the two systems. The results of the CORT antenna studies are summarized in a CAMROC-initiated report entitled "Conceptual Studies for a 400-Foot Diameter CORT Antenna" dated November 1966. The results of the Cassegrain antenna studies are summarized in this report.

Not only is the Cassegrain antenna superior to the CORT antenna, but in addition, one Cassegrain concept is seen to achieve great gains in economy and performance. This concept is examined in this report.

Although general feasibility and approximate cost have been established, many details require further study before a firm estimate of cost and performance can be made.

2. THE CONCEPT

The frequency range over which the antenna operates limits deflections far below those that can be economically met by brute force. A way of maintaining deflection within this limitation is required. The control methods that appeared feasible include:

- 1) Optimization of the distribution of material over the structure so as to produce a minimum RMS deflection set.
- 2) Compensation of length change in the structural elements that make the major contributions to deflection. This may be done by inserting jacks in some or all members, or by counterweighting.
- 3) Uncoupling of the reflector from the structural system so that deflection can be corrected independently of structural deflections.

Each method is feasible to the degree that deflections are predictable. Because the antenna is in a radome, deflections are sufficiently predictable to make any of the control methods practical. The choice of control methods, then, must be dictated by the economy, reliability, performance, and development possibilities of the entire system. The third method, in our opinion, provides an optimum combination of these somewhat conflicting criteria.

The uncoupled reflector surface is divided into individual triangular segments. The corner of each segment is kept in its correct position by jacks interposed between the segment and the supporting structure.

The reflector surface will be surveyed in a reference position, say face up, while the jacks are all in their home positions. If computed or measured deflections at various altitudes are then superimposed on the surveyed shape, the uncorrected shape of the reflector is known for these altitudes. This is all that is necessary for the computation of the jack extensions needed to produce a perfect paraboloid.

These curves of jack extension (actually rotation) versus altitude, stored in a computer, will be used to monitor the jack positions. In principle, the method is the same as that used to monitor the telescope attitude, except that the control may be several orders of magnitude less precise. For example, the rotation of the jack screw need not be known to more than $\pm 10^\circ$. This permits rugged and inexpensive hardware.

Curves that compensate gravity deflection will be of the form

$$R = A \cos \phi + B \sin \phi + C ,$$

in which R is the jack screw revolutions, ϕ the altitude angle, A and B are the constants dependent upon elastic behavior, and C is a constant dependent upon erection accuracy.

The curves can be modified or completely changed if necessary to account for non-linearity and discrepancies between computed and observed deflections. Because the computer driving the telescope knows altitude, azimuth, and real time, terms can be added to cover inertial and time-dependent factors.

If the jack-control function is too large for the computer, it can be performed by an inexpensive process-control computer connected by a communication link to the main computer.

In providing for the functioning of the antenna, this concept also offers the necessary advantages of:

Economy

- 1) The load-carrying structure can be optimized on cost rather than on deflection.
- 2) The antenna can be retuned by the use of the computer with no rigging.
- 3) Removal of the reflector from the structural system permits normal and therefore inexpensive techniques to be applied to the backup construction.

Performance

- 4) Deflections due to temperature and to loads other than gravity can be compensated, provided they are predictable and vary slowly with time.
- 5) Distortions caused by changes in loading, such as added capsules or new secondary reflectors, can be corrected.

Reliability

- 6) The sensitivity is a minimum; that is, an inaccurate correction cannot cause a magnified shape inaccuracy.
- 7) Compensation malfunction, such as a jack failure, cannot cause structural or mechanical damage and generally permits telescope operation with only a slight loss in gain.

Development possibilities

- 8) As better surface measurement techniques are developed, they can be immediately used, since all corrections are applied through computer software and require no hardware adjustments.
- 9) If continuous deflection monitoring becomes feasible, the antenna can be easily made to accept the system and be made precise regardless of the environmental changes through which it passes.

All the factors that contribute to antenna deflection can conceivably be compensated, at least partially. It would be well to discuss the degree to which all the deflections can be corrected in this concept.

The factors causing deflections are:

Gravity: These deflections are highly predictable and can be computed with accuracy in advance. The slight effects of the unknowable components, such as weight and elastic discrepancies, can be allowed for, if they can be measured.

Temperature change: Deflections are caused by a nonuniform temperature state in the structure. This can be due to a nonuniform time response to a temperature change, to a stratified temperature environment, or to the absorption of solar radiation. Observation may show that the effect is partly predictable and may possibly be a function of antenna position, time of day, date, and weather. If so, it can be compensated; if not, corrections based upon thermometer readings can be introduced into the computer a few times a day.

Inertial forces: Centrifugal forces due to both altitude and azimuth rotation and tangential forces due to accelerations cause small deflections. Although it may not be practical to measure the deflections, the small magnitude makes calculations sufficiently accurate. Compensation of the deflections can be performed by adding terms that are a function of the tracking parameters, and therefore functions of time.

Bearing and roller imperfections: These defects cause deflections if the parts are included in the structural system. If outside the system, except as a part of a statically determinate reaction, they cause rigid-body motions but no deflection. To a great extent the deflections can be correlated with altitude and azimuth position. If they can be measured, they can be considered a systematic error, and compensated.

Bolt-slip, metal creep, and hysteresis: Deflections due to these effects are generally unpredictable; however, a small part of the deflections may prove to be nonrandom and predictable. Such a determination could be made only after measurements in many positions are taken. The systematic component of these deflections may be indistinguishable from the bearing- and roller-caused deflections. The two will probably be lumped and compensated together in practice.

Dynamic deflections: Transients introduced by the drives may cause vibration. The vibrations are uncorrectable even though they are partially predictable. There seems to be no danger that this will occur, since the accelerations are very low, the backup structure is quite stiff, and the articulation by use of jacks introduces considerable damping to the structure.

3. COMPONENT DESIGN

3.1 General Configuration

The antenna as shown in Figures 1 and 2 consists of the following basic elements, which are further described in this section:

Reflector-surface panels attached to pyramidal backup assemblies.

Jack assemblies supporting the backup assemblies.

A reticulated shell backup structure on which the jack assemblies are supported and the two spine trusses that support the quadripod and deliver the antenna weight to the trunnion axis.

The secondary reflector and the quadripod.

Counterweight.

The azimuth and altitude drives and bearings.

The supporting tower.

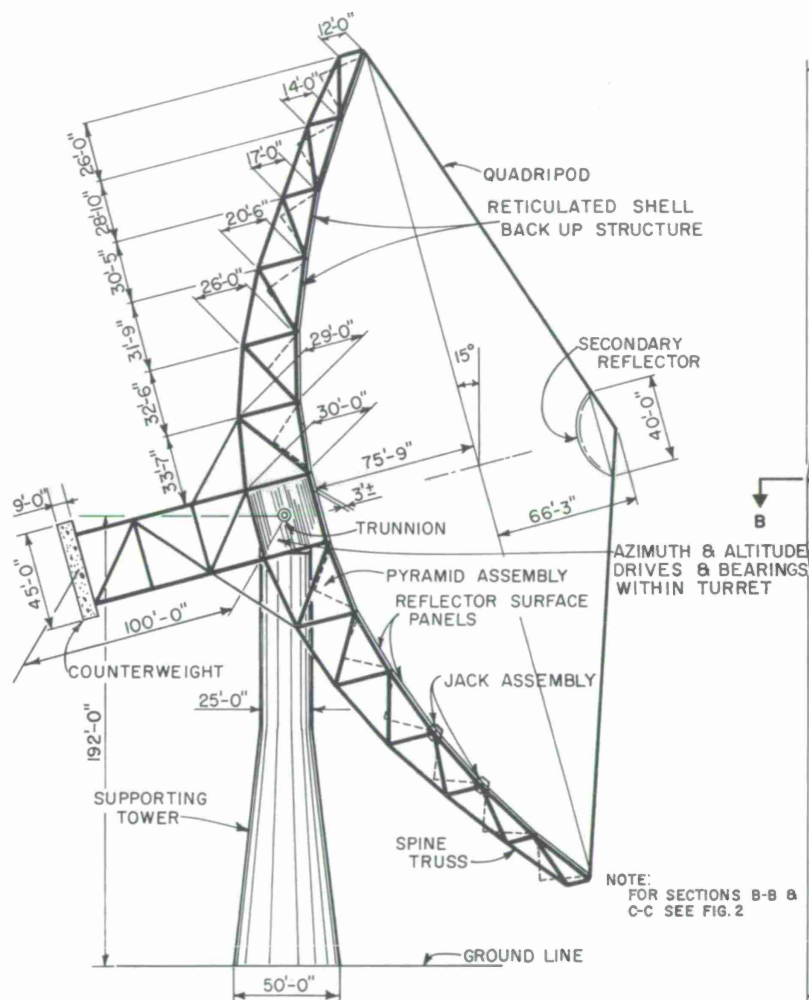
The radome.

3.2 Reflector Panels and Backup Assemblies

The reflector surfaces can be made of 2-inch-thick paper or aluminum honeycomb sandwich panels with 0.016-inch aluminum faceplates, or of aluminum faceplates with stiffeners. The weight of the panels will be 0.5 psf. If 1-inch-thick paper honeycomb with 0.01-inch aluminum faceplates is used, the weight can be reduced to 0.36 psf. For conservatism, a weight of 0.5 psf was used in this report.

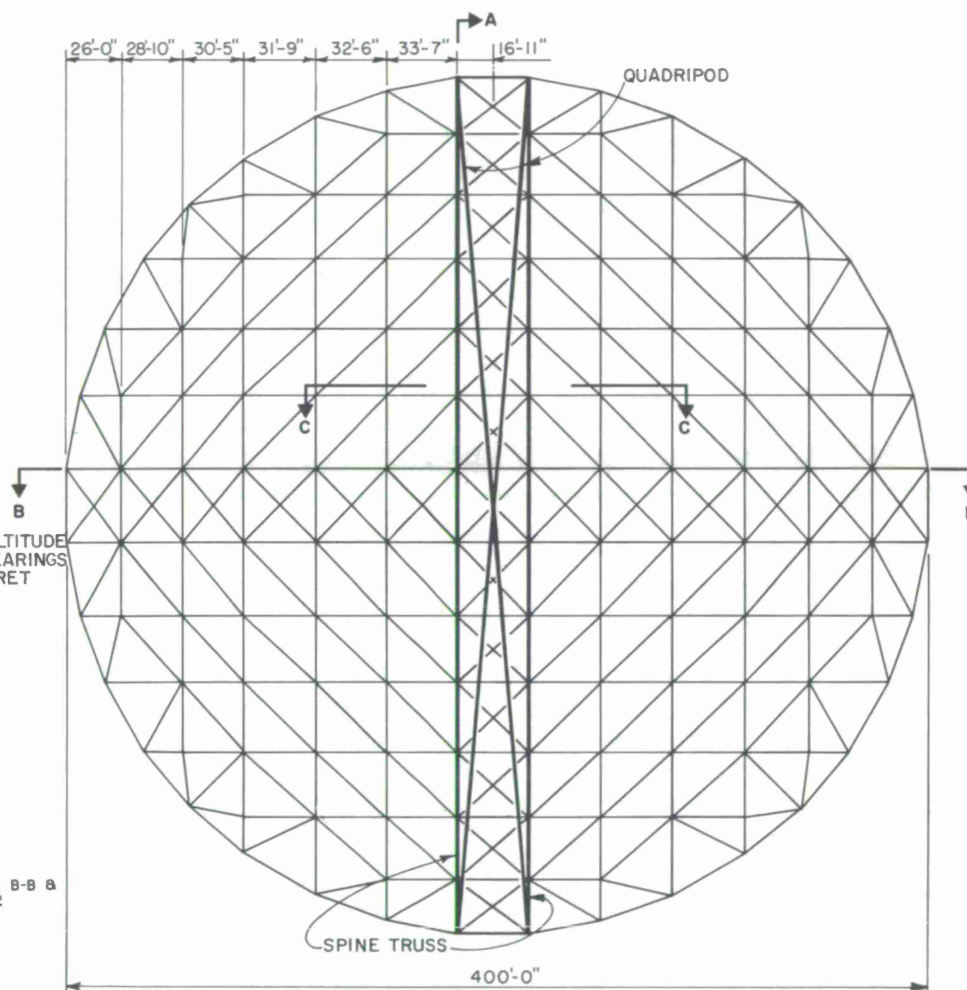
The panels are fabricated into triangular panels about 10 ft on a side and are attached to a pyramidal backup assembly, about 30 ft on a side.

C-5



SIDE VIEW A-A

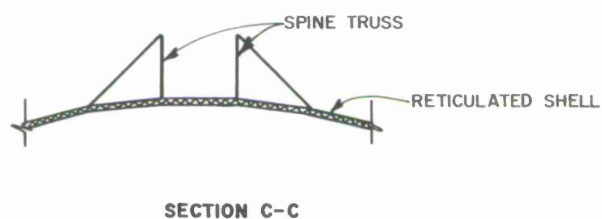
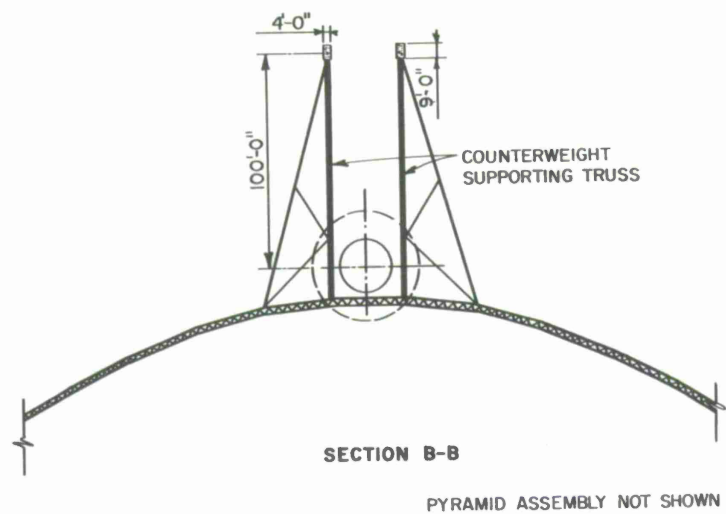
Figure 1. ANTENNA CONFIGURATION



FRONT VIEW

PYRAMID ASSEMBLY NOT SHOWN

Figure 1. Antenna configuration. (Based upon the early CAMROC specification for a +15° elevation angle.)



NOTE:
FOR SECTION LOCATIONS
SEE FIG. 1

Figure 2. Antenna configuration.

The pyramidal backup is shown in Figure 3. It is made of 6061-T6 drawn aluminum tubes. The sizes of the tubes for a typical interior panel are given in Table 1.

Table 1. Pyramid assembly

Members	Length	Diameter (inches)	Thickness (inch)	Area (inch ²)	Weight (lb/ft)
1 to 18 inclusive	10	3	0.028	0.263	0.300
-----19-----	15	4	0.042	0.528	0.603
20 to 22 inclusive	23	6-1/2	0.058	1.190	1.360
23 to 28 inclusive	18	5	0.042	0.660	0.751

The connections at the joints of the pyramid can best be made by one of the several patented connectors that are available. The connector illustrated is manufactured by Triodetic Structures Limited, Canada. It is an extruded aluminum hub that contains serrated slots into which the member ends can be fitted. The hub can join any number of members radiating at different angles. Two washers and a bolt prevent the tubes from slipping out of the hub.

The pyramid configuration has a high inherent rigidity for its weight. The configuration also places the structural weight as far as practicable toward the trunnion axis. This results in a lower counterweight and a smaller moment of inertia of the structure. The weight of the pyramid backup assemblies is about 0.82 psf, making the combined weight of the panels supported on the screws 1.32 psf.

The local maximum deflection of panels due to altitude rotation is about 0.0037 inch. The deflections of the pyramid backup, normal to the reflector surface during altitude rotation, were determined by computer. They are summarized in Table 2. The peak deflection after bias rigging will be 0.014 inch, and the RMS deflection of 1 panel will be in the order of 0.010 inch.

Table 2. Panel-point deflections normal to reflector surfaces (inch)

Point	Elevation + 90°	Elevation 0°	Difference
1	0	0	0
2	+0.0165	-0.0100	+0.0265
3	+0.0165	-0.0084	+0.0249
4	0	0	0
5	+0.0165	-0.0113	+0.0278
6	+0.0170	-0.0072	+0.0242
7	+0.0165	-0.0019	+0.0184
8	+0.0165	-0.0078	+0.0243
9	+0.0165	-0.0001	+0.0166
10	0	0	0

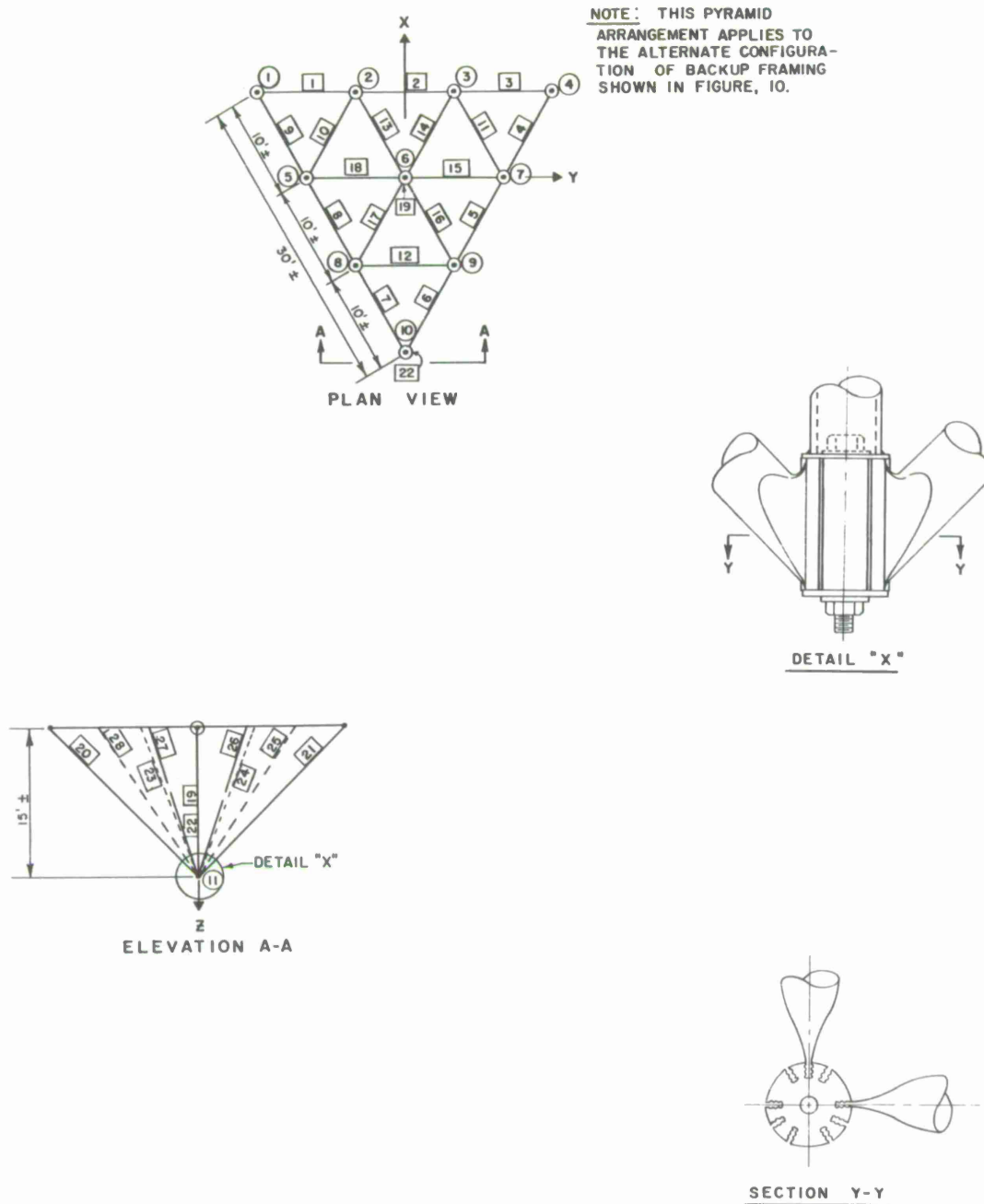


Figure 3. Pyramid assembly.

Manufacturing tolerances are as much a function of measurement as of fabrication. Because the rectangular panel assemblies are roughly 30 ft on a side, they may be precisely surveyed. The RMS manufacturing tolerance was therefore taken as 0.005 inch.

The RMS error of the aluminum panel, pyramidal backup system by itself will be of the order of 0.012 inch when the panel is in its worst position.

The connection of reflector panels to jacks is simplified by reducing the number of support points on each jack. This is accomplished by connecting the hypotenuses of pairs of triangular panels with a swivel joint to form articulated, square panels, as shown in Figure 4. Intermediate jacks need furnish only four points of support, and jacks at the periphery of the paraboloid need furnish only two.

Each articulated square panel must have a statically determinate support system in order to prevent its participation with the backup structure. This is accomplished by furnishing a Z reaction at all four corners (Z being the axis approximately normal to the paraboloid's surface), and X and Y reaction at one corner, and either an X or a Y reaction, whichever is appropriate for stability, at one of the other three corners.

Each rectangular panel corner is connected to the jack by a ball-and-socket detail, directly for X-Y-Z fixity, through a sliding plate for Z fixity, and through a guided, sliding plate for X-Z or Y-Z fixity (see Figures 5 and 6).

3.3 Reticulated Shell

Because deflection is compensated, stiffness is not a controlling factor in design of the backup shell. The shell is designed instead for strength and minimum cost. Although such a design is related to a least weight design, it is not the same.

The framing system and member makeup were both selected to permit fabrication and erection by most major steel companies. The members should then be selected within this constraint for minimum weight. The design used in this report is a first cycle of this optimization.

The general configuration of the reticulated shell framing system is shown on Figures 1, 2, 7, 8, and 9. This configuration was analyzed and estimated in this report. However, the alternate framing shown in Figure 10 should be studied before final design is started. It permits far more duplication of member pyramids and reflectors. The economy of duplication may outweigh the structural efficiency of the base concept.

3.3.1 Design

Moments, shears, and thrusts for all members for elevation angles of 15°, 30°, 45°, 60°, 75°, and 90° were found by the computer. The computer then determined the maximum stress combination in each member and designed it in accordance with the

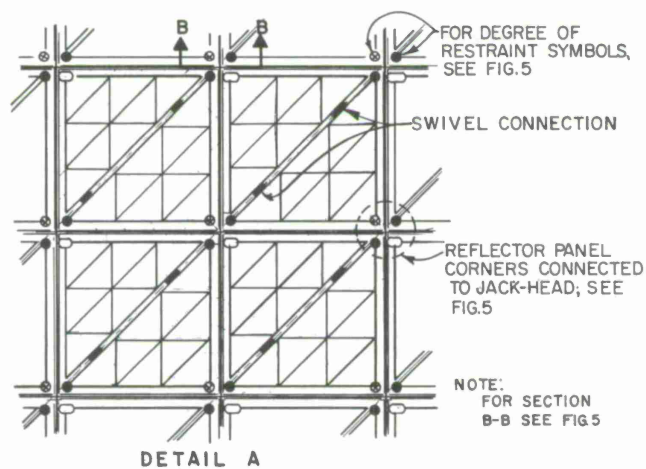
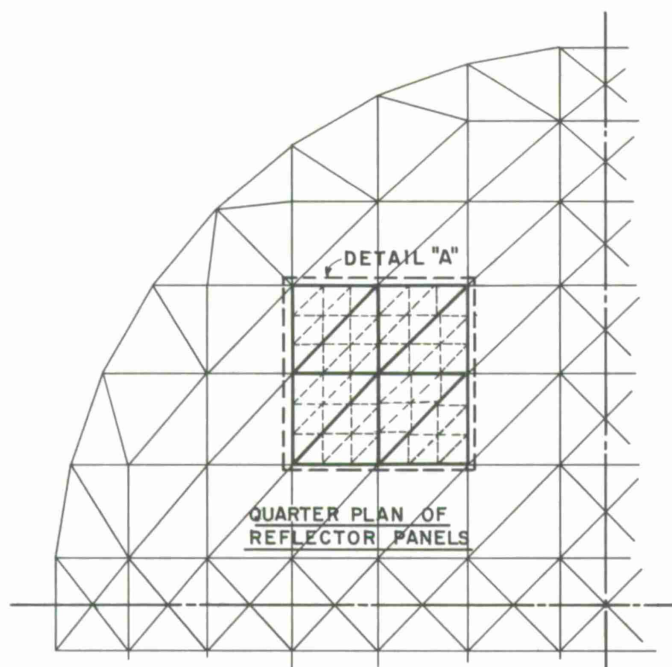


Figure 4. Reflector panel reactions.

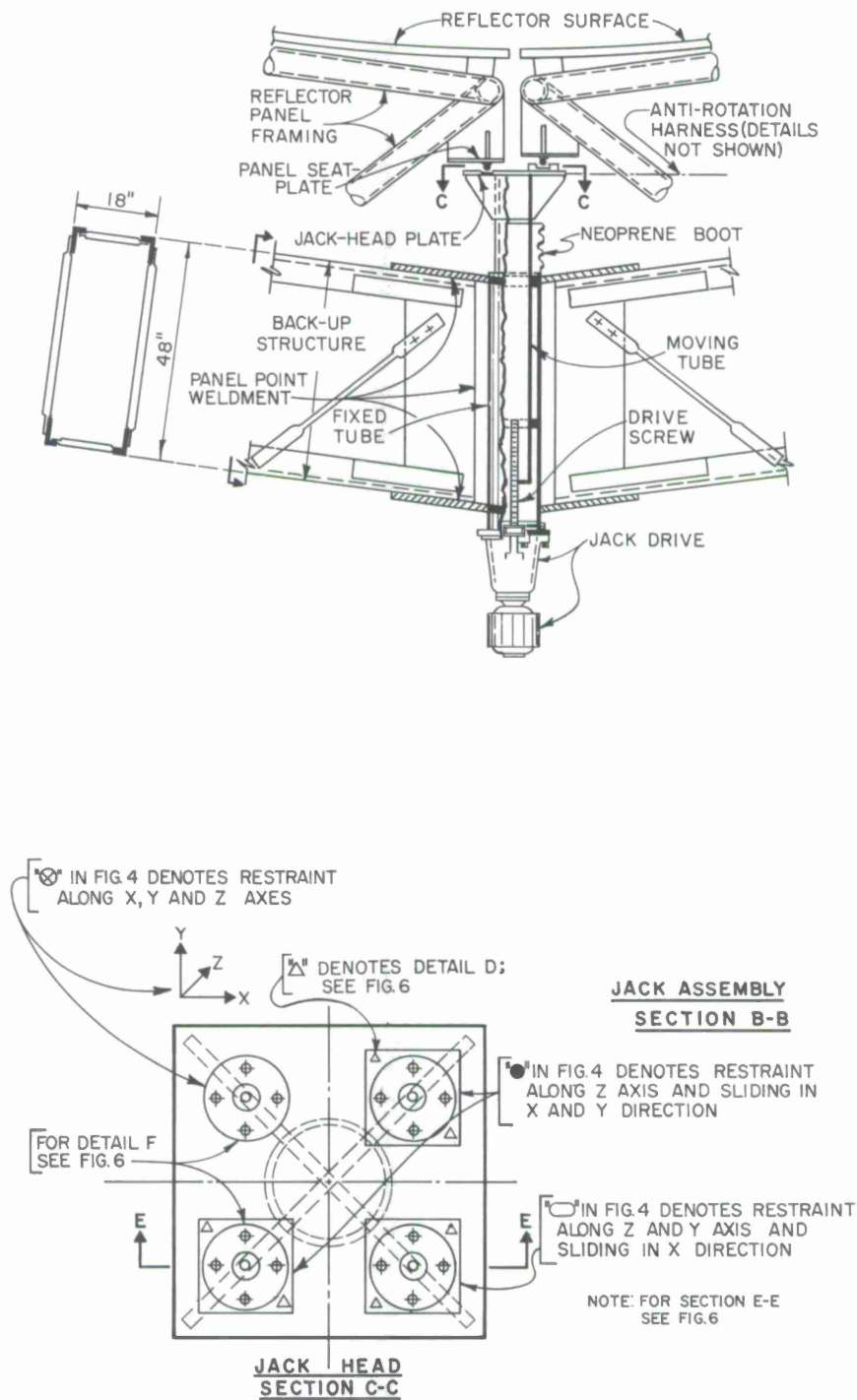


Figure 5. Details of panel and jack assembly.

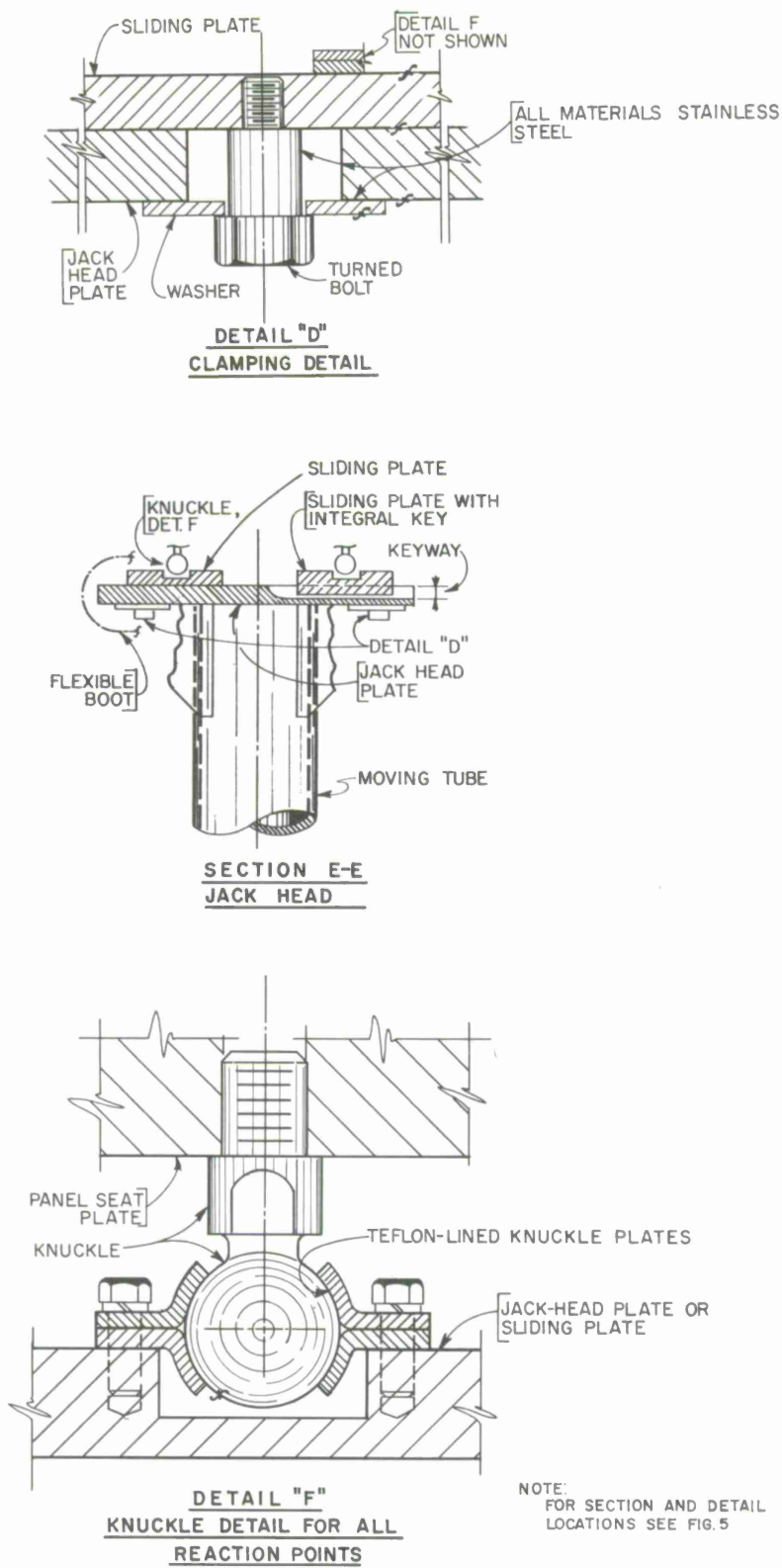


Figure 6. Details of panel and jack assembly.

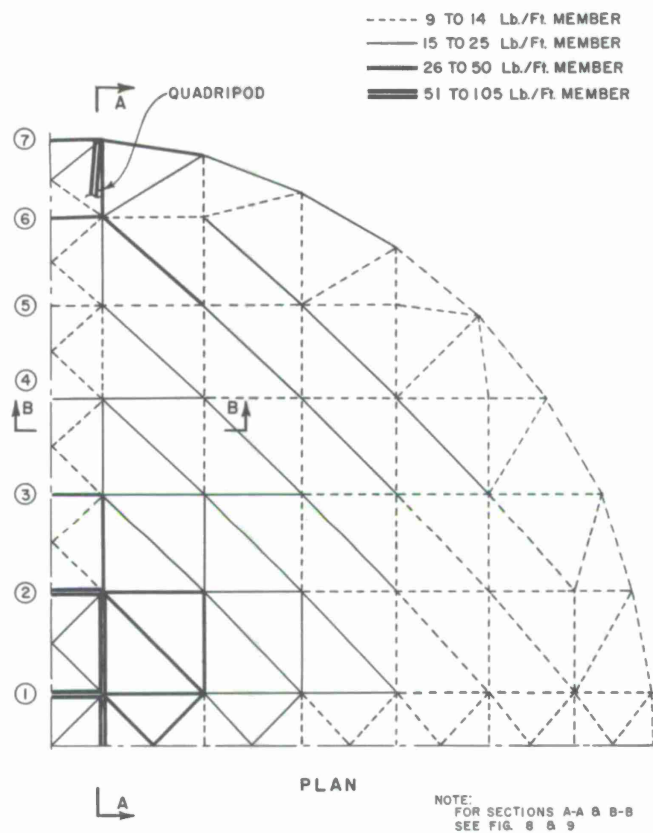


Figure 7. Reticulated shell member size.

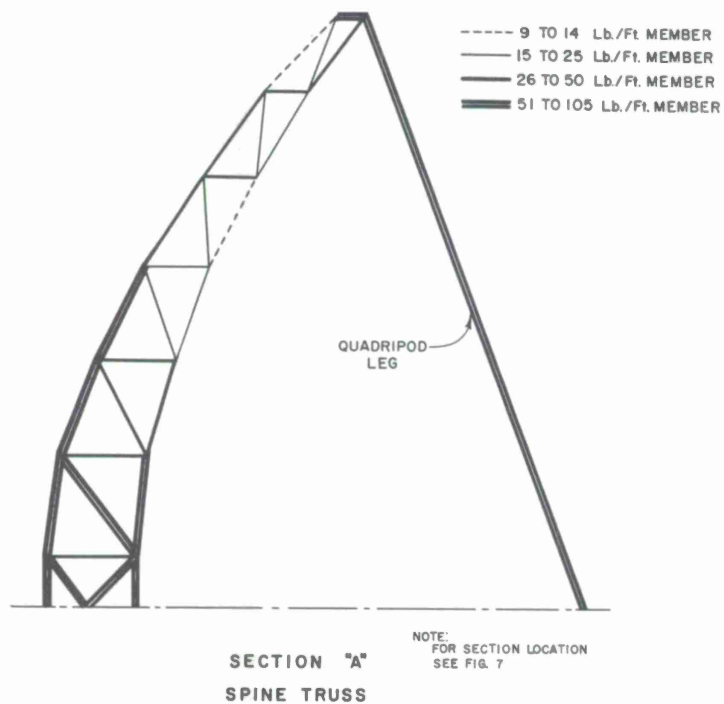


Figure 8. Reticulated shell member size.

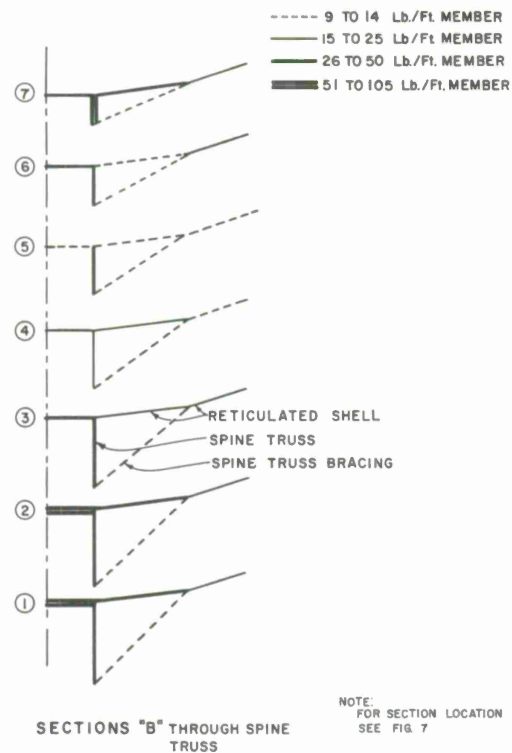


Figure 9. Reticulated shell member size.

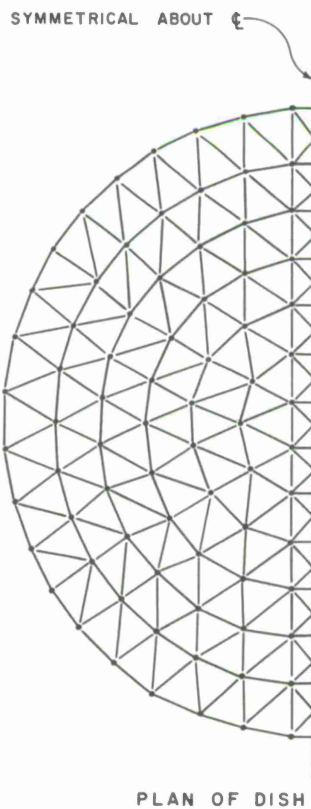


Figure 10. Alternative configuration.

1963 specifications of the American Institute of Steel Construction. There is a safety factor of about 1.6 intrinsic in these specifications. A low-alloy steel having a yield point of 55,000 psi was used.

The weights of all members are shown in Figures 7 through 9. The stresses in the backup members are primarily caused by the weight of the backup itself. A reduction in the cross-sectional area of the members does not appreciably affect the member unit stresses, since the cross-sectional area loss is offset by a corresponding weight loss. As a result, the cycle of member reduction must stop when a minimum member is reached, and the determination of the makeup of the minimum is a major factor in the economy. As can be seen in Figure 7, most members near the periphery are minima.

The minimum member used in this design consists of four angles placed at the corners of the rectangular cross section. One leg of the angle is 2 inches wide, the other 1-1/4 inches wide, and the thickness of the metal is 1/8 inch. The angles are tied together by tubes flattened at the ends for welding. The member is shown in Figure 5. Members heavier than the minimum are scaled up from the minimum by using heavier angles and lacing.

Lighter construction is possible and should be investigated in a final design stage. Very preliminary study of sheet-metal construction shows it to be lighter but more expensive.

In general, the depth and width of the member were determined by consideration of classical and snap-through buckling of the dish and by consideration of lateral buckling and bending of the member. All the members used are summarized in Table 3. Even the heaviest members, which occur near the spine truss, are relatively light and in fact are not far from what would be a minimum bridge truss member.

Table 3. Reticulated shell member sections.

Member type	Angles	Lacing		Depth (inches)	Width (inches)	Weight (lb/ft)
		Diameter (inches)	Thickness (inch)			
1	2 × 1-1/4 × 1/8	1.125	0.065	48	18	9.59
2	2 × 1-1/4 × 3/16	Varies	-----	48	18	13.58
3	2 × 1-1/4 × 1/4			48	18	17.94
4	2-1/2 × 2 × 5/16			48	18	24.93
5	2-1/2 × 2 × 5/16			48	18	31.16
6	3-1/2 × 3 × 1/4			48	18	37.13
7	3-1/2 × 3 × 5/16			48	18	45.93
8	4 × 3-1/2 × 5/16			48	18	53.55
9	5 × 3-1/2 × 5/16			48	18	60.93
10	5 × 3-1/2 × 3/8			48	18	72.59
11	6 × 3-1/2 × 3/8			48	18	81.40
12	7 × 4 × 3/8	1.875	0.500	48	18	94.72

3.3.2 Stiffness

Although proportioned for strength rather than deflection, the structure is stiff. If no compensation is used and the usual best-fit parabola assumptions are made to eliminate rigid-body components, the peak surface error would be a few inches and the RMS error would be less than 1 inch.

Three-dimensional framing provides rather high natural frequencies for all vibration modes. The frequencies were not calculated, since by inspection they will be far above the minimum requirements. Similarly, inertial effects were only approximated, their effects being nearly negligible.

3.3.3 Connections

Connection details are similar to those described in the two radome reports entitled "Large Diameter Rigid Radomes" dated April 1965 and "Large Diameter Rigid Radomes, Supplementary Report" dated May 1966. The central connection rod, however, was replaced by a tube to permit passage of the jack-moving tube. Although the details are not repeated here, the connection is shown in Figure 5.

3.3.4 Erection

Conventionally, space-frame roofs of this size and larger are erected on falsework towers. In this case, the central tower of the structure will replace one and possibly all the falsework towers. A central guyed derrick may be used to erect a substantial portion of the dish off of the temporarily stiffened spine truss, or a mast on top of the tower may be used to guy the partially erected structure while erection proceeds by crawler from the ground.

There will be obvious advantages to erecting the antenna and radome simultaneously. However, the vulnerability of the partially completed and fully completed antenna to wind and snow loads must be considered. Because erection presents no great difficulties, simultaneous erection was not studied in this preliminary stage.

The jacks that support the pyramids are to be provided with excess length so that they can function as shims. In this way all erection can be done according to normal structural methods and no undue precision demands need be placed on the erector.

3.4 Quadripod

The quadripod elements are shown in Figure 11. Each of the four legs is a 52-inch-deep truss with 3-inch-diameter solid round chords. Buckling normal to the 52-inch direction is prevented by low-dielectric Fiberglass tension members. This arrangement reduces the optical blockage due to the quadripod to 0.16%, a very low value.

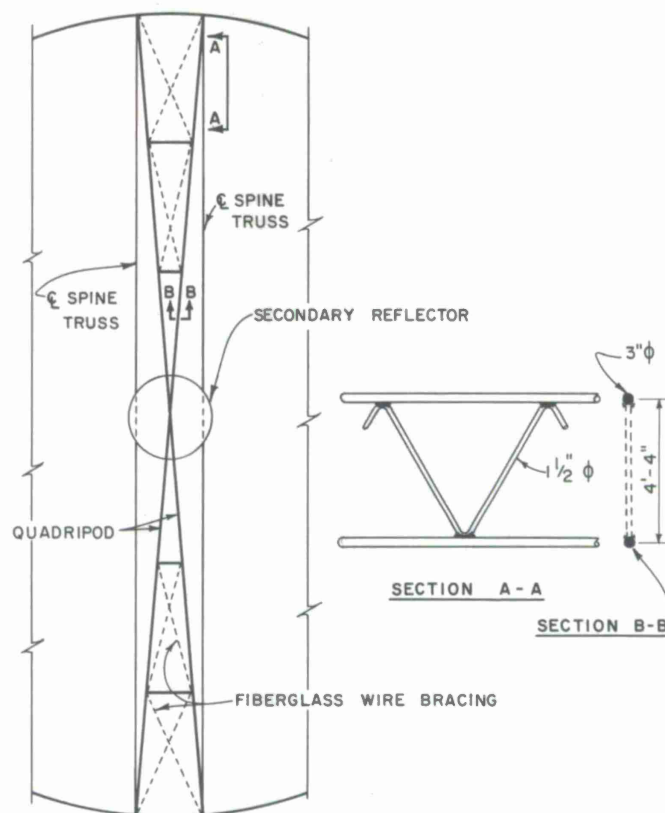


Figure 11. Quadripod.

An alternate framing system in which the intersection of the quadripod legs with the dish was spaced at 90° around the antenna was investigated. In this arrangement, the two legs not on the spine truss act as guys that carry the unstiffened edge of the dish. The saving in dish weight was overbalanced by the increase in blockage.

3.5 Counterweight

The center of gravity of the reticulated shell and quadripod is about 54 ft from the trunnion, and the center of gravity of the aluminum reflectors and pyramids is 56 ft from the trunnion. Their combined weight requires a counterweight of about 300 tons when placed on an arm at a distance of 100 ft back of the trunnion. This weight can be provided by about 150 yd^3 of stone concrete.

Because the antenna weight cannot be computed exactly and because the weight may change with future alterations, the counterweight will be made adjustable. This will be done by providing pockets in the concrete that are partially filled with lead.

Both the counterweight and its supporting arms are split to straddle the tower in the face-up position. The space between the arms is therefore unavailable for the electronic-equipment enclosure. However, the space immediately above the arms

(antenna in the horizon-looking position), the spaces on either side of the arms, and the space between trunnion axle and the reflector surface are all available.

3.6 Concrete Tower

The tower that supports the telescope is shown in Figures 12 and 13. A concrete structure was designed, and the cost estimated for this report. However, the very light loads that must be carried lend themselves to a steel structure as well. This possibility should be studied before a final design is started.

Unlike the moving structure above, the tower is subject to a constant load equal to the weight of the telescope and the counterweight. Strength and stiffness requirements both lead to extremely slender structures. For this reason, an earthquake causing an acceleration of 0.1 times gravity was added to the design criteria. Even this does not truly govern the tower proportioning that was selected to accommodate the hydrostatic bearing, the cable wrap, and the interior office space.

The walls are 12 inches thick to permit space for two layers of reinforcement in each face. The walls are of stone concrete and will have at least 1% vertical reinforcement to prevent creep. The foundation is a continuous ring whose size will depend upon the soil conditions at the site.

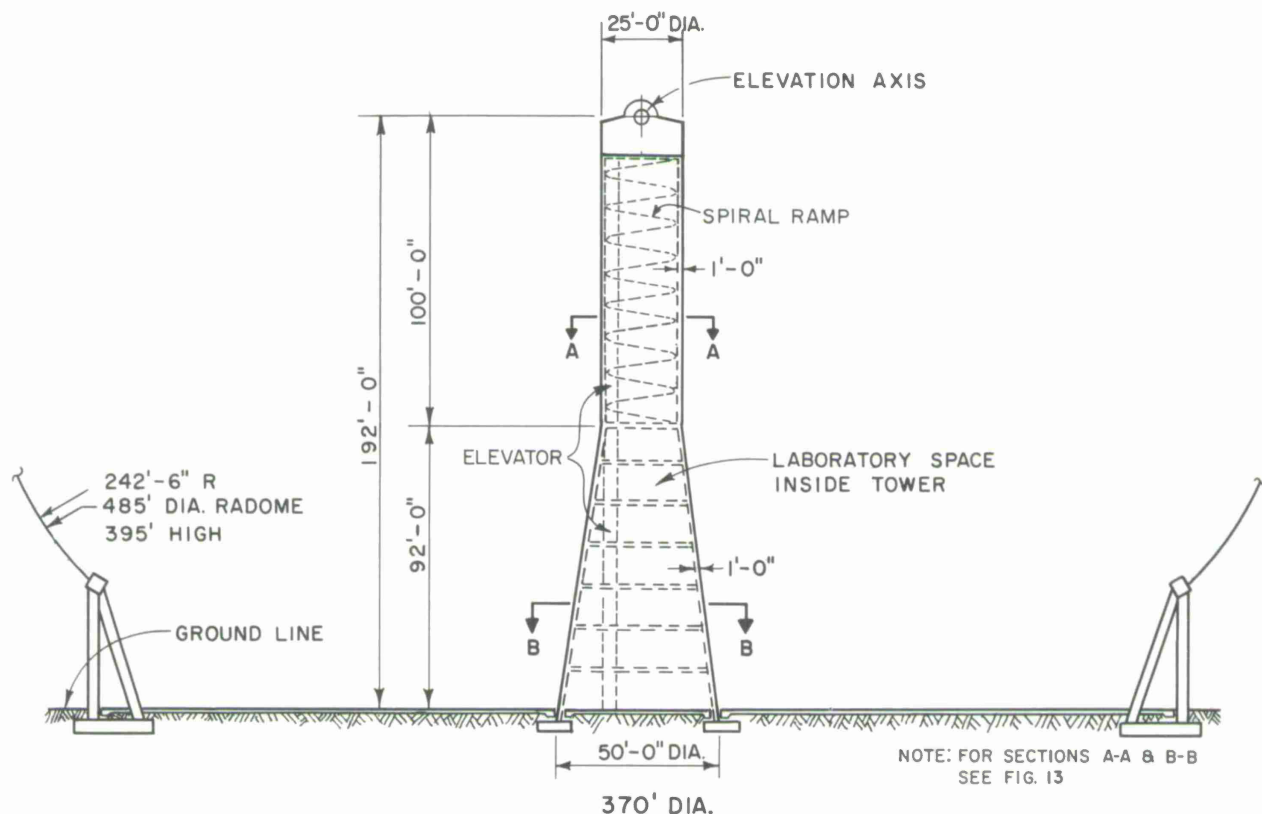


Figure 2. Tower and radome. (Based upon the early CAMROC specification for a + 15° elevation angle.)

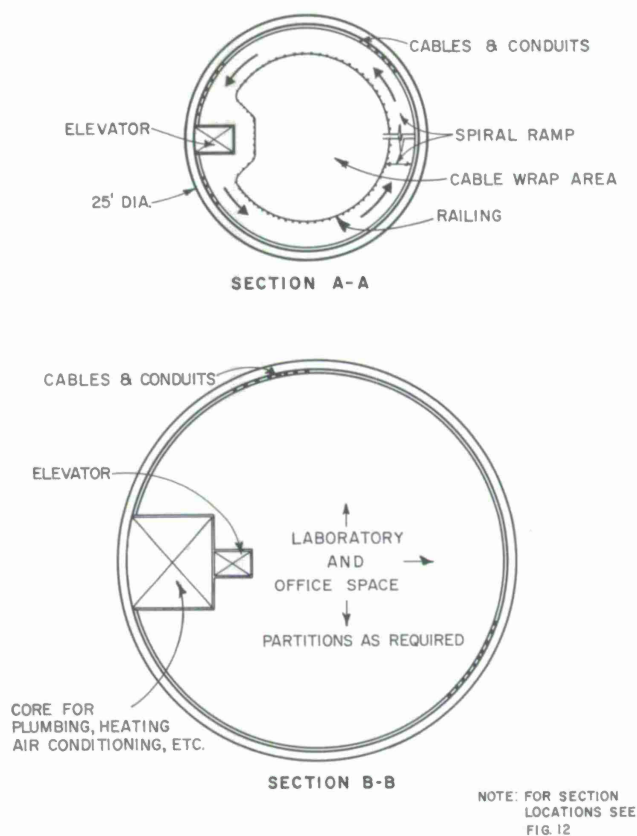


Figure 13. Tower sections.

The upper cylinder portion of the tower will be nearly filled by the suspended cables of the cable-wrap system. Conduit, coaxial cable, and wave guide attached to the inside of the walls will be accessible from a light spiral ramp. The elevator, which rises to the antenna proper, can be stopped wherever it crosses the ramp.

The lower conical portion is provided with seven floors for laboratory, office, and storage use. The actual number spacing and layout of the floors should be determined after detailed investigation of the functional requirements.

Large openings in the walls of the tower have only slight influence on its strength. Design development may show that they are needed for convenient access to the horizon-facing dish or to the electronic-equipment compartment when the dish is in the face-up position. They may also be desirable architecturally and psychologically in the laboratory and office areas.

3.7 Bearing and Drives

3.7.1 Elevation drive

The backup reticulated shell structure is supported at the center of each spine truss on trunnion axles, which are, in turn, anchored at the top of the concrete turret. Two

self-aligning bearings are required at each axle. A bull gear is attached to each spine truss so that during altitude rotation, both the wheels and the spine trusses rotate while the axles remain stationary. This arrangement provides ample space between the trunnion axles and the vertex of the paraboloid for the electronic-equipment capsule.

The bearings are about 20 inches in diameter, small enough to preclude the stiction problem.

Since the antenna structure above the elevation axis is counterweighted, the torque on the elevation drive is extremely small. The power required will be less than 10 hp. The counterweight can be unbalanced or made adjustable to prevent backlash.

The total weight of the structure above elevation axis is about 1,540,000 lbs.

3.7.2 Azimuth drive

The total load on the azimuth bearing is about 1,930,000 lbs.

To reduce friction and stiction during azimuth rotation, hydrostatic bearings are used. The bearings are located between the turret and the tower.

Either a bull gear or a squeeze drive can be used for the azimuth rotation. The drive is located at the bottom of the turret. Power required for the azimuth drive is estimated to be around 10 hp.

3.8 Secondary Reflector

The hyperboloid surface is made of aluminum honeycomb sandwich panels braced by aluminum ribs. It is attached to the quadripod by secondary framing.

The secondary reflector must be moved along two of its axes and rotated about the third in order to position it properly. It will therefore be supported on a system of jacks. It must also be monitored by the process-control computer to ensure its position at the focus of the best-fit paraboloid.

3.9 Radome

A spherical radome 485 ft in diameter and 395 ft high as shown in Figure 12 will be required to allow a minimum clearance of 20 ft from any point in the antenna at any elevation or azimuth angle to any point in the radome. The construction of the radome is assumed to be of the type described in the MIT Lincoln Laboratory-initiated reports on radomes, mentioned previously. The cost of the radome was obtained from the cost curves in these reports.

4. SURFACE COMPENSATION SYSTEM

Each of the jacks that support the reflector panels is a tube that slides within a backup structure connection tube. The moving tube is actuated by a drive screw in a thrust bearing on a fixed tube. Both are pressure lubricated and both have antibacklash take-up details. The arrangement is shown in Figures 4, 5, and 6.

The fixed tube in the backup connection is bored for pressure-lubricated bronze bushings. Hand holes permit access for inspection; the gasketed hand-hole covers protect the screw assembly and prevent escape of excess lubricant.

Each drive screw is coupled through a speed reducer to a two-speed fractional horsepower motor with a magnetic brake. The combination may be made of modified stock items. The modifications include a special housing, oil seals for multiposition use, and reduction of drive-shaft backlash. A manufacturer has evaluated the modifications premium as small.

4.1 Compensation Control

A process-control computer receives altitude, azimuth, and time information from the main computer, and program modification instructions from a console or remote typewriter. It also receives signals from a revolution counter within the speed-reducer assembly. The difference between the measured and the theoretical revolutions is computed, and one of three possible signals, depending on the difference, is sent out. The three possibilities are: jack forward, jack backward, or do not jack. Because the signal opens or closes relays, a signal to an advancing jack to advance will permit the motion to continue. A jack set in motion will stop only when a subsequent stop signal is received.

The operating cycle of the computer-jack system is as follows: On discovering a panel point deflected more than 0.028 inch off its theoretical position, the computer signals the jack controlling the point to move toward the correct position. It will re-examine the jack position every 10 sec and will turn the jack motor off when the jack has overcorrected by more than 0.025 inch. It continues examining this (and all other points) with a 10-sec period, responding to errors over 0.028 inch with an over-correction of 0.025 inch.

These intervals plus motions beyond these limits due to delayed computer discovery produce a dead band 0.030 inch each side of the mean. A random position within the band is ensured by the varying rate at which the points deflect, by a random monitoring sequence, and by a special starting sequence that positions the jacks randomly in the band.

The jacks operate in either direction, at a constant speed that is slightly greater than the speed of the fastest deflecting panel point. This speed establishes the maximum computer return period per jack. Too long a period will permit the jacks to exceed the limits of the ± 0.030 dead band.

The dead-band width is a first cycle of optimizing the requirements of small deflections, servo stability, and random deflections. It produces an RMS surface error of 0.017 inch.

This operating cycle requires a jack-screw rotation of $1/2$ rpm that will continue for at least 1 min and at most 3 min. The jack need never restart in less than $1-1/3$ min and will usually be idle for over 3 min. The computer must examine 148 points in 10 sec allowing 68 msec to compute error and signal a relay.

In the slewing mode, the logic and bandwidth will remain the same, but the jack will be speeded up by a factor of about 15 to ensure that the antenna is ready to track shortly after the slew stops. During the slew, the jacks may overshoot the dead band by about $1/8$ inch, requiring at most 2 min to return to a suitable surface. Most of this delay will take place while the antenna is slowing from slew to track and in practice should add less than 1 min to the slewing time.

The second major source of compensation error is the inaccuracy of the deflection calculations. Considering that the calculations can be augmented by direct measurement, the error may be conservatively taken as 1% of the deflection range about a mean position. The deflection range is far greater than the screw stroke, since it includes the rigid-body displacements of the telescope.

The range of the worst panel was found to be 15 inches. A small adjustment in the backup will reduce this peak value to about 10 inches. The peak calibration error will then be of the order of 0.10 inch, and the random error will be conservatively taken as 0.050-inch RMS.

4.2 Reliability

At this stage of the design, no estimate of mean time between failures of the jack system has been made. However, the overall reliability appears to be very high. The loads, accelerations, and velocities are all so small that each element of the assembly can be oversized at a small cost, making failure due to wear a minor factor. The assembly carries loads smaller than an automobile jack and is not much more complicated.

If the process-control computer is merely a part of the main computer, it will make practically no contribution to a reduction in reliability. A computer failure will already have been included in the aiming-system reliability. If it is a separate computer, its reliability is a factor that is manageable with redundancy.

In no event can a failure of a jack assembly or electronic component cause structural damage to the reflector or backup. This is due to the statically determinate support system of the pyramids. A low-probability motor or screw failure means at worst a short delay for repairs, and at best continued operation of the telescope with a 3% loss of gain.

4.3 Maintenance

Although the compensation assemblies are rugged, they should be inspected periodically and provision must be made for repair and replacement. This can best be done when the telescope is in the face-up position.

A practical means of access may be obtained by the permanent installation of a pair of light-moving radial scaffolds on either side of the spine truss. Each is an A-shaped frame contoured to the underside of the backup structure in its zenith-pointing position, rotating at one end on a rail encircling the concrete tower, and at the other end, on columns rolling on a rail atop the concrete ring girder of the radome foundation.

The pair of gantry scaffolds will be kept in the dead areas behind the antenna except when they are in use. Each is driven by a mechanism that is independent of the antenna. Arms from each gantry to toggle and limit switches mounted on the rotating head of the antenna tower actuate the gantry's movement and ensure that the backup structure cannot collide with it at any time. The motion of the gantries is intermittent and automatic. Manual control for positioning during maintenance can only be performed when interlock switches to the antenna sense that the antenna is pointing toward zenith and that neither the azimuth nor the altitude drive is operative.

The gantries are of light steel frame construction with drive mechanisms at the outer ends. Because their operation is intermittent, i. e. , moving a fixed distance, stopping, and recommencing motion only when the antenna again moves to their proximity, the drive, wheels, and rails may be standard commercial type.

Although the gantry scaffolds need be designed for only light maintenance loads, the constructor may be given the option of redesigning them for heavier loads and of using them for the construction of the antenna.

5. ERRORS

Nonrandom deflections are due to temperature, acceleration, and gravity deflections of the primary and secondary reflectors. They are treated as follows:

Temperature. Deflections are not covered in detail since they are partially susceptible to compensation and are partially controlled by a random heating-cooling system. Although the exact evaluation must be made in a more detailed study, there appears to be ample reserve in the deflection summary for temperature.

Acceleration. Deflections are very small. If an unusual tracking mode, not now contemplated, should cause significant deflection, they could be compensated.

Gravity deflection of primary reflector. Although nonrandom, the jacks will operate to make the mean of the total panel deflection zero, rather than to make the panel-corner deflections zero. This removes the bulk of the bias effect, permitting panel deflections to be treated as random.

The RMS deflection of a bias-rigged panel on the center of the dish is 0.010 inch. All other panels have smaller deflections. The RMS deflection for the whole reflector surface is estimated to be 0.006 inch before the jack reductions of the mean take place. This could reduce the deflection to a negligible value. However, in order to be conservative and to allow for some bias, an RMS value of 0.010 will be used.

Because the secondary reflector is a single structure, it can be made quite stiff. Although not designed, the RMS value of gravity deflection, with the mean moved by rigid-body compensation, is conservatively estimated at 0.08-inch RMS random.

The following errors are all taken as random. Those items not explained have been discussed elsewhere in the report.

PRIMARY REFLECTOR

<u>Initial survey.</u> Experience with the Haystack antenna indicated that the surface errors at the jack points only will be about	0.010-inch RMS
<u>Panel manufacturing error</u>	0.005-inch RMS
<u>Panel deflection:</u> due to gravity	0.010-inch RMS
<u>Readout error of jack rotation.</u> Allowing a 10° error in the shaft rotation for an 8 threads to the inch screw, the peak error will be 0.0034 inch and randomly distributed	0.002-inch RMS
<u>Jack dead band</u>	0.017-inch RMS
<u>Deflection calibration curve error</u>	0.050-inch RMS
<u>Miscellaneous.</u> Hysteresis, minor damage, etc.	0.005-inch RMS

SECONDARY REFLECTOR

<u>Initial survey.</u> Because the jack points to be surveyed are relatively few, the proportioning can be more accurate than for the primary reflector.	0.005-inch RMS
<u>Manufacturing error</u>	0.005-inch RMS
<u>Deflection due to gravity</u>	0.008-inch RMS
<u>Readout error of jack rotation.</u> Same as primary reflector.	0.002-inch RMS
<u>Jack dead band</u>	0.017-inch RMS

Deflection calibration curve error. Use
 1/2 of primary reflector error since this
 one point can be thoroughly checked in
 several positions 0.025-inch RMS

$$(RMS)_{Total} = \sqrt{(RMS)^2} = 0.064 \text{ inch}$$

If the assumption is made that the calibration error of the central 200 ft is halved, because jack strokes are more than halved, the RMS deflection becomes 0.047 inch.

6. DESIGN CRITERIA

The antenna system requirements and environment specifications as established by the MIT Lincoln Laboratory are as follows:

1) Sky coverage

Elevation: + 15° to +90°
 Azimuth: ± 300°

2) Velocity (°/sec)

	<u>Track</u>	<u>Slew</u>
Azimuth:	0.1	0.6
Elevation:	0.005	0.3

3) Acceleration (°/sec²)

	<u>Track</u>	<u>Slew</u>
Azimuth:	0.0001	0.05
Elevation:	0.00001	0.025

4) Speed range

The antenna will be capable of operating smoothly at all velocities from 0.001 °/sec to 0.25 °/sec.

5) Pointing accuracy

Operational peak pointing accuracy: 15 sec. This shall include the effect of gravity, temperature, axis-gearing readout tolerance, alignments, and servo tracking errors.

6) Operational Surface Accuracy

The permissible RMS (normal) of 0.12 inch overall and 0.08 inch for the center 200-ft-diameter area are to be budgeted in accordance with the following expression:

$$\frac{0.12 \text{ inch (0.08 inch for center portion)}}{\sqrt{(RMS_p)^2 + (RMS_s)^2}} =$$

RMS_p = RMS of paraboloid (normal)

RMS_s = RMS of secondary reflector (normal)

7) Structural dynamics

The lowest natural frequency of the antenna system can be 0.05 cps.

8) Electronic-equipment enclosures

Provision for 25,000 lbs of electronic gear plus access facility located behind the reflector

9) Ambient temperature

Survival: -40° F to +146° F

Operational: +45° F to + 85° F

10) Differential temperature

10° F top to bottom, 5° F side to side

11) Humidity

0% to 100%

12) Minimum f/D = 0.33313) Earthquake acceleration

0.1 times gravity

14) Structural design code

Steel: A. I. S. C. Specification for the Design, Fabrication and Erection of Structural Steel for Buildings (1963)

Aluminum: A. S. C. E. Specifications for Structures of Aluminum Alloys

7. COST ESTIMATES

7.1 Cost Items

For the cost estimate, it was assumed that the construction contracts are to be awarded in 1966. Applicable escalation of costs should be used when actual construction timing is determined. This is a valid procedure provided all cost estimates are based on the same assumption. The following items are included in the cost estimate.

- 1) Radome.
- 2) Structural steel.
- 3) Reflector surfaces.
- 4) Counterweights.
- 5) Structural compensation systems.
- 6) Altitude and azimuth:
 - a) bearing,
 - b) gear boxes,
 - c) rollers,
 - d) motors,
 - e) rails, tracks, or canals.

- 7) Major bearings (pintle or altitude).
- 8) Ladders and access or elevators, passageways.
- 9) Drive power wiring.
- 10) Cable-wrap system.
- 11) Hoists for equipment enclosure.
- 12) Hoists for repair and maintenance.
- 13) Brakes and bumpers.
- 14) 7 floors within tower for laboratories, offices, storage, etc. (structural portions only).
- 15) Drive control system.
- 16) Space for electronic-equipment enclosure.
- 17) Surface checkout and tuning.
- 18) Engineering.
- 19) Contingencies.

The following items were not estimated. They should be estimated by the CAMROC Committee or others and added to the enclosed estimate to obtain the overall antenna cost.

- 20) Coordinate conversion computer and data-reduction system.
- 21) Radome temperature-control system.
- 22) 7 floors within tower for laboratories, offices, storage, etc., architectural, heating, ventilation, air-conditioning, lighting, power, etc.
- 23) Electronic-equipment enclosures.
- 24) All RF equipment.
- 25) Station power (substation and standby).
- 26) Conduit and all wiring, except power and control wiring for jacks.
- 27) Lighting within radome and on antenna.
- 28) Site work:
 - a) access road,
 - b) parking,
 - c) utilities,
 - d) paving, grading, drainage, and landscaping.
- 29) Insurance.
- 30) Local taxes.
- 31) Real estate.
- 32) Power, except drives
- 33) Administration by CAMROC.
- 34) Off-site inspection and testing.
- 35) Borings and soil testing.

7.2 Cost Summary

The cost estimates for Items 1 to 19 inclusive of the fully compensated Cassegrain antenna are summarized in the following table.

Table 4. Cost estimates (preliminary)

The cost estimates for Items 1 to 19 are as follows:

Structural steel 867,900 lbs	@ \$ 1.50	\$1,302,000
Counterweight 120 yd ³	@ \$100.00	12,000
Reflector surface panels 148,200 ft ²	@ \$ 4.00	593,000
Reflector surface backup assembly 121,500 lbs	@ \$ 7.00	851,000
Secondary reflector surfaces 2,000 ft ²	@ \$ 20.00	40,000
Trunnion axle and support 62,000 lbs	@ \$ 1.50	93,000
Altitude bearings 4 × \$1,500		6,000
Altitude gear box, drive, bull wheel, etc.		40,000
Turret 185 yd ³ × 200		37,000
Azimuth bearings		70,000
Azimuth gear box, drive, etc.		60,000
Drive control system		200,000
Concrete tower 850 yd ³ × \$150.00		128,000
Jacks, push-rod, etc.		85,000
Cable at jacks, lubrication, etc.		50,000
Jack control system		110,000
Ladders, access, elevators, maintenance gantry		100,000
Drive, power-wiring, cable-wrap system		200,000
Hoist for equipment enclosure		50,000
Hoist for repair and maintenance		10,000
Brake and bumper		30,000
Space for electronic-equipment enclosure		18,000
Surface checkout and tuning		200,000
Antenna Cost		\$ 4,285,000
Radome		6,500,000
Radome floor		135,000
Ramps (within tower)		10,000
Laboratory . (within tower)		40,000
Radome Cost		6,685,000
Radome and antenna engineering, supervision of construction and contingencies (25%)		<u>2,743,000</u>
Total		<u><u>\$13,713,000</u></u>

APPENDIX D

CAMROC HAMMERHEAD ANTENNA CONCEPT

Prepared for
THE CAMBRIDGE RADIO OBSERVATORY COMMITTEE

December 1966

MIT LINCOLN LABORATORY
LEXINGTON, MASSACHUSETTS

TABLE OF CONTENTS

<u>Section</u>		<u>Page</u>
1	INTRODUCTION	D-1
2	SUMMARY AND CONCLUSIONS	D-2
3	PERFORMANCE CRITERIA	D-2
4	OPERATIONAL CHARACTERISTICS	D-3
5	PRELIMINARY DESIGN	D-6
6	MECHANICAL CHARACTERISTICS	D-25
7	DEFLECTION-MATED HYDROSTATIC BEARING INVESTIGATION . . .	D-36
8	ERECTION	D-41
9	WEIGHT REDUCTION	D-42
10	WEIGHT AND COST ESTIMATE	D-43
11	SIZE VERSUS WEIGHT AND COST RELATIONSHIPS	D-47

1. INTRODUCTION

A study of a concept for the CAMROC 400-ft antenna was undertaken at Lincoln Laboratory for the purposes of providing a basis for comparison with other concepts under consideration, of stimulating new ideas and their application to other concepts being studied by outside design firms, and possibly, but not primarily, of providing a concept for final design.

Deflections due to gravity loading are the major source of surface error of radome-enclosed antennas. As a dish travels from face-up to face-side position, the gravity loading may be considered as two major actions — weight relief producing a symmetrical outward deflection of the surface in the direction of the boresight axis, plus the downward gravity loading in face-side position, which results in deflections antisymmetrical about the elevation axis. The axes of symmetry and antisymmetry should be normal to the principal stiffness of the structure if it is to be efficient for this type of loading, and a series of deep parallel trusses aligned along a rigid elevation axis will provide this type of support.

The Hammerhead concept, named for the crane having a T-shaped horizontal boom on a tower, employs the system described above. The rigid elevation axis is provided by a horizontal boom that can rotate in azimuth on top of a tower. The vertical trusses rotate around this boom, which serves as an axle for the trusses. Since the trusses are counterweighted so that their center of gravity lies on the elevation axis, the loading on this axle does not change when the trusses rotate about it, and consequently the axle acts as a rigid member.

The vertical trusses are designed so that their outer portion will deflect into a shape having the same parabolic curve as the original surface but tilted downward at the ends. Compensation of deflections is then accomplished by jacks on two symmetrically located members of each truss that jack this curve back into its true position.

Use of these compensation techniques allows the supporting structure to be highly stressed and less stiff than conventional antennas, with a resulting economy of weight and cost, and adds a new species to the cost-versus-size curves for large antennas. Deflections are reduced by orders of magnitude. Independent studies of other compensation methods by Paul Weidlinger, Consulting Engineer, show similar benefits.

One particular advantage of the Hammerhead concept is its use in the construction of the radome — a crane can be mounted on rails on top of the Hammerhead truss, which can be rotated to locate the crane over the work. Another advantage is the capability of switching between types of RF systems, which can be located behind the vertex of the dish, inside the Hammerhead truss. In addition, air-handling equipment for environmental control inside the radome can be mounted on the Hammerhead.

2. SUMMARY AND CONCLUSIONS

A structural concept of a 400-ft antenna was studied at Lincoln Laboratory. A prime purpose of this in-house effort was to guide the consulting firms, working on other antenna concepts, into being sufficiently bold with a truly lightweight design.

Another result, most elemental, is the realization that lightweight surface panels mean a lightweight antenna and less cost. When the weight of panels in this concept was reduced from 1.25 to 0.5 psf, the total structural weight on azimuth bearings reduced from 2700 tons to 1430 tons, with a corresponding decrease in inertia and drives.

Further weight reduction is possible; if the counterweights are moved outward and the vertical trusses are redesigned, the total weight on azimuth bearings may drop to below 1000 tons. No reduction in inertia is anticipated by this change, and the system frequency will probably limit the possible reductions to somewhere around 1000 tons.

In the realization that these studies represent a substantial effort, it should be emphasized that considerably more effort should be devoted to an analysis of any system before a final design phase is started. The operation of the system, interchange of RF components, and future adjustments of the surface should be considered. A static and dynamic analysis of the final optimized structure, including all possible modes of vibration, should be completed using STAIR, MAST, or FRAN computer programs. Only when such an analysis shows acceptable results can it be safely assumed that the structure, when designed and built, will operate properly.

Cost-versus-size curves for 300-, 400-, and 500-ft-diameter antennas indicated that for this range of size, the cost varied with diameter raised to the 1.6 power.

3. PERFORMANCE CRITERIA

The following criteria were used for preliminary investigations:

- 1) Sky coverage
Elevation: $+15^{\circ}$ to $+90^{\circ}$
Azimuth: $\pm 300^{\circ}$
- 2) Angular velocity
Tracking: $0.25^{\circ}/\text{sec}$
Slew: $1.00^{\circ}/\text{sec}$
- 3) Angular acceleration
 $0.04^{\circ}/\text{sec}^2$
- 4) Speed range
The antennas will be capable of operating smoothly at all velocities from $0.001^{\circ}/\text{sec}$ to $0.25^{\circ}/\text{sec}$.
- 5) Operational peak pointing accuracy
15 sec. (This includes the effects of gravity, temperature, axis gearing, readout tolerances, alignments, and servo tracking errors.)

6) Operational surface accuracy

0.15-inch RMS (normal) - Overall system tolerance to be budgeted in accordance with the following expression:

$$0.15 = \sqrt{(\text{RMS}_p)^2 + (\text{RMS}_s)^2}$$

RMS_p = RMS of fixed paraboloid (normal)

RMS_s = RMS of secondary reflector (normal)

7) Structural dynamics

The lowest natural frequency of the antenna systems can be 0.1 cps.

8) Electronic equipment enclosure

Provision for 25,000 lbs of electronic gear plus access facility located behind the primary reflector.

9) Ambient temperatures

Survival: -40°F to $+140^\circ\text{F}$

Operational: $+45^\circ\text{F}$ to $+85^\circ\text{F}$

10) Differential temperatures

10°F top to bottom, 5°F side to side

11) Humidity

0% to 100%

For subsequent Hammerhead investigations, some of these criteria have been altered as follows:

	<u>Track</u>	<u>Slew</u>
Azimuth velocity	$0.1^\circ/\text{sec}$	$0.6^\circ/\text{sec}$
Elevation velocity	$0.005^\circ/\text{sec}$	$0.3^\circ/\text{sec}$
Azimuth acceleration	$0.0001^\circ/\text{sec}^2$	$0.05^\circ/\text{sec}^2$
Elevation acceleration	$0.00001^\circ/\text{sec}^2$	$0.025^\circ/\text{sec}^2$
Servo bandwidth	0.01 cps	-
System mechanical resonant frequency	0.05 cps	-

4. OPERATIONAL CHARACTERISTICS

4.1 Gravity Deflections

An error analysis of the Hammerhead antenna was performed by Simpson Gumpertz & Heger to determine the expected RMS of the surface.

In this analysis, the surface was assumed to be rigged so that the panel supports described a perfect paraboloid when the dish was in the 45° position. The RMS error was then computed for the zenith position with a 12-db taper in illumination.

A random sample of 45 points on the surface was selected for analysis, including points on the vertical trusses, on the purlins, and on the panels.

Input to the RMS computer program was calculated as follows:

For points on the vertical trusses, the compensated deflections normal to the surface caused by a change in gravity from 45° to face-up position were separated into three components (see Figures 5 through 8).

For points on the purlin trusses, the peak deflections of the purlin trusses (traveling from 45° to face-up position) were superimposed on the vertical-truss displacement.

For points on the panels, the total peak deflections in face-up position were added to the purlin-truss and vertical-truss deflections. Total peak, rather than change in deflection from 45° to face-up, was used because it was assumed that the panels could not be rigged.

The computer program first calculates the RMS error of the reflector referred to a corresponding perfect paraboloid. Next, the deflected surface is rotated as a rigid body to a best-fit position. Finally, the focal length is changed to find the best-fit perfect paraboloid corresponding to the deflected rotated surface, and the RMS error difference is calculated.

Results of the computer program are as follows:

RMS before best fit — 0.09979 inch,
 RMS after rotation — 0.090894 inch,
 RMS after change in focal length — 0.090812 inch.

These results do not include manufacturing tolerances, rigging errors, thermal distortions, or acceleration distortions of the surface.

Although the results are based on large approximations of the surface deflections, they indicate the general range of surface distortion and are conservative. In addition, it can be seen from the results that rotation and change in focal length account for only about a 10% improvement in the RMS error.

Now that it is recognized that the RMS error before "best fit" is the most significant portion of the total RMS error for the Hammerhead concept, any further work on this concept should consider the RMS (rather than the peak) error of individual panels and purlin trusses combined with vertical trusses.

4.2 Dynamic Deflections

Surface error due to acceleration forces in the structure was considered for elevation motion as follows: The elevation drives are located at trusses T25, adjacent to the tower. The torque tube connects the vertical trusses so they act together, and any twisting of the torque tube will produce a surface error at the outer vertical trusses,

especially at their tips. This error was found to be less than 0.2 inch (peak) at $0.04^\circ/\text{sec}^2$ acceleration. The resulting RMS error would be small, since only a small fraction of the surface will be affected.

In azimuth motion, the Hammerhead truss will bend, owing to the inertia of the vertical truss assemblies as well as to its own inertia. The inertia forces were hand calculated and applied as loads to the Hammerhead truss for a STIFFEIG computer run. The resulting deflected shape showed an insignificant deviation from a straight line. The bending stiffness of the torque tube would further reduce these deflections.

Deflections due to centrifugal force at maximum speed were investigated and were found to be nearly nonexistent, since the forces at the tip were only 0.00007 G at $0.2^\circ/\text{sec}$ speed.

Only the presumably major dynamic deflections were investigated, and all were found to be tolerable. A further design, however, should include the cumulative effects of dynamic loading on all the structural components.

4.3 Natural Frequency

One mode of vibration investigated was the "nodding" of the antenna. Inertias of each vertical truss with its associated panels, purlins, and counterweights were calculated by a computer program, and these lumped inertias were applied along the torque tube, combined with the inertias of the torque tube itself, and connected with springs representing the torsional stiffness of each section of the torque tube. To this system was added another spring representing the turret. The frequency of this combined system was calculated to be 0.63 cps. Not included were flexibility and inertias of drives, bearings, tower, and soil.

The vertical trusses were run through the STIFFEIG program individually for a frequency analysis, assuming rigid support at the bearings. Truss T25, together with the secondary reflector and its support trusses, had a natural frequency of 1.08 cps. Since this is located adjacent to the turret, at the stiffest part of the Hammerhead, its frequency appears satisfactory, since the total system frequency requirement is only 0.1 cps.

Another mode investigated was slewing, or azimuth motion. Horizontal bending of the Hammerhead truss was assumed to be a major contributor to this mode. Inertias of the vertical trusses and sections of the torque tube were lumped together with the inertias of the elements of the Hammerhead truss and applied at the stations along the Hammerhead truss. The motion in this case was antisymmetrical about the center line of tower, so half of the Hammerhead truss combined with the turret was used. Figure 18 shows the model that was run through the STIFFEIG program for a frequency analysis. The primary frequency for this system was 1.26 cps. Not included were inertias and spring

constants of the azimuth drive and bearing, tower, and soil. It is not expected, however, that these components will result in an order-of-magnitude change in frequency.

5. PRELIMINARY DESIGN

5.1 Surface Panels

In the Hammerhead concept, the surface panels and purlin trusses are not deflection compensated, and do not contribute structural stiffness via shell action. Their dead weight is the major contributor to gravity deflections and stresses in the supporting structural components. Lightweight panels, therefore, are a prime requisite for a successful design of this type.

The first pass at a design used panels made of 3-inch-thick aluminum honeycomb, weighing 1.25 psf, capable of supporting, without permanent deformation, a 300-lb man. The lightweight sheet aluminum panel shown in Figure 1 was used as a basis of comparison. It weighs 0.5 psf and must support the 300-lb man, but in doing so, may be distorted and must be repaired or replaced if accidentally stepped on. Since it is not essential that a man walk all over the surface, and walkways can be provided for access where necessary, it is felt that the advantages of lightweight panels outweigh the inconvenience of limited access.

Proof of these advantages appears in the following tabulation of reflector properties versus panel weight, and the improvement in deflection of vertical trusses is shown graphically in Figure 2.

Reflector properties versus panel weight

	<u>Original panels</u>	<u>Lightweight panels</u>
Panel weight	1.25 psf	0.50 psf
Panel deflection (gravity)	0.05 inch	0.06 inch
Purlin truss deflection (gravity)	0.05 inch	0.05 inch
Vertical truss deflection (compensated)	0.4 inch	0.20 inch
Total deflection (peak)	0.5 inch	0.31 inch
Bias-rigged deflection (peak)	0.25 inch	0.15 inch
Manufacturing and rigging (peak)	0.120 inch	0.120 inch
RMS deflection	0.15 inch	0.09 inch
Weight on elevation bearings	1525 tons	946 tons
Weight on azimuth bearings	2700 tons	1430 tons
Inertia about elevation axis	6.4×10^8 slug ft ²	4.0×10^8 slug ft ²

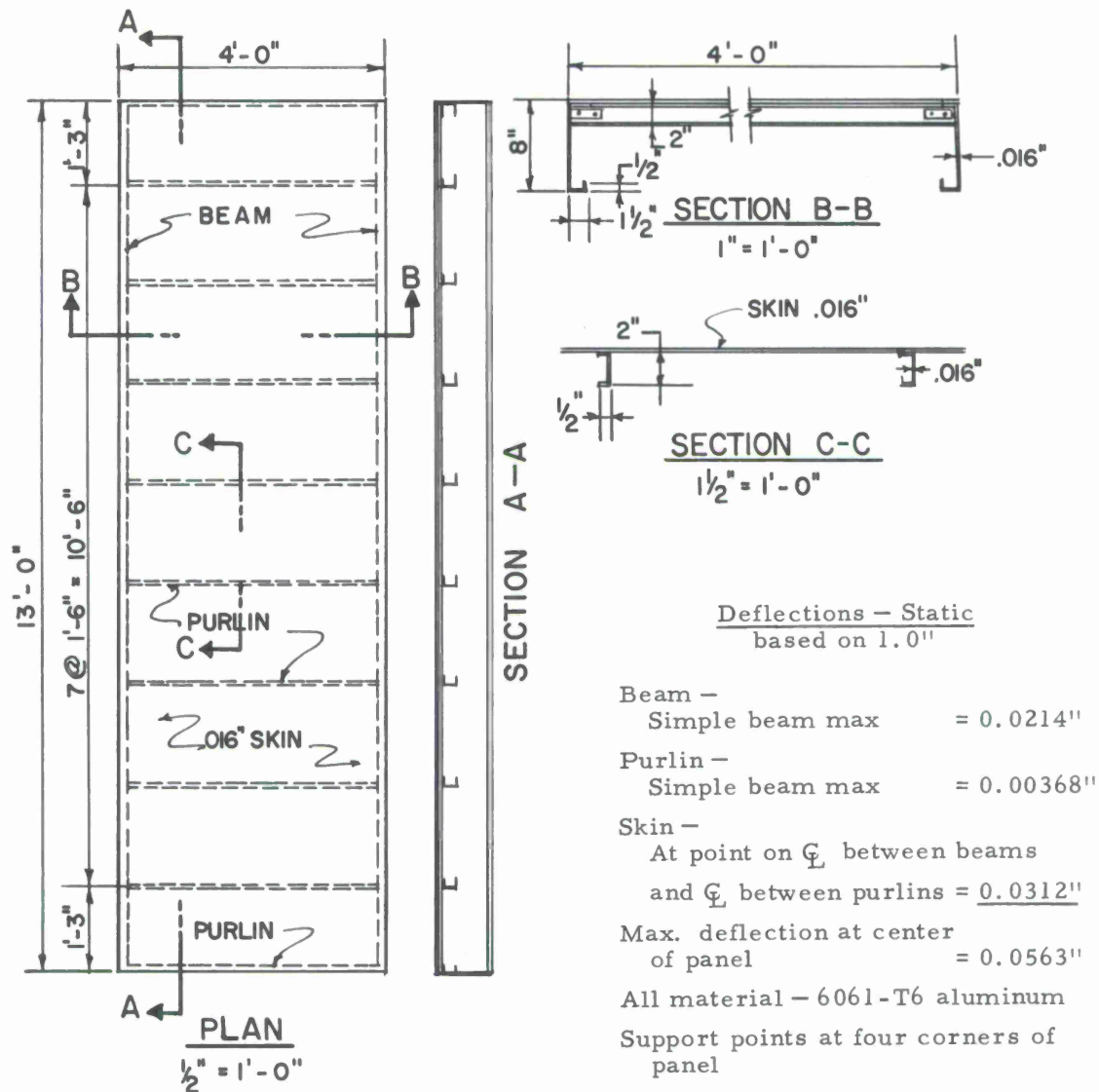


Figure 1. Aluminum surface panel for CAMROC Hammerhead antenna concept.

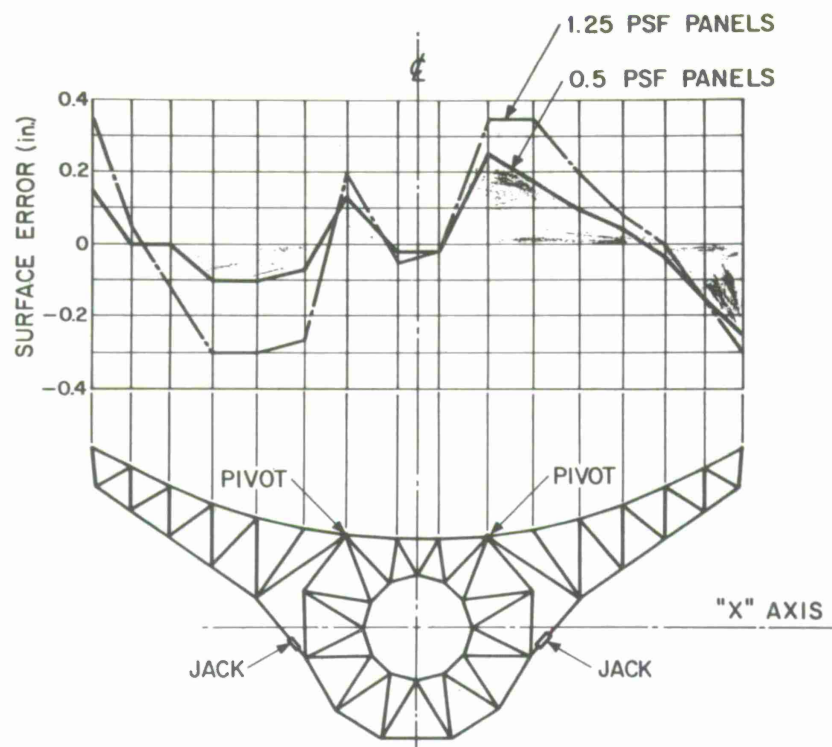


Figure 2. Panel weight versus surface error truss T75 face-up to face-side deflections, no bias rigging.

5.2 Surface-Panel Geometry

For most paraboloidal antenna reflectors designed to date, the circular symmetry of the structure has been exploited to minimize the number and types of surface panels required. If a surface substructure is to be avoided in the Hammerhead concept, it would appear that square or rectangular panels should be utilized. However, in the limit of doubly curved sections of the paraboloid, this would result in just four panels of any given type, one in each quadrant of the paraboloid.

In an attempt to minimize the number of types of rectangular surface panels required for Hammerhead, geometries other than sections of a paraboloid have been considered. For this purpose, a portion of the error budget for surface inaccuracies and deviations has been allotted to the resulting nonideal geometry of the surface panels. For the present, the geometrical RMS surface error has been assumed to be a maximum of 0.025 inch. If the total permissible RMS surface error is 0.075 inch, the contribution from all other sources than geometry will be limited to 0.0707-inch RMS. It is assumed that the Hammerhead reflector is a nominal 400 ft in diameter and has a focal length of 160 ft.

The simplest type of panel is a flat plate. However, a simple calculation indicates that the maximum edge dimension of a flat panel meeting the geometrical RMS error requirement of 0.025 inch is less than 4.0 ft. Since the surface area of the paraboloid is

approximately $137,000 \text{ ft}^2$, the number of panels required is in excess of 10,000. In an effort to reduce the number required and hence relieve installation and rigging problems, consideration was next given to singly curved panels. For this purpose, a length of 4 ft in the noncurved or flat dimension was assumed. This results in a maximum RMS error due to this approximation of 0.019 inch in the central region of the reflector where the radius of curvature of the paraboloid is a minimum.

As one increases the curved dimension of a rectangular plate beyond 4 ft, a second source of geometrical error becomes significant. This error results from the tilting about a chord of the curved dimension required to fit the flat dimension of the panels. A study of the trade-off in errors with panel dimensions has resulted in the selection of panel dimensions of 4 ft by 13 ft for demonstration of feasibility. Moreover, for a chord length of 13 ft in the curved dimension, use of a constant radius of curvature for two successive rows of panels rather than segments of a parabola introduces negligible additional surface errors.

To summarize, it has been determined that it is feasible to meet the geometrical RMS surface error of 0.025 inch utilizing 4-ft by 13-ft panels with the 13-ft dimension having a constant radius of curvature. Nine different types corresponding to different radii of curvature are required. The total number of panels involved is 2944 for an effective diameter of 420 ft. It should be noted that panels of this type require simple tooling and utilize standard-width flat sheet material for the actual surface.

5.3 Purlin Trusses

The purlin trusses shown in Figure 3 are triangular space frames approximately 13 ft per side, spanning 50 ft between vertical trusses. They will be spaced 13 ft apart so that the surface panels will span between members of each purlin truss (13 ft) and between the purlin trusses themselves (13 ft).

A preliminary computer run indicates that purlin deflections from face-up to face-side antenna positions will be 0.04 inch in the X and Y directions. Weight of trusses is approximately 1.2 psi of antenna surface. Member cross-section areas for this configuration are small; however, preliminary studies of available thin-wall steel tubes indicate that buckling criteria can be satisfied.

5.4 Vertical Trusses

The location of vertical trusses in the reflector backup structure is shown in Figure 4. These planar trusses are lined up 50 ft apart along the Hammerhead truss, and rotate about it in concert. Identification of these trusses is based on their distance from center of tower; i. e., truss T25 is located 25 ft from the azimuth axis.

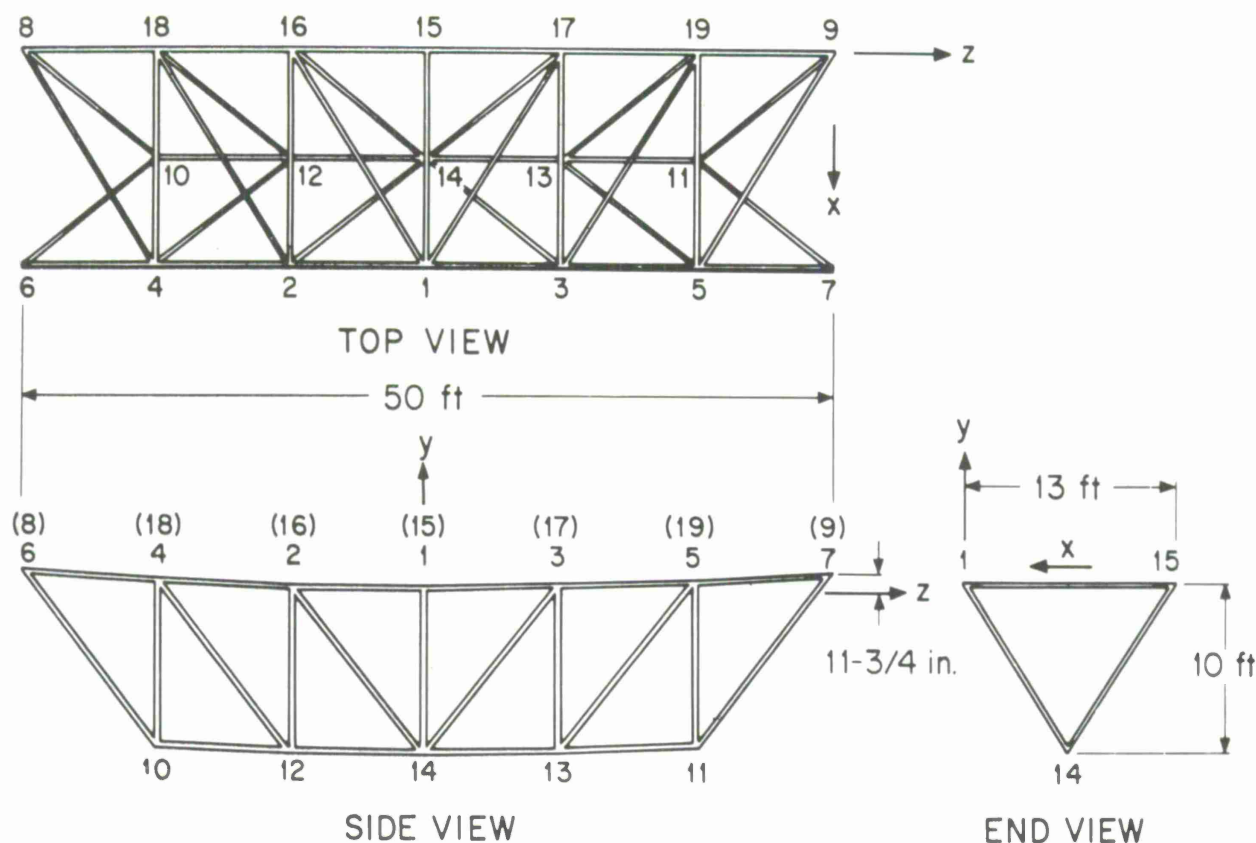


Figure 3. Purlin truss.

Each truss was run through the STIFFEIG computer program several times with variations of member areas and joint configuration. Gravity loads from surface panels, purlin trusses, and vertical truss members were applied at the joints of the vertical trusses, and deflections of the joints were computed for several elevation angles of the reflector. From this output of the computer, the changes in deflection from face-up position (zenith pointing) to various elevation angles were computed.

The deflection-compensation technique consisted of two jacks and pivots that rotated the ends of each truss (as free bodies) into a best-fit position. Vertical-truss outlines showing jack and pivot locations as well as compensated deflections are shown in Figures 5 through 8.

Figure 9 shows the graphical solution for compensated deflections. These were found by first making a layout of the gravity displacement; then optimum free-body rotation of the truss end about the pivot was found by trial and error; and the resulting joint displacement was scaled along a line normal to a radial line through the pivot to locate the compensated joint position. The distance from this position to the true (original) surface is the compensated deflection.

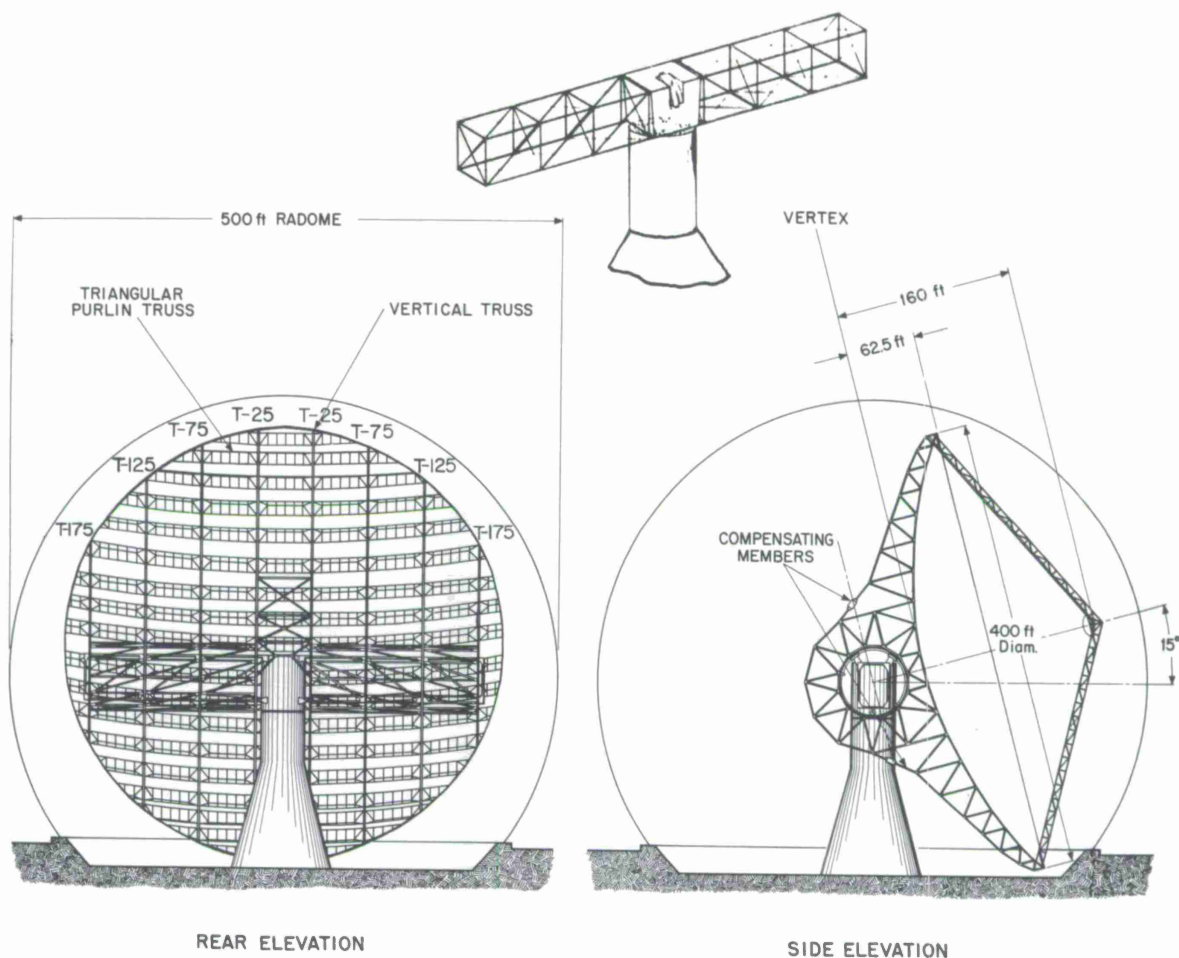


Figure 4. Vertical trusses are marked T25, etc., indicating distance from center of antenna or tower.

At truss T25 the interaction of the secondary reflector support, which prevented truly free-body rotation, was included in the compensation process.

The compensated deflections thus obtained were included in the RMS calculations.

The completed antenna is shown in Figure 10, with the vertical trusses in heavy outline.

5.5 Torque Tube

The torque tube is a cylindrical space frame connecting the vertical trusses so that they act together through changes in elevation angle of the reflector. The torque tube and vertical trusses rotate about the Hammerhead truss, which serves as an axle. In order to provide clearance for this rotation, the inside diameter of the torque tube must be about 60 ft.

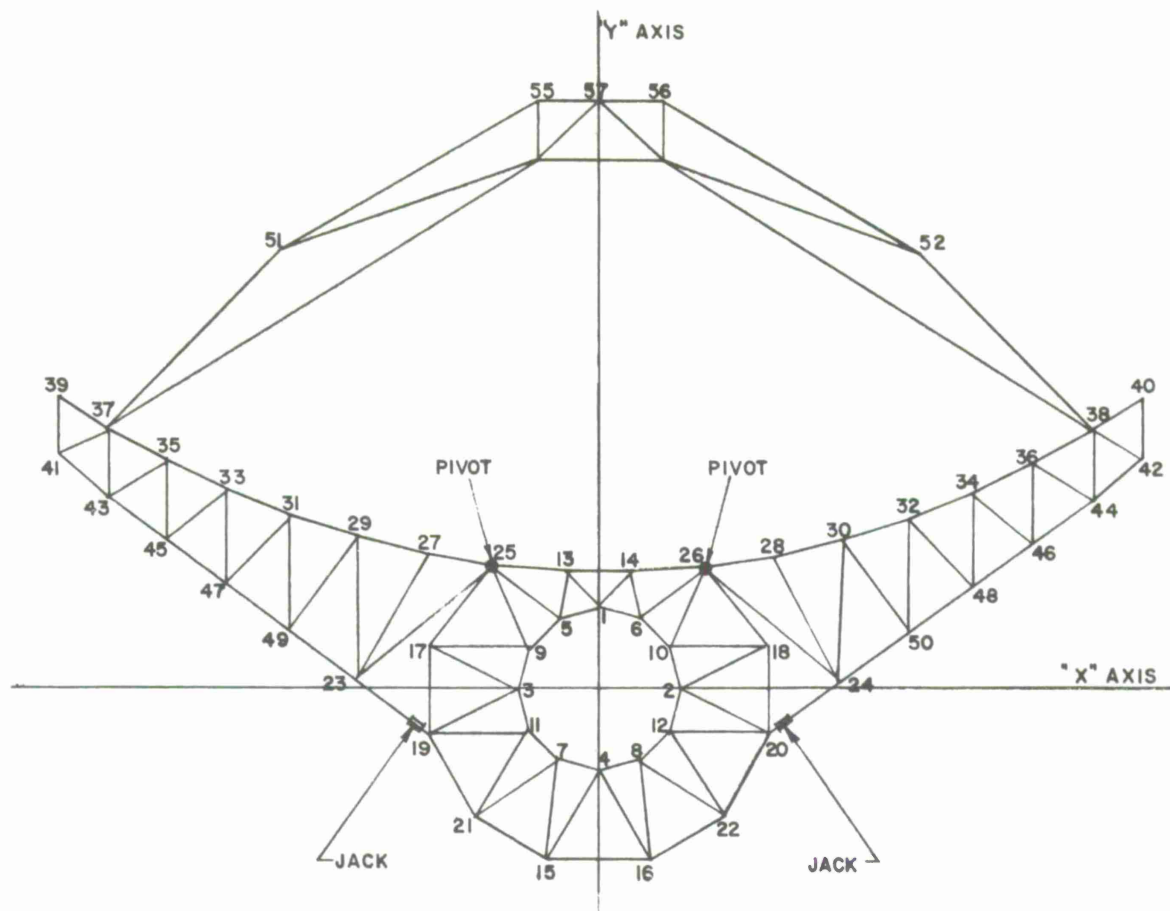


Figure 5. T25* compensated deflections (inches).

1. 25 psf panels					0. 5 psf panels		
Joint	Face-up	60° elev.	30° elev.	15° elev.	Joint	Face-up	45° elev.
13	0	0.05	-0.05	-0.09	13	0	0
14	0	-0.20	-0.13	-0.12	14	0	-0.13
25	0	0.32	0.25	0.30	25	0	0.25
26	0	-0.42	0.02	0.14	26	0	-0.15
27	0	0.20	-0.03	-0.06	27	0	0.05
28	0	-0.26	0.08	0.15	28	0	-0.07
29	0	0.10	-0.20	-0.28	29	0	-0.02
30	0	-0.20	0.10	0.13	30	0	-0.06
31	0	0.03	-0.28	-0.37	31	0	-0.15
32	0	-0.10	0.12	0.10	32	0	0
33	0	0.05	-0.25	-0.33	33	0	-0.13
34	0	-0.05	0.08	0.06	34	0	0
35	0	0.10	-0.11	-0.15	35	0	-0.10
36	0	0.05	0.05	0.03	36	0	0.02
37	0	0.21	0.25	0.30	37	0	0.02
38	0	0.05	-0.07	-0.03	38	0	-0.02

* Vertical truss located 25 ft from center of tower.

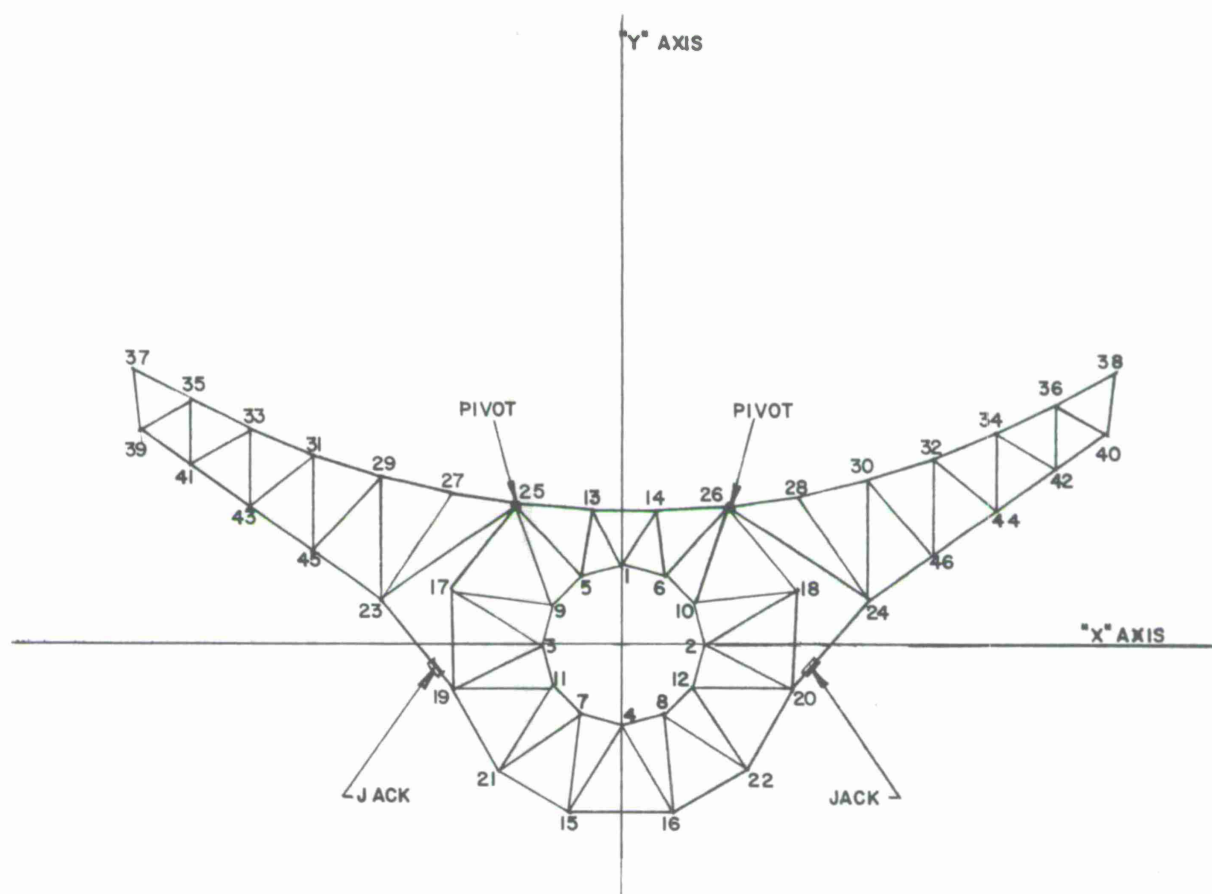


Figure 6. T75* compensated deflections (inches).

1. 25 psf panels					0. 5 psf panels		
Joint	Face-up	60° elev.	30° elev.	15° elev.	Joint	Face-up	45° elev.
13	0	0	0	-0.03	13	0	0
14	0	-0.17	-0.10	-0.04	14	0	-0.08
25	0	0.20	0.15	0.18	25	0	0.15
26	0	-0.30	0.07	0.21	26	0	-0.12
27	0	0.05	0.07	-0.16	27	0	0.02
28	0	-0.12	0.12	0.24	28	0	0
29	0	0	-0.21	-0.25	29	0	0
30	0	-0.10	0.12	0.16	30	0	0
31	0	0	-0.21	-0.25	31	0	-0.01
32	0	-0.02	0.10	0.09	32	0	0
33	0	0.03	-0.15	-0.13	33	0	0
34	0	0	0.05	0.02	34	0	0
35	0	0.08	0	0.02	35	0	0
36	0	0	-0.05	-0.10	36	0	0
37	0	0.15	0.20	0.28	37	0	0.05
38	0	0	-0.20	-0.28	38	0	0

* Vertical truss located 75 ft from center of tower.

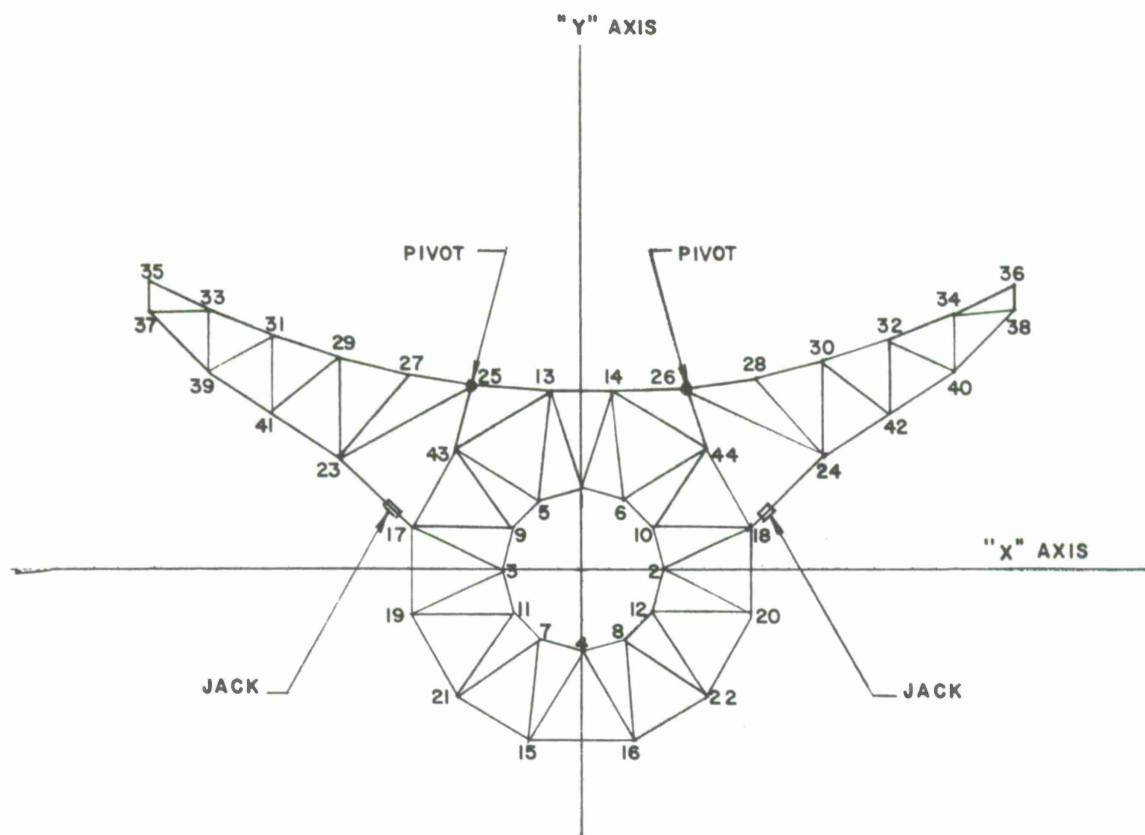


Figure 7. T125* compensated deflections (inches).

1.25 psf panels					0.5 psf panels		
Joint	Face-up	60° elev.	30° elev.	15° elev.	Joint	Face-up	45° elev.
13	0	0	-0.10	-0.02	13	0	0.03
14	0	-0.15	-0.25	-0.13	14	0	-0.03
25	0	0.26	0.20	0.23	25	0	0.10
26	0	-0.38	-0.15	0.08	26	0	-0.08
27	0	0.1	0	-0.03	27	0	0.02
28	0	-0.15	0	0.11	28	0	0
29	0	0	-0.25	-0.23	29	0	0
30	0	-0.05	0.05	0.10	30	0	0
31	0	0	-0.15	-0.14	31	0	-0.02
32	0	0	0.10	0.08	32	0	0.02
33	0	-0.05	-0.05	0	33	0	0
34	0	0.05	0.10	0.02	34	0	0.02
35	0	0.05	0.05	0.15	35	0	0.05
36	0	0.05	0	-0.13	36	0	0

* Vertical truss located 125 ft from center of tower.

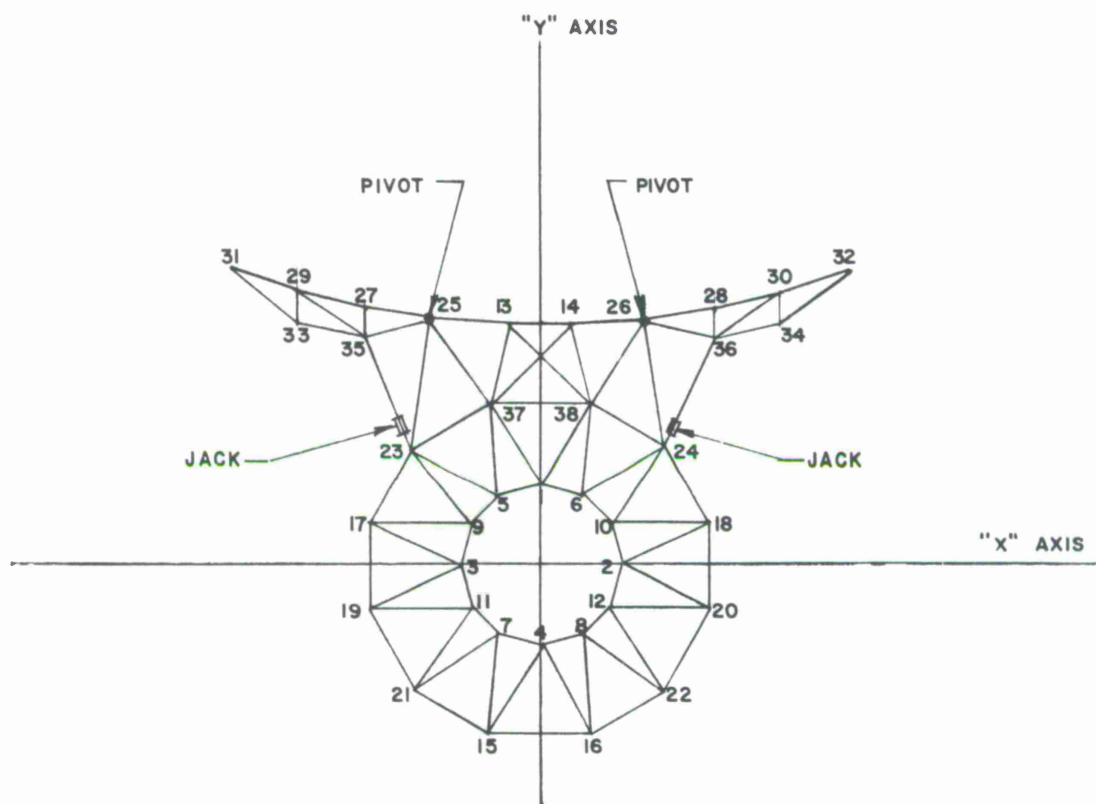


Figure 8. T175* compensated deflections (inches).

1.25 psf panels					0.5 psf panels		
Joints	Face-up	60° elev.	30° elev.	15° elev.	Joint	Face-up	45° elev.
13	0	0	0.09	0.04	13	0	0.03
14	0	0.12	-0.19	-0.12	14	0	-0.05
25	0	0.18	0.19	0.20	25	0	0.15
26	0	0.21	-0.28	-0.19	26	0	-0.10
27	0	0	-0.01	-0.04	27	0	-0.02
28	0	0.19	-0.19	-0.12	28	0	-0.02
29	0	0	-0.06	-0.03	29	0	0
30	0	0.04	-0.09	-0.03	30	0	-0.01
31	0	0.05	0	0.04	31	0	0
32	0	0.02	0	0.07	32	0	0.03

* Vertical truss located 175 ft from center of tower.

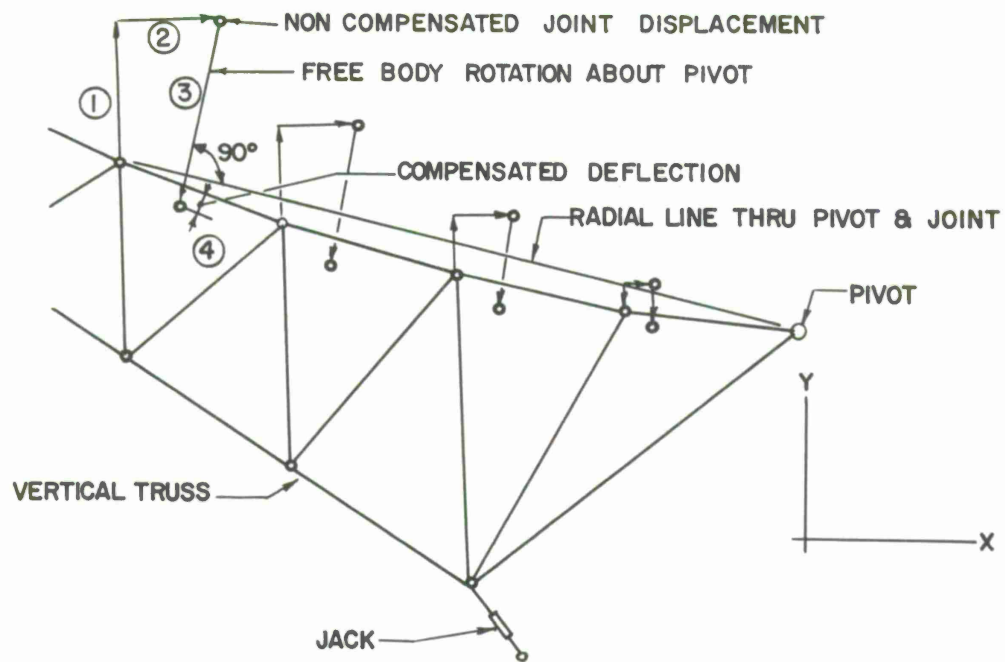


Figure 9. Graphical solution for deflection compensation of Hammerhead vertical trusses.

Steps for graphical solution:

1. y component of deflection from computer output is plotted at full scale.
2. x component of same deflection is plotted.
3. Plot free-body rotation about pivot for best fit of all points. (This is the compensation produced by the jack.)
4. Measure the compensated deflection normal to the surface.

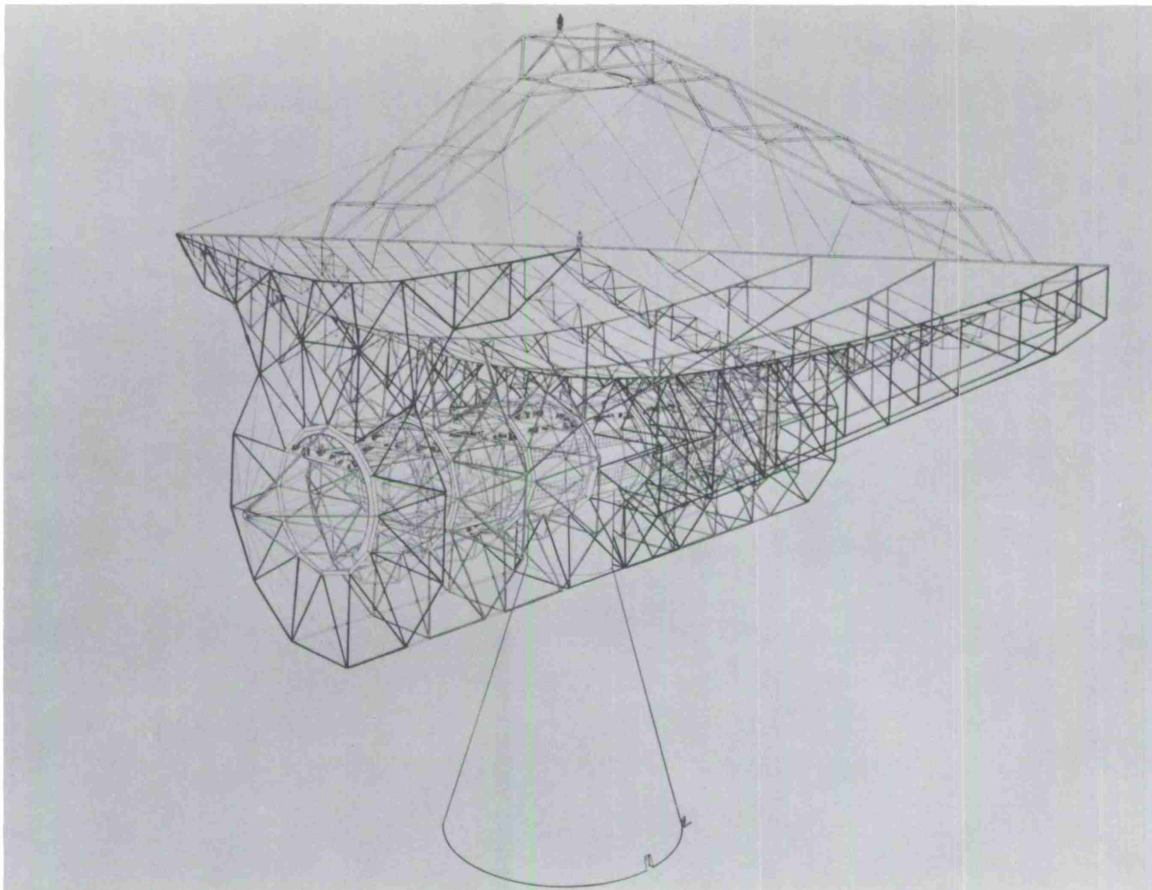


Figure 10. Vertical trusses (heavy outline) shown with completed Hammerhead antenna.

The torsional stiffness of the torque tube was established so that elevation drives would be required only at the inboard trusses (T25). When the elevation drives change speed, the acceleration forces will twist the torque tube, and this "wrap up" will rotate the outboard trusses with respect to the antenna surface and produce a maximum surface distortion at their tips. A 0.2-inch deflection at the tip of the outboard trusses would not significantly affect the RMS of the whole surface, so this was established as a design criterion for torsional stiffness of the torque tube. Investigation of the original concept of the torque tube (Figure 11) showed this to be no problem at the operational acceleration of $0.04^\circ/\text{sec}^2$.

The natural frequency in the nodding mode due to wrap up, assuming locked drive at T25 and lumped inertias of vertical trusses, was 0.65 cps. Cross-section areas of bars for this concept were 10 inches².

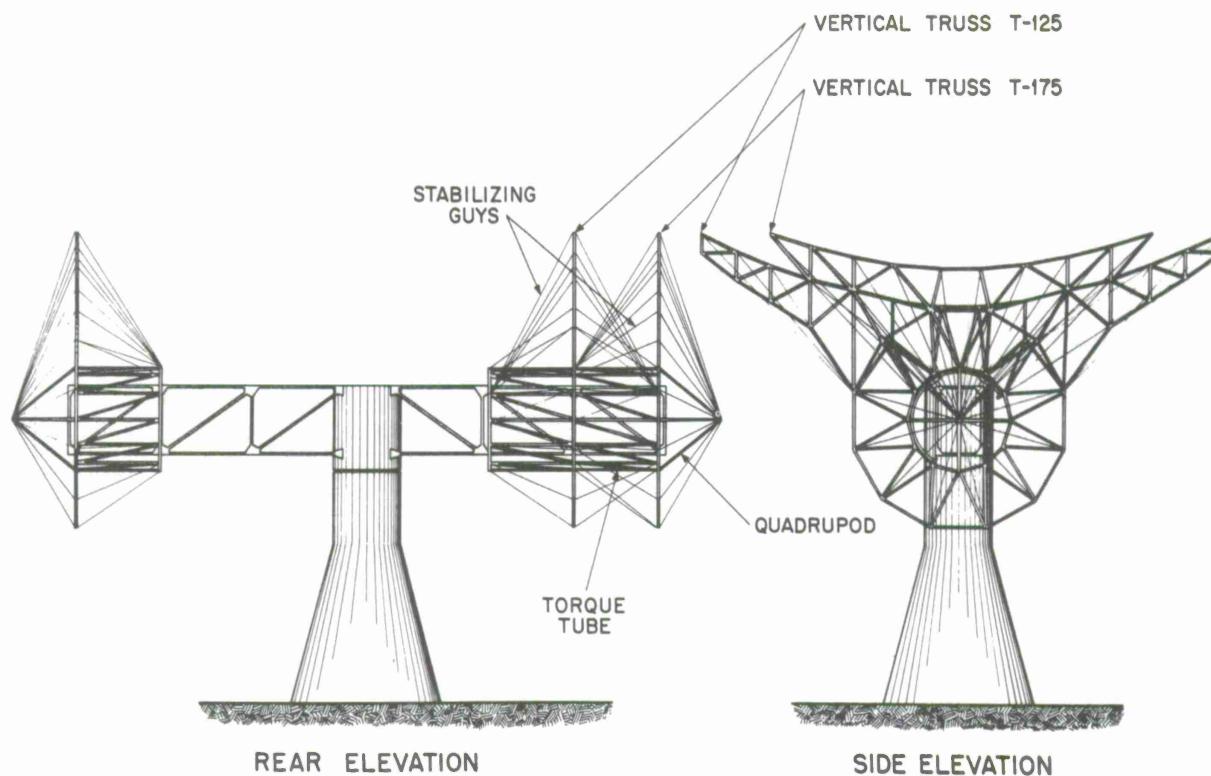


Figure 11. Outer trusses and torque tube.

An improved version of the torque tube is shown in Figure 12. Deflectional characteristics are the same as for the original concept, and instead of 10-inch² members, this configuration has areas of 3, 2.4, and 1.5 inches² in the three divisions between vertical trusses. Improvement was accomplished by changing the geometrical layout to produce a better helical slope of members, and by apportioning the areas of members for minimum tip deflection due to torsion. A light ring truss shown in Figure 12 (Section B-B) was added midway between vertical trusses for stability.

The completed antenna with the torque tube in heavy outline is shown in Figure 13.

5.6 Hammerhead

The Hammerhead, or axle, is mounted horizontally on azimuth bearings on top of the tower. Elevation bearings are mounted along this cantilever truss to support the vertical trusses that rotate about it. The design of this structure evolved from the layout shown in Figure 14. Changes in concept, such as weight saving due to lighter panels and a multiuse feed with laboratory space located within the Hammerhead, resulted in the concept shown in Figure 15.

The axle in this concept is 350 ft long, 29 ft wide, and 40 ft high. Laboratory space inside the Hammerhead will be about 8000 ft² with the two-story configuration shown, or a third floor with over 10-ft headroom may be added.

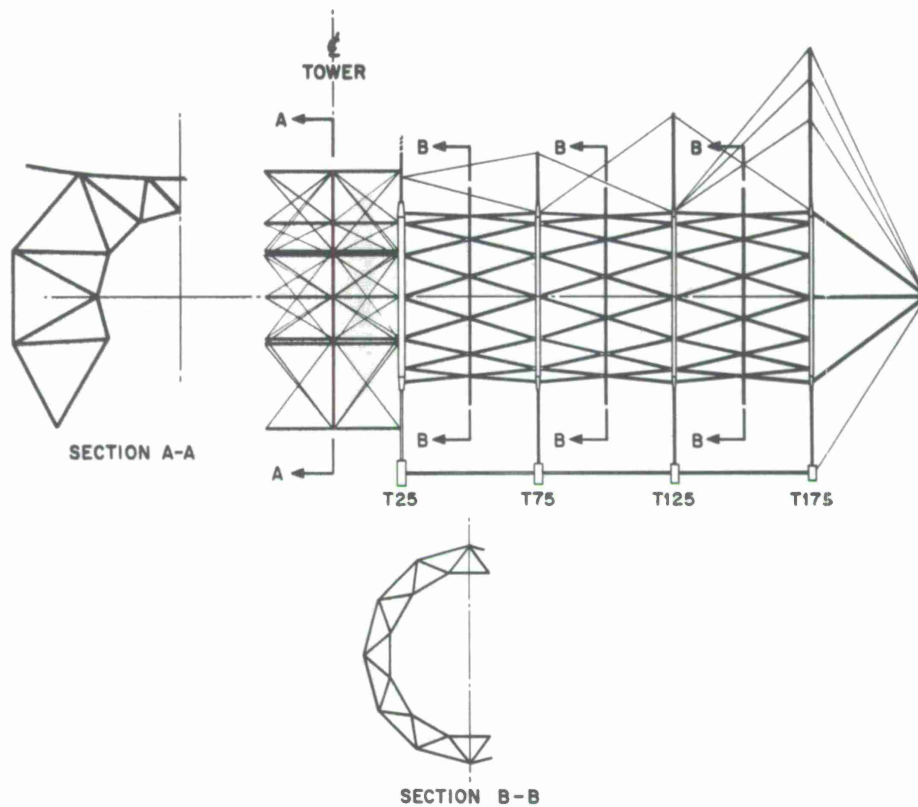


Figure 12. Outline drawing of torque tube for Hammerhead antenna.

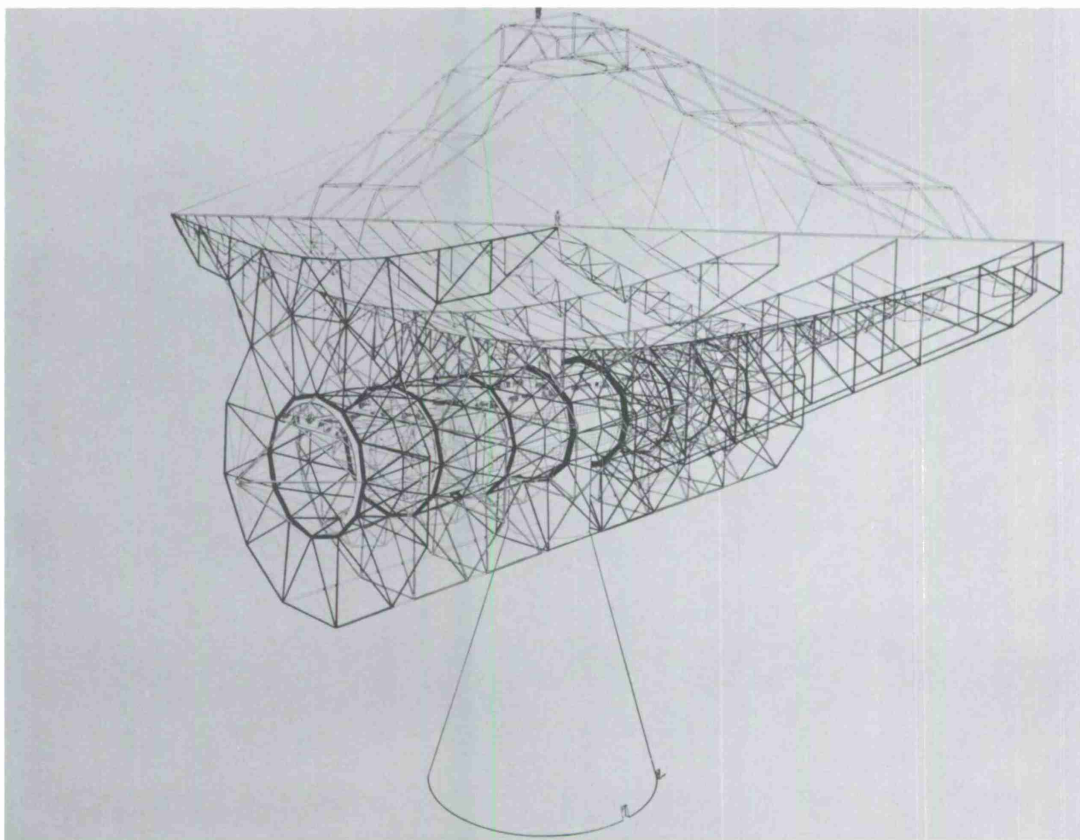


Figure 13. Torque tube (heavy outline) shown with completed Hammerhead antenna.

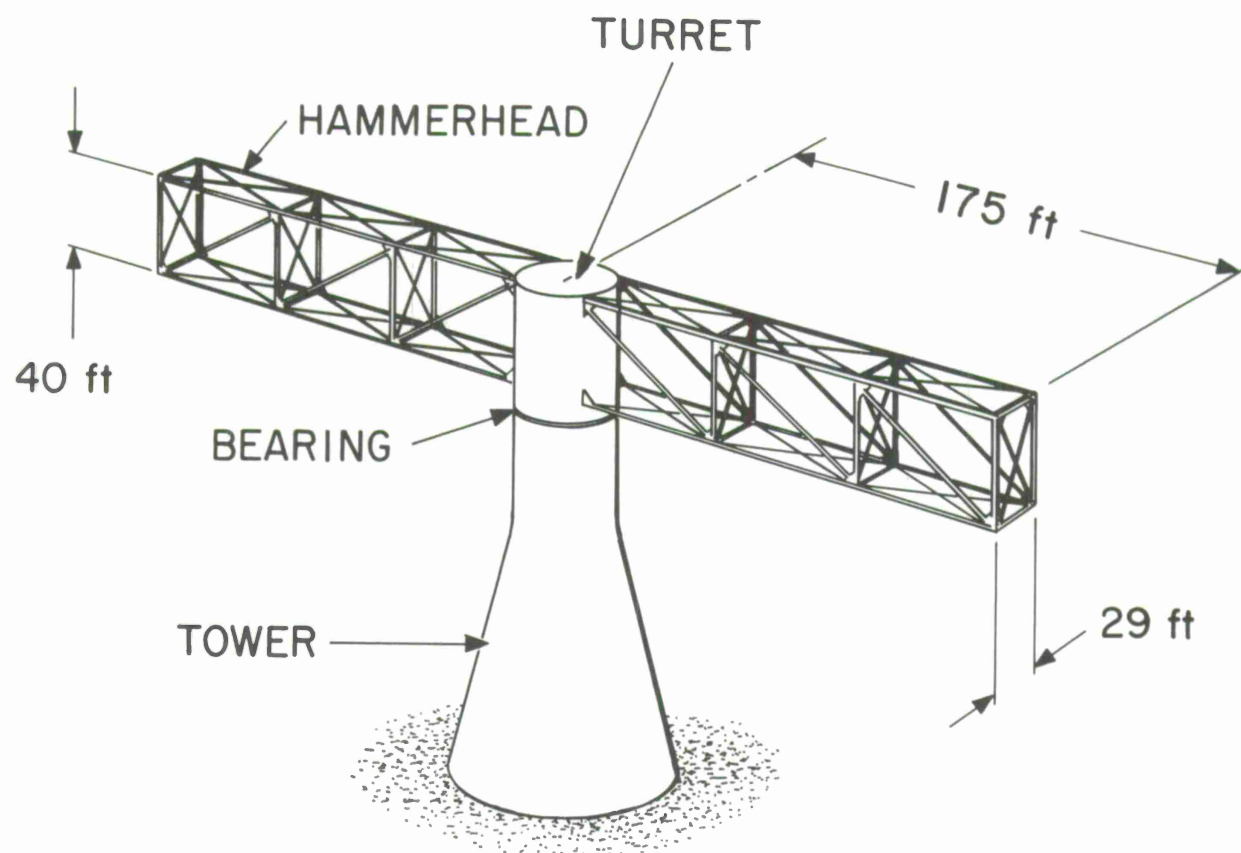


Figure 14. Hammerhead truss.

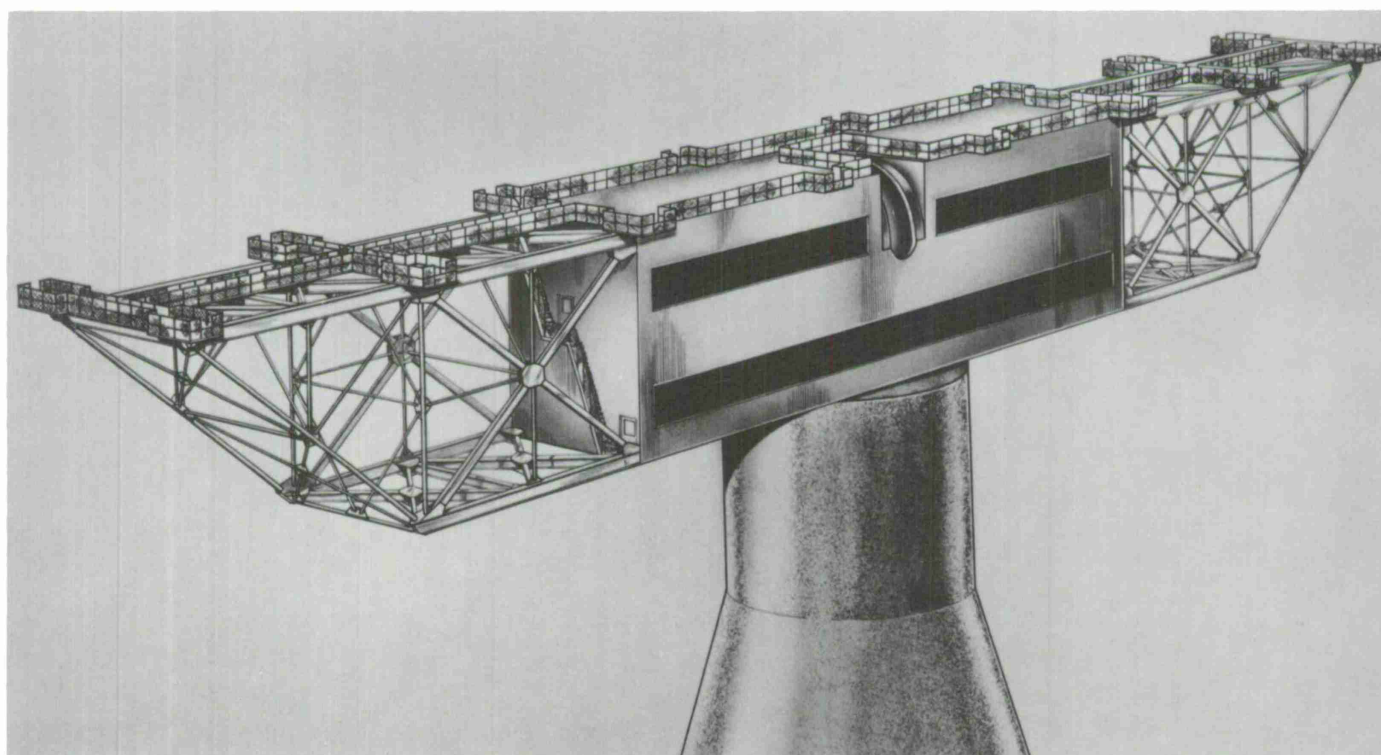


Figure 15. Hammerhead truss, showing possible laboratory behind antenna.

Since structural members of the Hammerhead are structural steel shapes or steel pipes and the layout is orthogonal, this part of the structure lends itself to standard building or bridge construction and some economy will be realized. Additional economy of weight and cost can be gained by reducing the laboratory space in the Hammerhead.

5.7 Turret

Eight structural concepts of the turret were studied. In the original one, a reinforced concrete turret shown in Figure 16, the hydrostatic bearings were mounted on the tower, with the track integrally built into the turret, running on top of the hydrostatic bearings. A change in concept, making the hydrostatic bearings part of the turret instead of the tower and making the track part of the tower instead of part of the turret, allowed four concentrated loads to be applied from above through the hydrostatic bearings, thus evolving a more efficient design.

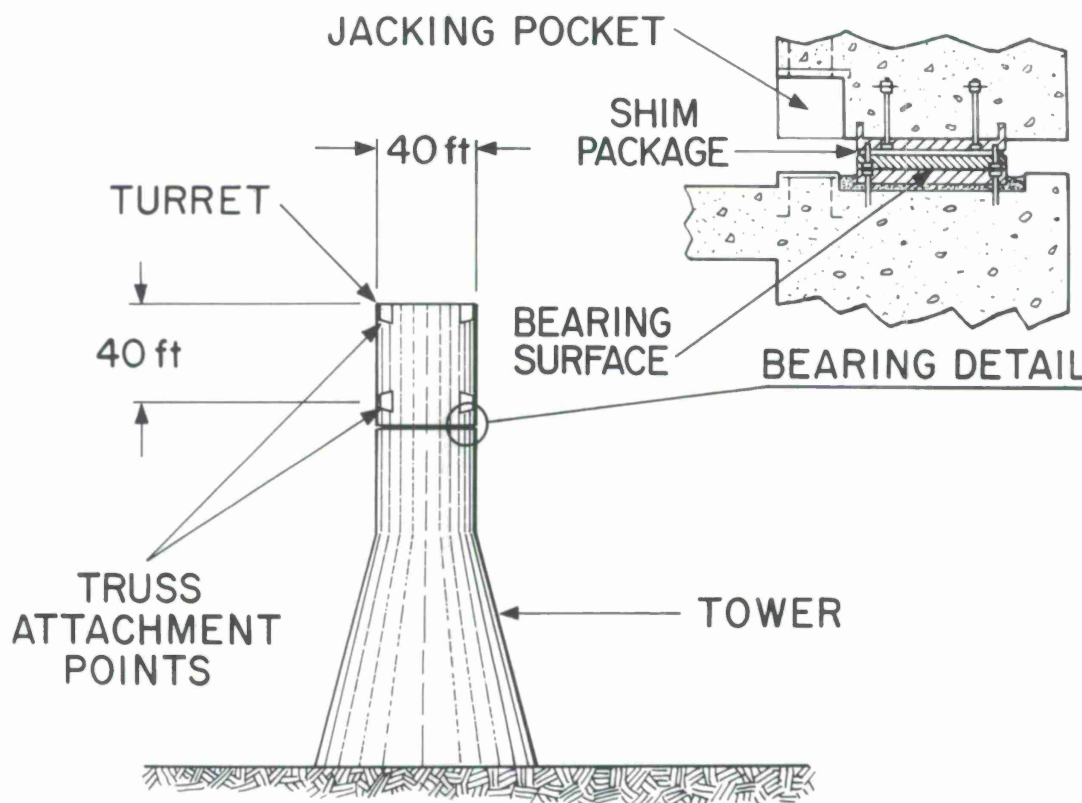


Figure 16. Concrete turret.

Figure 17 shows a schematic outline of the structural steel frame of the turret. Members in the rear faces are omitted for clarity. The four points at the base will be supported by hydrostatic bearings, and the Hammerhead truss ends will be attached to each side at the upper corners and lower support points. The slot in the upper front face

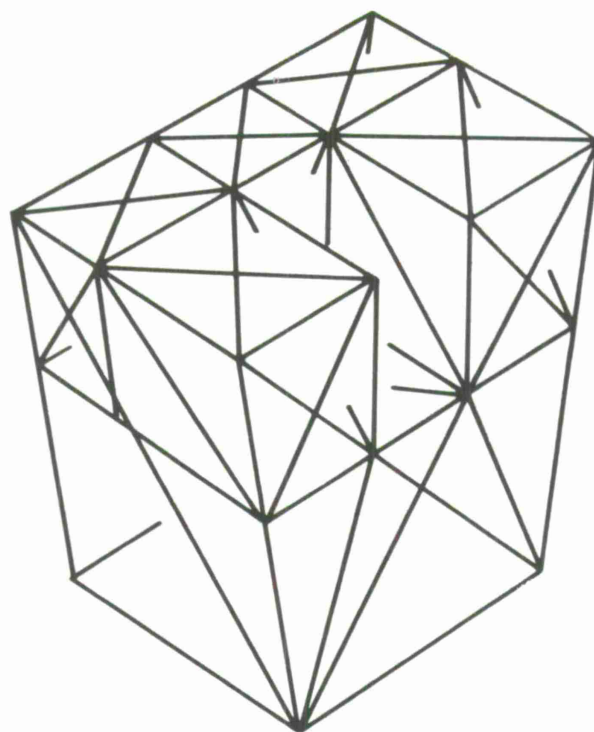


Figure 17. Isometric outline drawing of turret of Hammerhead antenna.
Slot at front is for feed horn.

will allow the feed horn to project through the turret and rotate in elevation with the reflector. Ample space is provided inside the turret, consisting of two or more floors for up to eight separate RF systems that can be plugged in without hoisting boxes up into the antenna.

The turret was analyzed using the STIFFEIG computer program to determine stiffness characteristics, and a simplified model was designed to have similar characteristics. This simplified model was combined with the Hammerhead to form the computer model shown in Figure 18. Lumped inertias representing the vertical trusses, surface construction, counterweights, and Hammerhead truss were added to the model, and it was run through the STIFFEIG program for a frequency analysis.

The lowest mode of frequency calculated for this model was 1.26 cps. This frequency will be reduced when flexibilities of drives, tower, and soil are included, and it appears that the resulting system frequency will be above 0.1 cps.

Deflection at the tip of the Hammerhead due to azimuth drive acceleration of $0.04^\circ / \text{sec}$ was calculated to be 0.01 inch, using the same model with applied loads representing the inertial loading.

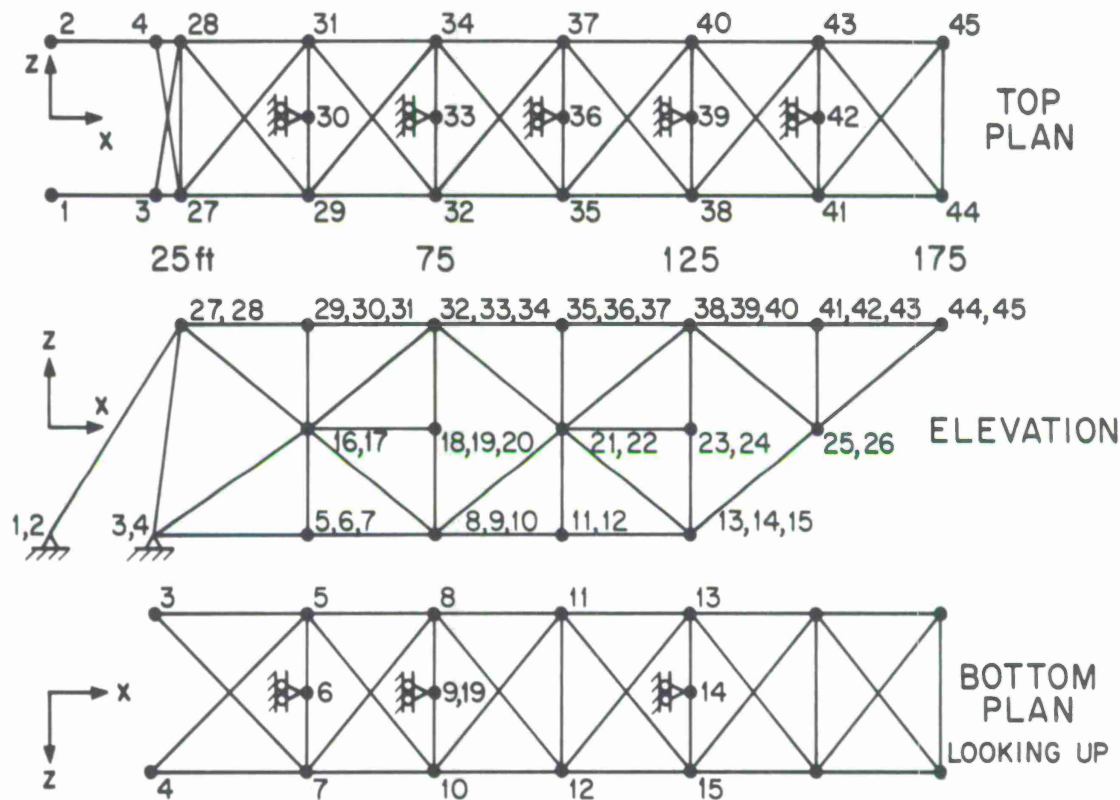


Figure 18. Computer model of Hammerhead truss and turret.

5.8 Tower

Studies of concrete versus steel towers for supporting large radars at moderate heights have generally concluded in favor of concrete for stability and thermal motion. Since the height of the tower for this concept is about that of a 13-story building, which is commonly built of concrete, it is assumed that this will be a logical choice of material.

Use of the tower for laboratory space will result in some overall economy. Elevators necessary for access to the antenna will also be used for access to the laboratory.

Figure 19 shows a possible design for a concrete tower. This design provides a 20-ft-high bay at the base to allow truck delivery of material to the elevator; above are stories with 10-ft ceilings. Total floor area inside the tower will be 61,000 ft². Of this available space inside the tower, it is estimated that 30,000 ft² will be finished laboratory space with air conditioning, heating, ventilating, acoustical-tile ceilings, asphalt-tile floors, and movable metal partitions. The remaining 31,000 ft² will be available for a machine shop, mechanical-equipment storage, and other storage use; the floors, walls, and ceilings of this part will be finished concrete. For comparison, the Haystack office and laboratory space has 4000 ft², computer areas 9000 ft², and mechanical-equipment areas 8000 ft².

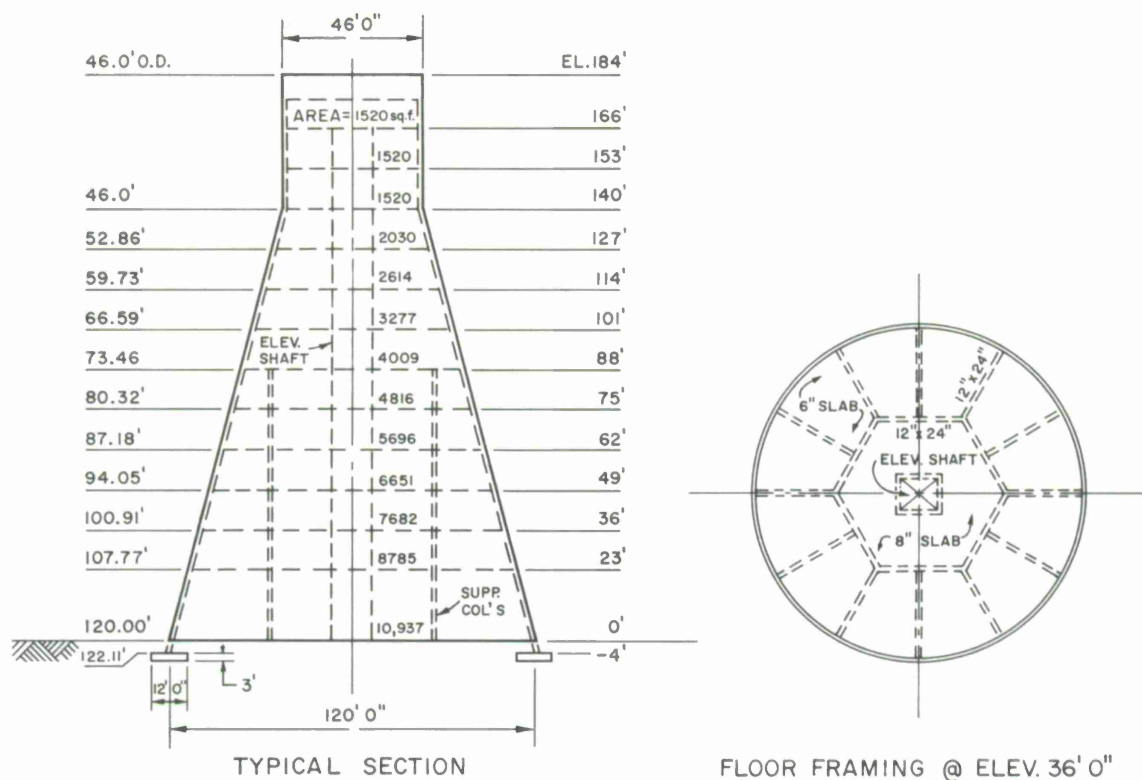


Figure 19. Concrete tower for Hammerhead antenna, showing cross section and typical floor framing, with floor elevations and areas.

Tower wall thicknesses of 6 and 12 inches were investigated. Although system mechanical frequency may dictate wall thickness, the comparison below indicates possible designs.

	<u>6-inch walls</u>	<u>12-inch walls</u>
Total concrete in tower	3200 yd ³	4100 yd ³
Concrete compressive stress at elevation 138*	450 psi	250 psi
Concrete compressive stress at base of tower	500 psi	300 psi
Width of foundation ring, assuming 2-ton soil press	9 ft	12 ft

*Section was selected at top of conical section of the tower. Stress is due to dead weight of concrete plus weight of antenna on azimuth bearing.

6. MECHANICAL CHARACTERISTICS

6.1 Rotating Support Elements

The primary concern in mechanically steering a Hammerhead antenna about both its axes of motion is that of minimizing friction. For the azimuth axis, nearly frictionless rotation can be ensured by adapting fluid-film hydrostatic bearings already in existence. However, the unique configuration of the elevation axis has no precedent that is readily adaptable, and designing a nearly frictionless system here will require a concerted design effort and analysis to develop and demonstrate its feasibility.

Figure 20 is a schematic of a typical station of the eight vertical trusses rotating around the Hammerhead truss and indicates that the rotating surfaces between the trusses and the support element are designed to contact each other at a 26-ft radius. Forces opposing rotation at this radius must be minimized so that as few restraints as possible are imposed on the drive system and its controls. To sustain this principle, a film of oil under pressure will be introduced between the sliding surfaces of the two elements. A design study undertaken to determine the feasibility of this concept had the following program objectives:

- 1) Establish oil-film requirements, including allowable variations in film thickness, oil-flow recess pressure, and power requirements.
- 2) Design preliminary pad and runner with possible schemes of pad configurations. Stability of these designs must be ensured.
- 3) Determine load distribution and distortions of runner. Compare results with requirements established in 1) and 2) above.
- 4) Consider fabrication and machining.
- 5) Consider installation and alignment of pads and runners.
- 6) Design basic hydraulic circuits, including subsystem components.
- 7) Make a preliminary cost estimate.

The services of Professor D. D. Fuller of Columbia University were solicited in this program, and his contributions have been most helpful. Although the program is still under way, enough progress has been made to report the following items:

1) Table 1 illustrates the film requirements for both elevation- and azimuth-bearing configurations. A variation of 20% in film thickness was established as maximum.

2) A pad configuration utilizing articulated pad surfaces as shown in Figure 20 was necessary in order to realign each pad for in-plane distortions of the runner surface. These distortions pertain to out-of-roundness of runner, assembly inaccuracies, and deflections of the runner as it rotates from 0° to 90° . Ring distortions were analyzed

by STIFFEIG for various elevation angles at each of the node points of the complete ring girder supporting the runner. Beam analysis was used to determine deflections between node points. Out-of-plane distortions (twisting of runner) will be held within design limits (loads are symmetrical and machining is within tolerance) and will not require any realignment.

3) By demanding a near equalization of the load on the two pad assemblies and by maintaining this load directly over the center of rotation, the stability of the antenna is ensured. This requires balancing the system for elevation rotation within a reasonable tolerance, once the center of mass of the reflector assembly has been made to coincide with the center of rotation.

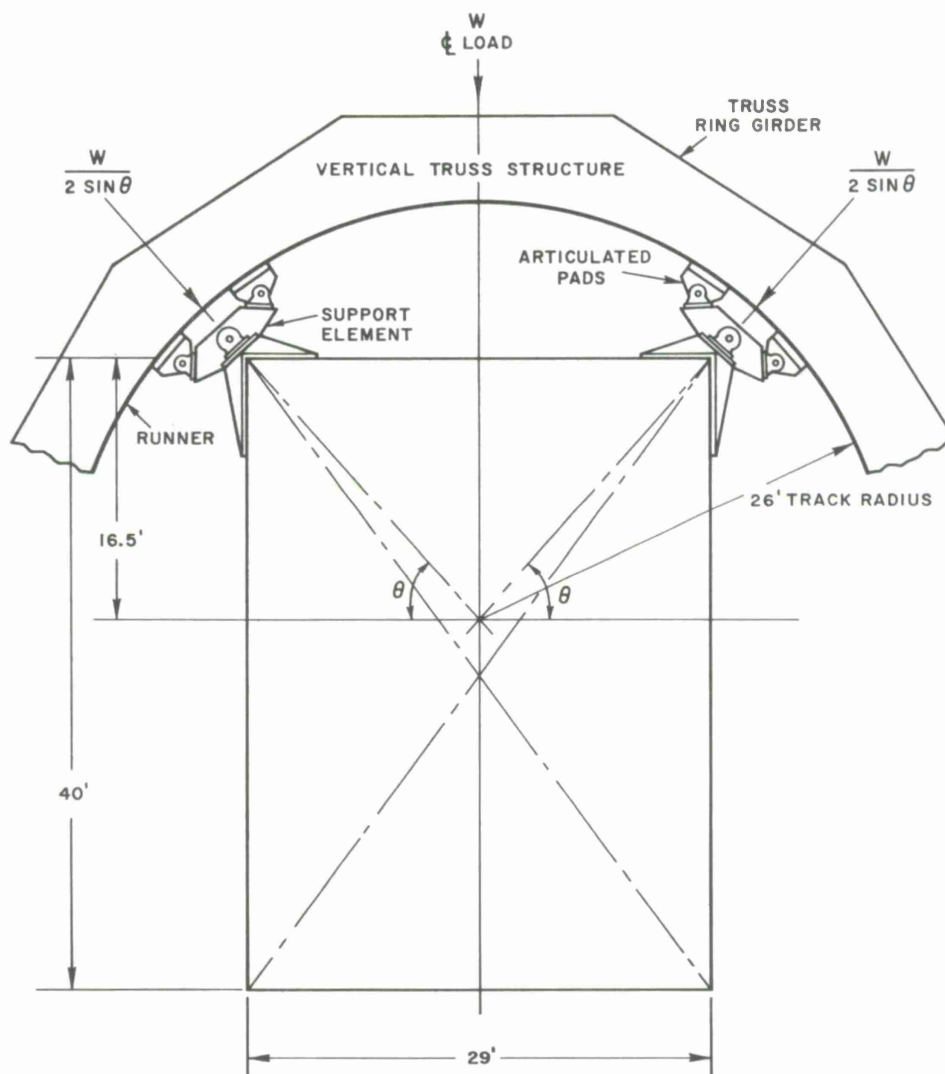


Figure 20. Elevation hydrostatic-bearing configuration.

Table 1. Preliminary design requirements for azimuth and elevation hydrostatic bearings

	Elevation	Azimuth
Total rotating weight	941 tons	1650 tons
Maximum pad load	175,000 lbs	825,500 lbs
Film thickness	0.010 inch	0.010 inch
Operating pressure	200-400 psi	500-600 psi
Flow rates/pad	Varies at each station	33 gpm
Total flow	140 gpm/16 pads	135 gpm/4 pads
Established total hp required	40-50	75-100

Computer studies are in progress to determine the possibility of designing deflection-mated surfaces for the runner and the pad for the elevation bearing. The objective here is to allow the runner and the pad to distort in concert with each other without exceeding the allowable variation of film thickness. A first cut at a grid-analogy investigation of a deflection-mated hydrostatic bearing for the elevation axis has been completed. The results are presented in Section 7 of this report. This approach, if successful, could result in the savings of many tons of steel that would have been required to produce the stiffness of a conventional-type bearing.

A second approach, utilizing a compliant surface in the pad, will be investigated to determine its feasibility for the elevation assembly only.

4) A cursory look at the elements comprising these systems indicates no unreasonable machining problems. Computer-controlled machines may be required to machine the sections that make up the length of runner.

5) Installation and alignment of the pad assemblies can be accomplished with optical means. The deflection of the Hammerhead truss, due to the dead weight of the structure, can be accounted for by cambering the truss or by simulating the reflector-assembly weight and removing an equivalent load of the parts as they are installed. Once initial alignment is achieved, and with theoretically no change in loading condition as the antenna rotates, the initial alignment should remain unaffected. Thermal considerations have not been evaluated, but in the rather controlled environment of the radome this should not present any major problem.

6) Figures 21 and 22 illustrate possible systems for hydraulic power supply and oil return for these elevation hydrostatic bearings. The basic hydraulic circuit illustrates a redundant system designed to supply continuous oil if the initial system fails during operation. Such a system, if sequenced properly, should increase system reliability. An alternate method featuring a direct supply from a pump to opposite recesses without any restrictions is under study. The return circuit is a two-stage system that utilizes a vacuum return to collect the major volume of oil and a gravity return to collect residual oil on the runner and that oil, if any, escaping the first return system.

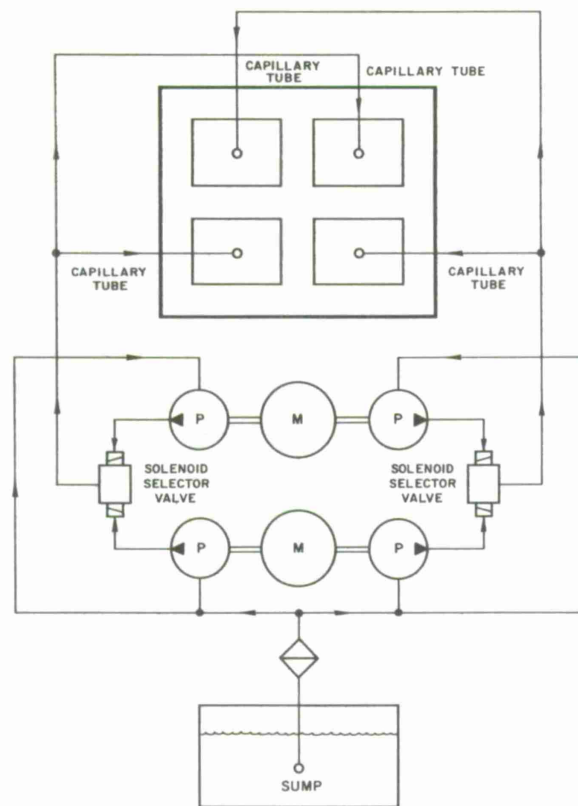


Figure 21. Schematic pressure-supply typical pad.

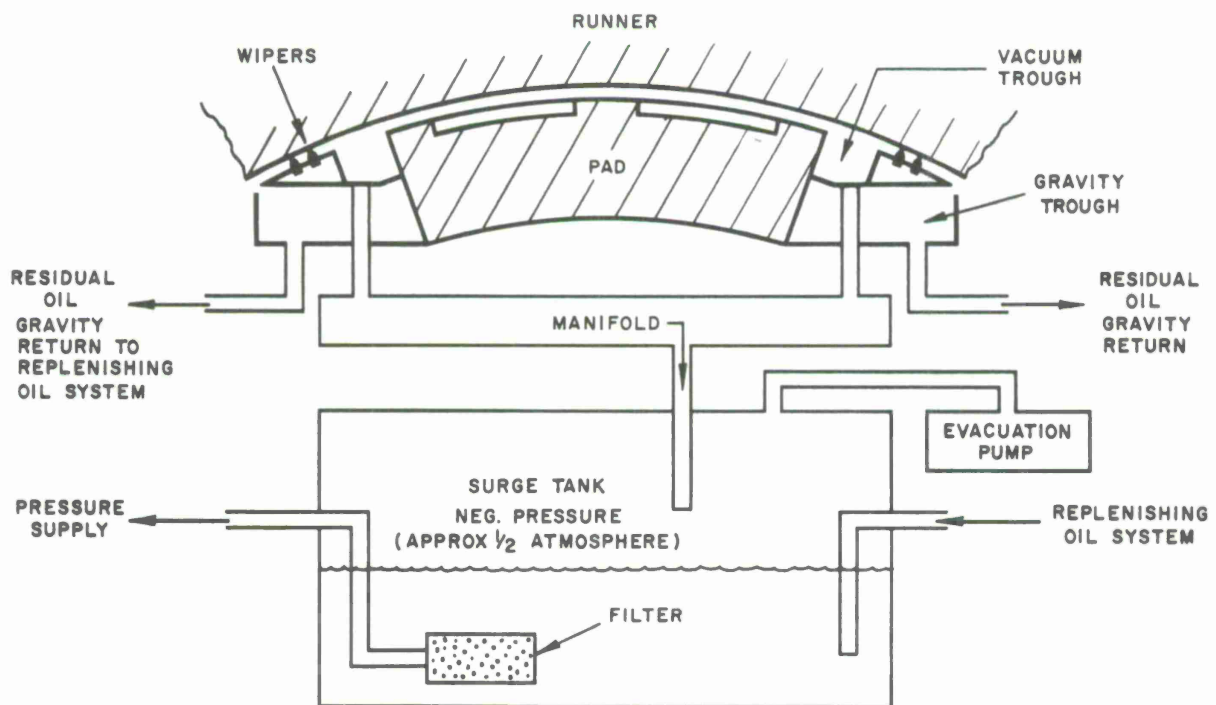


Figure 22. Typical elevation-pad schematic - a proposed oil-return system.

That the study to date has not uncovered any major problem areas indicates that the present design appears to be feasible, and that preliminary design and test programs should be undertaken.

The azimuth hydrostatic-bearing configuration, Figure 23, is a four-pad thrust bearing and is merely an application of bearing designs already in existence. No significant problem areas requiring further study are envisioned at this time. The radial loads will be reacted by either a fluid-film bearing or an antifriction bearing, neither of which should present any problems for immediate investigation.

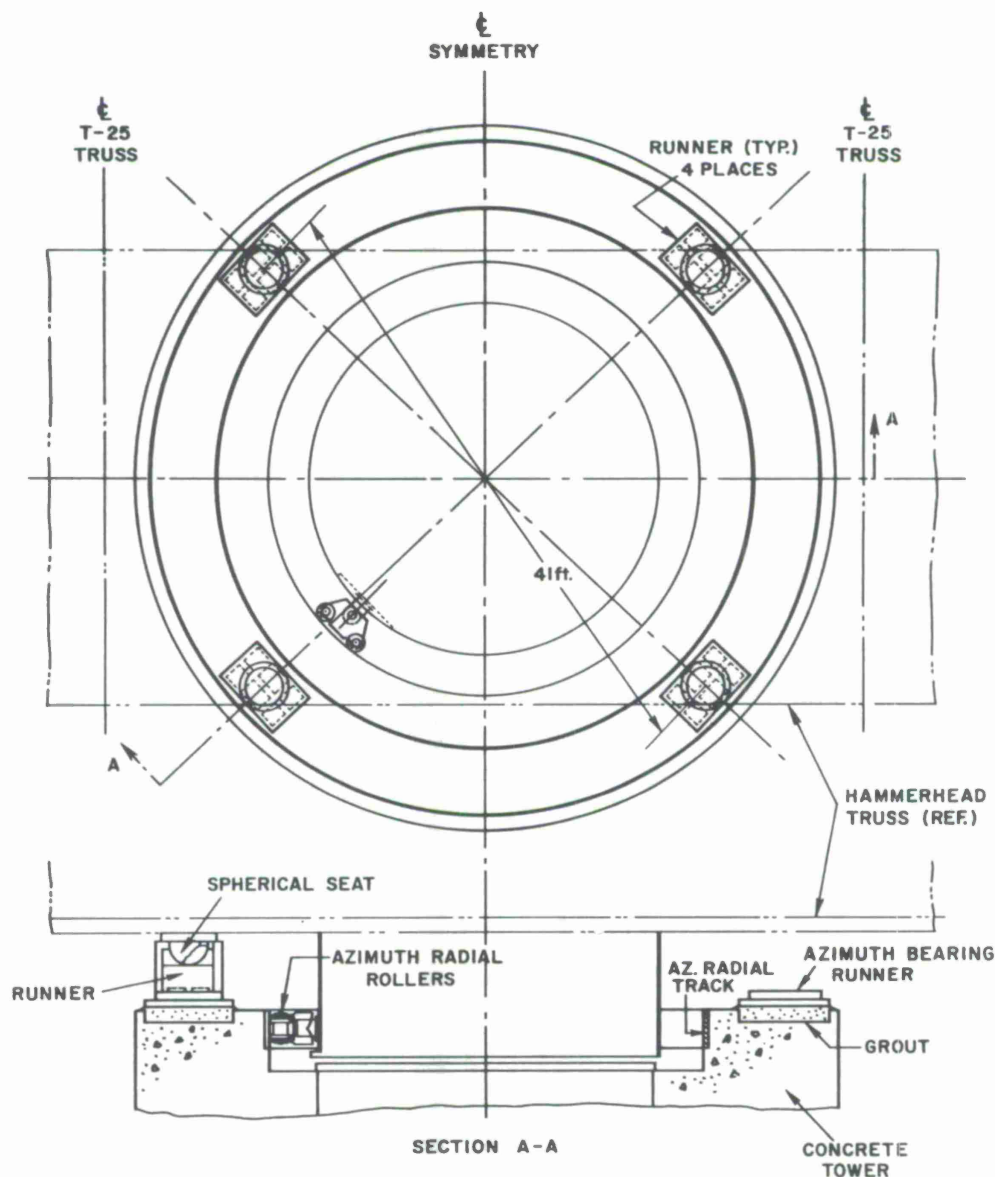


Figure 23. Azimuth hydrostatic-bearing configuration.

6.2 Drive Systems

Utilizing the principle of fluid-film bearings on both axes of motion has provided us considerable latitude in the design of the drive systems. The drive-system parameters are shown below:

	Track	Slew
Azimuth velocity $\dot{\theta}_{az}$	0.1°/sec	0.6°/sec
Elevation velocity $\dot{\theta}_{el}$	0.005°/sec	0.3°/sec
Azimuth acceleration $\ddot{\theta}_{az}$	0.0001°/sec ²	0.05°/sec ²
Elevation acceleration $\ddot{\theta}_{el}$	0.00001°/sec ²	0.025°/sec ²
Servo bandwidth (both axes)	0.002 cps	
Tracking error	0.003°	
Pointing accuracy	0.004°	
System mechanical resonant frequency	0.01 cps	

The drive system in this study is not optimized, since final selection would be determined by more detailed studies where performance can be evaluated more critically and economic trade-offs can be appraised more judiciously.

The ideal servo drive is that type of system where gear grains are eliminated between the load and prime movers, and viscous friction is the only form of friction to contend with. The direct-drive torque motor most nearly approaches this ideal and would be most applicable except for the fact that 50-ft-diameter torque motors do not exist. However, one can approach this type of drive in Hammerhead by inserting a single gear mesh between a torque motor and the elevation axis. This gear reduction, in the case of Hammerhead, consists of a 50-ft pitch-diameter internal bull gear, affixed to the two T25 trusses, and meshing with 8-inch pitch-diameter pinions. The eight trusses will be structurally coupled with a space-frame torque tube of proper stiffness. Figure 24 is a schematic representation of such a drive configuration. The two drive assemblies shown at each of the two T25 stations will be designed to operate with about a 10% bias torque for eliminating backlash. Each of the drive assemblies consists of two DC torquers on either side of the pinion for increased stiffness, reducing the physical size of the torquers and simplifying the design of the drive package. Figure 25 illustrates a typical elevation drive package.

To accommodate any bull-gear pitch-diameter perturbations resulting from runouts of gearing or distortion on ring truss, adaptive drives will be required and are illustrated in Figure 25. The rollers will ensure gear-tooth contact for any variation. The gear web must be compliant to allow the bull gear to align itself for any angular misalignment. The pivot for the drive will permit the assembly to rotate and accommodate any radial runouts. The drive assembly described above may be necessary for the

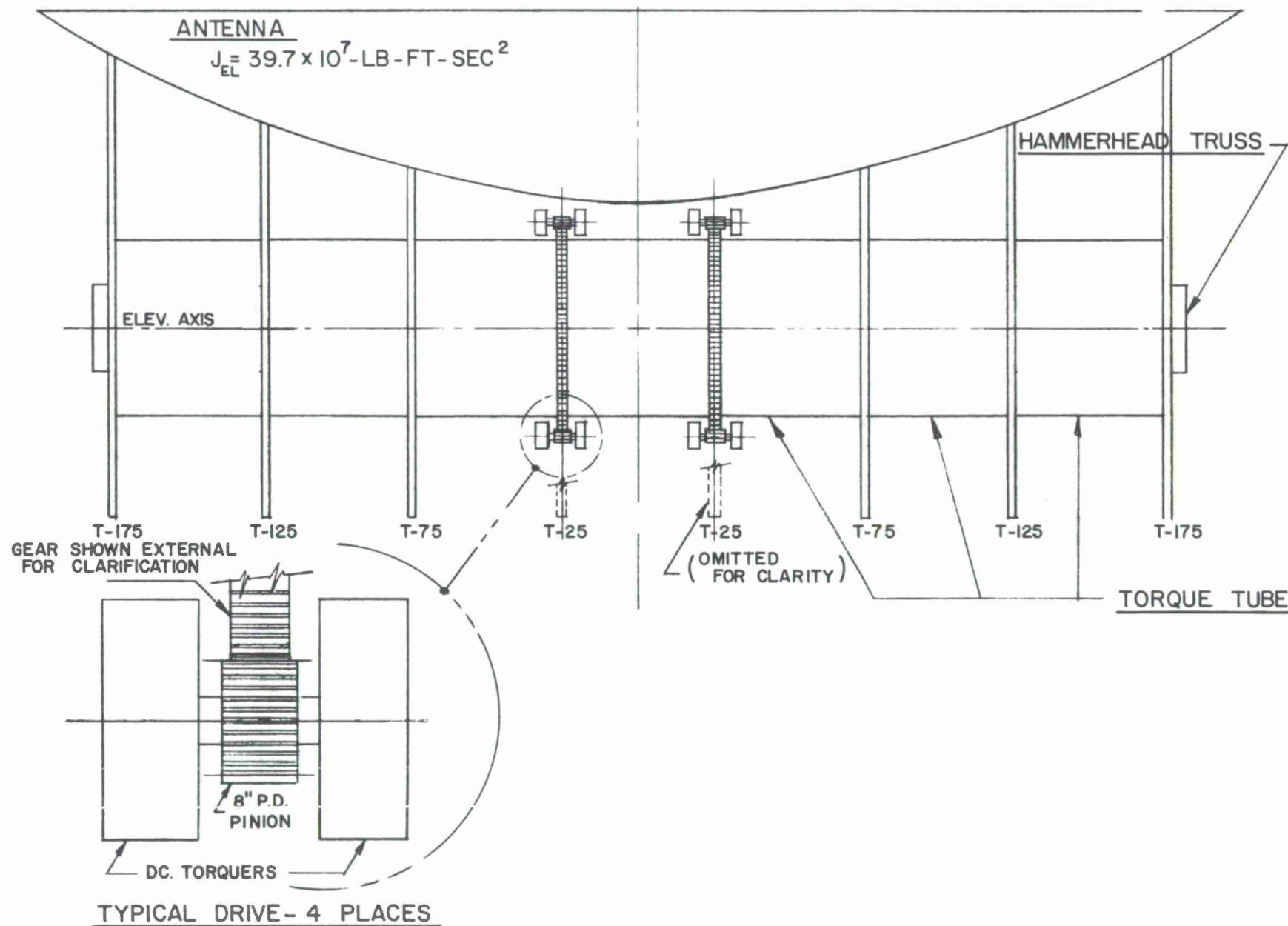


Figure 24. Schematic - elevation drive.

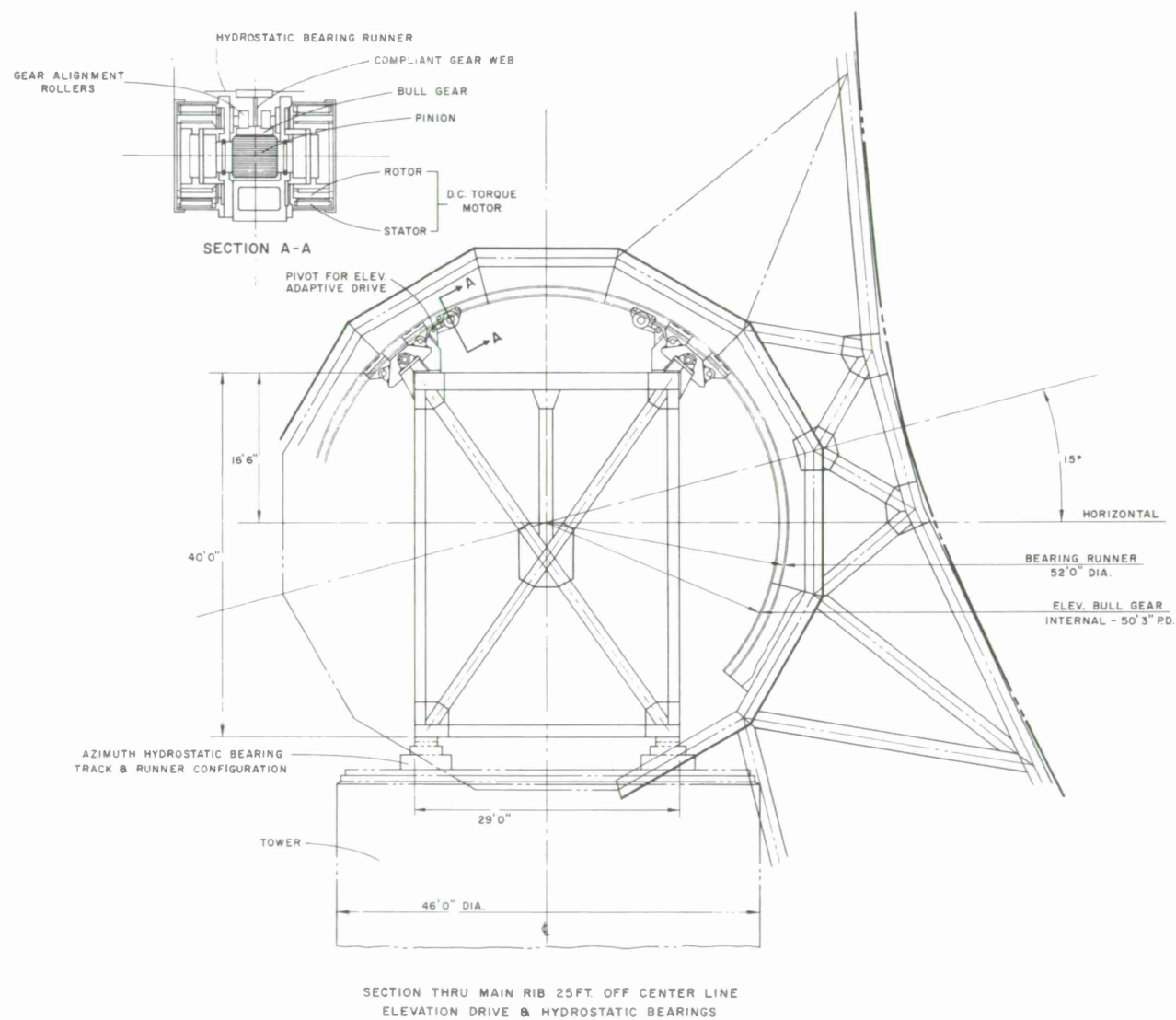


Figure 25. Elevation-drive and hydrostatic bearings.

azimuth drive. If the azimuth bull gear (30-ft pitch-diameter) can be machined with sufficient accuracy, it may be possible to eliminate the bias torque and use the DC torque arrangement above by itself.

The torque requirements for both drives are shown below.

Elevation Drive

$$\text{Slew Mode } \ddot{\theta} = 0.025^\circ/\text{sec}^2,$$

$$T_T = T_U + T_A + T_B,$$

where T_U = unbalanced antenna, T_A = acceleration torque, T_B = bias torque, and T_T = peak torque.

T_U , unbalanced antenna

Counterweights totaling 591,000 lbs will be required to "trim" the antenna. If each of the eight counterweights were trimmed to a precision of 50 lbs, it would introduce an unbalance of the antenna of 25,000 ft-lb. Although this unbalance may be decreased, these calculations will proceed as though the unbalance actually exists.

$$T_U = 25,000 \text{ ft-lb.}$$

T_A , acceleration torque

$$T_A = T_I + T_R + T_F,$$

$$T_I = J\ddot{\theta},$$

$$= 39.7 \times 10^7 \times \frac{0.025}{57.3}$$

$$= 174,500 \text{ ft-lb,}$$

where T_I = load inertia, T_R = rotor inertia, and T_F = viscous friction.

Using a DC torque motor

$$J_R = 3.1 \text{ lb-ft-sec}^2 \text{ (8 motors)}$$

$$T_R = J_R N_G^2 \ddot{\theta} \times 8$$

$$= 3.1(75)^2 \left(\frac{0.025}{57.3} \right) 8$$

$$= 65 \text{ ft-lb,}$$

$$T_F = 16 \text{ hydrostatic bearings},$$

$$T_F = F \times 26 \times 16,$$

$$F = \text{viscous friction}$$

$$\begin{aligned}
 F &= \mu A \frac{dv}{dh} \\
 &= \frac{271 \times 10^{-7} \times 784 \times 0.815}{0.010} \\
 &= 1.73 \text{ lbs}
 \end{aligned}$$

$$\begin{aligned}
 T_F &= 1.73 (26) (16) \\
 &= 720 \text{ ft-lbs} ,
 \end{aligned}$$

$$\begin{aligned}
 T_A &= 174,500 + 65 + 720 \\
 &= 175,285 \text{ say } 175,300 \text{ ft-lbs} ,
 \end{aligned}$$

T_B - bias torque (10% of peak torque)

$$\begin{aligned}
 T_B &= 0.1 (T_A + T_U) = 0.1 (175,300 + 25,000) \\
 &= 20,000 \text{ ft-lbs} ,
 \end{aligned}$$

$$\begin{aligned}
 T_T &= T_U + T_A + T_B \\
 &= 25,000 + 175,000 + 20,000 \\
 &= 220,000 \text{ ft-lbs} .
 \end{aligned}$$

Torque available - DC torquer - 375 ft-lbs

$$T = 375 \times 75 \times 8 = 235,000 \text{ ft-lbs} .$$

Maximum speed of torquer

$$\begin{aligned}
 N_M &= \frac{0.3}{360} \times 60 \times 78 \\
 &= 0.05 (78) = 3.9 \text{ RPM} .
 \end{aligned}$$

Azimuth Drive

$$\text{Slew Mode } \ddot{\theta} = 0.05^\circ / \text{sec}^2 ,$$

$$T_T = T_A + T_B ,$$

$$T_A = T_I + T_R + T_F ,$$

$$\begin{aligned}
 T_I &= J \ddot{\theta} = 80.0 \times \frac{0.05}{57.3} , \\
 &= 700,000 \text{ ft-lbs} .
 \end{aligned}$$

Using DC torque 3,000 ft-lbs

$$J = 26 \text{ ft-lb-sec}^2 - 4 \text{ motors} ,$$

$$\begin{aligned}
 T_R &= J_R N_G^2 \times 4 , \\
 &= 26 (60)^2 \frac{0.05}{57.3} \times 4 \\
 &= 330 \text{ ft-lbs} .
 \end{aligned}$$

$$\mu = 271 \times 10^{-7} \text{ Reyn SAE oil 20 at } 60^\circ \text{F}$$

$$A = 784 \text{ square inches}$$

$$V = V_{av} = \frac{0.3}{2} = 0.15$$

$$h = 0.010 \text{ inch}$$

$$V = 2 \text{ rn}$$

$$= 2 (26 \times 12) \left(\frac{0.15}{360} \right)$$

$$= 0.815 \text{ inch/sec}$$

$$T_F - 4 \text{ hydrostatic bearings} = 271 \times 10^{-7} \text{ Reyn SAE 20 oil at } 60^\circ \text{ F}$$

$$T_F + F \times 26 \times 4$$

$$\begin{aligned} F &= \mu A \frac{dv}{dh} \\ &= \frac{271 \times 10^{-7} \times 2400 \times 1.25}{0.010} \\ &= 6.95 \text{ lbs} \end{aligned}$$

$$A = 2400 \text{ ft}^2$$

$$V = V_{av} = \frac{0.6}{2} = 0.3 \text{ V/sec}$$

$$\begin{aligned} V &= 2\pi rn \\ &= 2\pi \times 20 \times 12 \times \frac{0.3}{360} \\ &= 1.25 \text{ inch/sec} \end{aligned}$$

$$\begin{aligned} T_F &= 6.95 \times 20 \times 4 \\ &= 556 \text{ ft-lbs} \end{aligned}$$

$$\begin{aligned} T_A &= 700,000 + 330 + 556 \\ &= 700,886 \text{ ft-lbs} \\ &\approx 701,000 \text{ ft-lbs} \end{aligned}$$

T_B, bias torque

$$\begin{aligned} T_B &= 0.1 (J_A + T_U) - (10\% \text{ peak torque}) \\ &= 0.1 (701,000) \\ &= 70,000 \text{ ft-lbs} \end{aligned}$$

$$\begin{aligned} T_T &= T_A + T_B \\ &= 701,000 + 70,000 \\ &= 771,000 \text{ ft-lbs} \end{aligned}$$

Friction of radial bearing has not been considered here since its magnitude would be rather small if hydrostatic bearings are used. Relatively small (10- to 12-ft diameter) antifriction bearings with low friction and stiction torques are possible.

Available torque:

$$\begin{aligned} T &= 3000 \times 4 \times 60 \\ &= 720,000 \text{ ft-lbs} \end{aligned}$$

Speed of torquer:

$$N_M = 0.6 \times 60/360 \times 60 = 6 \text{ RPM}$$

Motor friction torque has been omitted since its effect on the total will be negligible (4 ft-lbs and 12 ft-lbs for 375 ft-lb and 3000 ft-lb motors, respectively).

The almost infinite speed range of these DC torque motors, combined with the high torque/inertia ratio, relatively low damping and friction of the motors, elimination of gear trains with their inherent backlash, and friction and stiffness parameters are among the principal reasons for selecting this method of rotating the two axes of motion.

The calculations indicate the capability of these motors to meet the maximum torque requirements (7% overload in azimuth should not present any problems).

6.3 Controls

The antenna drives, the angular position indicators, and the control system for Hammerhead will comprise a closed-loop position servo system.

The drives, as previously presented, are DC torque motors in a series-parallel arrangement for sharing torque, with torque biasing to eliminate backlash. In general, the controls for these units are more simplified than those of AC servo drive units and should be relatively straightforward to design. Maximum uncontrolled slewing operation is well within the capability of the motors, and with their almost infinite speed range, any desired tracking velocity can be acquired easily.

Position control can be achieved by any one of various readout systems, among which are digital encoders (19-bit accuracy), a master equatorial control, and an inertial guidance and control system. With these three possibilities and the relatively quiet radome environment, no difficulties are anticipated here. Final selection would be dependent upon an integrated systems analysis.

Control of the antenna will be directed by a digital computer, which will offer the experimenter a choice of various control modes such as:

- 1) Scan mode, preprogrammed or real time.
- 2) Slave mode for interferometer studies.
- 3) Auto-track mode.
- 4) Computer-programmed mode.
- 5) Manual control for pointing.

7. DEFLECTION-MATED HYDROSTATIC-BEARING INVESTIGATION

7.1 Introduction

A new application of hydrostatic-bearing design is being investigated for possible use in large antennas. (A hydrostatic runner similar to that of the Hale telescope would be prohibitive if used in the superstructure of the Hammerhead antenna.) To overcome such limitations, the deflected shapes of track and pad plates are mated, so as to fit each other within acceptable oil-film tolerances. The first investigative approach was to analyze a 1-inch strip of track and pad as beam action (see Figure 26).

The purpose of this effort is to investigate a configuration that would better approximate the behavior of the pad and track, taking into account the effects of continuity of the track and the deflectional behavior of the plates under varying hydrostatic pressure. The configuration considered is shown in Figure 27, and the computer model is shown in Figure 28.

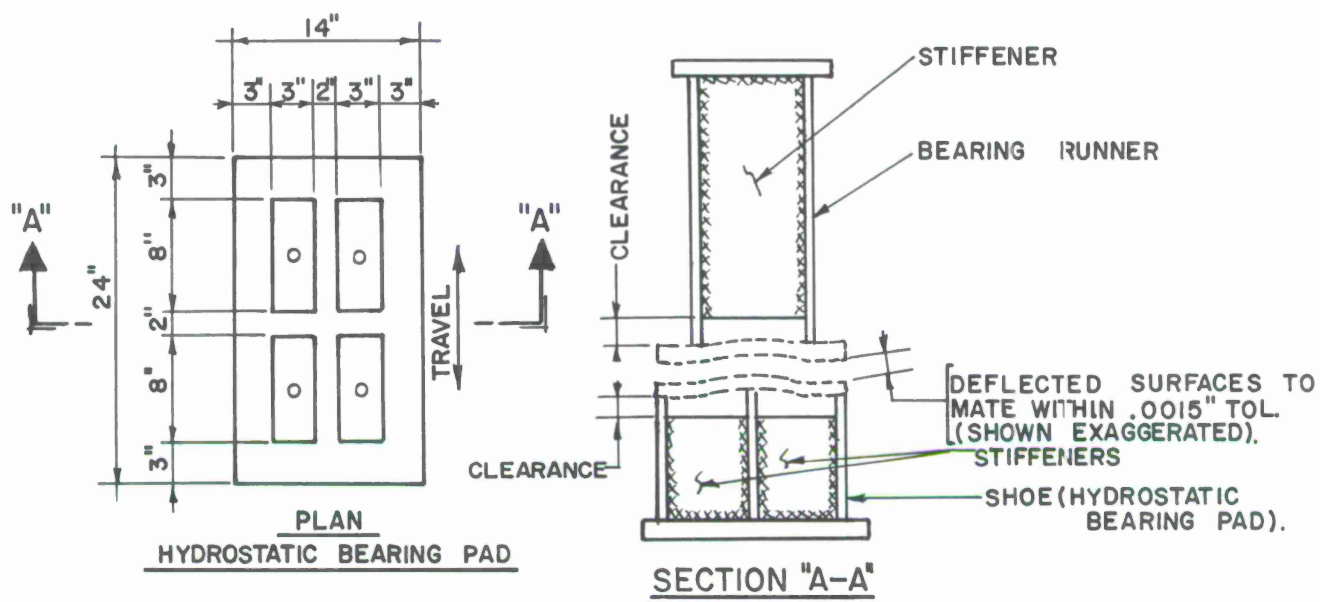


Figure 26. Deflection-mated hydrostatic bearing.

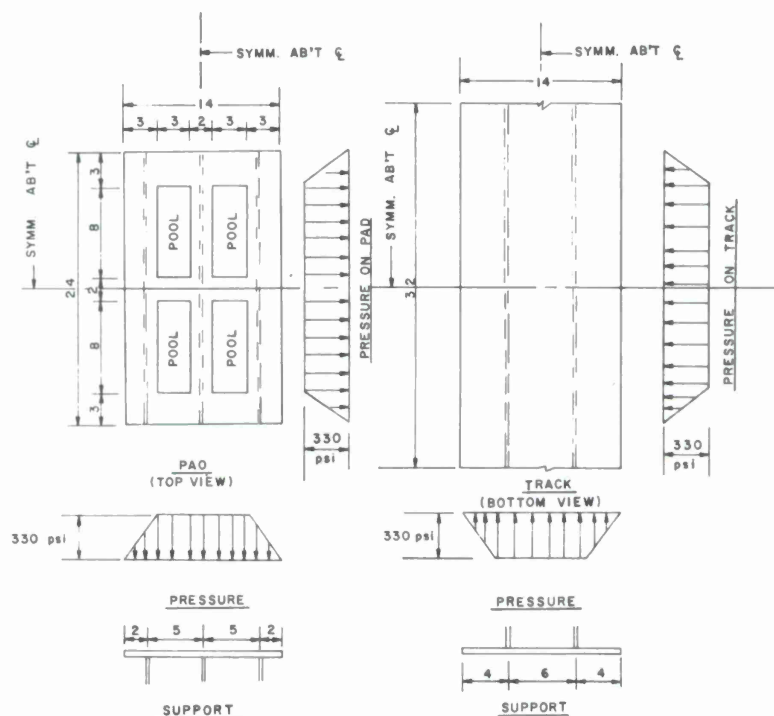


Figure 27. Prototype deflection-mated hydrostatic bearing and track.

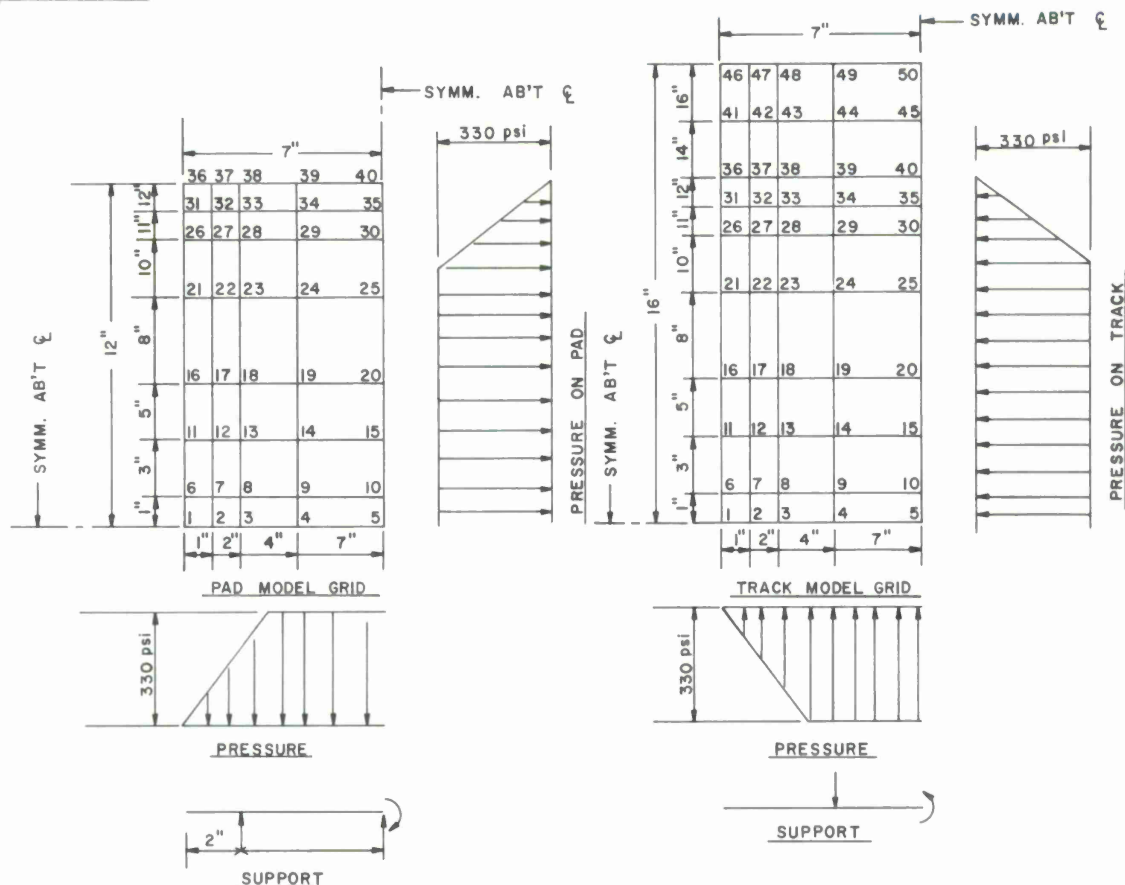


Figure 28. Computer model of deflection-mated hydrostatic bearing and track.

7.2 Conclusion

A computer-grid analysis indicates that a 0.500-inch-thick track plate coupled with a 0.705-inch pad plate will have a peripheral film-thickness deviation of 0.0016 inch under 330-psi hydrostatic pressure.

7.3 Recommendations

Try a 1/4-inch-thick track plate with 3 stiffeners, and optimize pad-plate thickness for minimum film thickness, using 4 stiffeners on pad. Investigate effects of local pressure changes due to film-thickness variation (an iterative procedure).

7.4 Method of Analysis

The models used for computer programs were planar grids consisting of bars with rigid joints. Bar stiffnesses for the grids were obtained by finding the moment of inertia of a strip of plate having a width equal to the distance between midpoints between joints on the grid, so that the overall grid stiffness would be the same as for the plate. Taking advantage of symmetry, only 1/4 of the pad and track were modeled, with appropriate edge restraints.

A STIFFEIG computer run was made for both pad and track models, assuming 1/2-inch plate thickness for both. The resulting deflections for the two models were tabulated and the film thickness at each point was computed. The deviations in thickness

at the points around the outside perimeter of the pad were considered critical, since the flow occurs between these points. Between and over pools were not considered so critical, since the oil is more stagnant at these points.

Bending of the track as a beam will occur between panel points of the vertical trusses. Deflections of the track due to this beam bending were computed and added to the deflections of the plates. Not considered were deflections of the track due to the deflections of the adjacent panel points on the vertical trusses that support the beams.

Calculation Procedure (see work sheet, Table 2)

Column 1: Joint numbers. Locations of joints are shown in Figure 28.

Column 2: Deflections of 1/2-inch track plates taken from STIFFEIG computer run. Supports are located as shown in Figure 28, at joints 4, 9, 14, 19, 24, 29, 34, 39, 44, and 49. Note zero deflections at these joints.

Column 3: Deflections of 1/2-inch pad plates taken from a separate STIFFEIG computer run. Supports at joints 3, 8, 13, 18, 23, 28, 33, and 38; also at 5, 10, 15, 20, 25, 30, 35, and 40. Note zero deflections at these joints.

Column 4: Subtract pad deflections from track deflections to obtain first pass at the film variation.

Column 5: In order to reduce the differences in deflection (film error), the pad plate is increased from 0.500 inch to 0.705 inch thick, increasing pad stiffness by a factor of 2.8. Divide column 3 by 2.8 to obtain deflections for the thicker pad plate.

Column 6: Subtract the new pad deflections from track deflections to obtain a new film error.

Column 7: In order to equalize positive and negative deviations, add a constant (-0.0016) inch to column 6.

Column 8: Considering the track as a beam, a computer run was made with two hydrostatic pads located symmetrically 1 inch each side of the beam center line, with a 2-inch space between pads. Deflections were calculated for each inch of beam, and beam deflections corresponding to joints on the grid entered in this column.

Column 9: The 24-inch-long pad will rotate to conform roughly to the beam deflection, so that its ends (if straight) touch the beam. This column gives coordinates of a straight line drawn between this 24-inch length on the deflected beam. Note that joints 36 through 40 at the edge of the pad have the same coordinates as the deflected beam, and that joints 1 through 5 have a maximum offset.

Column 10: The space between the curved beam (track) and straight pad is shown in this column, calculated by subtracting column 9 from column 8. Note that the center line of the pad (joints 1 through 5) shows maximum space between track and pad.

Table 2. Deflection-mated hydrostatic-bearing investigation work sheet showing film errors due to deflection of plates and track beam.

Points at perimeter indicated by an underline; questionable points indicated by *; points at stagnant flow indicated by () require some study.

1	2	3	4	5	6	7	8	9	10	11	12
Joint	Deflection of 1/2-inch track plate	Deflection of 1/2-inch pad plate	Film variation (both plates 1/2-inch)	Increase pad stiffness by 2.8 (pad plate will be 0.705-inch thick)	Film variation track plate = 0.500 pad plate = 0.705	Equalize plus and minus deviations (-0.0016)	Total deflection of track beam along pad	Tilted plane (straight line) along track with constant slope	Curvature of beam over pad	Film error with undeflected beam at main truss points	Film error with deflected beam at midspan
1	0.0021	0.0059	-0.0038	0.0021	0.0000	-0.0016	0.0435	0.0418	0.0017	-0.0016	<u>0.0001</u>
2	0.0011	0.0033	-0.0022	0.0012	-0.0001	-0.0017	0.0435	0.0418	0.0017	-0.0017	0.0000
3	-0.0001	0.0000	-0.0001	0.0000	-0.0001	-0.0017	0.0435	0.0418	0.0017	-0.0017	0.0000
4	0.0000	-0.0036	0.0036	-0.0013	0.0013	-0.0003	0.0435	0.0418	0.0017	-0.0003	(0.0014)
5	0.0063	0.0000	0.0063	0.0000	0.0063	0.0047	0.0435	0.0418	0.0017	0.0047	(0.0064)
6	0.0022	0.0059	-0.0037	0.0021	0.0001	-0.0015	0.0432	0.0415	0.0017	-0.0015	<u>0.0002</u>
7	0.0011	0.0033	-0.0022	0.0012	-0.0001	-0.0017	0.0432	0.0415	0.0017	-0.0017	0.0000
8	-0.0001	0.0000	-0.0001	0.0000	-0.0001	-0.0017	0.0432	0.0415	0.0017	-0.0017	0.0000
9	0.0000	-0.0038	0.0038	-0.0014	0.0014	-0.0002	0.0432	0.0415	0.0017	-0.0002	(0.0015)
10	0.0063	0.0000	0.0063	0.0000	0.0063	0.0047	0.0432	0.0415	0.0017	0.0047	(0.0064)
11	0.0024	0.0059	-0.0035	0.0021	0.0003	-0.0013	0.0428	0.0412	0.0016	-0.0013	<u>0.0003</u>
12	0.0013	0.0033	-0.0020	0.0012	0.0001	-0.0015	0.0428	0.0412	0.0016	-0.0015	0.0001
13	0.0000	0.0000	0.0000	0.0000	0.0000	-0.0016	0.0428	0.0412	0.0016	-0.0016	0.0000
14	0.0000	-0.0040	0.0040	-0.0014	0.0014	-0.0002	0.0428	0.0412	0.0016	-0.0002	(0.0014)
15	0.0064	0.0000	0.0064	0.0000	0.0064	0.0048	0.0428	0.0412	0.0016	0.0048	(0.0064)
16	0.0029	0.0056	-0.0027	0.0020	0.0009	-0.0007	0.0420	0.0405	0.0015	-0.0007	<u>0.0008</u>
17	0.0017	0.0032	-0.0017	0.0012	0.0005	-0.0011	0.0420	0.0405	0.0015	-0.0011	0.0004
18	0.0002	0.0000	0.0002	0.0000	0.0002	-0.0014	0.0420	0.0405	0.0015	-0.0014	0.0001
19	0.0000	-0.0042	-0.0042	-0.0015	0.0015	-0.0010	0.0420	0.0405	0.0015	-0.0001	(0.0014)
20	0.0065	0.0000	0.0065	0.0000	0.0065	-0.0049	0.0420	0.0405	0.0015	-0.0049	(-0.0034)
21	0.0033	0.0043	-0.0010	0.0015	0.0018	0.0002	0.0417	0.0396	0.0011	0.0002	<u>0.0013</u>
22	0.0021	0.0025	-0.0004	0.0009	0.0012	-0.0004	0.0417	0.0396	0.0011	-0.0004	0.0007
23	0.0006	0.0000	0.0006	0.0000	0.0006	-0.0001	0.0417	0.0396	0.0011	-0.0001	0.0010
24	0.0000	-0.0035	0.0035	-0.0013	0.0013	-0.0003	0.0417	0.0396	0.0011	-0.0003	(0.0008)
25	0.0055	0.0000	0.0055	0.0000	0.0055	0.0039	0.0417	0.0396	0.0011	0.0039	(0.0050)
26	0.0028	0.0032	-0.0004	0.0012	0.0016	0.0000	0.0397	0.0390	0.0007	0.0000	<u>0.0007</u>
27	0.0018	0.0018	0.0000	0.0006	0.0012	-0.0004	0.0397	0.0390	0.0007	-0.0004	0.0003
28	0.0006	0.0000	0.0006	0.0000	0.0006	-0.0010	0.0397	0.0390	0.0007	-0.0010	-0.0003
29	0.0000	-0.0018	0.0018	-0.0006	0.0006	-0.0010	0.0397	0.0390	0.0007	-0.0010	-0.0003
30	0.0033	0.0000	0.0033	0.0000	0.0033	0.0017	0.0397	0.0390	0.0007	0.0017	0.0024*
31	0.0024	0.0028	-0.0004	0.0010	0.0014	-0.0002	0.0386	0.0384	0.0002	-0.0002	<u>0.0000</u>
32	0.0015	0.0015	0.0000	0.0005	0.0010	-0.0006	0.0386	0.0384	0.0002	-0.0006	-0.0004
33	0.0005	0.0000	0.0005	0.0000	0.0005	-0.0010	0.0386	0.0384	0.0002	-0.0011	-0.0009
34	0.0000	-0.0013	0.0013	-0.0005	0.0005	-0.0011	0.0386	0.0384	0.0002	-0.0011	-0.0009
35	0.0021	0.0000	0.0021	0.0000	0.0021	0.0005	0.0386	0.0384	0.0002	0.0005	0.0007
36	0.0021	0.0025	-0.0004	0.0009	0.0012	-0.0004	0.0381	0.0381	0.0000	-0.0004	-0.0004
37	0.0013	0.0013	0.0000	0.0005	0.0008	-0.0007	0.0381	0.0381	0.0000	-0.0007	-0.0007
38	0.0004	0.0000	0.0004	0.0000	0.0004	-0.0012	0.0381	0.0381	0.0000	-0.0012	-0.0012
39	0.0000	-0.0008	0.0008	-0.0003	0.0003	-0.0013	0.0381	0.0381	0.0000	-0.0013	-0.0013
40	0.0012	0.0000	0.0012	0.0000	0.0012	-0.0004	0.0381	0.0381	0.0000	-0.0004	-0.0004

Column 11: Column 7 repeated for easy comparison. This represents the film deviation when pad is located on an undeflected part of the beam (track).

Column 12: Tabulated by adding columns 10 and 11 to show the combined film error due to beam and plate action.

Note that points around the perimeter of pad are within 0.0016 inch.

8. ERECTION

In this concept the erection of the radome and antenna are closely coupled, since the concrete tower, Hammerhead truss, and azimuth drive can be used as erection tools. The cost of scaffolding for an antenna and radome of this size can be a considerable amount, and the saving of this cost has been considered in the erection procedure. The sequence of erection shown in Figure 29 is admittedly oversimplified, but shows a general plan for erection of both the radome and antenna without a large scaffolding system.

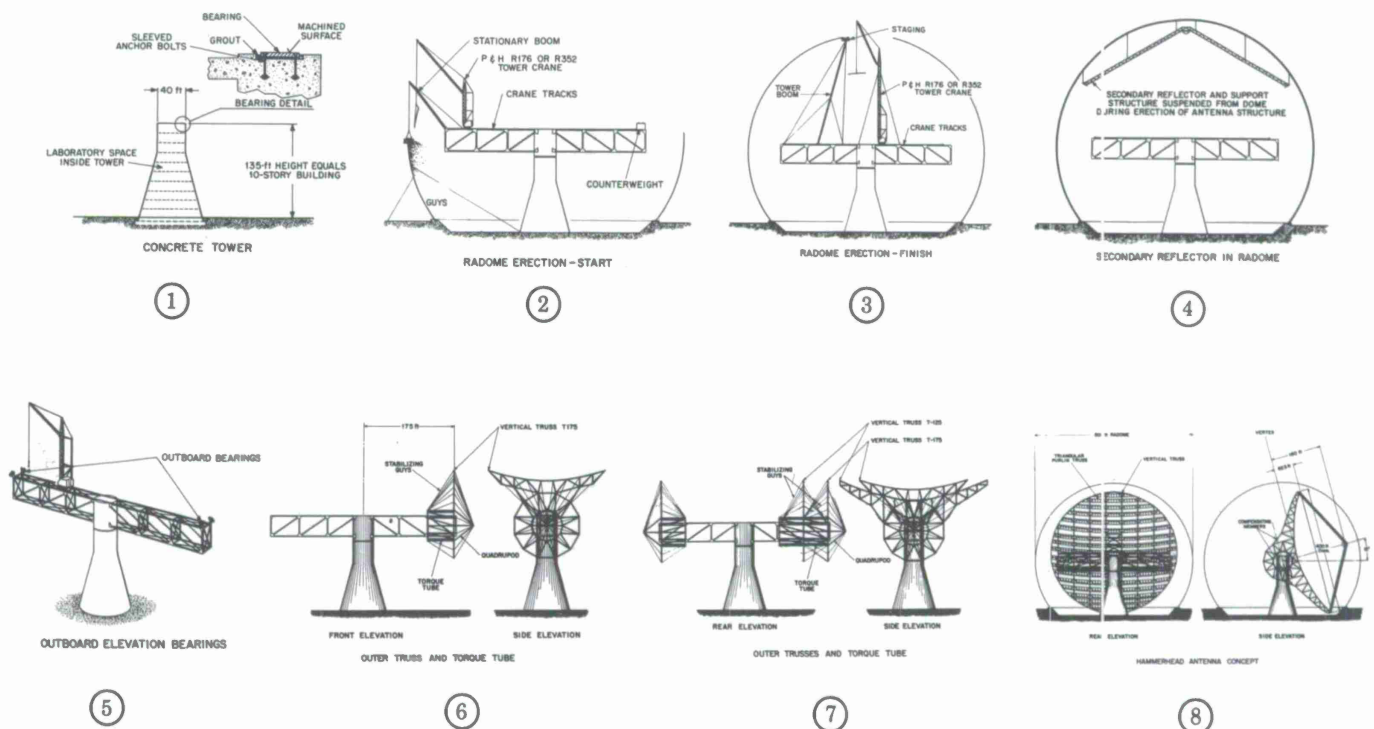


Figure 29. Sequence of erection of Hammerhead antenna and radome.

The phases of erection are as follows:

- 1) The concrete tower is erected and a track for the hydrostatic bearing is installed around the top of the tower. A radial bearing is installed at center line of the tower.

- 2) Following installation of the turret, azimuth drives, and Hammerhead structural steel frame, a standard crane is mounted on tracks that are attached to temporary beams on top of the Hammerhead. The crane can travel back and forth along these tracks, and the azimuth drive of the Hammerhead can locate the crane for erection of the radome.
- 3) A tower boom is used to support the staging for the construction of the upper part of the radome.
- 4) The secondary reflector and support structure are suspended from the dome during erection of the antenna structure. When the reflector nears completion, these will be lowered into place.
- 5) The outboard elevation bearings are installed first, and construction will progress inward toward the tower.
- 6) An outer truss and part of the torque tube are installed so that they will be a stable component when work at the other end of the Hammerhead is started.
- 7) Outer trusses at the other end of the Hammerhead are installed, and the construction effort shifts from one end of the Hammerhead to the other as construction works inward. Surface panels and purlin trusses are installed when two trusses at one end are erected. Stabilizing guys are a permanent part of the reflector.
- 8) Upon completion of reflector, the crane is lowered to the ground and all temporary tracks and supports have been removed. The secondary reflector spars are lowered into place and secured.

9. WEIGHT REDUCTION

Relocation of the counterweights to a point 126 ft from the elevation axis instead of the present 63 ft would halve the counterweights. The elevation-bearing loads would be reduced by about $1/3$, thus allowing a weight reduction in the heavy hub area of the vertical trusses and reducing distortions due to reactions of the elevation bearings. Since the vertical trusses have not changed in design since the 1.25-psf panels, a weight reduction of $1/3$ appears reasonable. The changes in weight on elevation bearings would be approximately as follows:

	Present weight (tons)	Factor	Possible weight
Surface panels	36.0	1	36.0
Purlin trusses	85.5	1	85.5
Vertical trusses	460.5	0.67	307.2
Torque tube	53.0	1	53.0
Guy strand and fittings	6.0	1	6.0
Counterweight	297.5	0.5	148.8
Secondary reflector	<u>3.0</u>	1	<u>3.0</u>
Total on elevation bearings	941.5		639.5

Loads on the Hammerhead truss will be reduced by about 1/3, allowing a comparable reduction in structural steel of Hammerhead and turret. If, in addition, the laboratory space is confined to the turret, the loading on azimuth bearing would be as follows:

	Present weight (tons)	Factor	Possible weight
Hammerhead truss	167.0	0.67	111
floors, walls, walkways	79.0	0	0
bearings	50.0	0.67	33
live load	80.0	0	0
Turret	159.0	0.67	106
floors, walls	27.0	1.25*	34
live load	<u>12.5</u>	1	<u>12.5</u>
Total Hammerhead and turret	574.5		296.5
Total on elevation bearings	941.5		639.5
Total on azimuth bearings	1516.0		936.0

* End walls must be provided.

Further, reduction in weight may be possible by reducing the Hammerhead truss in cross section, now possible with reduced loading on it. This would reduce the vertical truss hub diameter with consequent stiffening of the hub and more weight reduction of the vertical trusses and counterweights.

Since the inertias of the vertical trusses with panels and purlin trusses are not significantly reduced, and the inertias of the counterweights will be approximately doubled, it is probable that system natural frequency will limit the weight-reduction process.

A panel design weighing less than 0.5 psf can result in another downward spiral of weight, directly proportional to weight of panels.

Since the purlin trusses, like the surface panels, are part of the passive, noncompensated fill-in material between the vertical trusses, the saving in weight of the entire structure would result from reduction in weight of the purlin trusses. This weight reduction could be expressed by the relationship:

$$\text{Reduction factor} = \frac{\text{weight of panels} + \text{reduced purlins}}{\text{weight of panels} + \text{original purlins}}$$

10. WEIGHT AND COST ESTIMATE

Based on a preliminary structural analysis, a cost for the antenna was estimated. The following estimate presents the cost of this antenna, divided into four main sections:

- 1) Primary paraboloid, including the secondary dish.
- 2) Hammerhead truss.
- 3) Tower, foundation, and laboratory space.
- 4) Azimuth- and elevation-drive bearings and associated equipment.

The largest single item of cost is the fabrication and erection of the primary paraboloid. This cost was based primarily on the weight of the steel framework needed to

construct a 400-ft-diameter reflector, and the estimated weight, fabrication, and positioning cost of the aluminum surface of this reflector. It is believed that the weight used for this estimate is sufficiently conservative to allow for any minor deviations. The erection cost is based upon present high-rise building costs.

The machinery costs are based upon budgetary cost estimates from various concerns for these types of bearings and drives. The miscellaneous category includes such items as final adjustments and alignments, gravity compensation, elevators, electrical work, control systems, azimuth cable wrap (mechanical), and monitoring system for bearing and pumps. It is important to note that the following items have been excluded from the cost:

- 1) Power facilities.
- 2) Housing offices, and laboratory space in tower.
- 3) Access roads, water, and drainage.
- 4) Fire protection.
- 5) Parking and general utilities.
- 6) Communication systems.
- 7) RF equipments and associated equipment.
- 8) Computer and support equipment.
- 9) Cabling, instrumentation, and RF.
- 10) Radome costs.
- 11) Radome environmental control.
- 12) Real-estate costs.
- 13) Escalation factors due to yearly fluctuations of costs.

NOTE: Painting is not included because rust-inhibiting materials will be used.

The total antenna cost of \$8,880,000 includes engineering cost, engineering supervision, and contingency, and also includes 3000 ft² of laboratory space behind the vertex of the dish.

The following cost-estimate summary is based on Structural, Machinery, and Miscellaneous schedules, which are included.

COST-ESTIMATE SUMMARY

From structural schedule

1. Primary reflector	\$1,934,000
2. Secondary dish	100,000
3. Reflector support structures	127,000
4. Laboratory space behind reflector (3000 ft ²)	94,000
5. Tower, foundation	372,000
6. Azimuth bearing	262,000

COST-ESTIMATE SUMMARY (Cont.)

From machinery schedule

7. Azimuth drive	74,000
8. Elevation bearing	703,000
9. Elevation drive	106,000
10. Miscellaneous items	<u>1,233,000</u>
Construction Total	5,005,000
Engineering	1,250,000
Engineering supervision	850,000
Contingency 25%	<u>1,775,000</u>
Grand Total	\$8,880,000

STRUCTURAL SCHEDULE

	Weight	Cost	Subtotal	Total
1. Primary paraboloid				
a. Aluminum skin	76,500 lbs	\$ 5.00/lb	\$382,500	
b. Adjustable clips	3,000 req'd	50.00 each	150,000	
c. Steel purlins	86 tons	2,000/ton	172,000	
d. Structural steel	409 tons	1,000/ton	409,000	
e. Counterweights (concrete)	300 tons	50/ton	15,000	
f. Cables and connectors	6 tons	6,000/ton	36,000	
g. Torque tube	53 tons	3,000/ton	159,000	
h. Lifting and positioning				
(1) Structural members	892 tons	600/ton	535,200	
(2) Aluminum skin	3,000 panels	25/panel	75,000	
			Total	\$1,933,700
2. Secondary dish				
a. Estimated cost of 40-ft dish		\$92,000	\$92,000	
b. Lifting and positioning			8,000	
			Total	\$100,000
3. Reflector support structures (Hammerhead truss)				
a. Structural steel	326 tons	\$357/ton	\$122,500	
b. Adjusting			5,000	
			Total	\$127,000
4. Laboratory space behind reflector (3000 ft ²)				
a. Siding (18 tons)	7,200 ft ²	\$ 2.75/ft ²	\$19,800	
b. Floor (11 tons)	3,000 ft ²	5.25/ft ²	15,800	
c. Windows	930 ft ²	1.70/ft ²	1,600	
d. Fin, HVAC, Elect.	3,000 ft ²	19.00/ft ²	57,000	
			Total	\$94,200

STRUCTURAL SCHEDULE (Cont.)

	Area	Cost	Subtotal	Total
5. Tower, foundation				
a. Excavating and backfill	2,270 yds ³	\$ 2.75/yd ³	\$ 6,500	
b. Concrete work	3,200 yds ³	100/yd ³	320,000	
c. Bearing and drive anchorage			40,000	
d. Painting	460 square	12.50/square	6,000	
			Total	\$372,500

MACHINERY SCHEDULE

	Weight	Cost	Subtotal	Total
1. Azimuth bearing				
* a. Runner	}	-----	\$210,000	
b. Pads				
c. Pad supports				
d. Pumps	}	-----	31,500	
e. Motors				
f. Piping and controls				
g. Lifting and positioning	50 tons	\$420/ton	21,000	
	Average Cost: \$5,250/ton		Total	\$262,500
2. Azimuth drive				
a. Bull gear and support	7.5 tons	\$4,000/ton	\$ 30,000	
b. Pinions and assembly (2)			4,000	
c. Drive housing (2)			8,400	
d. Motors (4)			18,000	
e. Brakes (2)			2,000	
f. Lifting and positioning	15 tons	810/ton	12,200	
	Average Cost: \$4,950/ton		Total	\$ 74,200
3. Elevation bearings				
a. Runner	}	-----	\$600,000	
b. Pads				
c. Pad supports				
d. Pillow blocks				
e. Pad base	}	-----	53,000	
f. Pumps				
g. Piping and controls				
h. Lifting and positioning	120 tons	\$420/ton	50,250	
	Average Cost: \$5,850/ton		Total	\$703,250

* Does not rotate (25 tons).

MACHINERY SCHEDULE (Cont.)

	Weight	Cost	Subtotal	Total
4. Elevation drive				
a. Bull gear	6 tons	\$4,000/ton	\$24,000	
b. Pinions and assemblies (4)			8,000	
c. Drive housings (4)			16,800	
d. Motors (8)			36,000	
e. Brakes (4)			4,000	
f. Lifting and positioning	21 tons	810/ton	17,000	
	Average Cost: \$5,000/ton		Total	\$105,800

MISCELLANEOUS SCHEDULE

	Subtotal	Total
Final adjustment and alignment	\$300,000	
Gravity compensation (passive)	168,000	
Elevators	90,000	
Electrical work	100,000	
Control systems (azimuth and elevation drives)	350,000	
Azimuth cable wrap (mechanical)	100,000	
Monitoring system	100,000	
Buffer stop	25,000	
	Total	\$1,233,000

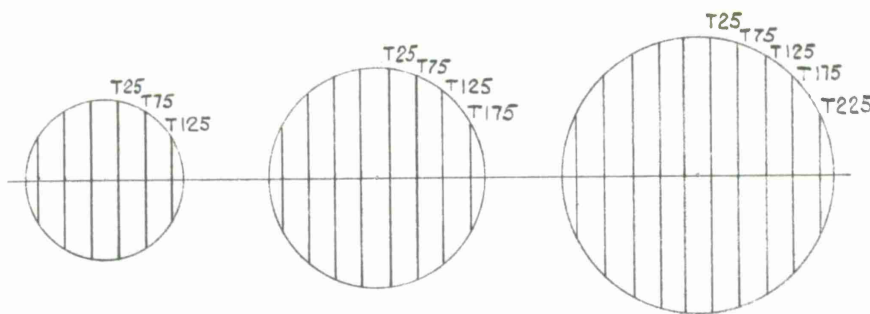
11. SIZE VERSUS WEIGHT AND COST RELATIONSHIPS

11.1 Size Versus Weight

Estimates of weight made for 300-, 400-, and 500-ft-diameter reflectors were based on each reflector's having identical panels (4 ft \times 13 ft) and purlin trusses (13 ft \times 50 ft), with vertical trusses spaced 50 ft apart along a Hammerhead. The bases for weight escalation are as follows:

Vertical trusses are considered as a series of uniformly loaded cantilevers for a stress design. Stress varies with square of length. The depth of trusses will vary directly with the length of the trusses. The length of the trusses will not vary directly with the diameter of the dish, except for trusses located at the center of the dish, as can be seen by inspection of the sketches in Figure 30. The areas and the lengths of members both vary directly with the length of truss. The weights tabulated are based, therefore, on truss-length squared. A comparison of total truss weights shows a cubic variation of weight with dish diameter.

Figure 30. Estimate of weight versus size.



	<u>300-ft diameter</u>	<u>400-ft diameter</u>	<u>500-ft diameter</u>
Vertical truss T25	99 tons	177 tons	276 tons
Vertical truss T75	59	105	177
Vertical truss T125	23	93	160
Vertical truss T175	0	85	117
Vertical truss T225	0	0	102
Surface panels	20	38	56
Purlin trusses	48	86	133
Torque tube	22	53	103
Guys and fittings	3	6	9
Counterweights	167	300	465
Secondary reflector	<u>1</u>	<u>3</u>	<u>5</u>
Total on elevation bearings	442	946	1603
Hammerhead truss and turret	137	326	636
Floors, walls (in Hammerhead)	29	29	29
Azimuth bearings and drive	22	40	62
Elevation bearings and drives	<u>50</u>	<u>89</u>	<u>139</u>
Total on azimuth bearings	680 tons	1430 tons	2469 tons

Surface panels will vary directly with the area of the dish, or with the dish-diameter squared.

Purlin trusses. Total weight will vary with the area of the dish.

Counterweights. Counterweight arm, or distance from elevation axis, will vary with the diameter. The distance from the center of gravity of the dish will also vary directly with the diameter, and the remaining variable is the weight of the surface, varying with the area. Therefore, the counterweights are assumed to vary with the square of the dish diameter.

Torque tube. The diameter of the torque tube will vary in size with the Hammerhead truss in order to provide clearance. The torsional stiffness will change as the square of the diameter if member areas remain constant, not quite matching the increase in inertia of the reflector. Since the length of the torque tube will directly affect the tip deflection, it seems reasonable to let the torque tube weight vary with the cube of the dish diameter.

Hammerhead truss. Since the length must increase in direct proportion to the dish diameter, and the loading will increase as the square of the dish diameter, the weight of the Hammerhead truss is assumed to vary with the cube of the dish diameter.

Weights of components of the antenna are tabulated in Figure 30, and curves of size versus weight are in Figure 31. It appears that the weight ratio lies between the square and the cube of the dish diameter, and at the 300- to 500-ft range, the curve shown in Figure 32 indicates that weight on azimuth bearing varies with the diameter to the 2.56 power.

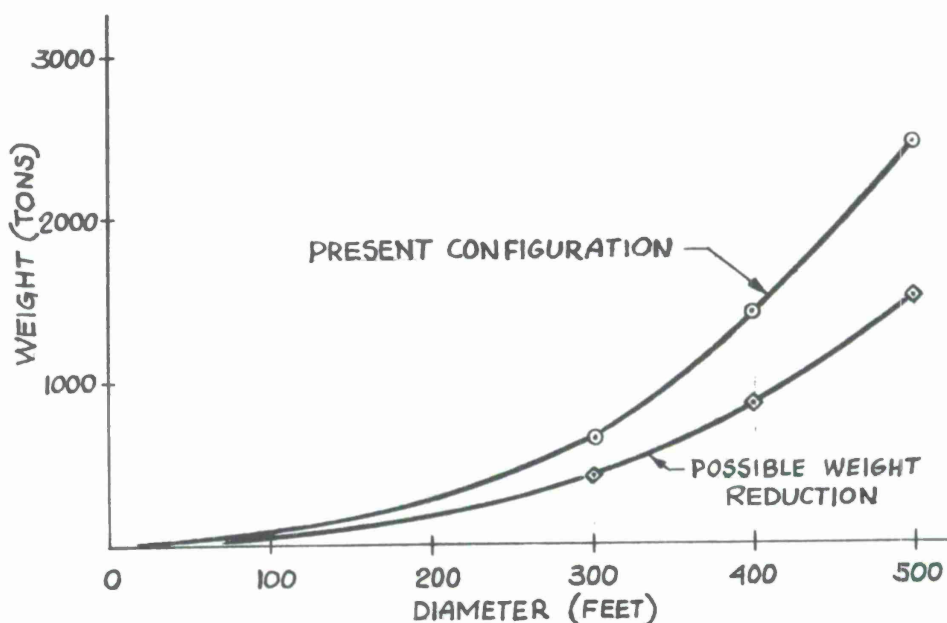


Figure 31. Curves of weight versus size of Hammerhead antenna configuration.

11.2 Size Versus Cost

Cost estimates for 300-, 400-, and 500-ft antennas with radomes of corresponding sizes are in Table 3. Not included in these estimates were RF equipment, site development, and other items excluded from the original cost estimate in Section 10. Cost escalation of components was approximately as follows:

Primary paraboloid. Cost based on weight-escalation factors.

Secondary dish. Cost based on square relationship for downward escalation, on cubic for upward.

Hammerhead truss. Cost based on weight.

Laboratory space in Hammerhead. Cost based on a constant 3000 ft².

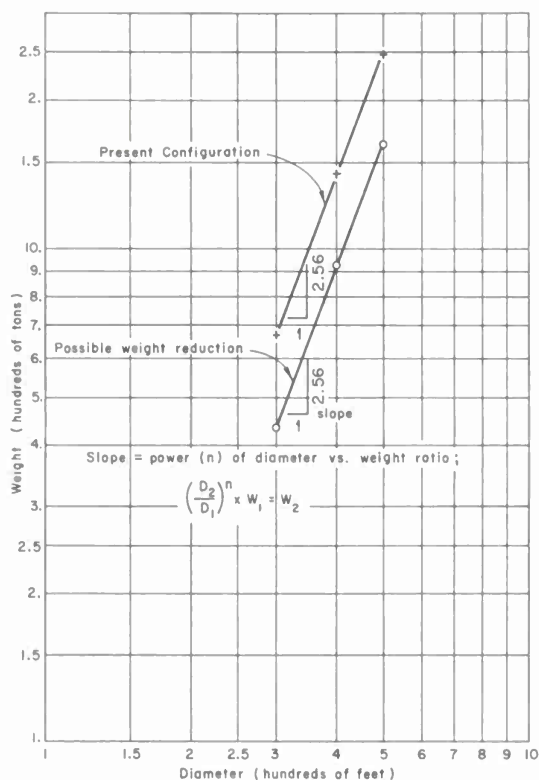


Figure 32. Logarithmic curves of weight on azimuth bearing versus diameter; Hammerhead antenna concept.

Tower, foundation. Cubic relationship, except bearing and drive anchorage, which varied directly with diameter.

Laboratory space in tower. Cost based on 30,000 ft² of laboratory space for all sizes of antenna.

Bearings and drives. Many items such as pumps and motors held constant; tracks varied with square of diameters; installation costs varied directly with diameter.

Miscellaneous items. Most items such as electrical work and control systems remained constant.

Logarithmic curves of cost versus size for the Hammerhead concept are shown in Figure 33: One curve is for the antenna, laboratory space, and radome; the other curve is for the antenna and radome only. Slopes of the curves indicate that costs vary with diameter raised to the 1.6 and 1.7 powers, respectively.

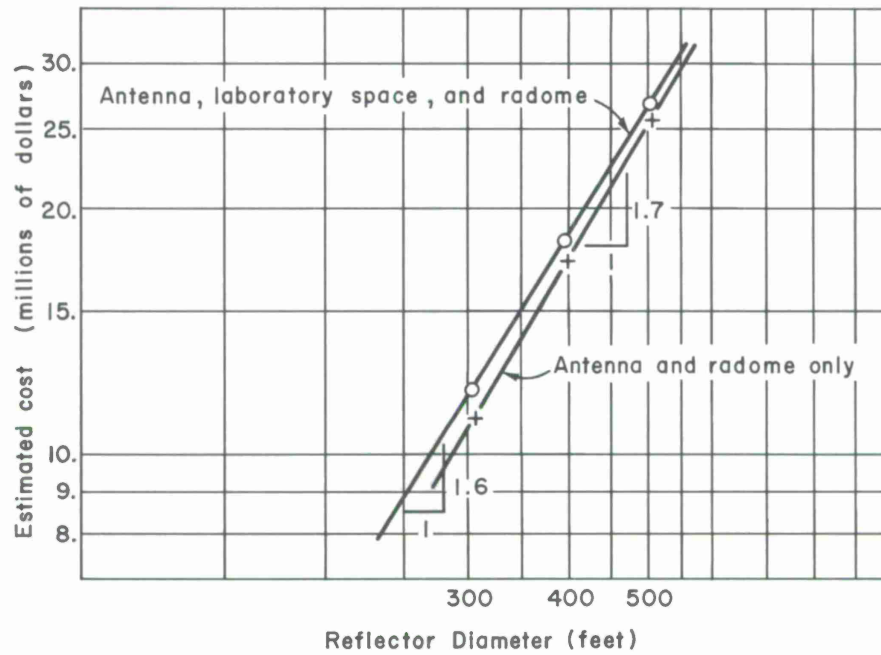


Figure 33. Logarithmic curves of cost versus size for the Hammerhead concept.

Table 3. Estimate of cost versus size.

<u>Primary reflector size</u>	<u>300-ft diameter</u>	<u>400-ft diameter</u>	<u>500-ft diameter</u>
1. Primary reflector	\$941,000	\$1,934,000	\$3,087,000
2. Secondary dish	56,000	100,000	195,000
3. Reflector support structures	56,000	127,000	243,000
4. Laboratory space behind reflector (3,000 ft ²)	94,000	94,000	94,000
5. Tower, foundation	170,000	372,000	693,000
6. Azimuth bearing	165,000	262,000	385,000
7. Azimuth drive	64,000	74,000	85,000
8. Elevation bearing	427,000	703,000	1,051,000
9. Elevation drive	96,000	106,000	116,000
10. Miscellaneous items	<u>1,050,000</u>	<u>1,233,000</u>	<u>1,433,000</u>
Construction Total	\$3,119,000	\$5,005,000	\$7,382,000
Engineering	1,000,000	1,250,000	1,600,000
Engineering supervision	700,000	850,000	1,100,000
Contingency 25%	<u>1,200,000</u>	<u>1,775,000</u>	<u>2,520,000</u>
Grand Total	\$6,019,000	\$8,880,000	\$12,602,000

<u>Radome size</u>	<u>414-ft diameter</u>	<u>550-ft diameter</u>	<u>687-ft diameter</u>
1. Radome	\$ 2,536,000	\$ 4,734,000	\$ 8,036,000
Air circulation and heating	<u>566,000</u>	<u>1,000,000</u>	<u>1,566,000</u>
Construction Total	\$ 3,102,000	\$ 5,734,000	\$ 9,602,000
Engineering	650,000	700,000	800,000
Engineering supervision	200,000	300,000	400,000
Contingency 25%	<u>1,000,000</u>	<u>1,685,000</u>	<u>2,700,000</u>
Total Radome Cost	\$ 4,952,000	\$ 8,419,000	\$13,502,000
Total Antenna and Radome	\$10,971,000	\$17,299,000	\$26,104,000

APPENDIX E

REPORT ON A CONCEPTUAL STUDY OF A
LARGE CASSEGRAIN ANTENNA

Prepared for
THE CAMBRIDGE RADIO OBSERVATORY COMMITTEE

December 1966

PAUL WEIDLINGER
NEW YORK, NEW YORK

TABLE OF CONTENTS

<u>Section</u>		<u>Page</u>
	SCOPE	E-1
1	CONTROL OF DISTORTIONS OF ANTENNA STRUCTURES	E-1
2	RMS TOLERANCE LIMIT OF SIMPLE STRUCTURES	E-4
3	FORCE-COMPENSATING CONCEPT.	E-6
4	SYSTEM DESCRIPTION	E-15
5	WEIGHT AND COSTS	E-21
6	CONCLUSIONS	E-22

SCOPE

This report contains a summary of the results obtained from a preliminary engineering feasibility study for a 400-ft-diameter radome-housed Cassegrain antenna. The study was executed under a contract with MIT, Lincoln Laboratory, in behalf of the Cambridge Radio Observatory Committee.

The report presents a concept of an antenna structure satisfying the following requirements:

<u>Sky coverage</u>	Elevation: $+15^{\circ}$ to 90° Azimuth: $\pm 300^{\circ}$
<u>Angular velocity</u>	Tracking: $0.25^{\circ}/\text{sec}$ Slewing: $1.00^{\circ}/\text{sec}$
<u>Angular acceleration</u>	$0.04^{\circ}/\text{sec}^2$ max (at 87°) $0.01^{\circ}/\text{sec}^2$ (typical)
<u>Operational pointing accuracy</u>	15 sec
<u>Operational surface accuracy</u>	RMS = 0.10 inch
<u>Mechanical resonant frequency</u>	< 0.05 cps
<u>Ambient temperature</u>	-40° F to $+140^{\circ}\text{ F}$ — survival $+45^{\circ}\text{ F}$ to $+85^{\circ}\text{ F}$ — operational
<u>Gradient</u>	10° F top to bottom, 5° F side to side

In the process of evolving the "force-compensating" concept, numerous other approaches were investigated and reviewed. Some of the details and ideas found in the course of this review are incorporated in the design of the antenna structure, and several of these are briefly described in the next section of this report.

The antenna structure concept presented in this report consists of a parabolic dish supported on a series of parallel backup trusses. The gravity distortion of these trusses is actively compensated by externally applied forces during rotation around the elevation axis. The details of this force-compensating concept are given in the body of the report, together with drawings and a description of the entire antenna structure and substructure. The report also contains detailed weight breakdown of the various components and an extrapolation of those weights in the 300-ft- to 500-ft-diameter range. It is found that the weight is directly proportional to the square of the dish radius, and significant increase in accuracy is achievable without comparable increase in cost.

1. CONTROL OF DISTORTIONS OF ANTENNA STRUCTURE

The control of system tolerance due to all causes of a large-diameter fully steerable Cassegrain antenna structure is the principal development and engineering challenge, and it has a major influence on the cost and feasibility of these instruments.

To achieve the design objectives, various techniques have been proposed, and many of these are considered and included in the design concept of all antenna structures. The most important of these follow.

(a) Elimination of Source of Distortions

An important part of distortion can be eliminated by protecting the antenna structure from large ambient temperature variations and temperature gradients and by protecting it from the effects of wind and weather in general. This is accomplished by housing the antenna in a radome. The influence of the radome on the cost and efficiency of the antenna has been previously evaluated by CAMROC. It was found that because of noise and temperature effects, a radome-enclosed antenna will have to be 6 to 10% larger in diameter to achieve an equivalent aperture efficiency. Since the cost of the radome appears to be approximately equal to the cost of the antenna, it was decided by CAMROC to restrict the present studies to radome-housed antenna structures. In view of the radome environment, wind and large temperature effects are, therefore, eliminated as a contributory cause of distortions. *

(b) Distortion Control of the Substructure

Rotation around the azimuth axis does not produce static deformations, and the substructure deformation can also be made largely independent of the elevation angle of the dish by bringing the elevation axis bearing to coincide with the center of gravity of the antenna dish. Further improvements can be made by appropriate details at these points to minimize torsional distortions caused by the torque of the elevation axis drive. This approach is used in the "Hammerhead Antenna" concept of Lincoln Laboratory.[†] A similar principle is used in the antenna concept presented in this report.

(c) Control of Panels and Stringers

These elements are usually of small dimensions as compared to the major antenna-dish backup structure, and consequently their contribution to the system error budget is minor. Nevertheless, because of the weight superimposed by these sub-assemblies on the backup structure, the weight stiffness of these elements merits serious studies. An excellent solution to this problem is proposed in Stetson's paper.[†]

* Procurement Specification CAMROC-2, MIT Lincoln Laboratory, Lexington, Massachusetts, March 8, 1966.

[†] Stetson, P., "CAMROC Hammerhead Antenna Concept," from Radomes and Large Steerable Antennas, Conference Proceedings, June 17-18, 1966, The Cambridge Radio Observatory Committee, Paper 5, Part IV, Session II - Antennas, pp. 162-180.

(d) Cambering and Bias Rigging

In controlling the surface tolerance of the antenna dish, cambering of the backup structure can bring about a significant reduction in the RMS deformation of these major elements. Generally it could be anticipated that by optimum cambering the RMS error can be reduced to approach the difference of the extremes of these values at the corresponding elevation angles ϕ_1 and ϕ_2 :

$$\text{RMS}_{\text{cambered}} = \text{RMS}(\phi_1)_{\text{max}} - \text{RMS}(\phi_2)_{\text{min}} \quad (1)$$

The actual reduction obtained seems to approach a factor of 5 for large RMS values in some cases that were investigated. It appears that reductions by a factor of 2 can be achieved in case of smaller RMS quantities. On the other hand, cambering and bias rigging, especially to optimal values, can significantly increase both shop fabrication and erection costs, and these must be compared to other means by which corresponding reductions of RMS errors are obtainable.

(e) Best Fitting

A further reduction of the RMS error of the reflecting surface can be obtained by best fitting the distorted surface at some or each elevation angle to a paraboloid of revolution of different focal length and by an appropriate rigid-body translation and rotation. The reduction of the RMS error that can be achieved by best fitting of a shell in the shape of a paraboloid of revolution is estimated at one order of magnitude.* For linear elements, i. e., plane trusses, it is found that a reduction by a factor of 5 may be attainable (see Section 2 of this report).

To achieve the required system tolerance it may be necessary to use all, or many, of the above-listed procedures. Since the weight contribution to the system error, and even more to the surface error, derives from the antenna-dish backup structure, special effort and techniques need to be applied to this component. At the present time the following approaches seem to be possible and promising.

(f) Maximum Stiffness

This approach is the conventional technique of design and it requires the achievement of maximum stiffness consistent with minimum weight. This method requires stringent and, therefore, costly fabrication and erection tolerances. At the present it appears that large, high-precision antennas cannot be built without at least the partial application of some of the compensating techniques described below.

*Mar, J. W., and Wan, F. Y. M., "The Influence of Shell Behavior on the Design of Large Antennas," from Radomes and Large Steerable Antennas, Conference Proceedings, June 17-18, 1966, The Cambridge Radio Observatory Committee, Discussion 4, Part V, Session III - Discussion, pp. 275-331.

(g) Control by Compensation of Displacements

At the extreme application of this method, the antenna backup structure is designed without regard to distortion requirements, and surface tolerance is achieved by controlled displacements of the panels of the surface itself. Each panel must be supported on jacks that are continuously adjusted to the required position during rotation around the elevation axis. This method requires elaborate servo systems and continuous monitoring of displacements.

(h) Control by Homologous Deformations

This method developed by S. von Hoerner takes advantage of the fact that it is possible to define the geometry and the cross-sectional area of the members of a space truss in a manner that a paraboloidal surface defined by the nodes of the truss will be continuously deformed, unhindered, into another family of paraboloids, at all elevation angles. The method in some respects is a further exploration of the previously described best-fitting procedure. Its application to an actual antenna structure has as yet to be attempted.

(i) "Exotic" Solutions

A number of unusual approaches have been proposed, such as the use of helium-filled structures, a spherical metal shell-radome combination floated on air, and a reinforced concrete structure supported on torroidal shells floated on water. While the advantage gained from these solutions is evident, a number of technological problems remain to be solved before they can be evaluated.

(j) Force-Compensating Concept

Distortions of the antenna surface can also be controlled by applying one or more external forces that vary with the elevation angle. In the ideal situation, i. e., with a sufficient number of compensating forces, the gravity deformations are independent of the elevation angle of the antenna, and it approaches that of a structure operating in a gravity field rotating with the elevation axis. If the compensating forces are at an optimum level, their effect approaches that of zero gravity. The most significant practical advantage lies in the relative simplicity of the control of the magnitude of compensating forces that are independent of the magnitude of distortions; and control, therefore, does not require continuous monitoring with respect to a fixed reference point. The preliminary design of the antenna structure presented in this report is based on the force-compensating concept.

2. RMS TOLERANCE LIMIT OF SIMPLE STRUCTURES

Since the major effort in the development of an economical antenna system is in the direction of obtaining an acceptable RMS surface tolerance within the most economical solution, certain basic considerations leading to initial estimates of limiting quantities are desirable.

Apart from the more exotic solutions, it is safe to assume that the minimum weight (and approximately minimum cost) could be achieved if the antenna backup structure were designed by strength considerations only, i. e., without regard to stiffness. The attainable RMS surface error of structures designed for strength only is, therefore, of fundamental importance in evaluating the efficiency of other designs. It turns out that the RMS deformation of linear elements (such as plane trusses) of constant strengths can be readily calculated without additional assumptions. Consider a plane cantilevered truss of span R and depth h designed for constant strength in bending. This implies a constant extreme fiber stress and, therefore, constant maximum strain ϵ_m . If the depth h is also constant along the span R , the structure will deform with a constant radius curvature, which for small deflections is given by

$$\delta(x) = \epsilon_m \frac{R}{h} R \left(\frac{x}{R} \right)^2, \quad (2)$$

and the peak deflection δ_m at $x = R$ is

$$\delta_m = \epsilon_m \frac{R}{h} R, \quad (3)$$

where the span-depth ratio R/h is an essential geometric design parameter. The RMS deflection can be calculated from Eq. (2):

$$\text{RMS} = \frac{1}{\sqrt{5}} \epsilon_m \frac{R}{h} R. \quad (4)$$

The ratio of peak to RMS deflection by Eqs. (3) and (4) is

$$\frac{\delta_m}{\text{RMS}} = \sqrt{5} = 2.24. \quad (5)$$

In steel structures operating at 15 to 20 ksi, average peak stress levels, the strain is bracketed between

$$5 \times 10^{-4} \leq \epsilon_m \leq 6.7 \times 10^{-4}. \quad (6)$$

For the lower value of ϵ_m Eq. (4) can be written as

$$\text{RMS} = 2.24 \times 10^{-4} \frac{R}{h} R. \quad (7)$$

If the deflection curve of Eq. (3) is best fitted to a straight line, the best-fit RMS is given by

$$\text{RMS}_{\text{best fit}} = \frac{1}{3\sqrt{2}} \text{ RMS} = 0.23 \text{ RMS} \quad (8)$$

The customary range of values of the span-depth ratio for backup trusses is

$$2 < \frac{R}{h} < 4 \quad (9)$$

and on Figure 1, approximate typical RMS values attainable for least weight designs are shown. The aim of further improvement is to produce lower RMS errors with weights comparable to those obtained by strength design only.

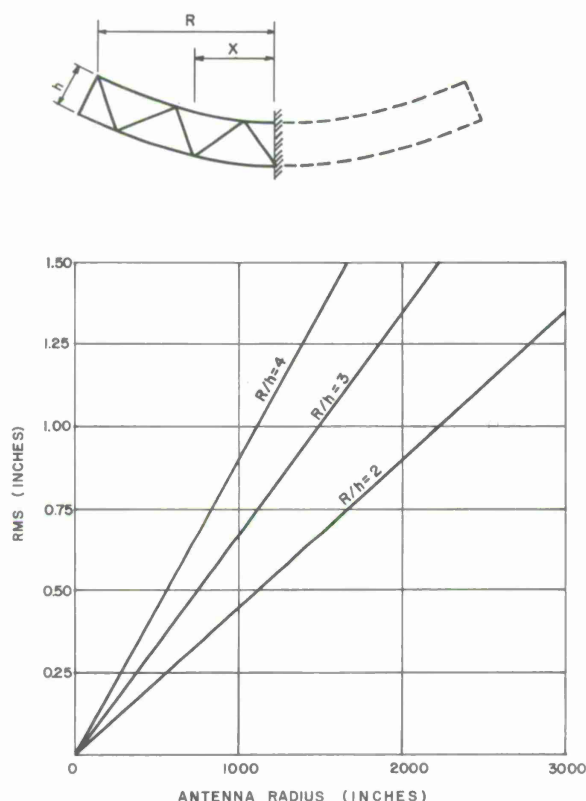


Figure 1. RMS deflection of simple structures.

3. FORCE-COMPENSATING CONCEPT

Consider a large parabolic antenna surface supported on a backup structure, subject to gravity forces. We divide the backup structure into a number of segments with the weight W of each such subdivision assumed to be acting at the center of gravity. If the antenna is rotated by the angle ϕ from its original position, the gravity vector \overline{W} will rotate by the same angle with respect to a coordinate system attached to the antenna. We now also introduce the external compensating force $F(\alpha, \phi)$ acting on the center of gravity at the angle α with respect to the coordinate system. The

resultant of the two vectors \overline{W} and \overline{F} is

$$\overline{R} = \overline{W} + \overline{F} . \quad (10)$$

The value of \overline{F} is continuously adjusted by control of the compensating system in such a manner that the resultant vector

$$\overline{R} = \text{constant} . \quad (11)$$

The gravitational distortion of the structure is now independent of the elevation angle, i. e., the structure behaves during rotation as if it were in a field rotating with it. The constant distortion introduced by the force R can be eliminated by cambering. In practical application, with a finite number of compensated points, gravity distortion will exist in the areas between such points. Since our aim is to obtain a structure in which the radial component of RMS deformations is to remain below a predetermined value, it is sufficient to control the radial component R_n of the resultant force only. For the condition

$$R_n = \text{constant} , \quad (12)$$

it is sufficient to define for each elevation angle ϕ the value of $F(\phi)$ only, while its direction α can remain constant throughout the rotation. The compensating forces F acting on the backup structure can be reacted on some other part of the same structure, and the entire system of truss and compensating forces constitutes a prestressed structure in which the intensity of the prestress is varied as a function of the elevation angle ϕ only. Since this variable prestress is now an internal force with respect to the entire structure, the system remains in equilibrium. The variable prestress produces internal distortions, but as long as the variation of the force F at a constant angle α satisfies the condition

$$F(\phi) = \frac{R_n - W \cos(\phi - \theta)}{\cos(\alpha + \theta)} , \quad (13)$$

where R_n is a constant normal component at an angle θ with respect to the axis, the distortion of the structure remains controlled at selected points (see Figure 2). During rotation of the antenna the intensity of the force $F(\phi)$ is continuously controlled at a predetermined value of each elevation angle and the force does not depend on displacements at the points of application or at the anchorage or displacements caused by the elongation of control rods through which the force is applied. This leads to a simple, open-loop control system depending on the magnitude of the force only.

To apply the principles described, we proceed by designing an antenna backup structure consisting of a series of parallel-plane trusses, perpendicular to the elevation

axis and symmetrical with respect to it. Each plane truss incorporates an anchorage point or pole (Figure 3), to which the compensating control rods are attached. The intensity of the force in each rod can be controlled either through a preprogrammed hydromechanical actuator or through gravity forces obtained through the truss counterweight. Each truss is designed for strength only; the approximate peak deflection can be obtained from Eq. (3), and the RMS deflection from Eq. (7) of Figure 1. The actual calculated radial component of the deflection is shown on Figure 4. The RMS radial deflection is 2.02 inches.

In order to study the effect of the position and the number of compensating forces, influence coefficients I_{ik} were calculated denoting the radial deflection of the k th joint due to a pair of symmetrical compensating forces applied to the symmetrical points i and i' . The deflection of the truss at joint k due to a pair of forces F_i at joints i and i' is

$$\delta_k = F_i I_{ik} \quad , \quad (14)$$

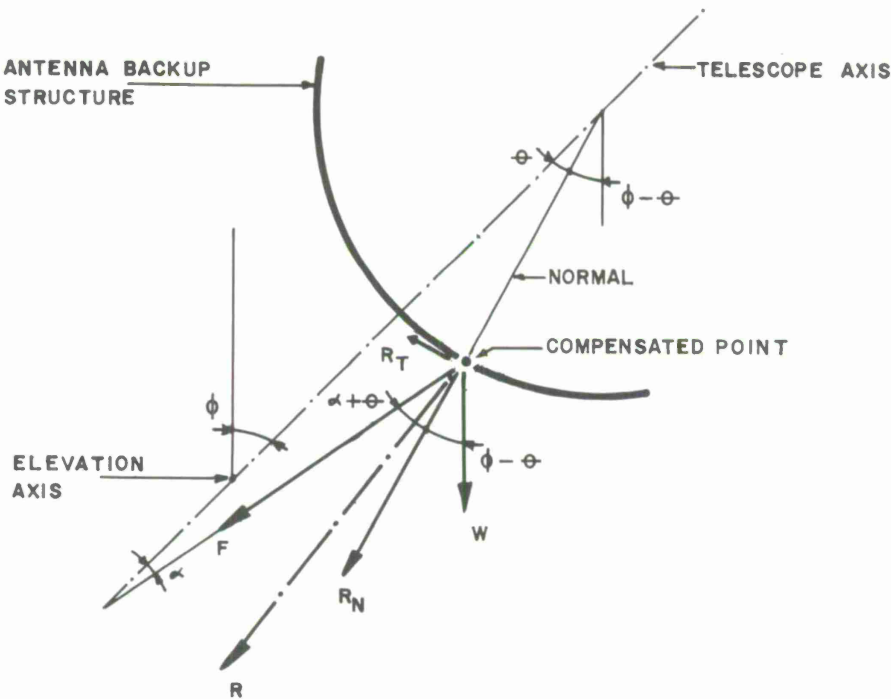


Figure 2. Compensating-force geometry.

and the compensated deflection δ_c of a joint at k , including the effect of gravity deformation δ_g and n pair of forces, is

$$\delta_c = \delta_g + \sum_{i=1}^{i=n} F_i I_{ik} \quad . \quad (15)$$

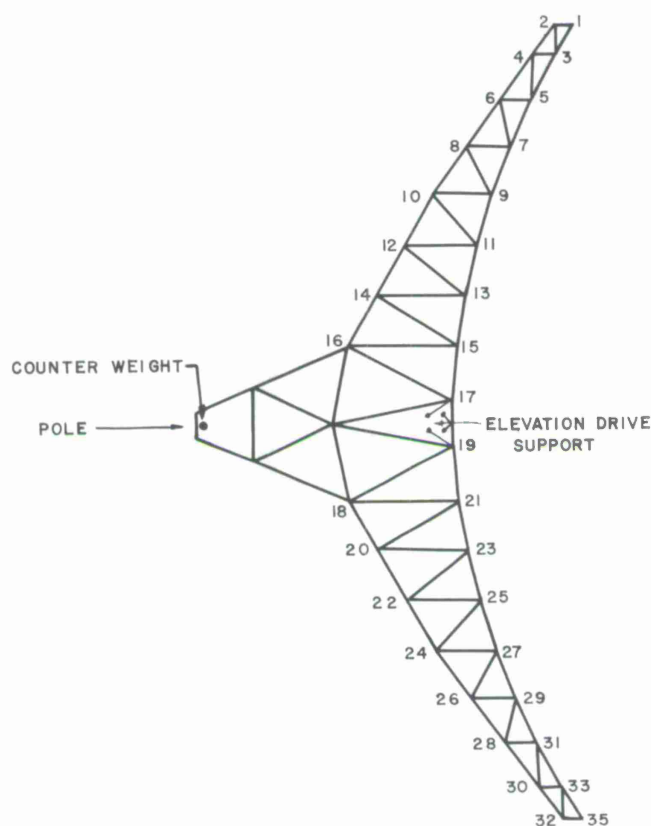


Figure 3. Typical truss.

A deflection curve, for $n = 3$ applied to the main truss of the antenna structure, is shown in Figure 9. In a symmetrical truss consisting of j pairs of joints, the number of all possible points of compensation is

$$\sum_{n=1}^{n=j} \frac{j!}{n!(j-n)!} = 2^n - 1.$$

In case of the truss shown in Figure 2, $j = 8$ and the number of combinations is 255. With the aid of the computer, these combinations can be scanned and the magnitude of the compensating forces and the RMS deflections for elevation angles $0 \leq \phi \leq 90$ calculated. The result of such calculations is shown on Table 1 for a maximum of 6 pairs of forces showing best combination, i. e., the one that gives the least RMS value together with the maximum value of any single compensating force and the sum of the absolute values of all compensating forces, measured in units of the total gravity load W on the truss. The sum of absolute values instead of the algebraic sum is given, because the compensating system as designed transmits tension only; consequently, the truss is bias rigged to adjust to this requirement.

Table 1. Effect of force compensation on typical truss

Number of pairs of forces	ϕ_m (2)	RMS deflection (inches)	RMS gain	Location of compensating forces at joint								$\frac{F_{i \max}}{W}$ (1), (3)	$\frac{\Sigma F }{W}$ (1)
				2	4	6	8	10	12	14	16		
0	0	2.020	1									0	0
1	0	0.280	7		*							0.47	0.73
2	75	0.050	40		*				*			0.90	1.60
3	0	0.028	72	*		*				*		1.23	2.28
4	0	0.020	101	*	*		*			*		1.23	2.28
5	0	0.011	183	*	*		*		*		*	33.00	68.0
6	0	0.010	202	*	*	*	*		*		*	33.00	68.0
7	0	0.010	202	*	*	*	*		*	*	*	33.00	68.0
8	0	0.010	202	*	*	*	*	*	*	*	*	33.00	68.0
<p>Note: (1) $W = 1.5 \times 10^6$ lbs.</p> <p>(2) ϕ_m: Elevation angle at maximum RMS.</p> <p>(3) Maximum force occurs at $\phi \neq \phi_m$.</p>													

Table 1 also shows the RMS gain, i. e., the ratio of the uncompensated RMS to the compensated RMS. As is to be noted from table 1 and from its graphic presentation in Figure 5, the RMS values approach a minimum value of 0.01 inch. The magnitude of compensating forces increases nearly linearly up to 3 pairs, but increases very rapidly at 5 pairs. With these data it seems reasonable to select 3 pairs providing an RMS = 0.028 inch, although 2 pairs with an RMS = 0.050 inch may also satisfy system-tolerance requirements.

It is to be noted that while in Figure 5 the RMS deflection approaches a nonzero limiting value with an increasing number of pairs of compensating forces, the value RMS = 0 is approached if nonsymmetrical combinations are also considered. The variations of the RMS deflection for $n = 3$ for various elevation angles ϕ are shown in Figure 6, and the variations of the 3 pairs of forces and the sum of their absolute values are given in Figures 7 and 8. The radial deflection of the half truss at $\phi = 0$ is shown in Figure 9.

From these studies, it is concluded that the gravity RMS deflection of the antenna backup structure can be controlled at any desired level, and very low surface distortion can be achieved with 2 or 3 pairs of compensating forces. It is also concluded that a significant increase in efficiency through a reduction of gravity distortions can be achieved without a significant increase in cost.

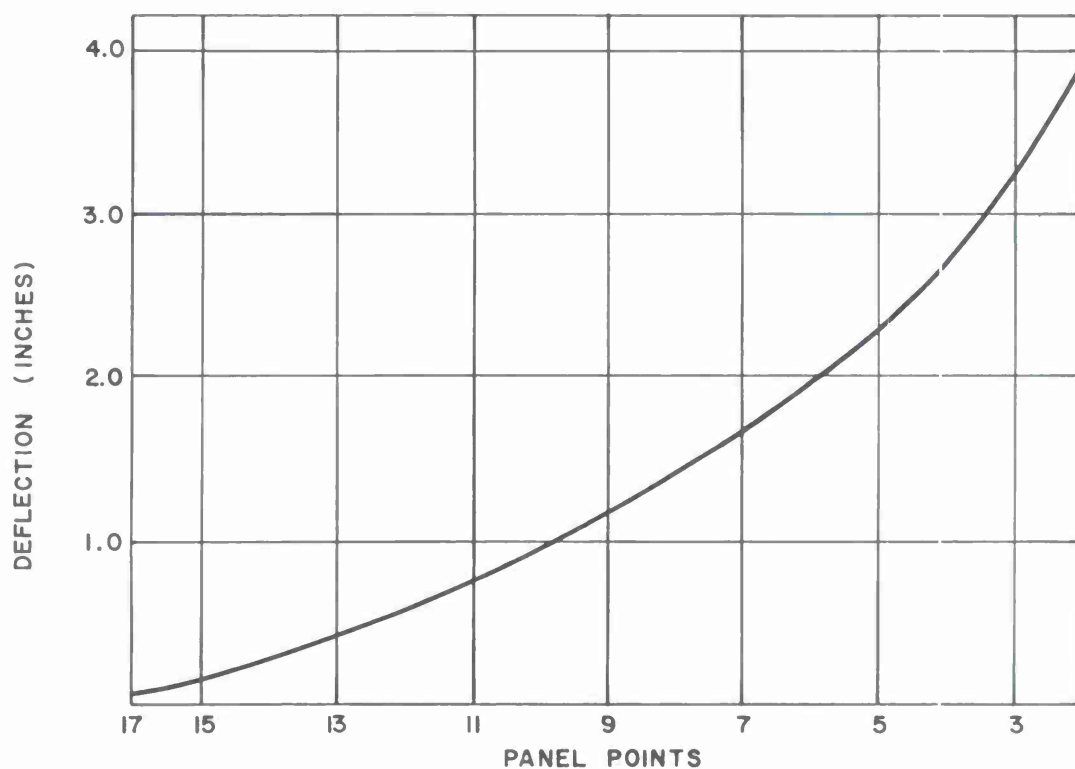


Figure 4. Deflection of half truss under gravity loads — face-up position.

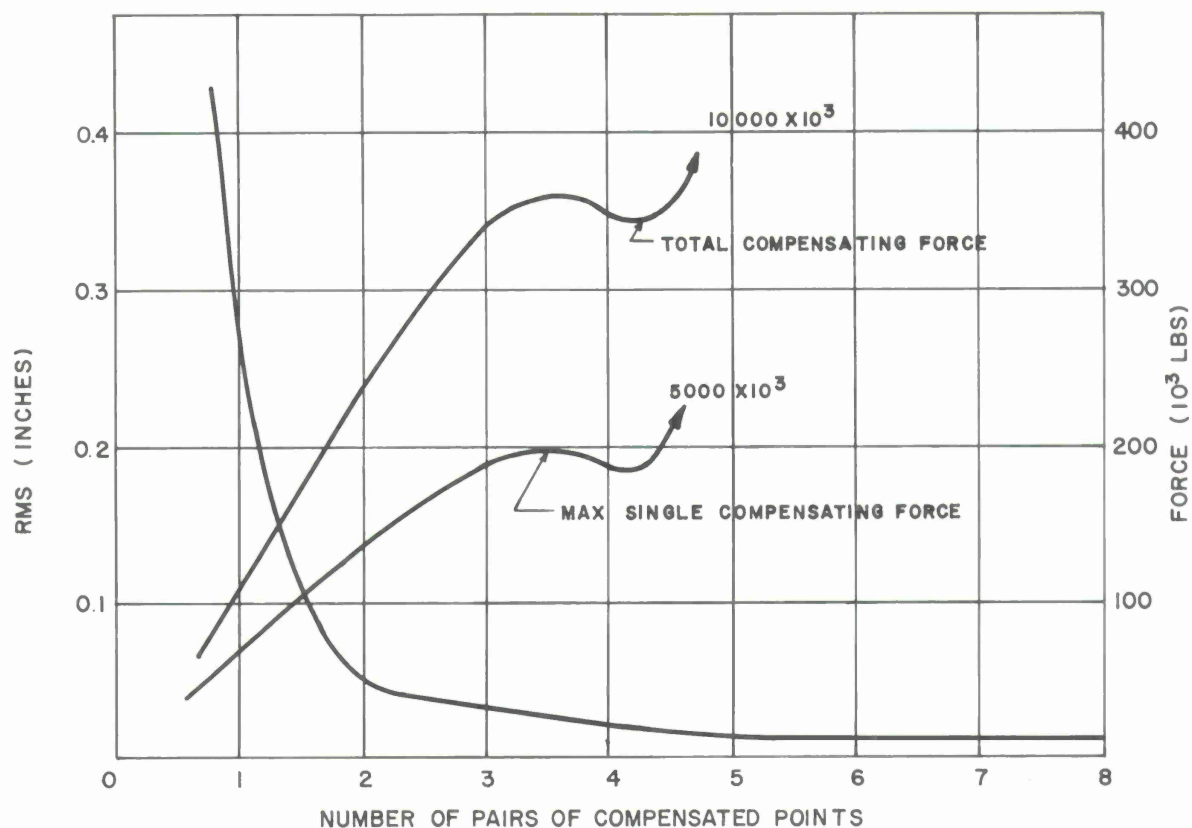


Figure 5. RMS deflection and force versus number of compensated points.



Figure 6. Variation of RMS versus elevation angle; compensating forces are applied at panel points 2, 6, 14, 20, 28, and 32.

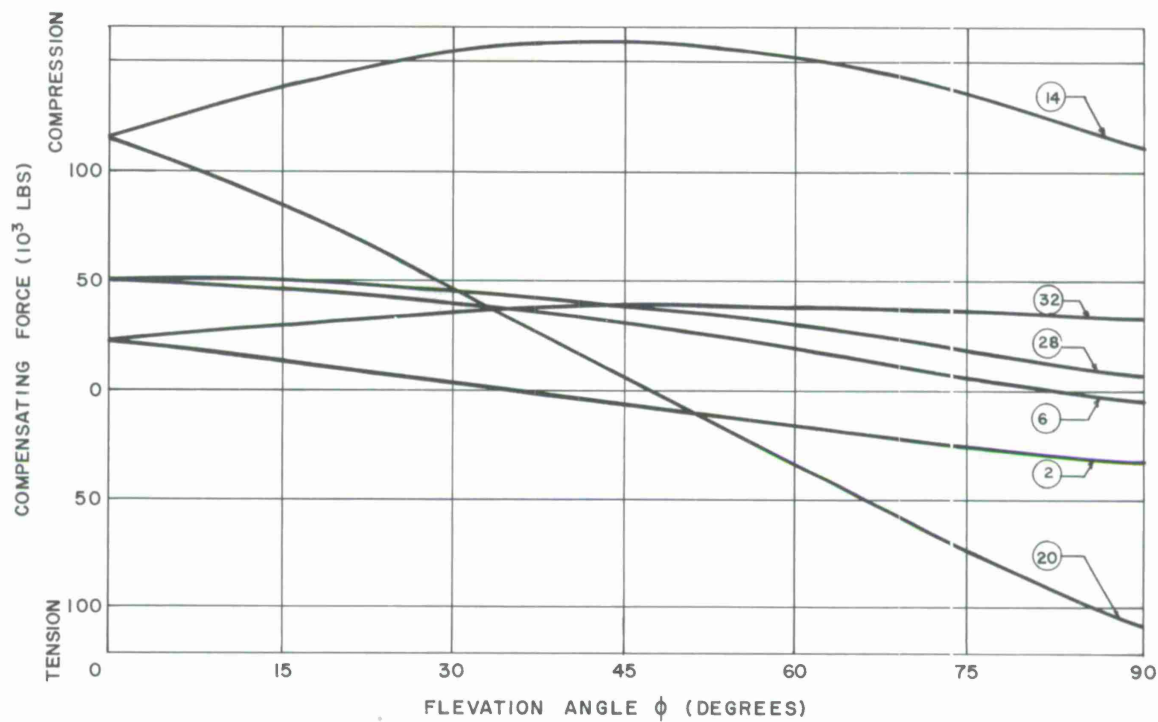


Figure 7. Compensating forces versus elevation angle.

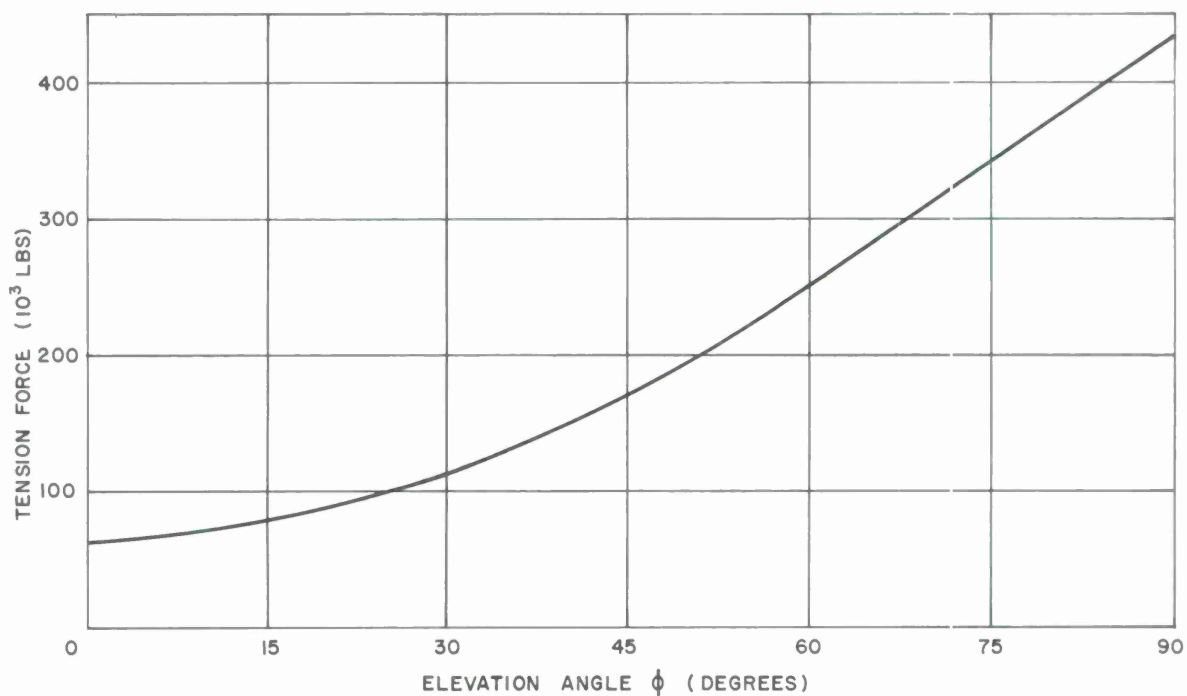


Figure 8. Total compensating force versus elevation angle.

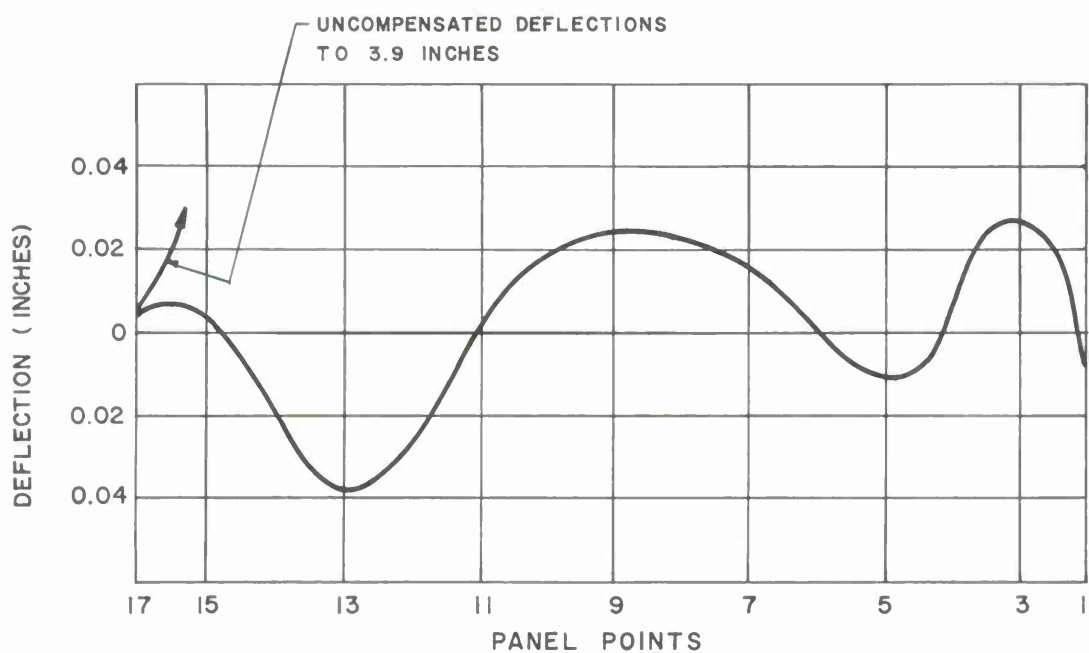


Figure 9. Deflection of half truss under gravity loads and six compensating forces — face-up position.

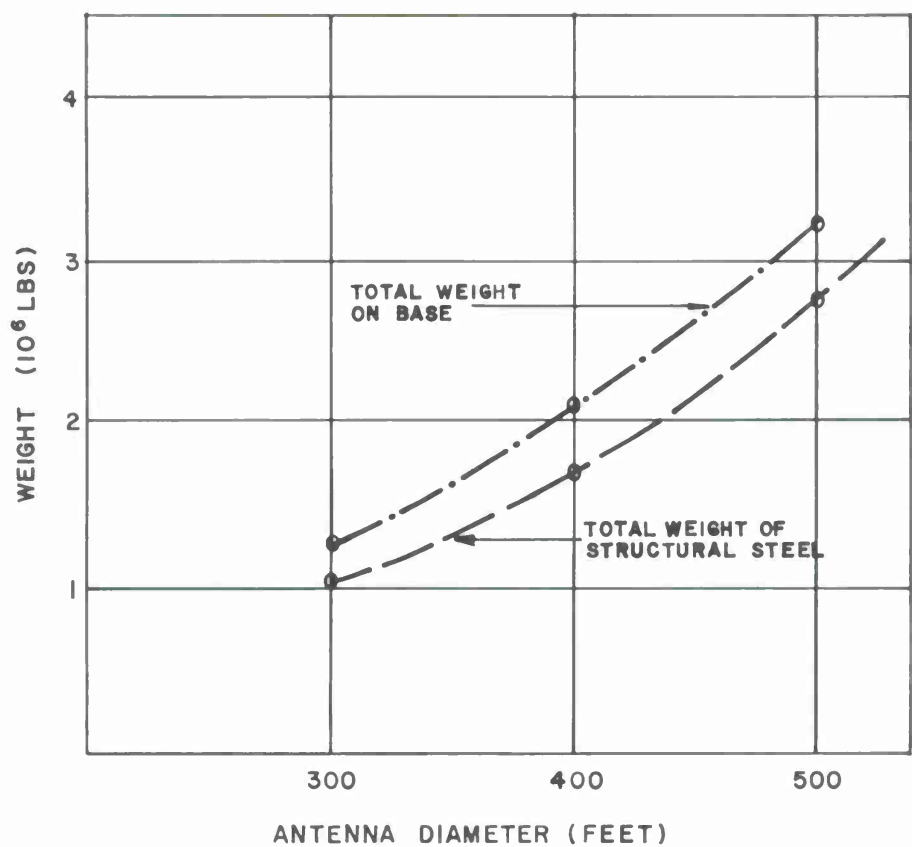


Figure 10. Weight versus diameter.

4. SYSTEM DESCRIPTION

4.1 Geometry

The method of controlling the RMS deformation of an antenna dish is, in principle, applicable to various types of structures. In its practical application to the CAMROC study, certain additional specific constraints are desirable. Since it is anticipated that a number of points on the antenna backup structure need to be compensated simultaneously, it is advisable, from the point of view of stability of the control system, to design an antenna structure consisting of essentially independent subassemblies that are uncoupled from each other with respect to deformation. Since the distortion of the antenna structure is governed by the rotation around the elevation axis, a series of independent axisymmetric structures (instead of a centrally symmetric space structure) have been selected. In effect, the antenna-dish backup structure consists of a series of parallel plane trusses supported on the elevation axis.

4.2 Compensating Force

There appear to be two practical methods by which the compensating force can be applied to the antenna backup structure. In both cases it is desirable that the compensating forces be applied in the form of tension only, and this is accomplished by appropriate bias rigging and prestressing of the individual backup trusses.

In one method, the application of the compensating forces is accomplished by an external power source. This requires the use of a hydromechanical or hydraulic power device. Control will be accomplished by means of a nulling-type electrical system and appropriate amplifiers. The magnitude of the force is precalculated for each altitude angle. The shaft of the elevation axis drive will be used to make available a noise-free voltage analog of the reflector altitude to control the compensating forces on the structure. It is estimated that the compensating forces will be obtainable within a required tolerance.

The second method does not require an external power source. In this approach the rolling weight on a fixed track is used to produce the required tension. The counterweight required for the vertical truss itself will be used as the weight required to provide the compensating force through suitable mechanical amplifying devices. This passive method of compensation (i. e., without external power source) can be used because the variation of the compensating force is a sine function of the elevation angle, as shown in Eq. (13) of this report.

4.3 Structure

Specific application of the force-compensating concept to a 400-ft-diameter parabolic Cassegrain antenna is shown in Drawings 1 to 4. The structure is divided into 2 major components, namely, that of the structure of the dish supported on an elevation

axis and that of the substructure consisting of a yoke and supporting towers, which, in turn, rest on azimuth bearing pads (Drawing 1).

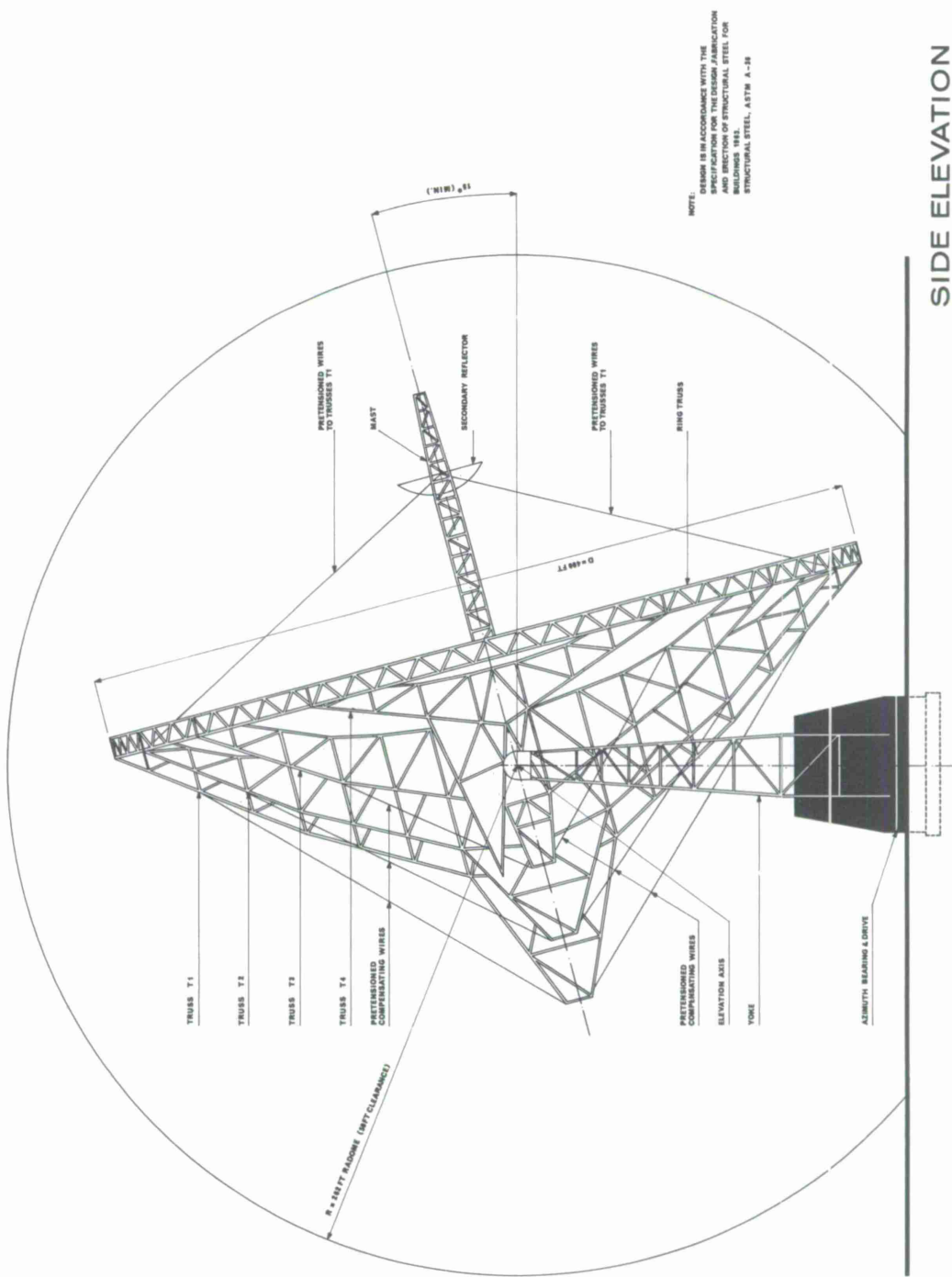
The antenna backup structure consists of purlins spaced at 13 ft on center and main vertical trusses spaced at 50 ft on center. The elevation axis on which the vertical trusses are supported is placed as close as possible to the vertex of the paraboloid, thus reducing the eccentricity of the center of gravity with respect to this axis, and consequently reducing the required counterweight. This arrangement also produces a more compact design with favorable dynamic properties, requiring a minimum radome radius. Achievement of the above objective also suggests the use of a minimum shaft diameter and this, in turn, requires closely spaced support towers of the shaft. These conditions are met by the substructure consisting of the yoke and the supporting towers (Drawings 2 and 4).

The design of the vertical trusses was controlled by strength. They are balanced with respect to their support (elevation axis) by counterweights. The tension in the compensating wires is reacted at a central pole supported by a protruding part of the truss. The deflection of each truss in its own plane is independent of the deflection of an adjacent truss; for this reason, each truss has its own compensating system. The vertical trusses are supported on an elevation axis, which consists of a triangular space truss and hollow shaft. To minimize bending and torsion in the axis, bearings for the axis and support points for the trusses are close to each other. The entire axis rotates as one unit, thus simplifying the problems of bracing. Owing to the truss action of the substructure supporting the dish, there is a horizontal thrust along the elevation axis that is taken up by a single stationary rod, running between the end points of the yoke through the hollow shaft of the elevation drive axis (Drawing 2).

The elevation axis is supported by towers. Each tower contains an elevation bearing and drive unit. Thus the axis is driven at a short distance from the support point where the torque is transmitted to a vertical truss. Azimuth rotations cause a radial, outward pointing, dynamic force (centrifugal), which causes tension in the elevation axis. This is a self-equilibrating force, and since the vertical trusses are rigidly connected to this axis, there is no need for thrust bearings.

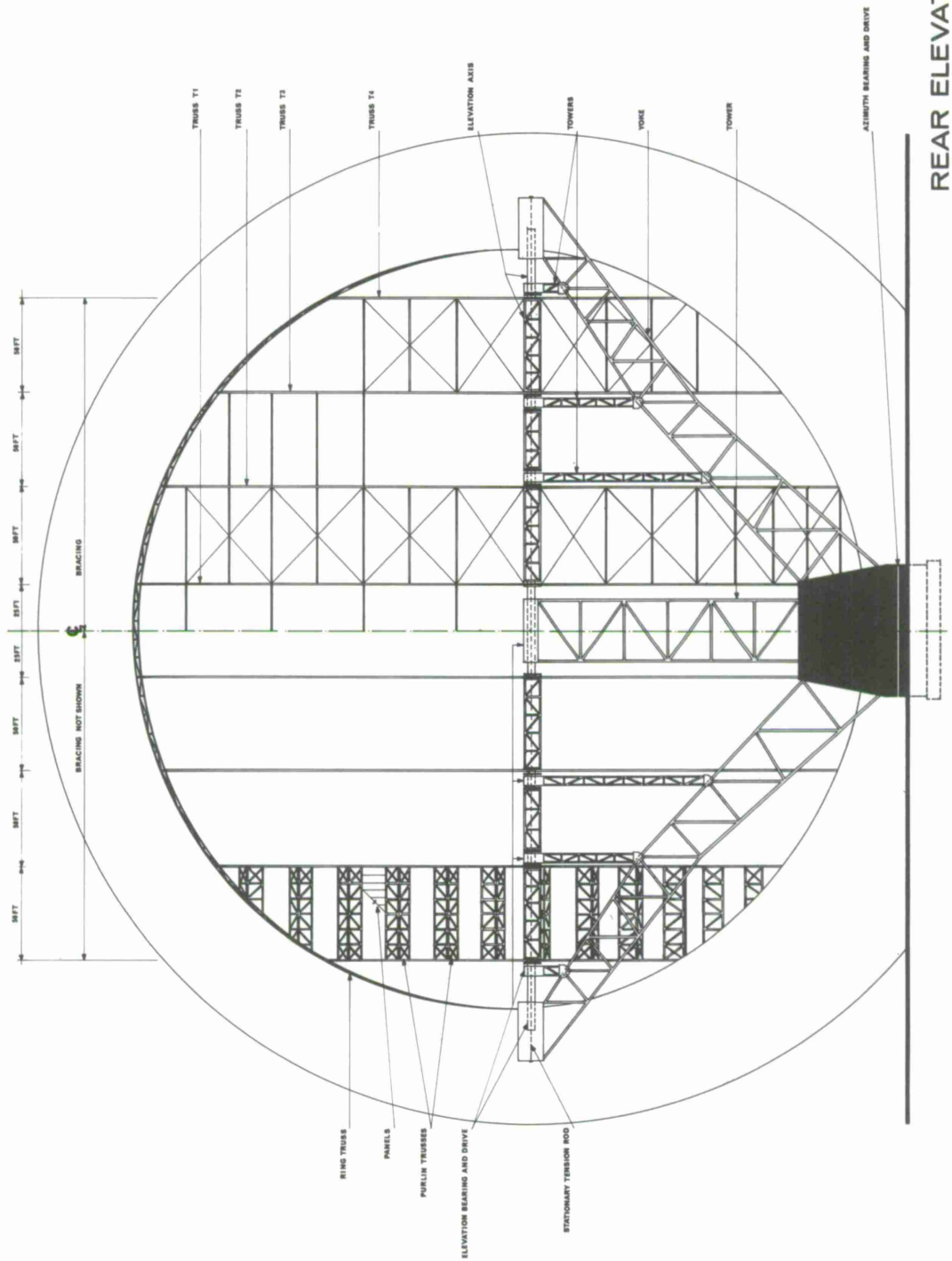
The towers are designed to transmit vertical loads to the yoke. They also participate in resisting deformations due to tangential dynamic loads in case of azimuth accelerations. Some portion of these loads is reacted by the beam action of the elevation axis in a horizontal plane.

The towers are supported on the yoke. The shape of the yoke is chosen in a manner that moments due to eccentrically applied compression and vertical loads largely compensate. It transmits the torque for azimuth drive to the ends of the elevation axis.



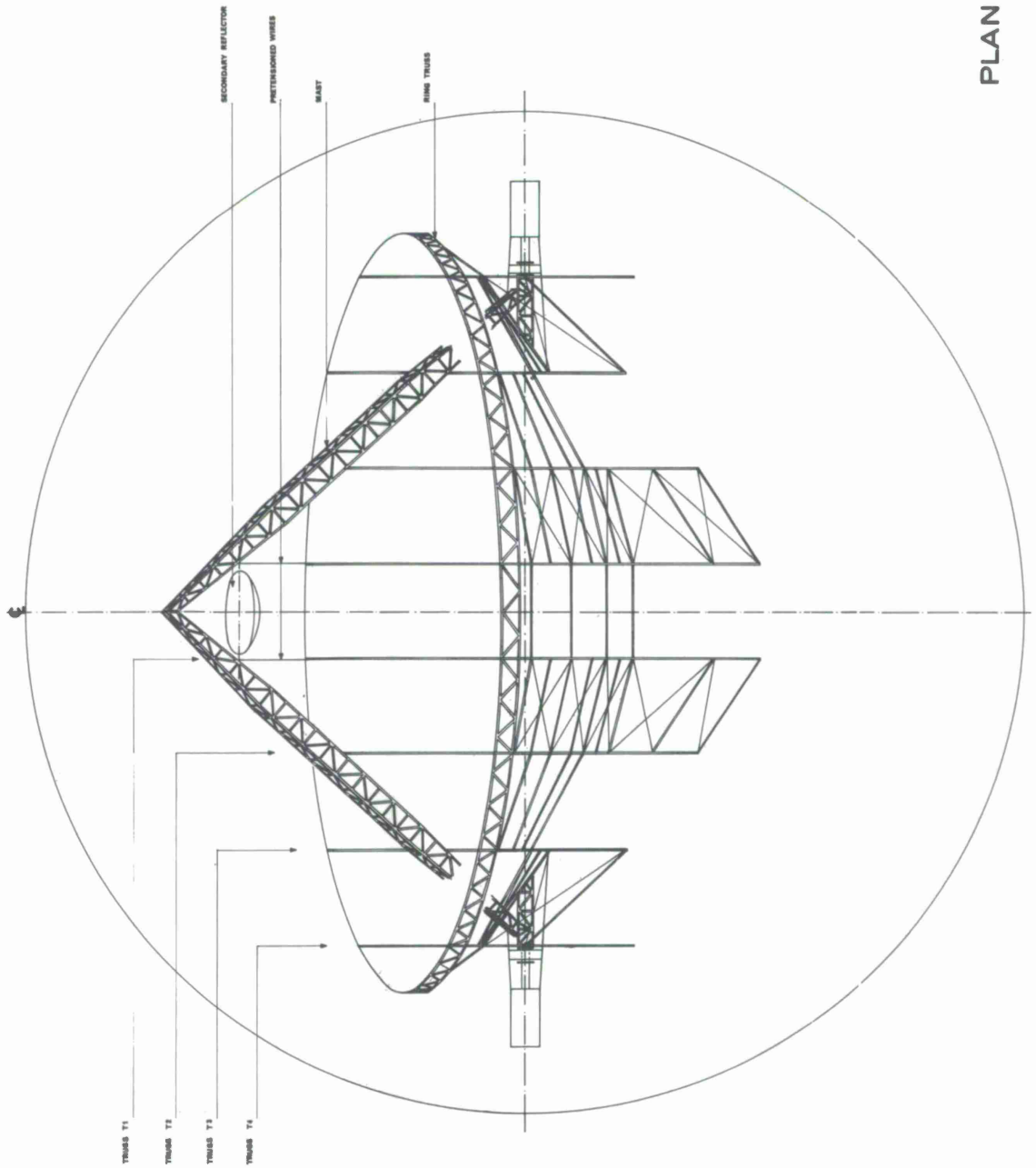
NOTE:
DESIGN IS IN ACCORDANCE WITH THE
SPECIFICATION FOR THE CONSTRUCTION
AND ERECTION OF STRUCTURAL STEEL FOR
BUILDINGS 1982.
STRUCTURAL STEEL, ASTM A-36

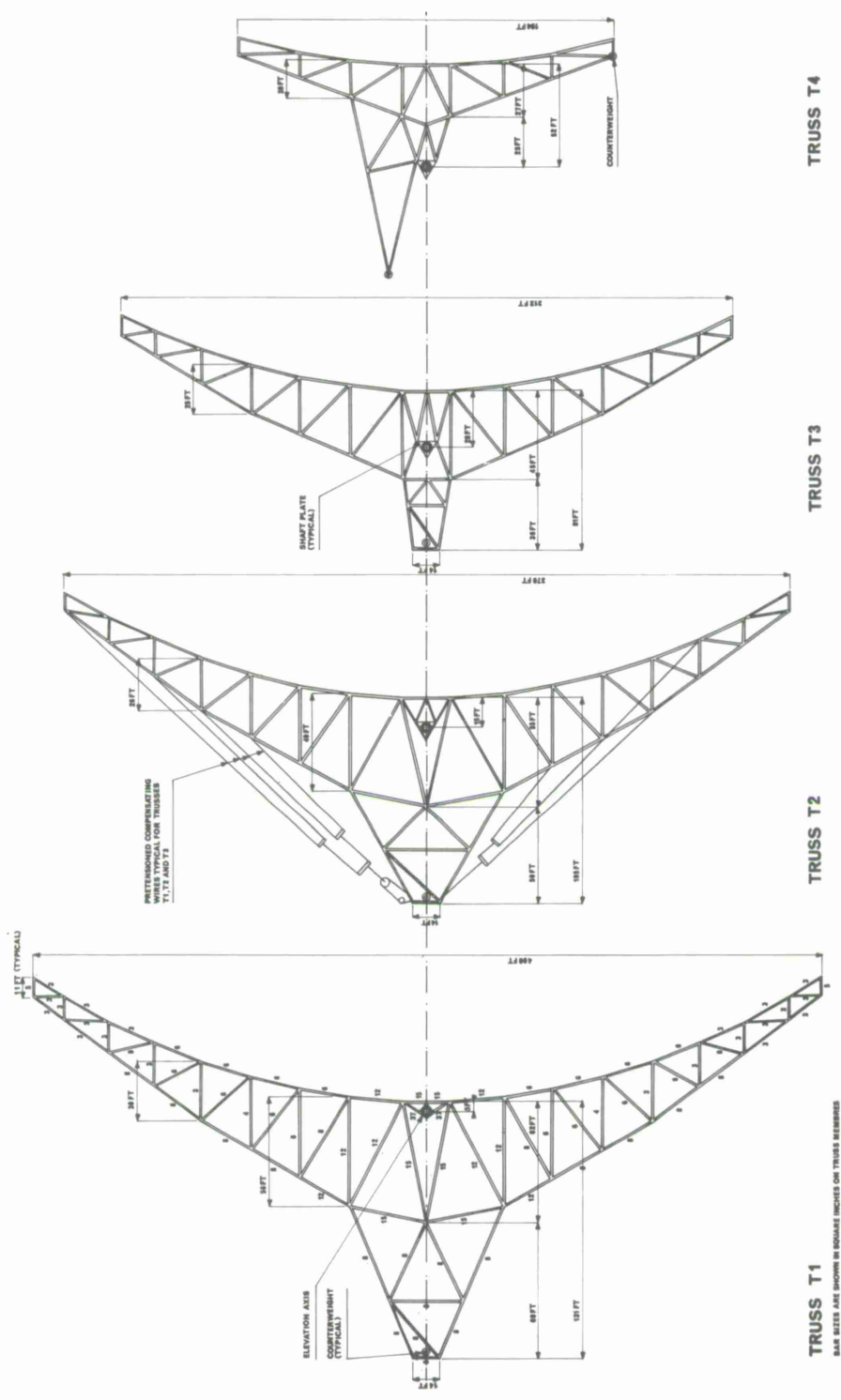
SIDE ELEVATION



REAR ELEVATION

PLAN VIEW





TRUSS T1

TRUSS T2

TRUSS T3

TRUSS T4

TRUSS ELEVATIONS

The yoke is supported on a cellular reinforced concrete structure in the shape of a conoid with a square upper and a circular lower surface. It will house electronic equipment, and the entire antenna is rotated on azimuth bearings at its lower circular surface.

Supports for the secondary reflector are provided in such a manner that a major portion of the load enters the elevation axis directly. Two compression masts and, in a perpendicular plane, two pairs of wires make up the supporting assembly. The variable force in the wires is compensated so that the resultant force acting on the truss is tangential rather than radial, resulting in negligible bending in the truss. Further advantage of this kind of support is that it allows the adjustment of the position of the secondary reflector on a vertical circular path. The vertical trusses are braced against the elevation axis and each other. The top chords are held in position by the purlin trusses, and the adjacent bottom chords are cross braced (Drawing 3).

The entire dish is "enclosed" by a ring truss, which also serves as a support for the purlin trusses in the peripheral areas of the paraboloid. In order to prevent interaction between adjacent vertical trusses, portions of the ring truss are connected by a combination of rigid and slip joints (Drawing 1).

Preliminary calculations indicate that inertial forces have a negligible influence on deformation and that the frequency of lower modes is well below the resonant frequency specified.

5. WEIGHT AND COSTS

The basic design of the CAMROC antenna is based on a 400-ft-diameter parabolic dish. Detailed calculations to establish the weight of the individual subassemblies were made. In order to assess the variation of the weight versus the diameter, additional calculations were obtained, partially by extrapolating from the 400-ft-diameter basic design, and partially by redesigning certain major members for this purpose. In extrapolating the values obtained from the 400-ft-diameter dish, it was assumed that the weight per square foot of panels and purlins is constant. The weight of the subsequent subassemblies was calculated by superimposing on them the weight carried by the subassembly and calculating the weight of the subassembly itself required to carry the superimposed loads. In this manner the total weight of the antenna was obtained for various diameters.

The weights indicated do not include the electronic equipment and the conoidal reinforced concrete base on the azimuth bearing.

At this stage of the study, it is not possible to obtain a reliable cost estimate; however, it is felt that the cost will probably be proportional to the weight of the structural steel alone. This item is given separately in the weight breakdown in Table 2 and is also shown on Figure 10. The cost of the hydromechanical control

system, assuming a maximum of 50 points controlled, has been estimated at \$250,000. This cost will be substantially reduced if the passive counterweight control system is used.

Table 2. Weight calculations

Diameter	Weight in 10^3 lbs		
	300 ft	400 ft	500 ft
Counterweight (concrete)	190	260	380
Panels (aluminum)	40	75	120
Truss bracing	100	180	280
Purlins	100	175	270
Total weight on trusses	430	690	1050
Trusses	370	420	570
Secondary reflector	25	50	100
Weight on elevation axis	825	1160	1720
Elevation axis	150	270	500
Towers	60	100	150
Yoke	230	500	900
Total weight on azimuth bearing (excluding concrete base)	1265	2030	3270
Total weight of structural steel only	1035	1695	2770

6. CONCLUSIONS

As a result of the preliminary study the following conclusions have been reached:

- 1) A 400-ft-diameter, radome-housed Cassegrain antenna can be designed and built to the CAMROC specifications.
- 2) Surface accuracy even beyond that specified is achievable without significant cost increase by the use of the force-compensating system.
- 3) The entire weight of the 400-ft-diameter antenna, excluding the reinforced concrete base, foundations, and electronic equipment, is 2×10^6 lbs.
- 4) The weight, and probably cost, of similar antennas in the 300- to 500-ft-range vary as the second power of the diameter.

- 5) The force-compensating concept appears to offer an economic method to obtain extremely high surface accuracies. Further development of many crucial details of this method are required, however, to improve its practicability and to explore its potential. In principle, the force-compensating method could also be applicable to very large-diameter antenna structures well beyond the range of the present study. It appears to be also well suited to large-antenna structures built of materials of low modulus of elasticity, such as aluminum and, conceivably, reinforced concrete.
- 6) The RMS tolerance can be further decreased and/or the intensity of compensating forces decreased by best fitting and bias rigging.
- 7) Because of the compact design of the structure, the radome size is reduced to a radius of 262 ft, including a clearance of 50 ft.
- 8) Since sufficiently low values of RMS deflections are achievable, the antenna structure can be fabricated within commercial structural-steel tolerances, resulting in a significant cost saving.
- 9) The compensating system may be used, if this turns out to be desirable, to reduce the effects of thermal distortions. This can be accomplished by activating the compensating control system through temperature-sensing devices placed on the backup structure.

APPENDIX F

PARAMETRIC STUDY OF A 400-FT-DIAMETER ANTENNA BASED ON
CSIRO PARKES CONFIGURATION

Prepared for
THE CAMBRIDGE RADIO OBSERVATORY COMMITTEE

December 5, 1966

SIMPSON GUMPERTZ & HEGER INC.
CAMBRIDGE, MASSACHUSETTS

ACKNOWLEDGMENT

We wish to express our appreciation to E. G. Bowen of the Radiophysics Division of the Commonwealth Scientific and Industrial Research Organization and to Freeman, Fox & Partners (Consulting Engineers) for supplying information on the Parkes antenna.

TABLE OF CONTENTS

<u>Section</u>		<u>Page</u>
1	INTRODUCTION.	F-1
2	DESCRIPTION OF THE PARKES ANTENNA	F-1
3	STRUCTURAL CONCEPT OF PARKES ANTENNA	F-3
4	EXTENSION OF PARKES STRUCTURAL CONCEPT TO CAMROC ANTENNA.	F-3
5	SIMPLIFIED MATHEMATICAL MODEL	F-5
6	METHOD OF STRUCTURAL ANALYSIS	F-5
7	ERROR ANALYSIS OF SURFACE.	F-8
8	OPTIMIZATION	F-10
9	CALCULATIONS AND RESULTS.	F-11
10	DESIGN DESCRIPTION	F-15
11	DISCUSSION.	F-23
12	CONCLUSIONS AND RECOMMENDATIONS	F-24

1. INTRODUCTION

A recent study by Simpson Gumpertz & Heger Inc. of the Commonwealth Scientific and Industrial Research Organization 210-ft antenna at Parkes, N. S. W., Australia (Figure 1), revealed that:

- 1) The structural behavior of the Parkes antenna can be predicted with good accuracy using existing computer techniques.
- 2) The basic structural configuration of the antenna is efficient and worthy of further investigation.

The investigation reported herein is a feasibility study involving the extension of the Parkes structural concept to an optimum design for the CAMROC antenna. The immediate objectives of this effort are:

- 1) To investigate the structural characteristics of the Parkes dish.
- 2) To utilize the basic structural concepts involved for a preliminary design of the CAMROC antenna.
- 3) To optimize this preliminary design by varying the relative stiffnesses of the different components of the antenna.
- 4) To select member sizes for and calculate the weight of the optimized design.

2. DESCRIPTION OF THE PARKES ANTENNA

The Parkes antenna is 210 ft in diameter and has a focal length of 86.10 ft. Its back-up structure consists of 30 radial trusses radiating from a cylindrical hub 23 ft in diameter and 20 ft long. To prevent excessive deflection of the hub, internal diaphragms are provided at the levels where the radial trusses are connected to the hub. Four systems of circumferential trusses and two ring beams intersect the radial trusses.

Supported on the radial trusses are two orthogonal systems of purlins. These purlins are shallow I-beams arranged in the form of 45° logarithmic spirals. The reflector surface consists of 10-mm-square mesh panels, made from 1-mm high-strength steel wires. The mesh is fastened with self-tapping screws to a system of circumferential and radial subpurlins. The subpurlins are supported on the top surfaces of the spirals by "adjusters" designed to permit rigging of the reflector surface.

The antenna has full azimuth coverage and a zenith-angle coverage of 0° to 60°. The weight of the structure supported by the elevation bearings is approximately 300 tons,

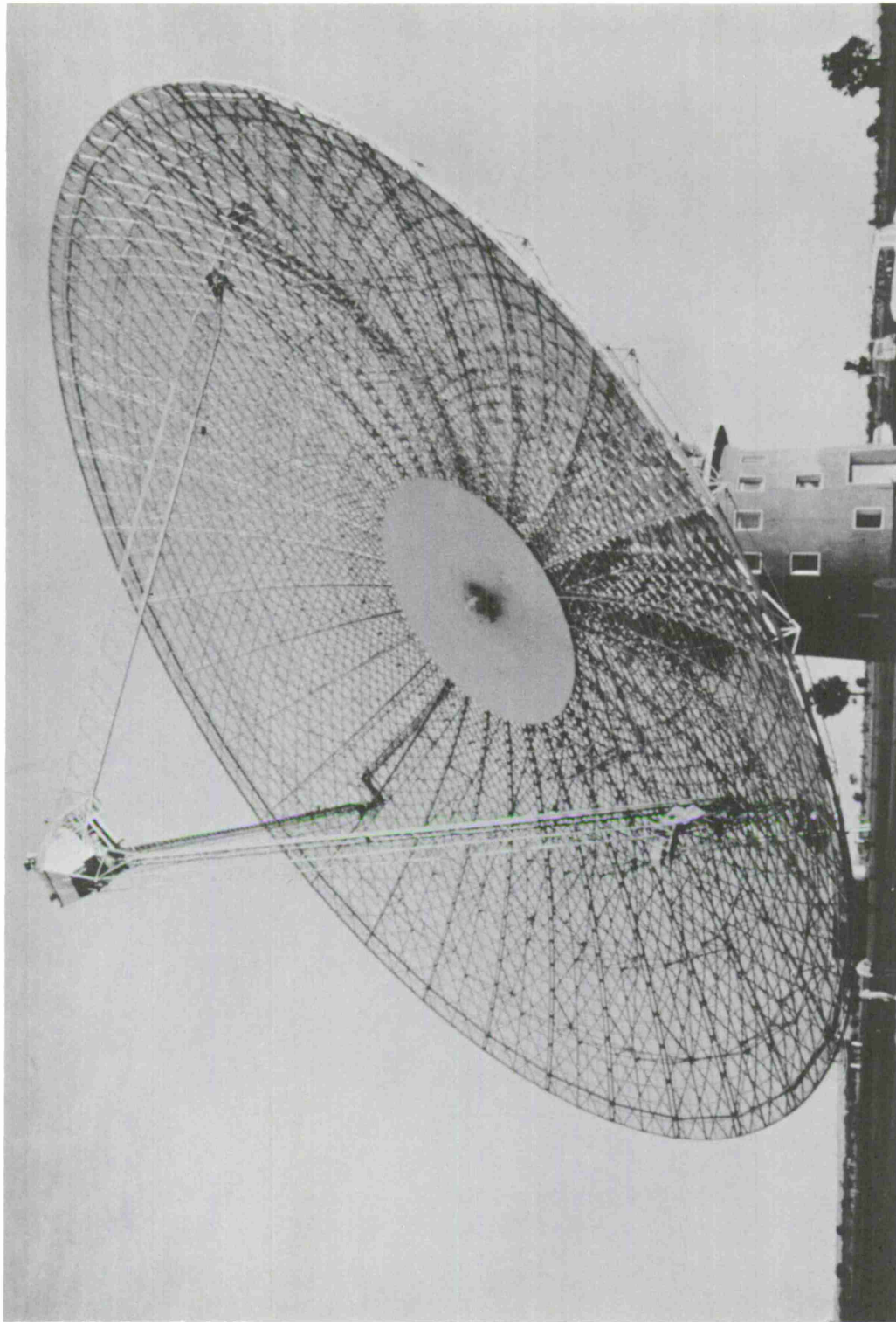


Figure 1. Parkes Radio Telescope

exclusive of the counterweight. The calculated maximum travel of the surface as the reflector tilts from 0° to 60° is ± 0.28 inch. For this calculation the reference paraboloid is positioned to minimize the RMS error of the surface.*

3. STRUCTURAL CONCEPT OF PARKES ANTENNA

The first step in the extension of the Parkes configuration to the CAMROC project is to obtain a thorough understanding of the structural characteristics of the principal elements of the existing antenna. To achieve this, a detailed mathematical model of the Parkes antenna was analyzed under the face-up and face-side dead loads. This model was the same as that used for the previous deflection analysis of the dish except for certain corrections in the support idealization and in the magnitude of the counterweight.* From this analysis the internal force paths were detected, and the behavioral characteristics and role of each element system were isolated. The results of this study are as follows:

- 1) The two systems of orthogonal spiral purlins act in an integrated manner as a shell capable of carrying the externally applied loads by in-plane forces. (All the in-plane stress resultants can be carried by direct tension or compression of the spiral purlins.)
- 2) The radial trusses carry part of the radial stress resultant, and they provide bending stiffness for the shell. They also supply an elastic support for the reflector and thus control the shape of the deflected configuration and limit the magnitude of the deflections.
- 3) The circumferential trusses do not carry a sizable part of the hoop force. Their main action is to prevent instability of the radial trusses by limiting deflections out of their planes.
- 4) The rim beams stiffen the structure at the edge.

4. EXTENSION OF PARKES STRUCTURAL CONCEPT TO CAMROC ANTENNA

For the purpose of this investigation, it is assumed that the CAMROC design diameter is 400 ft, the focal length-diameter ratio is 0.4, and the maximum allowable surface RMS is 0.10 inch.

As described above, the Parkes dish is 210 ft in diameter, weighs about 300 tons exclusive of the counterweight, and has a peak travel in going from 0° to 60° zenith angle of about 0.28 inch after eliminating the rigid-body motions of the reflector. If the antenna is assumed to be linearly scaled up in size, the stiffness of its members would increase linearly; its weight would increase as the third power and deflections as the square of the

*Simpson Gumpertz & Heger Inc., "Deflection Analysis of the CSIRO 210-foot Radio Telescope at Parkes, N. S. W. Australia," vol. 1, July 1965.

scale factor. Therefore, a direct enlargement of the Parkes dish to one 400 ft in diameter would result in a dish that would weight 2100 tons* and would have a peak travel of 1.02 inches in going from 0° to 60° zenith angle. It is important to note that the 400-ft CAMROC antenna is to have a zenith angle coverage of from 0° to 75°. Therefore, the expected peak travel would be 1.2 to 1.5 inches, and the expected RMS 0.4 to 0.5 inch. Even after bias rigging, this error is too large to satisfy the requirements of the CAMROC antenna.

It is apparent that optimization of the preliminary "scaled-up" design requires a reduction in both weight and surface RMS; however, a uniform reduction in the sizes of all members would produce a proportional reduction in stiffness and weight, and hence would cause no reduction of the RMS value.† To improve the dish, the distribution of stiffness and the geometry must be changed so as to optimize the total surface RMS.

The first scaled-up design was made in accordance with the general structural arrangement of the Parkes antenna. The geometry and the member sizes of the hub and the circumferential trusses were obtained directly from an appropriate enlargement of the present dish, but for the design of the spiral "shell" purlins and the radial trusses, it was noted that

- 1) An isotropic shell with uniform thickness in the face-side attitude deflects to a configuration that does not differ much from its original configuration after a rigid-body rotation if (a) the shell is free at its outer edge and simply supported at its inner edge, and (b) the bending distortions can either be eliminated or be confined to a small region.
- 2) If a truss has small shear deflections, the areas of its chords and the depth of the truss can be chosen to make its deflection curve approximately parabolic.

It was not considered desirable to include the weight of the secondary reflector assembly in the optimization study. The tripod leg loads should be delivered to the hub through an independent framework so as not to destroy the axisymmetry of the dish structure. An alternate arrangement would be to support the tripod legs directly on the radial trusses, but with deflection control devices in the latter to eliminate the effect of the secondary reflector assembly on primary reflector deflections.

*Note that this number does not include the counterweight.

†Since the weight of the reflector remains constant, a direct proportionality between weight and stiffness does not exist; therefore, the validity of this statement is only approximate.

5. SIMPLIFIED MATHEMATICAL MODEL

To study the effects of the variation of the parameters of interest, a simplified mathematical model of the CAMROC antenna was constructed. In general, a reduction in the number of degrees of freedom of a system, either in the form of discretization of a continuum or in the form of simplification of a discrete system, involves a certain "discretization error." This error increases as the number of degrees of freedom in the model is reduced. On the other hand, an extensive model is too awkward and costly to work with. To strike a balance between the cost of the investigation and the accuracy of results, a 130-node mathematical model of the CAMROC antenna, composed of pin-connected bars and plates that can take only in-plane forces, was constructed.

The principle involved in the reduction of the number of degrees of freedom is explained here for a radial rib of the Parkes antenna. The overall geometry of the model and prototype trusses is held the same (Figure 2). The areas of the bars in each panel of the model truss are computed separately. For each panel, there are four degrees of freedom, namely the axial and the transverse displacements of the two unsupported joints (Figure 2). The stiffness corresponding to each degree of freedom may be calculated in terms of the four unknown bar areas. The comparison of the deflections of the designed model and of the prototype is made in Figure 3 for a system of vertical and horizontal loads at all the joints of the top chord of the truss.

To check the accuracy and validity of the CAMROC mathematical model, a similar mathematical model of the Parkes antenna was constructed and the deflections obtained were compared to those of the more extensive one. This comparison is shown for two typical ribs in Figure 4.

6. METHOD OF STRUCTURAL ANALYSIS

The mathematical model was analyzed by a large-capacity structural analysis program. Although STRESS seemed at first to be the appropriate computer program, the degree of connectivity of this structure as well as the number of joint releases resulted in a time per IBM 7090 run of more than 1.5 hours. Subsequently, the computer program MAST was employed for the analysis. The computer time required for MAST was about 12 min on the IBM 7090. However, preparation of input for each MAST run involved more work than for a corresponding STRESS run. Later, this program was run on the IBM 360 computer at Lincoln Laboratory; the time per run was 11 min.

The MAST computer program, written for the IBM 7090 and 7094 computers, was developed by Simpson Gumpertz & Heger Inc. as an extension of STAIR. The latter program, originally developed by MIT Lincoln Laboratory for the analysis of pin-connected frameworks, uses the "stiffness method" of structural analysis.

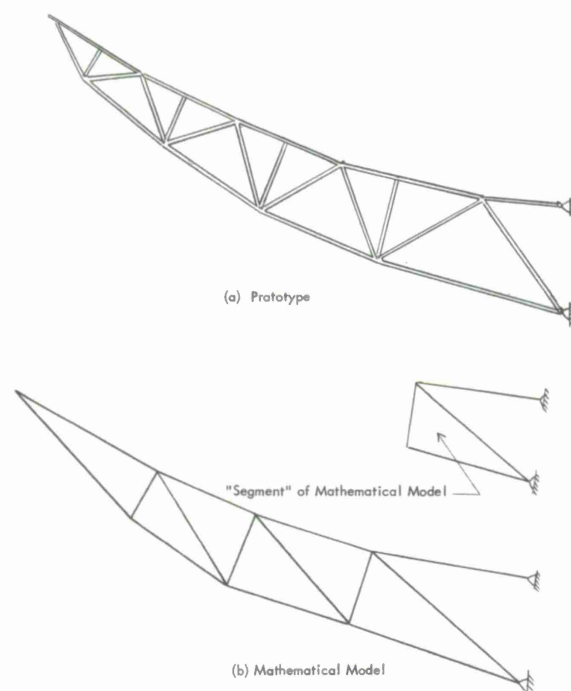


Figure 2. Comparison of configuration of a radial rib of Parkes antenna and of its model.

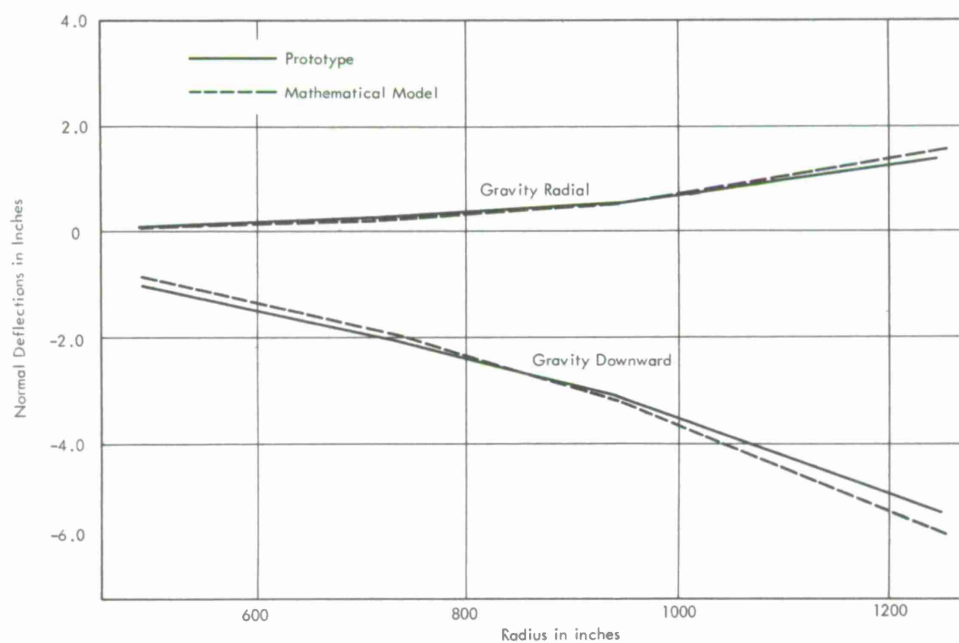


Figure 3. Comparison of normal deflections of a radial rib of Parkes antenna subjected to 100-kip loads at all top-chord joints with those of its model.

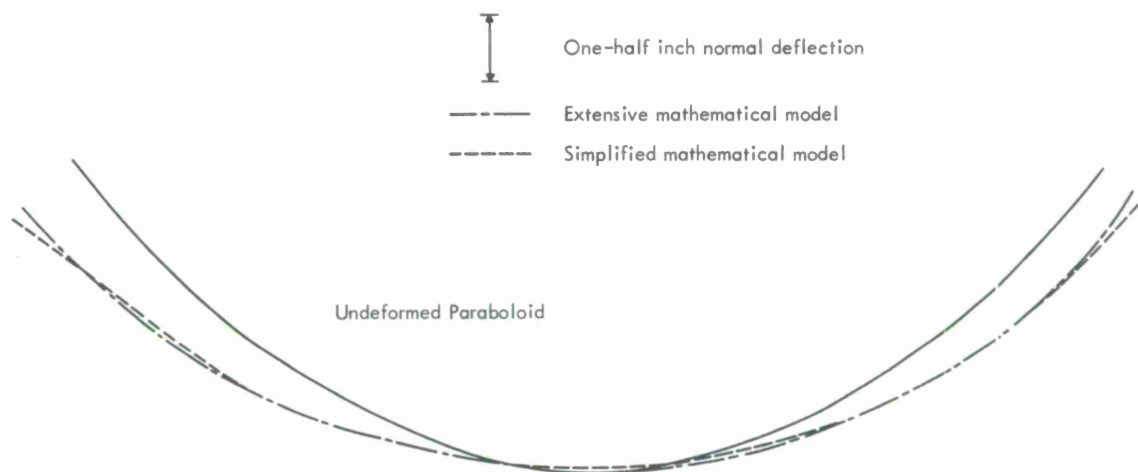


Figure 4. Normal deflection of reflector surface in face-up attitude.

MAST is designed for the analysis of large, linearly elastic space structures that can be idealized into assemblies of quadrilateral and triangular membrane and pin-connected bar elements connected at points (called nodes or joints). Using the stiffness technique, MAST generates and solves the simultaneous equations governing the behavior of such assemblages. The system has been tested and applied successfully to a large variety of structures.

MAST analyzes the idealized structure by first establishing the stiffness matrices for its elements. The stiffness matrix for a pin-ended bar is calculated in the conventional manner. The calculation of plate-element stiffness matrices, however, requires special discussion.

The stiffness matrix for a plate element relates its nodal forces to its nodal displacements. The nodal forces are concentrated forces that are statically equivalent to the edge loads corresponding to a stress state. The stress states determine the strain within the element and thus define the nodal displacements.

A stiffness matrix for a quadrilateral element was derived by Simpson Gumpertz & Heger Inc. for use in the MAST system. For planar quadrilateral elements, the stress states can be expressed in terms of five independent parameters as follows:

$$\begin{aligned} T_x &= c_1 y + c_2, \\ T_y &= c_3 x + c_4, \\ T_{xy} &= c_5, \end{aligned} \quad (1)$$

where c_1, \dots, c_5 are the five independent parameters (Figure 5).

The relationships between nodal displacements and nodal forces for triangular plates are given in the literature.^{*} In deriving this stiffness matrix, a constant stress state as shown in Figure 6 is assumed.

The solution proceeds by assembling individual element stiffness matrices to form stiffness matrices for previously designated groups, called "units," and solving for the nodal deflections. These in turn are substituted into element matrices to yield nodal forces and edge stresses. Finally, the validity of the results is tested by an equilibrium check of internal and external forces at each node.

7. ERROR ANALYSIS OF SURFACE

Weight distribution was optimized to obtain the minimum RMS of the effective surface travels when the antenna goes from face-up to face-side attitude. This quantity may be expressed by the following equation:

$$\text{RMS}^2 = \frac{\int_A f \lambda^2 dA}{\int_A f dA}, \quad (2)$$

where f is the illumination function, λ is the change in the RF path length with respect to the best-fit paraboloid in going from face-up to face-side attitude, and A is the area of aperture.

The surface illumination was assumed to have a paraboloid-on-pedestal distribution with a 12-db edge taper. The values of the function λ were computed at the surface nodes of the mathematical model as follows:

$$\lambda = 2n_z(\hat{n} \cdot \bar{u}), \quad (3)$$

where $\hat{n} = (n_x, n_y, n_z)$ is the unit normal vector and \bar{u} is the displacement vector with respect to the best-fit paraboloid.

^{*}Turner, M. J., Clough, R. W., Martin, H. C., and Topp, L. J., "Stiffness and Deflection Analysis of Complex Structures," Journ. Aeronaut. Sci., vol. 23, no. 9, September 1956.

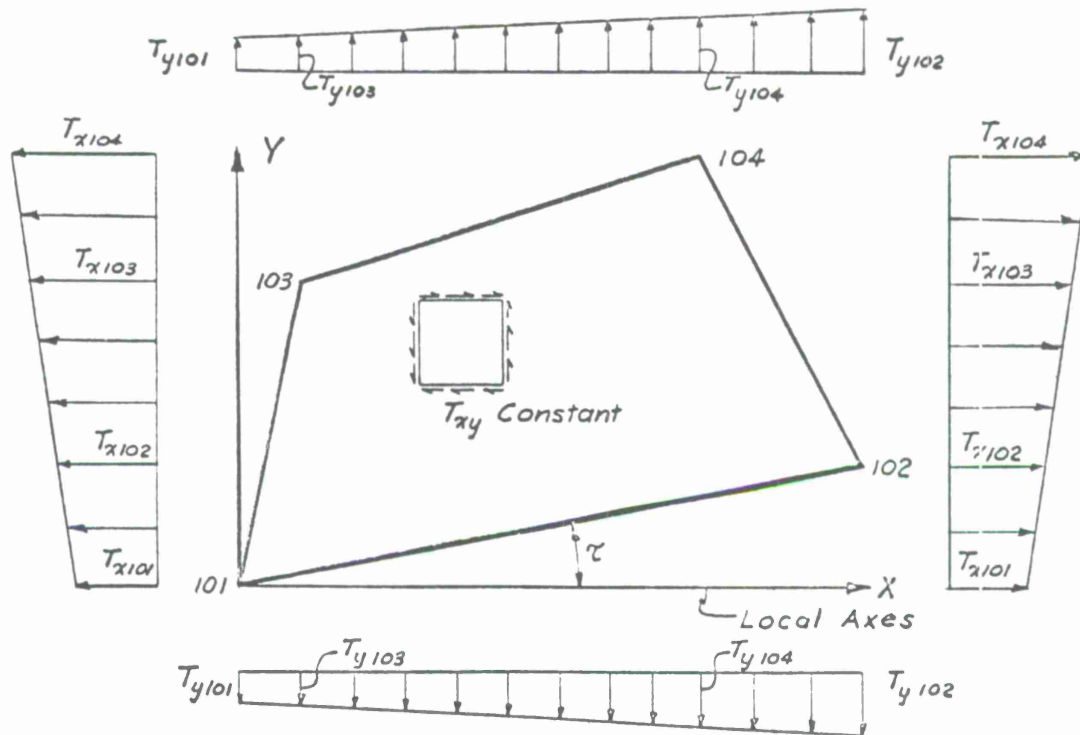


Figure 5. Geometry and stress distributions of a quadrilateral plate.

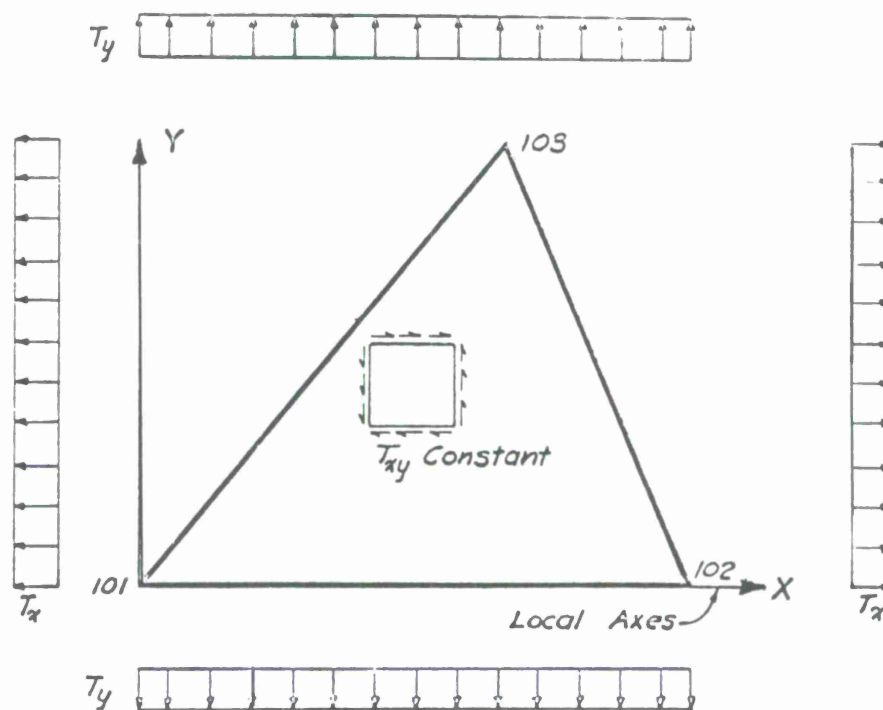


Figure 6. Geometry and stress distributions of a triangular plate.

The displacement with respect to the best-fit paraboloid can be expressed in terms of the magnitudes of the rigid-body displacements and the change in the focal length of the antenna as follows:

$$\bar{u} = \bar{u}_0 - (\Delta x) \hat{i} - (\Delta z) \hat{k} - (\Delta \theta_y)(z \hat{i} - x \hat{k}) + \left(\frac{\Delta f}{f}\right) z \hat{k} \quad (4)$$

where \bar{u}_0 is the displacement vector of the surface points, Δx the x displacement of the theoretical surface, Δz the z displacement of the theoretical surface, $\Delta \theta_y$ the y rotation of the theoretical surface, and $\Delta f/f$ the ratio of the increase in focal length to the original value.

The values of Δx , Δz , $\Delta \theta_y$, and $\Delta f/f$ are obtained by noting that at the location of the best-fit paraboloid we must have

$$\begin{aligned} \frac{\partial(\text{RMS}^2)}{\partial(\Delta x)} &= \int_A f n_z^2 n_x (\hat{n} \cdot \bar{u}) dA = 0 \quad , \\ \frac{\partial(\text{RMS}^2)}{\partial(\Delta z)} &= \int_A f n_z^3 (\hat{n} \cdot \bar{u}) dA = 0 \quad , \\ \frac{\partial(\text{RMS}^2)}{\partial(\Delta \theta_y)} &= \int_A f n_z^2 (\hat{n} \cdot \bar{u}) (z n_x - x n_z) dA = 0 \quad , \\ \frac{\partial(\text{RMS}^2)}{\partial(\Delta f/f)} &= \int_A f n_z^3 z (\hat{n} \cdot \bar{u}) dA = 0 \quad . \end{aligned} \quad (5)$$

These are four linear equations in terms of four unknowns Δx , Δz , $\Delta \theta_y$, and $\Delta f/f$ that can be solved simultaneously. The RMS is then calculated from Eq. (2).

8. OPTIMIZATION

For the purposes of the optimization process, the structural components of the antenna are classified by function and location into groups. The relative sizes of the members in any one group are determined by a prior analysis and are here considered invariable. Starting from a first trial design, the weight (and hence stiffness) of each group in turn is varied, and the resulting changes in surface RMS are calculated. (In the case of the hub, its height is held constant and its diameter allowed to vary.) In this manner, curves can be obtained that define, for each group, the relation between its weight and the surface RMS. From these curves, a revised trial design can be constructed in which the weight of each group is approximately that which gives the minimum RMS.

For refined design purposes, the technique described above is recycled until the revised trial design does not differ significantly in total weight and weight distribution from that resulting from the previous cycle. It is possible, of course, to introduce refinements or modifications in the group classifications at the end of any cycle. Relative

weights of members or of subgroups within each group, and individual geometric parameters can be included in the optimization.

The above procedure is not applicable to the radial trusses, which, within the range of interest, will ordinarily give a slightly (but continuously) decreasing RMS as their weight and stiffness are increased. To find the size and disposition of radial trusses corresponding to a minimum weight design, it is necessary to optimize several different trial designs, each with a different radial truss configuration.

9. CALCULATIONS AND RESULTS

On the basis of preliminary studies, certain modifications were made in the initial scaled-up design, resulting in a revised weight of about 1150 kips. A single optimization cycle then was performed on this revised trial design. The optimization process involved determination of the influence of each of the following parameters on the RMS of the reflector travels owing to tilting from face-up to face-side:

- 1) Weight of spirals.
- 2) Ratio of the area of inner spirals to the area of outer spirals (the outer spirals are defined as the spirals in the outer 80 ft of the dish radius).
- 3) Weight of circumferential trusses.
- 4) Diameter of hub.
- 5) Distributivity of counterweight load.

The results of the parametric studies are shown in Figures 7 through 10. The number and size of the radial trusses were not optimized. As indicated in the previous section, a separate optimization study would be necessary for these parameters; it was considered inappropriate to undertake such an effort in the scope of this preliminary investigation.

Figure 7 shows the effect of the weight of spirals on RMS. The contribution to RMS resulting from the bending of the spirals was neglected here; for spiral weights above the minimum indicated on the figure, this contribution does not exceed about 0.005 inch. It is apparent from the figure that the optimum weight of spirals is the minimum necessary to provide adequate bending stiffness.

The effect of altering the relative weights of outer and inner spirals is small, as is shown in Figure 9. Obviously, it would be desirable to terminate as many spirals as possible as they approach the hub.

The effect of the circumferential trusses on RMS is plotted in Figure 8. For the weight range considered, the influence of these trusses is apparently quite small.

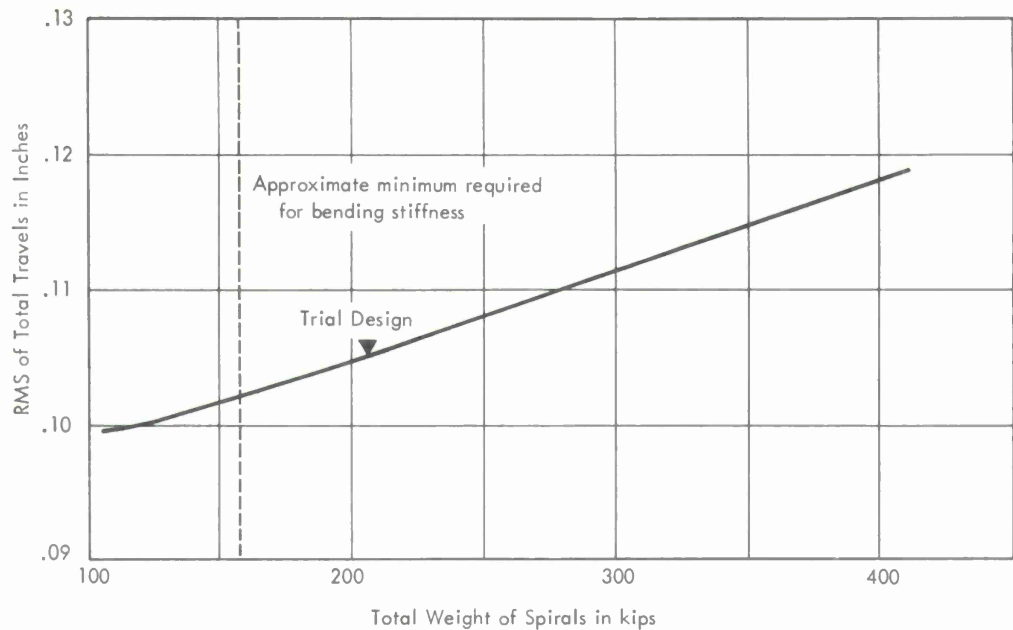


Figure 7. Variation of RMS of travels from face-up to face-side with total weight of spirals.

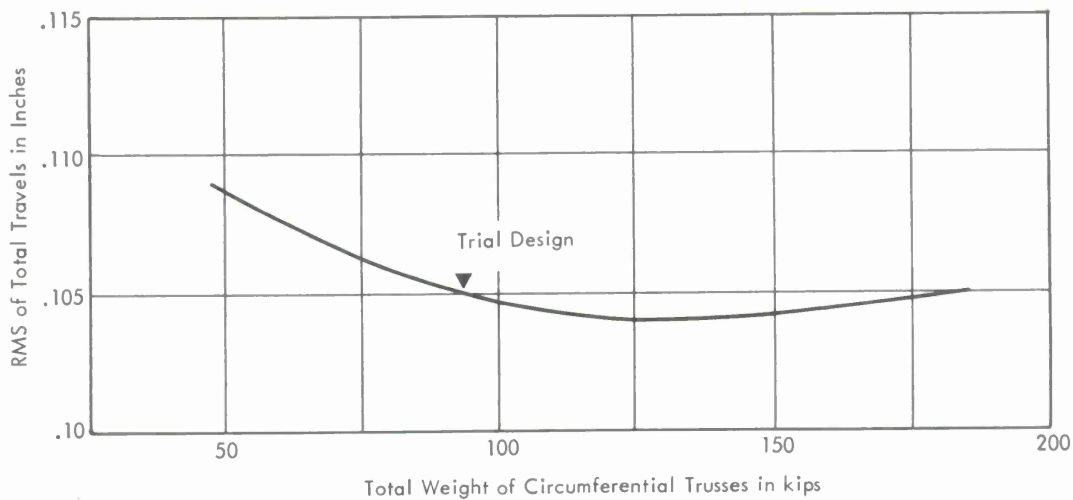


Figure 8. Variation of RMS of travels from face-up to face-side with weight of circumferential trusses.

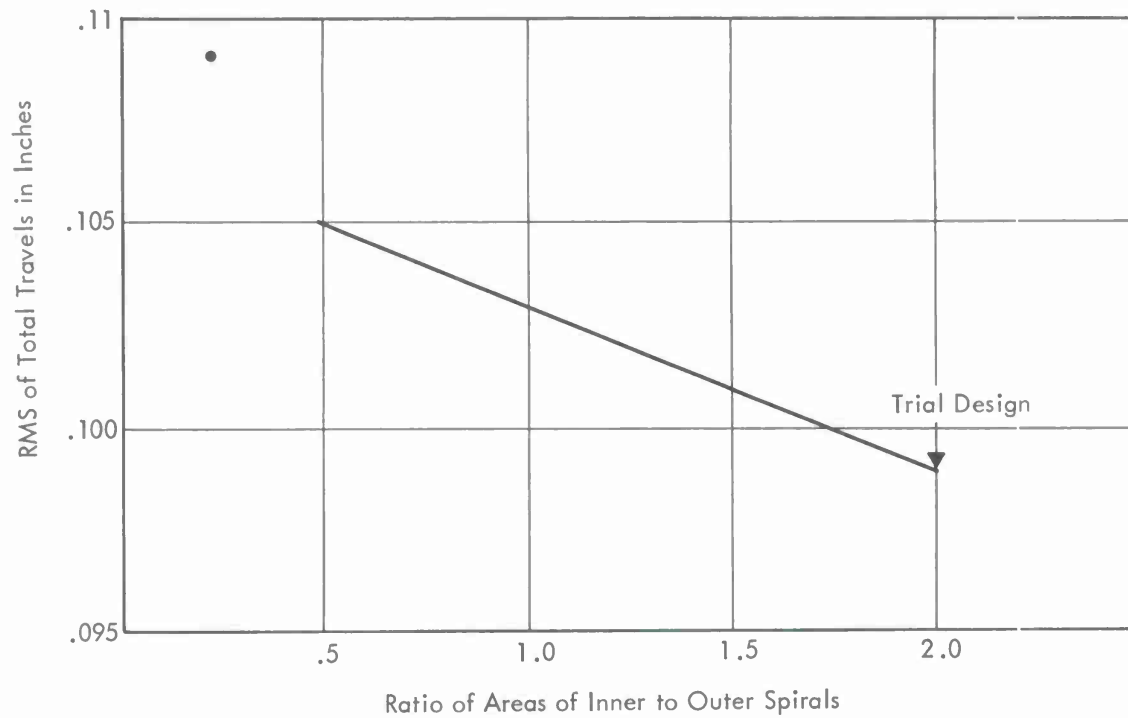


Figure 9. Variation of RMS of travels from face-up to face-side with ratio of areas of inner to outer spirals.

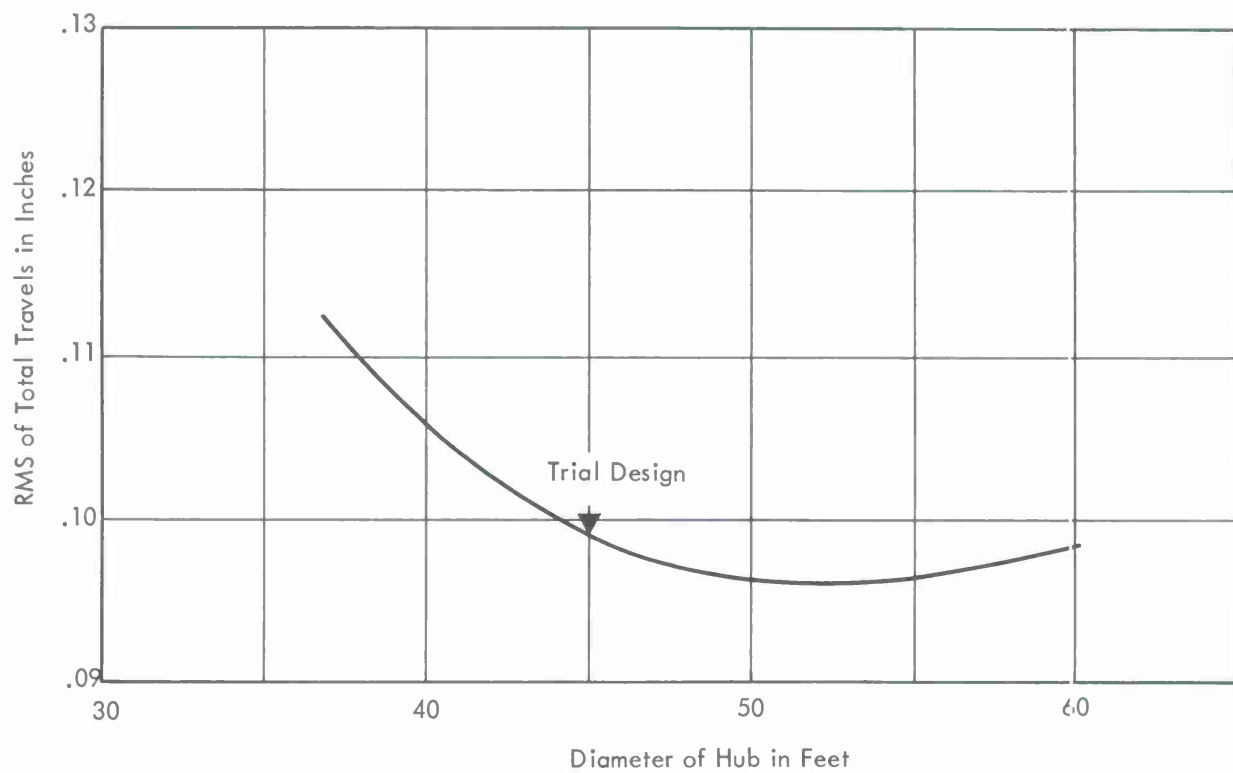


Figure 10. Variation of RMS of travels from face-up to face-side with size of hub.

The effect of distributivity of the counterweight was investigated by performing a surface-error analysis assuming a cosine distribution of counterweight load along the periphery of the hub, and comparing the results with those previously obtained for the concentrated counterweight load. The improved distributivity reduced the face-up-to-face-side travel from 0.104 inch to 0.100 inch.

On the basis of the optimization studies, certain modifications were made in the trial design, and their implications investigated. Contour plots of travels from face-up to face-side for the revised design (but with concentrated counterweight load and with hub diameter retained at the initially assumed value of 45 ft) are presented in Figures 11 and 12.

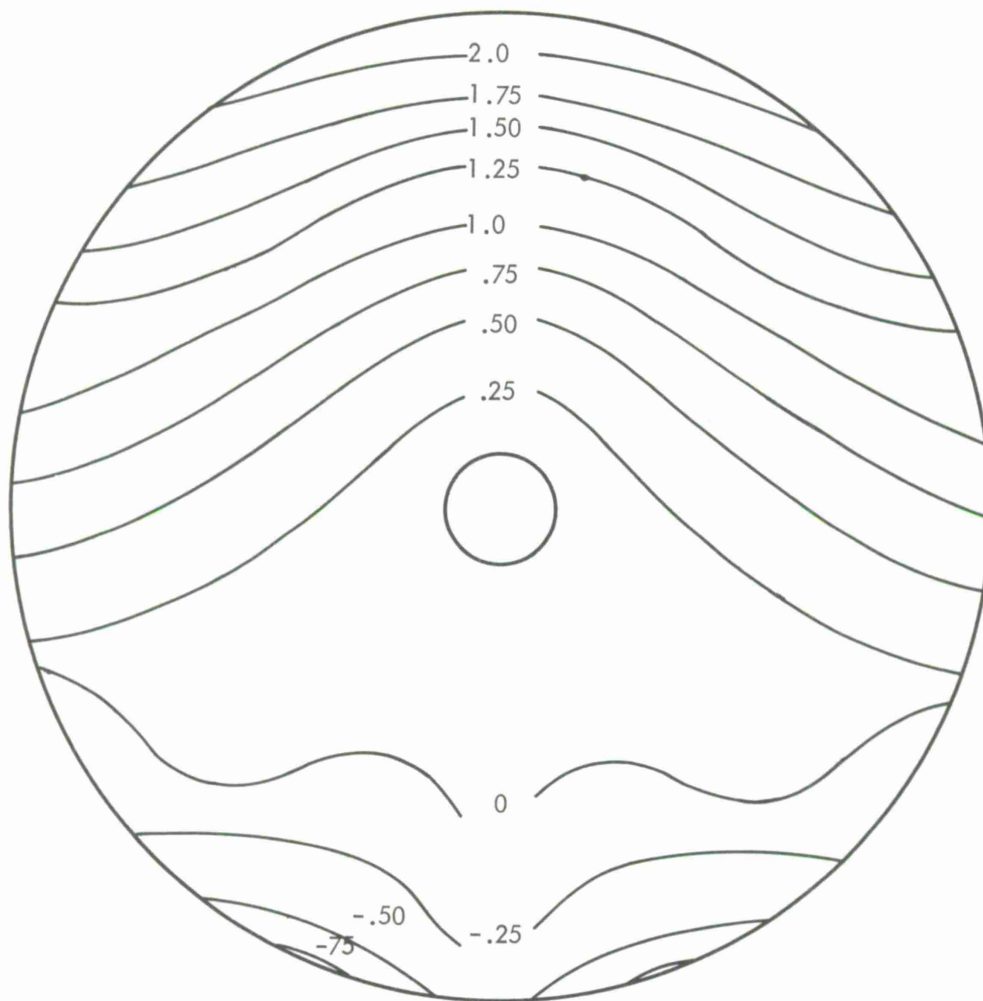


Figure 11. Contour map of z component of travels from face-up to face-side prior to best fitting.

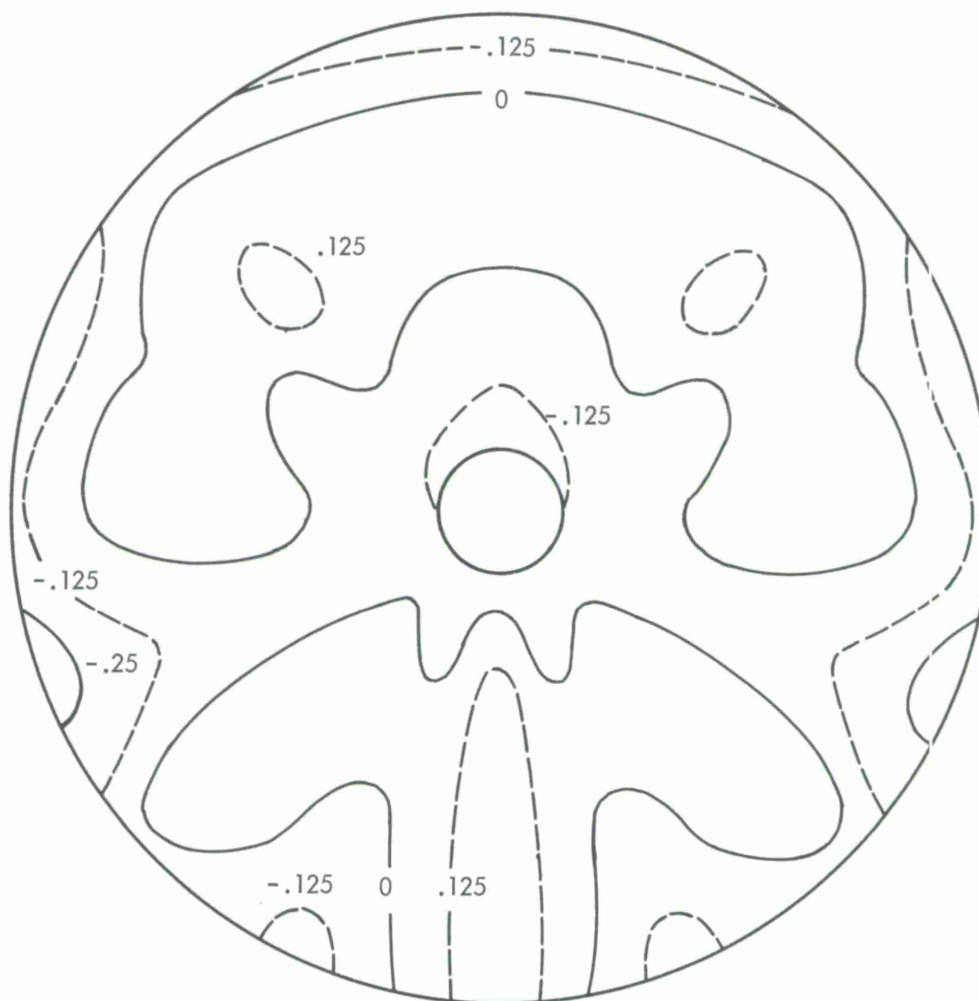


Figure 12. Contour map of effective surface error of travels from face-up to face-side.

After revising the hub diameter to 50 ft and distributing the counterweight load, the RMS of the surface nodes was found to be less than 0.06 inch. (This figure assumed the use of bias rigging in order to halve total travels.) The effect of the deflections of panels and members between nodes is to increase this value to 0.09 inch. Adding, by the root-sum-square rule, 0.03-inch RMS due to the random errors associated with manufacturing and rigging tolerances, the resulting RMS of the "optimized" design is less than 0.095 inch.

10. DESIGN DESCRIPTION

From the results of the parametric study described in the previous section, plus considerations of local bending effects, stability, and the RMS requirements for the antenna, further refinements were made in the trial design. The resulting design is described

below. It is emphasized that this design is presented only as a first approximation to a minimum weight design; as will be discussed in the next section, there is reason to believe that further study can result in appreciable further weight reduction.

The antenna has an assumed diameter of 400 ft and a focal length of 160 ft. The structure above the elevation axis consists entirely of 6061-T6 aluminum. Aluminum was selected rather than steel because the use of the latter would result in a large number of very thin sections.

Reflector Panels. The reflector consists of 15 annuli of approximately rectangular, independently supported panels about 13 ft long by 4 ft wide. The panels are omitted in the inner 20-ft radius, since this region is shaded by the secondary reflector. The panel design (Figure 13) is approximately the same as that developed by MIT Lincoln Laboratory for the proposed Hammerhead concept. Problems due to the difference between the thermal time constants of panel and backup structure favor this use of small panels capable of independent motion.

Circumferential Purlins. These members, which provide the support for the reflector panels, are fabricated of back-to-back double channels (Figure 14). The maximum deflection of the panel-circumferential channel assembly due to its own dead weight is about 0.063 inch.

Spiral Purlins. These provide support for the circumferential purlins and are in turn supported by the radial and circumferential trusses. They are arranged in two orthogonal systems, each consisting of 96 continuous members, extending from the face of the hub to the edge of the reflector. Notwithstanding the results of the parametric study, it was found necessary to make the outer spirals heavier than the inner ones, in order to hold their bending deflections to an arbitrary maximum of 0.02 inch. The added weight of spirals was partially compensated by a reduction in the sizes of the nearby circumferential trusses. The average maximum bending deflection of the spiral system due to transverse gravity loading is approximately 0.012 inch.

Circumferential Trusses. Six circumferential trusses are provided (Figure 15). Figure 16 shows a detail of the truss located at the 160-ft radius. The maximum deflection of the circumferential trusses is less than 0.005 inch.

Radial Trusses. The 48 radial trusses are laterally supported by the spiral purlins, the circumferential trusses, and a system of tensioned cables. Buckling of the members of the radial truss in its own plane is prevented by the addition of auxiliary members and cables. The top chord of the radial truss is designed for an average maximum bending deflection between nodes of about 0.012 inch and a peak deflection of less than 0.025 inch. The geometric configuration of a typical radial truss is shown in Figure 17. The general arrangement of the tensioned cable stays is given in Figure 15.

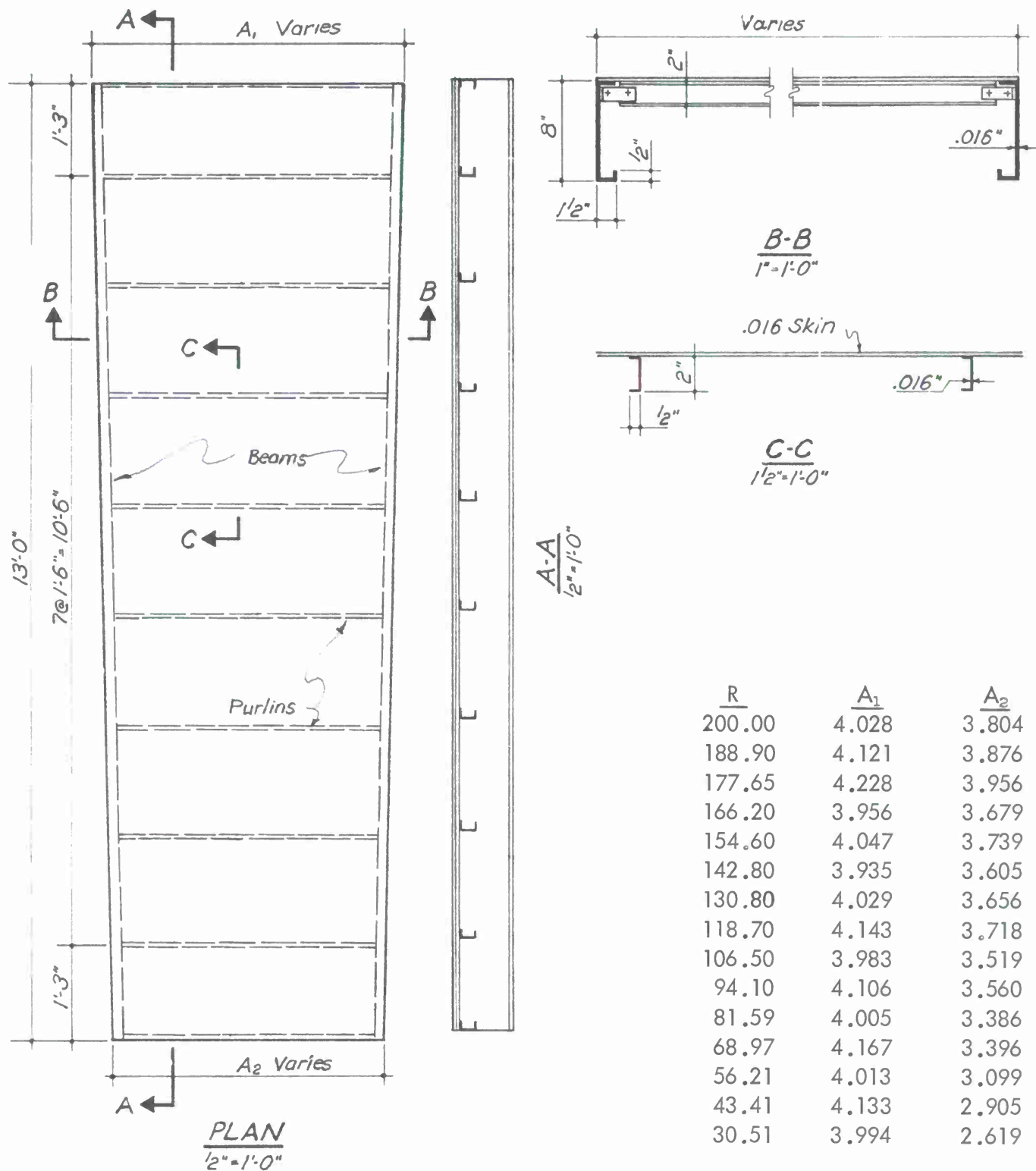


Figure 13. A typical panel of reflector.

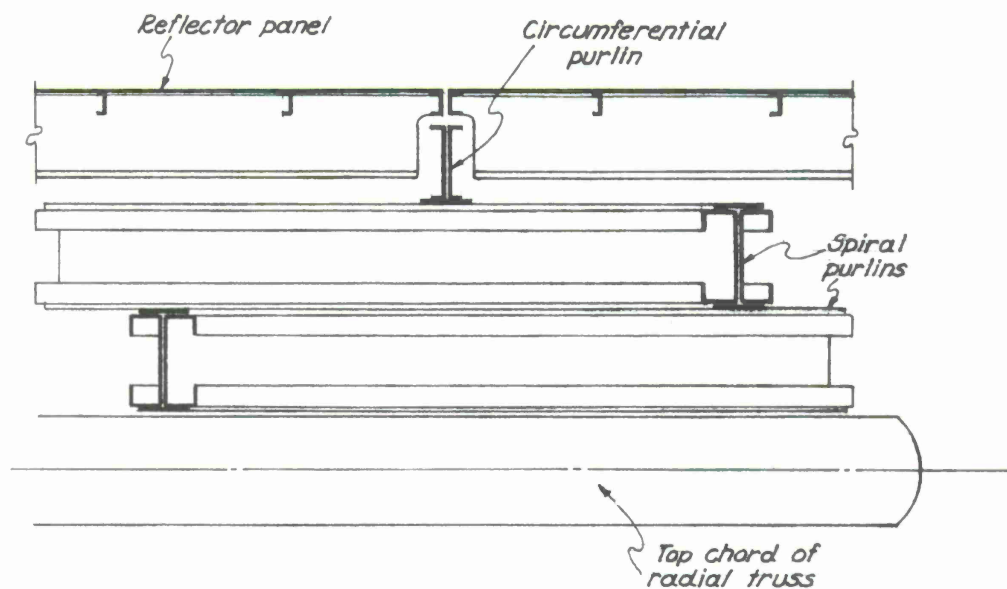


Figure 14. Arrangement of panels and spiral purlins.

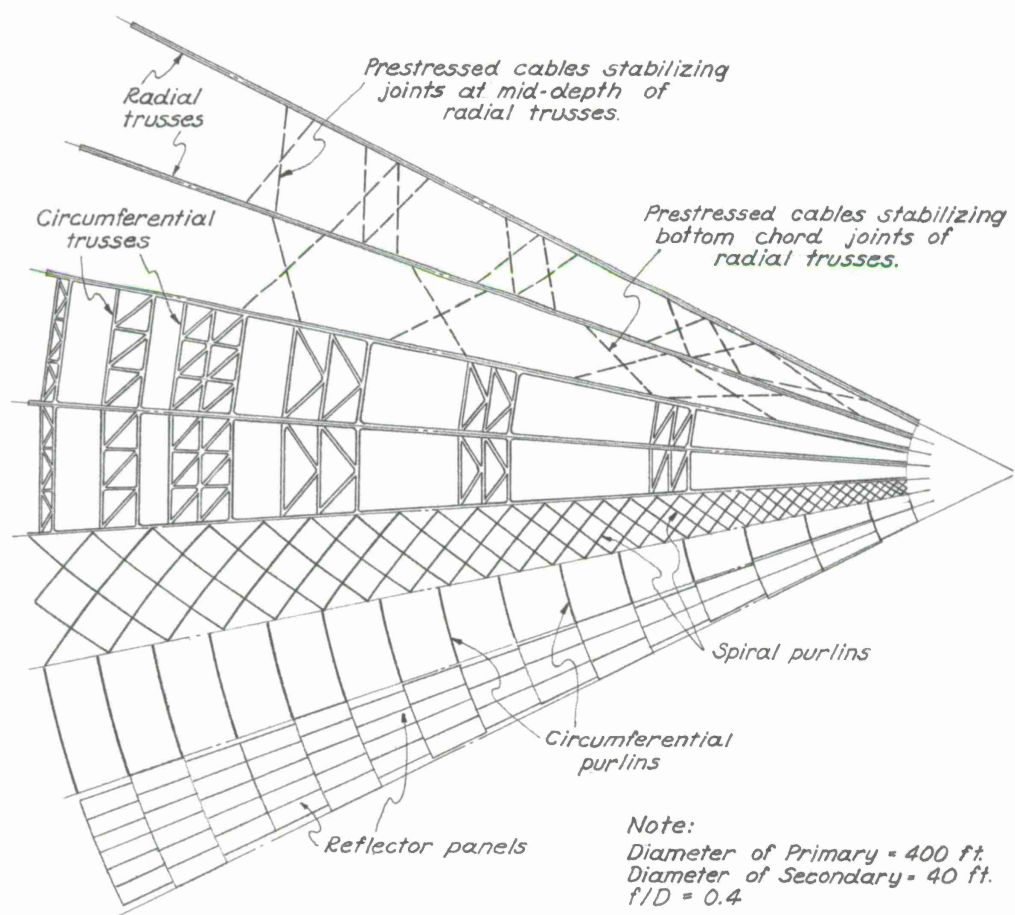


Figure 15. A schematic of reflector and backup structure.

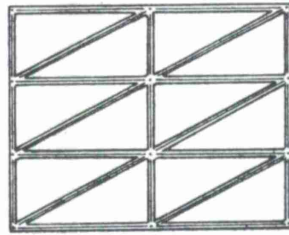


Figure 16. Circumferential truss at 160-ft radius.

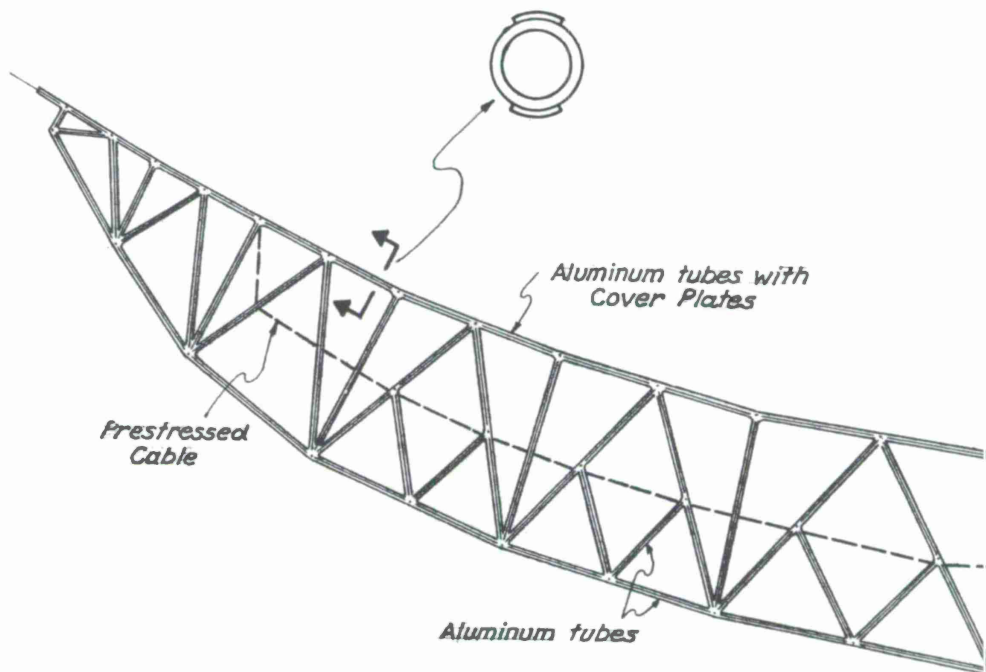


Figure 17. Typical radial truss.

Central Hub. The hub is a cylindrical structure 50 ft in diameter by 43 ft deep (Figure 18). The wall thickness of the cylinder varies with height, from 3/8 inch at the top to 1/2 inch at the base, in two increments. A system of 48 vertical stiffeners and three intermediate circumferential stiffeners braces the cylindrical skin against buckling.

Heavy circumferential ring beams are provided at the top and the base of the hub to provide reactions for the radial trusses. The upper ring is extended upward and welded to the spirals.

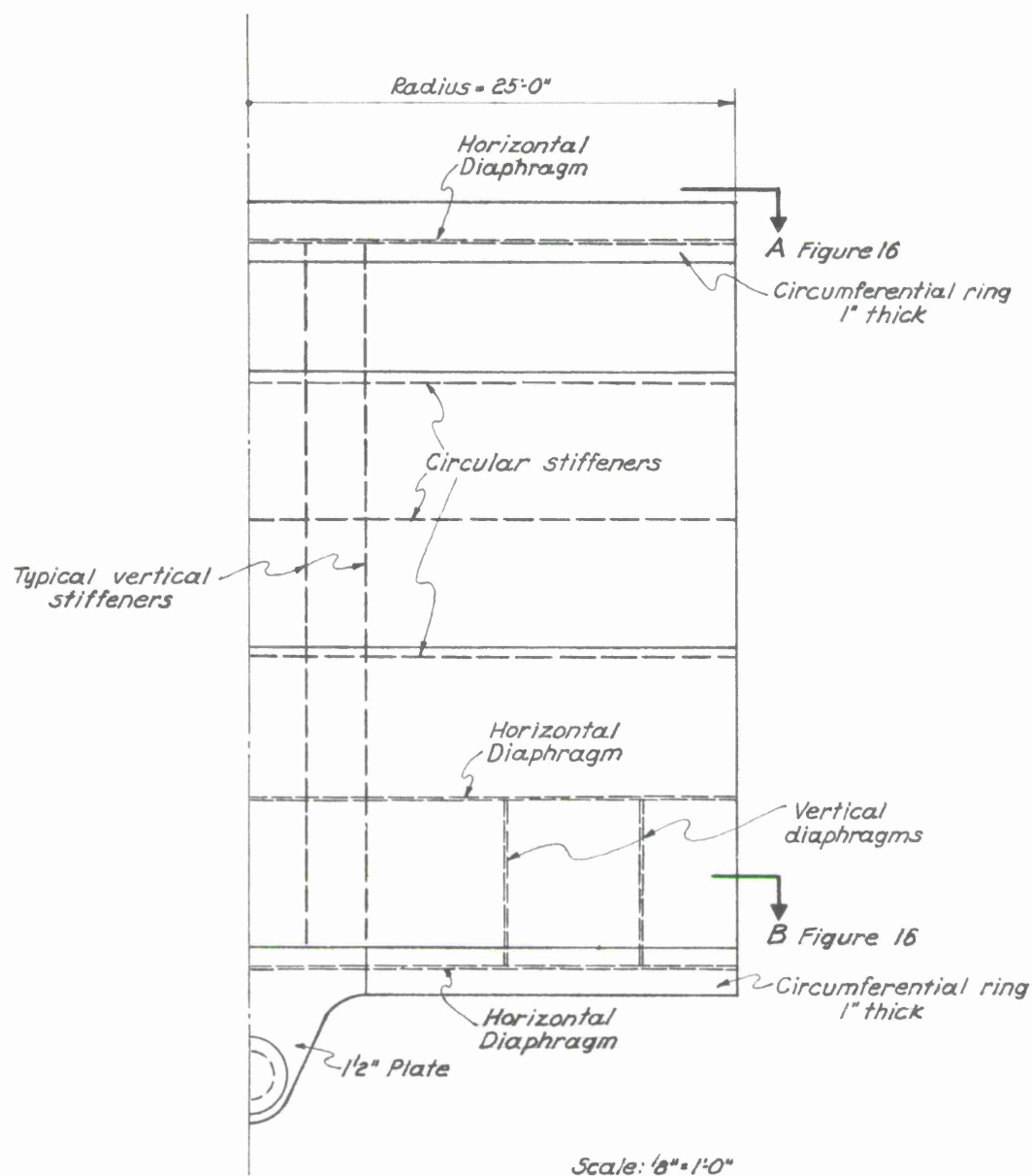


Figure 18. Hub - elevation view.

The radial rigidity of the hub is achieved by three diaphragms stiffened in both directions (see Figure 19). The lower two diaphragms, together with a system of vertical walls, provide for the efficient distribution of the counterweight load.

34

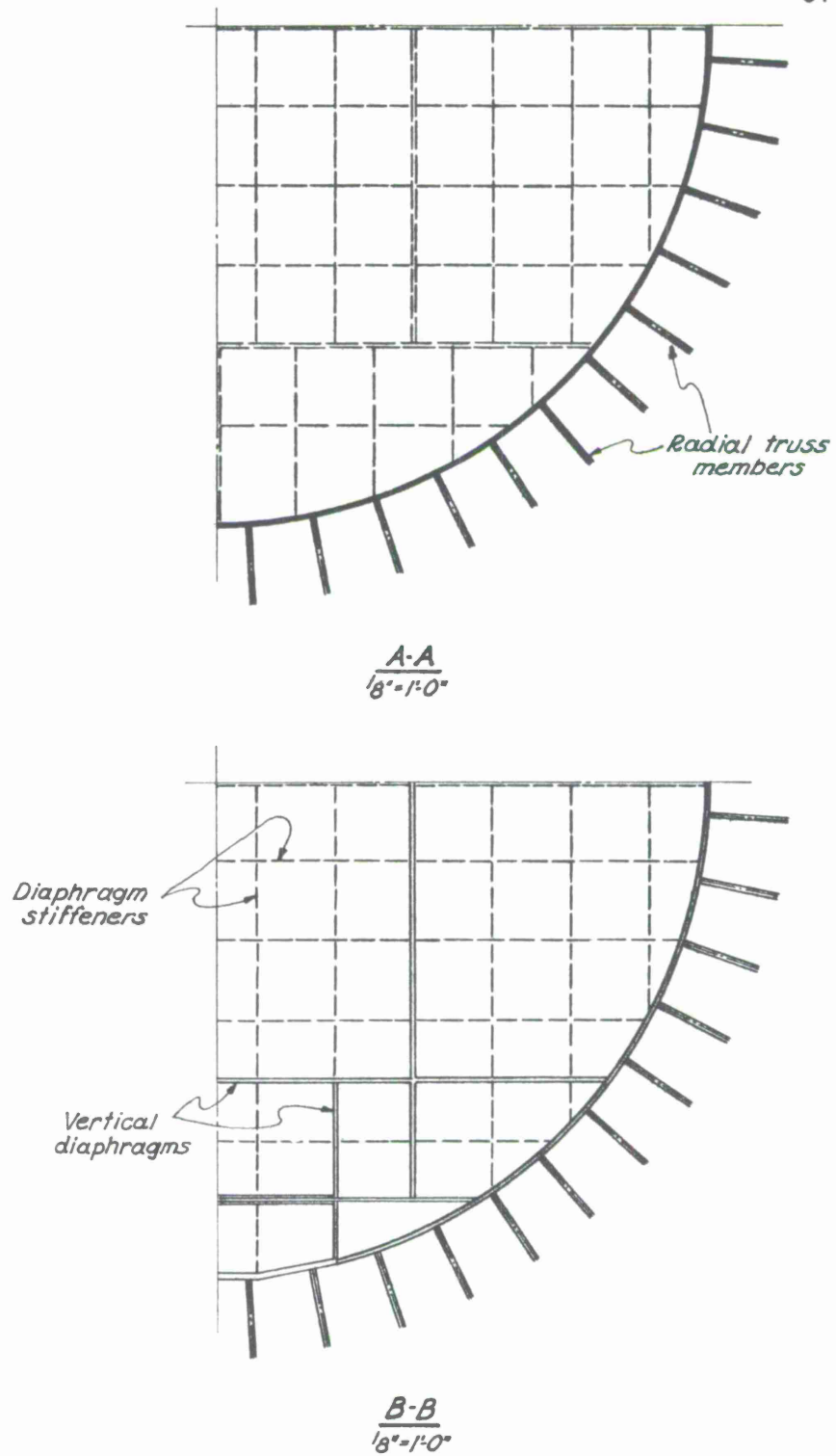


Figure 19. Hub diaphragms.

Connections. The connections between the members of the trusses are achieved by direct welding of the tubing (Figure 20). In estimating the weight of the hardware, it should be noted that the weights of the trusses are calculated assuming that every member extends fully between the center lines of the connecting members. This approximation is on the conservative side, since small sections ordinarily will be removed at both ends.

For joints where a large number of members meet, a special connection, as shown in Figure 20, was developed.

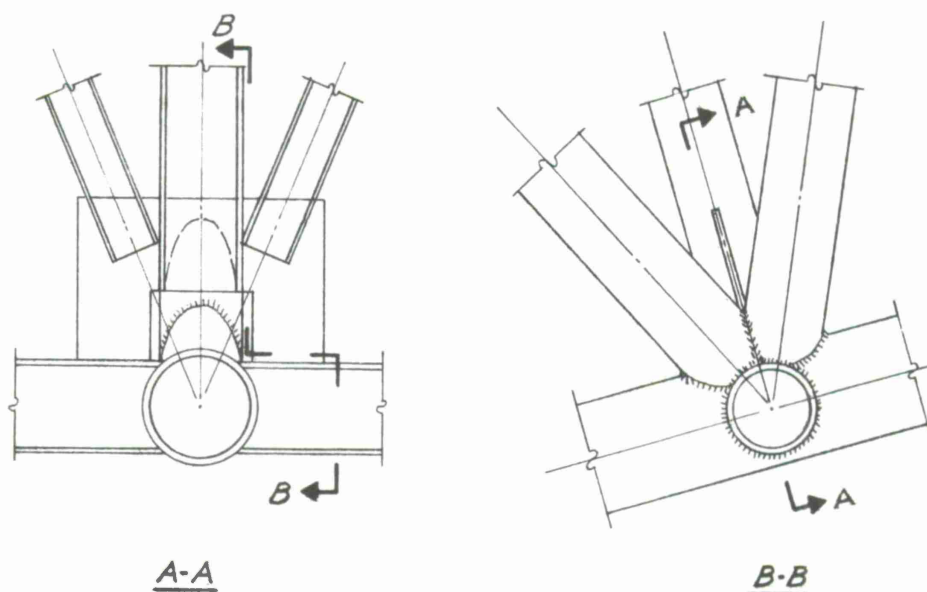


Figure 20. Typical connection between radial and circumferential trusses.

Weight. A weight breakdown for the design described above is given below:

Reflector panels and circumferential purlins	72 kips
Spirals	160 kips
Circumferential trusses	150 kips
Radial trusses including cables and secondary members	359 kips
Hub	129 kips
Hardware	<u>25 kips</u>
Total weight exclusive of the secondary reflector, tripod, and counterweight	895 kips

11. DISCUSSION

The Parkes antenna derives its efficient behavior in large part from the fact that its deformed configurations are approximately paraboloidal. The optimization process described previously in effect determines the distribution of stiffnesses that, within the constraints imposed by the assumed structural configuration and member groupings, will make the deformed configuration as nearly paraboloidal as possible.

It is apparent from the curves in Section 9 that the effect on RMS of varying the sizes of spirals or of circumferential trusses is rather small. The indication appears to be that the trial design on which the optimization was performed is already fairly well proportioned, and also (as may be expected) that the role played by spirals and circumferentials in an indoor dish is much less significant than in dishes exposed to wind loads.

The size of the hub has a strong influence on RMS. The larger hubs reduce the deflection, but they adversely affect the shape of the deformed surface. The smaller hubs result in larger absolute displacements and may fail to block the effect of the counterweight on surface distortions. Apparently, the optimum hub diameter for the configuration investigated is about 50 ft.

The cumulative effect of all the changes suggested by the optimization study is to reduce the surface RMS by about 30%.

It is emphasized that the radial truss configuration selected for the trial design was obtained from approximate preliminary studies and not from a formal optimization process. It is entirely possible that a significant reduction in the weight of the proposed design can be achieved by performing the optimization procedure of Section 9 on one or two trial designs in which the radial truss weight is materially reduced from that previously assumed. This should provide enough information to indicate the optimum weight of radial truss corresponding to the desired RMS.

The question of the effect of the size of the antenna on its cost for a given RMS has been raised. An approximate answer to this question can be obtained for the structural concept investigated herein by the following equation:

$$W = 895 \left(\frac{a^4}{2} + \frac{3a^2}{8} + \frac{a^{3.5}}{8} \right),$$

where a is the diameter of the dish in feet divided by 400, and W is the weight of the structure in kips. Therefore, for a 500-ft antenna, the total weight, exclusive of secondary reflector assembly and counterweight, would be 1785 kips; for a 300-ft antenna, the weight would be 395 kips.

The slope of the cost versus tolerance curve for the 400-ft antenna may be estimated at roughly one-to-one in the range of 0.075- to 0.150-inch RMS. Reduction in RMS may be achieved, for example, by increasing the depth of trusses; this reduces the deflection but increases the weight, resulting in an approximately linear effect on RMS.

The structural concepts of this antenna make it quite attractive as an out-of-radome dish. However, the preliminary investigation of the cost of such a dish reveals that the survival load will govern the design. The total weight of an out-of-radome antenna designed to withstand 100-mph winds will be significantly more than twice the weight of the indoor antenna.

12. CONCLUSIONS AND RECOMMENDATIONS

The design described in Section 10 is a first approximation to an optimum design of an indoor, 400-ft-diameter dish based on the Parkes configuration. The structure above the elevation axis consists entirely of 6061-T6 aluminum, and its weight is estimated at 895 kips, exclusive of the secondary reflector assembly. There seems to be a good probability that this weight can be further reduced by additional optimization studies.

The maximum RMS of the surface deviations for elevation angles between 0° and 90° , including the effect of deflection of structure between the nodes as well as the deflection of the node points and the random errors introduced during manufacturing and rigging, is estimated at about 0.095 inch.

The effect of size of the antenna on its weight is indicated by the estimate that an increase in the diameter to 500 ft would result in a weight of 1785 kips, while a decrease to 300 ft would correspond to a weight of 395 kips.

It is estimated that, within the range 0.075- to 0.150-inch RMS, the cost of a 400-ft antenna is roughly inversely proportional to the required RMS tolerance.

An extension of the effort reported herein should include the following tasks:

- 1) An optimization study of the structural configuration of the radial trusses.
- 2) Refined stiffness distribution optimization studies.
- 3) The design of the tripod and its supporting structural or mechanical components.
- 4) The design of mechanical systems and the design of the counterweight.
- 5) Vibration analyses.

APPENDIX G

ENGINEERING SUMMARY
OF A STUDY
FOR A 400-FT-DIAMETER RADOME-HOUSED RADIO TELESCOPE

Prepared for
THE CAMBRIDGE RADIO OBSERVATORY COMMITTEE

December 8, 1966

ROHR CORPORATION
ANTENNA DIVISION
CHULA VISTA, CALIFORNIA

ABSTRACT

A design and cost analysis has been conducted on a radome-housed 400-ft-diameter radio telescope.

The results have shown that significant cost and performance advantages can be gained if a large-diameter radio telescope is designed specifically for a radome environment. In fact, a total cost has been estimated at a low \$6.5 million, which is approximately \$40 million less than its environmental counterpart. The design is estimated to weigh approximately 1 million lbs total (excluding concrete pedestal).

From a performance standpoint, a radome-housed 400-ft-diameter telescope can be economically designed to meet the surface accuracy requirement of 0.100-inch RMS and a pointing-accuracy requirement of 15 arcsec (peak 3σ). In fact, a reflector concept that weighs approximately 0.7 psf, the "Rohr lightweight concept," has been developed.

The controlled radome environment permits utilizing engineering and manufacturing techniques that would not be advisable for an environmentally designed telescope. Without the controlled radome environment, meeting the pointing-accuracy requirement would be economically prohibited.

From the results of this study, a radome-housed telescope consisting of a standard parabola supported by an elevation-over-azimuth mount is recommended for the CAMROC program.

TABLE OF CONTENTS

<u>Section</u>		<u>Page</u>
1	INTRODUCTION	G-1
2	SUMMARY AND CONCLUSIONS	G-2
3	DESCRIPTION OF THE TELESCOPE	G-8
4	ANALYSIS AND RESULTS OF THE 400-FT-DIAMETER RADOME - HOUSED RADIO TELESCOPE	G-13
5	COST AND WEIGHT VERSUS SKY COVERAGE	G-51

1. INTRODUCTION

This report summarizes the engineering analyses conducted on a 400-ft-diameter radome-housed radio telescope. The antenna concept developed exploits fully the use of the radome environment. The end result is an extremely lightweight reflector structure, "the Rohr lightweight concept," which utilizes unique fabrication techniques tailored specifically to optimizing weight while maintaining minimum antenna cost.

A recent study entitled "Engineering Summary of a Study to Evaluate the Effects of a Radome Environment on the Performance and Cost of a Large-Diameter Radio Telescope" (see Appendix A) demonstrated the economic advantage of a radome environment for a large-diameter radio telescope.

This 400-ft-diameter radio telescope study substantiates the conclusions reached previously and amplifies the advantages of the radome environment to an ultimate conclusion resulting in a reflector backup structure that has an average weight of less than 0.7 psf of projected area.

The need for this study stems from the absence of data on large-diameter radio telescopes designed specifically for a radome environment. The study was patterned to assist CAMROC in determining the highest performance, most economical radio telescope concept and has explored optimum utilization of materials that may be applied.

The radio telescope specification developed for the program requires a surface accuracy of 0.150-inch RMS (0.100-inch RMS desired), and a pointing accuracy of 15 arcsec (3σ) repeatability. These tolerances include the nonrepeatability gravity load deflections, deflections due to tracking accelerations, thermal differential deflections, and servo and readout system errors. Maximum servo and drive-system requirements were $0.5^\circ/\text{sec}$ velocity and $0.05^\circ/\text{sec}^2$ acceleration for the azimuth axis, and $0.3^\circ/\text{sec}$ velocity and $0.025^\circ/\text{sec}^2$ acceleration for the elevation axis.

The radome: no-radome study referenced previously illustrated the significant effects of the radome environment on the design of a large-diameter radio telescope. The conclusions developed were:

- 1) Surface panel loads determine the performance and cost of an extremely lightweight reflector structure.
- 2) Despite its low modulus of elasticity, aluminum may be utilized economically for the reflector backup structure and feed support.
- 3) Member stresses are very low; therefore, L/r criteria are of extreme importance (where L is the length and r the radius of gyration).
- 4) The depth of the reflector structure should be reduced to minimize L/r and the total reflector weight and counterweight should be kept to a minimum.

- 5) Since gravity is the only distortion vector of importance, compensation devices must be investigated.
- 6) An optimized reflector-support girder and elevation-wheel assembly should be developed, resulting in circular gravity deflection contours and a homologous deflection pattern with minimum weight (locating the axis of rotation as close to the center of gravity of the reflector as possible will minimize counterweight).
- 7) Very low power drive and servo systems are required and should be carefully analyzed.
- 8) Axis frictions become major loads and affect the drive and servo design.
- 9) Unbalance torque is critical to the drive and servo design.
- 10) The absence of wind permits very low system stiffness characteristics.
- 11) The maximum antenna pointing error can be very small and therefore approach the 1/10 beamwidth requirement.

The objective of the present study, therefore, was to evaluate the effect of each of the above parameters on the design and cost of a 400-ft-diameter telescope. The study has satisfied the above purpose.

2. SUMMARY AND CONCLUSIONS

The effect of a radome environment on the design of a large-diameter radio telescope presents new and relatively unexplored structural and mechanical design approaches for radio-telescope applications. Owing to the absence of the wind environment, the structure need be capable of supporting only its own weight and the weight of the surface. This brings to the foreground completely new approaches in lightweight reflector design techniques, and low power drive concepts.

For example, by utilizing aluminum for the reflector surface and backup structure and by using special fabricated thin-walled tapered round tubular members for the reflector backup structure, a total weight for the components of 129,000 lbs or approximately 1 psf is possible. This is greater than 1 order of magnitude less than an equivalent environmentally designed telescope. Correspondingly, drive-power requirements of only 5 hp per axis, which is greater than 2 orders of magnitude less than the environmental counterpart, point out the significant advantage of the radome environment on the design of mechanical components. The resulting cost of this system is \$6.5 million excluding engineering, shipping, and profit. This represents \$13 million less than the more standard type of radome-housed telescope design that uses conventional structural techniques.

Figures 1 through 5 were extracted from the 210 radome: no-radome study (Appendix A), which resulted in a 5.8-million lb design costing approximately \$19.5 million. Based on this extrapolation, we could not fully realize the cost saving due to the radome environment. This 400-ft study has shown that the antenna weight can be further reduced to 1.1 million lbs (a factor of 5.3) and the cost reduced to \$6.5 million (a factor of 3.0). Significant to note is that the dollar per pound is rising rather sharply, which is as expected, even though the total cost is considerably less.

2.1 Recommendations and Further Investigations

This study, although limited in scope, represents a first real look at the economics of a radome on the design of a large-diameter radio telescope designed specifically for the radome environment. The cost has been firmly established and full advantage of the radome environment was utilized. Since the only vector that we are trying to overcome is gravity, the least-weight design would represent the best, technically and economically, which were the goals set for this study. Stress levels are very low owing to the absence of wind, and very lightweight member sections were developed, including a lightweight surface. The structural limitation of $L/r = 200$ presented one of the lower limits on member sizes, and hence on weight and cost, as was expected. The weight of the surface, however, emerged as the limiting criteria since its effect on performance of the lightweight structure was significant.

Since the conclusions reached are the result of a first trial design for a lightweight 400-ft-diameter radome-housed telescope, it is suggested that the following investigation be made in order to exploit full advantage of this concept:

- 1) The geometry of the 400-ft-diameter radio telescope "lightweight" concept needs optimization in order to develop the most efficient structure.
- 2) Since the tapered sections came through as being exceedingly efficient, they should be further investigated for cross section and various materials.
- 3) Since the external load from the surface panels represents a significant contribution to the deflections, steel- rather than aluminum-walled tapered tubular members should be investigated since this will reduce the deflection contributions from the panels by 2/3.
- 4) Compensation devices for the hyperbola, axial, and tilt (in order to best fit the reflector deflection) and within the structure need additional investigation. From an electrical standpoint, will the changing focal point require an adjustment at the feed and will it affect the curvature of the hyperbola?
- 5) Owing to the significant contribution from the surface panels to the deflections of the reflector, an investigation of alternate approaches with different materials (magnesium?) is warranted (i. e., similar to the two presented in this report).

Figure 1. Cost and weight summaries.

		Diameter	210 ft		100 m (328 ft)	
			Environmental*	Nonenvironmental†	Environmental**	Nonenvironmental
Cost	Weight	Millions of lbs	4.8	1.6	11.6	3.9‡
		Ratio	3	1	7.3	2.4
	(Less engineering and profit)	Millions of dollars	9.4	4.3	30.0	13.2
		Ratio: environmental nonenvironmental	2.20	1	2.28	1
		Approximate dollars/lbs	2.0	2.7	2.6	3.4
		Diameter	400 ft†		400 ft***	
			Environmental	Nonenvironmental	Nonenvironmental	
Cost	Weight	Millions of lbs	22	5.8	1.1	
		Ratio	13.8	3.7	0.7	
	(Less engineering and profit)	Millions of dollars	46.0	19.5	6.5	
		Ratio: environmental nonenvironmental	2.36	1	7.1	
		Approximate dollars/lbs	2.1	3.4	5.9	
<p>* Based on JPL contract — W. O. 420.</p> <p>† Based on MIT study — W. O. 748 (210-ft extrapolation).</p> <p>** Based on NRAO study — W. O. 215.</p> <p>*** Based on MIT study — W. O. 988.</p> <p>‡ Based on an equivalent stiffness extrapolation.</p>						

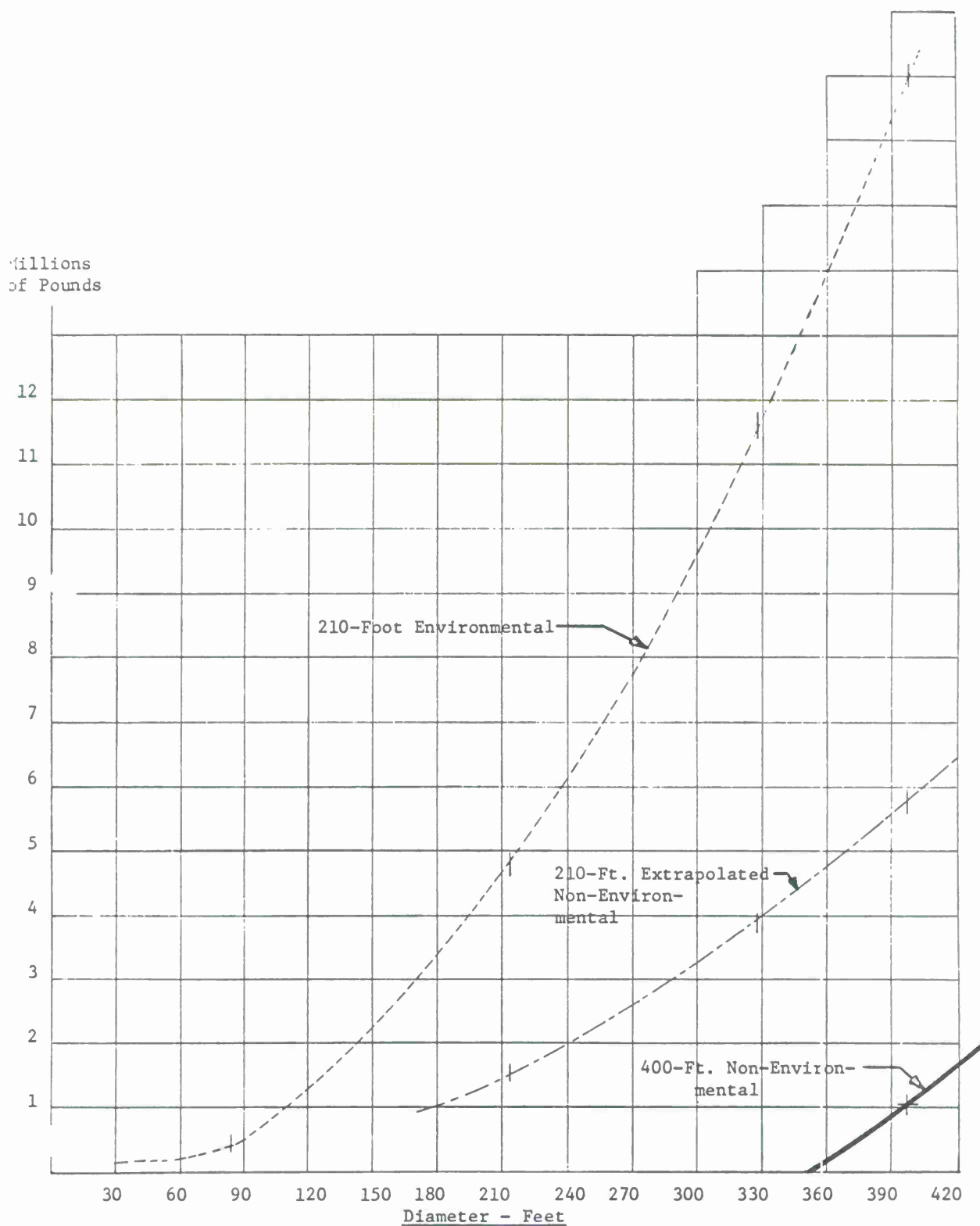


Figure 2. Large-diameter antenna study weight versus diameter curves.

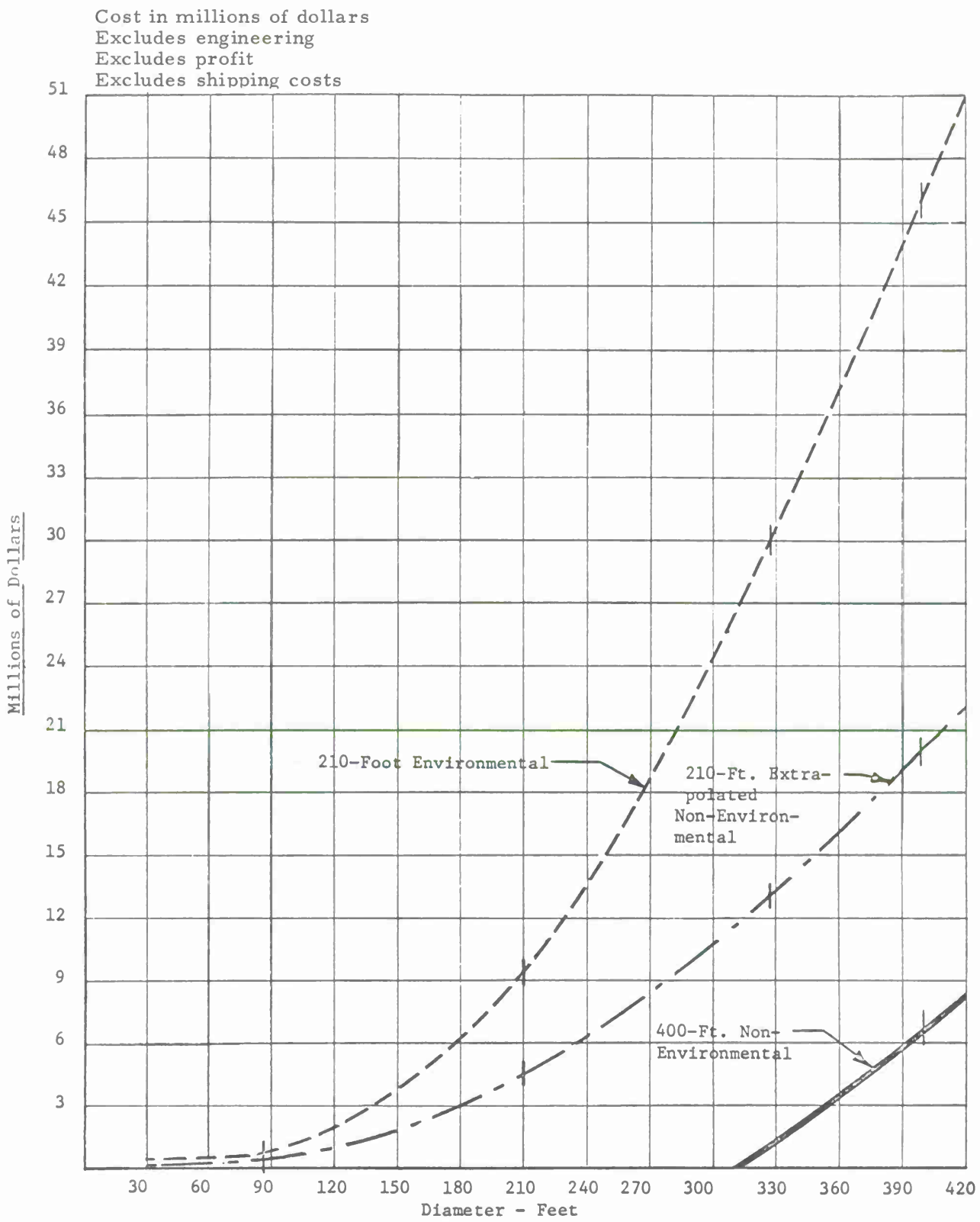


Figure 3. Total costs, in millions of dollars (excludes engineering, profit, and shipping costs).

Millions of dollars

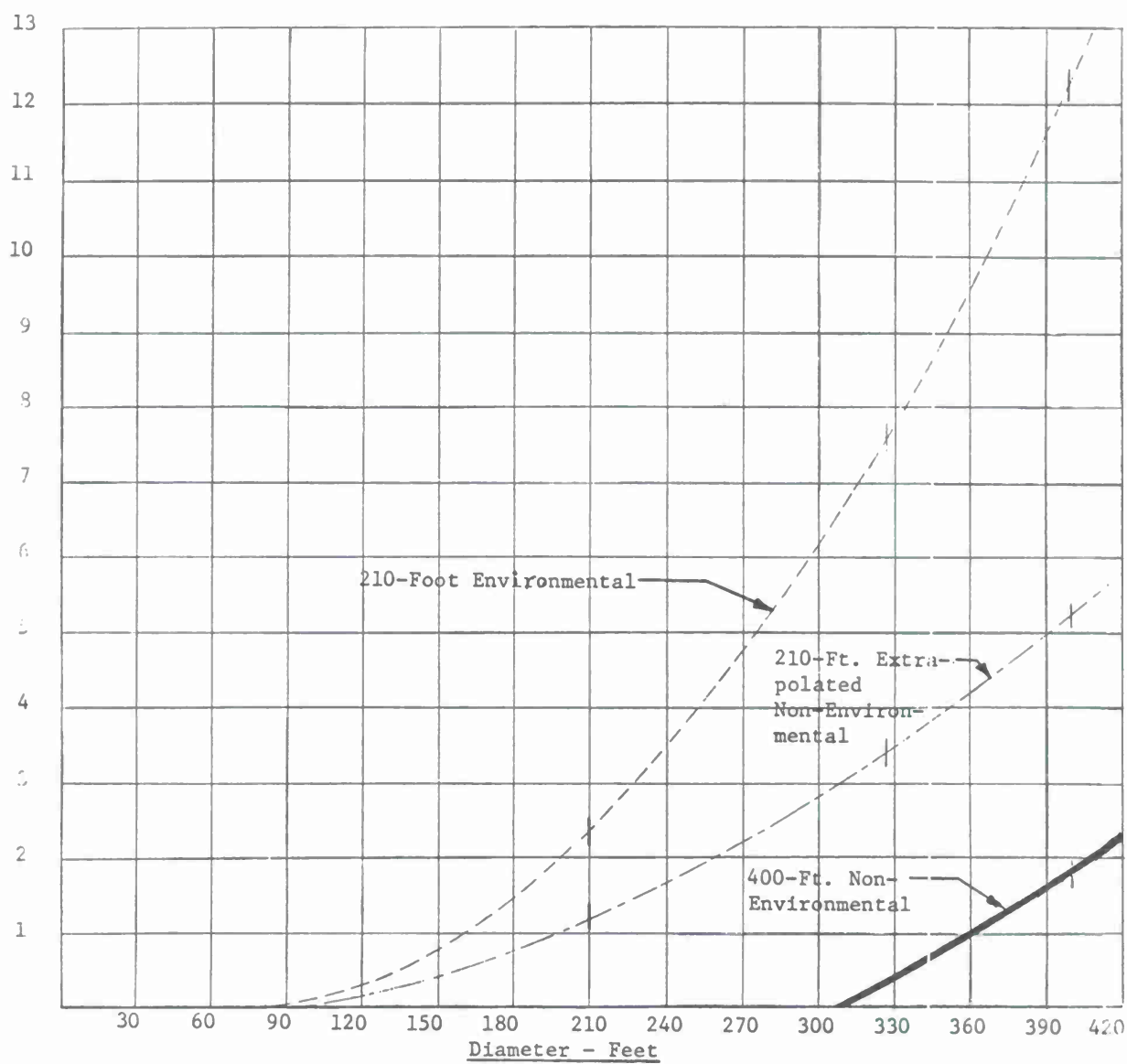


Figure 4. Erection costs.

Millions
of Dollars

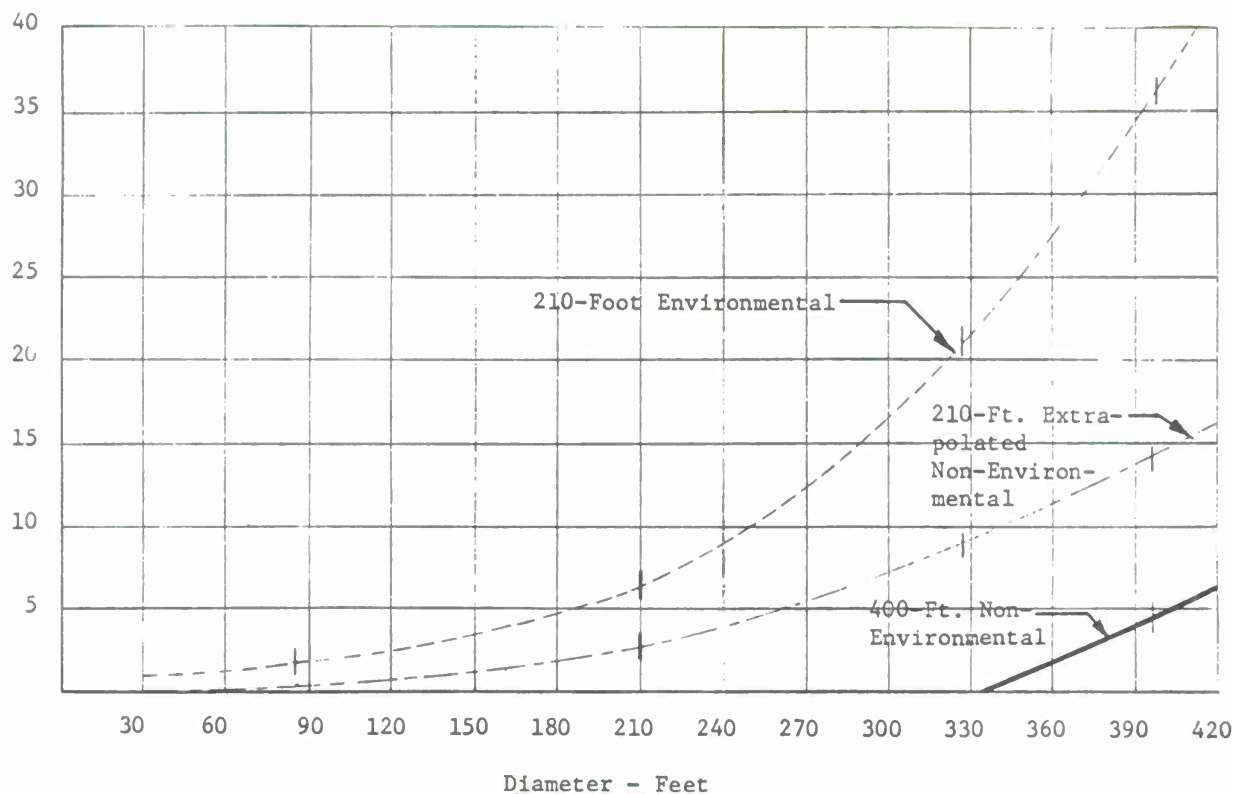


Figure 5. Manufacturing costs.

3. DESCRIPTION OF THE TELESCOPE

The radio telescope concept that evolved as a result of the study was computer analyzed to determine final performance characteristics. The structure (refer to SK-2122) is comprised of an aluminum bipod and an extremely lightweight aluminum reflector surface (however, a special surface-panel study was conducted and is reported on in Engineering Report No. W.O. 988-1) that consists of individually adjustable panels having a maximum span of 13 ft. The panels in turn are supported by a lightweight aluminum reflector backup structure comprised of thin-walled tapered tubular members. The reflector embodies 48 continuous aluminum radial rib trusses that are approximately 200 ft in length. The ribs are supported by a single-plane continuous aluminum ring girder 130 ft in diameter and 25 ft deep. The reflector structure is approximately 18 ft deep at the vertex. The axis of rotation is located 12 ft behind the vertex of the parabola and therefore is essentially contained within the plane of the backup structure. Consequently, the physical depth of the reflector at the center is 12 ft and consists of an aluminum center hub 20 ft in diameter and 12 ft deep. This center hub supports a lightweight feed cone and can easily be made to suit the particular electronic feed-equipment requirements.

As noted, 48 auxiliary aluminum radial ribs are required to keep the span of the surface panels from not exceeding 13 ft. Seventeen lightweight aluminum circular hoop trusses are used to tie the ribs together in conjunction with a series of spiral torsion braces that provide stiffness about the boresight axis of the reflector. The 130-ft-diameter aluminum ring girder is supported by the steel elevation wheel at 12 points. Geometrically, the girder consists of 12 planar trusses that form a circle; each radial rib is spliced to the girder at their common intersection points.

The steel elevation-wheel assembly is an integrated three-dimensional structure supported by the two elevation bearings. The elevation wheel supports the reflector at the aforementioned 12 circular girder reaction points plus 12 center hub reaction points. Basically, the wheel is a cone-type structure that consists of 12 members radiating from the apex of the cone (counterweight point) to the 12 circular girder support points. In turn, these 12 girder support points are tied back to the center hub with a plane of bracing that lies directly behind the reflector. The center wheel member connects the apex of the cone with the back of the center hub at 12 points. This geometry supplies three support points for each 400-ft-long rib, one at the center and two at the intersections of the circular girder. With the reflector pointed at horizon, the plane of bracing directly behind the reflector carries vertical loads directly to the elevation bearings without further distortions to the reflector structure.

The elevation-wheel assembly, which is 130 ft in diameter, provides a stable support for the reflector backup structure. The wheel facilitates erection of the backup structure, since the center 130-ft-diameter section of the reflector can be completely assembled on the elevation wheel simply by mating the 12 pads under the circular girder and at the back of the center hub. The elevation wheel eliminates the need for counterweight, since the steel wheel assembly counterbalances the reflector backup structure, surface, bipod, feed cone, and RF equipment.

The azimuth rotating structure or yoke provides two points of support for the elevation bearings and is supported at its base by four hydrostatic bearing pads that are on a nominal diameter of 40 ft. Each arm of the yoke is an open-framed four-sided space frame that is supported by the base assembly. The structure is approximately 40 ft \times 40 ft \times 25 ft and contains the elevation and azimuth drives, machinery, and the hydrostatic-bearing equipment.

The concrete pedestal is a shell nominally 52 ft in diameter. It is constructed of special high-modulus concrete to support properly the hydrostatic bearing runner. A small-diameter pintle bearing is located on the center line of the antenna at the top of the concrete pedestal. This bearing carries any horizontal thrust due to driving the antenna about the azimuth axis. It also defines the azimuth axis.

Azimuth and elevation drives are of the low-power dual-pinion electric antibacklash type (however, other radome-type low-power drive systems have been investigated; refer to Report W. O. 748-1). The drive motors are conventional DC motors controlled by SCR power amplifiers and solid-state control circuitry. SCR power amplifiers are used, since the radome environment allows for low drive power. An on-axis encoding system is utilized.

A cable wrap-up structure is contained within the pedestal structure. It is a drop-loop type that can accommodate all requirements for proper cable and plumbing facility to transfer across the axis.

3.1 Radio Telescope Characteristics

The following are the characteristics of the 400-ft radio telescope:

Type of mount	Elevation over azimuth
Diameter	400 ft
Focal length	169 ft - 5 inch
f/D	0.424
Sky coverage	
Elevation limits	15° to 90°
Azimuth limits	± 360°
Operational frequency	6000 Mc/sec
Wavelength	2 inches
RMS 1σ	0.150-inch specification (0.100-inch desired)
Axis alignment	
Azimuth axis to gravity	10 sec
Orthogonality elevation over azimuth	10 sec
Elevation axis to reflector axis	10 sec
Reflector panel manufacturing tolerance (1σ)	0.050 inch
Reflector panel field setting tolerance (1σ)	0.050 inch
Readout errors	
Mounting and couplings (peak)	3 arcsec
Encoder (W. G. -BD-19) peak	2-1/2 arcsec
Total RSS error peak	4 arcsec
Servo errors	
Tracking error (including friction, noise, etc.)	4.0 sec
Servo loop bandwidth (reference R-988-171)	0.04 cps
Pointing errors (peak)	15-sec repeatability

Structural resonant frequency	
Reflector: symmetrical mode	1.29 cps
antisymmetrical mode	1.33 cps
Azimuth and elevation — locked rotor	0.2 cps minimum (0.3 cps desired)
System stiffness (minimum)	2.0×10^8 ft-lbs/rad at axis
Drive characteristics	Tracking Slew
Azimuth velocity	0.1°/sec 0.6°/sec
Elevation velocity	0.005°/sec 0.3°/sec
Azimuth acceleration	0.0001°/sec ² 0.05°/sec ²
Elevation acceleration	0.00001°/sec ² 0.025°/sec ²
Axis inertias (structural)	
Azimuth	78.5×10^6 ft lbs sec ² (add 10% for alidade inertia)
Elevation	56.7×10^6 ft lbs sec ²
On-axis torque	
Friction	
Azimuth — breakaway	25,000 ft lbs axis
— running	20,000 ft lbs axis
Elevation — breakaway	10,000 ft lbs axis
— running	7,000 ft lbs axis
Drive horsepower (elevation)	5 total
(azimuth)	5 total
Type of drive	Electrically — antibacklash, two per axis, SCR amplifiers
Power requirements	
Peak operating	15 KVA
Environmental conditions	Radome operation
Miscellaneous	
98% humidity	
Sun	
Temperature	
Operational	+45°F to +85°F
Temperature differential	10°F top to bottom 5°F center to rim
Subreflector support — bipod	
Equipment load	4000 lbs (includes adjustment devices)
Focal-point deflection (Δ)	≈ 2.1 inches
Structural frequency	≈ 1.5 cps
Dead-load pointing error	- 2.20 arcsec
$\left[\theta \right] = \frac{\Delta(K) (M-1)}{MF}$	

Blockage	< 7%
Electronic-equipment shelter	20,000 lbs of electronic gear plus access facility located behind reflector
Reflector pointing error	295 arcsec
Resultant pointing error	
Reflector and hyperbola	295 arcsec - 220 arcsec = 75 arcsec (repeatability less than 10 arcsec)

MECHANICAL AND STRUCTURAL PARAMETERS

	Elevation axis	Azimuth axis	Units
Weights (structural and mechanical)	500,000	1,000,000	lbs
Mass moment of inertia (structural)	56,700,000	78,500,000 (plus 10% for alidade)	slug ft ²
Motor-to-axis ratio	35,000:1	17,500:1	
Friction torque			
Breakaway	121,000	240,000	inch lbs
Running	84,000	240,000	inch lbs
Inertia torque at axis at 0.05/sec ² for azimuth and 0.025°/sec ² for elevation	43,200	144,000	ft-lbs
Axis drive torques			
Nominal rated torque at each motor	916	916	ft-lbs
Maximum torques at each motor	6.1	12.1	ft-lbs
Rated hp drives total	5	5	hp
Drive system			
Reducer ratio	157:1	600:1	
Service factor used (life)	2	2	
Number of reducer assembly per axis	2	2	
Axis stiffness	10 ⁹	10 ⁹	ft-lbs/rad
Stiffness at each reducer	1.0 × 10 ⁴	2.0 × 10 ⁴	ft-lbs/rad at LSS
Axis bearings			
Nominal diameter	2	40	feet
Type	Spherical roller	Hydrostatic	

ESTIMATED WEIGHT TABLE - FINAL

Component	Weight (lbs)	Material
Structural weights		
Primary reflector	88,000	Aluminum
Primary reflector surface	41,000	Aluminum
Secondary reflector	2,000	Aluminum (\approx 40-ft diameter)
Structural weights (cont.)		
Bipod	13,000	Aluminum
Feed cone	<u>12,000</u>	Aluminum
Subtotal	158,000	
Elevation wheel	290,000	Steel
Counterweight	<u>10,000</u>	Trim weights
Subtotal on elevation axis	458,000	
Yoke	<u>260,000</u>	Steel
Total on pedestal	719,000	
Pedestal	8,300,000	Concrete (2100 yds)
Ladders, platforms, and walkways	50,000	Steel
Mechanical weights		
Elevation axis	42,000	
Azimuth axis	190,000	
On foundation	<u>200,000</u>	
Total elevation axis (+15%)	$500,000 \times 1.15 =$	580,000
Total azimuth axis (+15%)	$1,000,000 \times 1.15 =$	1,150,000
Total on foundation (+15%)	$1,200,000 \times 1.15 =$	1,380,000

4. ANALYSIS AND RESULTS OF THE 400-FT-DIAMETER RADOME-HOUSED RADIO TELESCOPE

Since for extremely large diameters the least weight structure represents the most economical, every attempt was made to develop the lowest possible weight, 400-ft-diameter reflector structure. Consideration was given to the failure or fatigue limits of the material. As stated previously, the radome-housed antenna must perform under the effects of gravity loads and reduced thermal loadings. However, reducing the gravity loading of the structure results in less stress and less deflection. Carrying this to its ultimate conclusion, a lower limit is approached, which is the practical restriction governing minimum sizes and materials that can be utilized. For example, structural local buckling or L/r considerations for selecting minimum member sizes places a restriction on the minimum structure possible. Consequently, a rather detailed analysis of this problem was undertaken, with the result being an extremely lightweight reflector design.

Figure 6 summarizes the significant results of the 400-ft-diameter radome-housed telescope study.

Figure 6. Results — 400-ft-diameter radome-housed radio-telescope analysis.

Component	Material	Major component weight breakdown (lbs)	Remarks
Surface	Aluminum	41,000	Only 0.3 psf
Reflector backup structure	Aluminum	88,000	Only 0.7 psf
Elevation wheel	Steel	290,000	
Elevation counterweight		Negligible	Trim weights only for fine adjustment
"Yoke" structure	Steel	260,000	
Pedestal	Concrete	8,300,000	2100 yds ³
Surface accuracy	Pointing accuracy	Structural dynamics	Drive power
Calculated 0.20 inch (1 σ)	Calculated 16 arcsec 3 σ (repeatability) 25 arcsec 3 σ (dead-load compensated)	Calculated Azimuth or ≈ 0.35 cps Elevation	5 hp per axis
Specified 0.150 inch (1 σ)	Specified 15 arcsec (3 σ) (repeatability)	Specified 0.3 cps	
Desired 0.100 inch (1 σ)		Minimum 0.2 cps (reflector ≈ 1.3 cps)	

4.1 Reflector

4.1.1 Aluminum versus steel

Since a large-diameter radio telescope designed specifically for the radome environment presented a relatively new and unexplored problem, it was necessary to question many of the so-called basic antenna precepts. The first question asked was: "Would the completed telescope be more economical if the reflector backup structure were of aluminum rather than the conventional steel structure?"

The material cost for aluminum is roughly six times that of steel; however, the overall lighter weight structure could reduce the cost of the elevation counterweight, the azimuth rotating structure, drives, bearings, pedestals, etc. Shipping the lighter structure could also be more economical, and the aluminum structure would not require processing for corrosion protection.

Because of the above reasons, it seemed plausible to investigate any cost advantages.

To make this evaluation, the 210-ft-diameter environmental antenna (see Appendix A) was used as a base. The question asked was: "If the members in the reflector backup structure were replaced size for size with aluminum, what would the total weight and possible cost reductions be?" Referring to Figure 7, notice that the weight reduction is a significant 36%, and referring to Figure 8, that the cost reduction, considering all factors, was 7.8%. It is noted that the performance of the two structures

being compared is identical for gravity-load deflections, and that in this case, the deflections due to the load from the surface panels are a small portion of the total.

Figure 7. Aluminum versus steel backup structure.*

Component \ Weight lbs	Steel structure (welded)	Aluminum structure (bolted)	Weight reduction
Reflector assembly	763,000	287,000	476,000
Elevation wheel	930,000	930,000	-
Elevation counterweight	600,000	250,000	350,000
Alidade	1,500,000	960,000	540,000
Totals	3,793,000	2,427,000	1,366,000

* Based on 210-ft-diameter antenna study.

Figure 8. Cost — aluminum versus steel.

The cost of the quadripod, surface panels, backup structure (steel-welded construction), elevation wheel, elevation counterweight, and alidade from the 210-ft-diameter program is \$2,640,000.00. The following chart indicates the difference in cost in the above components due to the material change.

Item	Welded-steel backup structure	Aluminum-bolted backup structure	Increase over (decrease) welded
Material	\$ 81,360.00	\$147,550.00	\$ 66,190.00
Labor	-	-	-
Processing	17,000.00	-	*(17,000.00)
Shipping	194,000.00	154,000.00	(40,000.00)
Erection	-	-	-
Counterweight	90,000.00	37,500.00	(52,500.00)
Alidade	450,000.00	288,000.00	(162,000.00)
Total	\$832,360.00	\$627,050.00	\$(205,310.00)

Total net reduction in cost is \$(205,310.00).

Total cost of above components revised and after reduction is \$2,434,690.00.

$$\% \text{ cost reduction} = \frac{\$2,640,000.00}{\$2,434,690.00} = 7.8\% \text{ reduction}$$

* Note: () means cost reduction.

The results were considered significant, and since both the steel and the aluminum structures will produce the same gravity deflections (except for the loads from the surface panels), it was concluded that an optimized aluminum-reflector backup structure supported by a steel elevation wheel would probably produce the most economical system.

4.1.2 L/r considerations

In order to investigate further weight reduction, a study was conducted to evaluate the weight advantage between standard structural shapes on one end of the scale and round tubes on the other, for constant radius of gyration. Referring to Figure 9, notice that there is a 10.6:1 weight advantage in favor of the round tube section. Because of this significant advantage, round tubes produce an overall economy system. It is pointed out, however, that the round member, while permissible for use in a radome environment, may be marginal in a wind environment due to the influence of the Von Karmon vortices, which give rise to possible excessive member-fatigue stresses.

Figure 9. Comparison of weight per linear foot, versus radius of gyration for standard available sections.

Standard aluminum sections	Weight (lbs/ft)	Area (inches)	Radius of gyration (inches)	Remarks
6-inch ϕ round tube 0.078-inch wall thickness	1.71	1.45	2.27	For approximately the same radius of gyration, a 10.6:1 weight reduction for round tubes versus double angles can be obtained
6-inch ϕ pipe (schedule 5)	2.62	2.23	2.35	
6-inch ϕ pipe (schedule 40)	6.56	5.58	2.25	
8 \times 8 wide flange	10.73	9.12	2.02	
2 angles 8 \times 6 \times 1/2	15.90	13.50	2.32	
2 angles 8 \times 5 \times 1/2	18.20	15.50	2.50	

4.1.3 Analysis of thin-wall sections

The lightweight member study was concluded by a final analysis that compared standard round tube sections versus thin-wall tapered tubular special fabricated sections. The question we asked was: "If the load capacity for the two types of sections were kept constant, would there be a significant weight difference?" Referring to Figure 10, notice that there is a 50% weight reduction for equal-capacity circular sections. For the total reflector backup structure, the use of standard round tube sections resulted in a weight of approximately 175,000 lbs versus 88,000 lbs for the thin-wall tapered tubular section.

An economic and producibility analysis of the lightweight aluminum members was undertaken (refer to SK-2114). The following five shapes were investigated:

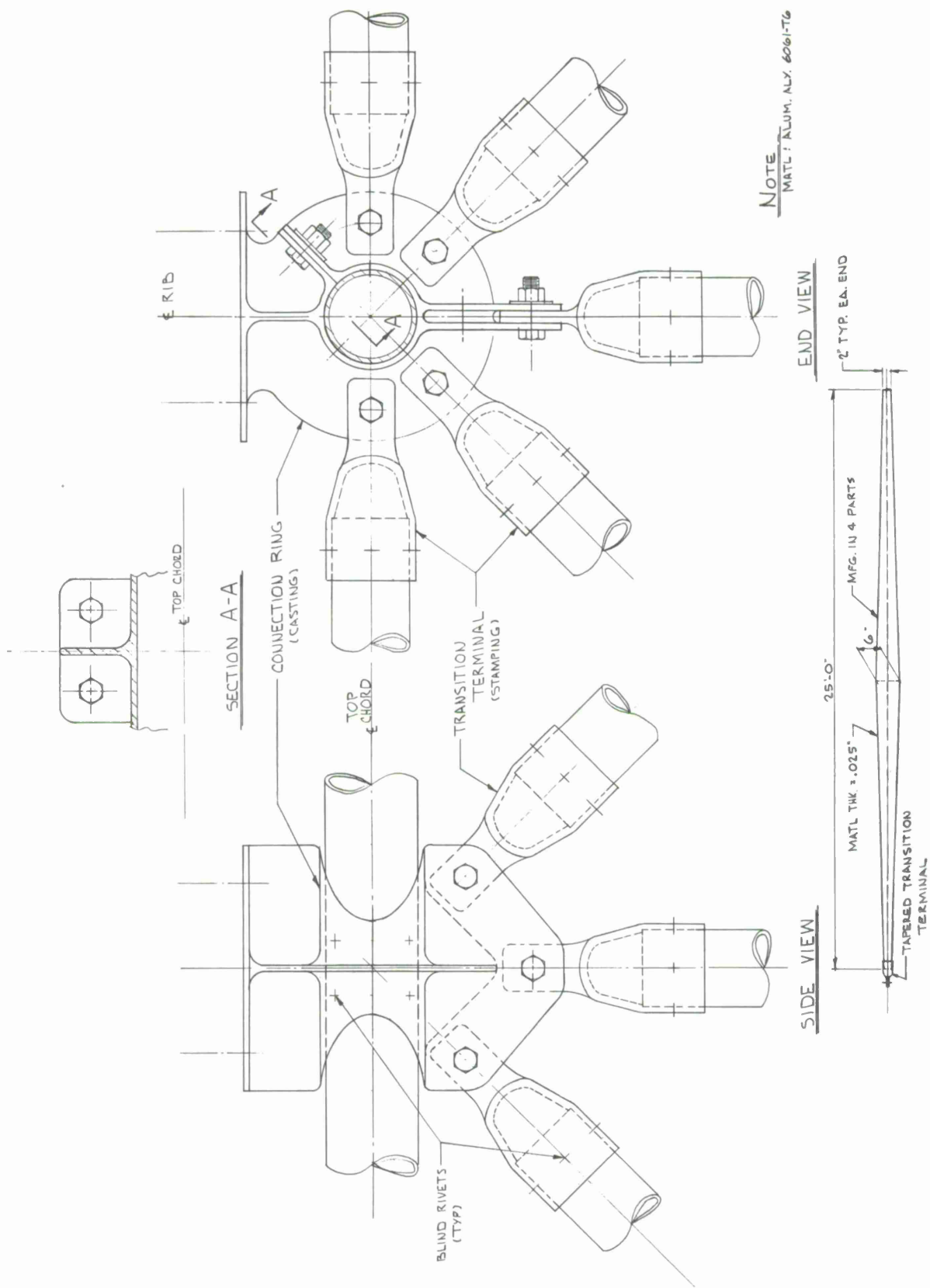
- 1) Standard round-tube sections (rolled or extruded).
- 2) Lightweight round tubes (thin-wall extrusions).
- 3) Corrugated tubes (special fabrication).
- 4) Tapered thin-wall tubular members (special fabrication).
- 5) Triangular truss sections (special fabrication).

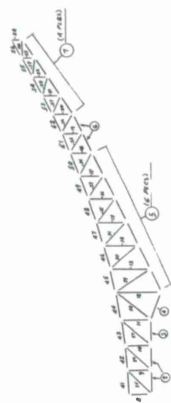
Because of the reduced material cost for the lightweight tapered tubular sections and because of the relative ease of connecting the narrow ends of this type of members, it proved to be the most economical. The analysis was conducted for hoop members

and girder members, and the material, tooling, and fabrication costs were all taken into consideration. Referring to SK-2114, Sheets 2 and 3, the actual estimated costs to manufacture trusses made of the standard round-tube section versus the tapered-tubular section showed a 30% cost advantage for the latter. Also, because of the connections for the narrow end of the tapered section, this type lends itself to standardization, since all member tapers and minimum end openings can be made identical. Since all connections have multiple members framing into it and if the member sizes range from 3-inch diameter to 8-inch diameter, the connection for the straight-type members becomes very big and represents a significant portion of the total weight. Also, thin-wall open-ended members may be advantageous from a temperature-differential standpoint.

Figure 10. Equal load-capacity comparison for standard round-tube sections versus thin-wall tapered round sections.

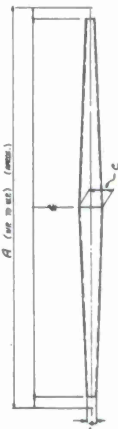
$P = A \times F_a$ $A = \text{Load capacity}$ $F_a = 51,000 / (L/r)^2$ $P = A \times \frac{51,000}{(L/r)^2}$ For equivalent load-capacity sections set $P_1 = P$		Substituting $A_1 \times \frac{51,000}{\left(\frac{L}{r_1}\right)^2} = A \times \frac{51,000}{\left(\frac{L}{r}\right)^2}$ $A_1 \times \frac{51,000 (r_1)^2}{(L)^2} = \frac{A \times 51,000 (r)^2}{(L)^2}$ Canceling like terms results in $A_1 r_1^2 = A r^2$	
Standard round-tube sections		Equivalent tapered tubular sections	
Size	$\frac{W}{\text{lb/ft}}$	Size	$\frac{W}{\text{lb/ft}}$
1-1/4-inch ϕ round tube 0.063	0.282	1-3/4-inch ϕ round tube 0.025	0.162
1-1/2-inch ϕ round tube 0.063	0.342	2-inch ϕ round tube 0.025	0.185
2-inch ϕ round tube 0.063	0.460	2-3/4-inch ϕ round tube 0.025	0.250
2-1/2-inch ϕ round tube 0.063	0.579	3-1/2-inch ϕ round tube 0.025	0.323
3-inch ϕ round tube 0.063	0.681	4-inch ϕ round tube 0.025	0.369
3-inch ϕ pipe (5)	1.048	5-1/4-inch ϕ round tube 0.025	0.485
4-inch ϕ pipe (5)	1.354	6-3/4-inch ϕ round tube 0.025	0.624
6-inch ϕ round tube 0.078	1.710	8-1/2-inch ϕ round tube 0.032	1.004
6-inch ϕ round tube 0.094	2.050	9-inch ϕ round tube 0.032	1.063
8-inch ϕ pipe (80)	15.010	12-inch ϕ round tube 0.160	7.090
Remarks: The member size used for this design shows an average weight reduction of approximately 2:1 in favor of the tapered tubular thin-wall members.			



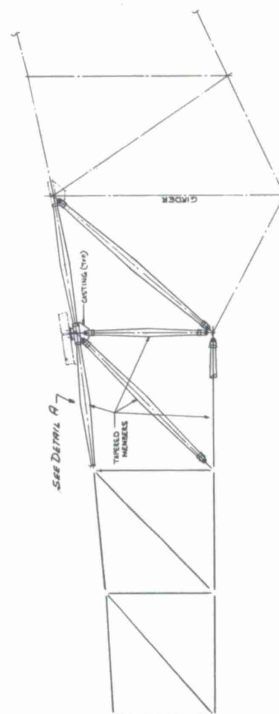


Exos A

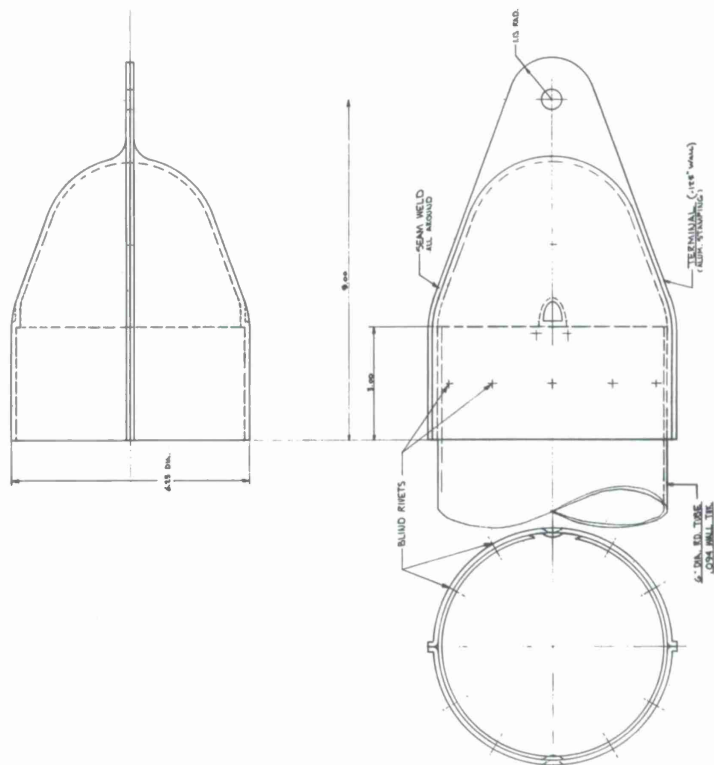
NOTE: "A" IS DIFFERENT FOR EACH PC. MARK BUT MAY BE SHOWN ALIKE IN MATERIAL HAND-OUT USED FOR ESTIMATING PURPOSE ONLY



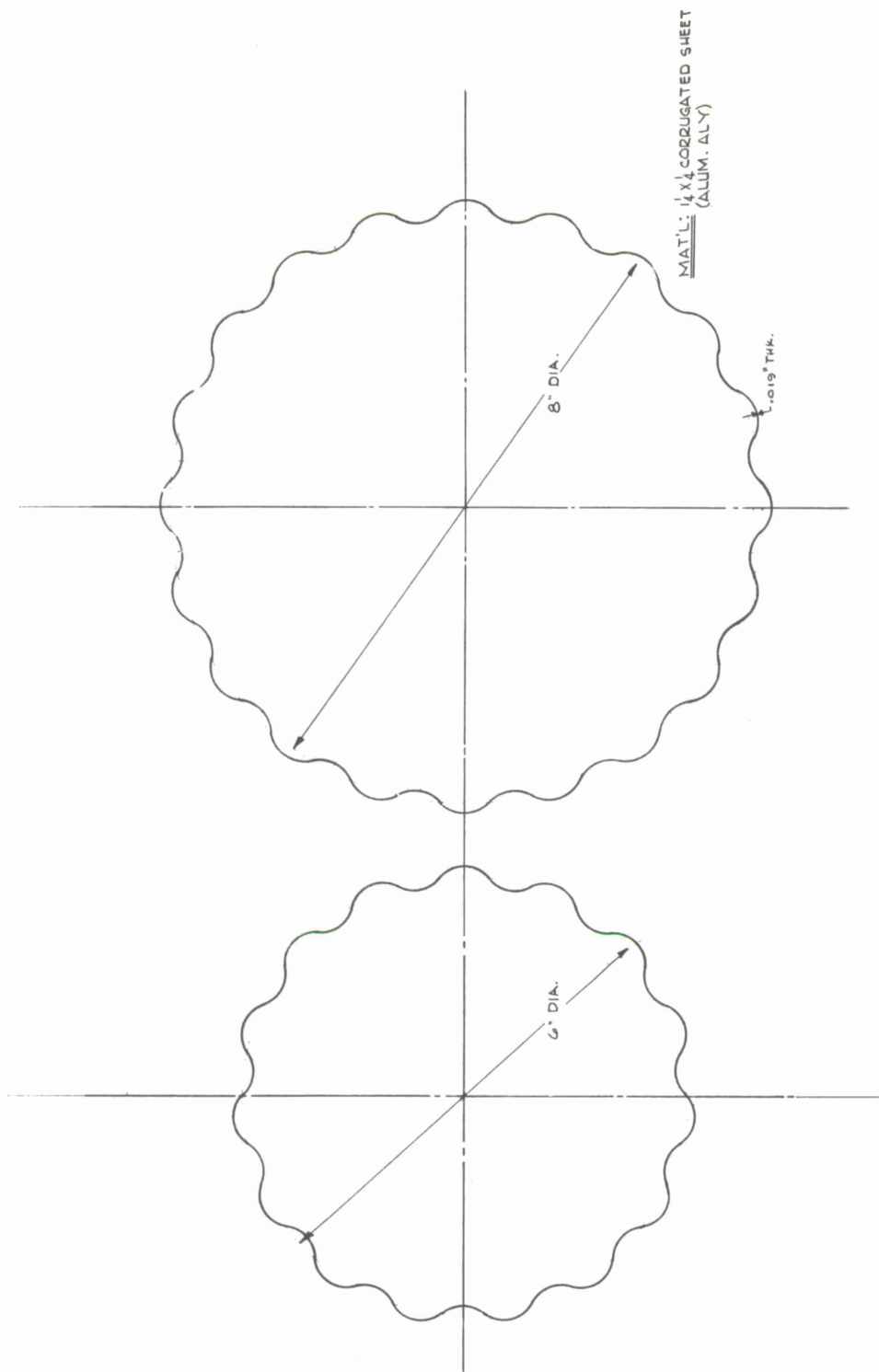
DETAIL A



LIGHTWEIGHT RIB CONSTRUCTION



STANDARD RIB MEMBER & TERMINAL

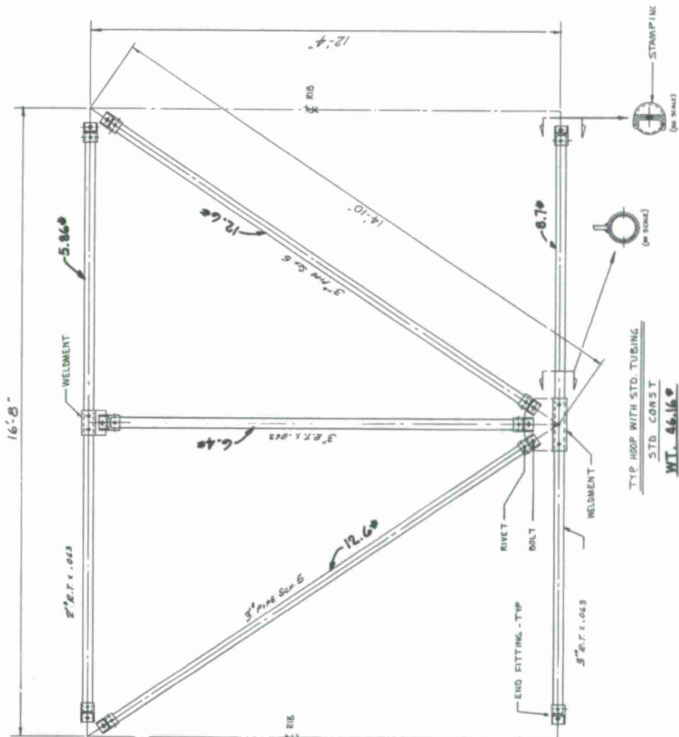
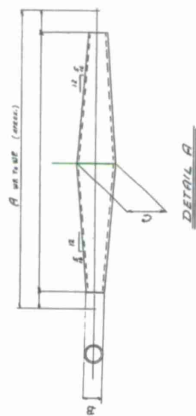


SK-2114.

ESTIMATED COST

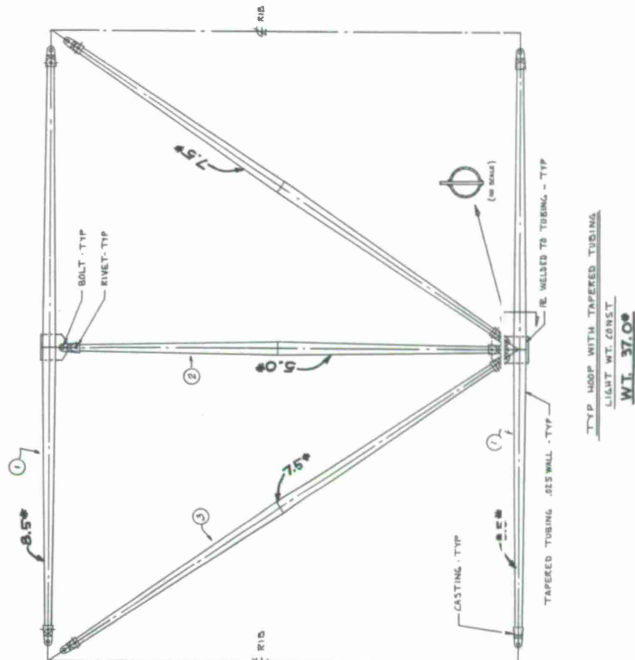
	STD. TIME (hrs)	FAB. SECTION
MAT'L	\$43.00	\$8.00
TOOLS	0	\$6.00
FAB.	\$4.00	\$20.00
TOTAL	\$47.00	\$34.00

INTERMEDIATE CLUSTER	
CASTING	\$150.00
STAMPING	\$60.00
WELDED	\$25.00



TYP HOOP WITH STD. TUBING
STD. CONST
WT. 46.16#
(per panel)

SK-2114.



TYP HOOP WITH TAPERED TUBING
LIGHT WT. CONST
WT. 37.0#
(per panel)

Three types of member connections were evaluated:

- 1) Castings.
- 2) Stampings.
- 3) Weldments.

The weldments appeared to be the most economical (refer to SK-2114, Sheet 3).

Figure 11 is a comparison of the component weights for the standard round-tube sections versus the thin-walled tapered membered section.

Figure 11. Component weights — standard versus tapered thin-walled sections.

	Tapered thin-walled sections	Standard round-tube sections	Remarks
Reflector surface	98,600 lb	98,600 lb	Based on 0.72 lb/ft ²
Backup structure	87,600 lb	176,700 lb	
Elevation wheel	<u>290,000 lb</u>	<u>290,000 lb</u>	Kept constant
Total	476,200 lb	565,300 lb	

4.1.4 Reflector-girder consideration

The geometry of the reflector's main support girder is critical when considering overall reflector performance. Several types of girders can be utilized:

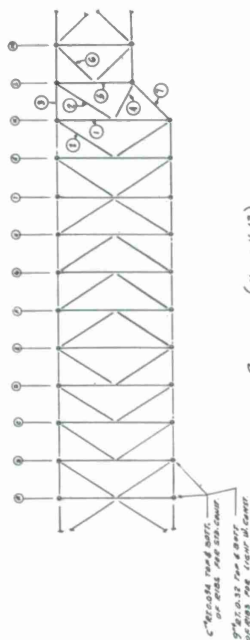
- 1) The circular- (planar-) shaped girder.
- 2) The square-, rectangular-, or diamond-shaped girder.
- 3) The ring girder.

If the reflector backup structure is supported at only two points, the shape of the girder is unimportant and either a ring, or a square, etc., may be used provided the girders are box-type structures that can take torsional loads. When the reflector girder is supported at multiple points, it is logical and efficient to use a planar girder in conjunction with continuous radial ribs. Advantages of this system include:

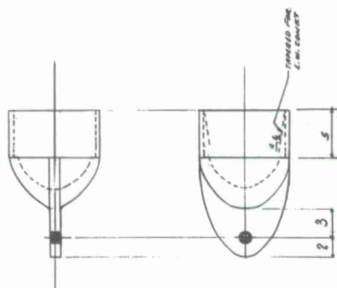
- 1) Secondary torsional loads on the girder, which are due to transfer of shear from the cantilever ribs, can be eliminated.
- 2) The planar ring or circular girder is more economical to fabricate and facilitates repetitive assemblies.

Figure 14 is a qualitative summary and has been utilized to determine the most efficient girder configuration. Based on this analysis, the most economical girder configuration is circular in conjunction with continuous radial ribs. An extensive analysis of this problem was conducted during the NASA/JPL 210-ft-diameter program. This work was reevaluated here.

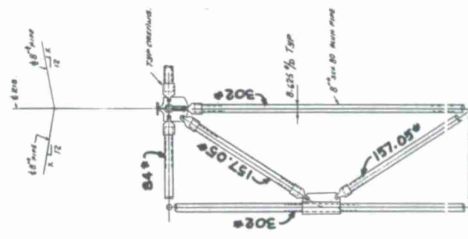
	STD. TIME (min)	FAB. SECTION
MAT'L	\$175.00 (one hour cap)	\$60.00
TOOLS	0	\$16.00
FAB.	\$10.00	\$30.00
TOTAL	\$185.00	\$120.00



GIRDER (Hoop No. 13)
ALL MATERIAL TO BE 8" NOM. PIPE SCH. 80 (EXCEPT NUTS) FOR STD. ENDSTANDARD
ALL MATERIAL TO BE 8" (SEE DET. A) (EXCEPT NUTS) FOR LOW ALLOY STEEL CIRC.

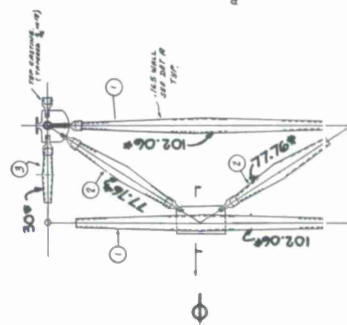


CASTING (ALUMINUM)



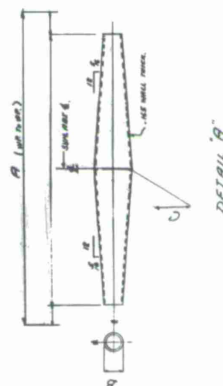
WT: 1002.10g

TYPE BAY OR GIEDER FOR
SFD. CONSTR.



WT. 389.640

TYPE BAY OF GIRDER FOR
LIGHT WEIGHT CONST.



DETAIL "A"

SK-2114.

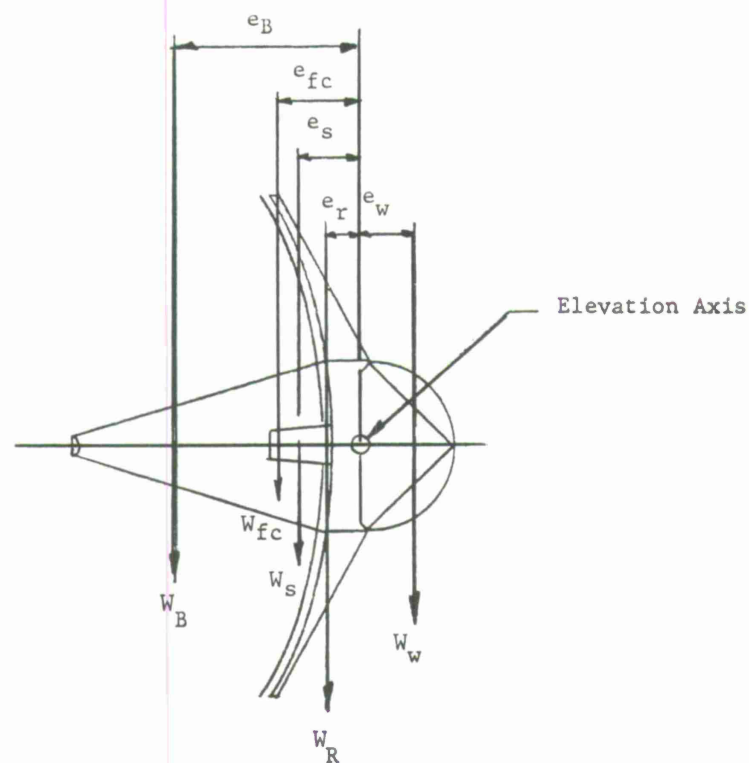


Figure 12. Reflector weights and mass moments of inertia – standard round-tube section.

Component	Symbol	W (K)	e (Pt)	W _e (K ¹)	IM _x (slug-ft ²)	IM _z (slug-ft ²)
Reflector	W_r	176.7	20.6	3640	36.7×10^6	63.9×10^6
Surface (0.725 psf)	W_s	98.6	42.3	4175	37.8×10^6	62.9×10^6
Wheel	W_w	290.0	-25.2	-7300	22.6×10^6	20.5×10^6
Total		565.3		515	97.1×10^6	147.3×10^6
Bipod		15	105	1575		
Feed cone		20	42	840		
Counterweight	$(2415 + 151) \div 55 = 53 \text{ K}$					

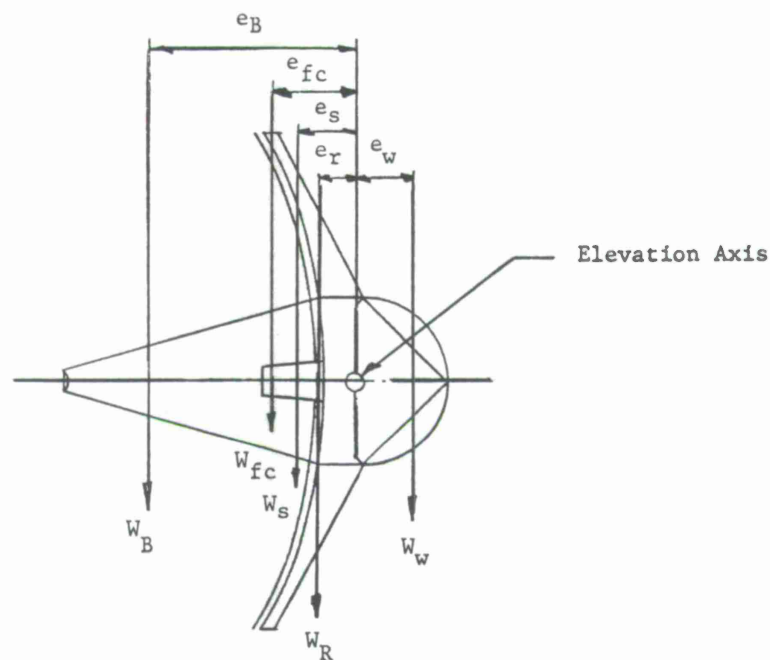





Figure 13. Reflector weights and mass moments of inertia — tapered thin-walled sections.

Component	Symbol	W (K)	e (Pt)	W _e (K ¹)	IM _x (slug-ft ²)	IM _z (slug-ft ²)
Reflector	W_r	87.6	20.6	1820	18.4×10^6	32.0×10^6
Surface (0.72 psf)	W_s	98.6	42.3	4175	37.8×10^6	62.9×10^6
Wheel	W_w	290.0	-25.2	-7300	22.6×10^6	20.5×10^6
Total		476.2		-1300	78.8×10^6	115.4×10^6
Bipod		15	105	1575		
Feed cone		20	42	840		
Counterweight	$(2415 - 1300) \div 55 = 20 \text{ K}$					

Figure 14. Reflector-girder configurations.

	(Planar) circular girder	Square, rectangular, or diamond	Ring girder
			
<u>Engineering considerations</u>			
Multiple-girder support points	✓	0	X
Torsional loading capability	✓	0	X
Hoop bracing efficiency	0	X	0
Structural-rib symmetry	0	X	0
Deflection pattern	0	0	X
Stress pattern	0	0	X
Weight	✓	0	X
Frequency	✓	0	X
Inertia	✓	0	X
Overall engineering efficiency	✓	0	X
<u>Fabrication and erection considerations</u>			
Girder complexities	✓	0	X
Rib complexities	0	X	0
Hoop complexities	0	0	0
Torsional bracing complexities	0	0	0
Overall economics	✓	0	X
<u>Summary – overall economics</u>	✓	0	X
✓ Most efficient; 0 Efficient; X Least efficient.			

As a result, it was concluded that the most economical girder configuration would be circular, with continuous radial ribs, the girder being supported at 12 points by the elevation wheel structure.

4.1.5 Elevation-wheel considerations

The elevation-wheel structural assembly is designed to transmit the reflector-drive forces to the elevation bearings. Primarily, however, it forms an integral portion of the reflector backup structure and therefore contributes significantly to the overall deflection pattern of the reflector structure. Consequently, this component is designed for extreme rigidity even though added weight may be incurred. While this results in a rather heavier structure, this weight is not so critical as it might seem, for most of the wheel structure lies on the counterweight side of the elevation axis and therefore contributes substantially toward counterbalancing the reflector. The elevation wheel is designed so that the deflections at the points of interface with the backup structure are equal. This optimizes the stiffness characteristics in the attempt to equalize its effect on the deflection contours of the reflector.

The elevation-wheel structure is the interface between the reflector's main girder and the two elevation bearings. To accomplish this efficiently, it should geometrically be cone shaped with the apex of the cone containing the elevation counterweight, while the ribs of the cone form the support points for the reflector's circular girder. A horizontal plane of bracing ties the ribs together (similar to the rim and spokes of a wheel) and contains the elevation axis. A center member for supporting the reflector's center hub is an integral portion of the elevation-wheel structure.

The radius of the elevation wheel should be set as close to the radius of gyration of the moving mass as is practical. For the structure under consideration, the mass moment of inertia is approximately 1820×10^6 psf and the total rotating mass is 500×10^3 lbs. Therefore,

$$r = \sqrt{\frac{I}{W}} = \frac{1820 \times 10^6}{500 \times 10^3} \text{ or } \approx 61 \text{ ft}$$

The total mass of the elevation wheel has been set at approximately 290,000 lbs of steel. This weight was selected for stiffness and to counterbalance completely the entire aluminum-reflector assembly, thus eliminating the need for counterweight.

4.1.6 Reflector geometry

The geometry of the reflector was established based on existing antenna designs. The following five characteristics define the geometry of the reflector:

- 1) Depth of structure at vertex.
- 2) Diameter of ring girder.
- 3) Depth of ring girder.
- 4) Radius of elevation-wheel structure.
- 5) Average weight per square foot of the backup structure and surface.

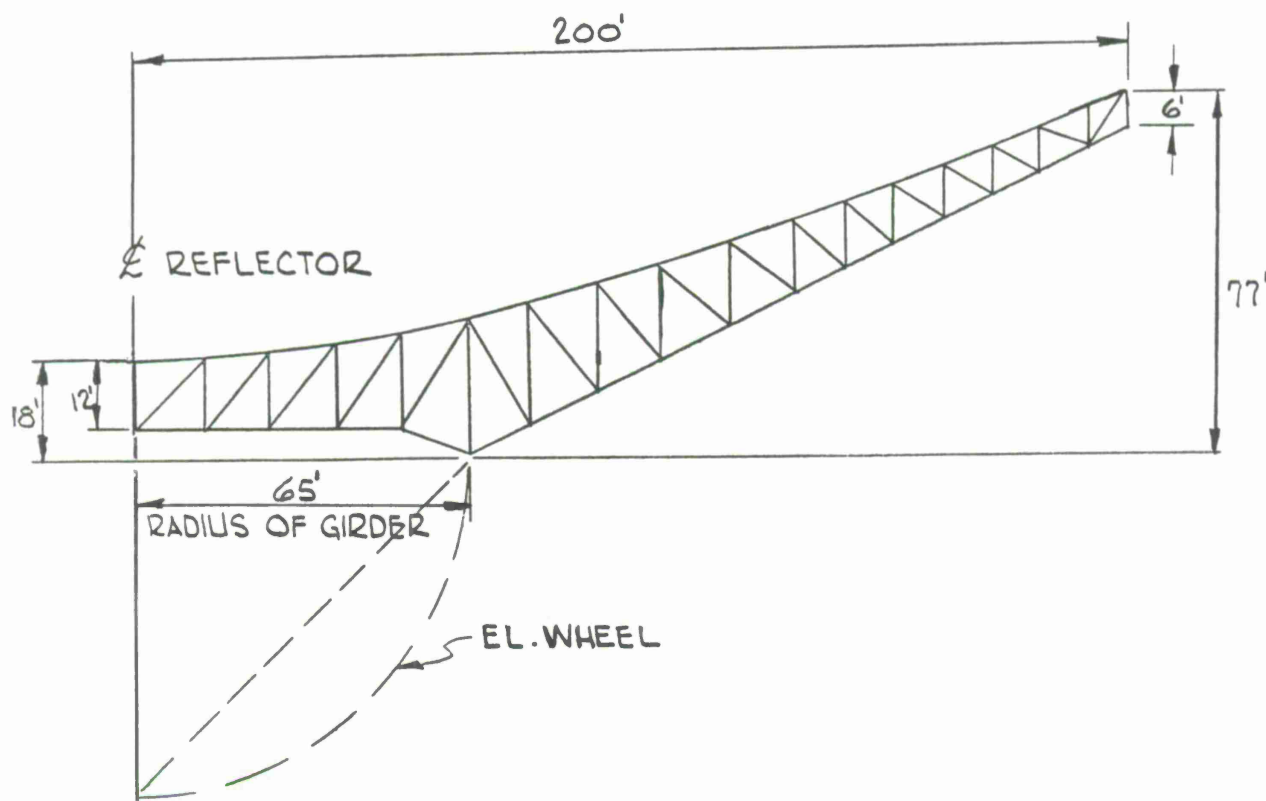
The antenna designs that were reviewed produced the following results:

Figure 15. Reflector geometry in terms of percent of diameter.

Characteristic	Average percent of diameter
Depth of structure at vertex	5-1/2
Diameter of ring girder	50
Depth of ring girder	7-3/4
Radius of elevation wheel	22
Average weight/ft ²	10 psf

The above was, however, based on environmentally designed antennas and therefore would not apply directly. Based on the above table and a preliminary estimate of the weight per square foot of the radome-housed antenna, the following geometry was developed and used for the final analysis conducted for the study:

- 1) Depth of structure at vertex — 12 ft
- 2) Diameter of ring girder — 130 ft
- 3) Depth of ring girder — 25 ft
- 4) Radius of elevation wheel — 65 ft



4.1.7 Two-dimensional analysis

A two-dimensional computer analysis of one typical 200-ft-long lightweight radial rib was conducted. The purpose was to study and evaluate the deflection characteristics of the rib, independent of the total structure, and to determine if there are any inherent structural disadvantages with this type of design. A complete three-dimensional analysis of the entire structure is not amenable to this type of isolated study; furthermore, the results can be used as guides in evaluating the expected performance of the complete three-dimensional analysis.

The radial rib characteristics that are of importance are:

- 1) The shape and magnitude of the deflection curve of the rib, due to its own weight, for both symmetric and antisymmetric loadings.
- 2) The shape and magnitude of the deflection curve of the rib, due to the external load from the surface, for both symmetric and antisymmetric loadings.

- 3) An estimate of the surface accuracy from Items 1 and 2 above.
- 4) Effect of the bipod reaction on the deflection characteristics of the rib.

Figure 16 summarizes the radial rib characteristics for this first trial design. For example, its weight is 1100 lbs and the weight of the hoops that react on the rib is 800 lbs. Total structural weight for a 7-1/2° sector is approximately 1900 lbs (10 lbs per linear foot). The corresponding tip deflections due to this loading are -4.34 inches for symmetric loadings and ± 2.21 inches for antisymmetric loadings. (Note: A negative deflection connotes displacement away from the focal point.)

The corresponding tip deflections due to a unit surface panel weight of 0.1 psf (284 lb per 7-1/2° sector) is -1.47 inch and ± 0.85 inch for symmetric and antisymmetric loadings, respectively. The surface panel unit weight, however, is approximately 0.725 psf for lightweight solid surface panels, or a total load of 2,050 lb per 7-1/2° sector. The corresponding tip deflections due to this loading are -10.6 inches and ± 6.4 inches for symmetric and antisymmetric loadings, respectively. For this first trial, the depth of the structure may have been decreased too much in deference to minimizing member length. However, the tapered sections have proved to be exceedingly efficient.

Figure 16. Summary of deflection characteristics of two-dimensional rib analysis.

<div style="display: inline-block; transform: rotate(-45deg); transform-origin: center;"> <div style="display: flex; align-items: center;"> <div style="writing-mode: vertical-rl; transform: rotate(180deg);">Loading condition</div> <div>Tip deflection</div> </div> </div>	Structure deflection due to own load - Δs	Structure deflection due to 0.725 psf panel load - Δp	Ratio $\Delta p / \Delta s$
Symmetric	- 4.34 inches	- 10.6 inches	2.45
Antisymmetric	± 2.21 inches	± 6.4 inches	2.90
Total load for 7-1/2° sector	Structure = 1900 lb = W_s	0.725 psf = 2050 = W_p	Ratio $W_p / W_s = 1.08$

Referring to Figure 16, the deflection and weight ratios between the structure and panels are far apart. This is because the rib weight varies from the lightest at the tip to heavier at center, whereas the reverse is the case for the distributed surface weight. Because of this and because of the lightweight structure, an upper limit is reached on the maximum allowable surface-panel weight that the rib can efficiently support. If the structural and panel deflections are approximately equal, this upper limit results in a 0.3-psf maximum panel weight, which may be difficult to achieve. A perforated panel has been designed for this weight target. See section 4.1.8 for its characteristics. Furthermore, if the aluminum tubular structure is replaced size for size with a steel tubular structure, the contribution of deflection from the panels will be reduced by 2/3. Further investigation is warranted.

To determine the effect of the above deflections on surface accuracy, the RMS for each case was evaluated. Referring to Figures 17 and 18, the RMS due to rigid-body motion, which is based on the original parabolic equation, is 1.53 inches for the structure alone and increases to 3.081 inches for the structure plus 0.3-psf panels, or 2:1 as stated. However, the RMS due to changing focal length (new parabolic equation) is 0.179 inch for the structure alone and 0.381 inch for the structure plus 0.3-psf panel.

Therefore, to achieve an accuracy that is even close to the CAMROC requirement, the RMS must be based on a changing focal length, which is a new curve. This means that the deflected points do fit a parabola rather closely. However, the corresponding focal length may be as much as 24 inches for the three-dimensional structure, and it varies (see Figure 19) for each elevation angle and therefore must be programmed. This, however, can readily be accomplished, since reflector deflections are extremely predictable and a mechanical cam device working off a gravity counterweight pivot can be devised.

Since the subreflector adjustment mechanism need not be servo controlled, it is a passive compensation device and may be the most economical and practical approach for compensating the zenith (symmetry gravity vector) rather than incorporating multiple compensating devices within the structure.

The horizon results do not follow the same pattern, since these deflections are antisymmetric and the best-fit focal length and the design focal length are one and the same. Consequently, compensation for antisymmetric loadings may not be accomplished by only subreflector tilt but also possibly by compensating the ribs (refer to Figure 20 - RMS Summary).

The conclusions reached above were based on the relative relationships between the stated deflection characteristics. The absolute magnitude of the deflections and the RMS values are indicative of maximum limits only and are greater than the actual three-dimensional structural analysis (a factor of 2 from previous experience; however, this may be much higher for this design owing to the relative stiffnesses between the hoops and lightweight ribs).

Since the bipod reactions represent a very large concentrated load, their effect on the deflection pattern of the rib was of concern especially in light of the low rib stiffness. The tip deflection of the rib due to this load is 2.41 inches and ± 0.81 inch for the symmetry and antisymmetry loading conditions, respectively. This magnitude of deflection represents 50% of the total structural deflection and therefore is not tolerable. Consequently, the bipod reactions should bypass the reflector backup structure and be directly supported by the steel elevation wheel (this has been accomplished on many of the Rohr low-tolerance 85-ft-diameter antennas currently in existence) (see Figure 21).

Weight of Rib	1100 lbs.
Weight of Hoops Supported by Ribs	800 lbs.
Weight of Surface Supported by Rib (.3 psf)	<u>850 lbs</u>
TOTAL	2750 lbs.

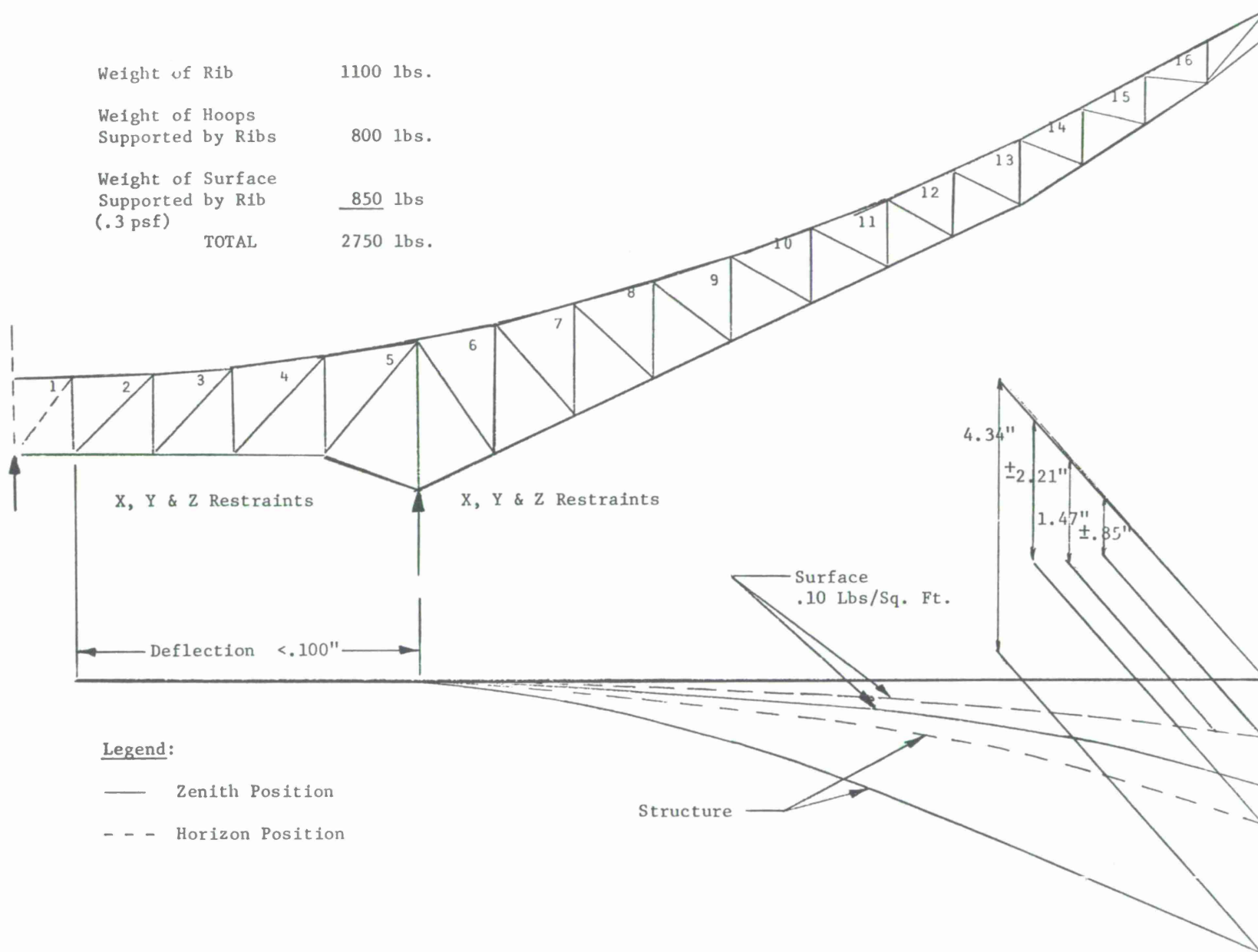


Figure 17. Two-dimensional dead-load deflection analysis; typical radial rib; 400-ft reflector. MIT W.O. 988. Reference: computer run 1494.

G-32

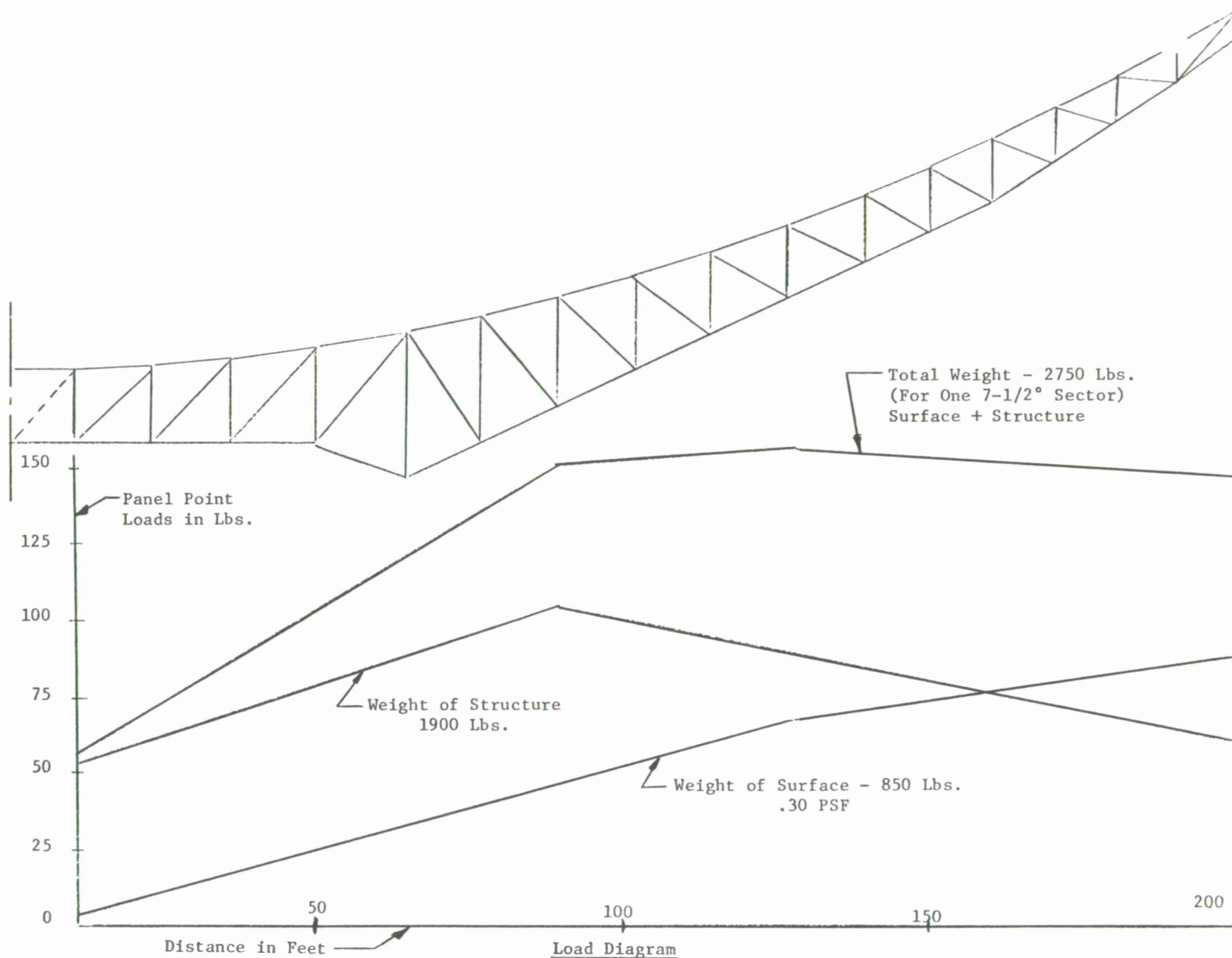


Figure 17.1. Load diagram for a 7-1/2° sector 400-ft reflector. MIT W.O. 988.
Reference: computer run 1494.

Figure 18. RMS summary two-dimensional analysis — symmetric loading.

Applied load	RMS before best fit (1 σ -inches)	RMS after best fit (1 σ -inches)	RMS after best fit and focal-length change	Focal-length change (inches)	Remarks
Structure	2.346	1.531	0.179	18	The minimum RMS is 0.381 inch Based on a new parabola equation $x^2 + y^2 = 4(172.4)Z$ Using a 0.3 psf surface panel
Surface	0.785	0.518	0.065	6	
Structure + 0.10 psf					
surface	3.240	2.142	0.346	25	
Structure + 0.20 psf					
surface	3.916	2.567	0.309	30	
Structure + 0.30 psf					
surface	4.696	3.084	0.381	36	

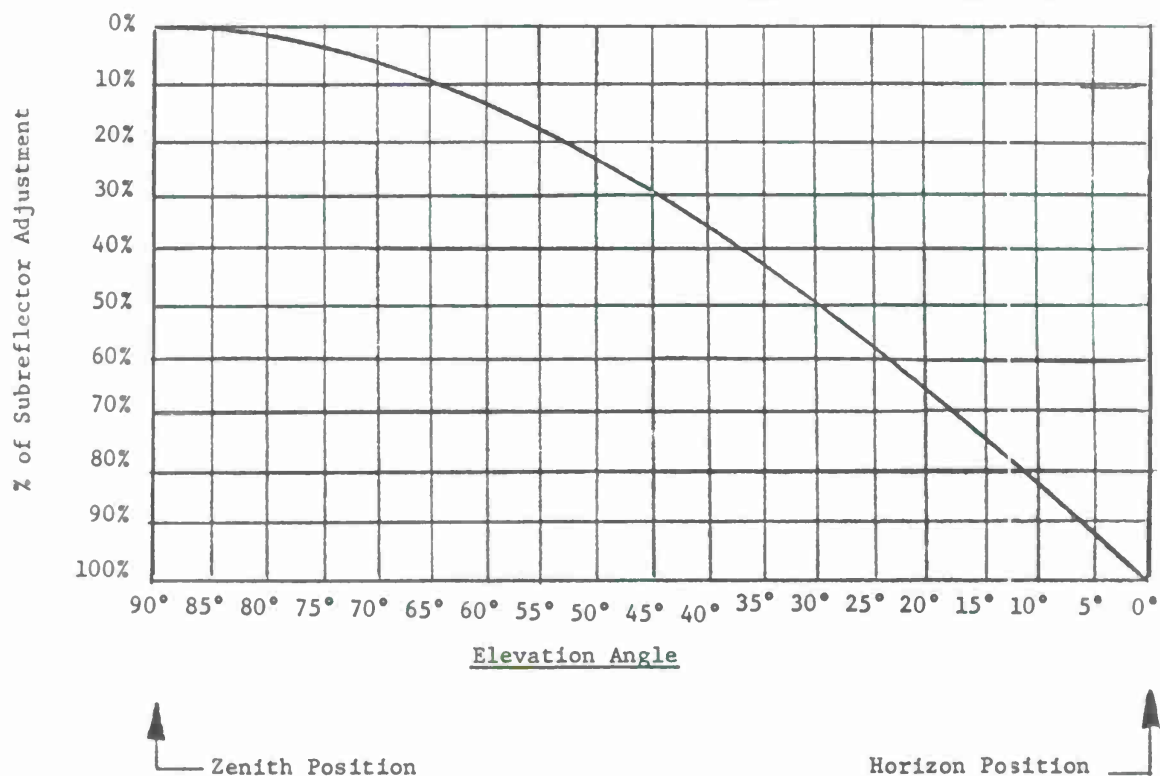
SUBREFLECTOR ADJUSTMENT

Figure 19. Subreflector compensation curve.

Figure 20. RMS summary two-dimensional analysis — antisymmetric loading.

Applied loads	RMS before best fit (1 σ -inches)	RMS after best fit (1 σ -inches)	Rotation at X-axis (rad)	Remarks
Structure	1.210	0.405	0.000738	The RMS of 0.902 inch may require rib compensation, and includes the 0.30 psf surface
Surface 0.10 psf	0.451	0.162	0.000272	
Structure + 0.10 psf surface	1.660	0.567	0.001010	
Structure + 0.20 psf surface	2.111	0.729	0.001282	
Structure + 0.30 psf surface	2.515	0.902	0.001519	

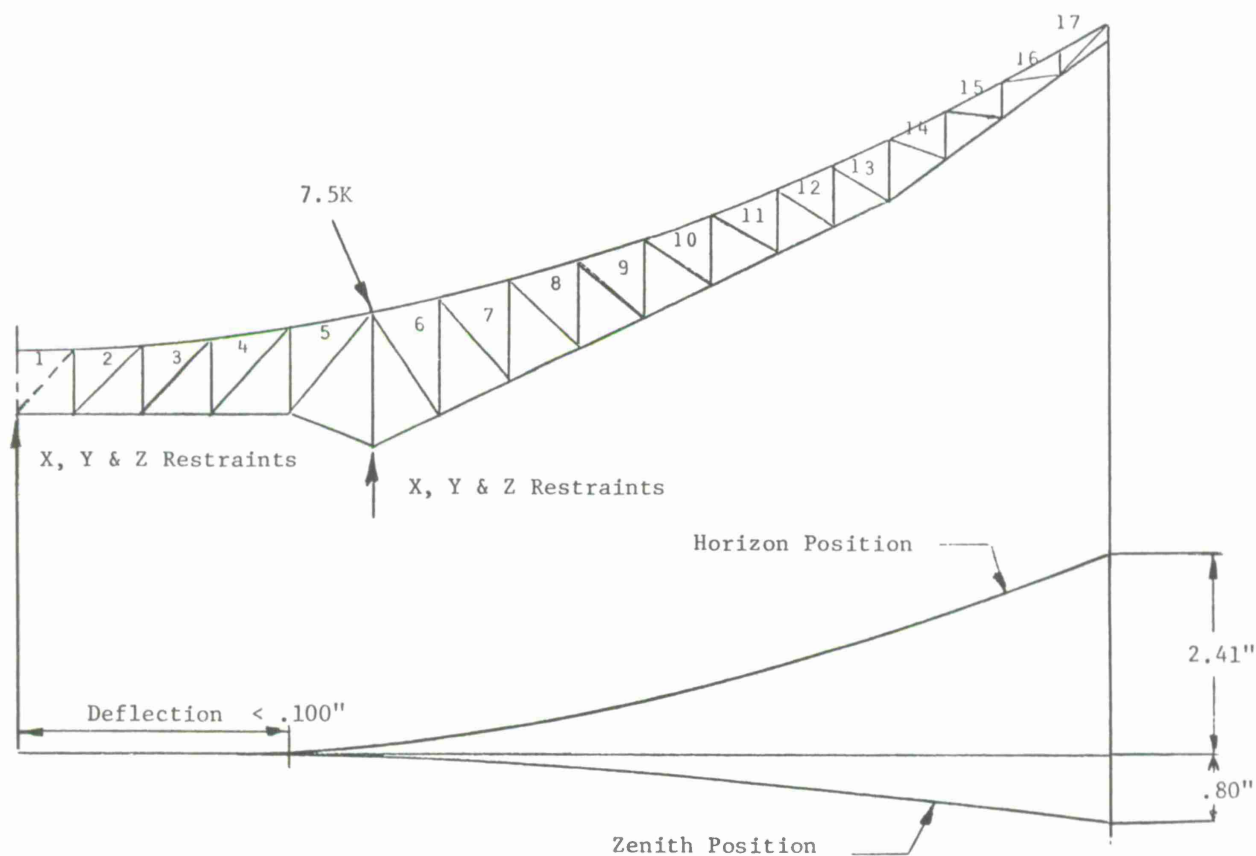


Figure 21. Dead-load deflection of rib due to bipod 400-ft reflector. MIT W.O. 988. Reference: computer run 1494.

The use of lightweight thin-walled sections may give rise to local high-stress levels and buckling problems; therefore, actual stress levels were of concern. Based on the maximum loading condition expected, the maximum stress levels were computed to be approximately 4000 psi with a 13,000 psi allowable. Local buckling for these thin-wall round tube members was also of concern, but was also found to represent a low stress level.

Referring to Figure 22, the reflector weights and the mass moments of inertia have been recomputed. Because of the reduction in surface-panel weight from 0.725 psf to 0.3 psf, the reflector weight has been reduced 57.8 K, which is 13% less than those shown on Figure 13, and the inertias are $\approx 30\%$ less.

4.1.8 Surface-panel considerations

To accommodate a reflector surface panel limited to a unit weight of 0.3 psf and having a peak deflection of approximately 0.130 inch (zenith to horizon) (0.160 inch was calculated for this initial trial), a 0.016-inch-thick perforated skin with 0.1-inch-diameter holes ($\lambda/20$ at 6000 MC) and 50% porosity was analyzed. The supporting frame members are 0.016-inch-thick formed aluminum channels, 6 inches deep around the perimeter, and intermediate support members are 2 inches deep placed on nominal 16-inch centers. The panel is approximately 4 ft \times 26 ft in length (trapezoidal in shape) with six support points.

An investigation of a 4-ft \times 26-ft-long panel with only two support points was made in an attempt to eliminate the need for the 48 intermediate ribs, which could result in a more economical reflector structure. However, the weight of this panel was prohibitively high and completely negated any advantage that may have been gained by eliminating this intermediate truss. Furthermore, most of the members that do make up the intermediate truss are required to reduce the L/r of the circular hoops that are transverse to this intermediate rib.

A peak deflection of 0.130 inch actually results in a maximum deflection change (if the panels are set at $\approx 45^\circ$ elevation angle) of $(0.7 \times 0.130) = 0.090$ -inch peak or an RMS of approximately 0.030 inch, which is the budgeted tolerance.

The curvature of this panel was investigated. A single curved panel will have a basic error from the theoretical contour that varies from a maximum of 0.074 inch to a minimum of 0.064 inch or a maximum RMS tolerance of approximately 0.025 inch (1σ). This tolerance represents approximately 50% of the maximum permissible panel manufacturing tolerance, which is targeted at 0.050 inch (1σ). However, the resulting cost favors the singly curved panel approach.

Therefore, all the panel-support members will have to be rolled to a radius and the panel must be curved in two directions. A 5°F thermal differential results in a deflection tolerance of 0.002 inch (1σ).

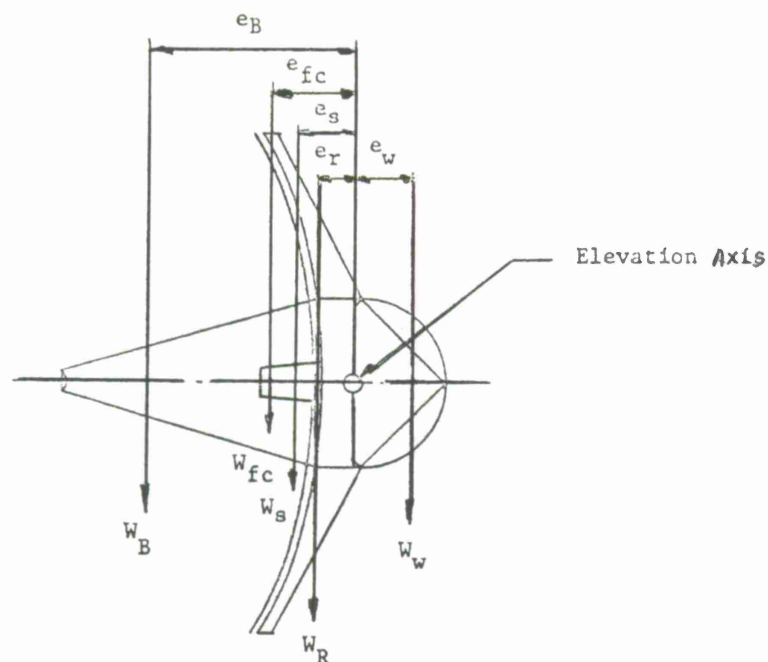


Figure 22. Reflector weights and mass moments of inertia — tapered thin-walled sections and lightweight surface.

Component	Symbol	W (K)	e (ft)	W _e (K ¹)	IM _x (slug-ft ²)	IM _z (slug-ft ²)
Reflector	W_r	87.6	20.6	1820	18.4×10^6	32.0×10^6
Surface (0.30 psf)	W_s	40.8	42.3	1730	15.7×10^6	26.0×10^6
Wheel	W_w	290.0	-25.2	-7300	22.6×10^6	20.5×10^6
Total		418.4		-3850	56.7×10^6	78.5×10^6
Bipod	W_B	15	105	1729		
Feed cone	$W_{F.C.}$	20	42	840		
Counterweight	-1181 ft. kip ÷ 55 ft = -21 K (tail heavy)					

Panel field-alignment tolerances will be held to 0.050-inch (1σ) RMS. Alignment will be accomplished at approximately midelevation travel to optimize gravity-load deflections of the reflector backup structure. This alignment tolerance includes the effects of optical errors, human errors, tooling errors, and panel thickness. These random errors result in approximately 4-arcsec (3σ) error for a distance of 200 ft. This tolerance is 0.046 inch (3σ) or 0.016 inch (1σ). In addition, an economic field-alignment tolerance that is compatible with the overall surface-accuracy requirement is approximately 0.045 inch (1σ). The combined surface alignment tolerance from all these effects is:

$$\begin{aligned} 1\sigma_A &= \sqrt{(0.016)^2 + (0.045)^2} \\ &= \sqrt{[(256) + (2000)]^2 \times 10^{-6}} \\ &= \sqrt{(2256)^2 \times 10^{-6}} \\ &\leq 0.050 \text{ inch} \end{aligned}$$

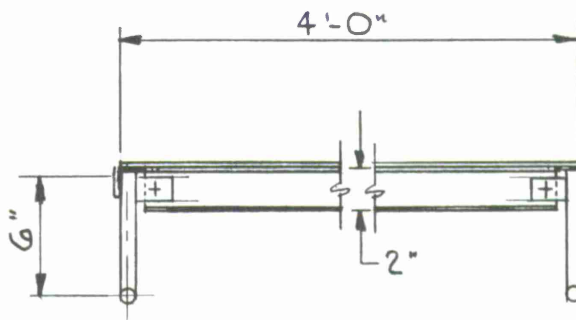
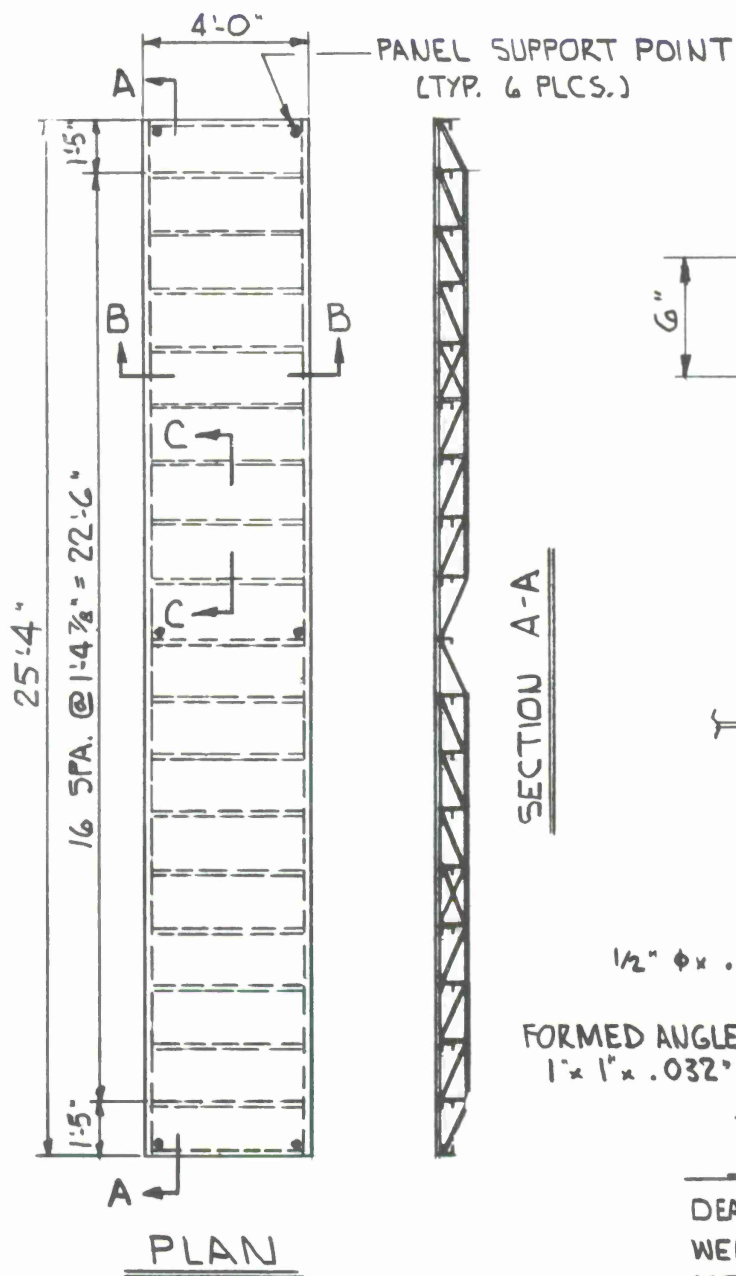
The combined accuracy from all error sources for the surface panels only is

$$\begin{aligned} \text{RSS } (1\sigma) &= \sqrt{(1\sigma_{DL})^2 + (1\sigma_A)^2 + (1\sigma_M)^2 + (1\sigma_T)^2} \\ &= \sqrt{[(0.030)^2 + (0.050)^2 + (0.050)^2 + (0.002)^2]} \\ &= \sqrt{[(900) + (2500) + (2500) + (4)] \times 10^{-6}} \\ &= \sqrt{(5909) \times 10^{-6}} \\ &= 0.077 \text{ inch} \end{aligned}$$

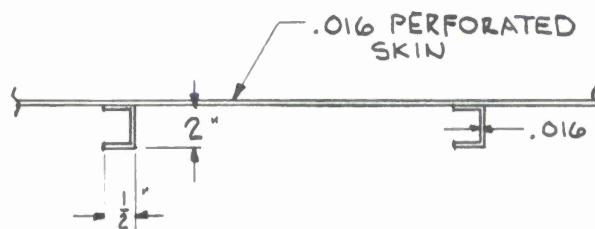
A study of the manufacturing techniques necessary to fabricate this panel pointed out that rolling to contour the thin-walled 6-inch-deep channel section was not practical. It was feared that the thin web was not stable enough to withstand the forces that will be developed during the rolling process. As a result, an alternate design was developed, which employs a lightweight trussed section in lieu of the 6-inch channel member consisting of a formed angle and thin-wall tubing.

4.1.9 Reflector three-dimensional analysis

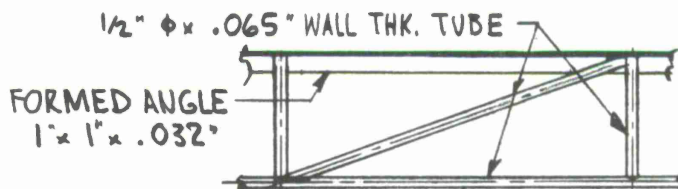
Utilizing the reflector geometry previously established, refer to SK-2122, a three-dimensional static analysis was conducted. The analysis was for one complete quadrant of the reflector and elevation-wheel assembly. A total of 500 joints and 1600 bars was analyzed. The computer programs employed were STAIR, STIFFEIG, and Path Length for determining the surface and pointing accuracies. These programs were handled by



SECTION B-B



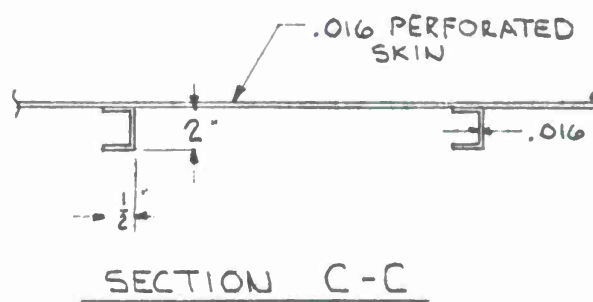
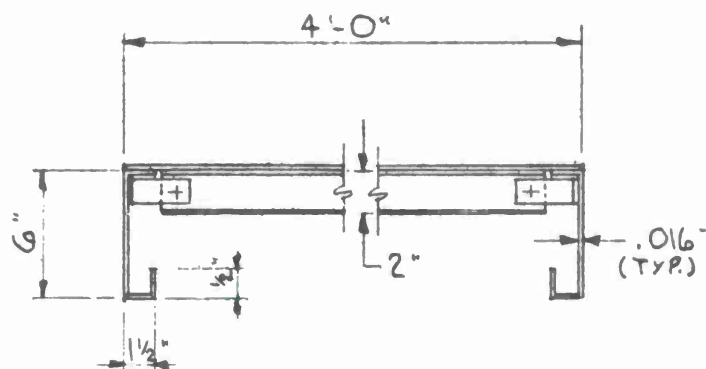
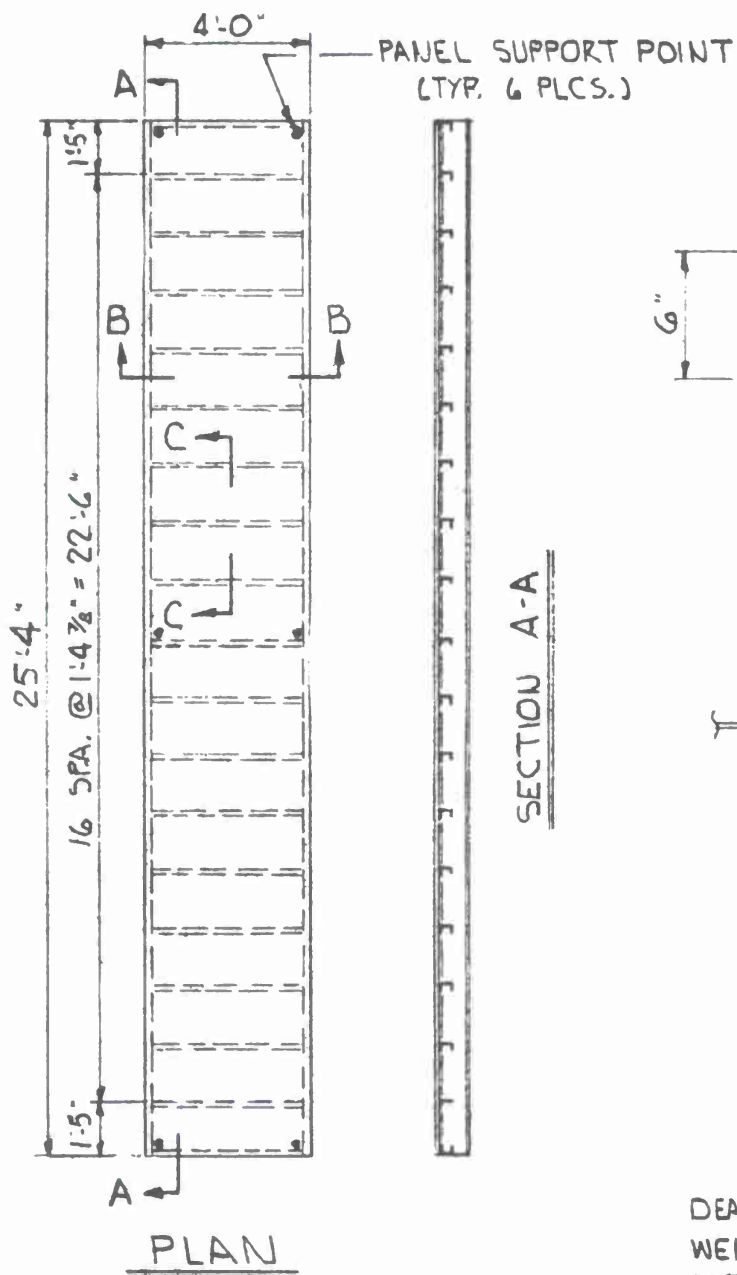
SECTION C-C



TYP. TRUSS DETAIL

DEAD LOAD DEFLECTION = .160"
WEIGHT OF PANEL = .270 P.S.F.
MFG. TOL. = .050" RMS (1 SIGMA)

4'-0" x 25'-4" SURFACE PANEL (ALTERNATE)



DEAD LOAD DEFLECTION = .160"
 WEIGHT OF PANEL = .270 P.S.F.
 MFG. TOL. = .050" RMS (1 SIGMA)

4'-0" x 25'-4" SURFACE PANEL

the Univac 1107 computer. Based on the static displacements of all structural joints located (221) at the reflector surface, the surface accuracy (RMS) and reflector pointing error were computed, using the path-length program.

The three-dimensional analysis for gravity loadings of the structure and the 0.3 psf surface panel indicates a peak deflection of 2.1 inches for the symmetrical condition (zenith-gravity on) and 3.2 inches for the antisymmetrical condition (horizon-gravity on). The RMS for each condition is 0.41 inch and 0.19 inch, respectively, without structural-compensation considerations. If the focal length (hyperbola) is preprogrammed (compensated) for an axial adjustment, throughout the entire range of travel, of approximately 2-1/2 inches, the RMS for the symmetrical condition reduces to 0.34 inch, defining a new parabolic equation, i. e., homology.

To optimize the reflector structural deflections, the surface panels will be aligned at midelevation travel in order to arrange the change in deflection from zenith to horizon. The RMS change from the optimum panel setting position, which is approximately 45° elevation angle, to either the zenith or 13° above the horizon calculates to an RMS of 0.166 inch. For this first trial analysis, these results were extremely encouraging, since the goal desired is definitely within the present state of the art and compensating the hyperbola only is readily achievable either mechanically (passive) or with a servo, depending on the economies.

As expected, the extremely lightweight ribs were stiffened considerably by the hoops. In fact, the peak deflections from the two-dimensional analysis were reduced by a factor of 10.5 for the symmetrical (zenith) condition and 2.3 for the antisymmetrical condition (see below).

Comparison of two-dimensional and three-dimensional analyses.

		Two-dimensional	Three-dimensional	Hoop factor
Maximum tip deflection	Zenith	8.72 inches	0.834 inch	10.5
	Horizon	4.74 inches	2.10 inch	2.3

The RMS including panels and structure from all error sources (refer to Figure 23) resulted in approximately 0.2 inch. Optimization of the structure will bring this tolerance below the 0.150 inch specified (0.100 inch desired).

To find the lowest natural frequency of the reflector and elevation-wheel assemblies, the structure, as used in the STAIR analysis, was simplified and modeled to fit within the size limitations of a three-dimensional structural dynamic analysis program called STIFFEIG. All the reflector-structure static displacements from the STAIR analysis were matched to the static displacements of the modeled structure. When the ratio of these deflections approaches unity, then the stiffnesses of the two structures are matched.

Once this compatibility is achieved, the structural dynamic analysis portion of the STIFFEIG program is run to determine the lowest six natural frequencies and the mode shape deflections of the reflector and elevation-wheel assembly. With these data reduced, reflector-elevation-wheel lumped parameter models can be developed for incorporation into the overall system lumped parameter models. The analysis was conducted for the zenith-position (SS boundary condition) and the horizon-position (AS boundary condition) dynamic models. The calculated natural frequency of the reflector assembly was 1.29 cps and 1.33 cps, respectively.

Figure 23. RMS table.
Final results of the CAMROC study.

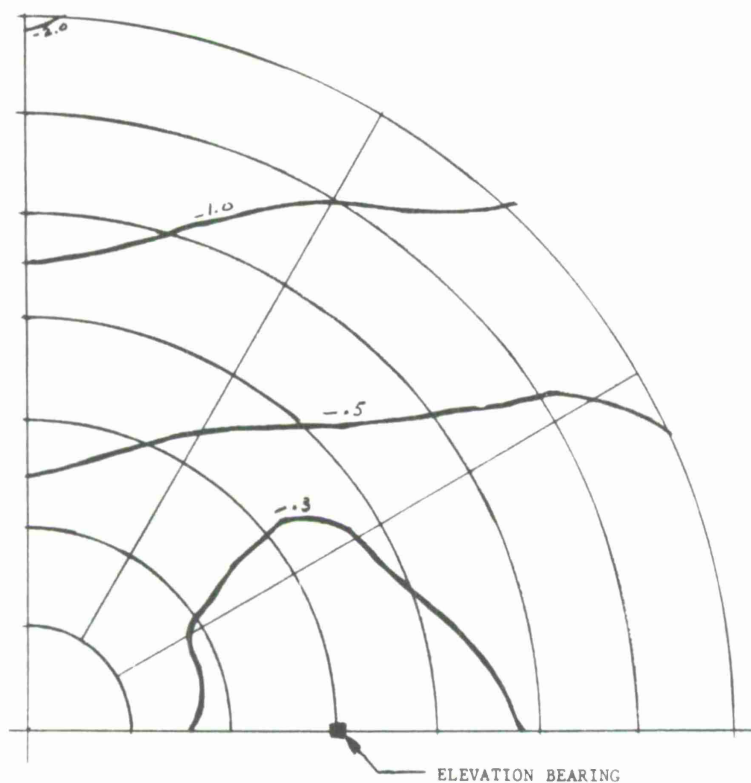
Error source 1 σ – RMS (inches)	Mfg. tolerance on the panels	Alignment tolerance on the panels	Gravity 44° to 15° above horizon	Thermals Δt = 5°F
Panels	0.050	0.050	0.030	0.002
Structure	-	-	0.166	0.010
Σ 1 σ	0.050	0.050	0.196	0.012
1 σ ² × 10 ⁻⁶	2500	2506	38400	144
Σ 1 σ ² × 10 ⁻⁶			43544	
RSS = √Σ 1 σ ² √0.043544 = 0.208 inch 1 σ				
CAMROC specification		0.150 inch (desired 0.100 inch)		

4.1.10 Azimuth structural considerations

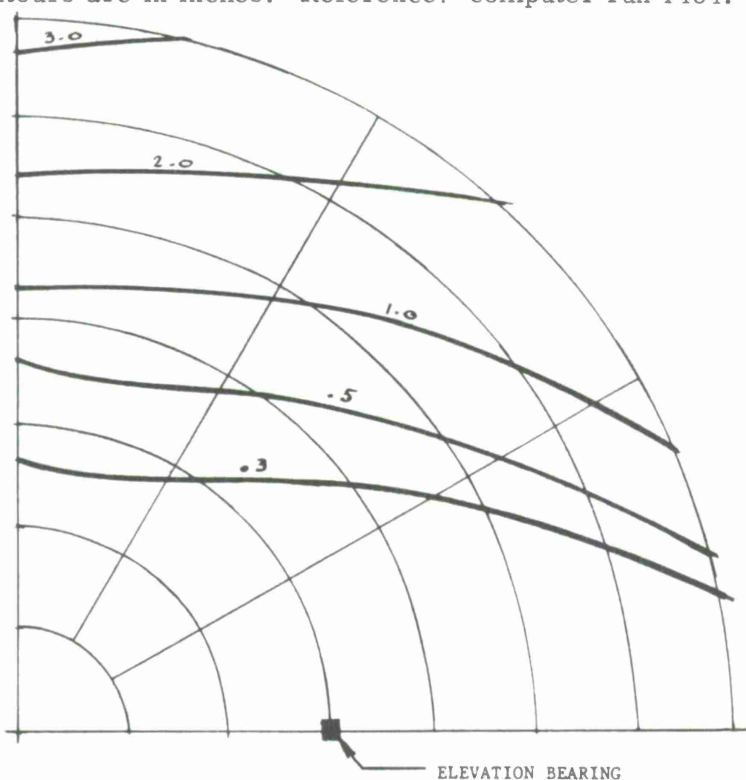
Three azimuth structures were considered:

- 1) The open-framed concept with 3 base-support points (refer to SK-2111).
- 2) The "yoke" type with 4 base-support points (refer to SK-2112).
- 3) The open-framed structure with a center-thrust bearing and stabilizers (refer to SK-2113).

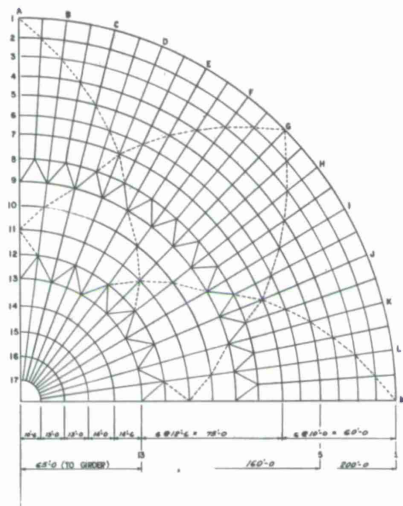
Owing to the absence of overturning moments on the azimuth bearing and the desirability of low-axis friction and minimum cost, the yoke-type concept supported by four hydrostatic bearing pads on a nominal diameter of 56 ft represents the most economical structure and was analyzed for this study. The lower portion of the yoke interfaces with the two yoke arms and the four hydrostatic bearing pads. It is a structure approximately 40 ft \times 40 ft \times 25 ft and houses the azimuth- and elevation-drive machinery and the hydrostatic-bearing equipment.



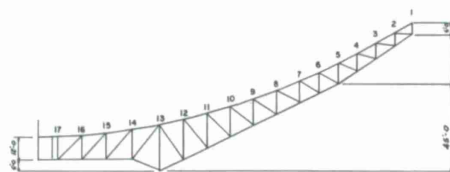
REFLECTOR CONTOURS - GRAVITY DEFLECTIONS - ZENITH POSITION
Contours are in inches. Reference: computer run 1484.



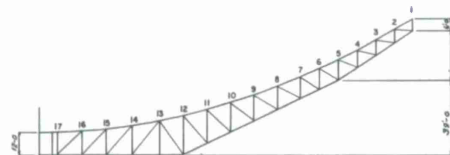
REFLECTOR CONTOURS - GRAVITY DEFLECTIONS - HORIZON POSITION
Contours are in inches. Reference: computer run 1485.



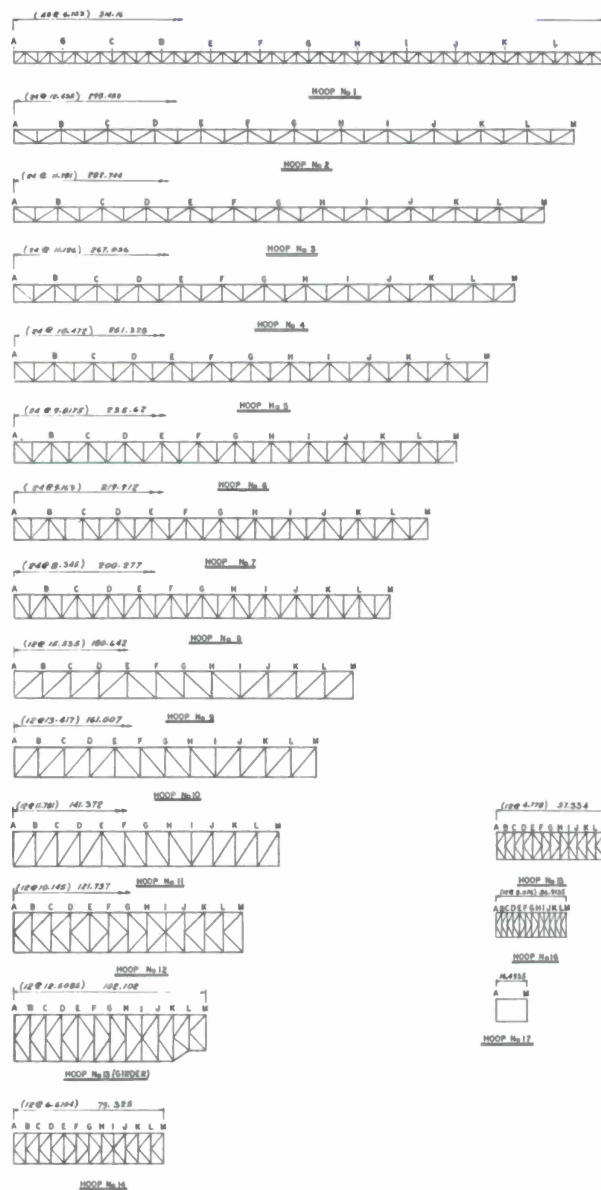
400' REFLECTOR



TYS. #18 FROM A TO K



TYS. #18 FROM A TO K



SK-2122.

The yoke structure was designed to support approximately 600,000 lbs of load. The yoke structure was analyzed as a three-dimensional pin-connected structure, and the mass, inertias, and deflection characteristics were computed for inputs into the system dynamic analysis.

4.1.11 Pointing accuracy and dynamic analysis

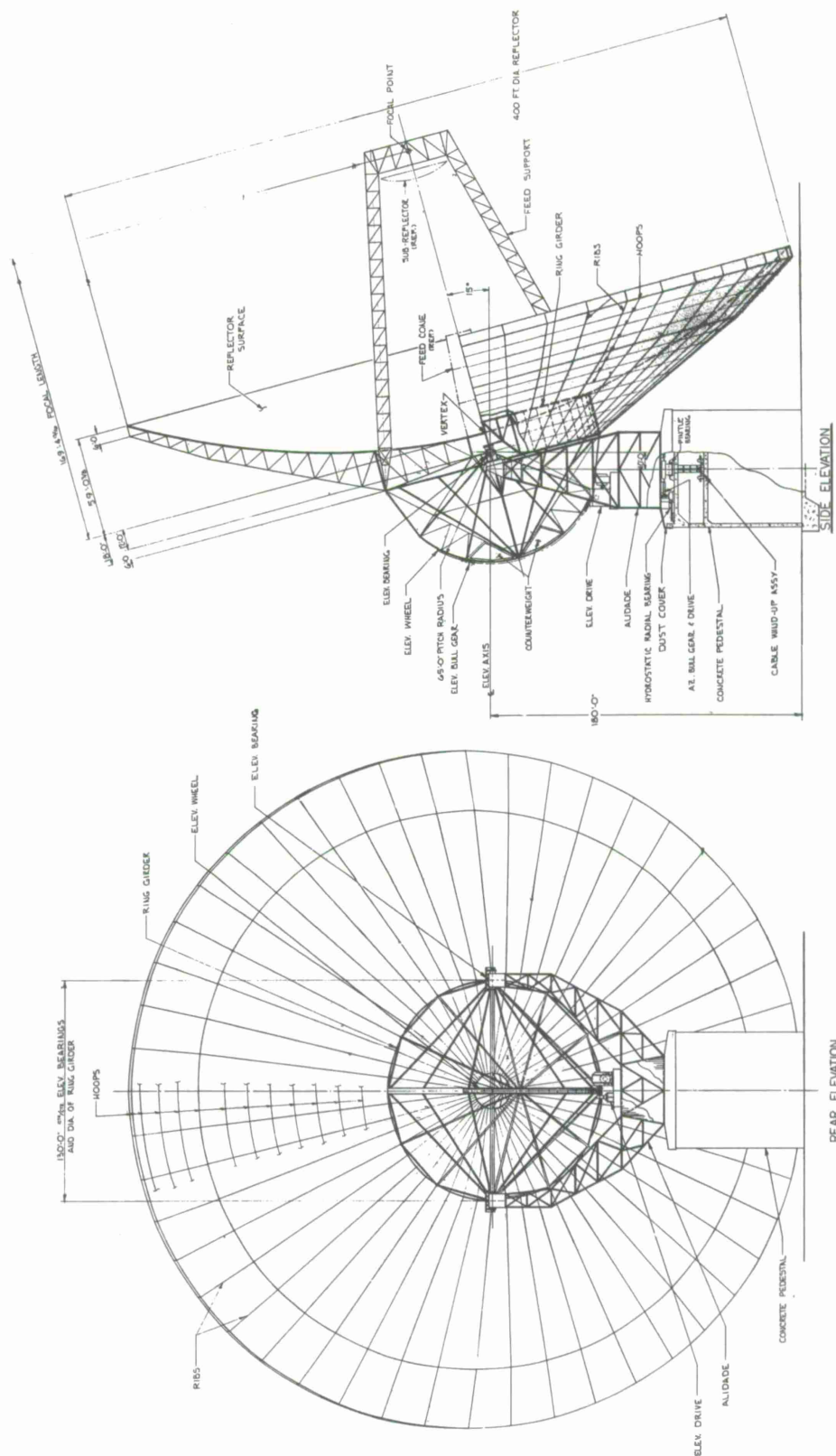
In the next phase of the study, the pointing accuracy was analyzed. The specification requires a peak error of 15 arcsec repeatability. This is a minuscule tolerance for a structure of this magnitude, and consequently represents a major problem area. The reflector assembly from a gravity-loading standpoint must be an extremely repeatable structure; therefore, it will be mandatory to calibrate out the gravity-load pointing error. To meet the pointing-accuracy requirement, the nonrepeatability of the reflector structure must be less than 10 arcsec. Assuming that 90% of the deadload error is calibratable, the maximum permissible pointing error for the reflector assembly would be 100 arcsec and would be the algebraic sum of the reflector, sub-reflector, and feed-cone pointing errors. The usual approach is to balance out the clockwise reflector pointing angle by the counterclockwise beam pointing angle due to subreflector translation.

Alignment of axes and datum planes must be held to less than 10 arcsec to accommodate calibration. Thermal differentials of only 2° on the structure can present a significant pointing error. For this structure, a 33-arcsec error has been calculated. It may, therefore, be necessary to control the entire structure thermally within a $\pm 1/2^\circ$ tolerance. This may be within the thermal-gradient characteristic of the radome environment. Control of this type would be impossible outside a radome. A precision on-axis readout encoding system (19 bit) having a total axis error of less than 5 arcsec is required. Axis errors from the servo system must also be kept to less than 5 arcsec. Axis frictions become very critical and must be kept as low as possible. The result of the pointing-error analysis indicates a peak error of approximately 16 arcsec is possible if the gravity and alignment errors are calibratable and thermals are held to less than $\pm 5^\circ$ (see Figure 24).

Since there is no wind acting on the antenna, all component parameters, except for the reflector, were based on stress, accuracy, and servo considerations only. The resulting mass, inertia, and stiffness characteristics were then determined and the locked rotor frequency of the system computed.

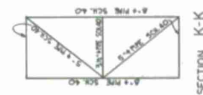
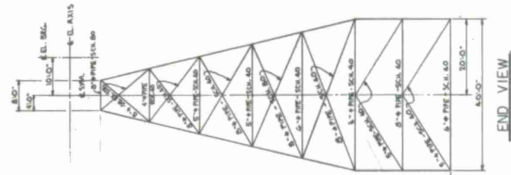
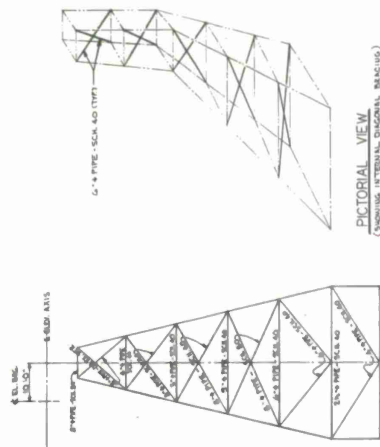
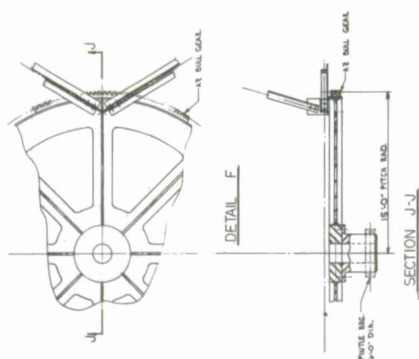
The servo accuracy requirement of 5 arcsec limited the acceleration lag error to approximately $1-1/2$ arcsec. This required that the lowest natural frequency (locked rotor) be approximately 0.2 cps.



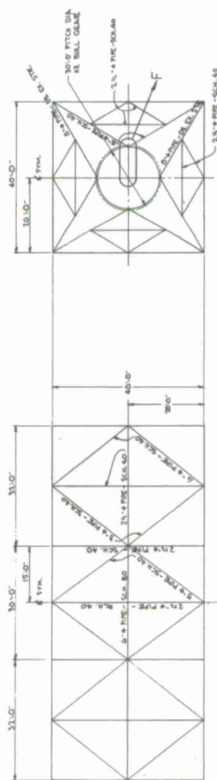


SK-2112.





SK-2129.



SECTION B-B

SECTION D-D

SECTION E-E

SECTION P-P

SECTION R-R

SECTION S-S

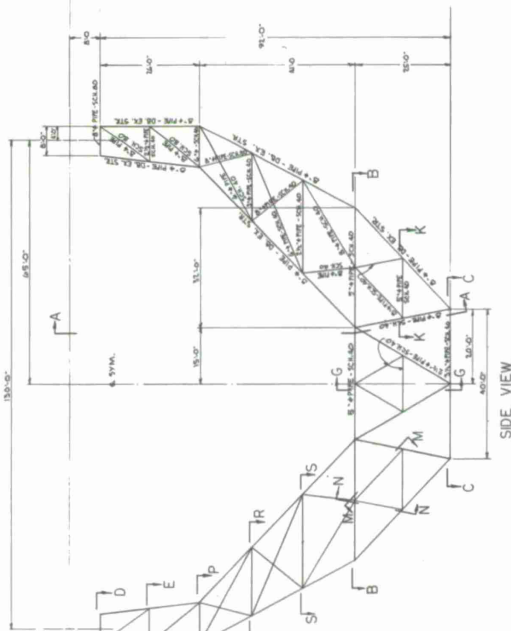


Figure 24. Pointing-accuracy table.

Elevation Axis				
Error source (arcsec) Component	Gravity (nonrepeatability)	Thermals 5° - Δt	Alignment*	Tracking
Reflector assembly	< 10	0 }	17	-
Antenna mount assembly	-	0 }		-
Servo system	-	-	-	5
Readout system	-	-	5	-
Σ 3 σ	10	0	< 18	5
(3 σ) ²	100	0	315	25
Σ (3 σ) ²		440		
RSS = √ Σ (3 σ) ²		√440 = 21		
Error source (arcsec) Component	Thermals 1/2° - Δt (thermal gradient)	Alignment	Tracking	
Reflector assembly	3	-	-	
Antenna mount assembly	8	-	-	
Servo system	-	-	5	
Readout system	-	5	-	
Σ 3 σ	11	5	5	
(3 σ) ²	121	25	25	
Σ (3 σ) ²		171		
RSS = √ Σ (3 σ) ²		171 = 13		
Resultant: Az + El = √440 + 121 = √611 = 25				
Note: Datum and axis alignments have been held to 10 arcsec maximum. Since axis alignment errors can be calibrated, it is assumed that 10% of the alignment errors will remain as residuals. This reduces the resultant space-pointing vector to approximately 16 arcsec, which is within the realm of meeting the specification goal of 15 arcsec.				
* RSS applies since alignment errors are random.				

For the dynamic analysis of the entire system, a 15-degree-of-freedom lumped parameter model was analyzed using two Rohr developed programs:

- 1) DYNEL for the elevation lumped model.
- 2) DYNAZ for the azimuth lumped model.

A group of differential equations describing the mass and stiffness characteristics of the lumped parameter model of the 400-ft antenna system are used to compute elements for the mass matrix A and stiffness matrix C. With these two matrices known, the natural frequencies of the model are solved using the eigenvalue subroutine CARAC5.

The results of the above analysis were approximately 0.35 cps for the elevation or azimuth axis. It is recommended that a minimum locked rotor frequency be specified as 0.3 cps to guard against discrepancies between the calculated versus the actual measured value.

4.1.12 Axis bearings

The elevation-axis bearings were designed to carry approximately 600 kips of total load (300 K per bearing). A nominal 24-inch-diameter SKF bearing has been selected. Axis frictions for this type of bearing are negligible. The bearings are structurally tied together with a through shaft to ensure proper load distribution and to provide the closing member across the yoke arms. Alignment targets, seals, etc., are included in the assembly.

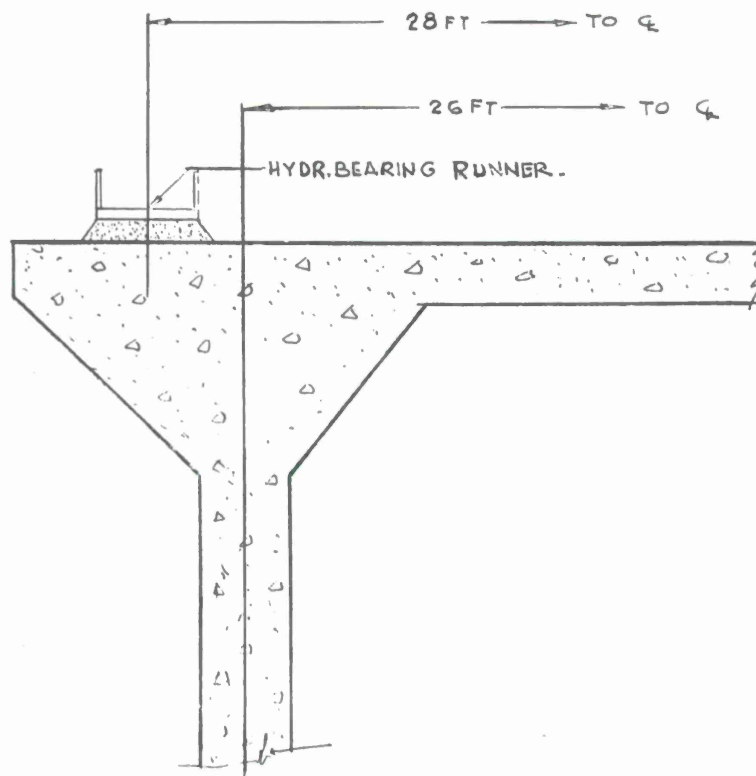
The azimuth-axis bearings consist of a center pintle that defines the azimuth axis and is a 6-ft-diameter roller bearing. To minimize axis frictions and to keep servo errors within tolerable limits, the thrust bearing must be of the frictionless type. For this application, a hydrostatic bearing consisting of four multiple recessed circular pads riding on a 56-ft-diameter steel runner separated by a thin film of pressurized oil is recommended. The bearing is designed for supporting approximately 1,000,000 lbs of load with adequate safety margin. Pumps, controls, reservoirs, heat exchangers, shut-down logic, etc., are included in the assembly.

4.1.13 400-ft drive, control, and servo-system considerations

As a result of the investigations made on the previous study, Appendix A, Sections 5.2 through 5.6, several radome drives were evaluated and a dual pinion electric anti-backlash drive system was recommended. Further investigation of alternate drive systems was conducted and is documented in the report titled "Additional Drive and Control Study," reference Report W.O. 748-1.

The cost and performance characteristics of the conventional gear-drive approach are included in this study.

The servo drive for each axis is a nominally rated 5-hp antibacklash system; two motors per axis provide maximum axis velocity of $0.3^{\circ}/\text{sec}$ in elevation and $0.6^{\circ}/\text{sec}$ in azimuth. The gear-drive systems are comprised of dual opposed pinions having a 3-inch face width bull gear. Drive motors are conventional DC motors controlled by SCR power amplifiers and solid-state control circuitry. An on-axis encoding system is utilized.

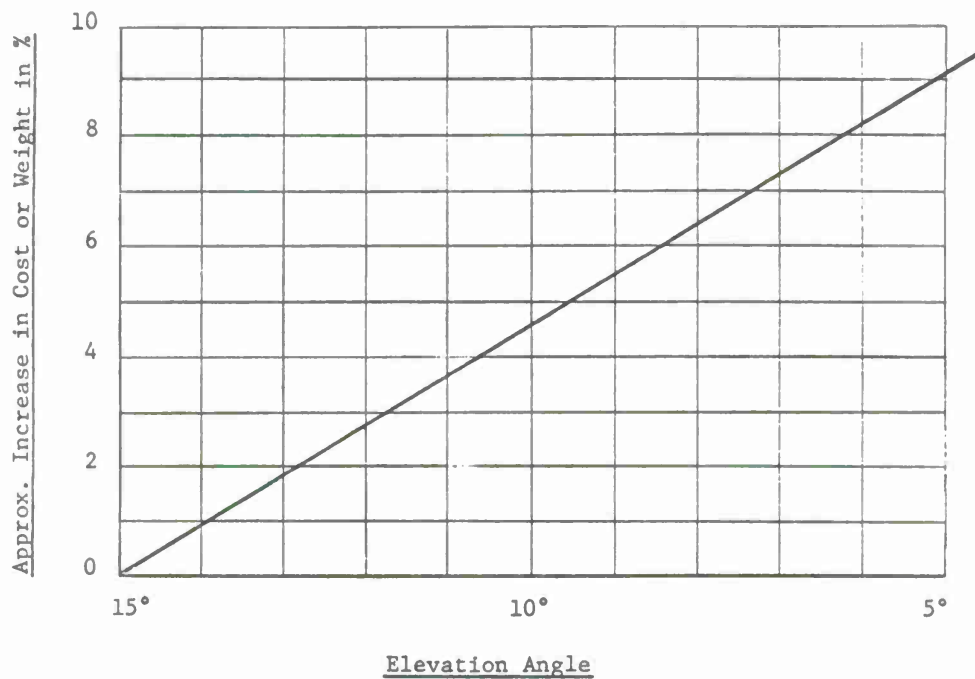


HYDROSTATIC BEARING AND PEDESTAL INTERFACE

5. COST AND WEIGHT VERSUS SKY COVERAGE

The effect of increasing the hemispherical sky coverage indicates that the cost or weight increases approximately 1% for each degree closer to the horizon. These increases are primarily the major structural components. Mechanical and servo components are unaffected by increasing sky coverage.

Figure 25. Percent of cost or weight increase versus elevation angle.



APPENDIX H

SCIENTIFIC PROGRAM FOR A
LARGE, STEERABLE PARABOLOID

Prepared for
THE CAMBRIDGE RADIO OBSERVATORY COMMITTEE

December 1966

CAMROC RADIO AND
RADAR ASTRONOMERS

TABLE OF CONTENTS

<u>Section</u>		<u>Page</u>
1	INTRODUCTION	H-1
2	APPLICATIONS TO RADIO ASTRONOMY	H-2
3	APPLICATIONS TO RADAR ASTRONOMY	H-21
4	BIBLIOGRAPHY	H-39

1. INTRODUCTION

The CAMROC choice of a large, fully steerable antenna is based on the results of scientific deliberations among the senior faculty and staff of the participating institutions. The choice results directly from the flexibility of the instrument. We anticipate serving a large user community, and the significance and variety of flow of scientific results from the NRAO 140-ft paraboloid and from the Parkes 210-ft paraboloid adequately demonstrate the scientific potential of the large paraboloid.

Use of smaller auxiliary antennas as interferometer elements is definitely planned as part of the CAMROC facility. This will permit further study of discrete sources with small angular size, including planets and extragalactic sources. A major consideration in the CAMROC scientific planning is the inclusion of radar as one of the fundamental objectives. We also plan interferometric experiments in radar as well as in passive radio astronomy.

The radio and radar discussions that follow are indicative of the scientific programs we would undertake if the CAMROC facility were available now. The programs outlined are those that are evident in 1967, although the proposed CAMROC telescope could not be available before the 1970's. As the advances in radio astronomy have clearly shown, new discoveries will undoubtedly alter the exact programs undertaken in the first few years of the life of the CAMROC facility. Nevertheless, the versatility of the large, precision, fully steerable paraboloid guarantees a powerful scientific instrument upon completion.

The material in this section is based on an earlier CAMROC document,^{*} but it has been condensed and revised where scientific progress warrants.

^{*}The Cambridge Radio Observatory Committee, "Objectives and Study Programs for a Regional Radio and Radar Astronomy Research Facility," Academic Year 1965/1966.

2. APPLICATIONS TO RADIO ASTRONOMY

2.1 Spectral-Line Studies

One of the rewarding aspects of radio astronomy as applied to the study of Galactic structure and physics of the interstellar medium has come from the detection (Ewen and Purcell, 1951) and the observation of the 21-cm line of neutral atomic hydrogen in its lowest levels. Not only have these studies led to the well-known maps of the Galactic hydrogen distribution prepared by Netherlands and Australian radio astronomers, but they have also provided detailed knowledge about the cloud structure and dynamics of the interstellar medium, the motions and hydrogen distribution of the Andromeda Nebula and Magellanic Clouds, and the hydrogen content of other nearby galaxies. Interest in radio spectroscopy of the interstellar medium has accelerated rapidly since the discovery in 1963 of the OH lines (Weinreb, Barrett, Meeks, and Henry, 1963), in 1964 of the recombination lines of atomic hydrogen by Soviet scientists (Dravskikh and Dravskikh, 1964; Sorochenko and Borodzich, 1964) and the recombination lines of atomic helium (Lilley, Palmer, Penfield, and Zuckerman, 1966). The success of these investigations has stimulated both radio astronomical searches for other lines and laboratory investigations to determine the frequencies of transitions of likely interstellar constituents. It is clear that interest in radio spectral lines will remain paramount for many years, and that one of the principal research programs of the proposed radio telescope will be concerned with further spectral-line investigations.

The study of the behavior of ground-state hydrogen in the vicinity of H II regions has received considerable attention in hydrogen-line research. Now, with the discovery of anomalously excited OH emission sources adjacent to thermal regions and with the possibility of studying the $n \rightarrow n-1$ type hydrogen recombination lines, there are many new possibilities for a detailed study of the physics of the interstellar medium. With the resolution of the proposed CAMROC antenna, a fruitful research objective for the CAMROC telescope will be selective probing within the larger H II regions to examine the interdependence of excited hydrogen and helium, ground-state hydrogen, the OH radical, and other constituents in the medium, as determined by radio spectroscopic techniques.

Spectral-line research objectives are unlimited with an antenna of the envisioned size and resolution. We view the proposed CAMROC instrument as a major step forward in the conduct of spectral-line research.

2.2 Observations of the OH lines

During 1965 and 1966, OH observations have provided some of the most unexpected results obtained in radio astronomy. In 3 years of observations many anomalies have been discovered, none of which has been satisfactorily explained, and it is virtually impossible to state what problems will be facing the OH observer 5 years from now.

We can, however, point out the present situation of the observations of the 18-cm lines of OH, and indicate the use that would be made of a large radio telescope if it were available now.

Present observations show that the spatial distribution of OH throughout the Galaxy can best be described as "spotty." Some 15 or so sources of either OH emission or absorption have been discovered in three years of observations, but this may be due to observational selection effects. Only four groups (MIT, Harvard, the University of California at Berkeley, and CSIRO in Australia) have been actively observing OH since its discovery, and they have tended to study a relatively small number of sources, since each successive series of observations has revealed new anomalies. The true extent of OH within the Galaxy is still to be determined.

Generally, the unexpected results obtained from the OH observations can be enumerated as follows:

- 1 There are intensity anomalies among the four OH lines that depart from theoretical productions by as much as 2 orders of magnitude.
- 2 There are OH-cloud motions in the region of the Galactic center at radial velocities quite different from those expected from studies of the H-cloud motions.
- 3 OH emission lines are found with brightness temperatures in excess of 2×10^6 ° K.
- 4 OH emission lines exist as narrow as 600 cps, corresponding to a thermal temperature of 5° K.
- 5 Strong circular polarization has been detected, often as much as 100% polarized, for all OH emission.
- 6 No polarization, linear or circular, has been detected for OH absorption.
- 7 Many of, if not all, the regions of OH emission have been discovered to have an angular extent less than 15 arcsec and to be associated with H II regions.
- 8 Some of the OH emission sources have been reported to be time varying.

None of these anomalies has a satisfactory explanation at the present time, although theories suggesting maser amplification on a cosmic scale appear to offer some promise.

Although some current OH investigations are not sensitivity limited, others are, and practically all OH observations are seriously resolution limited. The CAMROC facility would provide a direct increase in resolution of a factor of 3 over any radio telescope in the Northern Hemisphere that is capable of operating at the OH frequencies, excluding space-related antenna facilities. The capability of the CAMROC radio

telescope can be translated into an improvement in sensitivity by a factor of 9, which, in turn, implies a reduction of a factor of 81 in integration time for the same signal-to-noise ratio. This is an impressive number, for it means that data can be acquired 81 times faster than at present with the NRAO 140-ft radio telescope, for example. Integration times of 2 or 3 hours are not uncommon in spectral-line observations, but these could be accomplished in 1.5 to 2 min with a 400-ft antenna for the same signal-to-noise ratio. A clear-cut example of the advantage to be gained by the use of the CAMROC radio telescope is afforded by the recent detection of the lines of $O^{18}H$ in the spectrum of the Galactic center (Rogers and Barrett, 1966). These lines are approximately a factor of 500 weaker than the $O^{16}H$ lines and required 18 hours of integration to reveal the presence of one line. This same observation would require about 13 min with the CAMROC antenna. Thus, many details of the $O^{18}H$ lines would become capable of further investigation — details that are currently impossible to investigate because of the prohibitive time required on a large telescope.

Recent interferometric observations of the OH-emitting regions (Rogers, Moran, Crowther, Burke, Meeks, Ball, and Hyde, 1966; Cudaback, Read, and Rougoor, 1966) have shown that the angular size of the regions is less than 15 arcsec. This points up the utility of using the CAMROC antenna with an auxiliary antenna of smaller size as an interferometer to evaluate the positions and angular sizes of the emission regions. The determination of the angular sizes may require a mobile antenna to ensure sufficient base-line separation if angular sizes less than 5 arcsec are shown to be common.

The OH observations are relatively new and have produced unusual results, so that it is difficult to speculate on the course of future research. We can say with relative certainty, however, that even if all current OH anomalies are explained, others will appear and a facility such as the CAMROC antenna will be an invaluable tool with which to attack the new problems. This is clearly demonstrated in Figure 1, which shows the antenna temperature (proportional to the received power) observed for OH emission as a function of the effective area of the radio telescope used for the observation. Since the sources will be unresolved by the CAMROC radio telescope, the antenna temperature to be observed is indicated in Figure 1 (the antenna temperatures are normalized for a bandwidth of 10 kc). The large antenna temperature will allow many detailed studies, such as polarization and temporal variations, to be conducted.

2.3 Hydrogen-Line (21-cm) Research

The Galactic-latitude dependence of hydrogen-line spectra has been used to determine the distribution and content of gas perpendicular to the Galactic plane. Studies of this type have always been resolution-limited, and the proposed CAMROC antenna will contribute directly to more refined observations. An investigation of the geometrical "surface" defined by hydrogen throughout the Galactic disk is an objective where contributions may be expected from the proposed CAMROC antenna. For nearby

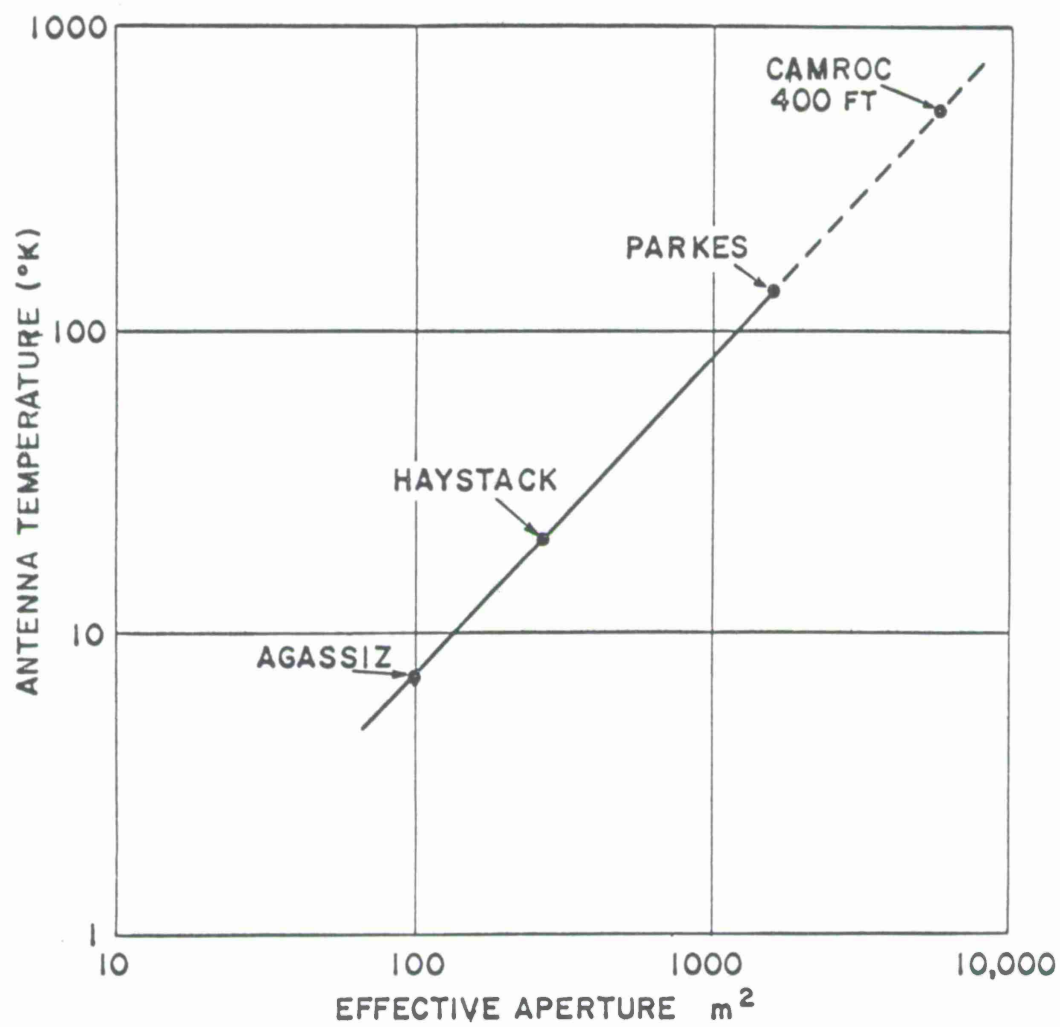


Figure 1. Peak intensity of +17 km/sec component in F(1 → 1) OH emission from W-49 linear polarization (10-kc bandwidth).

interstellar clouds, the resolution is sufficient to resolve and study the internal velocity characteristics within the clouds. With the high resolution afforded by the CAMROC antenna, we may also undertake investigations of the dependence of the state temperature of the hydrogen gas and its velocity characteristics within interstellar dust clouds.

One of the major capabilities of the CAMROC antenna will be to elevate the apparent antenna temperature of hundreds of discrete sources to amplitudes large enough to exhibit the absorption effects of microwave constituents in the interstellar medium. Absorption lines of this type not only provide information about the composition and physical conditions within the medium but also permit the assignment of minimum distances to the discrete sources. When these sources are Galactic, the minimum distances enable quantitative analysis of the total energy radiated by the source. Also, the absorption-line spectra are so steep that they are ideally suited for studies of the Zeeman effect. While studies thus far have necessarily concentrated upon the stronger discrete sources, the possibility of extending the absorption technique to arbitrary directions within the Galactic plane (because of the great number of sources available for such studies with the CAMROC antenna) will undoubtedly contribute to our knowledge of the interstellar medium.

The very large aperture of the proposed CAMROC antenna will bring the hydrogen-content signal strengths of several thousand extragalactic nebulae up to levels useful for study. In a recent investigation of atomic hydrogen in extragalactic nebulae, the maser-equipped Harvard 60-ft radio telescope positively detected 30 galaxies (Epstein, 1964). With the assumptions of a valid sample and a homogeneous distribution, approximately 10^4 galaxies are within the detectable range of the CAMROC radio telescope. The numbers are so large that the investigations may be carried out selectively. Hydrogen masses and internal-motion characteristics defined by neutral hydrogen can be studied as functions of the morphological type of extragalactic nebulae. This means that the 21-cm radio spectral-line studies can become a major part of extragalactic nebulae research.

2.4 Recombination Lines

In 1964, a new type of radio line was detected in the radio spectrum of H II regions. The lines originate as transitions between the principal levels of highly excited hydrogen. Typical values of the principal quantum number n are in the range ~ 100 to ~ 280 , corresponding to the CAMROC frequency range of interest, 6000 to 300 Mc. Since the existence of the lines requires a high degree of excitation of atomic hydrogen, the lines provide a valuable observational method for the study of the physical conditions of H II regions, and the lines may be detected in other regions of high excitation, for example, in planetary nebulae.

The recombination lines are numerous, occurring almost every 60 Mc/sec at decimeter wavelengths for those lines arising from changes of the principal quantum number of unity $\Delta n = 1$ (called α lines). Lines are also possible for which $\Delta n = 2, 3, 4, \dots$ (called β, γ, δ , etc.), but they are progressively less intense. The recombination lines are not restricted to atomic hydrogen. Similar lines occur for ionized and neutral helium. The CAMROC radio telescope, operating at 5-cm wavelength, will have a beamwidth of approximately 1.5 arcmin. This can be compared with the angular sizes of H II regions, many of which are substantially larger.

Similarly to the situation in OH, the study of recombination lines of hydrogen and helium is in its infancy, with groups in the USSR, NRAO, CSIRO, and Harvard contributing the first flow of results. Yet, from these early results, we know that we may determine electron temperature, state of turbulence, hydrogen-to-helium ratios, and Galactic distribution of H II regions. Most of these regions are hidden to optical measurements. Recent investigations at Harvard (Lilley, Menzel, Penfield, and Zuckerman, 1966) have revealed fundamental problems with the expected Stark broadening theory of such lines. Observations must be extended to very large principal quantum numbers with progressively weaker signals to evaluate the true broadening effects. In addition, important effects due to stimulated emission pose a significant observational challenge (Goldberg, 1966). The very large aperture and broad spectral capability of the CAMROC antenna are fundamental to future investigations of recombination lines.

2.5 Detection of Other Radio Lines

It seems likely that other resonance lines of interstellar molecules will have been discovered by the time the CAMROC radio telescope or other similar facility is operational. The search for new lines will always continue, and the CAMROC antenna will be a major instrument for this purpose. If other molecules are detected in absorption or emission from angularly small regions, as the OH observations seem to suggest, then the possibility of detecting such molecules is directly proportional to the collecting area of the antenna. This implies that the CAMROC radio telescope will have an advantage of at least a factor of 9 over any antenna in the Northern Hemisphere now capable of operation at 10- to 20-cm wavelength, excluding antennas whose primary function is related to the space effort.

At the present time, there are two molecular resonance lines that seem to be prime candidates for detection. Perhaps both lines will be detected in the next few years. The lines are the Λ -doublet levels of CH at an approximate frequency of 3200 Mc/sec and the Λ -doublet levels of SiH at an approximate frequency of 2400 Mc/sec. These lines are within the operational objectives of the CAMROC antenna when maximum utilization of the capabilities of the antenna is possible. It can be expected that the detection of new spectral lines, whether these lines or others, will be part of the CAMROC research program.

The study of spectral lines has contributed spectacular results to radio astronomy; antennas of 4- to 300-ft diameter have provided the flow of discoveries. Before the CAMROC machine is a reality, spectral-line radio astronomy will make many still-unknown advances. But regardless of the intervening years before construction, we know that the CAMROC telescope will eventually have a powerful advantage over previous instruments — its enormous aperture. The cloudy structure of the interstellar medium, H II and OH regions of small angular size, absorption spectra of discrete sources, and distant extragalactic nebulae all present research problems in which the signal-to-noise ratio increases as the square of the antenna diameter. When directed toward small targets, the CAMROC radio telescope will have a powerful advantage over existing instruments. For a given signal-to-noise ratio the CAMROC instrument will be almost 100 times faster than any other telescope in the United States.

The above-mentioned topics are not intended to be exhaustive, but they are typical of the interest of CAMROC radio astronomers in spectral-line research.

2.6 Continuum Observations

Striking additions to our scientific knowledge have been made during the last two decades through radio observations of the celestial-continuum emission. Dramatic events are implied by objects such as Cygnus A, once thought to be a pair of galaxies in collision and now suspected to be the remnants of a galactic explosion, or by the quasi-stellar objects (the so-called quasars), whose nature is still a subject of debate. Perhaps they are the explosions that herald the birth of the Cygnus-A type of object, or perhaps they are an entirely new class of objects, not galaxies as we know them but objects of galactic mass, collapsing because of their own gravitational field and destined to pass through the Schwarzschild limit and thereafter to be isolated from the rest of the universe.

Within our Galaxy, there are also continuum emitters that are more modest in scale but nonetheless of striking violence, such as the supernova remnants that we know as the Crab Nebula, the Cygnus Loop, and Cassiopeia A. These objects of modest visual appearance exhibit internal motions varying from hundreds to thousands of kilometers per second. Perhaps these disturbed clouds hold the clue to the origin of cosmic rays, for much of the electromagnetic radiation we receive appears to be generated by highly relativistic electrons, with energies in the 10-to 100-Bev range, circulating in magnetic fields within the supernova remnants.

Our Galaxy also provides a puzzle, for the radio sky is many orders of magnitude brighter than it should be, especially along the Milky Way. Furthermore, at the very center of our Galaxy there are peculiar radio sources whose nature we do not understand. Perhaps these may provide clues to the origin of all the radio galaxies, for the difference in radio emission between our Galaxy and Cygnus A is only 6 orders of magnitude.

All these radio discoveries show a common feature: the emitted radio noise is greater, often by factors of 10^{20} to 10^{30} , than we would have expected on the basis of prior knowledge. This unexpected intensity has enabled the astronomer to push outward in his explorations to a significant fraction of the entire visible universe. As this report is written, there is evidence that the initial explosion of the cosmos is, in fact, detectable by radio means. The programs envisioned for the CAMROC telescope will contribute significantly to these problems of cosmic scope.

2.7 Extragalactic Sources

The extraordinary character of the intense extragalactic radio sources such as Cygnus A and the quasi-stellar objects will certainly demand a large amount of observing time. We have little or no understanding of the physical natures of such objects, whose radio-noise power output is often comparable to their light output. It is this property that has enabled the radio astronomer to single out, for the optical astronomer, the most distant objects among the millions of possible candidates that appear on his photographic plates. The quasi-stellar objects, in particular, have enlarged our visible horizons, but the more "normal" objects, the radio galaxies, have also aided in expanding our horizons, since they, too, can be studied by spectroscopy at much greater distances than can normal galaxies. Several quasi-stellar sources (3C9, 0106 + 01, 1116 + 12) have been detected whose spectroscopic velocities appear to be 80% of the velocity of light, while a radio galaxy (3C295) has been seen whose red shift is 0.46. In the following section, it will be seen that the new instrument we are proposing will make possible the study of Cygnus A-type objects at such a great distance that they should appear to be receding at nearly 98% of the velocity of light.

One of the most exciting consequences of being able to view such distant objects is that we can hope to make crucial tests of many of the cosmologies that have been proposed during the last 50 years. Some predict a universe that presents the same aspect at all times, and hence we should find a similar population of radio sources at all distances. The angular sizes of radio sources do not diminish indefinitely in most of the "classical" cosmologies of general relativity, but pass through a minimum; and hence, as one increases the distance, the angular sizes should increase. In an Einstein-de Sitter universe (curvature and cosmological constant both 0), for example, the minimum is reached at a red shift $\Delta\lambda/\lambda$ of 5/4, or, equivalently, at a recession velocity of 65% of the velocity of light. The red shift at which minimum angular size occurs is dependent on the cosmological model, but each model makes definite predictions, which can be tested by observations of weak radio galaxies. Such distant galaxies would appear as extended objects of low surface brightness, with no optical identification. As an example, a source like Cygnus A, with a red shift of 8 in an Einstein-de Sitter universe, would appear as a double source with a separation of 2 arcmin between

components, and a surface brightness of 2° K. Low surface brightness objects such as this are difficult to detect by aperture-synthesis techniques, but would be easily recognizable with a paraboloid.

The study of the statistics of radio sources is also a relevant test of cosmological theories, but it is not so sensitive to the model because of the great dispersion in luminosity of radio sources. Meaningful statistics can be made only when the sample is large, and when, either by spectral studies or by other means, we can more accurately classify radio sources. A large paraboloid, with its great frequency flexibility, would be a powerful tool in sorting out, by spectral type and polarization properties, the sources observed in surveys of the type described in the following section.

2.8 Surveys

The large paraboloid, with its filled aperture, is especially useful in survey work because of the unambiguous character of the results. Side-lobe levels are low, and the problem of spurious responses is under better control than it is in other radio-telescope systems. In fact, we may regard surveys with a large paraboloid as useful companions, rather than as competitors, to surveys made by aperture-synthesis techniques. While the ultimate in resolution can be achieved only by aperture synthesis, there is a large and important area of overlap where the large paraboloid can "keep them honest." A further advantage of the large paraboloid is its flexibility; surveys will usually be made at several frequencies simultaneously and will include polarization measurements as well. Hence, additional physical information will contribute to the sorting of sources into different classes. Such a sorting is essential, for there appears to be such a variety of radio sources, with luminosities varying by a factor of 10^6 , that meaningful statistical studies must include more than simple counts of number at a given flux level. A survey of the entire sky would probably not be feasible, but surveys of selected areas, of sufficient extent to give a meaningful sample, would be a part of our program.

The number of observable sources depends upon whether the telescope is limited by confusion or by sensitivity. The distinction depends upon extrapolation from existing catalogs, and for the present study we use the "Parkes Catalogue of Radio Sources Declination Zone -20° to -60° " (Bolton, Gardner, and Mackey, 1964). The density of sources having a flux greater than $3 \times 10^{-26} \text{ W m}^{-2} \text{ sec}$ at a wavelength of 11 cm is 10 sources/ster. If a 400-ft telescope (aperture efficiency 50%) is used with a receiver whose RMS noise level is 0.01° K (a sensitivity that can be achieved today), sources of flux $2.4 \times 10^{-28} \text{ W m}^{-2} \text{ sec}$ will yield a signal-to-noise ratio of 5.

If the number-versus-flux relation $N(S)$ is known, the number of sources at this flux level can be predicted. Bolton, Gardner, and Mackey derive a power-law relation

$$N(S) = (\text{constant}) S^{-1.8} ,$$

which is steeper than the normal $S^{-1.5}$ relation usually assumed. Two different extrapolations can be made, one with the empirical (-1.8) power law, which yields a source density, at 11 cm:

$$N(2.4 \times 10^{-28}) = 54,000 \text{ sources/ster} ;$$

and a "theoretical" source density, corresponding to a static, isotropic universe, following a (-1.5) power law:

$$N(2.4 \times 10^{-28}) = 12,800 \text{ sources/ster} .$$

If we adopt a confusion criterion of 100 beamwidths source, the number of sources that would be observed, if the (-1.5) power law is valid, is less than the confusion limit at 11 cm by a small margin, while the number given by the (-1.8) power law exceeds the confusion limit. It is reasonable to conclude, therefore, that the number of observable sources will be limited by confusion and not sensitivity at wavelengths greater than 11 cm. The number will probably be limited by receiver sensitivity at 6 cm, except when maser radiometers are used.

It is instructive to compute the distance at which various types of radio sources would be observable, given the confusion limitation in Table 1. For these purposes, we adopt the radio source Virgo A, a giant elliptical galaxy with a blue jet in the center, an example of a "moderate" radio galaxy; the source Perseus A (NGC 1275), a radio galaxy that is somewhat more powerful intrinsically; and the radio source Cygnus A as an example of a very powerful radio emitter. The detectability of these objects is indicated in Table 2, which gives the flux of these sources at 11 cm, the observed red shift $z = \Delta\lambda/\lambda$, and the red shift at which these objects would be observable and still have a flux of $3 \times 10^{-28} \text{ wm}^{-2} \text{ sec}$, assuming an Einstein-de Sitter universe. The last column gives the corresponding velocity as a fraction of the velocity of light. Note that z can be greater than unity.

Table 1. Number of sources at the confusion limit ($\epsilon = 0.01$)

Paraboloid diameter	$\lambda = 10 \text{ cm}$	20 cm	50 cm
300 ft	6.8×10^4	1.7×10^4	2.7×10^3
400 ft	1.2×10^5	3.0×10^4	4.8×10^3
500 ft	1.9×10^5	4.7×10^4	7.5×10^3

Table 2. Red shifts ($z = \Delta\lambda/\lambda$) at which various classes of radio sources would still be easily detected by a 400-ft paraboloid*

	$S_{11 \text{ cm}}$	z_0	$z (3 \times 10^{-28})$	v/c
Virgo A	9.4×10^{-25}	0.004	0.22	0.20
Perseus A	7.4×10^{-26}	0.018	0.28	0.24
Cygnus A	7.6×10^{-24}	0.056	8.5	0.978
* Assuming an Einstein-de Sitter universe, source spectra proportional to $S^{-0.7}$, and no evolution in time.				

Although Virgo A is a relatively weak radio source, it would be observable at a distance nearly four times greater than the present distance of Cygnus A. The observability of the strong radio source Cygnus A, however, is far more striking, since it should be observable at a distance so great that the specific cosmological model would be important. For an Einstein-de Sitter universe, its velocity would be nearly 98% of the velocity of light, and for most other models, similarly dramatic velocities would be observable. Effects of the metric, such as the apparent enlarging of the source size mentioned previously, would be easily observable at these large red shifts. Undoubtedly, evolutionary effects are also important, and at our present stage of knowledge, we can only speculate on what these effects might be. Certainly, the ability to study objects whose age is only 2 or 3% of the present "age of the universe" is an exciting prospect.

The study of quasi-stellar sources by a large paraboloid should make important contributions to our understanding of these remarkable objects. At the present time, their nature is not understood, and their distance is still a subject of debate (Terrell, 1966; Burbidge and Hoyle, 1966; Woltjer, 1966). If their red shift is of cosmological origin, the extension of measurements to flux levels of $3 \times 10^{-28} \text{ W m}^{-2} \text{ cps}^{-1}$ will include large numbers of quasi-stellar objects at red shifts in the range $z = 8$ to 10. Studies to even lower flux levels and greater red shifts than this should be possible by use of interferometric techniques, utilizing secondary antennas at remote locations. The fringe visibility of resolved radio sources would be reduced greatly, while the quasi-stellar objects would be fully visible, thus allowing us to study them at flux levels considerably below conventional confusion levels.

If the quasi-stellar sources are not at great distances, but are relatively close companions, shot out of our Galaxy, their intrinsic luminosity is of the order of 10^{-5} the luminosity assigned to them cosmologically. The study of such objects in the neighborhood of other galaxies, if they represent rare galactic events, would again necessitate observations at very low flux levels. A large paraboloid, such as that envisaged for CAMROC, would have sufficient angular resolution to study families of such quasi-stellar objects surrounding galaxies well beyond the Virgo cluster.

2.9 Source Structure

Auxiliary antennas, used interferometrically with a large paraboloid, are of use, not only in extending quasi-stellar observations beyond the normal confusion limit, but also to make observations bearing on source structure. Observations at sufficiently frequent intervals along an adjacent base line allow complete aperture-synthesis studies, while observations at selected intervals allow us to make more rapid studies of sources whose approximate structure is known.

The simplest addition, a second auxiliary antenna to form a two-element interferometer, allows us to study sources with 6-arcsec resolution at 11 cm if a 2-mile base line is available. The area sampled in the fourier transform plane is a function of source declination and base-line orientation; an East-West base line gives the most symmetrical coverage in the polar regions, while an azimuth of 45° off North-South gives, for New England, the greatest information coverage over the entire sky.

Interferometric studies will not be limited to antennas on the site, however, and we should expect to be able to perform interferometry over base lines of hundreds or thousands of miles, using radio links up to 100 miles, and independent recording at greater distances, using highly stable local oscillators to maintain phase coherence. Large antenna areas are essential in such studies, to ensure an adequate signal-to-noise ratio. A joint MIT-Harvard-Lincoln Laboratory interferometer is now in use over a 12-mile base line; at Jodrell Bank in England observations are being carried out over an 80-mile base line; and experiments are under way at several laboratories, including the NRAO, to perform interferometry over thousand-mile base lines, using masers as local oscillators. The direction of the future is clear, and it is also clear that large paraboloids are best suited for this class of studies.

It is important to point out that, while most detailed source structures will have to be determined interferometrically, the larger scale features, 1 arcmin in size or greater, are the most difficult to measure interferometrically. The single paraboloid excels at determining these, the low-frequency spatial components, and it is in this respect that a large paraboloid should be regarded as an essential companion instrument to interferometers and aperture-synthesis arrays.

2.10 Polarization

Since at the confusion limit for the large paraboloid the signal-to-noise ratio is high, observations of the Stokes parameters will allow a complete polarization description of several tens of thousands of unresolved sources (Table 2) in the decimeter-wavelength band. These observations will be important also in Galactic studies through the individual determinations of a large number of Faraday rotation measures. The problem of separating out the rotation effects due to the interstellar medium from the rotation in the source itself is best attacked by studying a large number of radio sources

at all galactic latitudes, including those radio sources that lie behind neighboring galaxies such as M31. The rotation measure cannot be studied adequately by 2-frequency methods, as observations of Cygnus A have shown, and for such complex objects the frequency flexibility of the large paraboloid will prove invaluable.

Interferometric capability, using auxiliary dishes, provides an additional class of polarization observations, since distributions of polarization measure and rotation measure across a radio source give us additional knowledge of the magnetic field configuration in the source. Few observations of this nature have been attempted as yet, although such variations have been detected in Cygnus A, the Crab Nebula, and Centaurus A. The large signal-to-noise ratio that would be obtained with a 400-ft paraboloid would allow this limited list to expand remarkably. Confusion limitations on polarization measurements are more severe than for flux measurements, and have not been carefully formulated as yet, but a conservative criterion, of 500 beamwidths per source, allows one to study 2×10^4 sources at 11-cm wavelength before confusion considerations become serious.

2.11 Lunar Occultations

The observation of lunar occultations will undoubtedly be the most powerful technique for the high-resolution study of certain extragalactic discrete sources during the coming decade. Observations of the lunar occultation of discrete sources have already been used by several observers to provide accurate source positions and high-resolution strip-brightness distributions. The positional accuracy and the resolution of the lunar-occultation technique exceed those obtainable with current interferometers. However, this technique is limited to those sources in the moon's path.

An analysis of the signal-to-noise ratio for optimum resolution with a 400-ft paraboloid is summarized in Table 3 (cf. von Hoerner, 1964).

Table 3. Optimum resolution (arcsec) of sources by lunar occultation
(flux at the 3C wavelength of 1.68 m, $\text{wm}^{-2} \text{cps}^{-1}$)

Wavelength	10^{-26}	10^{-25}	10^{-24}
50 cm	0.63 arcsec	0.14 arcsec	0.029 arcsec
1 m	0.67	0.15	0.030
2 m	1.20	0.26	0.056
3 m	1.20	0.26	0.056

The practical usefulness of the 400-ft antenna in lunar occultation depends on obtaining bandwidths in excess of 1% in the meter-wavelength range. Considering irregularities on the lunar surface of ~ 200 m, their angular size is ~ 0.2 arcsec, which will limit resolution when the first Fresnel zone is of this order. At the level of $S_{3C} = 1$ flux

unit, several hundred sources will be occulted by the moon per year, for which strip distribution with ~ 1 -arcsec resolution should be observable over a wide wavelength interval. Positional accuracies will be limited by lunar-surface irregularities at this level. Approximately 1000 sources/year could be observed with a resolution better than 5 arcsec and with positions better than 1 arcsec.

2.12 Normal Galaxies

Studies of the distribution of radio emission in normal galaxies will extend our knowledge of the degree of similarity or dissimilarity of galactic systems. Such studies have already been undertaken with the 300-ft transit telescope of the NRAO, and from these studies it is clear that increased angular resolution is desirable, both to distinguish structural details more clearly and to distinguish chance background objects. The increased angular resolution will be greater than the ratio of the diameter of a 400-ft dish to a 300-ft dish, because of the shorter wavelengths at which the CAMROC instrument could be used. For the closer systems, such as M31 and M33, it will be possible to distinguish individual supernova remnants, of the types represented by the Crab Nebula and Cassiopeia A, whose fluxes are sufficiently large to be detectable at the distance of M31.

2.13 Scintillation Studies

The recent discovery that the irregularities in the solar corona cause scintillations in radio sources of small angular size has two implications. First, the angular sizes of small-angular-diameter radio sources can be studied quickly, in a qualitative way; and second, the structure of the outer corona, as far as the earth's orbit and beyond, can be investigated in a new way. Large signal-to-noise ratios are needed in order to obtain accurate scintillation spectra, and since the characteristic fluctuation times are of the order of a second, the best way to obtain the necessary signal-to-noise ratio is with a large paraboloid. The scintillation can be detected from meter wavelengths to decimeter wavelengths, and the fullest information is obtained from multiple-frequency observations. The subject is in its earliest stages, but the scintillation technique promises to be a powerful astrophysical tool.

2.14 Galactic Sources and the Galactic Background

The usefulness of a paraboloidal antenna is particularly evident when the object under investigation is of low surface brightness and the angular extent is large compared to the size of the main lobe. Low surface brightness necessitates the use of a completely filled aperture, while the mapping of sources of large angular extent requires rigorous control of side-lobe levels, a control most easily realized when the aperture is completely filled.

In our Galaxy, there are numerous examples of such large, low-surface-brightness objects, including supernova remnants, H II regions, and, as a limiting case, the Galactic background itself.

2.14.1 Galactic background

The Galactic noise background is composed, in part, of the superposition of all discrete radio sources in the universe, but a large fraction of the noise appears to come from a source of radio emissivity more or less continuously distributed throughout our Galaxy. It is likely that the Galactic background is closely related to the distribution of cosmic radiation in our Galaxy, since the radio noise is probably generated by synchrotron radiation from electrons of cosmic-ray energy circulating in Galactic magnetic fields. The radiation is initially polarized with the E vector perpendicular to the magnetic field, but since the radiation must traverse the interstellar medium between its point of origin and the earth, the polarization orientation can be affected by Faraday rotation. We can, therefore, summarize the observed phenomenon as follows: The distribution of intensity of the background radiation indicates the cosmic-ray electron density; the direction of polarization (corrected for Faraday rotation) shows the transverse magnetic-field orientation; and the Faraday rotation measures the product of ion density and longitudinal magnetic field. All these quantities are, of course, averages along the line of sight.

2.14.2 Polarization

The polarization of the Galactic background has been studied by the Leiden group (Berkhuijsen and Brouw, 1963) with the Dwingeloo 25-m telescope, and great complexity is evident in their observations. In some parts of the sky, most notably along the North Polar Spur, the direction of polarization changes rapidly in position, and the observations are certainly limited by resolution. There are at least two regions in the sky where some order is observed over an appreciably solid angle, but in most cases it seems that angular-resolution limitations are severe. At the frequency used, 408 Mc/sec, their beamwidth was 2° , which corresponds to a spatial resolution of 40 parsecs at a distance of 1000 parsecs, which is probably the order of magnitude of the effective distance over which these low-frequency observations apply. Faraday rotation within the Galaxy probably "smears out" the polarization of radiation arriving from more distant parts of the Galaxy. As we observe at higher frequencies, where Faraday rotation becomes less severe, the measurements refer to averages over greater and greater distances, although the observations become progressively more difficult because of the low surface brightness of the Galactic background.

A telescope in the 400-ft range should, at the lower frequencies, improve markedly on the Leiden results, which are resolution limited in most cases. The degree of observed polarization should be higher in many parts of the sky, since with the large

telescope we would be averaging over a smaller solid angle. We might hope that for discrete structures such as the North Galactic Spur a mapping of the magnetic-field configuration might be possible. The possibility of mapping the Galactic field in more extensive parts of the Galaxy can be tested only by observations with such an instrument.

2.14.3 Galactic sources

In addition to making polarization measurements, a large paraboloid can make real contributions to the study of the brightness distribution of the Galactic background. Part of the background is composed of discrete sources along the Milky Way, many of which are of appreciable angular size. Some are undoubtedly supernova remnants, which should be recognizable by their characteristically steep spectra, while many are H II regions that can be identified by their flat spectra. The supernova remnants range in size from the Cygnus loop, which is several degrees in angular extent, through objects such as HB21 and IC443, which are 0.5° in size, to the Crab Nebula, which would be barely resolvable with a 400-ft telescope at 3000 Mc/sec.

The number of Galactic sources, both thermal and nonthermal, that one might hope to resolve with a 400-ft telescope is limited by confusion, but should be approximately 1000. Wilson's catalog (1963) lists 110 sources, most of which were resolved by one of the California Institute of Technology 90-ft dishes. The resolution of a 400-ft dish would enable us to study these in detail in order to gain a better understanding of the structure of H II regions and supernova shells.

Studies of the continuous spectra of the Galactic sources will enable us to distinguish the H II region from the nonthermal regions over a large part of the Galactic disk, and thus will make possible a statistical analysis of the occurrence of supernova and H II regions. The relative frequency of supernova explosions and their distribution in space throughout the Galaxy are not well understood, but their importance to theories of stellar evolution and cosmic-ray origin lends particular interest to their study. The statistics of H II-region occurrence should be related to the star-formation rate, which can only be measured optically within a relatively small fraction of our Galaxy. The larger the paraboloid, the more effectively can these observations be made, since we must have sufficient resolution to distinguish the thermal and nonthermal sources as distinct objects.

2.14.4 Galactic halo

There are further problems connected with the background radiation that may not be directly dependent on having the very largest paraboloid at our disposal, but nevertheless will be profitably studied if we have such an instrument. One unresolved problem at the moment is the relative contribution from the Galactic disk and the Galactic halo. In fact, the existence of a Galactic halo has been questioned recently, and observations with NRAO's 300-ft transit telescope have been useful in studying the

problem. A transit telescope does have limitations, however, since we cannot eliminate the uncertainties caused by ground radiation. A large steerable paraboloid gives us more confidence in the observations, since independent checks on the ground-radiation contribution are possible.

2.15 Lunar and Planetary Observations

Radio observations have been fundamental in providing new information about the nature of planets. Beginning with the discovery of strong, nonthermal, time-varying radio emission from Jupiter, in 1955, the observations have been extended to Mercury, Venus, Mars, Jupiter, Saturn, Uranus, and Neptune, and cover the frequency range 5 Mc/sec to 100 Gc/sec. The results of these measurements have drastically influenced the course of future research, including observations from planetary spacecraft, because radio observations provided totally unexpected results. To realize the scope and impact of (passive) radio observations on planetary research, we need cite as examples only the unexpected detection of temperatures of 600°K at centimeter wavelengths for Venus, the discovery of polarized, nonthermal emission at decimeter wavelengths and the radio bursts at decameter wavelengths from Jupiter, or the more recent observations of significant radio emission from Neptune, considerably in excess of the expected equilibrium temperature.

2.15.1 Lunar observations

Lunar radio observations have been conducted since 1946 and have now been extended to cover virtually the entire radio spectrum from 170 Mc/sec to higher frequencies. The observations have been used to define the electrical properties of the uppermost layers of the lunar-surface material and to reveal localized regions of anomalous radio emission, presumably related to different surface material from surrounding areas.

In view of the planned lunar exploration to be conducted from lunar-orbiting spacecraft and lunar-landing parties in the decade of 1970, it is not anticipated that the CAMROC radio telescope will be primarily concerned with observations of the moon, except perhaps for specialized experiments in support of radar observations and/or the space program. Therefore, no further consideration of lunar radio observations will be presented here.

2.15.2 Planetary observations

The proposed CAMROC facility will be an ideal instrument to pursue further the problems of planetary radio astronomy. Knowledge of planetary phenomena is gained through observations of the intensity, spectrum, polarization dependence, and time dependence of the radio emission, and the CAMROC radio telescope will be well suited to observations of this nature. This is due to the large size and the versatility

of the proposed radio telescope. The large size ensures an adequate signal-to-noise ratio, and the versatility of a parabola ensures the capability of polarization and intensity measurements at several frequencies.

Characteristically, planetary thermal emission is first detected and studied at wavelengths of 10 cm or less, because the emission is stronger for the short centimeter wavelengths. Because of this, planetary radio spectra are not well determined for wavelengths longer than 10 cm, with the exception of those of Jupiter. The CAMROC radio telescope will be able not only to determine the spectra of several planets in the 10- to 50-cm wavelength range but also to perform those observations that require signal-to-noise ratios appreciably greater than unity, for example, polarization measurements. This point is illustrated in Table 4, where the antenna temperatures are tabulated at 10-cm and 20-cm wavelengths for the planets at mean inferior conjunction or opposition. For the computations of Table 4, an antenna diameter of 400 ft and an operating efficiency of 50% were assumed. Also presented in the table are the expected signal-to-noise ratios, with an RMS temperature sensitivity of 0.05°K assumed — a value now obtainable at the wavelengths considered. Future technological improvements may reduce this temperature and lead to larger signal-to-noise ratios than those presented in Table 4.

The values in Table 4 show clearly the potential of the CAMROC facility for planetary studies. The large signal-to-noise ratios for Venus and Jupiter show that the CAMROC antenna is not necessary for routine studies of these planets. However, large signal-to-noise ratios are indispensable for more sophisticated observations such as (1) polarization measurements, (2) detection of short-term time variations, (3) detection of radio spectral lines originating in planetary atmospheres, and (4) high-accuracy measurements of planetary phase effects over entire orbits.

Table 4 also shows that Mercury, Mars, and Saturn can be easily observed with the CAMROC telescope. Uranus and Neptune will also be detectable but will require integration. Thus, only Pluto will be beyond the limit of detectability with the proposed antenna, and even these may prove to be detectable if their radio emission is non-thermal or, at least, appreciably greater than estimated here.

Unfortunately, thermal emission from planetary satellites is at least 10^{-3} smaller than from the parent planet; therefore, its detectability is not eminent. However, if the satellite influences the emission from the parent planet, as is known to occur in the case of Io and Jupiter, then the CAMROC facility will be very appropriate for the detection and study of such effects.

Table 4. Expected antenna temperatures and signal-to-noise ratios for the CAMROC radio telescope

Planet	Brightness temperature	Semidiameter	Antenna temperature		Signal-to-noise ratio	
			$\lambda = 10$ cm	$\lambda = 20$ cm	$\lambda = 10$ cm	$\lambda = 20$ cm
Mercury	300° K	5.45	0.38° K	0.096° K	7.6	1.9
Venus	600	30.7	24.1	6.04	480	120
Mars	200	8.94	0.69	0.17	14	3.4
Jupiter	600	23.4	14.0	--	280	--
	3000	--	--	17.5	--	350
Saturn	200	9.76	0.82	0.20	16	4
Uranus	300	1.81	0.042	0.011	0.84	0.22
Neptune	150	1.06	7.5×10^{-3}	2×10^{-3}	0.15	0.04
Pluto	100	0.26	3×10^{-4}	7×10^{-5}	0.006	0.0015

3. APPLICATIONS TO RADAR ASTRONOMY

In order to maximize its great potential in radar astronomy, the CAMROC facility must be equipped with high-power radar transmitters, low-noise receivers, and data-processing computers. Naturally, the design of such an instrument will reflect the needs of users in many disciplines. We shall treat here those factors that are of direct concern to radar astronomy.

The discussion is in three sections. First, the radar planetary-detection problem is described and numerical values are presented for the various targets in the solar system. Second, the present capabilities of systems in use in radar astronomy are described, and several possible realizations for the CAMROC facility are set forth. Third, the various experimental possibilities opened by such radar systems are described.

3.1 Target Detectability

Basic to any experiment involving radar is the equation that relates the strength of the echo received to the properties of the target, its distance, and the observing equipment used. The radar equation can be written simply as the product of a "path-loss" term containing astronomical parameters beyond the experimenter's control and a second term containing the equipment characteristics. The path loss is given by

$$\frac{\sigma}{(4\pi r^2)^2} \quad , \quad (1)$$

where σ is the radar scattering cross section of the target, and r the distance between it and the observer. Expression (1) is the ratio of the reflected energy received in an antenna of unit capture area to the radio energy transmitted from an isotropic antenna (gain equal to unity). Supplying the other parameters then yields the radar equation for the actual received power:

$$\frac{P_t G_t A_r \sigma}{(4\pi r^2)^2} \quad , \quad (2)$$

where P_t is the transmitted power, G_t the gain of the transmitting antenna, and A_r the effective aperture of the receiving antenna. (The angular extent of the target is assumed small compared with the beamwidth of the antenna.) The quantity A_r is related to G_r , the gain of the receiving antenna, by

$$A_r = \frac{\lambda^2}{4\pi} G_r \quad , \quad (3)$$

where λ is the operating wavelength.

The cross section σ may depend importantly on the orientation of the target, on λ , and on other radar parameters. For example, since planetary targets are large, even relatively long radar pulses may not encompass simultaneously the entire range of delays presented by the visible surface. Similarly, rotation of the target causes an apparent relative radial motion of various portions of the surface that leads to a dispersion in the frequency spectrum of the reflected signal. If the receiving filter does not accommodate the full dispersion, signal energy will be lost. In both cases, the effective cross section is decreased.

The level of received power that is necessary to permit a reliable measurement depends, of course, on the competing noise. The noise, in turn, depends both on the equivalent temperature of the receiving system and on the time-bandwidth characteristics of the analyzing channel. Since these parameters vary widely between different systems and experiments, no single meaningful level can be quoted. To establish the order of magnitude, however, we may note that for a system temperature of 100°K , an analyzing bandwidth of 1 cps, and an integration time of 5 hours (realistic numbers for a current system observing Venus), the fluctuation in the determinations of the mean noise, referred back to the receiver input, is 10^{-23} w. To ensure reliable detection, the signal plus mean noise power should exceed the mean power of noise alone by approximately 10 standard deviations of the fluctuations in the noise level. Thus, for this case, the received power should be at least 10^{-22} w (or -190 dbm). When it is necessary to resolve individual regions on the surface of the target, as for precise measurements of delay to the nearest portion of the surface or for mapping (i. e., for determining the backscattered power from small regions on the surface), a very much stronger received power level may be required.

Figure 2 shows the path loss associated with various possible radar targets in the solar system and should be valid over a frequency range extending from at most 100 Mc/sec to at least 4000 Mc/sec, except for the targets shown in brackets with dotted lines. These "soft" targets, which include the sun and the planets Jupiter, Saturn, Uranus, and Neptune, have been shown under the assumption that their radar albedo is 0.10. Since their actual reflectivity is known (or suspected) to be a strong function of the frequency of the incident radiation or of the state of weather in the upper atmosphere of the target, the indicated path loss for these objects should be taken only as a starting reference for further estimation. Representative path losses for several minor planets during their close approaches to earth in the period 1966-1970 are also shown. (A similar set of calculations is being carried out for the period 1970-1980.) An albedo of 0.07 was assumed for all other bodies except Venus, for which the measured value of 0.14 was used, and earth, for which a value of unity (corresponding to the oceans) was assumed. As discussed more fully in a later section, the best current radar system (Haystack) can see down to about 364 db/m^2 . It is likely that the proposed CAMROC facility will exceed 390 db/m^2 .

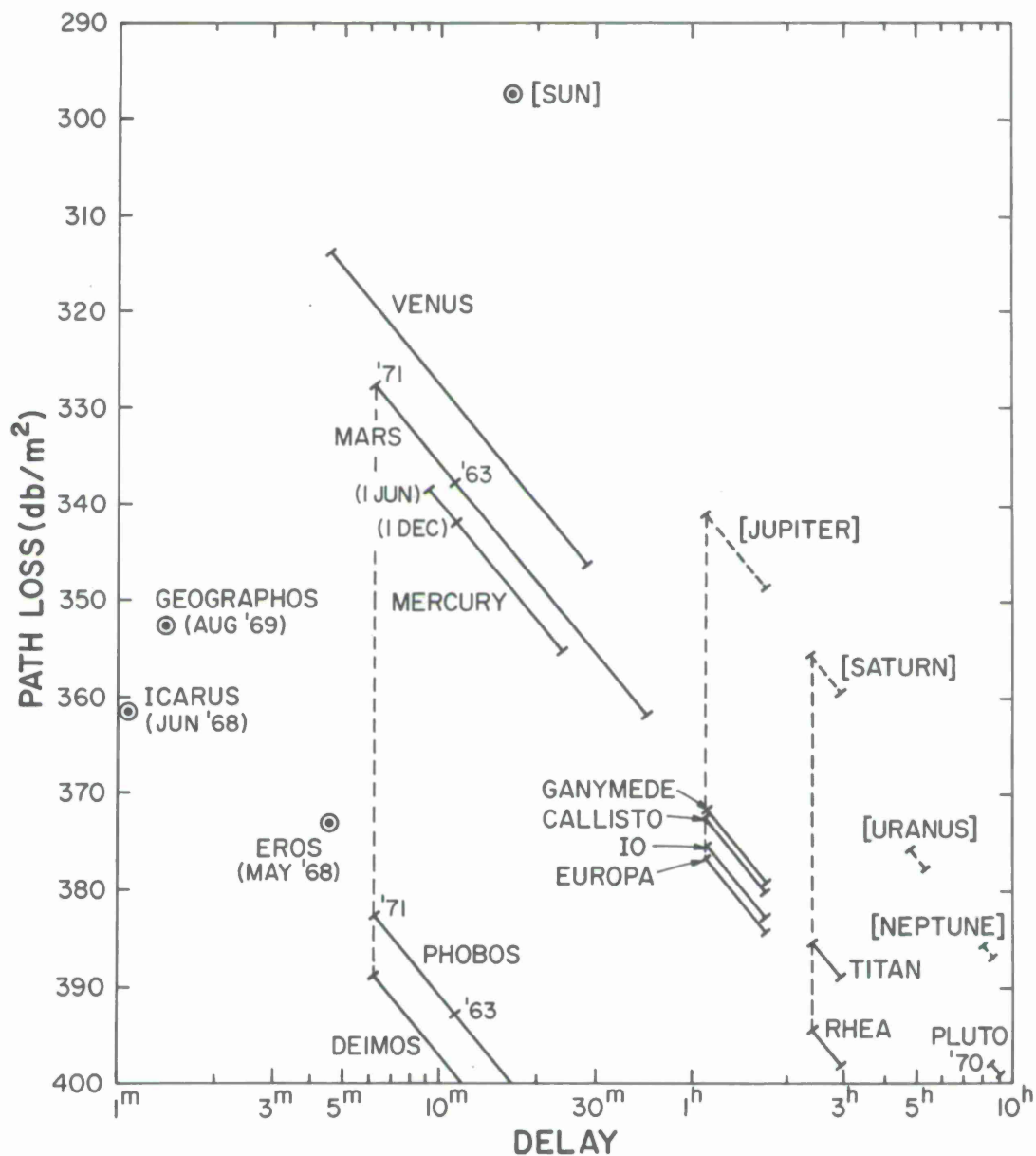


Figure 2. Radar path losses for solar-system targets as a function of echo delay. Minimum values associated with most and least favorable dates are shown for Mars and Mercury. Dotted bars and brackets indicate targets whose radar cross sections are unknown or highly variable; the values plotted were obtained under the assumption of 10% reflectivity and are given for reference only. The points for the minor planets refer to the close approaches to earth on the dates shown. For comparison, note that the path loss for the moon is 247 db/m².

A large radar may also be used to study the earth's ionosphere through the incoherent backscatter at short wavelengths. The experimental potential in this field is described below; here an approximate estimate of path loss is obtained. Since the ionosphere completely fills the radar beam, the transmitting gain does not enter, and the received power depends primarily on the receiving antenna aperture. Thus,

$$P_r \approx P_t A_r \left(\frac{\epsilon c \tau N \sigma_e}{16 \pi r^2} \right) , \quad (4)$$

where P_t , A_r , and r are as in Equation (2), ϵ is the beam efficiency of the transmitting antenna (typically between 0.7 and 0.8), c is the velocity of light, τ is the transmitted pulse width, N is the electron density, and σ_e is the scattering cross section per electron. The scattering cross section, in turn, may be expressed as

$$\sigma_e \cong \frac{\sigma_c}{1 + T_e/T_i} , \quad \frac{T_e}{T_i} \leq 3 , \quad (5)$$

where σ_c is the classical Thomson cross section ($\approx 10^{-28} \text{ m}^2$), and T_e and T_i are the temperatures of the electronic and ionic components, respectively, of the plasma. Relationship (5) is valid only when the wavelength of the incident radiation exceeds $4\pi \lambda_D$ (λ_D is the Debye length, approximately 2 mm in the F region).

The quantity in parentheses in Equation (4) may be viewed as a path loss; taking $\tau = 0.1 \text{ msec}$, $N = 10^5 \text{ electrons/cm}^3$, $T_e/T_i = 2$, and $r = 250 \text{ km}$ (typical F-region conditions) leads to 255 db/m^2 . The most sensitive current systems (in Puerto Rico and Peru) can overcome a path loss of about 275 db/m^2 for these assumptions in about 10 min of operation. The CAMROC facility should be at least 10 db better.

3.2 Radar Systems

Equations (2) and (3) show the received echo power for a target not resolved in angle to vary as

$$P_r \sim P_t \left(\frac{A}{\lambda} \right)^2 . \quad (6)$$

For planetary targets, therefore, a greater premium is placed on building a large aperture at the shortest reasonable wavelength than on having high transmitted power. Also, high angular resolution is rarely as important in radar astronomy as obtaining adequate signal strength, implying no strong requirement for distributed antennas, such as the Mills Cross.

Another important consideration in radar astronomy is the need for continuous tracking. The travel time for radio energy to a planet and back is usually so long that the target will have completely traversed a fixed antenna beam in the interval. In addition, with tracking, signal integration may be extended over many hours by use of digital techniques, with an associated improvement in signal-detection sensitivity that may be crucial. Finally, since radar astronomy is implicitly a study of time-variant phenomena, the antenna should have access to the major targets of interest at frequent intervals; the pursuit of radar astronomy may be severely prejudiced unless all portions of the ecliptic are available for many hours of observation each day. A large, fully steerable reflector admirably satisfies this requirement.

Equation (6) demonstrates that, provided other factors remain constant, the best performance will be obtained at the shortest wavelength for which the antenna maintains its efficiency. With recent improvements in technology it now appears that transmitter power and receiver performance are not likely to be affected significantly by the choice of operating frequency; thus, antenna performance and target characteristics will largely determine this parameter. In fact, the experimental objectives will require equipment at several frequencies, one of which is near the upper useful limit of the antenna.

Table 5 has been prepared to provide a comparison among systems that have been or soon will be used in radar astronomy. The target properties of reflectivity and dispersion in delay were assumed to be frequency independent. Although variation is observed for some planetary targets, this assumption enables a quick comparison that would be difficult to make otherwise. Taking into account the proportional change in Doppler spread that accompanies change in frequency, the signal-to-noise ratio for planetary targets varies as

$$(\text{SNR})_p \sim A^2 f^{3/2} N_0^{-1} P_{AV} L^{-1} T^{1/2} , \quad (7)$$

where A is the effective antenna aperture, f the operating frequency, N_0 the system noise temperature, P_{AV} the average transmitted power, L the two-way system losses, and T the total span of receiving time.

The detection sensitivities of most of the entries in Table 5 have been plotted against data in Figure 3 (which has been carried back to the first lunar-echo detection). Several measurement landmarks have been included. Note that the growth rate has been fairly steady at 5.5 db/year. What can be expected of the CAMROC radar? Table 6 has been prepared to explore several possibilities.

Table 5. Comparative sensitivities of various radar systems used in planetary research.

Facility	Year (as of Jan. 1)	Antenna diameter (ft)	Operating frequency (Mc/sec)	Effective gain (db)	A_{eff} (db/m ²)	2-way losses (db)	System noise (°K)	Average power (KW)	Peak power (MW)	Maximum observing time (hours)	Path loss threshold for 5σ detection† (Mercury/Venus) (db/m ²)
MIT*	1964	1800 × 220	38.26	34.5†	41.2	2.0	12,000	500	0.5	0.5	327
AIO 3**	1966	1000	40.12	37.0†	43.7	1.0	10,000	100	2.5	2.5	331
NBS ^x	1962	1000 × 500	49.92	40.0†	44.7	2.0	6,000	400	4.0	0.1	335
JB ^{xx}	1961	250	408	47.3	33.6	2.0	1,000	3	0.1	10	322
AIO 1**	1965	1000	430	55.0†	40.7	1.5	200	120	2.0	2.5	358
AIO 2**	1967	1000	430	58.0†	43.7	1.5	120	150	2.5	2.5	367
MH 1***	1961	84	440	37.5	23.2	2.0	240	150	2.5	10	325
USSR ^{xxx}	1963	8-50	~750	47.4	28.4	2.0	100	60	CW	10	338
MH 3***	1963	84	1295	47.3	23.6	1.2	70	150	5.0	10	339
JPL 1 [#]	1964	85	2388	54.2	25.4	0.5	30	100	CW	10	350
JPL 2 [#]	1967	210	2388	62.1	33.3	0.5	30	100	CW	10	366
HS 1***	1966	120	7750	66.1	26.9	0.5	100	100	CW	10	355
HS 2***	1967	120	7750	66.1	26.9	0.5	70	500	CW	10	364

* Phased dipole array; El Campo, Texas.

† Calculated as proportional to $A^2 f^{3/2} N_0^{-1} P_{AV} L^{-1} T^{1/2}$ (see text).

** Cornell University's fixed 1000-ft-diameter spherical reflector; feed movable $\pm 20^\circ$ from zenith; Arecibo, Puerto Rico.

† Average value, since actual instantaneous gain varies with zenith angle.

*** MIT Lincoln Laboratory's steerable paraboloid; Westford/Tyngsboro, Massachusetts.

^x National Bureau of Standard's phased array; near Lima, Peru.

^{xx} University of Manchester's steerable paraboloid; Jodrell Bank, England.

^{xxx} Soviet Union's 8 mechanically coupled steerable paraboloids; Crimea, USSR.

[#] CIT - Jet Propulsion Laboratory's steerable paraboloid; Goldstone Lake, California.

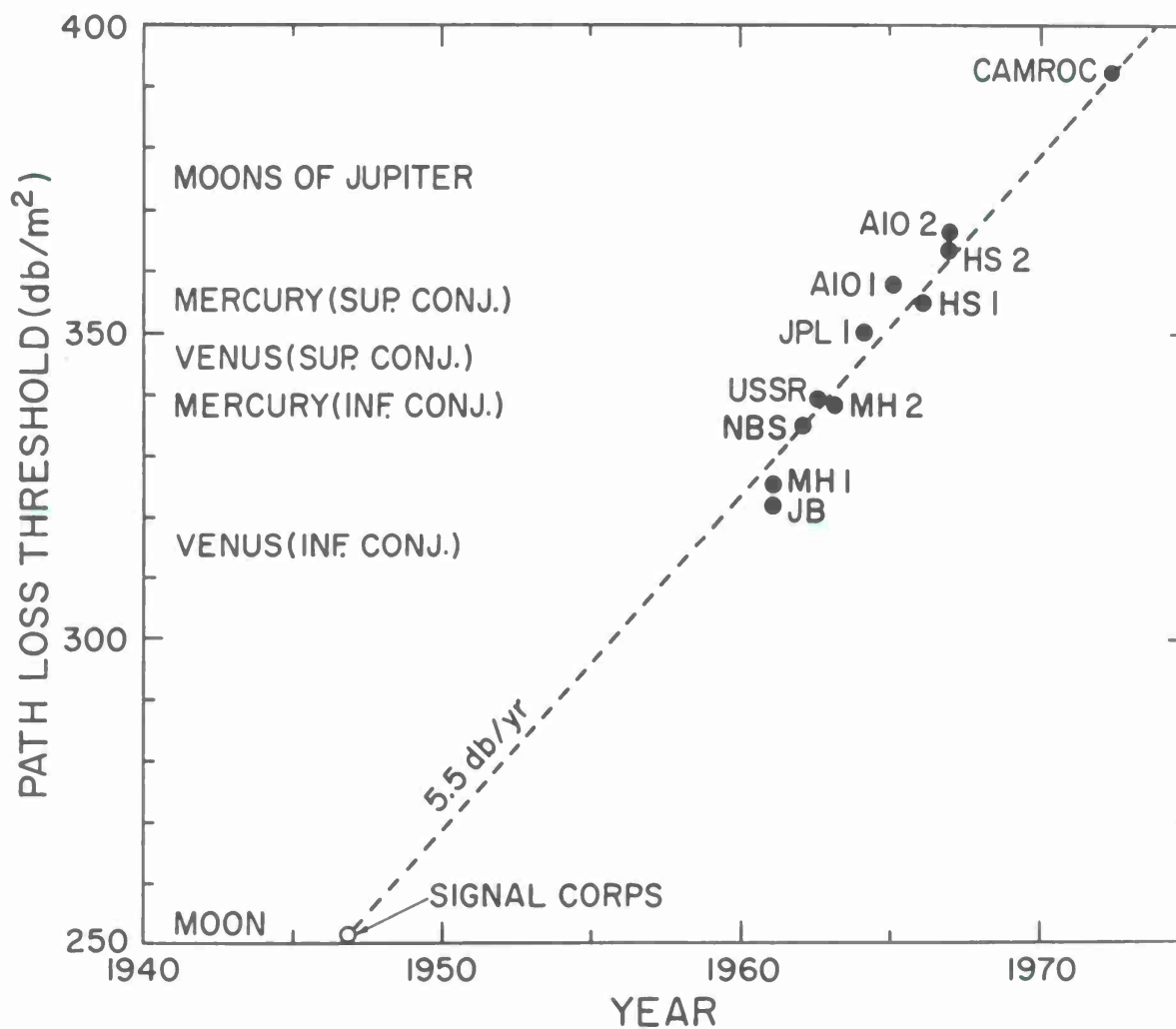


Figure 3. Growth in radar detection sensitivity over the last two decades. Abbreviations refer to entries in Table 5. Path losses for various major experimental landmarks are shown along the ordinate.

Table 6. Possible operating parameters and sensitivities of the CAMROC planetary radar system

Configuration	Antenna diameter (ft)	Operating frequency (Mc/sec)	Antenna beam-width	Effective gain (db)	A _{eff} (db over 1 m ²)	2-way losses (db)
CAMROC I	600	4000	1!7	75.1	41.6	0.5
CAMROC II	500	4000	2!0	73.5	40.0	0.5
CAMROC III	400	4000	2!5	71.6	38.1	0.5
CAMROC UHF	500	440	20'	54.4	40.0	1.0
CAMROC VHF	500	40	3°5	33.6	40.0	1.0

Configuration	System noise (°K)	Average power (MW)	Peak power (MW)	Maximum observing time (hours)	Path loss threshold for 5σ detection (db/m ²)
CAMROC I	40	1	30	10	395.4
CAMROC II	40	1	30	10	392.2
CAMROC III	40	1	30	10	388.4
CAMROC UHF	120	1	30	10	371.0
CAMROC VHF	10,000	1	30	10	336.0

The main operating frequency for the CAMROC configuration has been chosen at 4000 Mc/sec, where the loss contributed by surface inaccuracies is expected to be low. For an anticipated RMS surface error of 3 mm, there will be little radar improvement to be gained by operating at shorter wavelengths. A careful consideration of many factors, including the desirability of high peak powers, has led to the choice of 4000 Mc/sec as probably the most desirable single operating frequency. For radar astronomy, side-lobe level is of little consequence until the antenna noise temperature is affected. In fact, the optimum feed for radar astronomy would distribute the illumination uniformly across the reflector aperture (but would avoid spillover) and would lead to a principal side-lobe level only 17 db below the main beam.

In the study of the ionosphere, systems may be compared according to the following relationship, which holds for incoherent ionospheric backscatter when the operating wavelength is greater than $4\pi \lambda_D$:

$$(\text{SNR})_I \sim P_{pk} A_f^{-1/2} F^{1/2} N_0^{-1} L^{-1} \quad (8)$$

Here, P_{pk} is the peak transmitted power, F is the duty factor of the transmitter, and the other quantities are as defined in Equation (7). On this basis, for example, the AIO 2 and NBS facilities (Table 5) would have $(\text{SNR})_I$ values 8.6 and 16.5 db,

respectively, greater than the MIT Lincoln Laboratory 220-ft-diameter fixed paraboloid operated at 440 Mc/sec; the unique bistatic system (935 Mc/sec) operated by CNET at Nancy, France, has a corresponding value of -8.0 db. Relationship (8) contains several assumptions that are not fully satisfied in many experimental situations, but serves as an approximate guide in evaluating the relative experimental possibilities of various systems. Perhaps its greatest failure may be in comparing facilities operating at widely different frequencies. As in planetary radar, the new information gained on the nature of the target at a different frequency may greatly outweigh the penalty in sensitivity, so that frequency diversity should be sought in its own right.

3.3 Experimental Objectives

With the radar-detection capability that is implicit in a CAMROC system, an enormous range of experimental possibilities exists. These are treated only briefly in the following subsections, since a full discussion is not possible here. Detailed descriptions of current achievements in planetary radar astronomy have, however, been given by Thomson (1963), Goldstein (1964a), and Pettengill and Shapiro (1965). Solar observations have been described by James (1966), ionospheric work by, e.g., Evans and Loewenthal (1964), and radar meteor work by Evans (1965).

3.3.1 "Hard" targets

A CAMROC facility will permit substantial improvements to be made in the accuracy of echo delay and frequency-shift measurements. The corresponding refinements possible in the orbits and related parameters of the inner planets will permit more decisive tests to be made of gravitational theories, in particular the general theory of relativity (GTR). A stringent bound (about 1 part in 10^{11} per year) on any possible time variation of the gravitational constant will also be obtainable from several years of such data. The predicted general relativistic effects of gravitational fields on light rays (as discussed by Shapiro, 1964) can be tested with at least an order of magnitude improvement in accuracy over any experiment likely to have been made prior to CAMROC's becoming operational.

Dual-frequency experiments using the inner planets as targets will also enable the average properties of the interplanetary medium to be monitored. When a planet passes through superior conjunction, the path of the radar signal penetrates the solar corona; such occurrences, which are rather frequent for Mercury, will enable the properties of the coronal plasma to be studied. The sensitivity of a CAMROC-like facility is necessary for such work.

The technique of delay-Doppler radar mapping has been refined for the moon, to a point where it can yield information concerning the surface that is only slightly coarser in resolution than that afforded by the best earth-based optical telescopes. For Venus, where optical observation, even from orbiting planetary probes, is precluded

by the heavy cloud cover, such techniques could prove of immense value and might supply the only practicable method for mapping the surface. The fact that all portions of Venus, Mercury, and Mars are visible on occasion from the earth at varying aspects (in contrast to the moon, where only slightly more than half the surface may be studied with very limited variation in aspect) adds even further to the interest. To extend such techniques in a useful way to these planets, however, it will be necessary to have the extreme sensitivity of a CAMROC facility and to include an interferometer in the receiving-system configuration to remove the hemispheric ambiguity inherent in delay-Doppler maps. Only one direction of the base line (generally southerly) need be considered, since rotation of the earth will supply a sufficient variation in the angles of projection onto the visible disk. A base line of less than several kilometers should be adequate to supply the resolution needed at 4000 Mc/sec for the inner planets, and a diameter of about 100 feet should provide sufficient signal. Thus the interferometric requirements are similar to those for radio astronomy.

The increased accuracy offered by a CAMROC facility will also permit very precise determinations to be made of the sizes and shapes of the inner planets. Such information is of great interest for studies of the bulk geophysical properties of these targets and, in particular, will help in understanding the anomalous spin of Venus, which is apparently in resonance with the relative orbital motions of Venus and the earth (i. e., Venus' axial rotation is apparently controlled by the earth).

The CAMROC facility will permit a meaningful search to be made for relatively small objects that may be trapped, at least temporarily, in the vicinity of the L4, L5 libration points of the earth-moon system. Because of the rapid (f^4) decrease in radar cross section with decrease in frequency for small particles, the highest available frequency should be used for such explorations.

An important area of investigation that may be totally untouched before the completion of the CAMROC facility involves the detection of the satellites of Jupiter. These moons almost certainly should prove "hard" targets whose detection is predictable reliably. Figures 2 and 3 and Table 6 show that the proposed CAMROC facility is likely to have ample sensitivity to observe Ganymede and Callisto over all parts of the planet's orbit. Io and Europa should also be visible to radar during times of Jovian opposition. Although two reports have appeared claiming the radar detection of Jupiter itself (Goldstein, 1964b; Kotel'nikov, 1964), these have not been confirmed, and in any event, the uncertainties in the echoing mechanism and its actual location with respect to the planetary center of mass would render such detections useless for orbital work. Delay and frequency-shift measurements with respect to the larger Jovian satellites, on the other hand, will permit their orbits, as well as those of Jupiter, to be determined with sufficient accuracy to direct space probes to their immediate vicinity. At present, for

example, the satellites' orbits are not known to the required accuracy. Such improvements in the determination of the orbits will also provide useful information on the mass and details of the gravitational field of Jupiter.

Of even greater potential importance to astronomy is the use of Jupiter's satellites as tools to study the complex atmosphere of the giant planet. Occultation techniques have long been used for this purpose, but only recently (with Mariner 4 behind Mars) has the power of coherent measurement been brought to bear in this field. Echoes obtained from the major satellites during occultation could contribute substantially to our knowledge of the density distribution of both the atmosphere and the ionosphere of Jupiter. In addition to the obvious measurements of signal attenuation and phase-path distortion, a determination of the differential Faraday rotation should yield data on the distribution of magnetic fields in the Jovian ionosphere. The periods of the large satellites are short (approximately 1 week), and the orbits are not highly inclined to the ecliptic. Thus, opportunities for observation of an occultation are frequent. Because of the severe restriction on integration time, the most sensitive of the possible CAMROC configurations (see Table 6) will be necessary to exploit this technique effectively.

Other "hard" targets that may be visible to the CAMROC radar include Phobos (of Mars), Titan (of Saturn), and a number of minor planets when the geometries are favorable. For such observations to have sufficient signal-to-noise ratios to be useful, the most sensitive CAMROC configuration is probably necessary. Determining precise orbits for several of the minor planets should prove a useful task both for improving our understanding of the dynamics of the solar system (needed for the most precise tests of gravitational theories) and for the purpose of directing space probes to their vicinity.

Not to be overlooked also is the possibility of using "triple-bounce" lunar measurements to investigate the "far-field" scattering properties of the earth. As the earth rotates and the sublunar point migrates, it will be possible to study, through this technique, the scattering behavior of terrestrial oceans (in different sea states), jungles, and deserts. In this sense, the measurements may serve to help understand observations of the other planets. Finally, it seems likely that lunar probes and orbiters will be easily visible as radar targets to the CAMROC radar, i.e., lunar orbiters whose telemetry may have failed and readily be observed (without the need of extensive integration). Prolonged observation of these "dead" objects can lead to improved knowledge of the lunar gravitational potential even though men may have reached the lunar surface by that time.

The CAMROC radar could provide the first possibility of observing a comet nucleus — if one exists — directly from the earth. Of the 85 comet passages observed in the 10-year period 1951-1960, 2, at their minimum observed distances from the earth,

are calculated to give minimum path losses of 382 and 384; 4 less than 390; and 5 in the range 390 to 400 db/m². These calculations are based on Öpik's well-known formula for nuclear radii and on an assumed albedo of 0.07. Although the latter may well be higher because of ices remaining in the nucleus, the radii may well be lower. Nevertheless, within a 10-year period, there is a reasonable probability that the CAMROC radar could help to resolve the age-old problem of the nature of comets.

3.3.2 "Soft" targets

Chief among the soft targets is the sun. Current observations by radar have been entirely confined to the frequency range 25 to 40 Mc/sec, and it seems that only in the lower VHF range, where absorption in the corona before reflection is minimal, can echoes be expected from a homogeneous distribution of plasma. Because of the larger apertures already in use for observations in the frequency range 25 to 50 Mc/sec (see the first three entries in Table 5) than would be available from CAMROC (Table 6), CAMROC should probably not be instrumented with a transmitter at these long wavelengths. A further deterrent may be the severe constraints imposed on a radome design appropriate for decametric wavelengths. But substantial inhomogeneities in the solar corona exist, and with the great sensitivity offered by the proposed CAMROC configuration it is highly likely that reflections from these inhomogeneities may be found at 440 Mc/sec and even at 4000 Mc/sec.

Other soft targets that may be studied with the CAMROC facility are Jupiter, Saturn, Uranus, and possibly Neptune — at least for the most sensitive CAMROC configuration. The reflection properties of these planets are not known. However, taking into account the high relative sensitivity of the proposed facility at both the UHF and the S bands (see Table 6), it seems likely that echoes may be received at favorable times from most of these targets. If so, the signals should prove valuable in understanding phenomena taking place in the upper atmospheres of the major planets, and possibly may be correlated with the occultation measurements mentioned earlier for Jupiter.

Although no reliable predictions of radar cross section are available, it would be worthwhile also to search for echoes from the ionized material in the heads of comets.

3.3.3 Meteors

The CAMROC radar could be used to study meteors. Their echoes behave differently at UHF (see Evans, 1965) and at VHF, offering opportunities for learning about the interaction of small, high-speed particles with the upper atmosphere, as well as yielding information on meteor orbits and mass distributions. Evans has estimated that MH 1 (see Table 5) was able to detect a meteoric line density q as low as $10^{12.7}$ el/m, or through the relation

$$M_p = 39.40 - 2.5 \log q \quad , \quad (9)$$

a meteor of photographic magnitude 7.7.

Comparing the CAMROC UHF configuration of Table 6 with MH 1 shows an improvement in sensitivity (at the same frequency) for the former of about 46 db, thus implying observations of line densities possibly as low as $10^{8.1}$ el/m. This value is some 75 times lower than the minimum now observable by the best current VHF system (Eshleman and Gallagher, 1962) and corresponds to a photographic magnitude of about 19.2 if Equation (9) is extrapolated into this region. Thus, the CAMROC facility may permit studies of meteor trails substantially fainter than any now observable either by radio or by optical techniques.

At some point, as the mass of the impinging meteor is reduced, its ionizing efficiency will drop markedly, thereby leading to a slowing-down process by molecular impact with little or no accompanying ionization. Studies with the CAMROC facility of meteor number against echo intensity may well find a failure in the empirical law determined for larger meteors, which might be attributable to this phenomenon in the case of small meteors.

3.3.4 Ionosphere

The strength of incoherently scattered echo power as a function of altitude can be used to determine the electron-density distribution throughout the ionosphere, provided that the relative electron and ion temperatures T_e and T_i are known. Where the ratio T_e/T_i is a function of height, the effective cross section of the electrons will vary, as given in Equation (5), and will lead to a density profile that requires correction. By measuring the spectra of the signals reflected from a given height, it is possible to determine T_e/T_i , the ion temperature T_i , and, in some cases, the ionized molecular species as well. Thus, this technique can lead to measurements of electron density, ionic composition, and electron and ion temperatures as functions of altitude (Evans and Loewenthal, 1964).

To determine the shapes of the spectra, a long pulse (with narrow associated spectrum) is required, whereas for good height resolution, a short pulse is required. By use of a higher operating frequency, the width of the signal spectra will be increased, thereby allowing shorter pulses (with better height resolution) to be employed. Unfortunately, at 4000 Mc/sec the wavelength λ will approach the Debye length and will limit the vertical extent of the measurements. The height resolution can also be improved by tilting the antenna so that the ionosphere is explored obliquely. At an elevation of 30° , a 4000-Mc/sec CAMROC radar should be able to determine the temperature distribution in the lower ionosphere (below 300 km) with a height resolution of better than 5 km, and

a 440-Mc/sec radar, the temperature in the upper F region at 30-km intervals. Thus, although perhaps only slightly more sensitive than the Arecibo instrument, the CAMROC system could have a far superior height resolution.

Two further types of ionospheric measurements deserve mention. The first depends on the existence of a pair of peaks in the backscatter spectrum that are symmetrically displaced above and below the operating frequency by the plasma frequency corresponding to the height under observation. These peaks should be observable and would yield information both on the electron density (independently of the determination derived from the backscatter intensity) and on the electron scale height (Perkins, Salpeter, and Yngvesson, 1965). The second type involves a sufficiently strong interaction with the ionosphere to produce a measurable amount of heating (Farley, 1963). One of the difficulties in obtaining an observable effect with current systems lies in the extremely rapid, lateral conduction of heat out of the small illuminated region, by electron diffusion. This diffusion could be largely controlled by aligning the radar beam with the earth's magnetic field. The two existing sites (AIO and NBS) where sufficient antenna aperture and power are available to explore this effect, however, are located in the tropics and are restricted in their field of view, so this parallelism is not geometrically possible. The large steerable antenna and the northerly siting of the proposed CAMROC facility allow this condition to be met easily.

3.3.5 Aurora and field-aligned irregularities

The location of the proposed instrument is suitable for viewing auroral ionization and weak field-aligned ionization at E-region heights. Previous radar studies of the aurora at UHF (e.g., Leadabrand, Schlobohm, and Baron, 1965) have thus far failed to provide a conclusive theory of auroral scattering. Weak field-aligned ionization at E-region heights has been reported by a number of workers using UHF radar equipment. The large increase in sensitivity of a CAMROC UHF capability as compared to all existing facilities employed for this work may yield considerable clarification of existing observations, as well as uncover some new phenomena.

3.4 Conclusion

A large steerable antenna with an aperture diameter of 400 to 600 ft, suitable for operation at 4000 Mc/sec can be used for many useful experiments in radar astronomy that would otherwise not be possible. These experiments are summarized in Table 7. The system requirements for radar work appear to be quite compatible with the needs of radio astronomy, provided sufficient flexibility is provided at the focus to enable relatively rapid changing from radio- to radar-operating modes. Even with assumptions that appear to be very conservative for 5 years hence, the momentum of steady growth of 5.5 db/year, which has held over the past 20 years, can be maintained.

Table 7. Brief summary of proposed CAMROC radar experiments

Target	Objectives of study	Frequency (Mc/sec)	
		4000	400
A. Hard targets			
1) Inner planets (Mercury, Venus, earth, Mars)	a) gravitational theories b) orbits c) size, shape, rotation of target d) mapping of surfaces e) interplanetary plasma f) solar corona (by occultation) g) planetary atmospheres	X X X X X X X	X X X X X X
2) Jovian satellites (Ganymede, Callisto, Io, Europa)	a) orbits of satellites (and of Jupiter) b) size, shape, rotation c) surface properties d) Jovian atmosphere (by occultation) e) Jovian mass and gravitational field	X X X X X	
3) Moon-earth (triple-bounce)	a) earth's radio reflection properties	X	X
4) Minor planets	a) orbits b) size, shape, rotation c) surface properties	X X X	
5) Comets	a) nucleus	X	
6) Objects at earth-moon libration points	a) detection b) orbits	X X	
B. Soft targets			
1) Sun	a) outer regions	X*	X*
2) Outer planets (Jupiter, Saturn, Uranus, Neptune)	a) outer regions; perhaps surface	X	X*
3) Comets	a) outer regions	X*	
4) Meteors	a) atmospheric interaction b) occurrence/intensity distribution	X X	X X
C. Ionosphere	a) density b) temperature c) composition d) relaxation times	X X X X	X X X X
*Indicates attempts should be made, even though the likelihood of success may be small.			

To carry out the proposed experiments in the most efficient fashion, two transmitters will be required: (1) a high-priority system at approximately 4000 Mc/sec, to be installed first, and (2) a lower priority system at approximately 400 Mc/sec. These should achieve the highest average power that the technology of the period permits, we hope in excess of 1 Mw.

3.5 Related Uses: Space Experiment

3.5.1 Deep-space communication

There are several important experiments involving deep-space probes in which a large terrestrial receiving antenna has an important, if not crucial, role. Almost all of the probes launched thus far have been characterized by data rates of the order of 1 to 10 bits/sec at extreme ranges. Generally speaking, these are orders of magnitude too small to accommodate the information capable of being generated by the instruments on board the probe. One of the primary measurements proposed for reconnaissance missions to such planets as Mars involves the transmission of television pictures of the planet's surface. A marked reduction in both the proposed quality and rate of picture transmission is predictable because of the lack of gain in the transmission circuit. The power on board the vehicle is limited mostly by weight considerations to 10 to 100 w. The use of highly directive antennas aboard the vehicle makes the vehicle more complicated insofar as attitude control and stabilization are concerned, and raises questions about reliability and lifetime. Even with transmitter powers of ~ 50 w and vehicle antennas having gains of 15 or 20 db, the transmission rate is only some tens of bits per second at ranges of several astronomical units, with terrestrial receiving antennas with diameters in the 100- to 210-ft range. It is evident that greatly increased antenna apertures will be required if increased data rates to deep-space probes are to be obtained or, conversely, if the ranges are to be greatly increased.

To be more precise, for a noise temperature of 100° K at 2 Gc a 10-db gain antenna aboard the vehicle, a path length of ρ a. u., a spectral power density of 1 w/cps, the required dish diameter D to give a signal-to-noise ratio of 15 db is $D = 100 \rho$ ft. If the probe is not a simple fly-by type but is to be a planetary orbiter or launcher, then it is conceivable that communication with the probe would be required at the maximum range from the planet to earth. The required apertures for such missions to the three nearest planets are tabulated below.

Planet	Path at superior conjunction	Aperture required for $S/N = 15$ db, and $P_T/\Delta f = 1$ w/cps vehicle antenna gain	
		10 db	0 db
Venus	1.7 a. u.	170 ft	510 ft
Mars	2.7 a. u. *	270 ft	810 ft
Jupiter	6.2 a. u.	620 ft	1860 ft

* For 1971.

Some of the more probable or more attractive missions involving simple spacecraft at very great distances from the earth are discussed below.

3.5.1.1 Solar probes

There is serious study now being given to orbiting about the sun a very simple un-oriented spacecraft carrying only a power supply and a transmitter. The purpose is to measure the properties of interplanetary space by transmitting signals through the extended corona to a terrestrial receiver. The simplicity of the spacecraft and its low ERP require a large receiving antenna on earth to obtain the necessary transmission gain. The large aperture is required not only for high gain but also for high angular directivity to discriminate between the signals from the probe near conjunction and the very high noise contributions from the sun. Initial experiments are to be done at metric wavelengths, but eventually the shorter wavelengths will also be attractive for the transmission of reference signals for tracking and telecommunication purposes. A range of wavelengths is involved with the longer wavelengths being more important for measuring purposes, since they are nearer the plasma frequencies in the coronal regions of interest, and the shorter wavelengths being used for reference and communication purposes. A large-aperture paraboloid is about the only kind of antenna that will accommodate signals on such different wavelengths. One of the principal quantities to be measured is the relative delay between similar signals on each of two transmitted frequencies. The accuracy and the resolution with which such delays can be measured are directly a function of the gain of the receiving antenna. Similarly, the time over which the signals must be averaged is also a function of the aperture of the receiving antenna. In situations in which the medium is changing rapidly, as in the inner corona, it is desirable to use very large aperture antennas so that the averaging time will be short.

3.5.1.2 Planetary orbiters

At such time as spacecraft are made to orbit the near planets, a number of very simple transmission experiments to measure the properties of the planetary surface and possibly its atmosphere become possible. In the simplest situation, the vehicle is unoriented and transmits isotropically on several different frequencies. A very large antenna is then required on earth for reception. From the direct transmission, the period of the orbiter about the planet can be determined from the occultation of the signal by the planet, and some measure of the planet diameter, particularly of interest in the case of Venus, could also be obtained. With a range of transmitted wavelengths available, the properties of the planetary atmosphere may also be studied. It would be desirable to conduct such experiments over a long period of time, which implies a very simple spacecraft to obtain the required lifetime. Maximum earth-planet ranges would be involved and very large wide-band receiving apertures are indicated. A further variation of the experiment involves the observation of signals reflected from the planet,

as well as those directly transmitted. The intensity of the reflection from the planet would be expected to be 15 to 20 db below the direct-ray intensity and would require an even larger dish for its observation. If the reflected ray could be observed, some valuable data on the reflectivity and roughness of the planet's surface could be obtained.

4. BIBLIOGRAPHY

BENNETT, A. S.

1962. The revised 3C catalogue of radio sources. *Mem. Roy. Astron. Soc.*, vol. 68, pp. 163-172.

BERKHUIJSEN, E. M., AND BROUW, W. N.

1963. Measurements of the galactic polarized radiation at 75 cm. *BAN*, vol. 17, pp. 185-202.

BOLTON, J. G., GARDNER, F. F., AND MACKEY, M. B.

1964. The Parkes catalogue of radio sources declination zone -20° to -60° . *Australian Journ. Phys.*, vol. 17, pp. 340-372.

CUDABACK, D. D., READ, R. B., AND ROUGOOR, G. W.

1966. Diameters and positions of three sources of 18-cm OH emission. *Phys. Rev. Lett.*, vol. 17, pp. 452-455.

DRAVSKIKH, Z. V. D., AND DRAVSKIKH, A. F.

1964. An attempt of observation of an excited hydrogen radio line. *Astron. Zirk.*, vol. 282, pp. 2-4.

EPSTEIN, E. E.

1964. Atomic hydrogen in galaxies. *Astron. Journ.*, vol. 69, pp. 490-526.

ESHLEMAN, V. R., AND GALLAGHER, P. B.

1962. Radar studies of 15th-magnitude meteors. *Astron. Journ.*, vol. 67, pp. 245-248.

EVANS, J. V.

1965. Radio-echo studies of meteors of 68-centimeter wavelength. *Journ. Geophys. Res.*, vol. 70, pp. 5395-5416.

EVANS, J. V., AND LOEWENTHAL, M.

1964. Ionospheric backscatter observations. *Planet. Space Sci.*, vol. 12, pp. 915-944.

EWEN, H. I., AND PURCELL, E. M.

1951. Observation of a line in the galactic radio spectrum. *Nature*, vol. 168, p. 356.

FARLEY, D. T.

1963. Artificial heating of the electrons in the F region of the ionosphere. *Journ. Geophys. Res.*, vol. 68, pp. 401-413.

GOLDBERG, L.

1966. Stimulated emission of radio frequency lines of hydrogen. *Astrophys. Journ.*, in press.

GOLDSTEIN, R. M.

- 1964a. Radar studies of the planets. *Rev. Geophys.*, vol. 2, pp. 579-592.
1964b. Radar observations of Jupiter. *Science*, vol. 144, pp. 842-843.

HÖGLUND, B., AND MEZGER, P. G.

1965. Hydrogen emission line $n_{110} \rightarrow n_{109}$: Detection at 5009 megahertz in galactic H II regions. *Science*, vol. 150, pp. 339-348.

HOYLE, F., AND BURBIDGE, G. R.

1966. On the nature of the quasi-stellar objects. *Astrophys. Journ.*, vol. 144, p. 534.

JAMES, J. C.

1966. Radar studies of the sun at 38 Mcps. *Astrophys. Journ.*, vol. 146, pp. 356-366.

KELLERMAN, K. I.

1964. The spectra of non-thermal radio sources. *Astrophys. Journ.*, vol. 140, pp. 969-991.

KOTEL'NIKOV, V. A.

1964. Dokl. Akad. Nauk (SSSR), vol. 155, p. 1037.

LEADABRAND, R. L., SCHLOBOHM, J. C., AND BARON, M. J.

1965. Simultaneous very high frequency and ultra high frequency observations of the aurora at Fraserburgh, Scotland. *Journ. Geophys. Res.*, vol. 70, pp. 4235-4284.

LILLEY, A. E., MENZEL, D. H., PENFIELD, H., AND ZUCKERMAN, B.

1966. Detection of hydrogen emission lines $n_{159} \rightarrow n_{158}$ and $n_{157} \rightarrow n_{156}$ in galactic H II regions. *Nature*, vol. 209, pp. 468-470.

LILLEY, A. E., PALMER, P., PENFIELD, H., AND ZUCKERMAN, B.

1966. *Nature*, vol. 211, pp. 174-175.

MILLS, B. Y., SLEE, O. B., AND HILL, E. R.

1958. A catalogue of radio sources between declinations $+10^\circ$ and -20° . *Australian Journ. Phys.*, vol. 11, pp. 360-387.

PERKINS, F. W., SALPETER, E. E., AND YNGVESSON, K. O.

1965. Incoherent scatter from plasma oscillations in the ionosphere. *Phys. Rev. Lett.*, vol. 14, p. 579.

PETTENGILL, G. H., AND SHAPIRO, I. I.

1965. Radar astronomy. *Ann. Rev. Astron. Astrophys.*, vol. 3, pp. 377-410.

ROGERS, A. E. E., MORAN, J. M., CROWTHER, P. P., BURKE, B. F., MEEKS, M. L., BALL, J. A., AND HYDE, G. M.

1966. Interferometric study of cosmic line emission at OH frequencies. *Phys. Rev. Lett.*, vol. 17, pp. 450-452.

ROGERS, A. E. E., AND BARRETT, A. H.

1966. Radio detection of interstellar $O^{18}H^1$. *Astron. Journ.*, to be published in November issue.

SHAPIRO, I. I.

1964. Fourth test of general relativity. *Phys. Rev. Lett.*, vol. 13, pp. 789-791.

SHAPLEY, H., AND AMES, A.

1932. A survey of the external galaxies brighter than the thirteenth magnitude.
Harvard Ann., vol. 88, no. 2, pp. 41-75.

SOROCHENKO, R. L., AND BORODZICH, E. V.

1964. Paper presented at IAU General Assembly, Hamburg, Germany, August-September (in press).

TERRELL, J.

1966. Quasi-stellar objects: possible local origin. Science, vol. 154, p. 1281.

THOMSON, J. H.

1963. Planetary radar. Quart. Journ. Roy. Astron. Soc., vol. 4, pp. 347-375.

VON HOERNER, S.

1964. Lunar occultations of radio sources. Astrophys. Journ., vol. 140,
pp. 65-79.

WEINREB, S., BARRETT, A. H., MEEKS, M. L., AND HENRY, J. C.

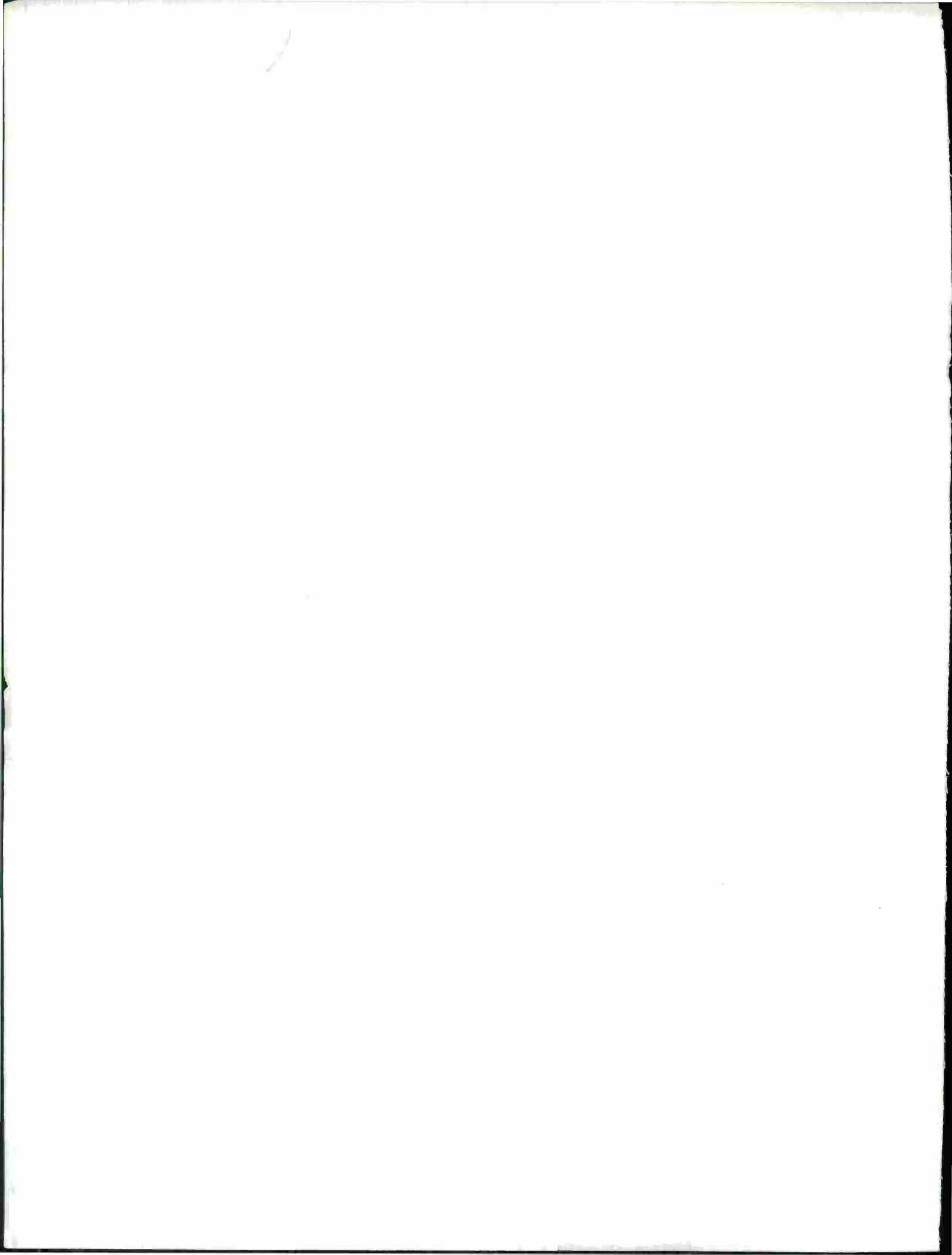
1963. Radio observations of OH in the interstellar medium. Nature, vol. 200,
pp. 829-831.

WILSON, R. W.

1963. Catalogue of radio sources in the galactic plane. Astron. Journ., vol. 68,
pp. 181-185.

WOLTJER, L.

1966. Inverse compton radiation in quasi-stellar objects. Astrophys. Journ.,
vol. 146, p. 597.



DOCUMENT CONTROL DATA - R&D

(Security classification of title, body of abstract and indexing annotation must be entered when the overall report is classified)

1. ORIGINATING ACTIVITY (Corporate author) Lincoln Laboratory, M.I.T., for the Cambridge Radio Observatory Committee, Cambridge, Massachusetts		2a. REPORT SECURITY CLASSIFICATION Unclassified	
		2b. GROUP None	
3. REPORT TITLE A Large Radio-Radar Telescope - CAMROC Design Concepts, Volume I*			
4. DESCRIPTIVE NOTES (Type of report and inclusive dates) Progress Report			
5. AUTHOR(S) (Last name, first name, initial) Committee Members of Harvard University, M.I.T., M.I.T. Lincoln Laboratory, and Smithsonian Astrophysical Observatory			
6. REPORT DATE 15 January 1967		7a. TOTAL NO. OF PAGES 472	7b. NO. OF REFS 55
8a. CONTRACT OR GRANT NO. NSF Grant No. 5832 and in part under AF 19(628)-5167		9a. ORIGINATOR'S REPORT NUMBER(S) CAMROC Report 1967-1, Vol. I	
b. PROJECT NO.		9b. OTHER REPORT NO(S) (Any other numbers that may be assigned this report)	
c.		ESD-TR-68-23	
d.			
10. AVAILABILITY/LIMITATION NOTICES This document has been approved for public release and sale; its distribution is unlimited.			
11. SUPPLEMENTARY NOTES * See ESD-TR-68-24 for Volume II.		12. SPONSORING MILITARY ACTIVITY National Science Foundation, Washington, D.C. with partial support from Air Force Systems Command, USAF	
13. ABSTRACT This document summarizes the engineering design studies relating to a large, fully steerable radio telescope. Engineering and economic considerations are detailed which led to the use of a radome to protect a 400-foot diameter, 5-cm, fully steerable parabolic antenna. The electromagnetic performance of the metal space-frame radome is discussed in detail, and the design of five different parabolic reflector configurations is described.			
14. KEY WORDS radio telescope radio astronomy instrumentation radio telescope sky noise considerations large steerable antenna radomes (metal space-frame) computer programmed structural analysis precision structures electromagnetic scattering rain effects on radomes deflection compensation			

